NAG 1-343

CCMS-90-06

VIRGINIA TECH
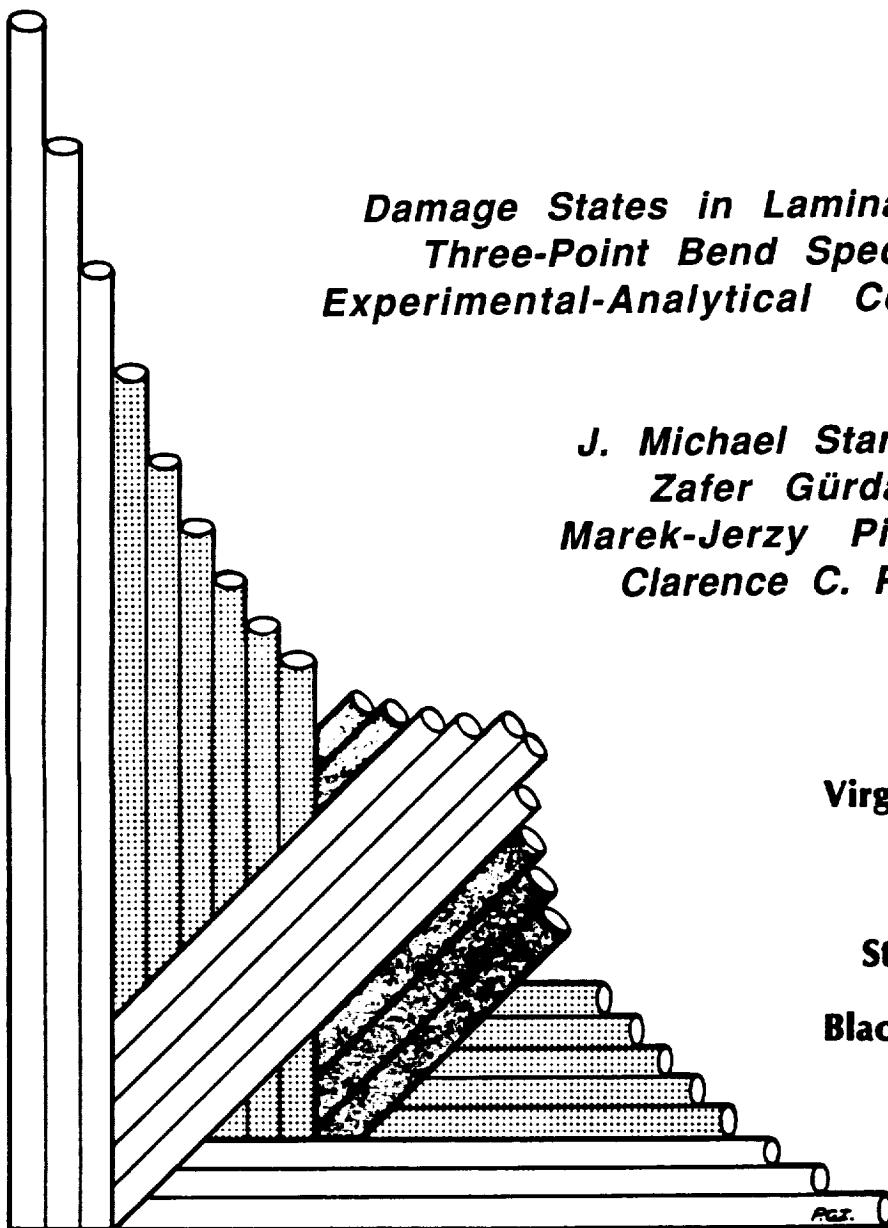
VPI-E-90-11

CENTER FOR COMPOSITE MATERIALS AND STRUCTURES

Damage States in Laminated Composite Three-Point Bend Specimens - An Experimental-Analytical Correlation Study

J. Michael Starbuck
Zafer Gürdal
Marek-Jerzy Pindera
Clarence C. Poe

Virginia Polytechnic Institute and State University

Blacksburg, Virginia 24061

July 1990

College of Engineering
Virginia Polytechnic Institute and State University
Blacksburg, Virginia 24061

July 1990

CCMS-90-06
VPI-E-90-11

Damage States in Laminated Composite Three-Point Bend Specimens - An Experimental-Analytical Correlation Study

J. Michael Starbuck[1]
Zafer Gürdal[2]
Marek-Jerzy Pindera[3]
Clarence C. Poe[4]

Department of Engineering Science and Mechanics

Prepared for: Mechanics of Materials Branch
                  National Aeronautics and Space Administration
                  Langley Research Center
                  Hampton, Virginia 23665-5225

[1] Graduate Student, Department of Engineering Science and Mechanics,
Virginia Polytechnic Institute and State University. Blacksburg
VA 24061-0219

[2] Associate Professor, Department of Engineering Science and Mechanics.
Virginia Polytechnic Institute and State University, Blacksburg.
VA 24061-0219

[3] Assistant Professor, Department of Civil Engineering. University
of Virginia, Charlottesville, VA 22901

[4] Senior Researcher, Mechanics of Materials Branch, NASA Langley
Research Center, Hampton, VA 23665-5225
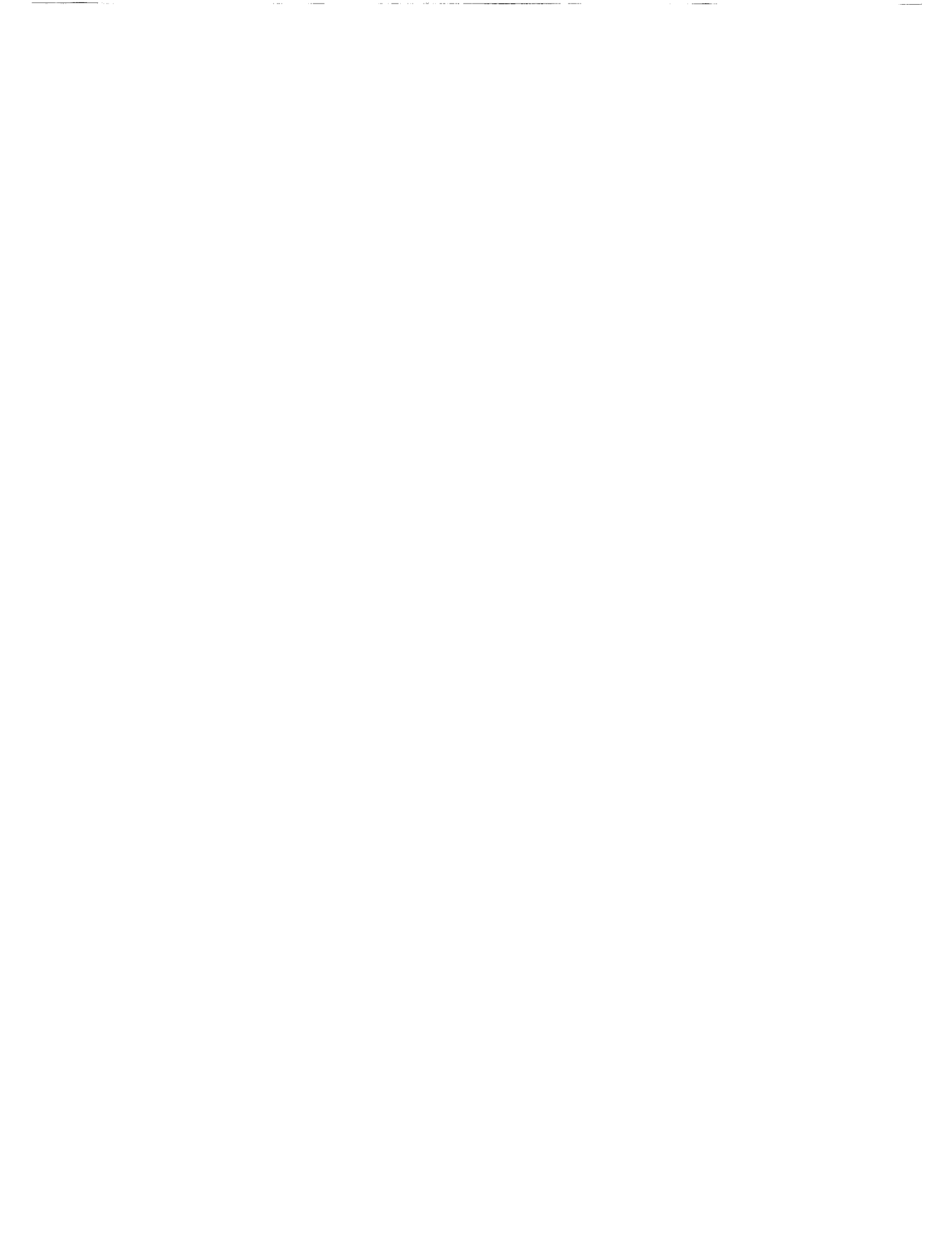
Abstract

Damage states in laminated composites were studied by considering the model problem of a laminated beam subjected to three-point bending. A combination of experimental and theoretical research techniques was used to correlate the experimental results with the analytical stress distributions. The analytical solution procedure was based on the stress formulation approach of the mathematical theory of elasticity. The solution procedure is capable of calculating the ply-level stresses and beam displacements for any laminated beam of finite length using the generalized plane deformation or plane stress state assumption. The beam lamination can be any arbitrary combination of monoclinic, orthotropic, transversely-isotropic, and isotropic layers. Prior to conducting the experimental phase of the study the results from preliminary analyses were examined. Significant effects in the ply-level stress distributions were seen depending on the fiber orientation, aspect ratio, and whether or not a grouped or interspersed stacking sequence was used.

The experimental investigation was conducted to determine the different damage modes in laminated three-point bend specimens. The test matrix consisted of three-point bend specimens of 0° unidirectional, cross-ply, and quasi-isotropic stacking sequences. The dependence of the damage initiation loads and ultimate failure loads were studied, and their relation to damage susceptibility and damage tolerance of the beam configuration was discussed. Damage modes were identified by visual inspection of the damaged specimens using an optical microscope. The four fundamental damage mechanisms identified were delaminations, matrix cracking, fiber

breakage, and crushing. The correlation study between the experimental results and the analytical results were performed for the midspan deflection, indentation, damage modes, and damage susceptibility. The correlation was primarily based on the distribution of the in-plane component of shear stress, τ_{xz}. The exceptions were for the case of a very small aspect ratio (less than 1.0) where the crushing model of damage was predicted based on the maximum contact pressure, and for very large aspect ratios (greater than 12.0) where a maximum tensile bending stress criterion was used for predicting the damage initiation loads.

Acknowledgements

Table of Contents

List of Illustrations

List of Tables

Chapter I

Introduction

Composites, although they benefit from being lighter and stiffer than most commonly used metals, are highly susceptible to damage induced by impact loads. Of primary interest is the type of damage occurring beneath the surface of contact which often cannot be detected by visual inspection. This includes any damage that may occur on the back surface which corresponds to the interior of a composite structure not accessible for visual inspection. In a laminated composite, the type of damage generally varies as it progresses through the structure depending on the stacking sequence and ply orientation. The manner in which the damage changes from one ply to another is important in determining failure modes and the residual response of the structure.

This study is aimed at investigating the damage modes in a laminated beam which is subjected to a concentrated load that simulates an impact condition. The motivation behind this study along with the research objectives are presented in this chapter. A statement of the problem and the approach used to solve the problem are also outlined. A review of the literature on analytical solution methodologies and damage descriptions in composite beams is given in Chapter 2. A brief review is also given for the contact problem involving anisotropic

bodies. Chapter 3 contains the formulation and solution procedure used for finding the stresses and displacements in a laminated beam under a quasi-static distributed load simulating a low velocity impact. The formulation is based on the mathematical theory of elasticity using a stress function approach. Preliminary results presented in Chapter 4 illustrate the effect of geometry, shear coupling, and stacking sequence on the stress distributions in the beam. These are in the form of either through-the-thickness stress distributions or stress contours. The experimental phase of the investigation is outlined in Chapter 5, where the test matrix and testing procedure are described. The resulting load versus displacement curves and indentations are given. Also, the damage initiation and ultimate failure loads are determined, and a discussion of the damage susceptibility and damage tolerance of the laminated beams is provided. On the basis of visual observations the type of damage occurring in each specimen is described and documented. In Chapter 6 the correlation between analytical predictions for the stress distributions and experimental results is presented. The relationship between load and displacement is correlated using a stepwise incremental loading procedure and a nonlinear relationship between the applied increment of load and the contact patch. The experimentally observed damage and damage susceptibility is explained in terms of the predicted local stress states. Remarks which summarize this investigation are offered in Chapter 7.

1.1 Motivation

1.1.1 Damage and Damage Tolerance

The capability of a structure to sustain load after it has been subjected to an impact which produces damage is a measure of the structure's damage tolerance. In order to design a

structure which is considered to be damage tolerant, its response to a specific damage inducing impact load and residual strength must be predictable. Equally important, however, is the predictability of the damage initiation, i.e, extent and nature of the initial induced damage. Any factors affecting initiation of damage, subsequent growth and/or arrest, and stability must be determined in order to assess a structure's susceptibility to damage and damage tolerance. This information is also beneficial in making service life predictions and for determining inspection intervals. Composite cylinders such as a solid rocket booster and stiffened panels found in aircraft fuselages are two of the most commonly addressed composite structures. Knowledge of the local stress distributions in the vicinity of the impact location during and after the impact is needed to describe and understand the impact induced damage, and to predict the structural response of these structures.

Response of composite laminates to impact damage has been studied mostly experimentally, resulting in empirical relations for the residual strength as a function of the impact energy, or resulting in the development of threshold curves for the residual strength. However, in order to develop a damage tolerance criterion for prediction of residual strength of any laminate under a prescribed impact load, an appropriate theoretical model based on complete understanding of the type and extent of the initial damage and progression of the initial damage upon subsequent loading is required. A theoretical model for a structure should consider geometric effects, the influence of stiffeners or boundary conditions on the stress state, and the effect of loading paths or applied tractions. The two most important material characteristics of a composite structure required for predicting residual strength are its material properties and strengths in the principal material directions.

In the case of a laminated composite structure, the local or ply-level stress state in the neighborhood of the impacted area and the stacking sequence are important factors to be considered in understanding damage susceptibility and damage tolerance. To completely define the ply-level stress state in an arbitrary laminated structure, modifications are needed to existing analytical tools for calculating stress distributions and displacements. Determining

the local three-dimensional stress states in an entire composite structure requires very complicated and expensive forms of analyses. Also, the testing of typical structural composite geometries for experimentally determining the damage around an impact site is very expensive and limited to a small number of test specimens. Consequently, depending on the type of structure and loading being considered, different analytical models and ideal geometries are desirable. Once the impact-induced damage has been characterized for ideal cases, this will form a basis which can then be extended to more complicated composite structures. For example, to study the local behavior and damage state between two stiffeners of a stiffened panel in a fuselage, a three dimensional analysis based on plate theory assumptions could be used. However, in some instances additional assumptions can be made on the stress state which further simplifies the analysis and reduces the problem to two dimensions. Consequently, the basis for a better understanding of a composite's structural response to impact loads, and associated damage mechanisms and failure modes may be generated by analyzing the ideal geometry of a laminated beam.

1.1.2 Quasi-static Loading

A major concern over the past decade has been with the response of a composite structure subjected to foreign object impact damage (FOD). This includes the extent of damage in a composite structure resulting from FOD and its residual strength. In trying to solve this problem, a better understanding of the contact phenomenon resulting from an impact load is needed. There are various types of applied loadings which can produce damage in a composite structure depending on the impact velocity, dimension and shape of the foreign object, and the relative hardnesses of the two contacting bodies. The failure mode and extent of damage strongly depends on the contact force which is imposed on the composite structure. The field of impact dynamics generally deals with small diameter objects and high velocity impactors, e.g., projectiles, where the duration of impact is small compared to the structure's

period of natural vibration. For this type of loading, the transient response of the structure is required and the propagation of stress waves must be considered. The damage resulting from high velocity impacts is generally very localized and concentrated near the contact area.

The experimental determination of dynamic contact forces is difficult because of the wide range of load parameters and penetration effects. However, for low velocity impacts involving large diameter objects, the damage due to impact can be simulated using a quasi-static loading which is easier to monitor and control in a test environment. If the duration of impact is long compared to the structure's period of natural vibration, the local deformations occur elastostatically and elastodynamic effects can be neglected. In this case, a quasi-static loading can be applied to the structure and the results of a static analysis will accurately represent the local stresses and structural response in the neighborhood of the contact area for this kind of loading. An experimental investigation based on quasi-static loading was performed by Yang and Sun [1] which resulted in a static indentation law for composite laminates. This was an empirical approach which modelled the experimental data by power laws. For a special case of the Hertz contact problem, where a rigid isotropic sphere is in contact with an elastic isotropic half-space, the contact force is proportional to the indentation raised to the 3/2 power [2].

$$F = k\alpha^n \tag{1}$$

where $n = 3/2$, F is the contact force, α is the indentation, and k is the proportionality constant which depends on the properties of the contacting bodies. Yang and Sun's results showed that $n = 3/2$ was also valid for a graphite/epoxy laminate and a steel indenter. Subsequent work by Tan and Sun [3] used this static indentation law for an impact analysis of a laminated composite plate. Based on their experimental results and comparisons with a dynamic finite element analysis, the static indentation law was shown to be valid for low velocity impacts. A quasi-static approach was also used by Schonberg, Keer, and Woo [4] for studying low velocity impact of transversely-isotropic beams and plates. In addition, C. C. Poe Jr. [5] simu-

lated low velocity impact damage in a thick graphite/epoxy laminate using quasi-static loading conditions.

1.2 Objectives

The present investigation is concerned with simulating low velocity impact loading on a composite structure using a quasi-static approach. The problem under consideration treats the composite structure as a model problem using a laminated beam for the analysis and experiments. The beam is finite in length (see Figure 1) and consists of a specified lamination containing layers which are either monoclinic, orthotropic, transversely-isotropic, or isotropic. The applied load is located at the midspan and is representative of the contact stress distribution resulting from static indentation. In comparison to the Hertz problem, the contact is between a rigid cylinder and a layered elastic beam. Damage states in laminated beams produced by a quasi-statically applied load are studied by conducting experiments on three-point bend specimen geometries.

The major objective of this investigation is to develop a better understanding of damage states and the damage susceptibility of laminated three-point bend specimens under quasi-static loading. A structure's susceptibility to damage is a measure of how easily damage is induced. Once damage is present in a structure, the question of how well it is tolerated with regard to ultimate failure needs to be addressed. Therefore, the objective of the present study also includes the investigation of a laminated beam's tolerance to damage. As mentioned above, the approach selected is a combination of theoretical and experimental research. The objective of the theoretical portion is to develop the necessary analytical tools for determining sub-laminae stress states near points of concentrated loading and study the effects of stacking sequence, specimen geometry, and boundary conditions on the local stress distributions. For
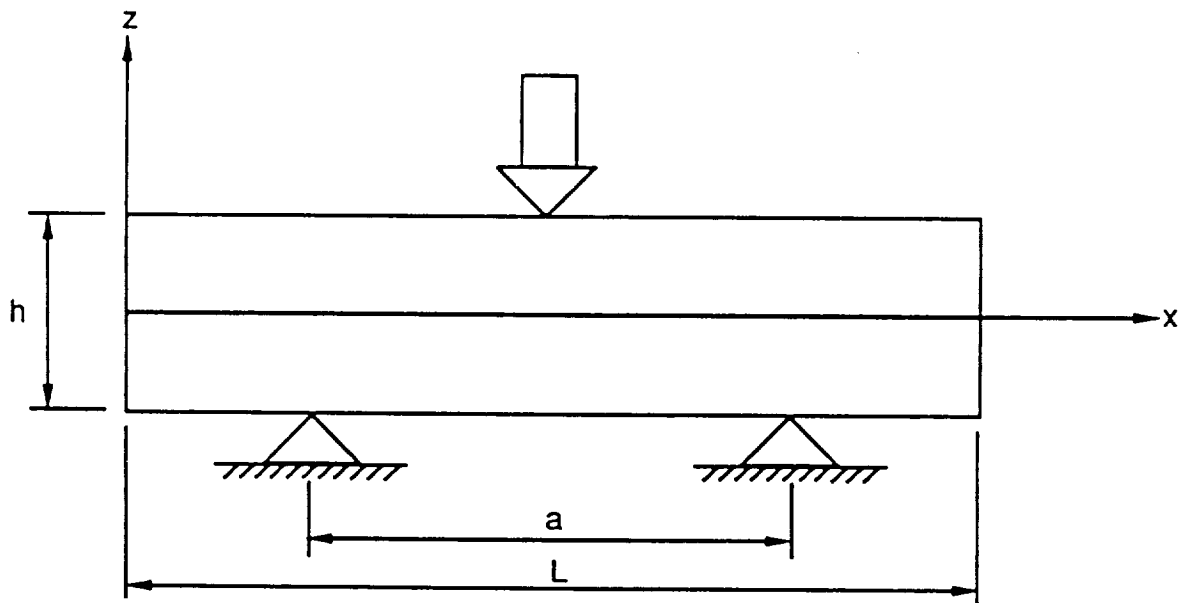
Figure 1.   Laminated beam geometry.

the experimental phase of the research, the objective is to identify damage modes from an extensive testing program. The initial damage is defined to occur when the laminated beam first experiences a reduction in load carrying capacity. The test matrix covers a wide range of specimen thickness to length and thickness to support-span ratios, and various lamination sequences. Subsequent correlations between the observed local damage in the test specimens and their corresponding damage initiation loads with predicted sub-laminae stress distributions are made.

Chapter II

Literature Review

Several investigative tools are required to study the damage produced by low velocity impact in composite laminates using a quasi-static approach. Different ways of treating the boundary conditions and applied loadings, and different solution procedures may be considered in developing a theoretical model for analyzing laminated beams. Analytically, the solution should provide the stress distributions and displacements in a laminated beam, both globally and locally in the vicinity of the applied load. Experimentally, the descriptions of damage and the changes in damage modes for different beam geometries should be investigated. Based on the analytical stress distributions corresponding to an experimentally measured load and correlation with observed damage states, a better understanding of the initiation of damage and damage susceptibility in composite beams subjected to a quasi-static load can be obtained.

2.1 Stress Analysis

The stress distributions and displacements in a composite beam which is subjected to a concentrated load have been determined by past researchers using various techniques and approximations. To obtain local and interlaminar stresses composite beams must be considered as layered media and a ply-level analysis must be performed. Global responses can be obtained by modelling the beam as being homogeneous with anisotropic properties. An overview of the approaches taken can be divided into three categories. Analytical techniques in the mathematical theory of elasticity are the foundations for one approach. The second approach is based on numerical techniques for solving the elasticity equations, such as the finite element method or finite differences. The last approach which has been used is an extension of classical laminated plate theory to the problem of a beam in bending. Whichever approach is used, solutions to problems associated with concentrated loads in the form of a point or line load must deal with a singularity at the contact point. However, a point load is an idealized case, whereas, the actual test conditions correspond to some type of distributed load. The determination of the applied loading distribution requires an investigation of the contact problem for anisotropic bodies.

2.1.1 Analytical Techniques

2.1.1.1 Problem Formulation

Elasticity solutions to two-dimensional problems are either based on a displacement formulation or expressed in terms of stress functions. The displacement formulation is used for solving a class of boundary-value problems where the displacements are prescribed on the

surface of an elastic body. The resulting internal stresses and displacements at every point in the body are found by solving the system of Navier's equations. The governing Navier's equations [6] are obtained by expressing the equilibrium equations in terms of displacements. For this class of problems, compatibility is satisfied by the assumed form of the displacements. A second class of boundary-value problems in elasticity is considered when the applied tractions are given on the surface of the body. The governing equations are the Beltrami-Mitchell equations [6] formulated in terms of stresses. A stress function is defined in terms of the stress components which identically satisfies the equilibrium equations. Since not every solution to the equilibrium equations will satisfy compatibility, the compatibility equations are employed to derive the governing differential equations.

Three analytical techniques which have been used to solve boundary-value problems in elasticity are: series expansions, transform techniques (both finite and infinite), and influence function techniques. In general, exact elasticity solutions using the above techniques only exist for ideal geometries and usually involve infinite regions. For example, a Fourier series expansion or Fourier transform technique works for rectangular geometries. Finite boundaries are often treated by making approximating assumptions and both homogeneous and layered media can be considered. For a laminated beam, anisotropic elasticity solutions are obtained for a single layer and then continuity of tractions and displacements at the interfaces are imposed.

2.1.1.2 Influence Function Approach

Influence function techniques result in the reduction of the problem to a system of integral equations in terms of some unknown variable, e.g., distribution of tractions. This was the approach used by Benjumea and Sikarskie [7] to solve several problems in plane orthotropic elasticity. The solution for a plane orthotropic region subjected to surface tractions was formulated using two different influence (Green's) functions, i.) functions which were defined to

be singular on the boundary, ii.) functions which were singular in the interior, both of which are only known for simple regions. Fredholm integral equations of the first kind were obtained when singular functions on the boundary were considered. For isotropic materials these are easily converted to the second kind which is the form suitable for numerical calculations. However, for the case of orthotropic materials, this is much more difficult and singular functions in the interior were considered. The major limitation of this approach is that it is difficult to obtain the influence functions for complicated geometries.

Rizzo and Shippy [8] determined the stress distributions in an orthotropic body using the modified potential theory and an adaptation to anisotropic elasticity. They used Green's solution [9] to the governing field equations of plane anisotropic elasticity and then coupled this with a desired solution corresponding to the given boundary conditions through Betti's reciprocal theorem [6]. For a well posed mixed boundary value problem, this produced a singular vector integral equation defined on the boundary of an arbitrary orthotropic body. Once this integral equation was solved for the unknown boundary tractions and/or displacements not initially prescribed, the displacement field was obtained by a boundary integral of the Somigliana type (Love [10]). Numerical results were presented for the problems of an elliptical inclusion in an infinite matrix, an infinite orthotropic plate with a hole subjected to hydrostatic pressure, and an orthotropic ring subjected to uniform shear on its inner boundary and a fixed outer boundary.

In contrast to the biharmonic formulations of elasticity, deriving a system of integral equations is not limited to two-dimensional stress states and is easily applied to multiply-connected domains, e.g., inclusions. If numerical techniques are used in the integral equation method then it has an advantage over a finite element formulation in that it produces a system of algebraic equations which is of lower order. This is because the equations are applicable on the boundary of the region being considered and not in the interior. However, the coefficient matrix is not banded as in the case of the finite element method and the techniques used for solving banded systems of equations cannot be applied. Only single-layered beams were

analyzed in References [7] and [8] and numerical integration techniques are generally required when more complicated geometries are being considered. Therefore, to perform a layered analysis for an arbitrary laminated beam by solving a system of integral equations would be computational inefficient.

2.1.1.3 Stress Function Approach

Many types of problems in the mathematical theory of elasticity have been solved for isotropic materials using stress functions. This generally involves the use of Fourier series for periodic loading and Fourier integrals for nonperiodic loading with harmonic functions. The distribution of shear stresses in unidirectional composite beams under three-point flexure was studied by Tarnopolskii, et al [11] using a stress function approach, taking into account the local effects of loading and anisotropy. The assumed form of the stress function satisfied the boundary conditions around a rectangular region cut-out from an infinite half-plane. Solutions were obtained for homogeneous isotropic and anisotropic regions, and comparisons were made between the two. Results of Reference [11] showed that the shear stress profile through the thickness for the anisotropic case differed considerably from being parabolic. Also, the results showed that by increasing the span length-to-depth aspect ratio of an anisotropic beam the maximum shear stress was reduced and the location was shifted toward the mid-plane, $x = 0$ (see Figure 1). Furthermore, the maximum shear stress was shown to increase if the stiffness of the material in transverse tension/compression was increased.

Conway [12] studied several problems for orthotropic plane stress using the Airy's stress function and made analogies with the isotropic cases. In particular, he analyzed a deep beam using a doubly infinite system of equations. The final solution to this set of equations was shown to be similar to Timoshenko's bending of a uniformly loaded clamped rectangular plate. Kasano, et al [13] extended Conway's work [12] for a two-dimensional Fourier series elasticity analysis of an orthotropic beam under three-point bending. The concentrated loads and sup-

ports were represented by a uniform stress distributed over a small length using a Fourier series, and hyperbolic functions represented the through the thickness part of the solution. A similar approach was used by Whitney [14] for a finite length, single layer orthotropic beam under three or four-point bending. The unknown constants in the expression for the stress function were determined from the boundary conditions and interfacial continuity. The boundary conditions were exactly satisfied on the top and bottom surfaces but the bending stress conditions on the ends of the beam were only approximately satisfied. Sullivan and Van Oene [15] considered the case of a generally orthotropic beam, i.e., unidirectional with off-axis fibers, under plane stress conditions. This was based on Whitney's work [14] where the stresses were derived from a stress function which satisfied the orthotropic analogue of the biharmonic equation and a Fourier series representation.

Kasano, et al [16] also investigated solutions to two-dimensional orthotropic elasticity problems using stress functions but in the form of Fourier integrals. Kasano considered the problem of an infinitely long orthotropic beam subjected to a concentrated load. In general, a singular point exists at the location of a concentrated load and the solution is in terms of divergent integrals. However, by using a transformation of coordinates and superimposing the solution for an orthotropic half-plane subjected to a concentrated load, a solution was obtained as the sum of a closed form integral and a convergent integral. The boundary conditions were satisfied by using the method of Fourier transforms to determine the form of the stress function. Yu [17] studied the local effects of a concentrated load applied to an infinitely long orthotropic beam by also considering an integral form of Airy's stress function. The problem of an infinite beam in bending was solved using superposition of the Boussinesq-Flamant problem for an infinite-half orthotropic plane under a singular load with the problem of an infinite strip cut out of the half-plane. The solution of the Boussinesq-Flamant system with reverse loading was superimposed on the bottom surface of the infinite strip. The boundary conditions were represented by Fourier integrals and consequently the solution was also in terms of Fourier integrals.

It was stated previously that Airy's stress function can be expressed in terms of Fourier series or Fourier integrals depending on the periodicity of the applied loading. A polynomial Airy's stress function was shown by Rao [18] to be suitable for analyzing rectangular laminated beams under a polynomial type of loading. The beam had clamped-clamped boundary conditions and each layer was assumed to be specially orthotropic in a state of generalized plane stress. The effects of relative stiffness and thickness of layers, boundary conditions, and continuity conditions at the interfaces were investigated.

Various solution procedures have been discussed using the stress function approach in the mathematical theory of elasticity. The primary limitation in applying these approaches to the problem of an arbitrary laminated beam subjected to three-point bending are the ideal geometries previously considered and the assumed boundary conditions. Solutions have been obtained for infinite strips or layered infinite regions. Finite geometries have been modelled by a rectangular cut-out region of an infinite half-plane or for only a single layer. Also, none of the approaches for a layered medium take into account the local effects of the support reactions.

2.1.1.4 Displacement-based Solutions

The problem of determining stresses and strains in an isotropic beam of rectangular cross-section under any system of load when the problem could be reduced to two dimensions was thoroughly investigated by Filon [19] using a Fourier series expansion. A displacement formulation was used where the solution to Navier's equations was expressed in terms of unknown functions. The unknown functions were then determined using a Fourier series expansion in terms of hyperbolic and circular functions. The Fourier transform technique is based on transforming the governing differential equations, e.g., Navier's equations (Chatterjee, et al [20]), to the Fourier domain using the Fourier transform. Expressions for the

stresses and displacements are obtained in the transformed domain and then transformed back to the real domain.

An exact solution within the framework of linear elasticity was obtained by Pagano [21] for the problem of cylindrical bending of a laminated plate. Orthotropic layers whose axes of material symmetry were parallel to the plate axes were considered and a state of plane strain was assumed. The plate was simply-supported on the ends and a normal traction was applied on the upper surface. Results were compared with classical lamination theory (CLT) and it was shown that for large aspect ratios CLT converged to the elasticity solution. A more general type of loading, which included approximating a point load by a uniformly distributed load over a small finite distance, was considered by Pagano and Wang [22] using the cylindrical bending model along with a Fourier analysis. The effect of shear coupling in cylindrical bending of an anisotropic laminated plate was also investigated by Pagano [23]. For general conditions of material symmetry, a state of plane strain cannot exist and a generalized plane deformation analysis was used. As discussed by Leknitskii [24], none of the six stress components vanish identically for this material state. The solution was obtained using a displacement formulation where a displacement field was assumed which satisfied the governing field equations and the the boundary conditions. The governing differential equations were then derived from the equilibrium equations using the constitutive and strain-displacement relationships. Applying the problem of cylindrical bending to the problem of a laminated beam subjected to three-point bending is limited by the assumed boundary conditions. The ends of the beam, i.e., $x=0$ and L (see Figure 1), are assumed to be simply-supported along the entire end-face of the beam from $z=-h/2$ to $z=h/2$, and the resultant shear force at the ends of the beam, i.e., the integral of the τ_{xz} shear stress distribution through the thickness at $x=0$ and L, maintains global equilibrium with the applied loading on the top surface. Consequently, overhang effects and the effects of supporting the beam on the bottom surface cannot be considered.

2.1.2 Numerical Approaches

2.1.2.1 Finite Element Method

An alternative to the analytical approaches discussed in the previous sections is to use numerical methods to solve the governing elasticity equations. The finite element method was used by Berg, Tirosh, and Israeli [25] to study the validity of the ASTM D 2344 short beam shear test (SBS) for composites. This standard test was designed for isotropic beams and is based on Bernoulli-Euler beam theory. Classical beam theory predicts a parabolic through-the-thickness shear stress distribution and the standard test assumes the failure to be dominated by this stress component. Therefore, the measured load at which fracture occurs determines the interlayer shear strength of the material. A finite element analysis was performed in Ref. [25] for a unidirectional beam having a span length-to-height aspect ratio, a/h, of four using an orthotropic elastoplastic continuum model. The fibers were oriented parallel to the x-axis (see Figure 1). The contact force was assumed to be a uniformly distributed traction over a small arc length, d. The results of this investigation showed that the actual in-plane shear stress distribution, τ_{xz}, does not differ much from beam theory at a location midway between the support and the loading nose. However, classical Bernoulli-Euler beam theory does fail to properly describe the distribution and location of maximum shear stress on planes closer to the contact point. The results presented also predicted a large transverse compressive stress, σ_{zz}, which causes fracture to take place under conditions of combined compression and shear in the vicinity of the loading nose. Consequently, the measured fracture load cannot be used in determining the shear strength of the material because this is not a pure shear failure. In some cases, large compressive bending stresses, σ_{xx}, were predicted under the applied loads which could produce a pure compression dominated failure in the form of fiber microbuckling.

2.1.2.2 Finite Differences

Sandorff [26] studied St. Venant effects in orthotropic beams using the finite difference method to determine stresses and displacements. He considered a state of plane stress and used a stress formulation approach where the equations of equilibrium were identically satisfied by defining an Airy's stress function. Invoking compatibility for a two-dimensional stress state resulted in a biharmonic equation to solve for the Airy's stress function. The governing biharmonic equation for the plane problem of orthotropy was shown by Mitchell [27] to have the same form as the biharmonic equation of the plane isotropic problem. The differential operator was equivalent to the isotropic problem but in the orthotropic case the constant co-efficients were different. In Reference [26], the solution to the biharmonic equation was expressed as a boundary value problem for an orthogonal matrix of interior points and then relaxation techniques were applied. The elasticity equations and constitutive relations were then expressed in finite difference form to find the stresses and displacements. Only unidirectional beams having fibers parallel to the x-axis (see Figure 1) were analyzed. However, as stated in Reference [26], for many cases the same approach applies to multi-ply laminates if the behavior is approximated by assuming the beam to be homogeneous, specially orthotropic. The external load was expressed by a triangular load distribution using a 3-term finite difference approximation. The results for the transverse stress, i.e., σ_{zz}, directly under the external load were shown to be about 15% higher than that predicted from the Boussinesq-Flamant relation [28] for a semi-infinite region. The through-the-thickness distribution for the shear stress, τ_{xz}, at a cross-section adjacent to the loading, showed the maximum value to be located just below the top surface of the beam. This was a severe deviation from the parabolic shear stress distribution obtained from Bernoulli-Euler beam theory. Also, the bending stress, σ_{xx}, distribution through-the-thickness was shown to have a large deviation from beam theory with a peak compressive value approximately three times greater. The stress distribution results presented in Reference [26] showed that St. Venant effects were more important in composite materials. If the net-section warpage was large and

unrestrained, the bending stress varied linearly through the thickness, and if warpage was restrained the distribution was nonlinear. Overhang effects were also studied for short beam shear specimens, concluding that too short of an overhang would result in beam failure before the fracture load associated with the interlayer shear strength of the material was reached. Consequently, the stress state was not dominated by the shear stress and the failure mode was not due to pure shear. This result was based on the net bending moment being zero at the support and in the overhang but the constraint against warpage provided by the overhang together with the introduction of a reaction load at the support caused local disturbances in the normal and shear stress distributions. This type of behavior acted to increase the beam's effective stiffness.

The numerical techniques discussed above illustrated the St. Venant effects in composite beams and the shortcomings of classical beam theory for calculating stresses. In comparison to an isotropic beam, the stress concentrations resulting from the applied loading and supports extended over a larger portion of the beam. However, only unidirectional homogeneous orthotropic beams under plane stress conditions were considered. As previously discussed for numerical evaluation of a system of integral equations, using these methods to perform a layered analysis would be computationally inefficient and not recommended due to the large finite element mesh or finite difference grid required.

2.1.3 CLT Approaches

Whitney, et al [29] analyzed the flexural test specimen for laminated composite materials by considering the beam as a special case of a laminated plate. Assumptions were made based on classical lamination theory and a pure bending type of loading was applied, i.e., $M_x \neq 0$, $M_y = M_{xy} = 0$ (see Figure 2). For beams having a large length to width ratio, a/b, it was assumed that the component of displacement in the z-direction depended only on the x-

coordinate, i.e., $w = w(x)$. The work of Reference [29] basically dealt with defining the bending properties of composites for simply-supported beams under three or four-point bending. The effects of transverse shear deformations were included and a shear correction term was defined which was equivalent to the correction term in Timoshenko beam theory. Accounting for transvere shearing deformations provided additional beam deflections and made the beam less stiff, which was shown by Whitney and Pagano [30] to be important for composite beams in three-point bending. The beam's stiffness was calculated using homogeneous isotropic beam equations which were modified to account for stacking sequence. This was analagous to Pagano's work [31] where he concluded that layered beams in which plies were oriented symmetrically about the midplane and the orthotropic axes of material symmetry were parallel to the beam edges, i.e., $0°$ or $90°$ plies, could be analyzed by classical beam theory with the bending stiffness EI being replaced by an equivalent stiffness using an effective bending modulus. The effective bending modulus was a function of stacking sequence and depended on the D_{ij} terms defined by lamination theory. Similar results were obtained by Adams and Miller [32] for the influence of transverse shear in hybrid composite materials. The analysis used by these authors was also derived from classical laminated anisotropic plate theory with an extension to include effects of transverse shear in the three-point beam bending problem. The approach was based on an approximate method developed for thick laminated plates having an assumed displacement field corresponding to the conditions of cylindrical bending, i.e., plane strain in the xz-plane with applied transverse tractions being constant in the y-direction. The laminates were assumed to be symmetric and when off-axis plies were included the D_{16} and D_{26} terms were assumed to be small and neglected for simplications. Also, for the case of a generalized plane strain analysis the three strain components, $\varepsilon_y, \gamma_{yz}, \gamma_{xy}$, were neglected. The presented results included beam deflections, flexural moduli, flexural energy and shear strain energy. The transverse shearing stresses were shown to have a predominant effect on the flexural modulus and the strain energy. It should be noted that the highly anisotropic nature of composite beams causes them to be more dependent upon transverse shearing stresses when subjected to three-point flexure than similarly loaded homogeneous

isotropic beams. The major limitation of a CLT based approach is the beam or plate theory solutions presented above cannot model the local effects due to transversely applied loads.

2.1.4 Contact Problems

2.1.4.1 Isotropic

In order to accurately describe and understand the possible damage states in a composite beam, the actual stress distribution and deformations under the loading nose and at the support points must be investigated for prescribing the boundary conditions in the analytical model. Hertz [2] in 1881 determined the stresses produced when two smooth bodies are pressed together. He solved this problem for the case of isotropic bodies by making suitable approximating assumptions and applying some known results of potential theory. The basic Hertz problem has been predominantly utilized for isotropic bodies where the elastic contact stress problem has been defined to be Hertzian if:

1. Bodies are homogeneous, isotropic, obey Hooke's law and experience small strains and rotations.

2. Contacting surfaces are frictionless

3. Dimensions of the deformed contact patch remain small compared to the principal radii of the undeformed surfaces.

4. Deformations are related to the stresses in the contact zones as predicted by the linear theory of elasticity for half-spaces.

5. Contacting surfaces are continuous, and may be represented by second degree polynomials prior to deformation.

2.1.4.2 Anisotropic

For anisotropic bodies, the basic Hertz problem was not considered for many years presumably because it could not be reduced to a potential theory problem except for the transversely
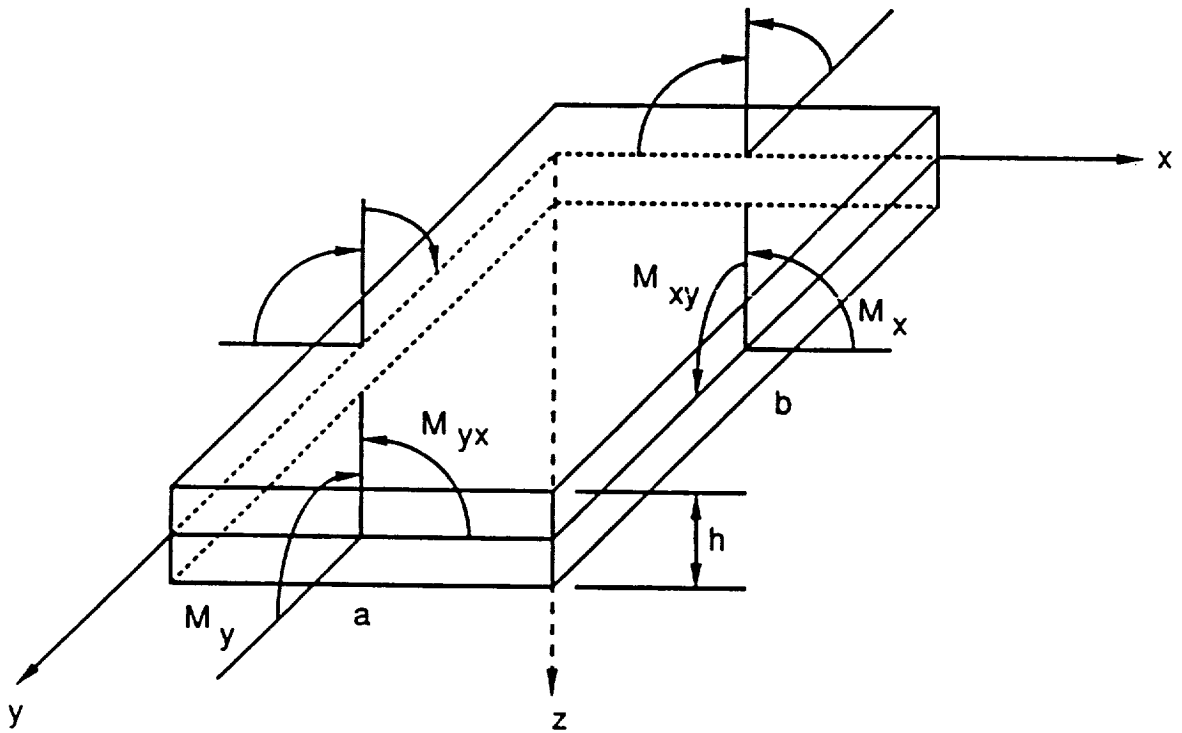
Figure 2. Laminated plate subjected to in-plane loading.

isotropic case. Sveklo [33] showed that a Hertzian approximation for a transversely isotropic body produced a normal component of surface displacement due to a concentrated normal load which was inversely proportional to the radial distance measured from the load point. Green and Zerna [9] studied the two-dimensional anisotropic contact problem for the case of indentaton by a rigid punch. Willis [34] considered the Hertz problem for generally anisotropic bodies using the Fourier transform method. The functional form of the pressure distribution between the bodies was found explicitly and determination of the resulting displacements was reduced to numerically evaluating contour integrals. For isotropic bodies, Hertz reduced the problem by the semi-inverse method of assuming that the contact area was an ellipse with an elliptical pressure distribution. This type of distribution was known to give the correct form of displacements according to potential theory. Willis [34] showed that by assuming an elliptical distribution for the general case of anisotropy the correct form of displacements could also be obtained. Chen [35] also assumed Hertzian contact to find the stresses in anisotropic materials due to indentation. He showed that in certain important practical situations the stress functions for isotropic and for anisotropic materials were of the same form. Consequently, the expressions for the pressure distribution underneath the punch were independent of the material properties of the half-space. For the anisotropic case it was shown that the stress distributions inside the body were generally not symmetric even though the external loading was. Chen presented results in the form of maximum shear stress contours where the largest value occurred on the axes of symmetry at a depth of approximately 4/10 the contact width for the case of isotropy. Conversely, for anisotropic materials the largest value did not necessarily lie on the axis of symmetry.

Another solution for plane anisotropic contact problems was developed by Miller [36] using the Green's function approach. The problem was assumed to be for two anisotropic cylinders in contact and included the effects of sliding friction. The method used was based on complex variable techniques in elasticity and the solution was expressed in terms of piecewise analytic functions. This was a mixed boundary value problem due to the contact between two

anisotropic bodies. The solution obtained included the displacements corresponding to the singular solution of a concentrated force in an anisotropic half-plane. Sankar [37,38] derived an approximate Green's function for the surface displacements in an orthotropic beam by superposition of the half-plane solution and beam theory. For small contact lengths he assumed that the contact stress distribution was elliptical, i.e., Hertzian. A relationship between the contact force and contact length was derived and was seen to be significantly affected by the curvature of the deflected beam. Therefore, this relationship was revised by considering contact between two curved bodies. In his approach, elasticity equations were used to describe the local behavior and beam theory was used for the global behavior. The Young's modulus, E_1 controls beam behavior with the 1-direction corresponding to the beam axis, whereas, E_2 controls local deformations with the 2-direction corresponding to the direction of the applied contact force. Consequently, for small E_2/E_1 values the local indentation dominated and the deviation from the Hertzian solution was small. Inclusion of shear deformations increased the contact area for a given contact force but reduced the amount of indentation, i.e., shear deformations added to the beam bending effects. Similar effects were seen for higher length to width ratios.

2.2 Damage Descriptions

Failure mechanisms and damage due to either static bending or low velocity impact have been investigated by several authors for the case of simply-supported composite beams. Two distinct modes were reported by Parry and Wronski [39] as failure mechanisms in unidirectional carbon fiber composite beams. One was a tensile mode which resulted from fiber breaks and debonding. The second was a compression mode combining fiber shear and/or buckling with compression creases or kinking. Kinking is a mechanism of transverse deformation where shear takes place initially parallel to the principal stress axis. Kink bands

generally develop in a diagonal fashion from rotation and failure of fibers by buckling, and eventually lead to the formation of interlaminar cracks.

Shih and Ebert [40] defined flexural failure mechanisms for unidirectional glass/epoxy beams under four-point bending. A flexural tensile mechanism was described by fiber pull-out, transverse matrix cracking, and longitudinal matrix cracking. Microbuckling of fibers was the predominant flexural compressive mechanism. A tensile failure due to flexure was associated with a strong interfacial shear strength, whereas, a poor interfacial shear strength led to a shear failure mode. It was also noted that the dependence of interlaminar shear strength on interfacial shear strength was larger than that of the longitudinal compressive strength which in turn was larger than that of the longitudinal tensile strength.

Two different failure modes were identified by Tarnopolskii, et al [11], for three-point bending of a composite beam made of glass-plastic materials. One was layer separation and the second was peeling of surface layers within the compression zone followed by global fracture. This was said to be caused by a local loss of stability with an accompanying breakdown of the polymer interlayer.

The effect of fiber orientation on the impact strength of off-axis composites was studied by Mallick and Broutman [41]. The material system was E-glass/epoxy and both static and dynamic flexure were considered. The static results indicated a "lift-off" phenomenon in off-axis specimens, i.e., as the load increased the specimens twisted which lifted the corners off the supports. For the dynamic flexure tests, the progression of damage was described by cracks initially forming parallel to the off-axis fibers causing the 0° fibers to break which eventually led to failure.

Greszczuk and Chao [42] investigated low-velocity (FOD) impact damage in graphite fiber reinforced composites using a quasi-dynamic approach. This approach involved determining the time-dependent surface pressure distribution under the impactor, time-dependent internal

stresses in the target caused by the surface pressure, and failure modes in the target caused by the internal stresses. Analytical studies were performed for different material systems to determine the influence of fiber and matrix properties on the impact response. A failure criterion based on distortional energy theory showed that the matrix properties strongly influenced the extent of damage and a high strength, low modulus matrix was required to minimize damage. In general, thin laminates failed on bottom due to bending stresses and thick laminates failed near the top due to contact stresses. Greszczuk also concluded that an accurate determination of the damage zone required a multi-layer heterogeneous orthotropic analysis.

Browning et al [43] performed an SEM investigation on a thick 50-ply short beam shear (SBS) specimen made of AS-1/3502 graphite/epoxy, and tested with a span length-to-depth aspect ratio of 4. The failure surface was characterized by resin deformation and microcracking. The failure surface features of the resin deformation were similar to fracture surfaces related to interlaminar failure. The microcracks appeared predominately at the fiber-resin interface, circumferentially surrounded the fiber, and radiated out into the matrix. Short beam shear tests were also conducted for thin 16-ply beams of the same material and aspect ratio and the test specimens consistently failed in a non-shear dominated mode. The only evidence of damage was local indentation under the loading nose. Therefore, it was concluded that although the SBS test is widely used for characterizing interlaminar failure and measuring "apparent" interlaminar shear strength, thin unidirectional beams usually do not fail in this manner and thick specimens or alternative test procedures must be used.

2.3 Summary

To investigate low velocity impact damage in composite beams using a quasi-static approach the knowledge of local stress states and an understanding of failure mechanisms is required.

The review of published work by previous researchers indicated shortcomings in their approaches which resulted in the inability to accurately and efficiently predict the stress distributions in a finite length laminated beam which contained off-axis layers. Primarily, solutions for homogeneous and/or infinite regions were developed which cannot predict ply-level stress distributions nor account for end-face boundary conditions associated with a finite region. For a layered analysis the numerical techniques required in using an influence function approach or finite elements are computationally inefficient. However, the distribution of stresses in a three-point bend specimen having an arbitrary lamination sequence and a finite length can be obtained by combining different aspects from several of the previously discussed analytical approaches. In the following Chapter, Whitney's solution [14], which was developed for a finite length orthotropic unidirectional beam and included the reactions at the support points, is extended to the case of a laminated beam. To properly account for the presence of off-axis plies in the lamination sequence, the stress-function based plane strain solution in [14] is modified for a state of generalized plane deformation. This approach parallels Pagano's displacement-based cylindrical bending analysis [23] which had the shortcoming of requiring the beam to be simply-supported only at the ends, i.e., no overhang. The concentrated loads located at the three contact points are modelled by assuming Hertzian contact, e.g., an elliptical distribution over the contact length, instead of the uniform distribution assumed in [14] and [23]. Once the stresses are known and experiments have been conducted to ascertain the location and type of damage, a correlation study between the theoretical and experimental results can be performed. The results of the correlation study should provide a better understanding of damage in laminated composite beams.

Chapter III

Analytical Procedure

3.1 Introduction

The determination of stresses in the interior of an elastic body when the tractions are specified on the surface of the body is a well defined problem in the theory of elasticity. The boundary-value problem being considered is illustrated in Figure 3, where the tractions, $T^{(n)}(x)$, are given on the surface of the body S, and the body force, $F(x)$, is given in the interior of the body. The governing equations are:

Equilibrium:

$$\sigma_{ij,j} + F_i = 0 \tag{1}$$

Constitutive relationship:

$$\sigma_{ij} = C_{ijkl}\varepsilon_{kl} \tag{2}$$

Strain-Displacement:

$$\varepsilon_{ij} = \frac{1}{2}(u_{i,j} + u_{j,i}) \tag{3}$$

Compatibility:

$$\varepsilon_{ij,kl} + \varepsilon_{kl,ij} - \varepsilon_{ik,jl} - \varepsilon_{jl,ik} = 0 \tag{4}$$

In using a stress formulation approach, a stress function or functions can be defined which will identically satisfy the equations of equilibrium. However, not every solution to the equilibrium equations will satisfy compatibility and the compatibility equations must be employed. The governing equation or equations are obtained by substituting the constitutive relationships into the compatibility equations and simplifying the expressions using the equilibrium equations.

Since one can always find a particular integral to the inhomogeneous equations when $F_i \neq 0$ and since the equations are linear, assume that a particular solution is known and set $F_i = 0$. For the case of isotropic bodies and a two-dimensional stress state, the equations of equilibrium are identically satisfied by defining an Airy's stress function, $U(x,z)$, as follows:

$$\sigma_{xx} = \frac{\partial^2 U(x,z)}{\partial z^2} \qquad \sigma_{zz} = \frac{\partial^2 U(x,z)}{\partial x^2} \qquad \tau_{xz} = -\frac{\partial^2 U(x,z)}{\partial x \partial z} \tag{5}$$

The problem can then be reduced to the fundamental biharmonic boundary value problem of finding $U(x,z)$ such that:

$$\begin{aligned} \nabla^4 U = 0 \ \ in \ \mathcal{R} \quad &(a) \\ U_{,\alpha} = f_\alpha(S) \ \ are \ given \ on \ C \quad &(b) \end{aligned} \tag{6}$$

where C is the part of boundary S where the tractions are prescribed. For the case of anisotropic bodies and general conditions of material symmetry (see Lekhnitskii [24]) equation (6) is no longer valid and a second stress function must be defined. In the case of a laminated
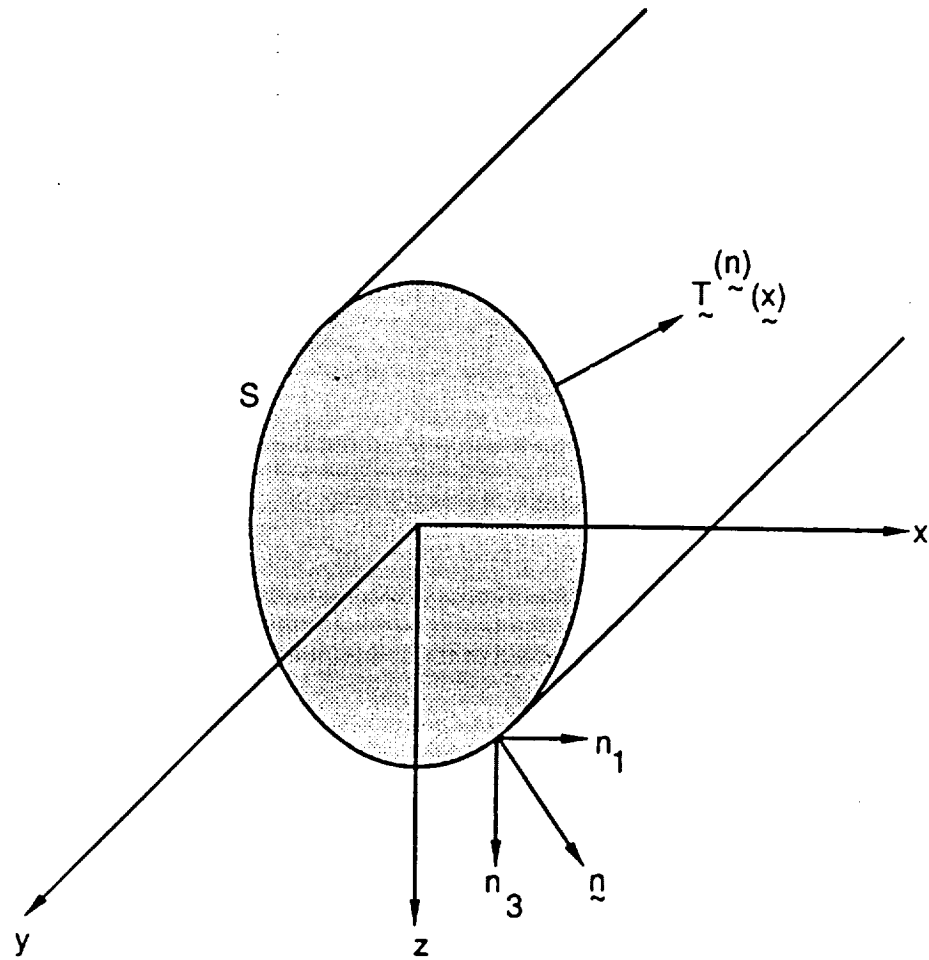
Figure 3. First fundamental boundary-value problem in elasticity.

medium the solution to this problem is applied to the individual layers and continuity of tractions and displacements at the interfaces is imposed.

Pagano [21,22,23] has derived plane strain and generalized plane deformation elasticity solutions for the cylindrical bending problem using a displacement formulation. However, the assumed form of the displacements cannot be used in cases where the ends of the beam are allowed to extend beyond the supports. In the cylindrical bending problem the simple supports are approximated by the particular boundary conditions that Pagano uses and the resultant shear stress distribution on the end faces of the beam maintains global equilibrium with the applied loading. Whitney's [14] approach includes the effects of an overhang but only for a homogeneous single-layered orthotropic beam under plane strain or plane stress conditions. In the present investigation a solution for an arbitrary laminated beam of finite length is obtained by extending Whitney's previous development for plane strain to generalized plane deformation in order to account for the possibility of including off-axis plies.

3.2 Solution for Monoclinic Layers

3.2.1 Governing Differential Equations

Following Whitney's [14] analysis and using a stress formulation, the prescribed tractions are expressed by infinite Fourier series and the solution is obtained in terms of two nondimensional stress functions. A state of generalized plane deformation in the xz-plane (see Figure 4) is considered in order to satisfy the three equilibrium equations for a monoclinic layer. For the case of orthotropic, transversely-isotropic , and isotropic layers the solution reduces to the form obtained by considering plane strain conditions.
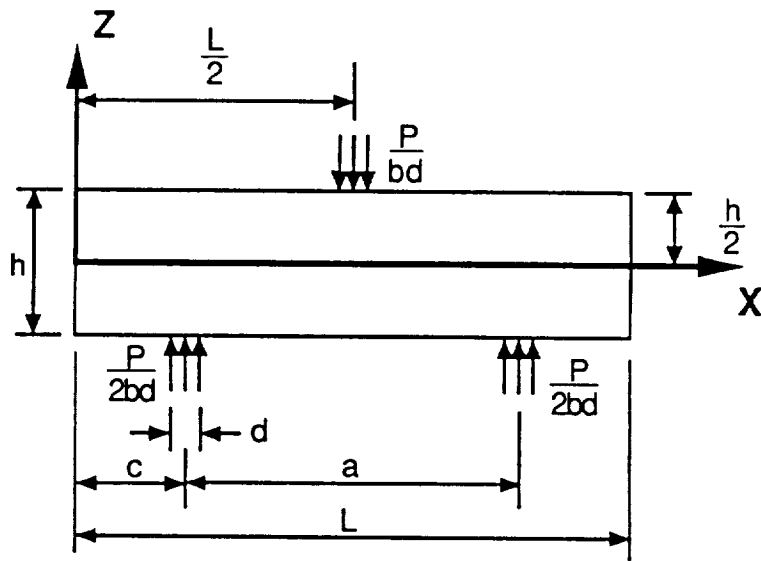
Figure 4.   Three-point bend specimen geometry.

For the generalized plane deformation analysis, the three displacement components, u, v, and w in the x, y, and z directions, respectively, are assumed to be only functions of the in-plane coordinates, x and z.

$$
\begin{aligned}
u &= u(x,z) \\
v &= v(x,z) \\
w &= w(x,z)
\end{aligned}
\tag{7}
$$

Consequently, the only vanishing component of strain is ε_y and σ_{yy} can then be expressed in terms of the other stress components. This results in a reduced 5 x 5 compliance matrix similar in form to the plane strain reduced compliance matrix and the constitutive equations become:

$$
\begin{array}{cc}
\varepsilon_x & \quad R_{11}\ R_{13}\ 0\ \ \ 0\ \ R_{16}\quad \sigma_{xx} \\
\left\{\begin{array}{c}\varepsilon_z \\ \gamma_{yz} \\ \gamma_{xz}\end{array}\right\} = \left[\begin{array}{ccccc}R_{13} & R_{33} & 0 & 0 & R_{36} \\ 0 & 0 & R_{44} & R_{45} & 0 \\ 0 & 0 & R_{45} & R_{55} & 0\end{array}\right]\left\{\begin{array}{c}\sigma_{zz} \\ \tau_{yz} \\ \tau_{xz}\end{array}\right\} \\
\gamma_{xy} & \quad R_{16}\ R_{36}\ 0\ \ \ 0\ \ R_{66}\quad \tau_{xy}
\end{array}
\tag{8}
$$

where R_{ij} are related to the transformed compliances as follows:

$$
\begin{aligned}
R_{ij} &= \overline{S}_{ij} - \frac{\overline{S}_{i2}\overline{S}_{j2}}{\overline{S}_{22}} \qquad i,j = 1,3,6 \\
R_{44} &= \overline{S}_{44} \\
R_{45} &= \overline{S}_{45} \\
R_{55} &= \overline{S}_{55}
\end{aligned}
\tag{9}
$$

This resulting constitutive relationship now reflects the shear coupling between the in-plane normal strains and the out-of-plane shear stresses. It should also be noted that none of the stress components vanish identically. For the case of plane stress in the x-z plane, R_{ij} is simply replaced by $\overline{S}_{ij}$, the transformed compliance matrix.

The six components of stress are functions of x and z only, and the three equations of equilibrium become:

$$\frac{\partial \sigma_{xx}}{\partial x} + \frac{\partial \tau_{xz}}{\partial z} = 0$$

$$\frac{\partial \tau_{xy}}{\partial x} + \frac{\partial \tau_{yz}}{\partial z} = 0 \qquad (10)$$

$$\frac{\partial \tau_{xz}}{\partial x} + \frac{\partial \sigma_{zz}}{\partial z} = 0$$

These equations are identically satisfied by defining two nondimensional stress functions, Φ and Ψ, as follows:

$$\sigma_{\zeta} = \frac{R}{S} \frac{\partial^2 \Phi}{\partial \eta^2} \qquad \sigma_{\eta} = \beta \frac{\partial^2 \Phi}{\partial \zeta^2} \qquad \tau_{\zeta\eta} = -\frac{\partial^2 \Phi}{\partial \zeta \partial \eta} \qquad (11)$$

$$\tau_{\zeta\chi} = \frac{\partial \Psi}{\partial \eta} \qquad \tau_{\chi\eta} = -\frac{\partial \Psi}{\partial \zeta}$$

The nondimensional stresses in equation (11) are defined as:

$$\sigma_{\zeta} = \frac{bh^2}{Pa} \sigma_{xx} \qquad \sigma_{\eta} = \frac{bd}{P} \sigma_{zz} \qquad \tau_{\zeta\eta} = \frac{bh}{P} \tau_{xz} \qquad (12)$$

$$\tau_{\zeta\chi} = \frac{bh}{P} \tau_{xy} \qquad \tau_{\chi\eta} = \frac{bL}{P} \tau_{yz}$$

and the nondimensional coordinate system is defined to be:

$$\zeta = \frac{x}{L} \qquad \eta = \frac{z}{h} \qquad \chi = \frac{y}{b} \qquad (13)$$

The Cartesian coordinate system used and beam dimensions are shown in Figure 4 and the remaining nondimensional quantities in the above expressions are:

$$\beta = \frac{d}{L} \qquad S = \frac{a}{h} \qquad R = \frac{L}{h} \qquad (14)$$

A direct consequence of the generalized plane deformation formulation is that two of the compatibility equations are not identically satisfied. Using the differential operator notation

given by Lekhnitskii [24], the resulting governing coupled partial differential equations are given by:

$$L_4 \Phi + L_3 \Psi = 0 \quad (a)$$
$$L_3 \Phi + L_2 \Psi = 0 \quad (b)$$

(15)

where the differential operators are defined as:

$$L_4 = R_{11} R^4 \frac{\partial^4}{\partial \eta^4} + (2R_{13} + R_{55})R^2 \frac{\partial^4}{\partial \zeta^2 \partial \eta^2} + R_{33} \frac{\partial^4}{\partial \zeta^4}$$

$$L_3 = R_{16} R^3 \frac{\partial^3}{\partial \eta^3} + (R_{36} + R_{45})R \frac{\partial^3}{\partial \zeta^2 \partial \eta}$$

$$L_2 = R_{66} R^2 \frac{\partial^2}{\partial \eta^2} + R_{44} \frac{\partial^2}{\partial \zeta^2}$$

(16)

Note, that for an orthotropic layer, R_{16}, R_{36}, and R_{45} are zero, the L_3 differential operator vanishes and the two partial differential equations become uncoupled. This is also the case for transversely-isotropic and isotropic layers. For monoclinic layers and generalized plane deformation, a sixth order partial differential equation is obtained by eliminating one of the stress functions in equations (15a) and (15b), e.g.,

$$(L_4 L_2 - L_3^2)\Phi = 0$$

(17)

It is easily shown that the second stress function, Ψ, must also satisfy an equation having this form.

3.2.2 Solution For Stress Functions

Solutions for the stress functions are found by assuming they have the form of a polynomial plus an infinite series which is expressed in terms of an unknown function through the thickness and a trigonometric function along the span. These forms are chosen in a way which

allows for satisfaction of the governing partial differential equation and the applied traction conditions. The solution for Φ was given by Whitney [14] and is repeated here for the purpose of clarity.

$$\Phi(\xi, \eta) = A_o \frac{\xi^2}{2} + B_o \frac{\eta^2}{2} + C_o \frac{\eta^3}{6} + \sum_{m=1}^{\infty} g_m(\eta) \cos p_m \xi \tag{18}$$

where $p_m = 2m\pi$, A_o, B_o, and C_o are unknown constants, and $g_m(\eta)$ has the same form given by Whitney but now involves a summation of six terms corresponding to the six roots of the characteristic equation. Substituting this expression for the stress function into equation (17), the solution for $g_m(\eta)$ is of the form:

$$g_m(\eta) = \sum_{j=1}^{6} K_{mj}(\cosh \lambda_j \mu_m \eta + \sinh \lambda_j \mu_m \eta) \tag{19}$$

where $\mu = \frac{p_m}{R}$ and K_{mj} are unknown constants, and λ_j are the roots of the following characteristic equation:

$$-A\lambda^6 + B\lambda^4 + C\lambda^2 + D = 0 \tag{20}$$

where

$$
\begin{aligned}
A &= R_{16}^2 - R_{11}R_{66} \\
B &= 2R_{16}(R_{36} + R_{45}) - R_{66}(2R_{13} + R_{55}) - R_{11}R_{44} \\
C &= R_{33}R_{66} + R_{44}(2R_{13} + R_{55}) - (R_{36} + R_{45})^2 \\
D &= - R_{33}R_{44}
\end{aligned}
\tag{21}
$$

Using the change of variable,

$$y = \lambda^2 - \frac{B}{3A} \tag{22}$$

the characteristic equation is reduced to a cubic equation having the form:

Analytical Procedure

$$\gamma^3 + r\gamma + s = 0 \qquad (23)$$

where

$$r = -\frac{B^2}{3A^2} - \frac{C}{A}$$
$$s = -\frac{2B^3}{27A^3} - \frac{CB}{3A^2} - \frac{D}{A} \qquad (24)$$

For most commonly used composite materials, the relationship

$$\frac{s^2}{4} + \frac{r^3}{27} < 0 \qquad (25)$$

is true and equation (23) will have three real and unequal roots. For materials having prop-

erties such that this quantity is positive the roots will be imaginary. If the quantity in equation

(25) is zero there will be repeating roots. The resulting values for the case of real character-

istic roots in equation (23) are:

$$y_j = 2\sqrt{\frac{-r}{3}} \cos\left\{ \frac{1}{3}[\phi + 2(j-1)\pi] \right\} \qquad j = 1,2,3 \qquad (26)$$

where

$$\phi = \cos^{-1}\left[\frac{-s\sqrt{27}}{2(-r)^{\frac{3}{2}}} \right] \qquad (27)$$

Substituting equation (26) into equation (22) results in six distinct characteristic roots occurring

in plus and minus pairs. By redefining the unknown constants, K_{mj}, to simplify the ex-

pressions when evaluated at the interfaces, i.e., $\eta = \pm \frac{1}{2}$, the solution for $g_m(\eta)$ can be rewrit-

ten in the following form:

$$g_m(\eta) = \sum_{j=1}^{3} \left(A_{mj} \frac{\cosh \lambda_j \mu_m \eta}{\cosh \dfrac{\lambda_j \mu_m}{2}} + B_{mj} \frac{\sinh \lambda_j \mu_m \eta}{\sinh \dfrac{\lambda_j \mu_m}{2}} \right) \tag{28}$$

where A_{mj} and B_{mj} are unknown constants.

The solution for the second stress function, Ψ, can be found by assuming a form similar to the first stress function which was given in equation (18), i.e.,

$$\Psi(\xi, \eta) = D_o \xi + E_o \eta + F_o \frac{\eta^2}{2} + \sum_{m=1}^{\infty} h_m(\eta) \cos p_m \xi \tag{29}$$

where D_o, E_o, and F_o are another set of unknown constants. As stated previously, this function must also satisfy a sixth order partial differential equation of the form given by equation (17) and the solution for $h_m(\eta)$ can immediately be written as:

$$h_m(\eta) = \sum_{j=1}^{3} \left(C_{mj} \frac{\cosh \lambda_j \mu_m \eta}{\cosh \dfrac{\lambda_j \mu_m}{2}} + D_{mj} \frac{\sinh \lambda_j \mu_m \eta}{\sinh \dfrac{\lambda_j \mu_m}{2}} \right) \tag{30}$$

where C_{mj} and D_{mj} are unknown constants and λ_j are the same roots of the characteristic equation determined previously. The two stress functions were shown to be coupled in equations (15a) and (15b) and by substituting equations (18) and (29) into equation (15b) it can be shown that the following relationships must exist between the unknown constants.

$$C_{mj} = L_j p_m \coth \frac{\lambda_j \mu_m}{2} B_{mj} \tag{31}$$

$$D_{mj} = L_j p_m \tanh \frac{\lambda_j \mu_m}{2} A_{mj} \qquad (32)$$

$$F_o = -\frac{R_{16}}{R_{66}} R C_o \qquad (33)$$

where

$$L_j = \frac{\left(R_{36} + R_{45} - R_{16}\lambda_j^2\right)\lambda_j}{R_{66}\lambda_j^2 - R_{44}} \qquad (34)$$

3.2.3 Stresses

Now by substituting the nondimensional forms of the two stress functions given in equations (18) and (29) into equation (11) the following expressions for the stresses in a monoclinic layer can be found.

$$\sigma_\xi = \frac{R}{S}\left\{B_o + C_o\eta + \sum_{m=1}^{\infty}\sum_{j=1}^{3} \mu_m^2 \lambda_j^2 \left(A_{mj} \frac{\cosh \lambda_j \mu_m \eta}{\cosh \frac{\lambda_j \mu_m}{2}} + B_{mj} \frac{\sinh \lambda_j \mu_m \eta}{\sinh \frac{\lambda_j \mu_m}{2}}\right)\cos p_m \xi\right\} \qquad (35)$$

$$\sigma_\eta = \beta\left\{A_o - \sum_{m=1}^{\infty}\sum_{j=1}^{3} p_m^2 \left(A_{mj} \frac{\cosh \lambda_j \mu_m \eta}{\cosh \frac{\lambda_j \mu_m}{2}} + B_{mj} \frac{\sinh \lambda_j \mu_m \eta}{\sinh \frac{\lambda_j \mu_m}{2}}\right)\cos p_m \xi\right\} \qquad (36)$$

$$\tau_{\zeta\eta} = \frac{1}{R}\sum_{m=1}^{\infty}\sum_{j=1}^{3} p_m^2 \lambda_j \left(A_{mj}\frac{\sinh \lambda_j\mu_m\eta}{\cosh \dfrac{\lambda_j\mu_m}{2}} + B_{mj}\frac{\cosh \lambda_j\mu_m\eta}{\sinh \dfrac{\lambda_j\mu_m}{2}} \right)\sin p_m\zeta \qquad (37)$$

$$\tau_{\zeta\chi} = E_0 - \frac{R_{16}}{R_{66}}RC_0\eta + \sum_{m=1}^{\infty}\sum_{j=1}^{3}\lambda_j\mu_m p_m L_j\left(A_{mj}\frac{\cosh \lambda_j\mu_m\eta}{\cosh \dfrac{\lambda_j\mu_m}{2}} + B_{mj}\frac{\sinh \lambda_j\mu_m\eta}{\sinh \dfrac{\lambda_j\mu_m}{2}} \right)\cos p_m\zeta (38)$$

$$\tau_{\chi\eta} = -D_0 + \sum_{m=1}^{\infty}\sum_{j=1}^{3} p_m^2 L_j\left(A_{mj}\frac{\sinh \lambda_j\mu_m\eta}{\cosh \dfrac{\lambda_j\mu_m}{2}} + B_{mj}\frac{\cosh \lambda_j\mu_m\eta}{\sinh \dfrac{\lambda_j\mu_m}{2}} \right)\sin p_m\zeta \qquad (39)$$

3.2.4 Displacements

Since this is a stress formulation, the corresponding displacement field is found by integrating the strains.

$$u(x,z) = \int \varepsilon_x dx + u_0(z)$$

$$v(x,z) = \int \gamma_{xy} dx + v_0(z) \qquad (40)$$

$$w(x,z) = \int \varepsilon_z dz + w_0(x)$$

By expressing the strains in terms of the nondimensional stresses, the equations for the nondimensional displacement components are obtained as follows:

$$\bar{u}(\xi, \eta) = \int^{\xi} \left(\bar{R}_{11} RS\sigma_\xi + \frac{\bar{R}_{13}}{\beta} \sigma_\eta + \bar{R}_{16} R\tau_{\xi\chi} \right) d\xi + u_o(\eta) \tag{41}$$

$$\bar{v}(\xi, \eta) = \int^{\xi} \left(\bar{R}_{16} RS\sigma_\xi + \frac{\bar{R}_{36}}{\beta} \sigma_\eta + \bar{R}_{66} R\tau_{\xi\chi} \right) d\xi + v_o(\eta) \tag{42}$$

$$\bar{w}(\xi, \eta) = \int^{\xi} \left(\bar{R}_{13} S\sigma_\xi + \frac{\bar{R}_{33}}{R\beta} \sigma_\eta + \bar{R}_{36} \tau_{\xi\chi} \right) d\eta + w_o(\xi) \tag{43}$$

where

$$\bar{u} = \frac{E_2 b}{P} u \quad \bar{v} = \frac{E_2 b}{P} v \quad \bar{w} = \frac{E_2 b}{P} w \quad \bar{R}_{ij} = R_{ij} E_2 \tag{44}$$

The unknown functions of integration in equations (41), (42), and (43) are determined in the following manner. The function $u_o(\eta)$ is determined from the symmetry condition on the x-displacement component about the midspan of the beam, i.e.,

$$\bar{u}(\tfrac{1}{2}, \eta) = 0 \tag{45}$$

The functions $v_o(\eta)$ and $w_o(\xi)$ are determined by requiring that the displacements be compatible with the following constitutive relationships.

$$\frac{\partial w}{\partial x} + \frac{\partial u}{\partial z} = \gamma_{xz} = R_{45}\tau_{yz} + R_{55}\tau_{xz} \tag{46}$$

$$\frac{\partial v}{\partial z} = \gamma_{yz} = R_{44}\tau_{yz} + R_{45}\tau_{xz} \tag{47}$$

Note that the expression for the out-of-plane displacement component, v, given by equation (42), was obtained by integrating the shear strain γ_{xy} along the length of the beam. Satisfying equations (46) and (47) produces two constants of integration. The constant obtained from integrating equation (46) with respect to x is solved for by using the rigid support condition, i.e.,

$$\overline{w}\left(\frac{c}{L}, -\tfrac{1}{2}\right) = 0 \tag{48}$$

Integrating equation (47) with respect to z produces a constant in the expression for the v displacement component which is a rigid body translation term and is set equal to zero to prevent any rigid body motion in the y-direction. Performing the integrations and satisfying the above conditions gives the following displacements for a monoclinic layer.

$$\overline{u} = \left[\overline{R}_{11}R^2 B_o + \left(\overline{R}_{11} - \frac{\overline{R}_{16}^2}{\overline{R}_{66}} \right)R^2 C_o \eta + \overline{R}_{13}A_o + \overline{R}_{16}RE_o \right](\zeta - \tfrac{1}{2})$$

$$+ \sum_{m=1}^{\infty}\sum_{j=1}^{3} (\overline{R}_{11}\lambda_j^2 - \overline{R}_{13} + \overline{R}_{16}\lambda_j L_j)\left(A_{mj}\frac{\cosh \lambda_j \mu_m \eta}{\cosh \dfrac{\lambda_j \mu_m}{2}} + B_{mj}\frac{\sinh \lambda_j \mu_m \eta}{\sinh \dfrac{\lambda_j \mu_m}{2}} \right)p_m \sin p_m \zeta \tag{49}$$

$$\overline{v} = \left(\overline{R}_{16}R^2 B_o + \overline{R}_{36}A_o + \overline{R}_{66}RE_o \right)\zeta - \frac{\overline{R}_{44}}{R}D_o \eta$$

$$+ \sum_{m=1}^{\infty}\sum_{j=1}^{3} (\overline{R}_{16}\lambda_j^2 - \overline{R}_{36} + \overline{R}_{66}\lambda_j L_j)\left(A_{mj}\frac{\cosh \lambda_j \mu_m \eta}{\cosh \dfrac{\lambda_j \mu_m}{2}} + B_{mj}\frac{\sinh \lambda_j \mu_m \eta}{\sinh \dfrac{\lambda_j \mu_m}{2}} \right)p_m \sin p_m \zeta \tag{50}$$

$$\bar{w} = \bar{R}_{13}RB_o\eta + \left(\bar{R}_{13} - \frac{\bar{R}_{36}\bar{R}_{16}}{\bar{R}_{66}}\right)RC_o\frac{\eta^2}{2} + \left(\bar{R}_{11} - \frac{\bar{R}_{16}^2}{\bar{R}_{66}}\right)R^3\frac{C_o}{2}(\xi - \xi^2)$$

$$+ \frac{\bar{R}_{33}}{R}A_o\eta + \bar{R}_{36}E_o\eta - \bar{R}_{45}D_o\xi + G_o \tag{51}$$

$$+ \sum_{m=1}^{\infty}\sum_{j=1}^{3}\left(\bar{R}_{13}\lambda_j - \frac{\bar{R}_{33}}{\lambda_j} + \bar{R}_{36}L_j\right)\left(A_{mj}\frac{\sinh \lambda_j\mu_m\eta}{\cosh \dfrac{\lambda_j\mu_m}{2}} + B_{mj}\frac{\cosh \lambda_j\mu_m\eta}{\sinh \dfrac{\lambda_j\mu_m}{2}}\right)p_m\cos p_m\xi$$

where

$$G_o = \bar{R}_{13}R\frac{B_o}{2} - \left(\bar{R}_{13} - \frac{\bar{R}_{36}\bar{R}_{16}}{\bar{R}_{66}}\right)R\frac{C_o}{8} + \left(\bar{R}_{11} - \frac{\bar{R}_{16}^2}{\bar{R}_{66}}\right)R^3\frac{C_o}{2}(\delta_2^2 - \delta_2)$$

$$+ \frac{\bar{R}_{33}}{R}\frac{A_o}{2} + \bar{R}_{36}\frac{E_o}{2} + \bar{R}_{45}D_o\delta_2 \tag{52}$$

$$+ \sum_{m=1}^{\infty}\sum_{j=1}^{3}\left(\bar{R}_{13}\lambda_j - \frac{\bar{R}_{33}}{\lambda_j} + \bar{R}_{36}L_j\right)\left(A_{mj}\tanh \frac{\lambda_j\mu_m}{2} - B_{mj}\coth \frac{\lambda_j\mu_m}{2}\right)p_m\cos p_m\delta_2$$

3.3 Solution for Orthotropic Layers

3.3.1 Governing Differential Equations

For orthotropic, transversely isotropic, and isotropic layers the solutions for the stresses and displacements are obtained in exactly the same manner outlined above with two noteworthy exceptions. The stress functions become uncoupled and in the case of transversely-isotropic and isotropic layers, the characteristic equation has repeated roots. The out-of-plane shear stress components are now uncoupled from the in-plane strain components as a result of the

planes of material symmetry associated with these layers. Considering a state of generalized plane deformation in the xz-plane, the constitutive relationships can be written as:

$$\left\{ \begin{matrix} \epsilon_x \\ \epsilon_z \\ \gamma_{xz} \end{matrix} \right\} = \left[\begin{matrix} R_{11} & R_{13} & 0 \\ R_{13} & R_{33} & 0 \\ 0 & 0 & R_{55} \end{matrix} \right] \left\{ \begin{matrix} \sigma_{xx} \\ \sigma_{zz} \\ \tau_{xz} \end{matrix} \right\} \tag{53}$$

$$\left\{ \begin{matrix} \gamma_{yz} \\ \gamma_{xy} \end{matrix} \right\} = \left[\begin{matrix} R_{44} & 0 \\ 0 & R_{66} \end{matrix} \right] \left\{ \begin{matrix} \tau_{yz} \\ \tau_{xy} \end{matrix} \right\} \tag{54}$$

where R_{ij} are the reduced plane strain compliance terms, defined as follows:

$$R_{ij} = \overline{S}_{ij} - \frac{\overline{S}_{i2}\overline{S}_{j2}}{\overline{S}_{22}} \qquad i,j = 1,3$$
$$R_{44} = \overline{S}_{44} \tag{55}$$
$$R_{55} = \overline{S}_{55}$$
$$R_{66} = \overline{S}_{66}$$

Again for the case of plane stress in the xz-plane the R_{ij} are replaced by $\overline{S}_{ij}$, the transformed compliance terms.

Following the same procedure as for the monoclinic layers, the two compatibility equations which need to be satisfied result in two uncoupled partial differential equations in terms of the stress functions.

$$L_4\Phi = 0$$
$$L_2\Psi = 0 \tag{56}$$

3.3.2 Solution for Stress Functions

The corresponding characteristic equations are:

$$R_{11}\lambda^4 - (2R_{13} + R_{55})\lambda^2 + R_{33} = 0 \qquad (57)$$

$$R_{66}\lambda^2 - R_{44} = 0 \qquad (58)$$

For an orthotropic layer, the roots to these equations are:

$$\lambda_{1,2}^2 = \frac{(2R_{13} + R_{55}) \pm \sqrt{(2R_{13} + R_{55})^2 - 4R_{11}R_{33}}}{2R_{11}}$$

$$\lambda_3^2 = \frac{R_{44}}{R_{66}} \qquad (59)$$

The expressions for the stress functions can now be written as:

$$\Phi(\xi, \eta) = \frac{A_o}{2}\xi^2 + \frac{B_o}{2}\eta^2 + \frac{C_o}{6}\eta^3 + \sum_{m=1}^{\infty} g_m(\eta) \cos p_m\xi \qquad (60)$$

$$\Psi(\xi, \eta) = D_o\xi + E_o\eta + \sum_{m=1}^{\infty} h_m(\eta) \cos p_m\xi \qquad (61)$$

where the constant F_o appearing in equation (29) is now zero and

$$g_m(\eta) = \sum_{j=1}^{2}\left(A_{mj} \frac{\cosh \lambda_j\mu_m\eta}{\cosh \frac{\lambda_j\mu_m}{2}} + B_{mj} \frac{\sinh \lambda_j\mu_m\eta}{\sinh \frac{\lambda_j\mu_m}{2}} \right) \qquad (62)$$

$$h_m(\eta) = A_{m3} \frac{\cosh \lambda_3 \mu_m \eta}{\cosh \dfrac{\lambda_3 \mu_m}{2}} + B_{m3} \frac{\sinh \lambda_3 \mu_m \eta}{\sinh \dfrac{\lambda_3 \mu_m}{2}} \tag{63}$$

3.3.3 Stresses

Substituting equations (60) and (61) into equation (11) gives the expressions for the in-plane stress components; σ_ξ, σ_η, and $\tau_{\xi\eta}$, which are the same as for a monoclinic layer but with the summation on j being from 1 to 2. The out-of-plane shear stresses for an orthotropic layer are:

$$\tau_{\xi\chi} = E_o + \sum_{m=1}^{\infty} \lambda_3 \mu_m \left(A_{m3} \frac{\sinh \lambda_3 \mu_m \eta}{\cosh \dfrac{\lambda_3 \mu_m}{2}} + B_{m3} \frac{\cosh \lambda_3 \mu_m \eta}{\sinh \dfrac{\lambda_3 \mu_m}{2}} \right) \cos p_m \xi \tag{64}$$

$$\tau_{\chi\eta} = -D_o + \sum_{m=1}^{\infty} p_m \left(A_{m3} \frac{\cosh \lambda_3 \mu_m \eta}{\cosh \dfrac{\lambda_3 \mu_m}{2}} + B_{m3} \frac{\sinh \lambda_3 \mu_m \eta}{\sinh \dfrac{\lambda_3 \mu_m}{2}} \right) \sin p_m \xi \tag{65}$$

For transversely isotropic or isotropic layers in the xz-plane, $\bar{S}_{11} = \bar{S}_{33}$, $\bar{S}_{12} = \bar{S}_{23}$, $\bar{S}_{44} = \bar{S}_{66}$, and $\bar{S}_{55} = 2(\bar{S}_{11} - \bar{S}_{13})$, which results in the following equality:

$$(2R_{13} + R_{55})^2 - 4R_{11}^2 = 0 \tag{66}$$

Therefore, the characteristic equation in equation (57) will have repeated roots and the solution for the function $g_m(\eta)$ becomes:

$$g_m(\eta) = (A_{m1} + A_{m2}\eta) \frac{\cosh \lambda_1 \mu_m \eta}{\cosh \dfrac{\lambda_1 \mu_m}{2}} + (B_{m1} + B_{m2}\eta) \frac{\sinh \lambda_1 \mu_m \eta}{\sinh \dfrac{\lambda_1 \mu_m}{2}} \tag{67}$$

where

$$\lambda_1^2 = \frac{2R_{13} + R_{55}}{2R_{11}} \tag{68}$$

The expression for $h_m(\eta)$ is the same as given by equation (63) but with $\lambda_3 = 1$. Note, that for an isotropic layer the root λ_1 will also be equal to 1. The stresses can now be written as:

$$\sigma_\xi = \frac{R}{S} \left\{ B_o + C_o \eta + \sum_{m=1}^{\infty} \lambda_1^2 \mu_m^2 g_m(\eta) \cos p_m \xi \right.$$

$$\left. + 2 \sum_{m=1}^{\infty} \lambda_1 \mu_m \left(A_{m2} \frac{\sinh \lambda_1 \mu_m \eta}{\cosh \dfrac{\lambda_1 \mu_m}{2}} + B_{m2} \frac{\cosh \lambda_1 \mu_m \eta}{\sinh \dfrac{\lambda_1 \mu_m}{2}} \right) \cos p_m \xi \right\} \tag{69}$$

$$\sigma_\eta = \beta \left\{ A_o - \sum_{m=1}^{\infty} p_m^2 g_m(\eta) \cos p_m \xi \right\} \tag{70}$$

$$\tau_{\xi\eta} = \sum_{m=1}^{\infty} \frac{p_m^2 \lambda_1}{R} \left[(A_{m1} + A_{m2}\eta) \frac{\sinh \lambda_1 \mu_m \eta}{\cosh \dfrac{\lambda_1 \mu_m}{2}} + (B_{m1} + B_{m2}\eta) \frac{\cosh \lambda_1 \mu_m \eta}{\sinh \dfrac{\lambda_1 \mu_m}{2}} \right] \sin p_m \xi$$

$$+ \sum_{m=1}^{\infty} p_m \left(A_{m2} \frac{\cosh \lambda_1 \mu_m \eta}{\cosh \dfrac{\lambda_1 \mu_m}{2}} + B_{m2} \frac{\sinh \lambda_1 \mu_m \eta}{\sinh \dfrac{\lambda_1 \mu_m}{2}} \right) \sin p_m \xi \tag{71}$$

and the equations for $\tau_{\zeta\chi}$ and $\tau_{\eta\eta}$ are the same as for an orthotropic layer given by equations (64) and (65).

3.3.4 Displacements

The constitutive relationships in equations (53) and (54) and the strain/displacement equations (3) are used to obtain the following integral expressions for the displacements.

$$\bar{u} = \int \left(\bar{R}_{11} RS\sigma_\xi + \frac{\bar{R}_{13}}{\beta} \sigma_\eta \right) d\xi + u_o(\eta) \tag{72}$$

$$\bar{v} = \int \bar{R}_{66} R\tau_{\xi\chi} d\xi + v_o(\eta) \tag{73}$$

$$\bar{w} = \int \left(\bar{R}_{13} S\sigma_\xi + \frac{\bar{R}_{33}}{R\beta} \sigma_\eta \right) d\eta + w_o(\xi) \tag{74}$$

The functions u_o, v_o, and w_o are found by using equations (45) and (48), but the displacements must now be compatible with:

$$\gamma_{xz} = R_{55}\tau_{xz} \tag{75}$$

$$\gamma_{yz} = R_{44}\tau_{yz} \tag{76}$$

The resulting displacements for an orthotropic layer are:

$$\bar{u} = \left[R^2 \bar{R}_{11}(B_o + C_o \eta) + \bar{R}_{13} A_o \right](\xi - \tfrac{1}{2})$$

$$+ \sum_{m=1}^{\infty} \sum_{j=1}^{2} p_m \left(\bar{R}_{11} \lambda_j^2 - \bar{R}_{13} \right) \left(A_{mj} \frac{\cosh \lambda_j \mu_m \eta}{\cosh \dfrac{\lambda_j \mu_m}{2}} + B_{mj} \frac{\sinh \lambda_j \mu_m \eta}{\sinh \dfrac{\lambda_j \mu_m}{2}} \right) \sin p_m \xi \qquad (77)$$

$$\bar{v} = \bar{R}_{66} R E_o \xi - \frac{\bar{R}_{44}}{R} D_o \eta$$

$$+ \sum_{m=1}^{\infty} \bar{R}_{66} \lambda_3 \left(A_{m3} \frac{\sinh \lambda_3 \mu_m \eta}{\cosh \dfrac{\lambda_3 \mu_m}{2}} + B_{m3} \frac{\cosh \lambda_3 \mu_m \eta}{\sinh \dfrac{\lambda_3 \mu_m}{2}} \right) \sin p_m \xi \qquad (78)$$

$$\bar{w} = \bar{R}_{13} R \left(B_o \eta + C_o \frac{\eta^2}{2} \right) + \frac{\bar{R}_{33}}{R} A_o \eta + R^3 \bar{R}_{11} \frac{C_o}{2} (\xi - \xi^2) + G_o$$

$$+ \sum_{m=1}^{\infty} \sum_{j=1}^{2} p_m \left(\bar{R}_{13} \lambda_j - \frac{\bar{R}_{33}}{\lambda_j} \right) \left(A_{mj} \frac{\sinh \lambda_j \mu_m \eta}{\cosh \dfrac{\lambda_j \mu_m}{2}} + B_{mj} \frac{\cosh \lambda_j \mu_m \eta}{\sinh \dfrac{\lambda_j \mu_m}{2}} \right) \cos p_m \xi \qquad (79)$$

where

$$G_o = \bar{R}_{13} R \left(\frac{B_o}{2} - \frac{C_o}{8} \right) + \frac{\bar{R}_{33}}{R} \frac{A_o}{2} + \bar{R}_{11} R^3 \frac{C_o}{2} (\delta_2^2 - \delta_2)$$

$$+ \sum_{m=1}^{\infty} \sum_{j=1}^{2} p_m \left(\bar{R}_{13} \lambda_j - \frac{\bar{R}_{33}}{\lambda_j} \right) \left(A_{mj} \tanh \frac{\lambda_j \mu_m}{2} - B_{mj} \coth \frac{\lambda_j \mu_m}{2} \right) \cos p_m \delta_2 \qquad (80)$$

The displacements for transversely isotropic and isotropic layers are:

$$\bar{u} = \left[\bar{R}_{11} R^2 (B_o + C_o \eta) + \bar{R}_{13} A_o \right](\xi - \tfrac{1}{2})$$

$$+ \sum_{m=1}^{\infty} \left(\bar{R}_{11} \lambda_1^2 - \bar{R}_{13} \right) g_m(\eta) p_m \sin p_m \xi$$

$$+ 2 \bar{R}_{11} R \sum_{m=1}^{\infty} \lambda_1 \left(A_{m2} \frac{\sinh \lambda_1 \mu_m \eta}{\cosh \dfrac{\lambda_1 \mu_m}{2}} + B_{m2} \frac{\cosh \lambda_1 \mu_m \eta}{\sinh \dfrac{\lambda_1 \mu_m}{2}} \right) \sin p_m \xi \qquad (81)$$

$$\bar{v} = \bar{R}_{44} R E_o \xi - \frac{\bar{R}_{44}}{R} D_o \eta$$

$$+ \sum_{m=1}^{\infty} \bar{R}_{44} \left(A_{m3} \frac{\sinh \lambda_3 \mu_m \eta}{\cosh \frac{\lambda_3 \mu_m}{2}} + B_{m3} \frac{\cosh \lambda_3 \mu_m \eta}{\sinh \frac{\lambda_3 \mu_m}{2}} \right) \sin p_m \xi \qquad (82)$$

$$\bar{w} = \bar{R}_{13} R \left(B_o \eta + C_o \frac{\eta^2}{2} \right) + \frac{\bar{R}_{33}}{R} A_o \eta + R^3 \bar{R}_{11} \frac{C_o}{2} (\xi - \zeta^2) + G_o$$

$$+ \sum_{m=1}^{\infty} p_m \left(\bar{R}_{13} \lambda_1 - \frac{\bar{R}_{33}}{\lambda_1} \right) \left[(A_{m1} + A_{m2}\eta) \frac{\sinh \lambda_1 \mu_m \eta}{\cosh \frac{\lambda_1 \mu_m}{2}} + (B_{m1} + B_{m2}\eta) \frac{\cosh \lambda_1 \mu_m \eta}{\sinh \frac{\lambda_1 \mu_m}{2}} \right] \cos p_m \xi \qquad (83)$$

$$+ R \sum_{m=1}^{\infty} \left(\bar{R}_{13} + \frac{\bar{R}_{33}}{\lambda_1^2} \right) \left(A_{m2} \frac{\cosh \lambda_1 \mu_m \eta}{\cosh \frac{\lambda_1 \mu_m}{2}} + B_{m2} \frac{\sinh \lambda_1 \mu_m \eta}{\sinh \frac{\lambda_1 \mu_m}{2}} \right) \cos p_m \xi$$

where

$$G_o = \bar{R}_{13} R \left(\frac{B_o}{2} - \frac{C_o}{8} \right) + \frac{\bar{R}_{33}}{R} \frac{A_o}{2} + R^3 \bar{R}_{11} \frac{C_o}{2} (\delta_2^2 - \delta_2)$$

$$+ R \sum_{m=1}^{\infty} \left(\bar{R}_{13} + \frac{\bar{R}_{33}}{\lambda_1^2} \right) (B_{m2} - A_{m2}) \cos p_m \delta_2 \qquad (84)$$

$$+ \sum_{m=1}^{\infty} p_m \left(\bar{R}_{13} \lambda_1 - \frac{\bar{R}_{33}}{\lambda_1} \right) \left[\left(A_{m1} - \frac{A_{m2}}{2} \right) \tanh \frac{\lambda_1 \mu_m}{2} - \left(B_{m1} - \frac{B_{m2}}{2} \right) \coth \frac{\lambda_1 \mu_m}{2} \right] \cos p_m \delta_2$$

The above expressions for the in-plane stresses and displacements in orthotropic, transversely-isotropic, and isotropic layers are identical to the expressions obtained if the following plane strain assumptions are made:

$$\varepsilon_y = \gamma_{xy} = \gamma_{yz} = 0 \qquad (85)$$

Then the out-of-plane displacement, v, and the two out-of-plane shear stress components, τ_{xy} and τ_{yz}, become zero and only one stress function is required in the formulation. Also, if the

coupling terms in the generalized plane deformation analysis for a monoclinic layer are assumed to be small, i.e., neglecting shear coupling effects, then the above orthotropic solution becomes an approximate solution which assumes plane strain conditions for an off-axis ply. In this case, the out-of-plane shear stresses are nonzero and are expressed in terms of the in-plane stress components using equation (8), i.e.,

$$\tau_{yz} = -\frac{R_{45}}{R_{44}}\tau_{xz}$$
$$\tau_{xy} = -\frac{R_{16}\sigma_{xx} + R_{36}\sigma_{zz}}{R_{66}}$$

(86)

3.4 Solution for Laminated Beam

3.4.1 Determination of Unknown Constants

For a laminated beam containing N layers, the previously derived solutions for the stresses and displacements are applied to each individual layer. For the kth layer, the six unknown coefficients, $A_{mj}^{(k)}$ and $B_{mj}^{(k)}$ in equations (28), (62), (63), and (67) are determined from the boundary conditions on the top and bottom surfaces and from the continuity of stresses and displacements at the interfaces. The applied tractions acting on the top surface and at the two supports satisfy global equilibrium and are initially assumed to be uniformly distributed over a distance d and expanded into an infinite series as follows (see Figure 4):

$$f_i(\xi) = -\frac{2P}{bd}\left(\frac{\beta}{2} + 2\sum_{m=1}^{\infty}\frac{1}{p_m}\sin\frac{p_m\beta}{2}\cos p_m\delta_i \cos p_m\xi\right) \quad i = 1,2$$

(87)

where $\delta_1 = \frac{1}{2}$ for three-point bending and $\delta_2 = \frac{c}{L}$, and where i equals 1 and 2 for the top and bottom surfaces, respectively.

The boundary conditions are:

$$\sigma_\eta^{(1)}(\xi, \frac{1}{2}) = \frac{bd}{P} f_1(\xi) \tag{88}$$

$$\sigma_\eta^{(N)}(\xi, -\frac{1}{2}) = \frac{bd}{P} f_2(\xi) \tag{89}$$

$$\tau_{\xi\eta}^{(1)}(\xi, \frac{1}{2}) = 0 \tag{90}$$

$$\tau_{\xi\eta}^{(N)}(\xi, -\frac{1}{2}) = 0 \tag{91}$$

$$\tau_{\chi\eta}^{(1)}(\xi, \frac{1}{2}) = 0 \tag{92}$$

$$\tau_{\chi\eta}^{(N)}(\xi, -\frac{1}{2}) = 0 \tag{93}$$

The interfacial continuity conditions are:

$$\sigma_\eta^{(k)}(\xi, -\frac{1}{2}) = \sigma_\eta^{(k+1)}(\xi, \frac{1}{2}) \tag{94}$$

$$\tau_{\xi\eta}^{(k)}(\xi, -\frac{1}{2}) = \tau_{\xi\eta}^{(k+1)}(\xi, \frac{1}{2}) \tag{95}$$

$$\tau_{\chi\eta}^{(k)}(\xi, -\frac{1}{2}) = \tau_{\chi\eta}^{(k+1)}(\xi, \frac{1}{2}) \tag{96}$$

$$\bar{u}^{(k)}(\xi, -\frac{1}{2}) = \bar{u}^{(k+1)}(\xi, \frac{1}{2}) \tag{97}$$

$$\bar{v}^{(k)}(\xi, -\frac{1}{2}) = \bar{v}^{(k+1)}(\xi, \frac{1}{2}) \tag{98}$$

$$\bar{w}^{(k)}(\xi, -\frac{1}{2}) = \bar{w}^{(k+1)}(\xi, \frac{1}{2}) \tag{99}$$

Applying these condtions results in a 6N x 6N system of linear algebraic equations, corresponding to the infinite series part of the expressions, which is solved for the 6N unknown constants. The nonseries terms in these conditions result in:

$$A_o^{(k)} = -1.0 \tag{100}$$

$$D_o^{(k)} = 0.0 \tag{101}$$

for k = 1 to N and in a (4N - 1) x (4N - 1) system of linear algebraic equations in terms of $B_o^{(k)}$, $C_o^{(k)}$, $E_o^{(k)}$, and $G_o^{(k)}$ (the constant of integration obtained when integrating ε_z for k $\neq$ N). There are 4N unknowns yet to be determined, therefore four more equations are needed. Three equations are obtained by applying the traction free end-face boundary conditons at ζ = 0 or 1. Due to the symmetry of the problem only ζ = 0 is considered. These conditions are approximately satisfied by requiring that the resultant normal force, resultant shear force, and resultant moment vanish in the integral sense and not pointwise, i.e.,

$$\sum_{k=1}^{N} \int_{-\frac{1}{2}}^{\frac{1}{2}} \sigma_{\zeta}^{(k)}(0, \eta) d\eta = 0 \tag{102}$$

$$\sum_{k=1}^{N} \int_{-\frac{1}{2}}^{\frac{1}{2}} \tau_{\zeta\chi}^{(k)}(0, \eta) d\eta = 0 \tag{103}$$

$$\sum_{k=1}^{N} \int_{-\frac{1}{2}}^{\frac{1}{2}} \sigma_{\zeta}^{(k)}(0, \eta)(\eta + \bar{\eta}^{(k)}) d\eta = 0 \tag{104}$$

Analytical Procedure

where $\bar{\eta}^{(k)}$ is the nondimensional distance measured from the midplane of the beam to the center of the kth ply (see Figure 5). Performing the integration results in:

$$\sum_{k=1}^{N} \left(B_o^{(k)} + 2 \sum_{m=1}^{M} \bar{B}_m^{(k)} \right) = 0 \tag{105}$$

$$\sum_{k=1}^{N} \left(E_o^{(k)} + 2 \sum_{m=1}^{M} \bar{E}_m^{(k)} \right) = 0 \tag{106}$$

$$\sum_{k=1}^{N} \left(C_o^{(k)} + 12 \sum_{m=1}^{M} \bar{C}_m^{(k)} + 12 \bar{\eta}^{(k)} B_o^{(k)} + 24 \bar{\eta}^{(k)} \sum_{m=1}^{M} \bar{B}_m^{(k)} \right) = 0 \tag{107}$$

where, for a monoclinic layer:

$$\bar{B}_m^{(k)} = \sum_{j=1}^{3} \lambda_j^{(k)} \mu_m^{(k)} A_{mj}^{(k)} \tanh \frac{\lambda_j^{(k)} \mu_m^{(k)}}{2} \tag{108}$$

$$\bar{E}_m^{(k)} = \sum_{j=1}^{3} p_m L_j^{(k)} A_{mj}^{(k)} \tanh \frac{\lambda_j^{(k)} \mu_m^{(k)}}{2} \tag{109}$$

$$\overline{C}_m^{(k)} = \sum_{j=1}^{3} B_{mj}^{(k)} \left(\lambda_j^{(k)} \mu_m^{(k)} \coth \frac{\lambda_j^{(k)} \mu_m^{(k)}}{2} - 2 \right) \tag{110}$$

For an orthotropic layer, $\overline{B}_m^{(k)}$ and $\overline{C}_m^{(k)}$ are the same as the monoclinic case but with the range on the j index being from 1 to 2, and

$$\overline{E}_m^{(k)} = B_{m3}^{(k)} \tag{111}$$

For transversely isotropic and isotropic layers the expressions become:

$$\overline{B}_m^{(k)} = \lambda_1^{(k)} \mu_m^{(k)} A_{m1}^{(k)} \tanh \frac{\lambda_1^{(k)} \mu_m^{(k)}}{2} + \frac{B_{m2}^{(k)}}{2} \left(\lambda_1^{(k)} \mu_m^{(k)} \coth \frac{\lambda_1^{(k)} \mu_m^{(k)}}{2} + 2 \right) \tag{112}$$

$$\overline{C}_m^{(k)} = \lambda_1^{(k)} \mu_m^{(k)} \frac{A_{m2}^{(k)}}{2} \tanh \frac{\lambda_1^{(k)} \mu_m^{(k)}}{2} + B_{m1}^{(k)} \left(\lambda_1^{(k)} \mu_m^{(k)} \coth \frac{\lambda_1^{(k)} \mu_m^{(k)}}{2} - 2 \right) \tag{113}$$

and the value for $\overline{E}_m^{(k)}$ is the same as an orthotropic layer given in equation (111). The last equation is obtained by applying the rigid support condition to the Nth layer. This corresponds to using either equation (52), (80), or (84), depending on the type of layer.

3.4.2 Program Development

A program was written to perform the required numerical calculations in the above solution procedure. The material properties, beam geometry, and ply dimensions are input along with the desired loading. Once the reduced compliances are calculated, the characteristic roots are determined. A check is made to make sure that the material properties are such that real roots are obtained. The 6N x 6N system of linear equations is setup and solved for the 6N
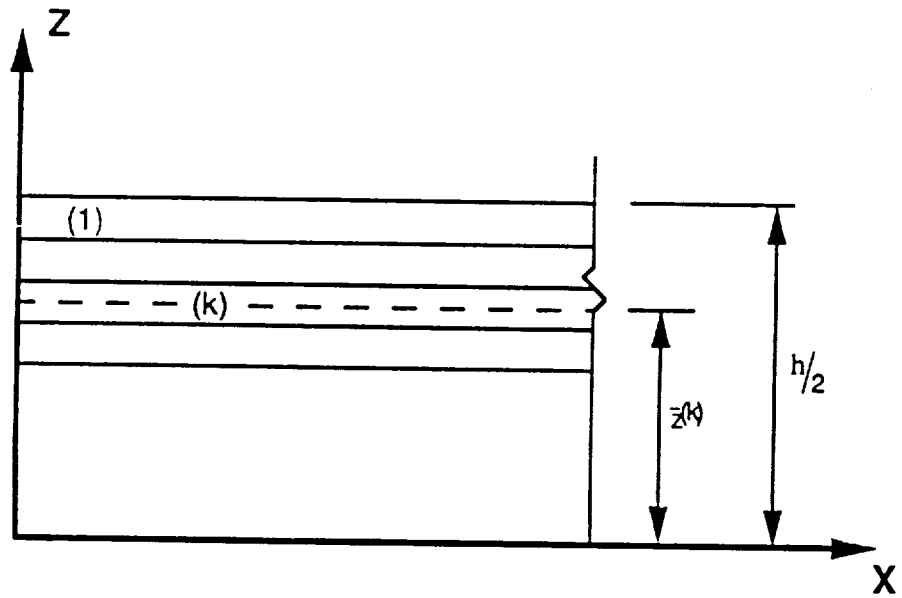
Figure 5.   Local coordinate system.

unknowns using an algorithm for unsymmetric banded coefficient matrices. If M terms are needed in the infinite series for convergence, then this system is solved M times. Convergence was based on the agreement between the applied traction on the top surface and the resulting σ_{zz} stress distribution along this same surface. Figure 6 shows the case for M equal to 50 terms where the applied load is uniformly distributed over a distance d = 0.02 in. and the resulting σ_{zz} distribution has been normalized by the applied stress. This figure demonstrates that more terms are needed in the truncated series as the maximum value of σ_{zz} underestimates the applied value and exhibits an oscillating behavior. In Figure 7, 400 terms were used in the series and a much better correlation with the applied loading is obtained. Similar results were also obtained for the bottom surface tractions at the two support locations. Once these 6N unknowns are resolved the remaining 4N unknowns are found by solving the 4N x 4N system of linear equations. This system only needs to be solved once but does not have the advantage of being assembled into a banded form. The resulting stress distributions and displacement fields in the Cartesian coordinate system are then calculated either through the thickness, along the span, or contours.

Verification of the program was carried out by checking global equilibrium at constant x cross-sections and at constant z cross-sections. This included checking the resulting stresses to see if they satisfied the applied boundary conditions. The solution was also verified to be independent of material properties for an isotropic layer and in addition, the satisfaction of interfacial stress and displacement continuity was checked. Additional confirmation was achieved by comparing the results for an orthotropic beam with the results presented by Whitney [14]. In the case of transversely-isotropic and isotropic layers, and for the generalized plane deformation state in off-axis plies, the results were compared with an infinite beam solution derived on the basis of the infinite Fourier transform technique [20]. In each of these comparisons extremely good correlation was demonstrated.
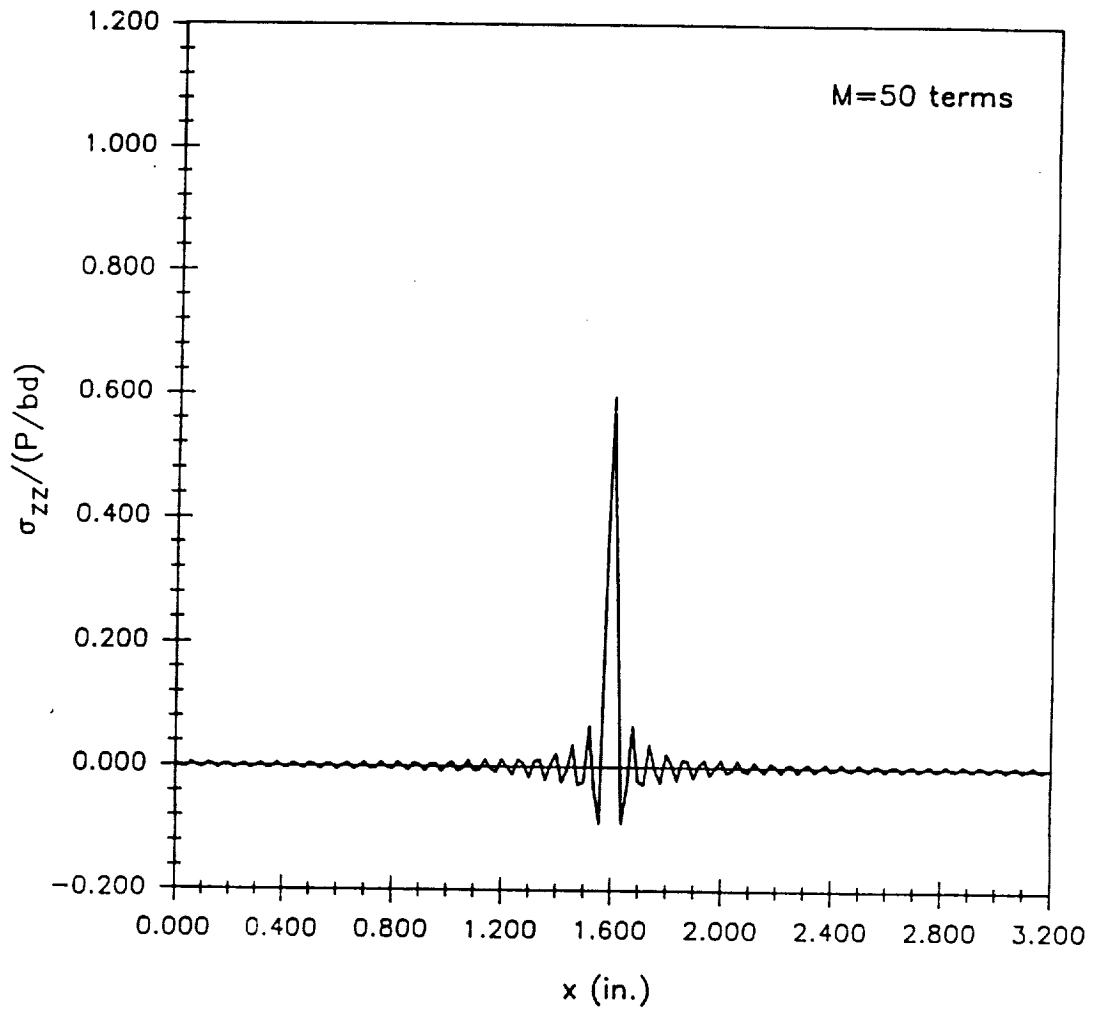
Figure 6. Fourier series representation of uniform load (M=50 terms).
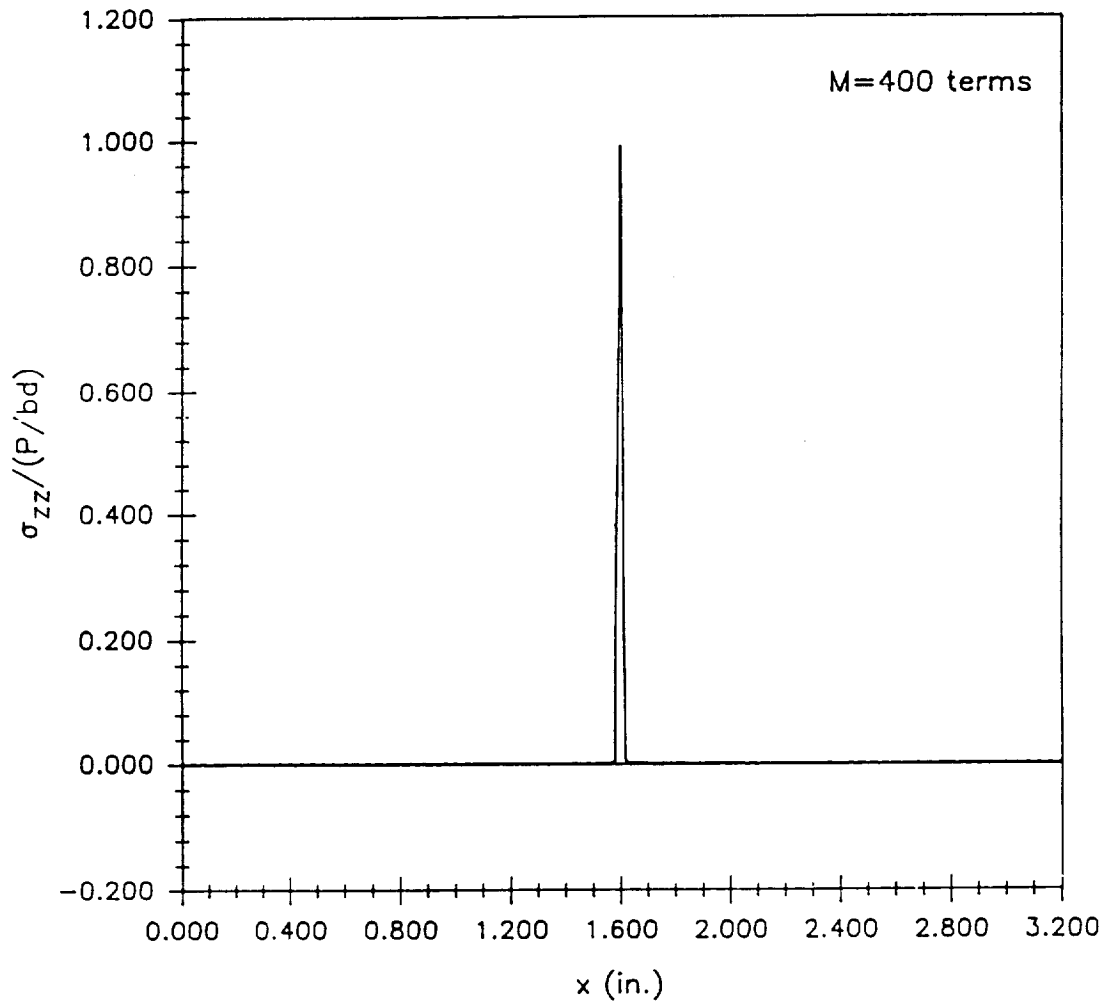
Figure 7. Fourier series representation of uniform load (M=400 terms).

Chapter IV

Preliminary Analytical Results

4.1 Introduction

In order to ascertain the dependence of the local or sublaminae stress states on the beam geometry, support conditions, and external tractions, the solution procedure developed in Chapter 3 was applied to various laminated and unidirectional three-point bend specimens. The principal specimen parameters studied were the fiber orientation, stacking sequence, distance between the supports, and the type of external loading expressed in terms of the boundary conditions. The effect of shear coupling resulting from the presence of off-axis layers on the local stress state was also determined. As mentioned previously in the derivation, the type of laminae can be either isotropic, transversely-isotropic in the xz-plane (see Figure 4), orthotropic, or monoclinic, i.e., an off-axis ply in the xy-plane. The stacking sequence can include any combination of these and be either interspersed or grouped. Layers which have fibers oriented parallel to the x-axis, i.e., 0°, are orthotropic. A transversely-isotropic layer is characterized by fibers running parallel to the y-axis, i.e., 90°. The distance between the

supports is associated with the amount of beam overhang and also defines an aspect ratio as the span length divided by the overall heigth of the beam, i.e., a/h.

In the development of the elasticity solution, a laminated beam subjected to three-point bending was modelled by specifying applied tractions at the two support points which, along with the loading on the top surface and the traction free end-face conditions, satisfied global equilibrium. In the investigation of shear coupling effects, beams with no overhang are studied and the analytical results from the elasticity solution are compared with Pagano's [23] solution for cylindrical bending. In the cylindrical bending problem, the boundary conditions for three-point bending are approximated and the resultant shear stress distributions on the end faces of the beam maintain global equilibrium with the applied loading. The consequences of expressing the boundary conditions in these two different ways is addressed.

4.2 Preliminary Analyses

4.2.1 Through the Thickness Distributions

The initial numerical calculations which employed the elasticity solution showed how the different in-plane stress components varied through the thickness of a unidirectional $0°$ beam. The material system used for this analysis was AS4/3501-6 Graphite/Epoxy. The material properties in the principal material directions were:

$$E_1 = 21.0\ MSI$$
$$E_2 = 1.5\ MSI$$
$$E_3 = 1.5\ MSI$$
$$G_{12} = 0.8\ MSI$$
$$G_{13} = 0.8\ MSI$$
$$G_{23} = 0.4\ MSI$$
$$\nu_{12} = 0.3$$
$$\nu_{13} = 0.3$$
$$\nu_{23} = 0.55$$

The beam had an overall length of $L=3.2$ inches and a height of $h=0.16$ inches. The applied tractions on the top surface and at the supports were assumed to be uniformly distributed over a small finite distance d which was taken to be equal to 0.02 in.. This was the same value used by Whitney in his results using an elasticity solution for an orthotropic beam [14]. Distributions for the bending stress, σ_{xx}, normalized by the applied stress, for four different aspect ratios: $a/h = 20.0$, 10.0, 1.0, and 0.5 are shown in Figure 8. These results are for a x-location which corresponds to the termination point of the uniformly distributed load. The maximum compressive and tensile values occur on the top and bottom surfaces, respectively, and are largest for the aspect ratio of 20.0 where bending effects govern the beam's global response. However, the magnitudes of the maximum tensile and compressive stresses are different and the distribution is nonlinear. This differs from the classical beam theory results which predicts a linear distribution and equal magnitudes of maximum compressive and tensile stresses. For the four different aspect ratios considered, the magnitude of the maximum bending stress predicted by the elasticity solution is approximately three times greater than the value obtained from beam theory. However, this is a localized effect and at a sufficient distance away from the concentrated load the classical beam theory results are recovered. For aspect ratios less than or equal to 1.0, the bending stress is approximately zero except for areas located close to the bottom surface and especially the top surface.

The distribution through the thickness of the normal component of stress, σ_{zz}, for the same x-location as in Figure 8, normalized with respect to the applied stress, is presented in Figure
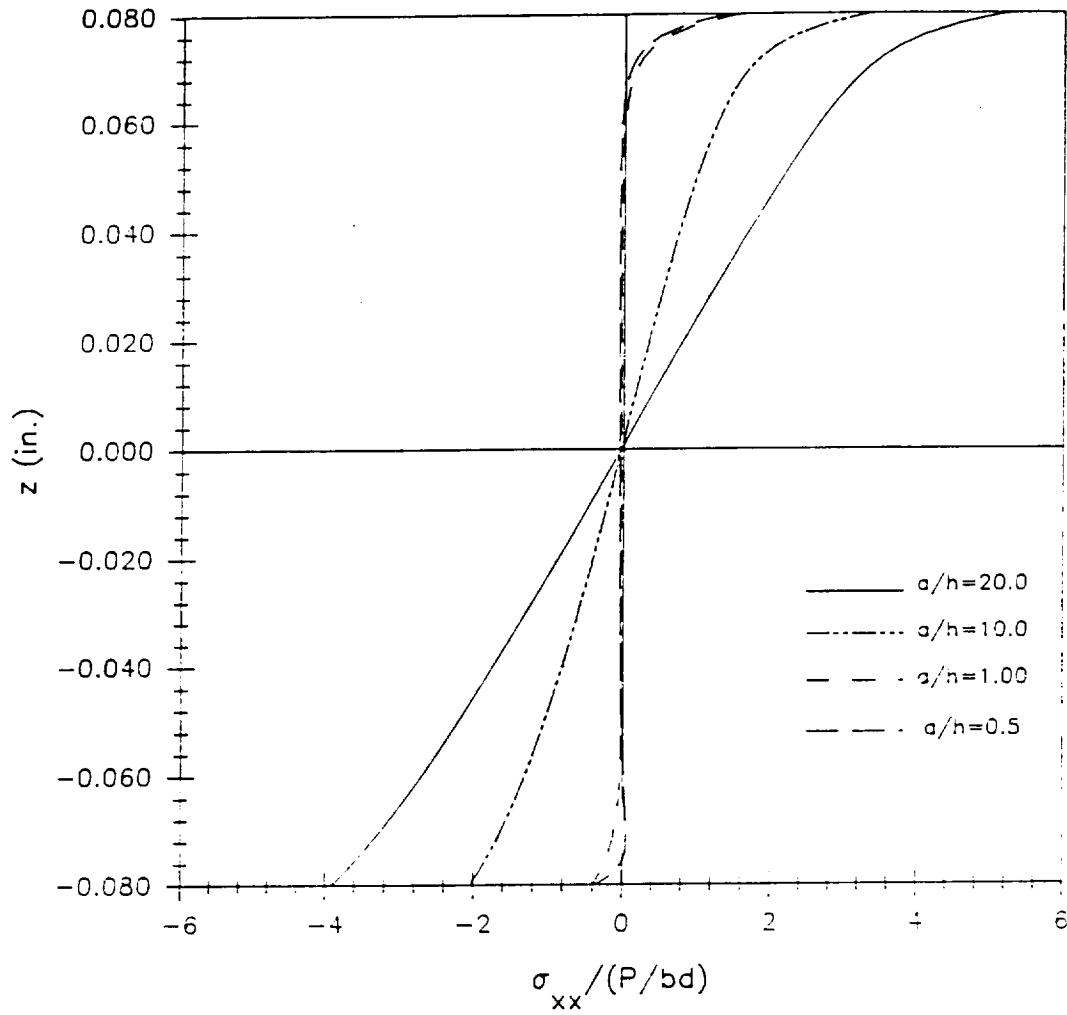
Figure 8.   Distribution of σ_{xx} through the thickness for an orthotropic beam.

9. The maximum value for this stress component occurs at the top surface and when the aspect ratio is less than or equal to 1.0 the effect of the bottom support changes the distribution as seen in Figure 9. The magnitude of the maximum value when normalized by the applied stress is equal to 0.5 at this x-location due to the Fourier series representation of a uniformly distributed load. There is no significant change in the distribution through the thickness until the distance between the supports becomes less than the height of the beam. The shear stress, τ_{xz}, distribution through the thickness, normalized with respect to the applied stress, behaves much in the same fashion as the normal stress σ_{xx} at the given x-location. This is demonstrated in Figure 10, which shows that the maximum value occurs below the top surface and not at the midplane of the laminate as predicted from beam theory. Also, the distribution is not parabolic as classical beam theory results indicate. However, as in the case for the bending stress, the elasticity solution for τ_{xz} coincides with beam theory at a sufficient distance away from the load point and the supports.

4.2.2 Shear Stress Contours

A better illustration of the local stresses in the vicinity of the applied load is needed because stress components in this area vary rapidly in both the x and z directions. This was accomplished by plotting stress contours in the neighborhood of the applied load for different types of beams. Of particular interest was the in-plane shear stress, τ_{xz} , which exhibited a rapid change in magnitude close to the top surface of the beam (see Figure 10). The four types of laminates analyzed were: isotropic, 0° unidirectional, cross-ply, and quasi-isotropic. The overall beam dimensions were the same as used in obtaining the previous results with the span length-to-depth aspect ratio, a/h, being equal to 1.0. Also, the applied tractions were still assumed to be uniformly distributed over a distance d = 0.02 inches. Figure 11 shows the resulting τ_{xz} stress contour for the case of an isotropic beam. The maximum value has a magnitude of 14 psi for a unit applied load and is located at the point of discontinuity in the surface
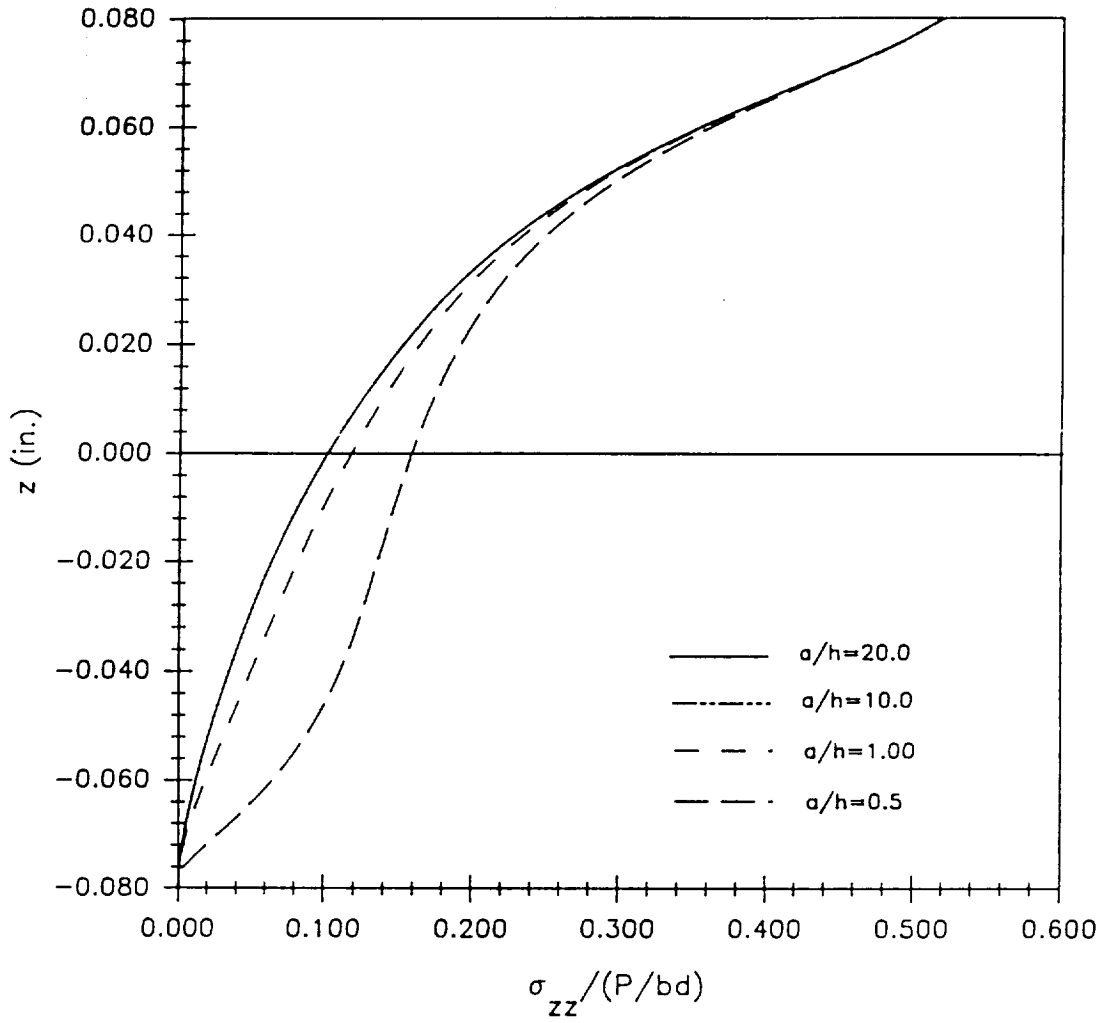
Figure 9. Distribution of σ_{zz} through the thickness for an orthotropic beam.
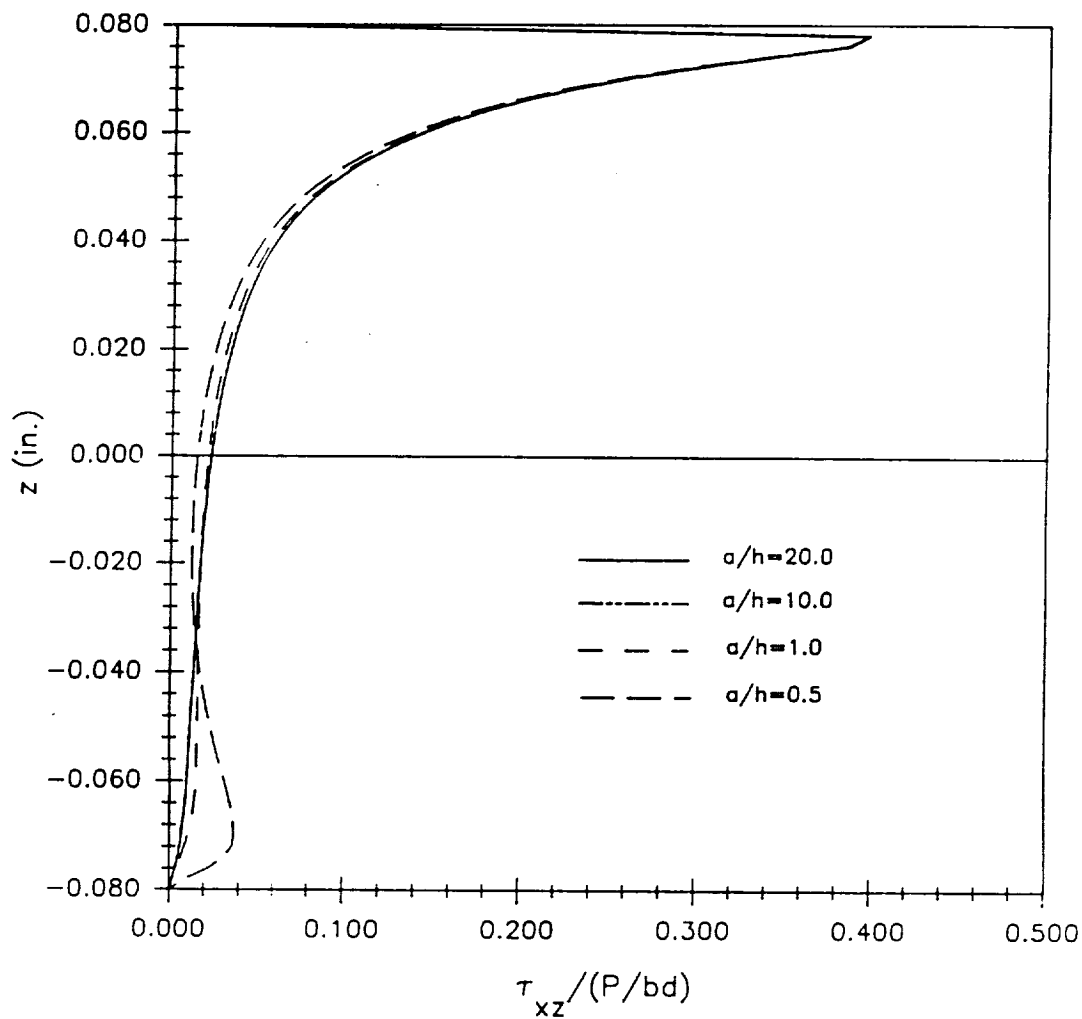
Figure 10. Distribution of τ_{xz} through the thickness for an orthotropic beam.

tractions and just below the top surface. For the same loading conditions, the solution for the 0° unidirectional beam predicts a larger maximum value for the shear stress τ_{xz} and shifts the location of the maximum stress closer towards the upper surface of the beam, as shown in Figure 12. This is in agreement with observed shear failures seen in previously published experimental results [39]. The contour plot in Figure 13 shows the effect of placing a transversely-isotropic, i.e., 90°, ply below a top layer which has a fiber orientation of 0°. In comparison with the unidirectional 0° beam results, the magnitude and location of the maximum shear stress are relatively unaffected. For the case of a quasi-isotropic laminate having a stacking sequence of $[0/\pm45/90]_s$, the magnitude of the maximum shear stress increases slightly up to 20 ksi, as illustrated in Figure 14, but the location remains the same as in the 0° beam.

Another component of stress or, in this case, combination of stresses of concern is the maximum shear stress, τ_{max} in the xz-plane which acts on the plane bisecting the angle between the two principal stresses. Some of the experimental results published in the literature (cf. Reference [5]) have attributed one of the basic failure modes in beams to the location and magnitude of the maximum shear stress. Figure 15 presents the maximum shear stress contour for an isotropic beam which is subjected to a unit load and has an aspect ratio of 1.0. This figure illustrates that the maximum shear stress contour is symmetric about the midspan of the beam and the maximum contour is located approximately 0.01 inches below the top surface. In comparison, Figure 16 shows that for a 0° unidirectional beam having the same geometry and subjected to the same loading, the maximum shear stress occurs on the top surface with very high gradients in the neighborhood of the applied load. Also, the magnitude is almost three times greater in comparison with the results for the isotropic beam. The larger magnitude is associated with the bending component of stress, σ_{xx} , having a much larger value in the 0° composite beam when compared to an isotropic beam subjected to the same loading.
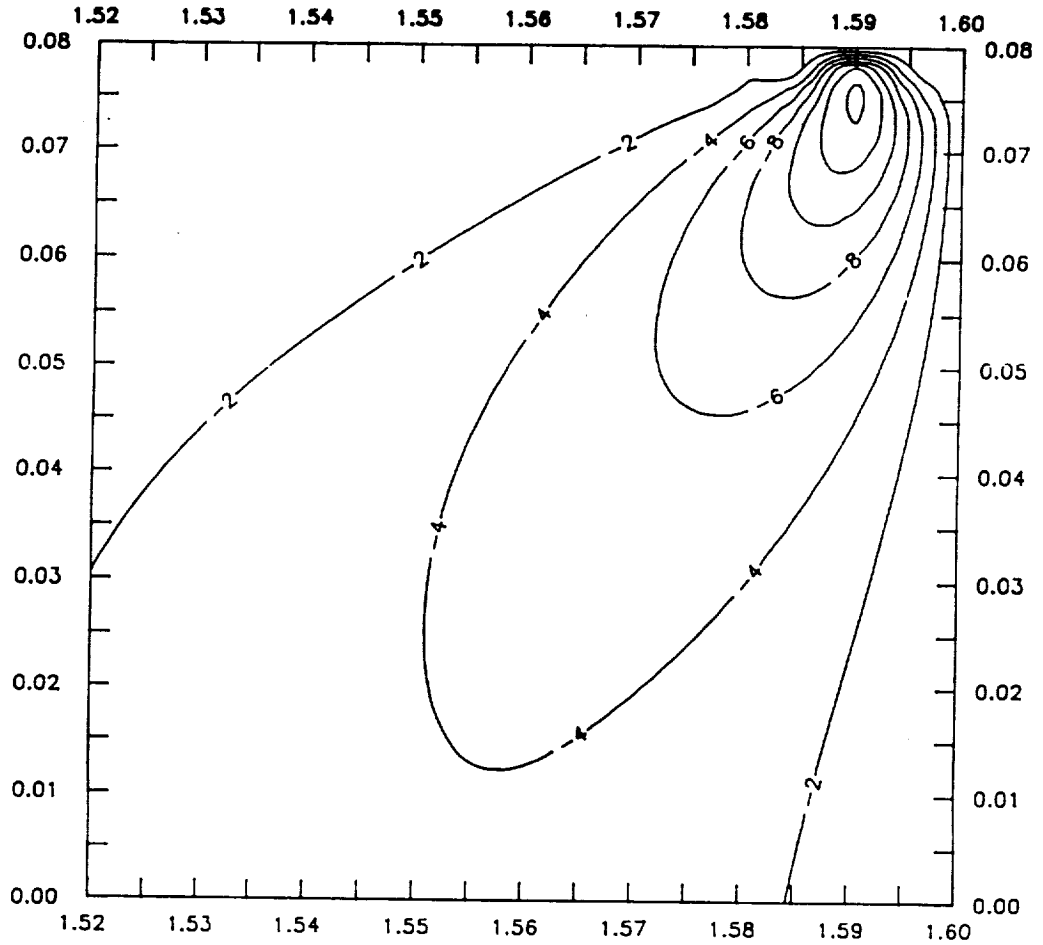
Figure 11. Shear stress contour, τ_{xz} (ksi) for an isotropic beam having an aspect ratio of a/h = 1.0 and subjected to a 1 kip load.
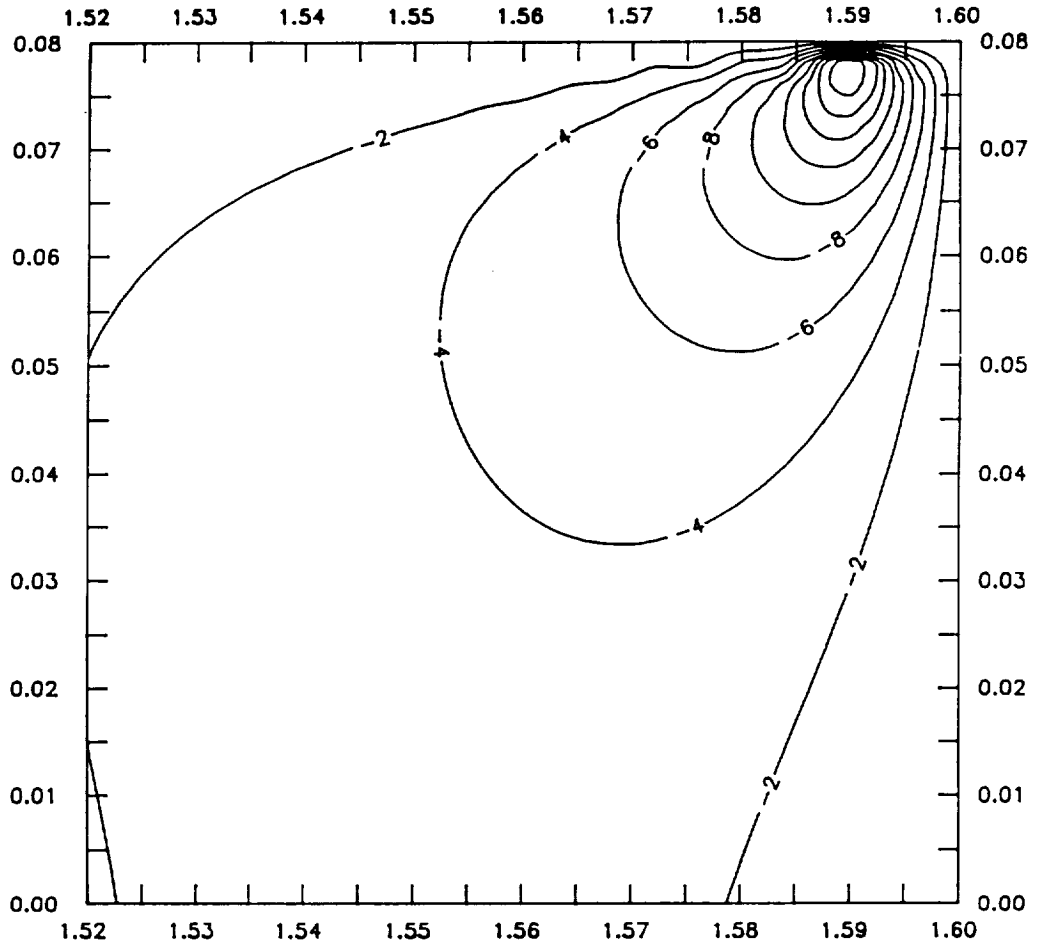
Figure 12. Shear stress contour, τ_{xz} (ksi) for an orthotropic beam having an aspect ratio of $a/h = 1.0$ and subjected to a 1 kip load.
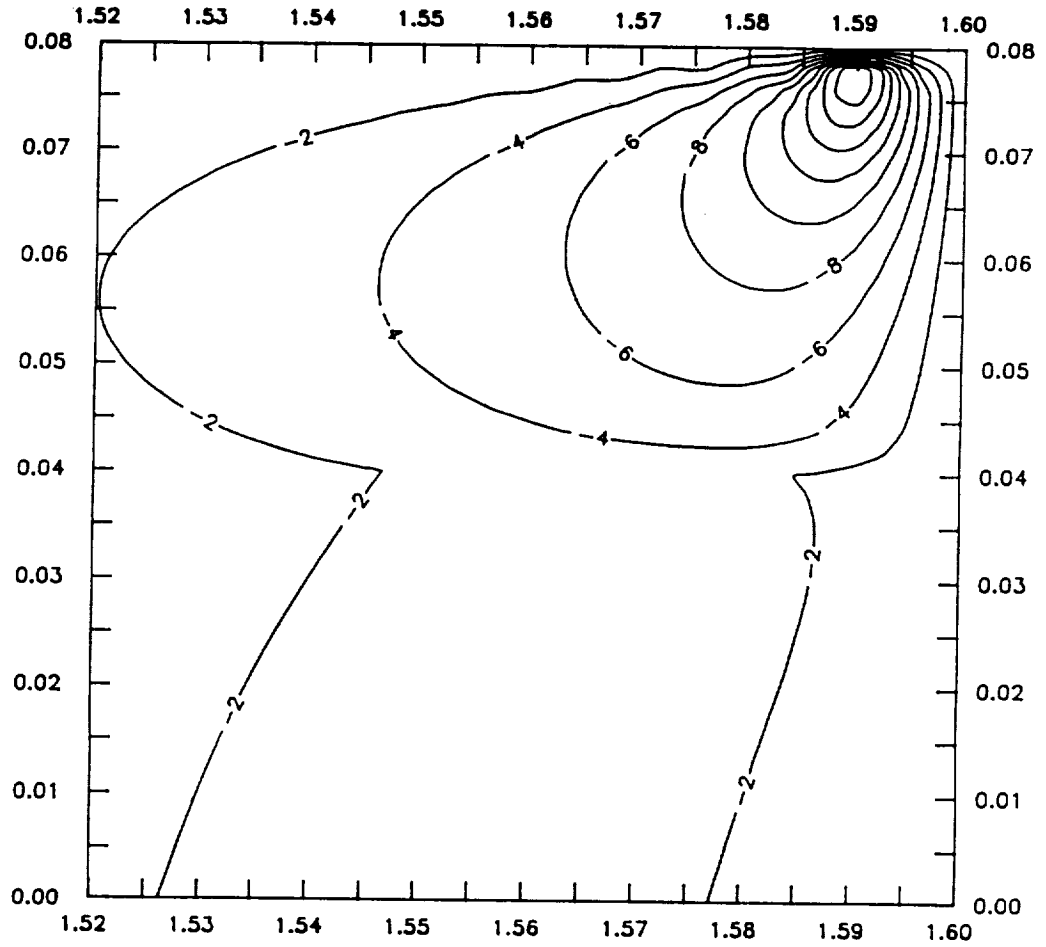
Figure 13. Shear stress contour, τ_{xz} (ksi) for a cross-ply beam having an aspect ratio of a/h = 1.0 and subjected to a 1 kip load.
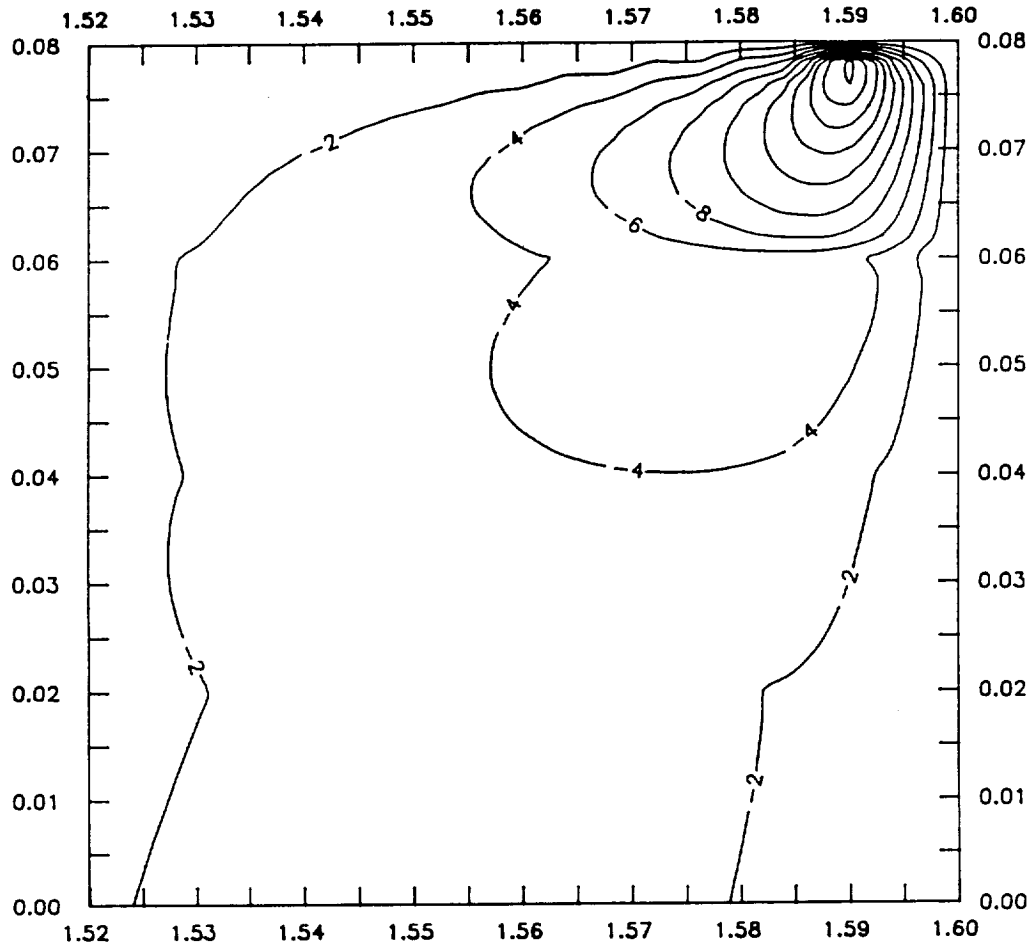
Figure 14.   Shear stress contour, τ_{xz} (ksi) for a quasi-isotropic beam having an aspect ratio of a/h=1.0 and subjected to a 1 kip load.
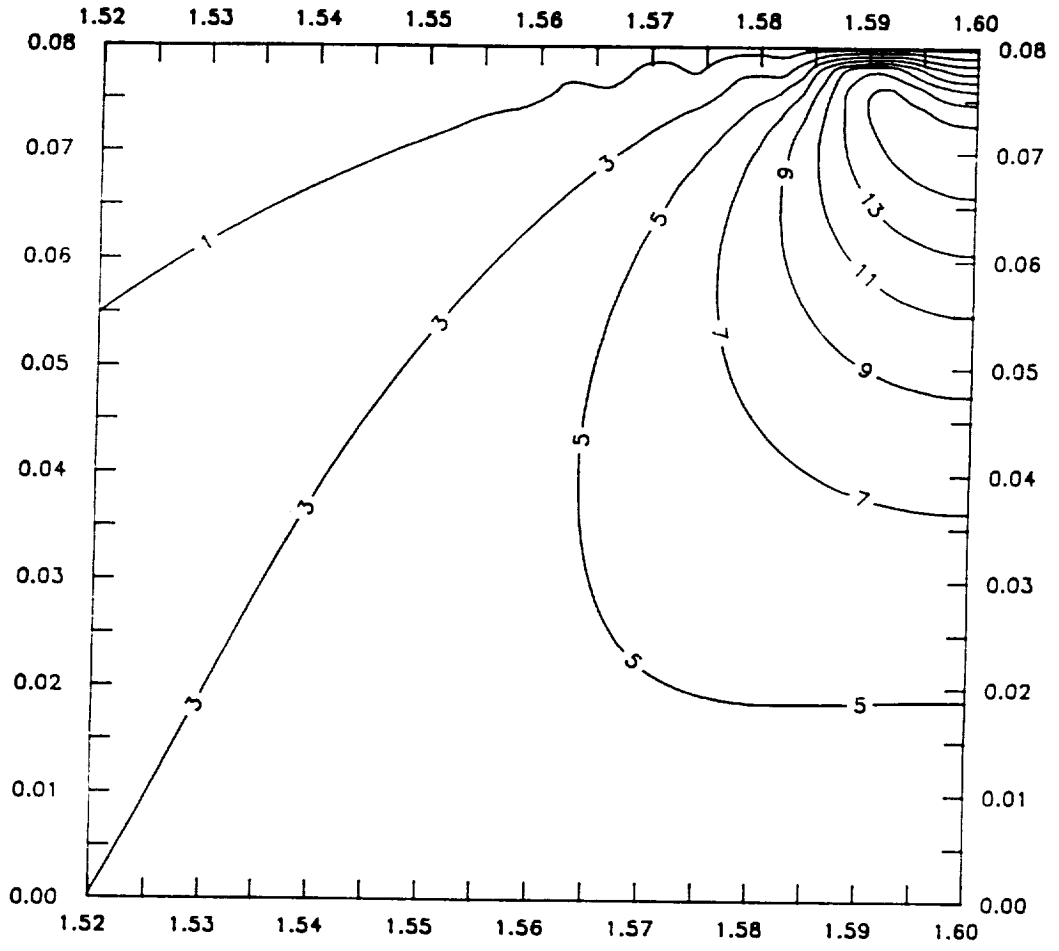
Figure 15. Maximum shear stress contour, τ_{max} (ksi) for an isotropic beam having an aspect ratio of a/h=1.0 and subjected to a 1 kip load.
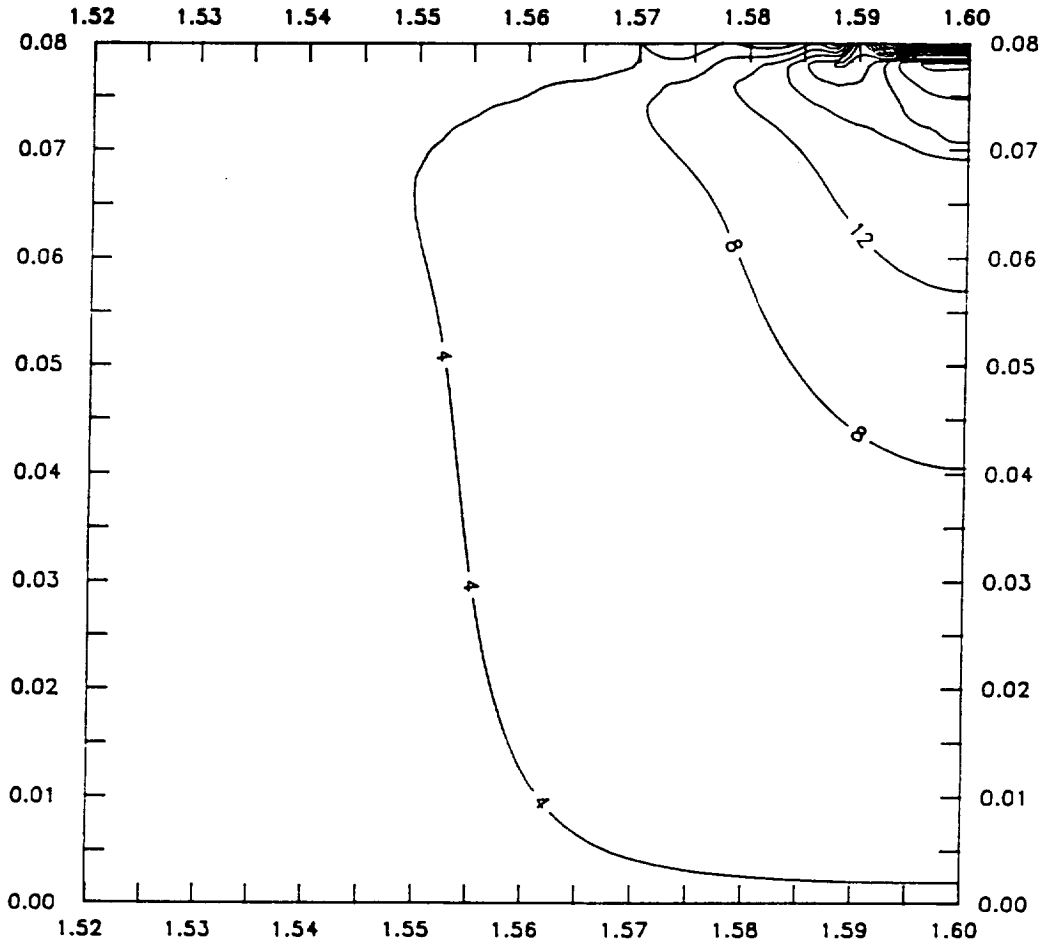
Figure 16. Maximum shear stress contour, τ_{max} (ksi) for an orthotropic beam having an aspect ratio of a/h = 1.0 and subjected to a 1 kip load.

4.3 Shear Coupling Effects

To study the effect of shear coupling on the stress state in a laminated beam under three-point bending, unidirectional beams which had different aspect ratios and different fiber orientations were examined. First, the dependence of different stress components and their corresponding maximum values, and the dependence of the midspan deflection on the beam geometry were investigated for different aspect ratios. The aspect ratios considered for this study ranged from $a/h = 3.125$ up to 18.75. The beams were all unidirectional with no overhang and the applied loading was uniformly distributed over a small finite distance, $d = 0.02$ inches, as in the preceding cases. The analysis was carried out for $0°$, $30°$, $60°$, and $90°$ fiber orientations. Second, the dependence of local stresses and deformations on the fiber orientation of a unidirectional beam were determined. For this part of the analysis the smallest and the largest aspect ratios, $a/h = 3.125$ and $a/h = 18.75$, respectively, were considered. The beam's response was investigated using both the two-dimensional elasticity analysis developed in the present study and by the cylindrical bending analysis discussed by Pagano [23]. As described in the beginning of this chapter, the two approaches apply different boundary conditions to satisfy global equilibrium. The two different analyses were performed in the shear-coupling investigation to study the effect of different end-face boundary conditions on the results. The effect of shear coupling in both of the above investigations was determined by calculating the difference between the results based on plane strain assumptions and the generalized plane deformation results. This was used as the determining factor because the plane strain assumptions neglect the effect of any shear coupling by using an orthotropic solution for the beams having fibers oriented at an off-axis angle.

4.3.1 Beam Deflection

The maximum midplane deflection at the beam's midspan is plotted as a function of aspect ratio in Figure 17 for the four different fiber orientations stated earlier. The deflections have been normalized with respect to the classical beam theory results using the axial Young's modulus of the beam, i.e., E_x. For the off-axis beams, this required rotating the properties in the principal material directions to the Cartesian xyz-coordinate system. Recalling Figure 4, the aspect ratio of the beam is defined as the beam's span length divided by the height, i.e., a/h. Figure 17 illustrates that the results for the generalized plane deformation and plane strain analyses coincide for $0°$ and $90°$ fiber oriented beams. This is because the solution for the two different strain states reduces to the same form in these two particular cases. For the off-axis cases the plane strain analysis predicts larger displacements than the generalized plane deformation solution. One reason the plane strain results are larger is because the out-of-plane shearing strains, i.e., γ_{xy} and γ_{yz}, are assumed to be zero for a state of plane strain. Consequently, a larger portion of the work input to the system is expended for the w deflection, rather than strain energy stored due to the out-of-plane, i.e., y-direction, deformations, and larger displacements in the z-direction are produced. Also, this figure shows that the plane strain laminated beam results approach the classical beam theory value, i.e., a normalized displacement equal to 1.0, for very high aspect ratios. This is true even for the off-axis beams where the plane strain assumption has neglected any effect of shear coupling. With a generalized plane deformation analysis, on the other hand, the deflection approaches a constant value as the aspect ratio becomes large which is less than the beam theory value. This constant value is different for the two off-axis fiber orientations considered. It should also be noted that for aspect ratios as high as 12, the deflection in the $0°$ beam is still about 40% larger than the value predicted from classical beam theory which neglects shear deformations.
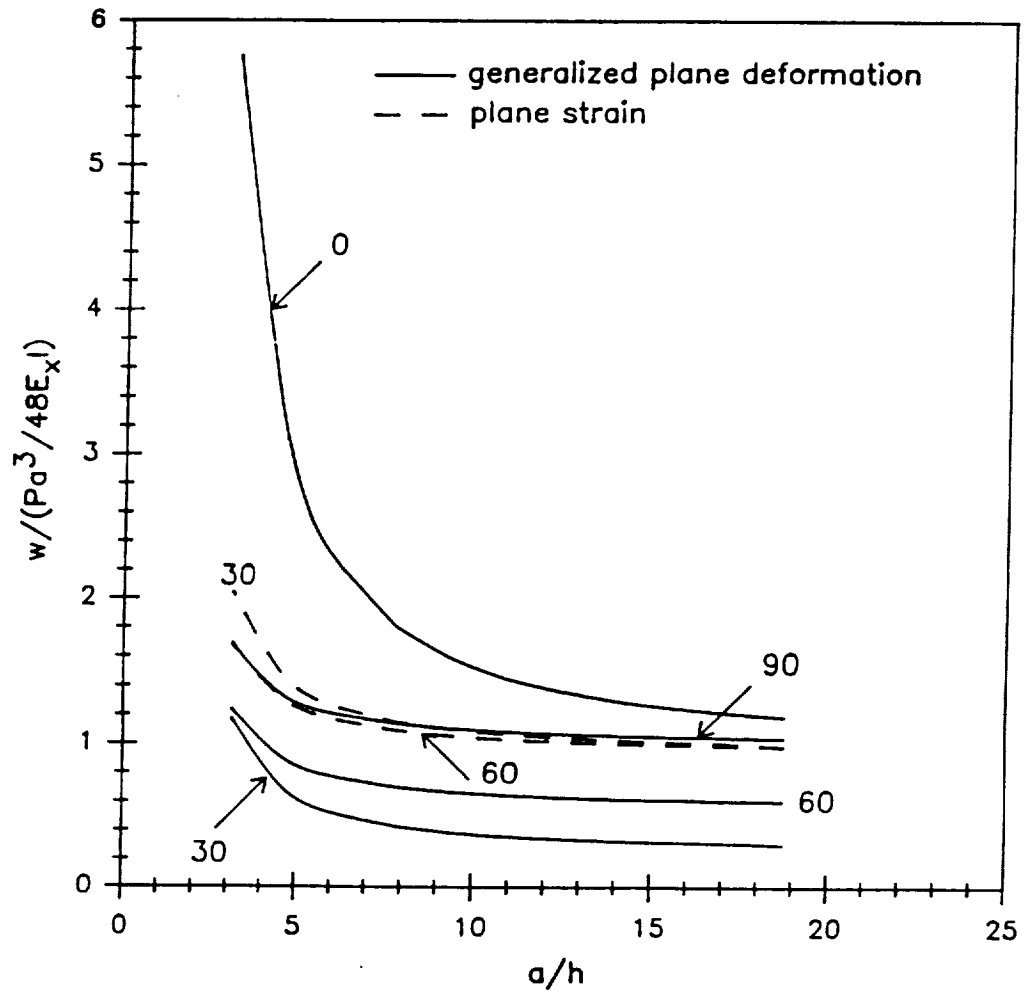
Figure 17. Midspan deflection, w (in.), as a function of the beam's aspect ratio, a/h.

The percentage difference between generalized plane deformation and plane strain for the two off-axis beams as a function of aspect ratio is plotted in Figure 18 and shows that the difference approaches a constant value as the aspect ratio of the beam increases. This behavior is the same for both the laminated beam analysis developed in the present study and the cylindrical bending analysis of Pagano [23]. However, the effect of shear coupling is greater for the cylindrical bending type of boundary conditions. The difference between generalized plane deformation and plane strain is less for the smaller aspect ratios than for the larger aspect ratios, i.e., the effect of shear coupling on the deflection is less severe in beams having small aspect ratios. This is true because for small aspect ratios the beam deflection is primarily due to shear deformations in the xz-plane rather than the bending deformation, and shear deformations in the xz-plane are not expected to be affected by the plane strain assumptions. In addition, high aspect ratio beams have larger bending stresses than small aspect ratio beams, and the magnitude of the bending stress is significantly influenced by having the fibers oriented at some off-axis angle.

Presented in Figure 19 are the differences, Δw, between the generalized plane deformation results for the deflection and the corresponding plane strain results as a function of fiber orientation, for two aspect ratios. For the small aspect ratio of $a/h = 3.125$, the maximum difference between generalized plane deformation and plane strain occurs at a fiber orientation of approximately 40°. The maximum difference occurs for fibers oriented at approximately 35° for the large aspect ratio of $a/h = 18.75$. The large variation in the difference between generalized plane deformation and plane strain as the angle of the fibers changes shows that the effect of shear coupling on the midspan deflection strongly depends on the fiber orientation. The greatest difference, 70%, is seen for an aspect ratio of $a/h = 18.75$ and the cylindrical bending analysis. Also, for the entire range of fiber angles, excluding 0° and 90°, the cylindrical bending results are affected more by shear coupling in comparison with the present beam solution. Additionally, for the range of aspect ratios studied and all fiber orientations, if shear coupling effects are not accounted for in the cylindrical bending and present laminated

C-2

Figure 18. Difference between a plane strain analysis and a generalized plane deformation analysis for the midspan deflection as a function of aspect ratio.

beam analyses then larger midspan beam deflections are predicted. One further note, the present laminated beam solution predicts larger deflections than the cylindrical bending analysis for all aspect ratios and fiber orientations considered.

4.3.2 Normal Stresses

The maximum compressive bending stress, σ_{xx}, which occurs on the top surface and at the midspan of the beam, was normalized with respect to the classical beam theory result and plotted as a function of aspect ratio in Figure 20. For the 30° and 60° beams it is seen that the generalized plane deformation analysis predicts larger bending stresses when compared to the plane strain results. This behavior is seen in Figure 20 to be true for the entire range of aspect ratios considered and is opposite of what was seen in the midspan deflection. That is, accounting for the shear coupling effects in off-axis beams increases the bending stress. Examining the curves for the off-axis beams and considering a given aspect ratio, the bending stress predicted from the plane strain analysis is closer to the classical beam theory value, i.e., a normalized stress value of 1.0, than the result obtained from the generalized plane deformation analysis. Figure 21 shows the difference between generalized plane deformation and plane strain for five of the stress components as a function of aspect ratio for the case of a beam having fibers oriented at 30°. The same results but for a fiber orientation of 60° are given in Figure 22. These two figures show that the difference between generalized plane deformation and plane strain for σ_{xx} is greater for smaller aspect ratios. For the range of aspect ratios considered, this difference is larger for the case of the 30° beam than for the 60° beam. The difference between generalized plane deformation and plane strain for the bending stress is plotted versus the fiber angle in Figure 23. For the two different aspect ratios, a/h equal to 18.75 and 3.125, the cylindrical bending results for the bending stress are less than the values obtained from the present laminated beam analysis for all fiber orientations. For an aspect ratio of a/h = 18.75, the maximum difference between generalized plane defor-

Figure 19. Difference between a plane strain analysis and a generalized plane deformation analysis for the midspan deflection as a function of fiber orientation.

mation and plane strain is for a fiber orientation of approximately 25°. For the case of a small aspect ratio, a/h = 3.125, this maximum difference occurs at about 30°.

The maximum value of the out-of-plane normal component of stress, σ_{yy}, which is located on the top surface of the beam, was normalized with respect to the applied stress, P/bd, and plotted versus the aspect ratio in Figure 24. It is seen that this component of stress is larger for the off-axis fiber oriented beams than for the 0° and 90° unidirectional beams for all aspect ratios. For the case of a 0° fiber orientation, σ_{yy} is seen to be independent of the aspect ratio. This figure also shows that the plane strain analysis predicts a larger σ_{yy} stress component than does generalized plane deformation for all aspect ratios for both the 30° and 60° beams, i.e., neglecting shear coupling overestimates the σ_{yy} stress. For the off-axis fiber orientations the magnitude of the out-of-plane normal stress increases as the aspect ratio of the beam increases. This increase is seen to be much larger for the case of a beam with a fiber orientaton of 60° when compared to a 30° beam. Figures 21 and 22 show that the difference between generalized plane deformation and plane strain for σ_{yy} increases as the aspect ratio of the beam is increased. Accordingly, the σ_{yy} stress component is affected more by shear coupling in the higher aspect ratio beams. In Figure 25 the difference between the generalized plane deformation result and the plane strain result for the out-of-plane normal stress is plotted as a function of fiber orientation. Note that there is no significant difference between the cylindrical bending results and the present laminated beam results. For the case of a small aspect ratio, a/h = 3.125, the plane strain analysis predicts larger values of σ_{yy} as compared to the generalized plane deformation analysis for fibers oriented at angles up to 65°. For fiber orientations between 65° and 90° the generalized plane deformation analysis predicts larger values. When the aspect ratio of the beam is large, i.e., a/h = 18.75, the above result is also true except now the change in sign of the difference occurs at a fiber orientation of approximately 73°. For both of these aspect ratios the shear coupling effects on the component of stress σ_{yy} are maximum for the unidirectional beams having a fiber orientation somewhere between 35° and 45°.

Figure 20. Maximum bending stress σ_{xx} normalized by beam theory predictions as a function of aspect ratio.
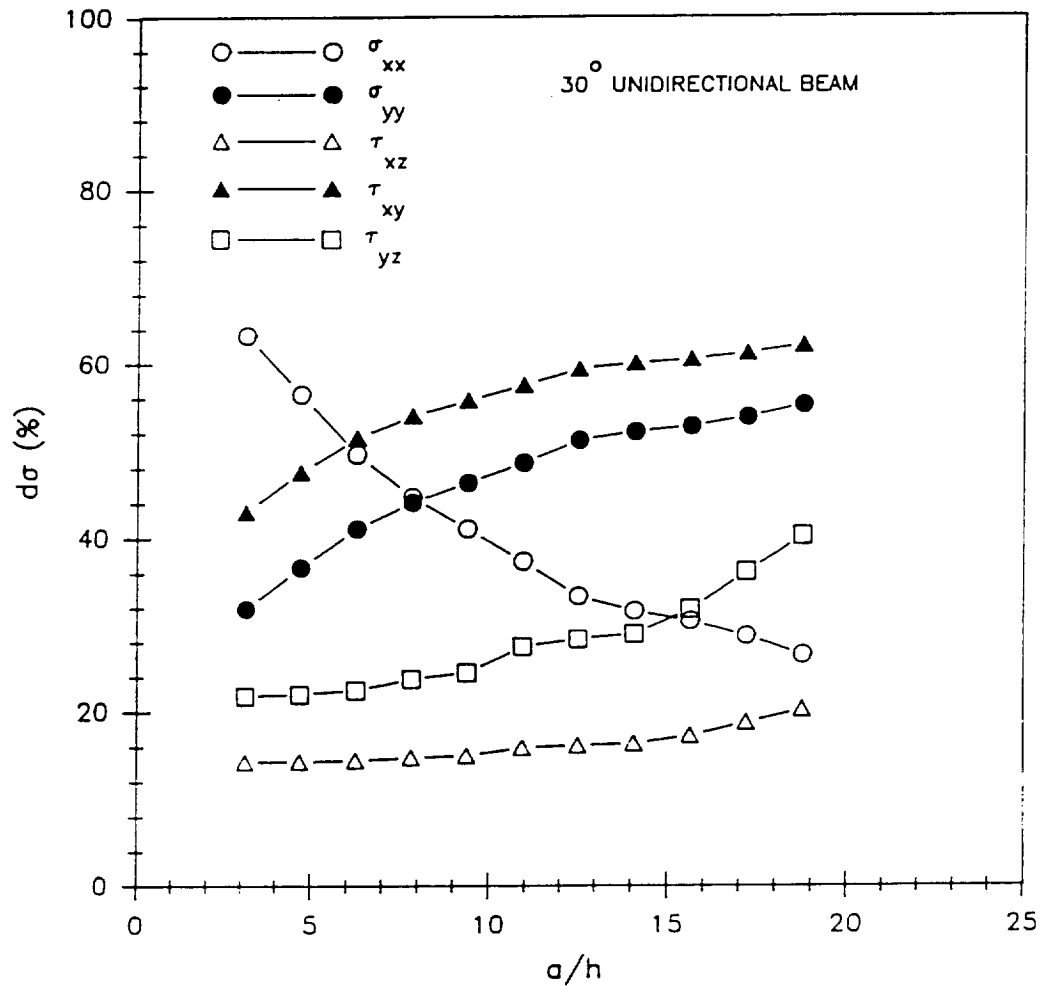
Figure 21. Difference between a plane strain analysis and a generalized plane deformation analysis for the components of stress as a function of aspect ratio in a 30 ° beam.
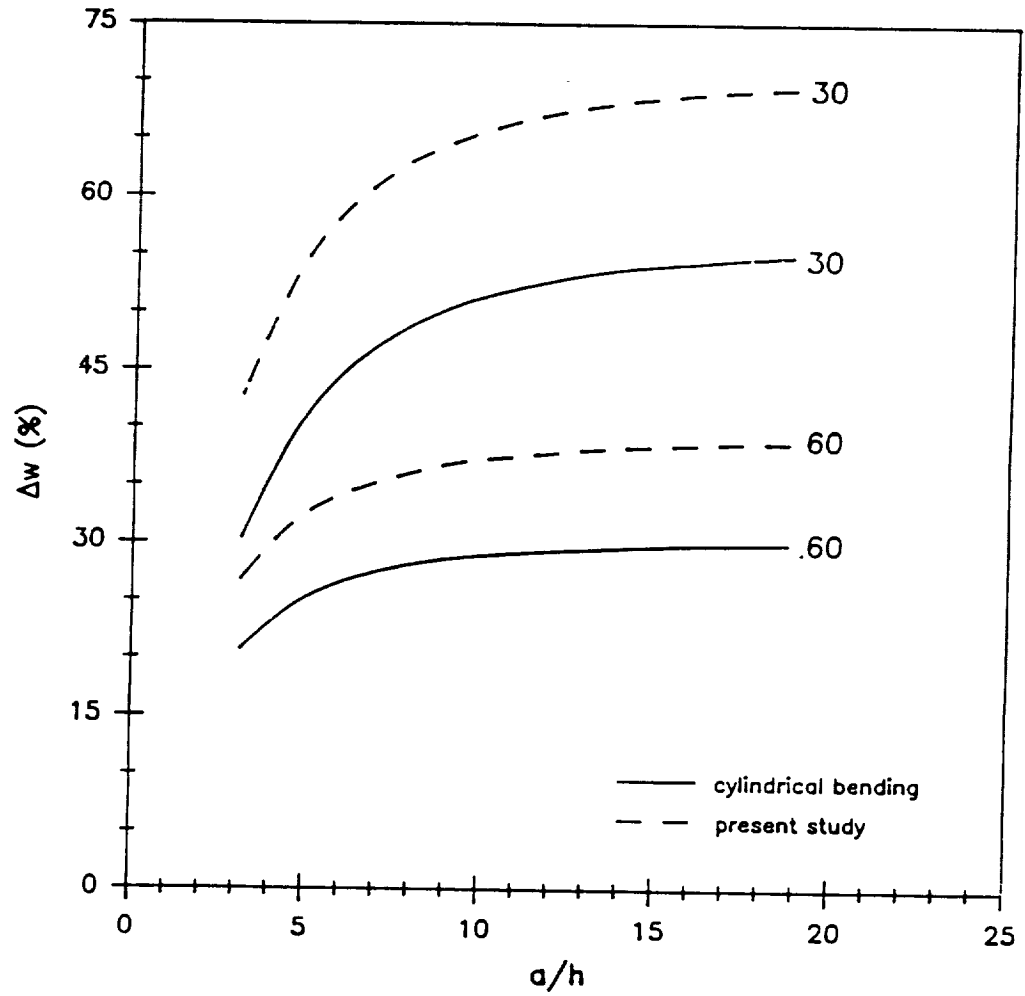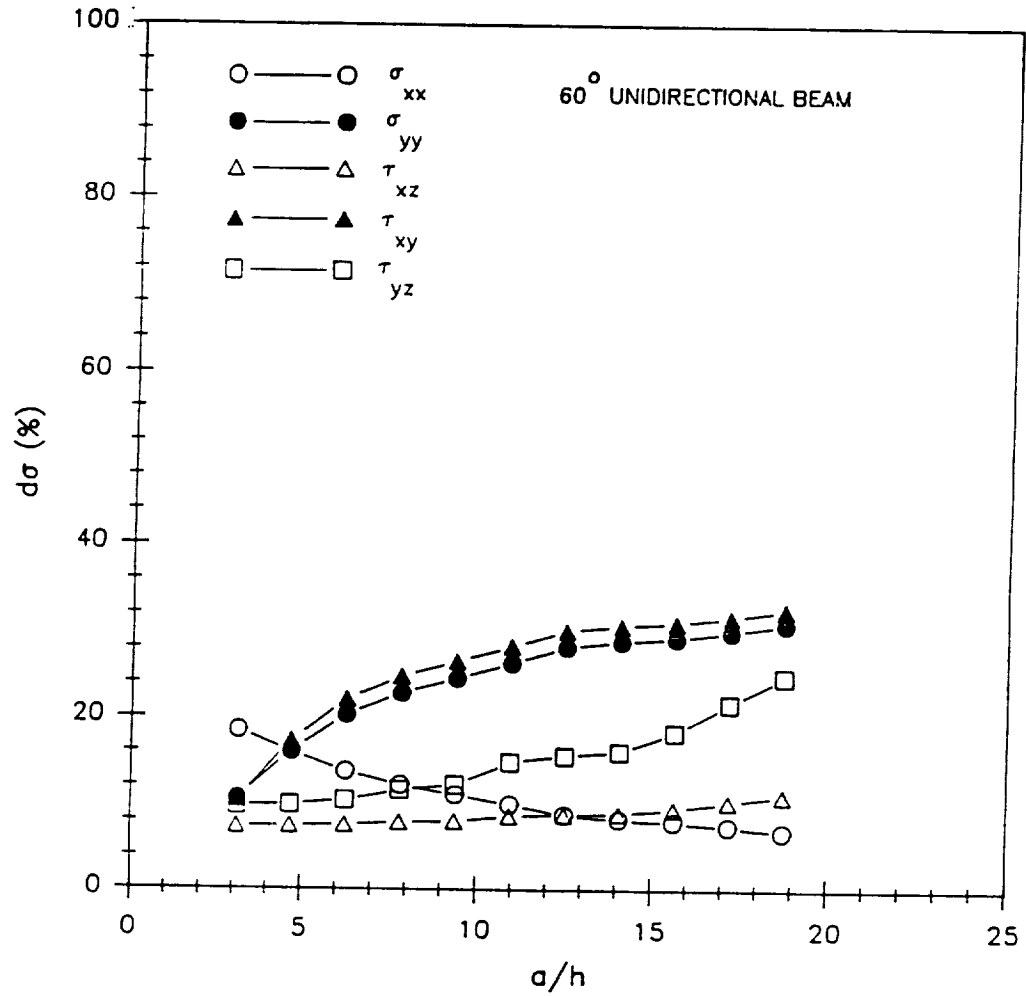
Figure 22. Difference between a plane strain analysis and a generalized plane deformation analysis for the components of stress as a function of aspect ratio in a 60 ° beam.

Figure 23. Difference between a plane strain analysis and a generalized plane deformation analysis for σ_{xx} as a function of fiber orientation.

Figure 24. Maximum normal stress σ_{yy} normalized by the applied stress as a function of aspect ratio.

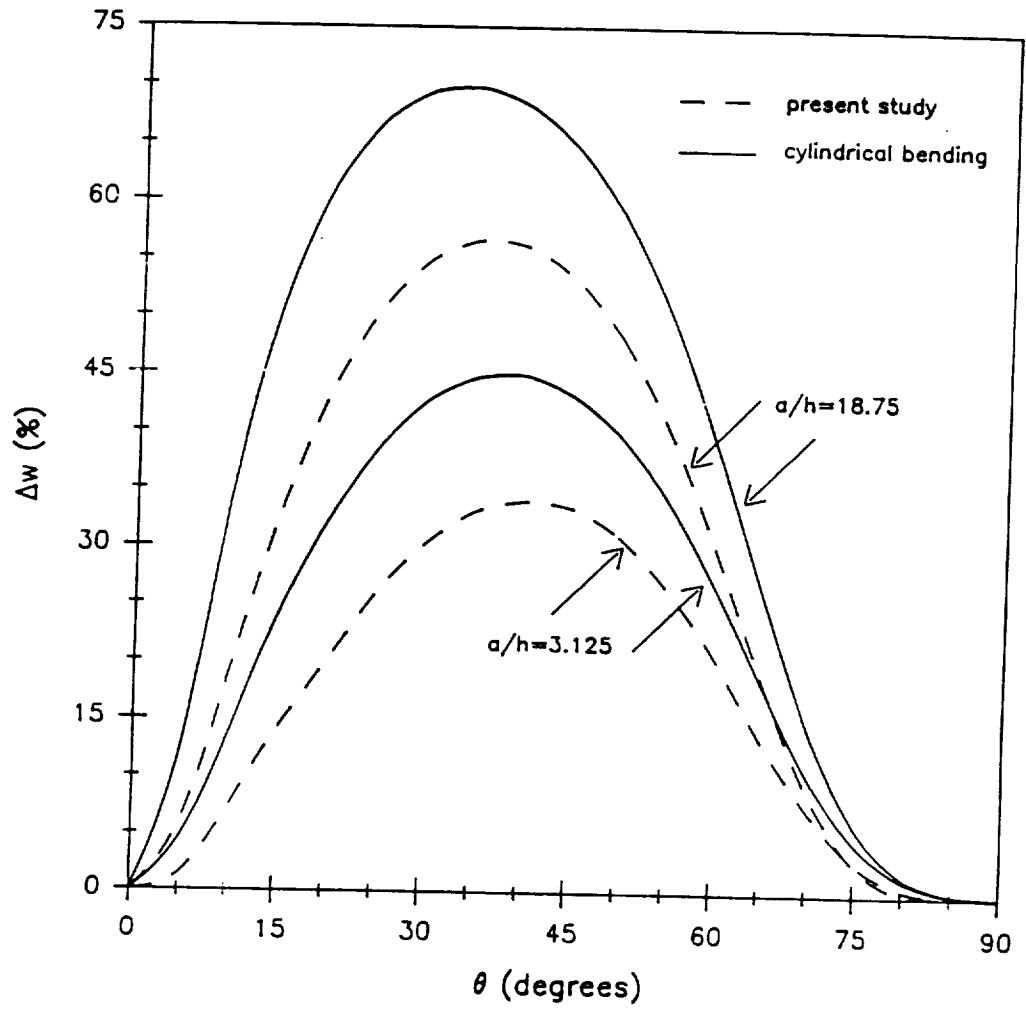**Figure 25.** Difference between a plane strain analysis and a generalized plane deformation analysis for σ_{yy} as a function of fiber orientation.

4.3.3 Shear Stresses

The maximum in-plane shear stress, τ_{xz}, was shown in Section 4.2.2 to be located below the top surface of the beam and underneath the point of discontinuity of loading on the top surface. This differs from the classical beam theory result, which as previously stated, predicts a parabolic stress distribution through the thickness and a maximum value located at the midplane of the beam. Also, the expression for τ_{xz} derived from classical beam theory is independent of the x-coordinate, i.e., position along the span of the beam which differs from the elasticity solution. The dependence of the maximum in-plane shear stress on the aspect ratio of the beam is shown in Figure 26 for the four different fiber orientations. These maximum values have been normalized with respect to the maximum value calculated from beam theory. As was shown for the bending component of stress, generalized plane deformation predicts a larger component of shear stress in comparison to plane strain for all the different fiber orientations and aspect ratios. Consequently, shear coupling effects produce an increase in the in-plane component of shear stress. Also, this figure shows that the results for τ_{xz} from the laminated beam analysis developed in the present study are larger than the classical beam theory results and never approach the beam theory prediction even for very high aspect ratios. It should be noted that the location dependence has been relaxed for the normalization used in this figure. In other words, the maximum beam theory value is not at the same location as the maximum shear stress value determined from the laminated beam analysis. Referring back to Figures 21 and 22, the difference between generalized plane deformation and plane strain for τ_{xz} and a given fiber orientation does not depend strongly on the aspect ratio of the beam. This difference is approximately constant up to an aspect ratio of 10, then slightly increases as the aspect ratio is increased. The effect of fiber orientation on the difference between the in-plane shear stresses for generalized plane deformation and plane strain is demonstrated in Figure 27. This figure also shows that this difference, i.e., the effect of shear coupling, is greater for the present laminated beam analysis than for the case of cy-

lindrical bending when the beam has a large aspect ratio. For beams having a small aspect ratio, the cylindrical bending analysis predicts larger shear coupling effects.

For the $0°$ and $90°$ unidirectional beams the out-of-plane shear stresses, τ_{xy} and τ_{yz}, are zero. Recall that for these types of beams the generalized plane deformation analysis is reduced to the form of a plane strain analysis. For the case of an off-axis fiber oriented beam, the maximum value for τ_{xy} is located on the top surface of the beam. The maximum value for the other out-of-plane shear stress, τ_{yz}, is located beneath the top surface near the point of discontinuity in the applied loading as in the case of the in-plane shear, τ_{xz}. Since the component of shear stress τ_{xy} is not a quantity normally associated with classical beam theory, the results for the maximum values have been normalized with respect to the applied loading and are shown as a function of beam aspect ratio in Figure 28. This figure shows that for the two different off-axis orientations and for all aspect ratios the plane strain analysis predicts larger values for τ_{xy} than does the generalized plane deformation. Therefore, if shear coupling effects are neglected then the magnitudes for τ_{xy} will be over estimated. Also, the magnitude of the maximum value of τ_{xy} increases as the aspect ratio of the beam increases. For the plane strain results this increase is larger for the case of a beam having a fiber orientation of $30°$ when compared to the $60°$ beam. This increase is smaller when the generalized plane deformation results are considered. The difference between generalized plane deformation and plane strain as a function of the aspect ratio for τ_{xy} is similar in behavior to that of the out-of-plane normal stress, σ_{yy} as shown in Figures 21 and 22. In Figure 29 the difference between generalized plane deformation and plane strain for τ_{xy} is plotted versus the fiber angle. Similar conclusions which were drawn from Figure 27 concerning the out-of-plane normal stress σ_{yy} apply also to τ_{xy} as seen from Figure 29.

The other out-of-plane component of shear stress, τ_{yz}, is much smaller in magnitude when compared to the other two shear stresses. Its maximum value was normalized with respect to the applied stress and plotted in Figure 30 for the two off-axis beams as a function of aspect ratio. The magnitude of τ_{yz} decreases slightly as the aspect ratio of the beam is increased.
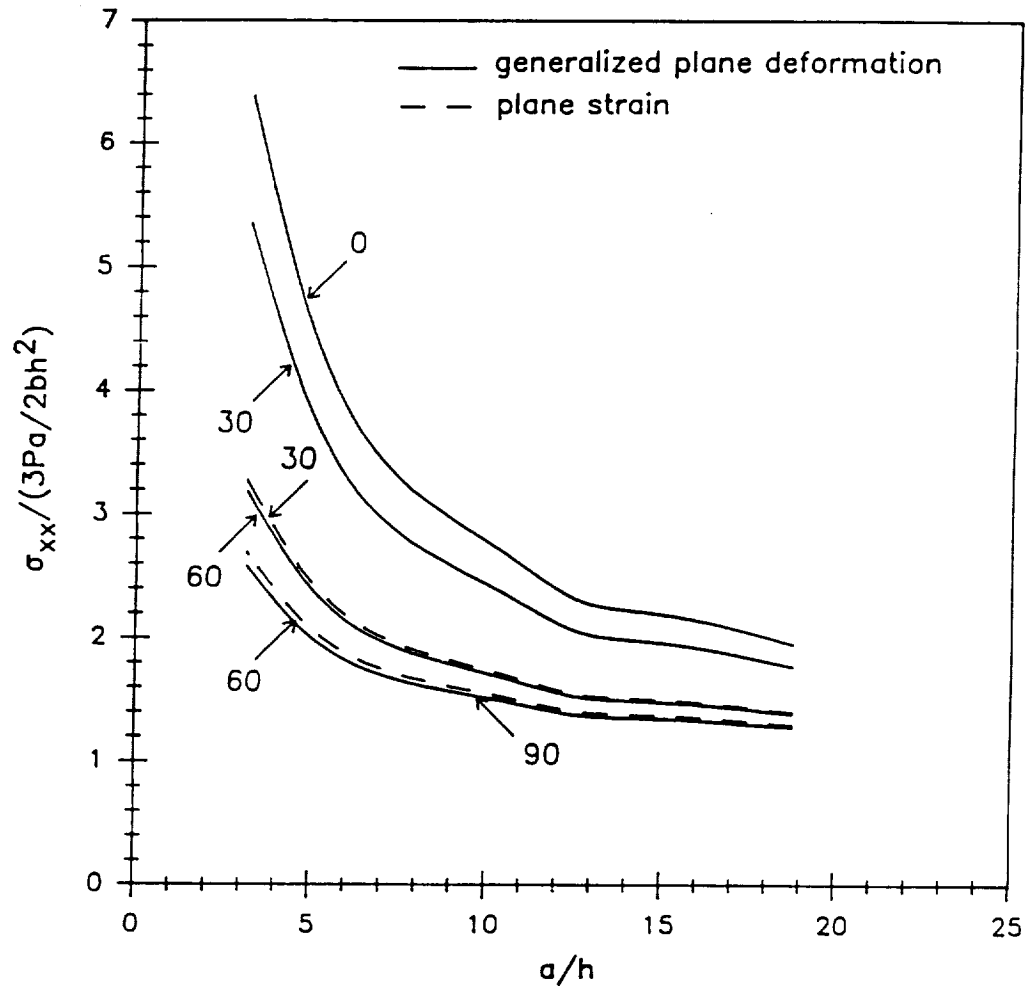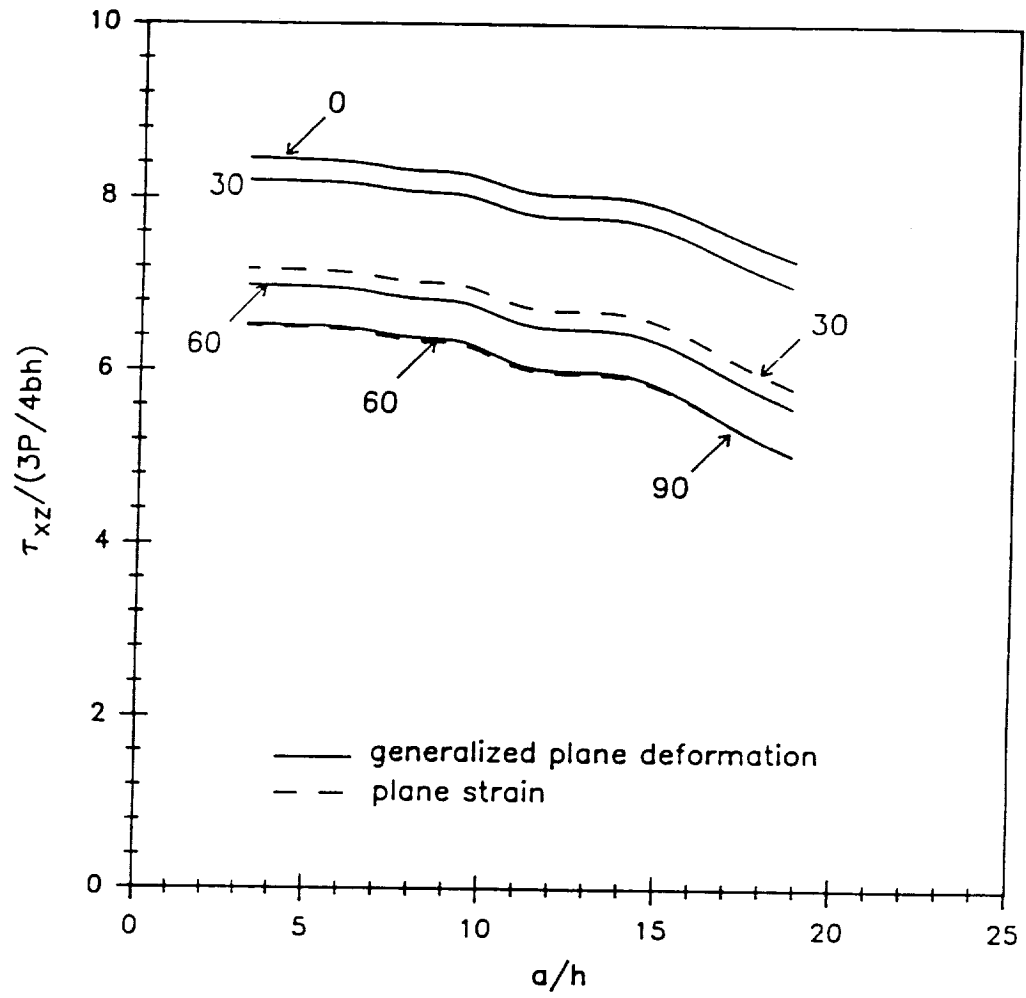
Figure 26. Maximum shear stress τ_{xz} normalized by beam theory predictions as a function of aspect ratio.
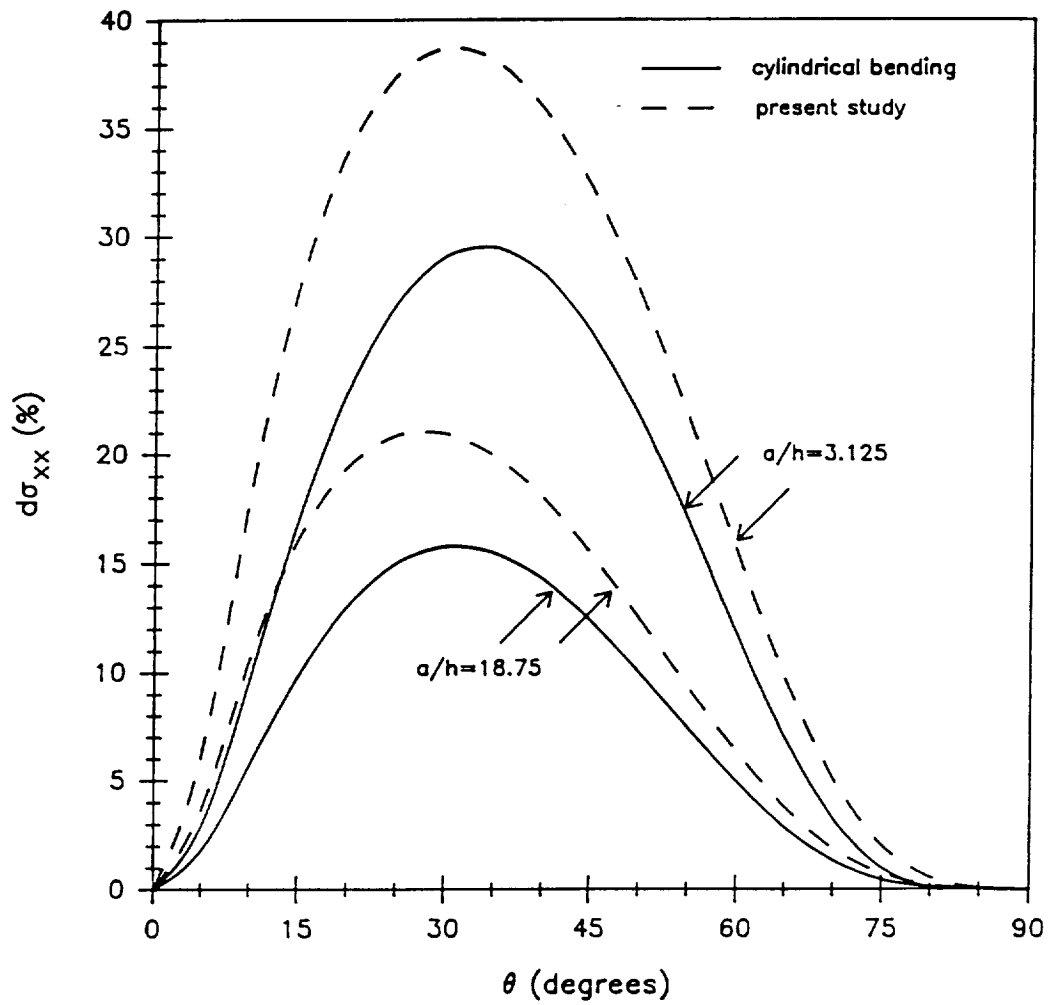
Figure 27. Difference between a plane strain analysis and a generalized plane deformation analysis for τ_{xz} as a function of fiber orientation.
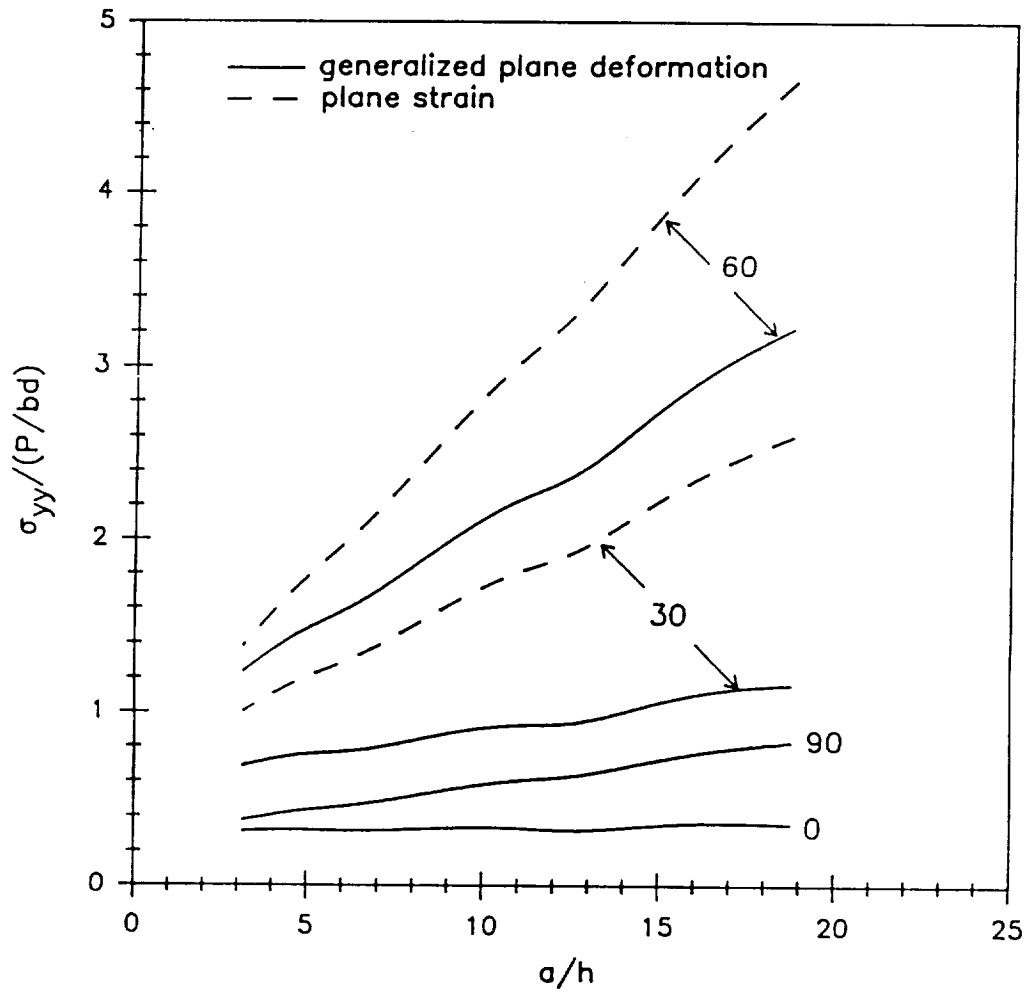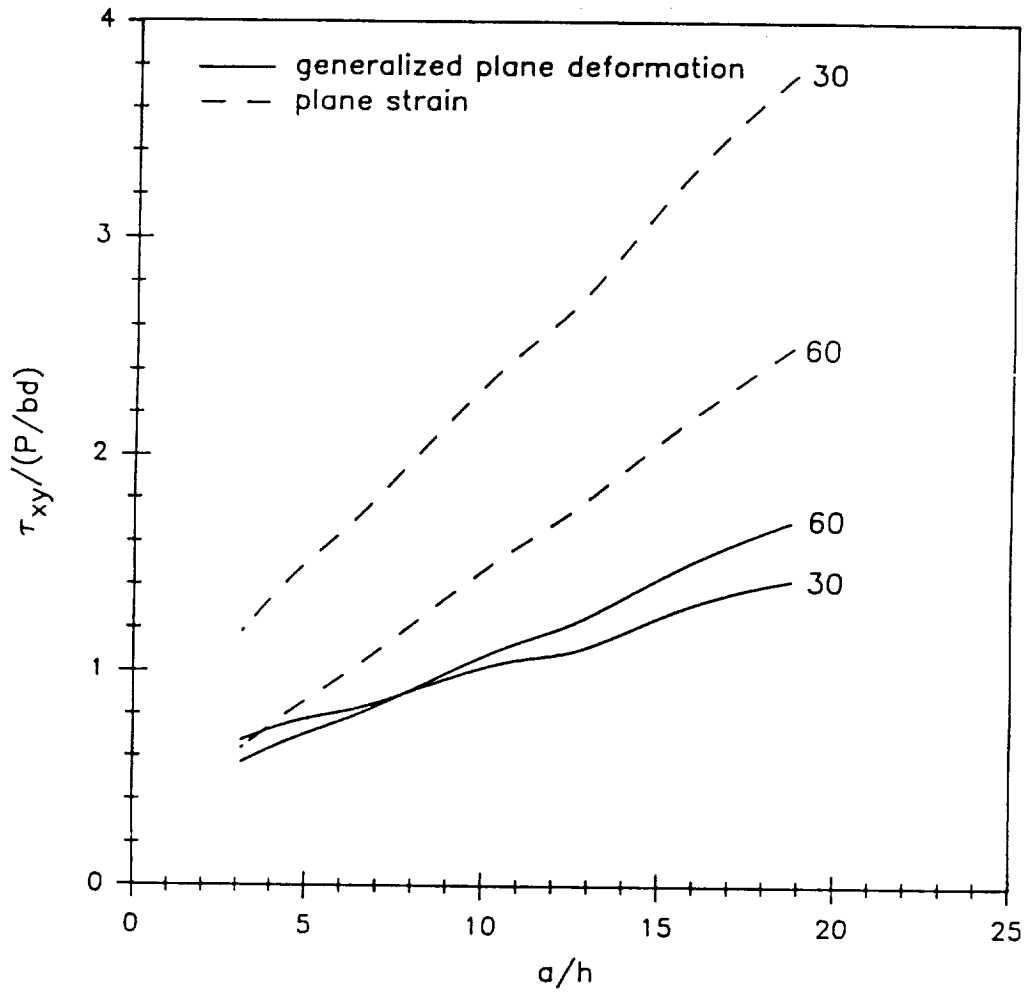
Figure 28. Maximum shear stress τ_{xy} normalized by the applied stress as a function of aspect ratio.
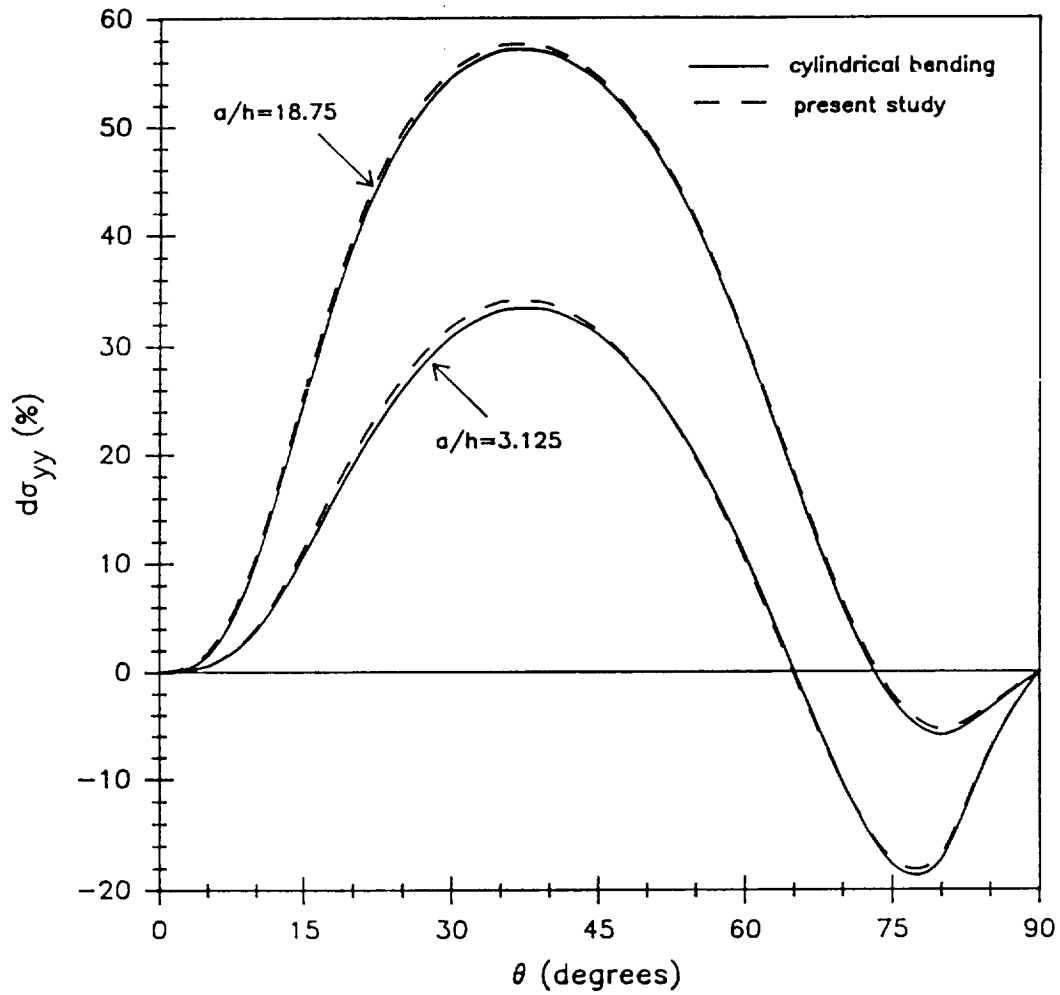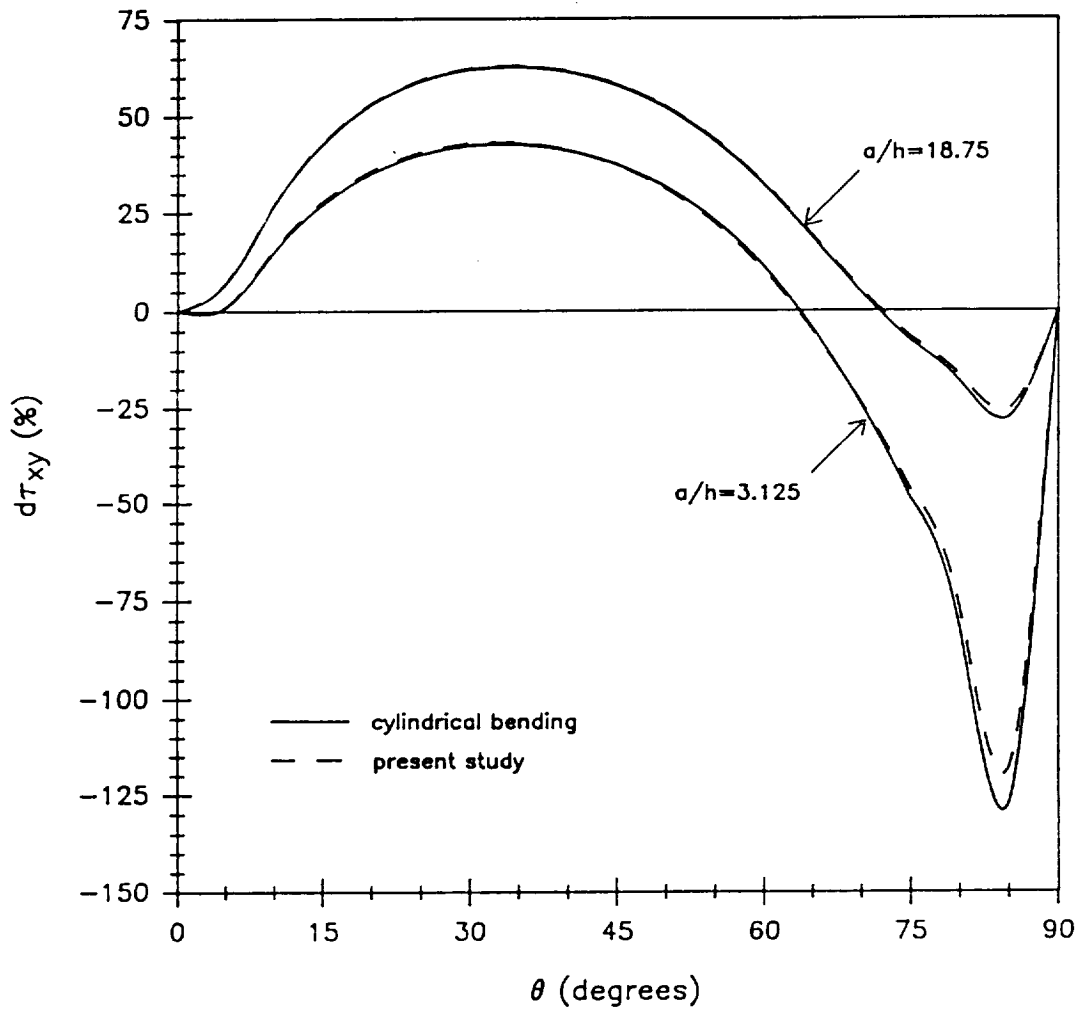
Figure 29. Difference between a plane strain analysis and a generalized plane deformation analysis for τ_{xy} as a function of fiber orientation.

For both the 30° and 60° beams the generalized plane deformation analysis predicts larger values than plane strain for all aspect ratios. In reference to Figures 21 and 22, the difference between generalized plane deformation and plane strain for τ_{yz} is seen to increase as the beam aspect ratio is increased. Figure 31 shows how this difference between generalized plane deformation and plane strain depends on the fiber orientation for two different aspect ratios. For both the large aspect ratio and the small aspect ratio, the present laminated beam analysis predicts a smaller difference than the cylindrical bending analysis for all fiber orientations. For the small aspect ratio and for fiber orientations greater than about 68°, the plane strain analysis gives larger values of τ_{yz} than does generalized plane deformation. Similar observations hold for the large aspect ratio, with the plane strain values being greater than the generalized plane deformation values for angles greater than approximately 73°.

4.4 Stacking Sequence Effects

As outlined in the introductory comments of this chaper, one phase of the analytical investigation consisted of determining stacking sequence effects on the local stress state. Consequently, supplementary studies were conducted for a series of quasi-isotropic laminated beams to ascertain the effects of grouping plies together. The lamination sequences were: $[0/45/-45/90]_{6s}$, $[0_6/45_6/-45_6/90_6]_s$, $[0/60/-60]_{6s}$, and $[0_6/60_6/-60_6]_s$. The $[0/\pm45/90]$ series of beams had an overall length L equal to 4.8 inches and height h of 0.24 inches, whereas, the $[0/\pm60]$ beams were 3.6 inches in length and had a height of 0.18 inches. In accordance with the earlier investigations in Section 4.2, the overall lengths were chosen such that when the supports were located at the ends of the beam the span length-to-depth aspect ratio was equal to 20.0. The different dimensions were a direct consequence of maintaining the same aspect ratio between the two series of beams for the purpose of making comparisons. Through-the-thickness stress distributions were generated at an x-location which corre-
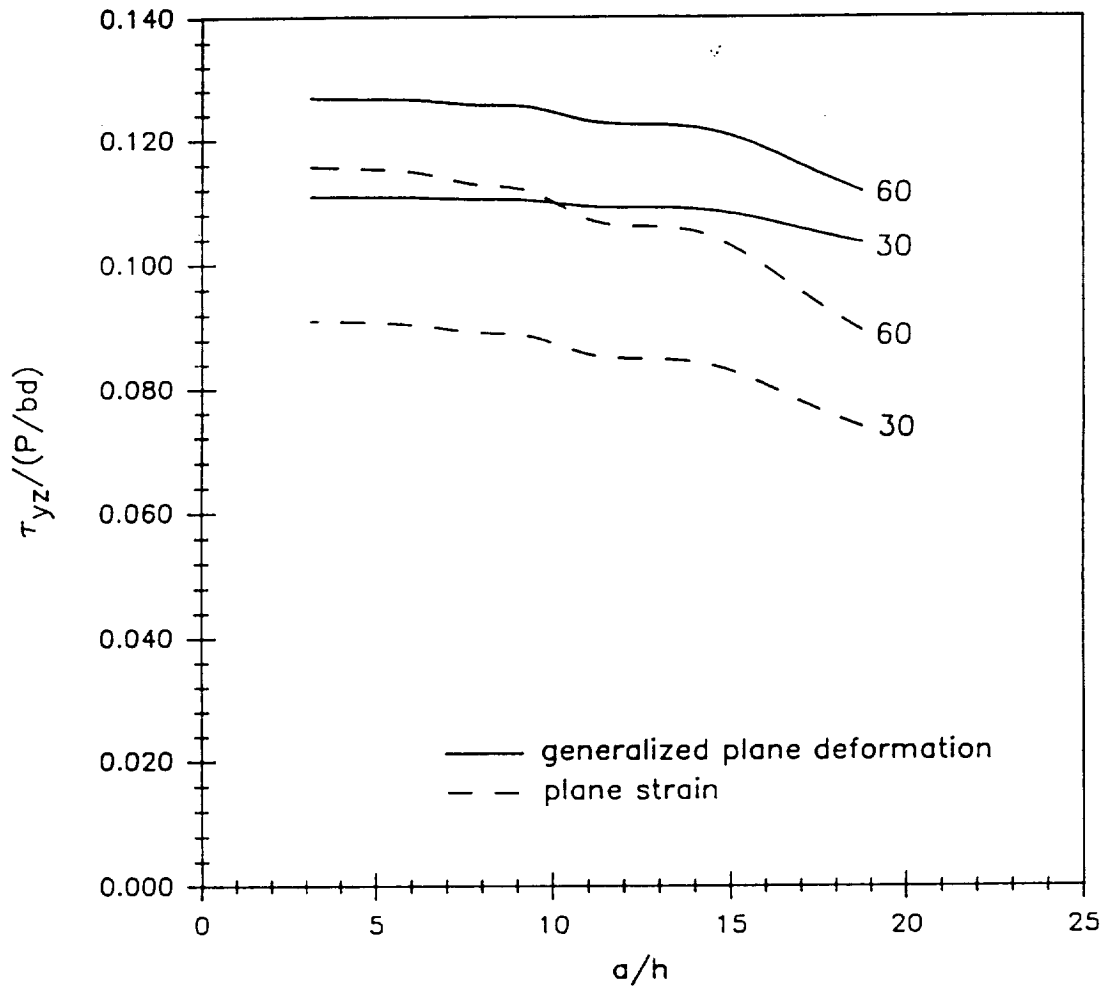
Figure 30. Maximum shear stress τ_{yz} normalized by the applied stress as a function of aspect ratio.
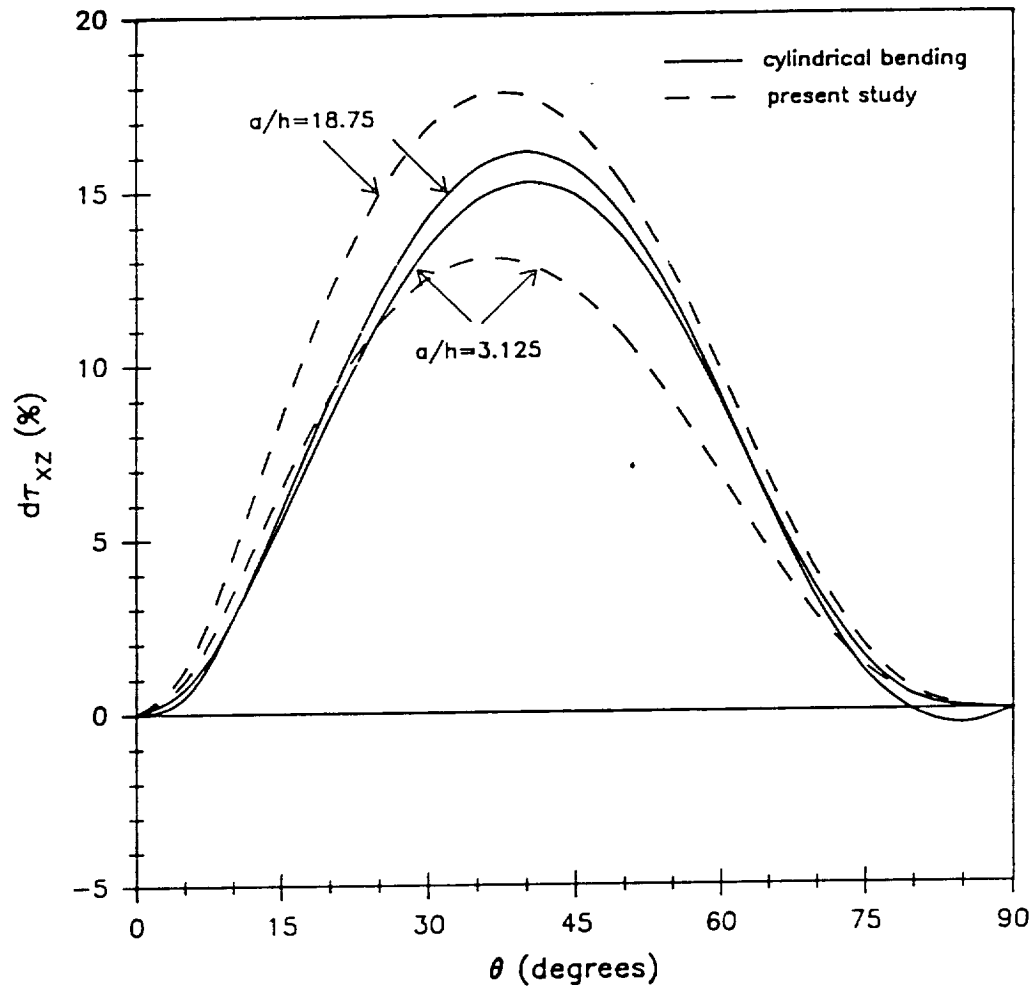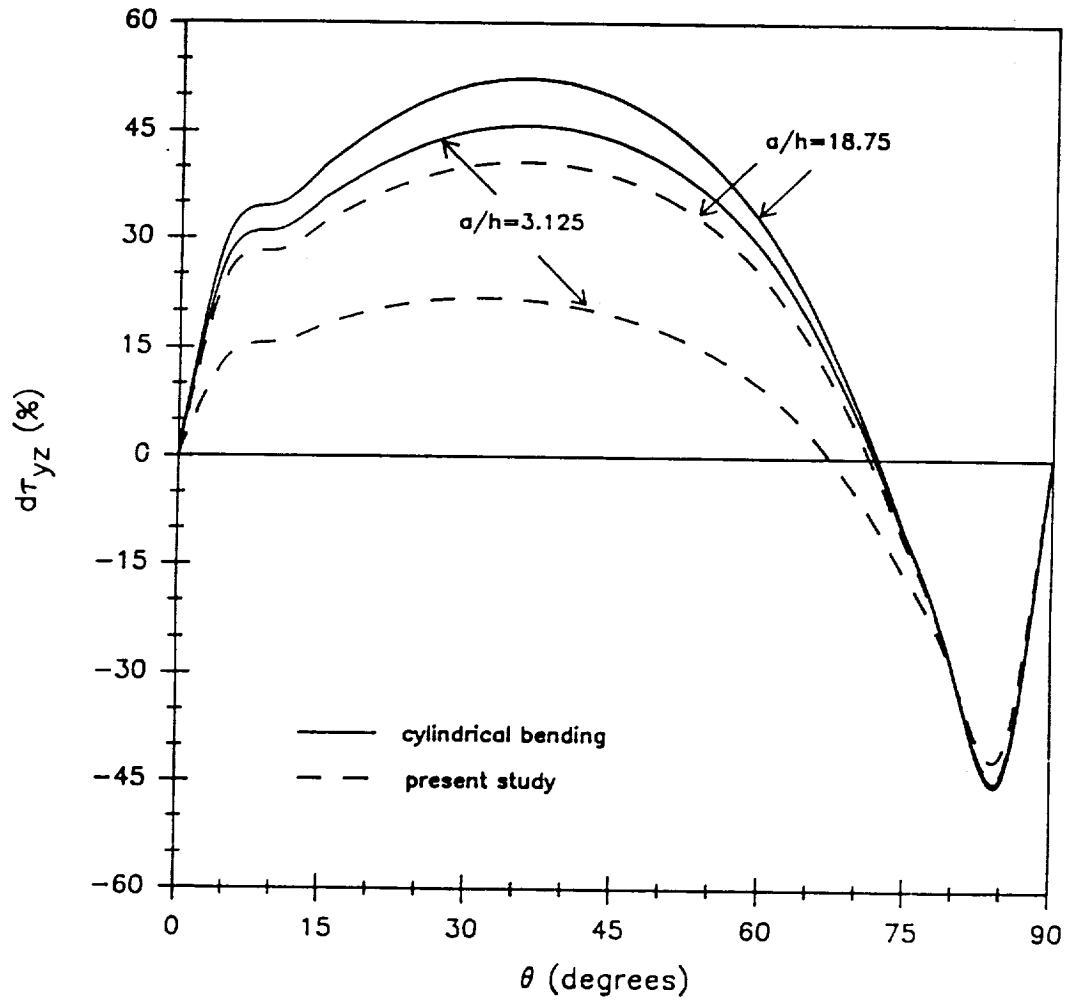
Figure 31. Difference between a plane strain analysis and a generalized plane deformation analysis for τ_{yz} as a function of fiber orientation.

sponded to the point of discontinuity in the applied traction on the top surface and comparisons were made between the different laminates. Also, in accordance with the earlier investigations, four different a/h aspect ratios were considered, i.e., 20.0, 10.0, 1.0, 0.5. For the three components of stress which are continuous across the interfaces, i.e., σ_{zz}, τ_{xz}, τ_{yz}, there were no significant changes in the distribution through the thickness between the different aspect ratios until the a/h aspect ratio became less than or equal to 1.0. The opposite was seen for the stress components in the xy-plane (Figure 4), i.e., σ_{xx}, σ_{yy}, τ_{xy}, which are discontinuous stress components, where the distribution through the thickness strongly depended on the aspect ratio when it was greater than 1.0.

4.4.1 Discontinuous Interfacial Stresses

Comparisons between the bending stress, σ_{xx}, distribution through-the-thickness, normalized by the applied stress, for the grouped and interspersed [0/45/-45/90] laminates are shown in Figures 32 and 33, for beam aspect ratios of a/h = 20.0 and 1.0, respectively. In the case of the larger aspect ratio, the maximum compressive bending stress located at the top surface is reduced when the plies are grouped together. In addition, grouping the plies together reduces the magnitude of the bending stress in the off-axis plies. Conversely, when the aspect ratio equals 1.0 the magnitude is approximately the same between the grouped laminate and the interspersed laminate. Similar behavior was seen for the [0/60/-60] laminates. Figure 34 shows the maximum compressive bending stress, normalized with respect to the applied stress, as a function of beam aspect ratio for the four different laminates. For aspect ratios which are characteristic of slender beams, i.e., a/h > 10, the maximum compressive bending stress strongly depends on the stacking sequence and the ply thickness. Also, the quasi-isotropic laminates containing ±60 plies have a larger bending stress in comparison to the ±45 cases.

Figure 32. Through-the-thickness distribution for σ_{xx} normalized by the applied stress for a/h = 20.0.
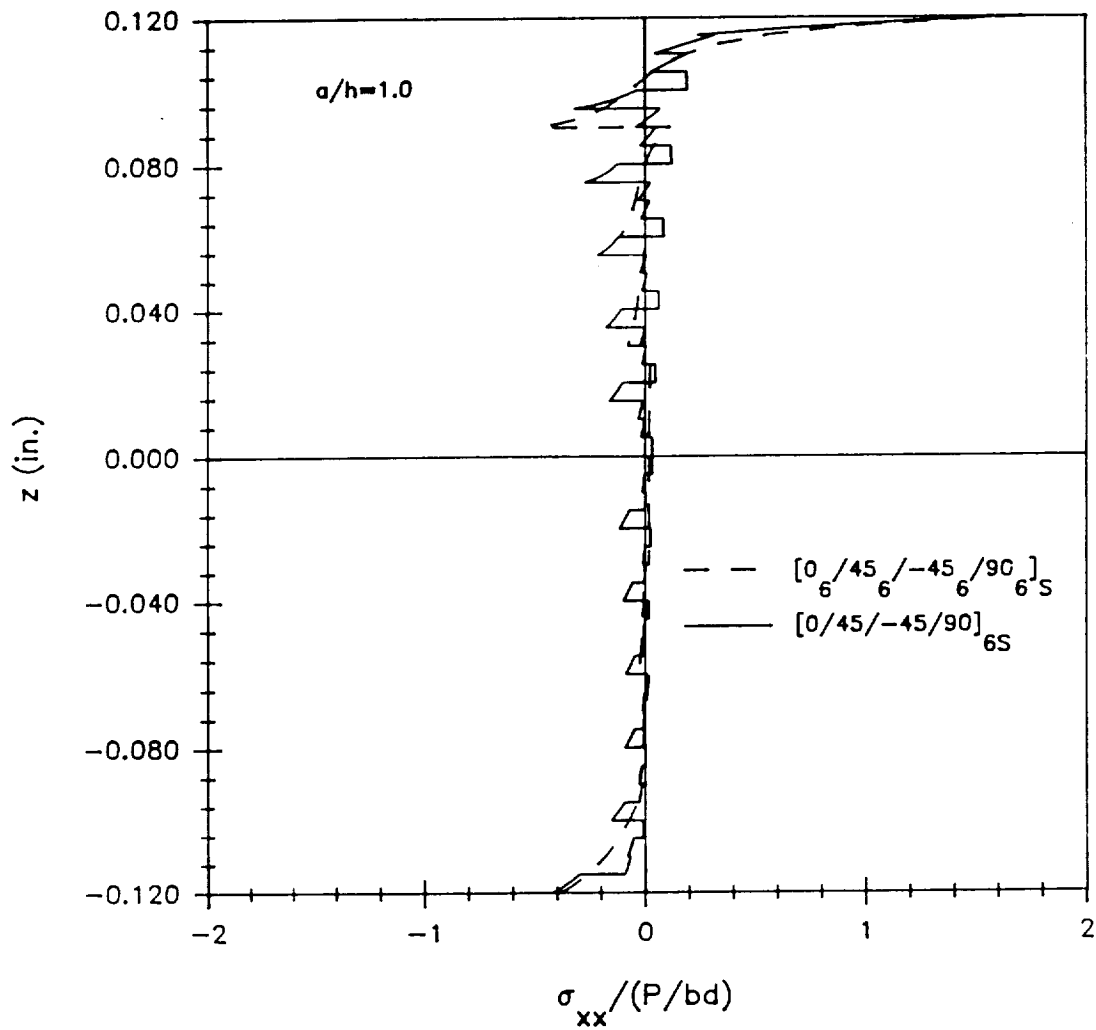
Figure 33. Through-the-thickness distribution for σ_{xx} normalized by the applied stress for a/h = 1.0.
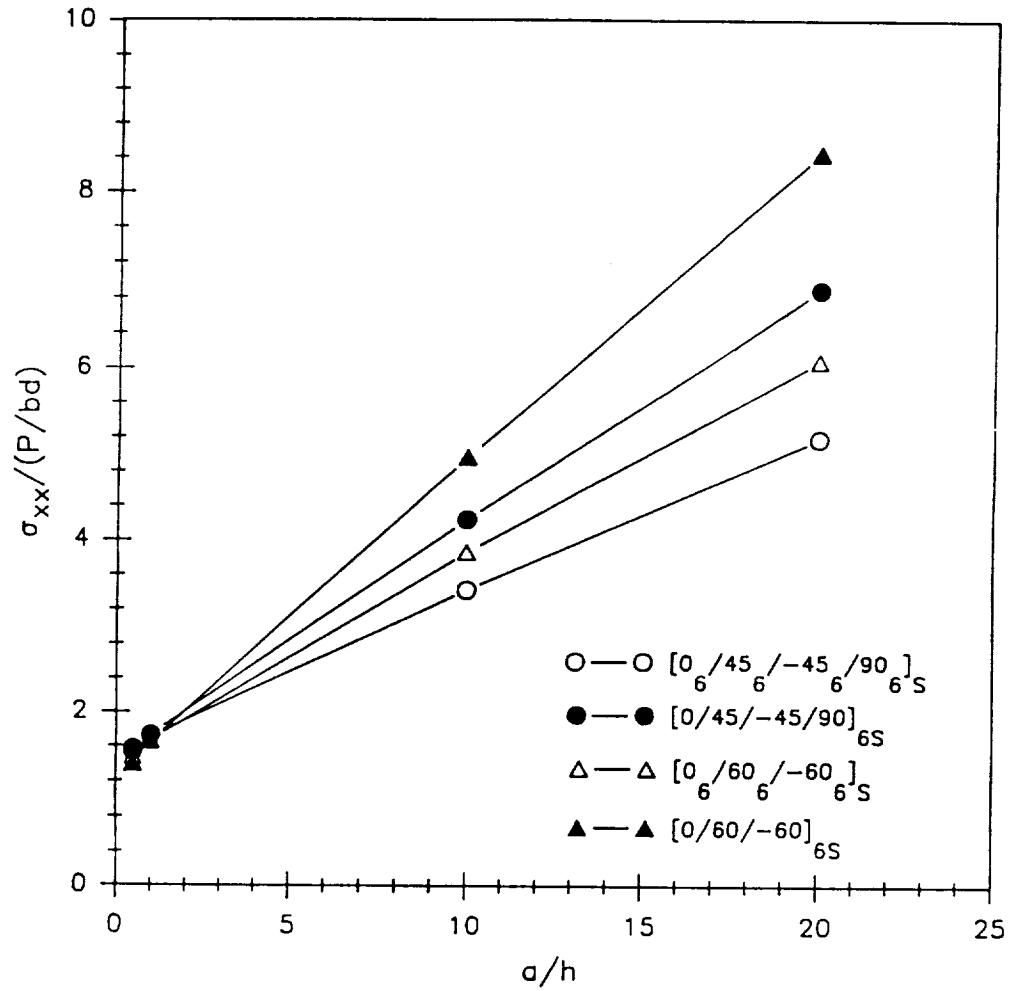
Figure 34. Maximum compressive bending stress normalized by the applied stress as a function of aspect ratio.

The results for the out-of-plane normal stress, σ_{yy}, normalized by the applied stress, for the grouped and interspersed [0/45/-45/90] laminates having an aspect ratio, a/h = 20.0, are shown in Figure 35. For an aspect ratio equal to 1.0 the results are presented in Figure 36. Figures 35 and 36 show that grouping plies together significantly reduces the magnitude of σ_{yy} in the off-axis plies. This was also true for the [0/60/-60] laminates analyzed. The maximum value of σ_{yy} is located at the first interface below the top surface for both the grouped and interspersed laminates and for a/h > 1.0. The magnitudes of σ_{yy}, normalized by the applied stress, at the location of the first interface in the four different laminates are plotted in Figure 37 as a function of the aspect ratio. The results for the [0/60/-60] laminates are slightly smaller in comparison to the [0/45/-45/90] results in both the grouped and interspersed cases. This figure also demonstrates that grouping the plies together significantly reduces the magnitude of σ_{yy} at the location corresponding to the first interface, especially for the larger aspect ratios. As the aspect ratio of the beam becomes small, the effects of the ply thickness and the stacking sequence are reduced. Similar conclusions can be drawn from Figures 38, 39, and 40, where the results are presented for the τ_{xy} component of stress.

4.4.2 Continuous Interfacial Stresses

A comparison of the results for the through-the-thickness distribution of σ_{zz}, normalized by the applied stress, for the grouped laminates with [0/45/-45/90] and [0/60/-60] stacking sequences are presented in Figure 41. The results shown are at an x-location which corresponds to the point of discontinuity in the applied load on the top surface. For this component of stress there was not a significant difference between the grouped and interspersed cases. The results for the beams having an aspect ratio of 0.5 show the effect of the applied tractions located at the bottom surface supports. In both the large aspect ratio case, a/h = 20.0, and the small case, a/h = 0.5, the local effects of the applied traction on the top surface diminish more rapidly in the [0/45/-45/90] laminates in comparison to the [0/60/-60] laminates.
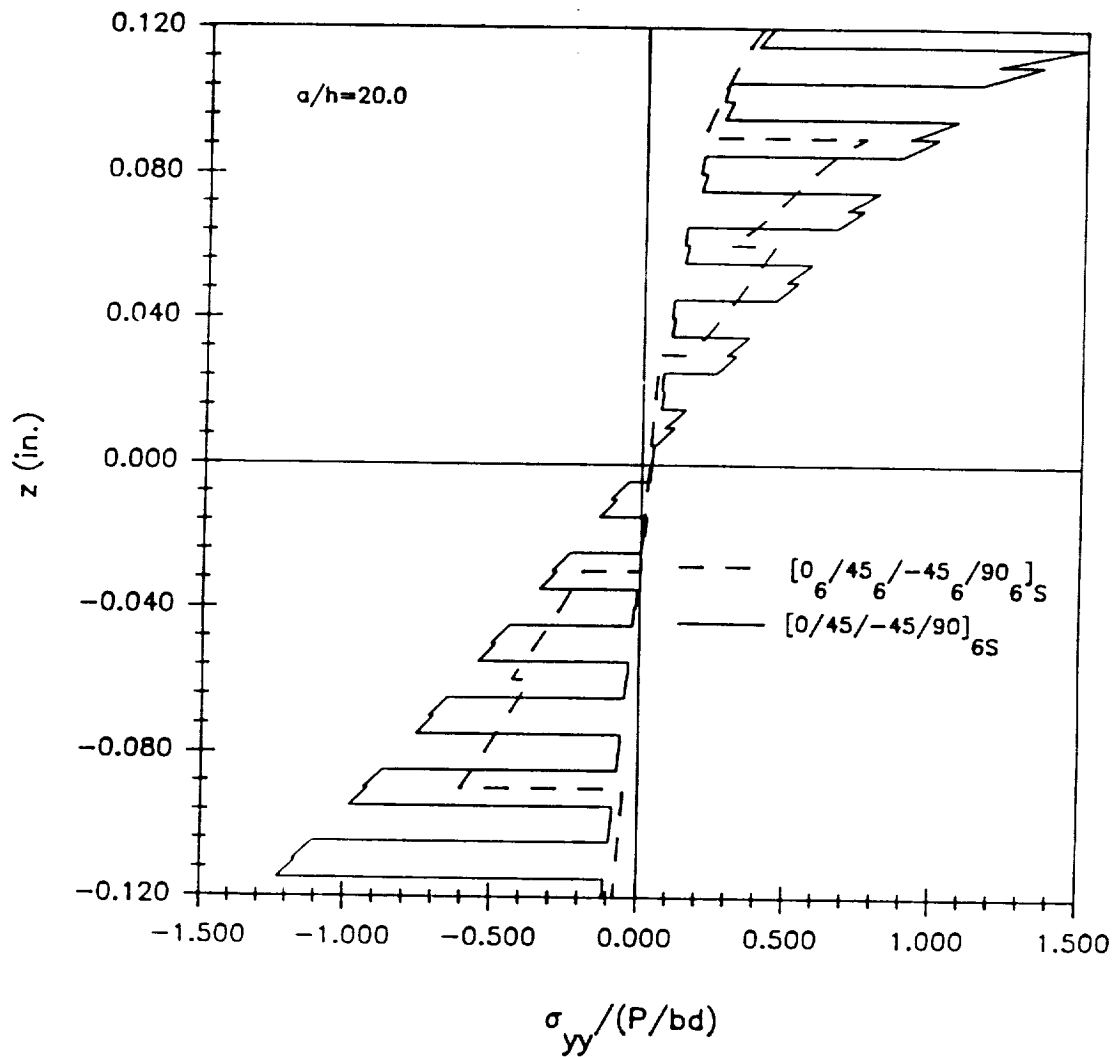
Figure 35. Through-the-thickness distribution for σ_{yy} normalized by the applied stress for a/h = 20.0.
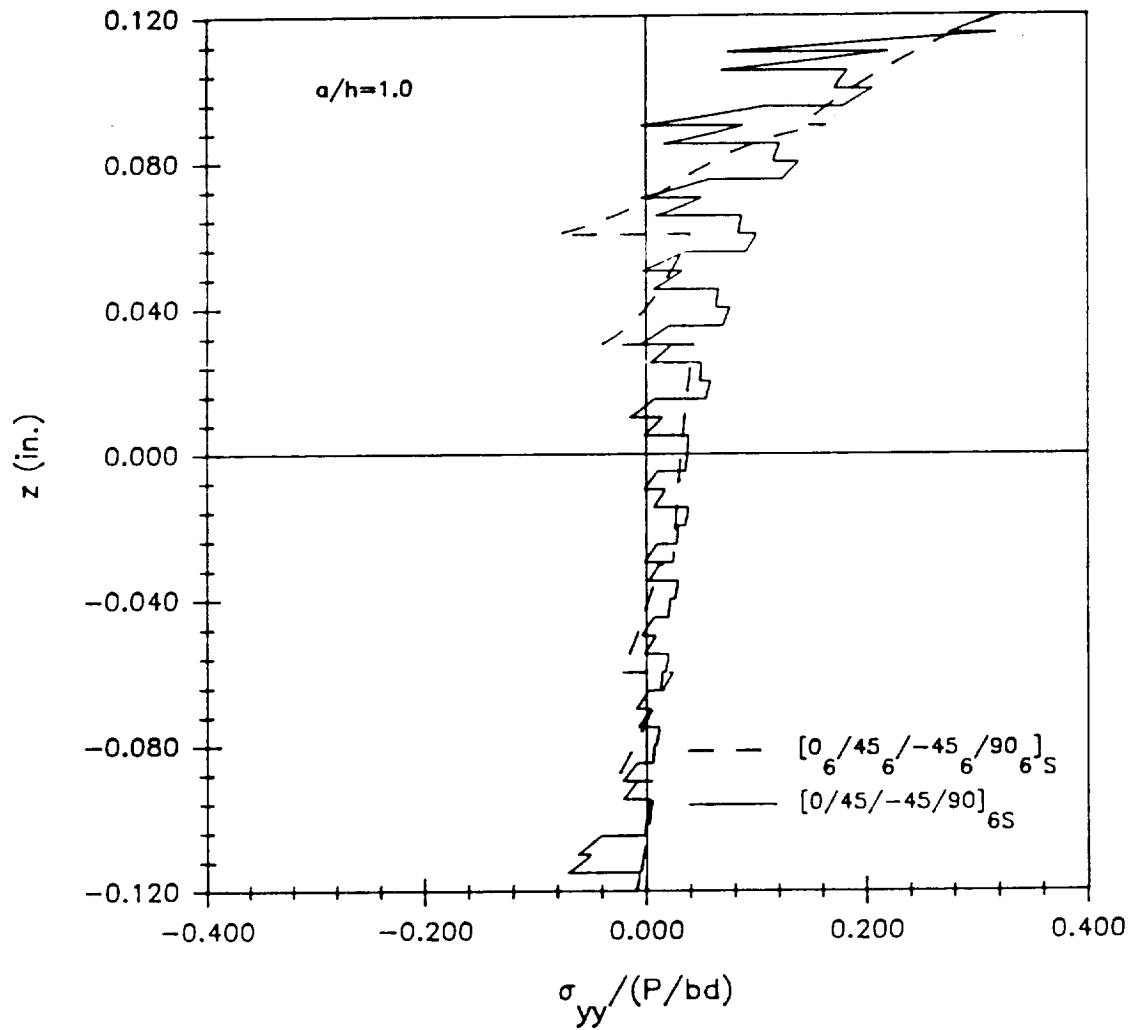
Figure 36. Through-the-thickness distribution for σ_{yy} normalized by the applied stress for $a/h = 1.0$.
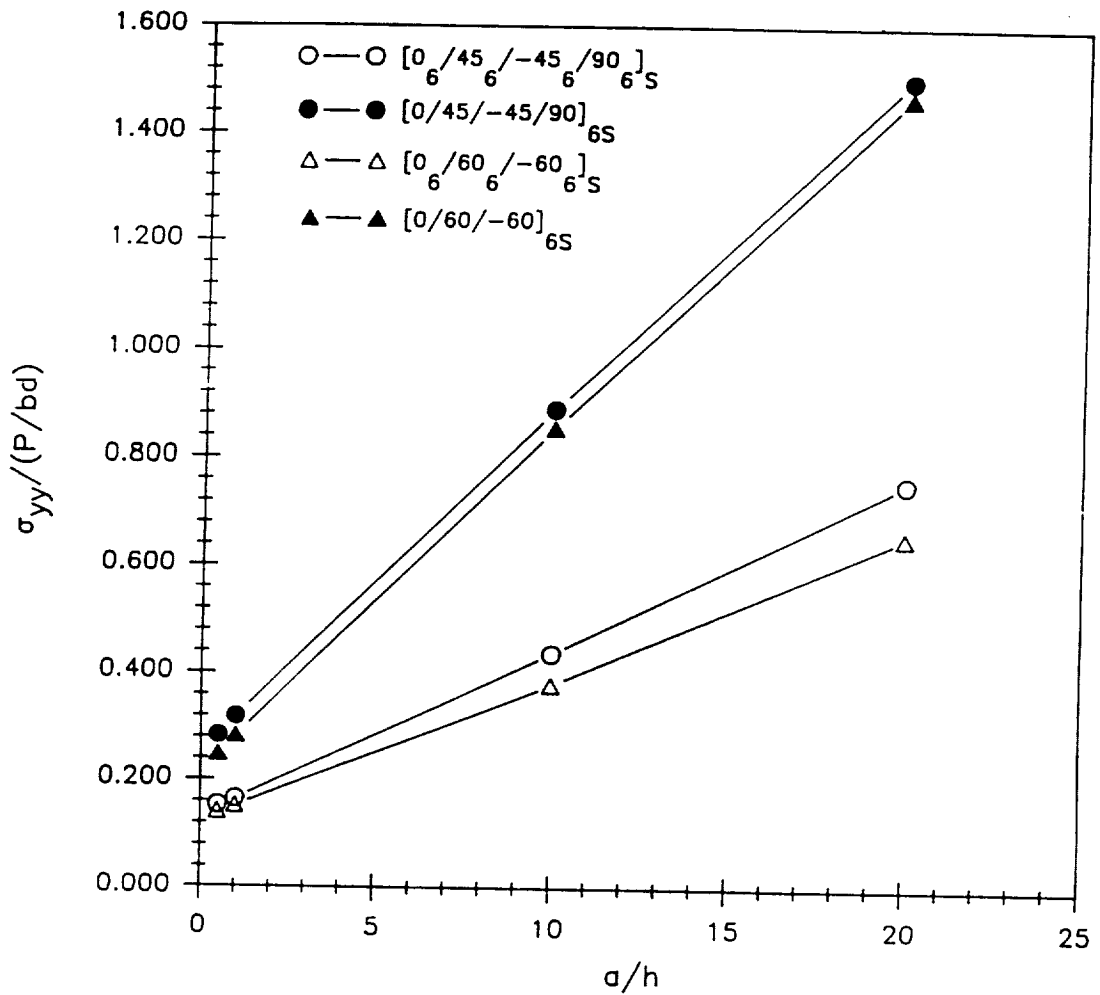
Figure 37. Magnitude of σ_{yy} at the first interface normalized by the applied stress as a function of aspect ratio.
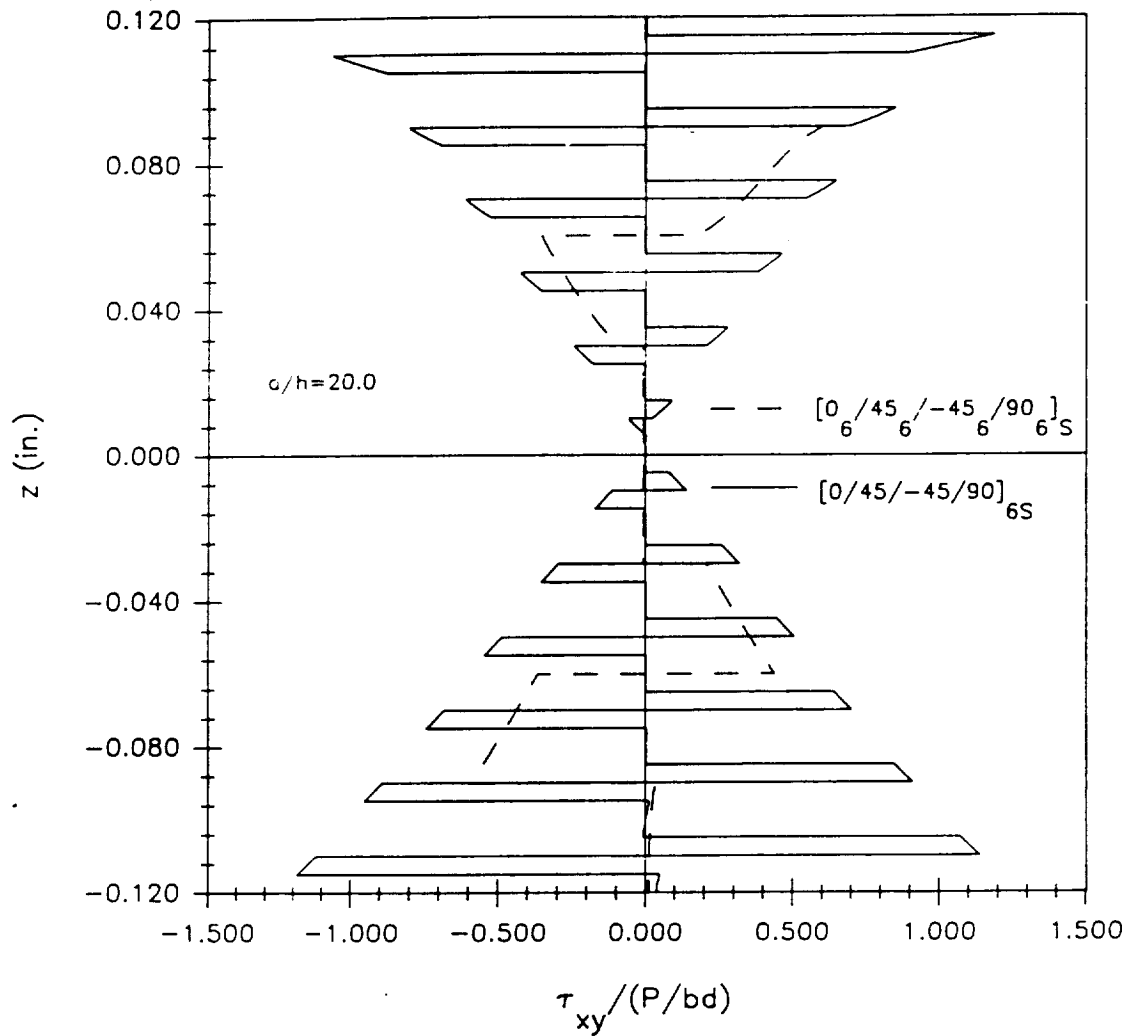
Figure 38. Through-the-thickness distribution for τ_{xy} normalized by the applied stress for a/h=20.0.
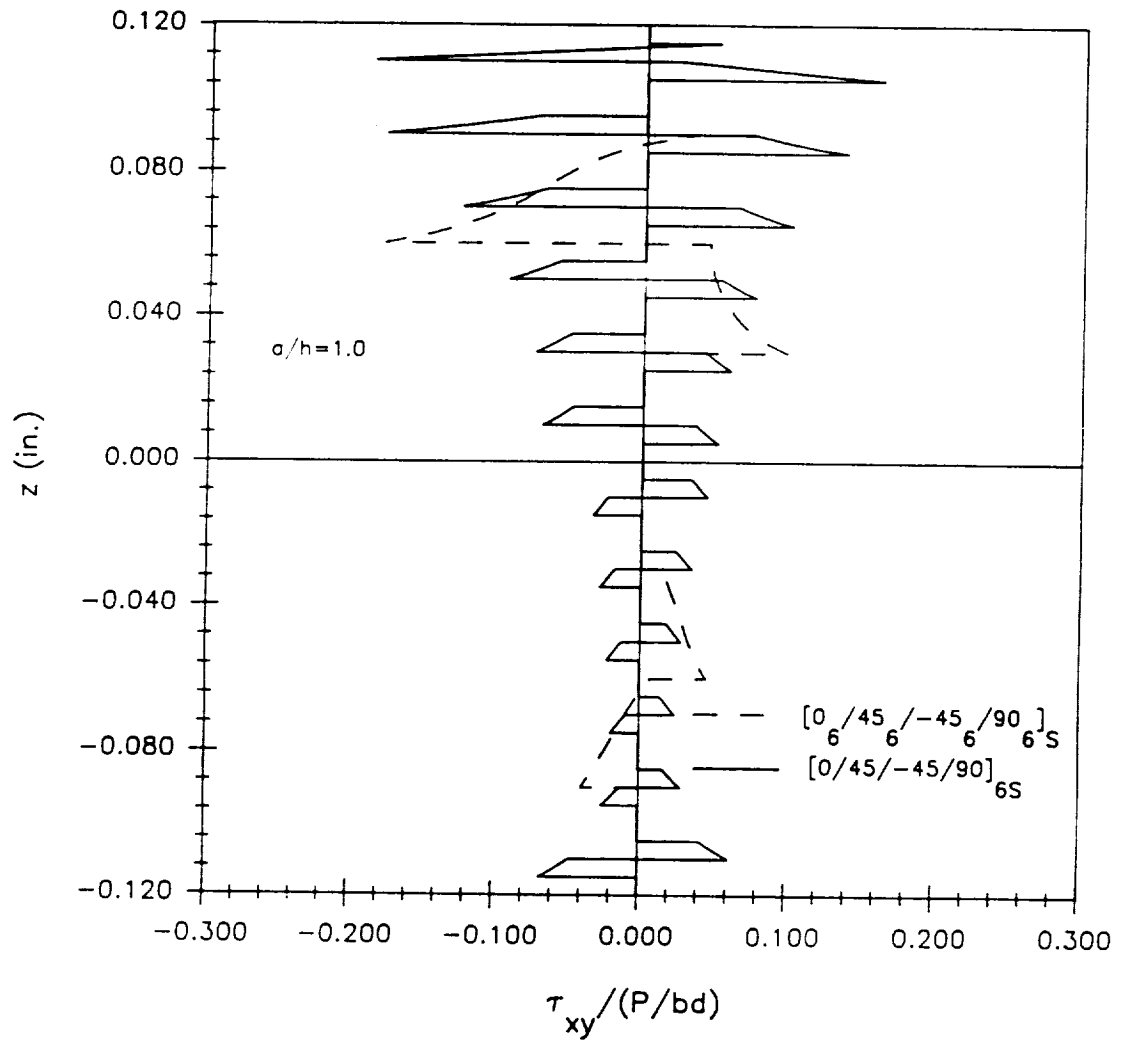
Figure 39. Through-the-thickness distribution for τ_{xy} normalized by the applied stress for a/h = 1.0.
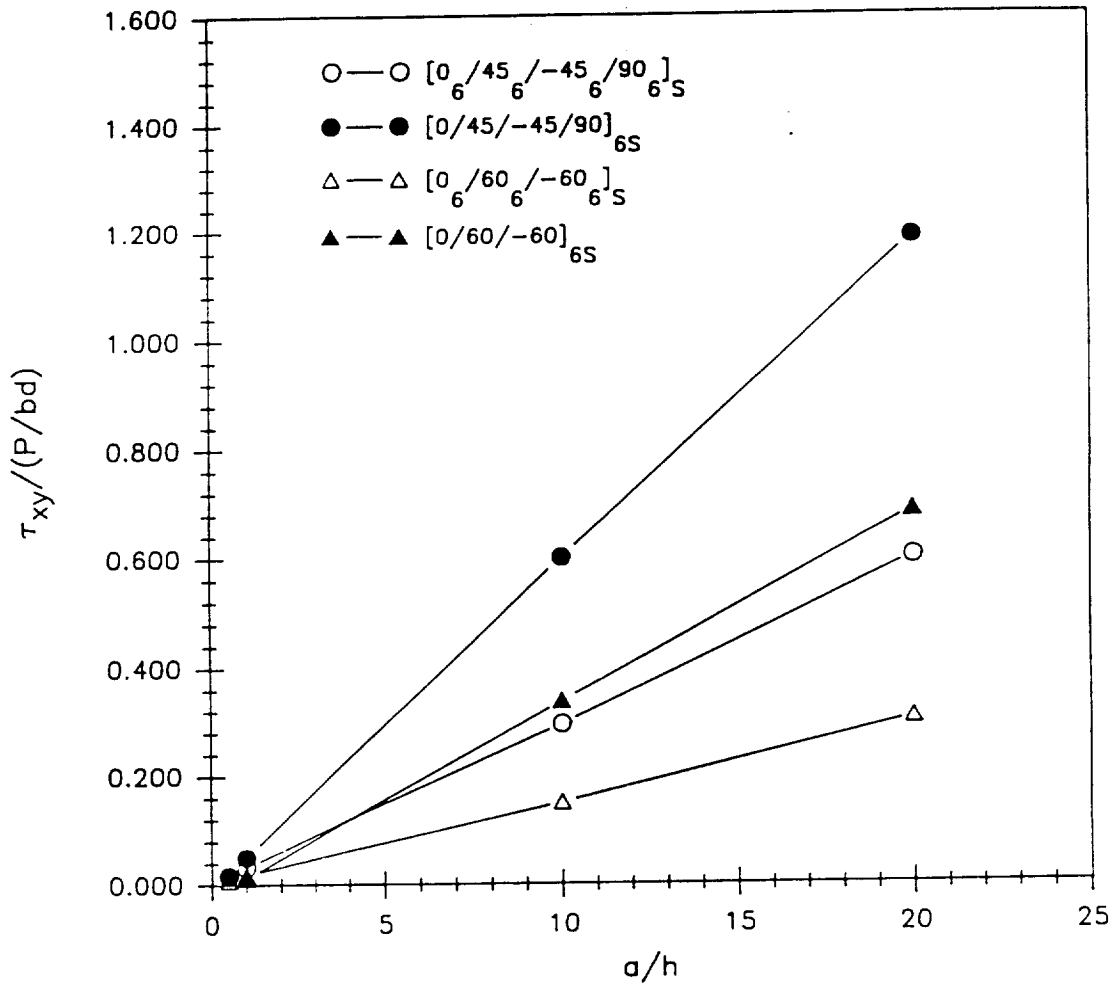
Figure 40. Magnitude of τ_{xy} at the first interface normalized by the applied stress as a function of aspect ratio.
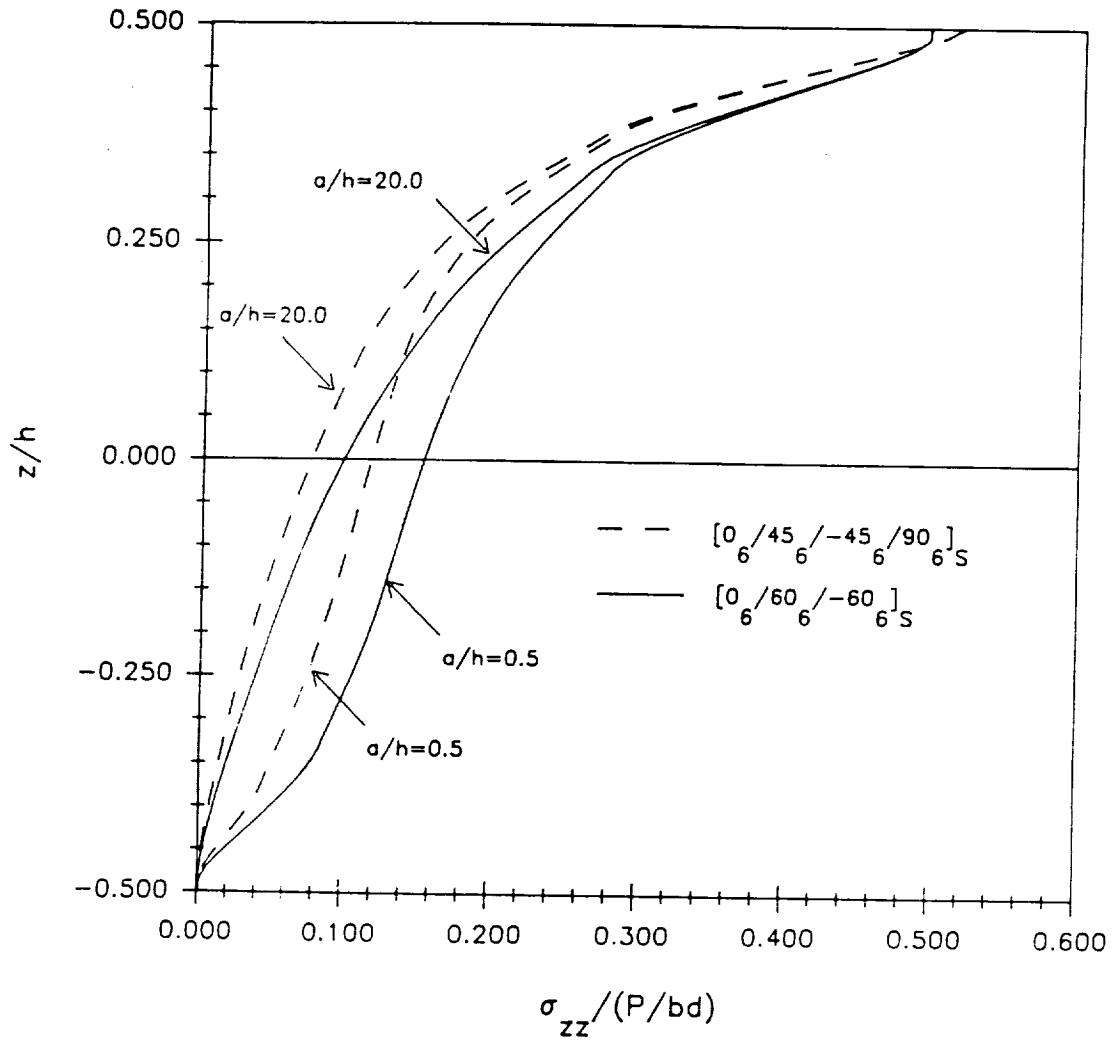
Figure 41. Through-the-thickness distribution for σ_{zz} normalized by the applied stress for a/h=20.0 and 0.5.

As previously mentioned, for the given x-location the through the thickness distributions for the two shear stress components, τ_{xz}, τ_{yz}, are not a strong function of the aspect ratio until this ratio becomes less than 1.0. Even for cases when a/h < 1.0, the only effect is in the form of a very localized disturbance in the neighborhood of the bottom support. The through the thickness distributions for τ_{xz}, normalized with respect to the applied stress, in the four different types of laminates are compared in Figure 42 for an aspect ratio equal to 20.0. The distributions are for an x-location which corresponds to the point of discontinuity in the applied loading. Similar results are shown in Figure 43 for the other component of shear stress, i.e., τ_{yz}. The maximum value for τ_{xz} is shown in Figure 42 to be located directly beneath the top surface of the beam. The magnitude of τ_{xz} is slightly reduced by grouping the plies together and is smaller in the [0/45/-45/90] laminates. Figure 43 shows that the grouped laminates have a significantly smaller maximum value for τ_{yz} in comparison to the interspersed laminates. Also, the magnitude for τ_{yz} is smaller in the [0/45/-45/90] laminates compared to the [0/60/-60] case.

4.5 Closing Comments

The analytical results presented in this chapter were obtained using the elasticity solution developed in Chapter 3 for analyzing various laminated beams. The local stress states were determined for various beam geometries subjected to three-point bend loading conditions. The preliminary analyses investigated the geometric, shear coupling, and stacking sequence effects on the stress distributions. Significant effects were seen in the displacements and the local stresses depending on the fiber orientation, span length-to-depth aspect ratio, and whether or not a grouped or interspersed stacking sequence was used.
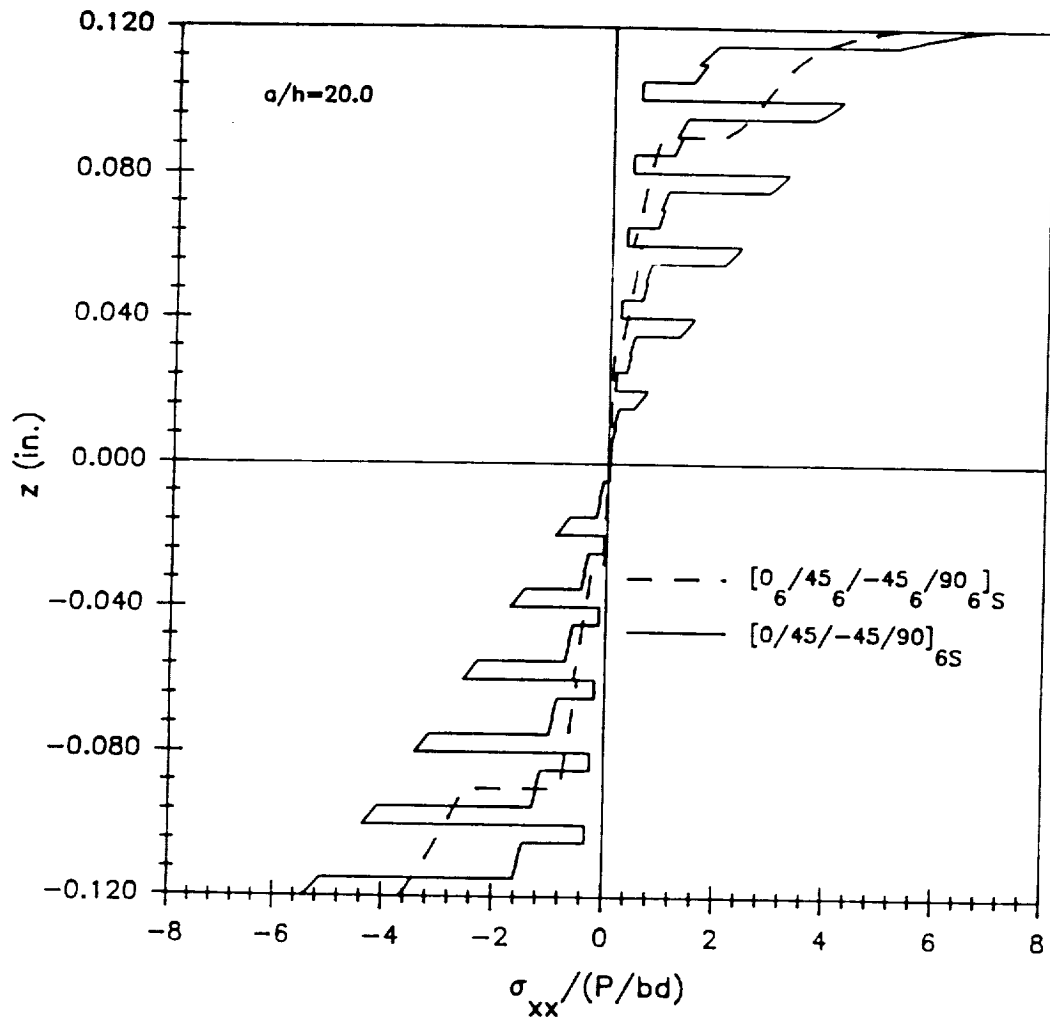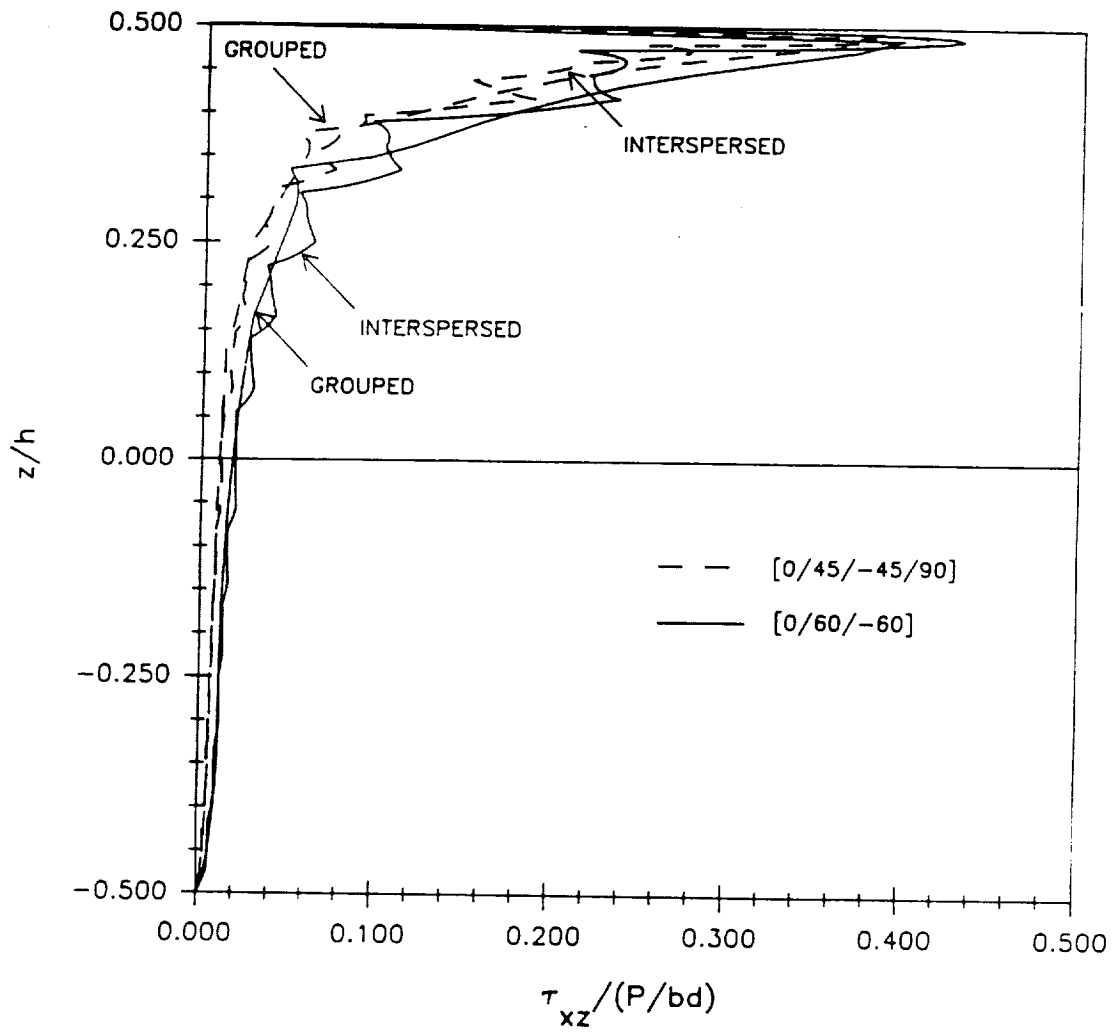
Figure 42. Through-the-thickness distribution for τ_{xz} normalized by the applied stress for a/h = 20.0.
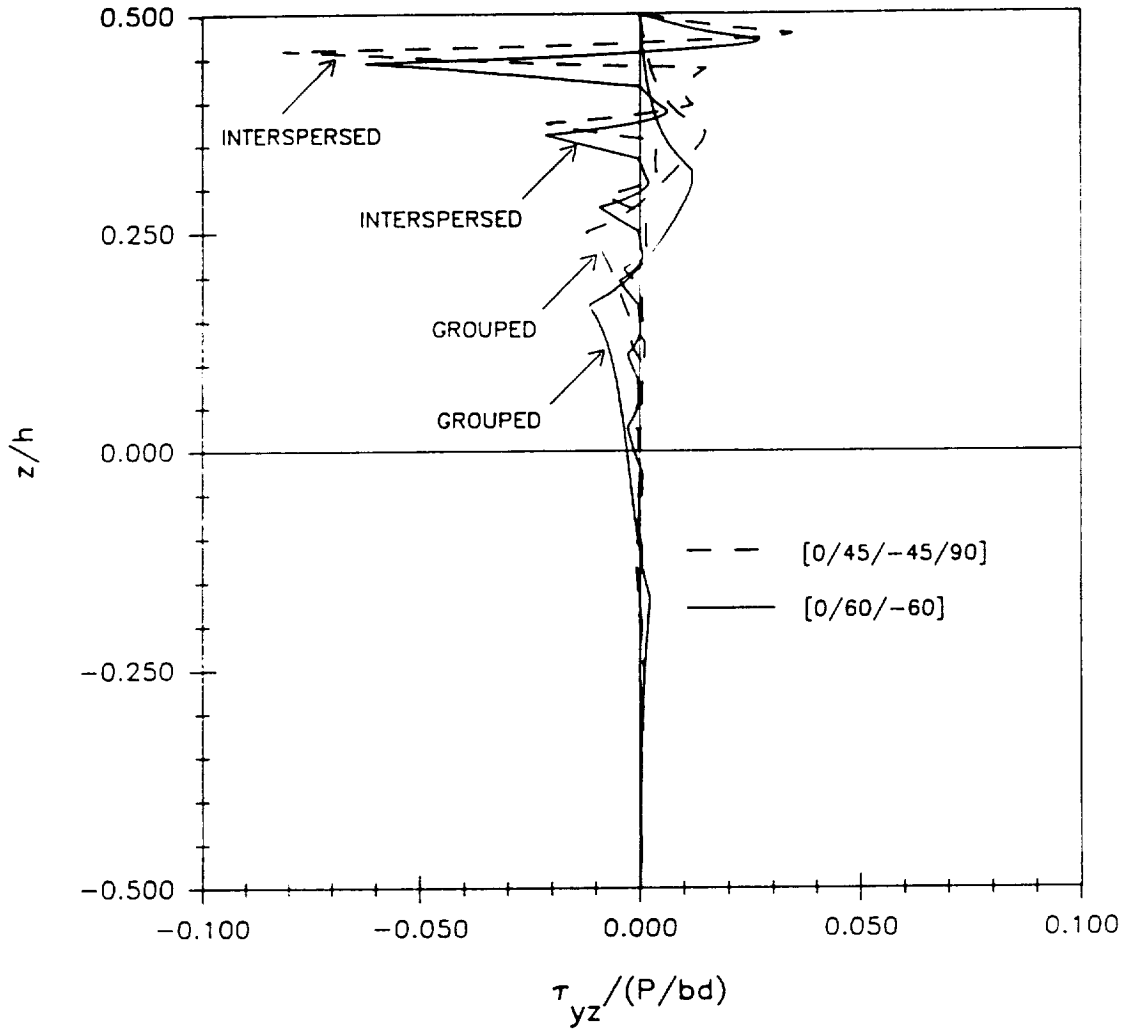
Figure 43. Through-the-thickness distribution for τ_{yz} normalized by the applied stress for a/h = 20.0.

It was shown that for a unidirectional $0°$ beam the bending component of stress, σ_{xx}, largely depended on the distance between the supports, whereas, the normal component of stress, σ_{zz}, and the in-plane shear stress, τ_{xz}, were insensitive to this distance until it became less than the overall height of the beam. The location and magnitude of the maximum shear stress, τ_{xz}, was demonstrated to be a function of the stacking sequence or type of beam. The location of the maximum shear stress was shown to be below the top surface and associated with very high gradients in the vicinity of the concentrated load. The maximum shear stress contour for a $0°$ unidirectional beam was shifted closer to the top surface and had a larger magnitude when compared to an isotropic beam solution. In considering a cross-ply beam, the $90°$ ply beneath the top $0°$ ply had a negligible effect on the magnitude and location of the maximum shear stress. For the quasi-isotropic case, the $45°$ layer produced a slight increase in the magnitude of the maximum shear stress.

When unidirectional laminates consisting of monoclinic layers were considered, i.e., off-axis plies, the results presented showed significant shear coupling effects for a wide range of off-axis fiber orientations. The generalized plane deformation analysis predicted smaller midspan beam deflections in comparison to the plane strain predictions. Consequently, a plane strain analysis which neglects shear coupling effects due to the presence of off-axis layers, makes the beam appear to be softer. These effects decreased as the span length-to-depth aspect ratio of the beam decreased. As mentioned previously, for this type of layer none of the stress components vanished and it was shown that the maximum out-of-plane shear stress, τ_{xy}, had a larger magnitude than its in-plane counterpart, τ_{xz}. Also, an increase in the bending stress, σ_{xx}, was seen as a result of shear coupling in off-axis beams. These results clearly demonstrate the importance of including shear coupling effects in the analysis by performing the more complicated generalized plane deformation analysis.

The effect of stacking sequence on the local stress state was analyzed by considering grouped and interspersed layers in laminated beams having either a $[0/\pm45/90]$ or $[0/\pm60]$ basic ply grouping. The components of stress which are continuous across the interfaces of a lami-

nated beam were seen to be independent of the span length-to-depth aspect ratio when this ratio was greater than 1.0 and for an x-location which corresponded to the point of discontinuity in the applied loading. Conversely, the distribution of the discontinuous stresses in the beam strongly depended on the span length-to-depth aspect ratio. When comparing the stress distributions in a grouped stacking sequence beam to those in an interspersed beam, the effect of grouping layers of equal fiber orientation together was demonstrated by a reduction in the maximum bending stress and a reduction in the magnitude of τ_{xy} in the off-axis plies. However, these grouping effects on the stress state decreased as the span length-to-depth aspect ratio of the beam was made smaller.

As a result of the preliminary analytical investigation, the local stress dependencies described above indicated that different lamination sequences would require testing in the experimental phase of the study. The testing of three-point bend specimens having similar geometries to the beams analyzed in this chapter is an essential part of describing and understanding damage in laminated composite beams. Once the type and location of damage has been identified, and the corresponding applied load at initiation of damage measured, the results can be correlated with the theoretical predictions for the local stress states.

Chapter V

Experimental Investigation

5.1 Testing Program

The analytical procedure developed in Chapter 3 has the capability of predicting the local stress distributions in a laminated beam subjected to surface tractions which are represented by a Fourier series expansion. Results were presented in Chapter 4 for the case of a load uniformly distributed over a small finite distance at the midspan. The reactions at the two support points were also modelled by a uniformly distributed load. To investigate the damage initiation and damage mode in laminated beams, the local stress distributions need to be correlated with the predominant form of initial damage observed for a given beam geometry. This involves determining components of stress or combinations of stresses that are associated with the experimentally observed damage states. Therefore, the second phase of the investigation was concerned with conducting a testing program for laminated beam three-point bend specimens to investigate the damage initiation, forms of damage, and effects of the initial damage on the ultimate failure. Effects of different geometries and lamination param-

eters on the damage initiation load and final failure load as well as damage modes were investigated. Also, beam geometries which experienced extensive damage before the actual ultimate failure occurred were identified. In these cases, the actual stresses in the beams at failure may drastically differ from the predicted stresses using a linear elastic analysis. Then the analytical approach used in the correlation study would not be valid for computing the local stress states at load levels greater than the damage initiation load.

The test matrix for the experimental investigation contained eight different quasi-isotropic stacking sequences, one cross-ply laminate, and one unidirectional lay-up, as shown in Table 1. This matrix was based on the consideration of possible effects of lamination sequence, beam thickness, distance between support points, and layer thickness on the beam's response. Thus, the test matrix was classified into four groups aimed towards studying these effects. The first classification group considered different classes of laminates and consisted of the $0°$ unidirectional beams, the cross-ply beams, and the thickest interspersed quasi-isotropic laminates, i.e., $[0/\pm45/90]_{2ss}$ and $[0/\pm60]_{3ss}$. The second group included the quasi-isotropic laminates with the total number of layers being different and addressed the effects of the beam's thickness on the response. In reference to Table 1, the second group was comprised of the $[0/\pm45/90]_{2ss}$, $[0/\pm45/90]_{1ss}$, $[0/\pm45/90]_{ss}$, $[0/\pm60]_{3ss}$, $[0/\pm60]_{2os}$, and $[0/\pm60]_{ss}$ laminates. The effects of stacking sequence and layer thickness were studied by considering interspersed and grouped stacking sequences. Therefore, group three contained the following laminates: $[0/\pm45/90]_{2ss}$, $[0_s/45_s/-45_s/90_s]_{ss}$, $[0/\pm60]_{3ss}$, and $[0_s/60_s/-60_s]_{7s}$. The fourth group actually encompassed the entire test matrix and pertained to the investigation of span length effects on the beam's response.

The overall beam dimensions were 6.0 inches in length, 1.0 inch wide, and had a thickness which corresponded to the total number of plies. The beams were tested using four different distances between supports, e.g., 5.5, 3.0, 1.0, and 0.5 inches. This produced a range of aspect ratios, a/h (see Figure 4, Chapter 3), from approximately 0.5 up to 25.0. Note that the ASTM standard short beam shear test recommends a span length-to-depth ratio of 5.0. Two tests

were conducted for each configuration, one monotonically up to the initiation of damage followed by unloading and one monotonically up to ultimate failure. The initiation of damage was experimentally defined to be either the point at which the first drop in load was experienced or when the first audible sound of cracking was heard. Only the ultimate failure test was conducted for the $[(0/90)_8/(90/0)_8]_{3s}$ cross-ply laminated beams.

The beam specimens were cut from 8.0 x 12.0 inch panels of AS4/3501-6 Graphite/Epoxy. The laminates were layed-up by the Composites Model and Development Section (CMDS) at NASA Langley Research Center. Prior to machining the specimens, all panels were C-scanned by the Materials Processing and Development Section (MPDS) at NASA Langley Research Center and were judged to be satisfactory. It should be noted that of the 10 panels processed, the $[0_5/45_5/-45_5/90_5]_{ss}$ and $[0/\pm60]_{8s}$ laminates showed the highest percentage of voids. All specimens were measured using a vernier caliper to determine the final dimensions after machining. Five measurements were taken across the width and the thickness, and their average values documented.

The identification of damage in the specimens and failure modes was based on the data collected during the testing and post-test inspection of the specimens using an optical microscope. The magnitude of through-the-thickness deformation plus the indentation under the load was experimentally determined by calculating the difference between the top and bottom surface displacements. This will be discussed in more detail later on in this chapter. The damage was documented by taking photomicrographs of the edges of the specimens in order to illustrate the type and location of damage. A Nikon SMZ-10 stereoscopic microscope was used in conjunction with a Nikon Microflex HFX photomicrographic attachment and Polaroid 4 X 5 land film.

Table 1. Test Matrix

Stacking Sequence	h (in.)	a_1/h	a_2/h	a_3/h	a_4/h
$[0/\pm45/90]_{2ss}$	1.00	5.50	3.00	1.00	0.50
$[0_s/45_s/-45_s/90_s]_{ss}$	1.00	5.50	3.00	1.00	0.50
$[0/\pm45/90]_{1ss}$	0.60	9.17	5.00	1.67	0.83
$[0/\pm45/90]_{6s}$	0.24	22.92	12.5	4.17	2.08
$[0/\pm60]_{3ss}$	1.05	5.24	2.86	0.95	0.48
$[0_s/60_s/-60_s]_{7s}$	1.05	5.24	2.86	0.95	0.48
$[0/\pm60]_{20s}$	0.60	9.17	5.00	1.67	0.83
$[0/\pm60]_{8s}$	0.24	22.92	12.5	4.17	2.08
$[0_{150}]$	0.75	7.33	4.00	1.33	0.67
$[(0/90)_8/(90/0)_8]_{3s}$	0.96	5.73	3.12	1.04	0.52

5.2 Testing Procedure

Based on the preliminary analytical results presented in Chapter 4, the various specimen geometries outlined in the above test matrix were expected to produce different forms of damage. Testing such a wide range of geometries was facilitated by designing a test fixture for three-point bending. The key features of the test fixture were varying support locations and easy interchangability of contact radii. A slotted base plate was used for mounting and positioning the two bottom surface supports. The supports were located equidistance from the centerline of the load point and secured in place using recessed bolts on the bottom of the base plate. A one inch diameter hole was drilled in the center of the base plate for insertion of a DCDT displacement transducer for the measurement of the bottom surface displacement relative to the support points. The transducer was held in place with a set-screw. The loading nose was attached to a 1½ inch by 2 inch rectangular steel bar using four ¼ inch diameter

bolts. The two supports and loading nose had a ¼ inch radius, were 1½ inches wide, and were measured to have a Rockwell hardness of 20 on the C-scale. The photograph in Figure 44 shows the details of the fixture and a typical beam specimen geometry.

The rectangular steel bar was mounted between two L-shaped gripping plates. The gripping plates were part of the crosshead arrangement on a MTS 100 kip hydraulic test stand used for conducting the tests. The set-up for the testing equipment, test fixture, and data acquisition are shown in Figure 45. All of the specimens were tested with the 100 kip MTS Controller on stroke control and with the function generator ramp rate set at 1.3 mm/min. This is the loading rate recommended by the ASTM D 2344-84 standard for short beam shear tests. The load and stroke ranges for each test depended on the beam geometry of the particular specimen being tested.

The experimentally collected data consisted of the applied load, and both top surface and bottom surface beam displacements. The bottom displacement was measured by the DCDT displacement transducer mounted on the base plate as previously described (see Figure 44). Transducers having different ranges were used depending on the distance between the support points. For the specimens tested with a span length of 5.5 inches and 3.0 inches a transducer having ± 0.100 inches of travel was employed. For a 1.0 inch span length a transducer having a range of ± 0.050 inch was used because the size of the ± 0.100 inch transducer body was greater than the thickness of the base plate. Consequently, the supports could not be placed an inch apart without interfering with the transducer body. When the span length equaled 0.5 inches no transducer could be placed between the support points to measure bottom surface displacements. When a transducer was used it was in conjunction with a DCDT Summing Amplifier. Initially, it was assumed that the compliance of the machine and test fixture were negligible and that the stroke motion would accurately represent the top displacement. However, when testing specimens with small aspect ratios, the resulting small order of magnitude beam deflections were such that the compliance or so-called "lost motion" of the system had to be properly taken into account.
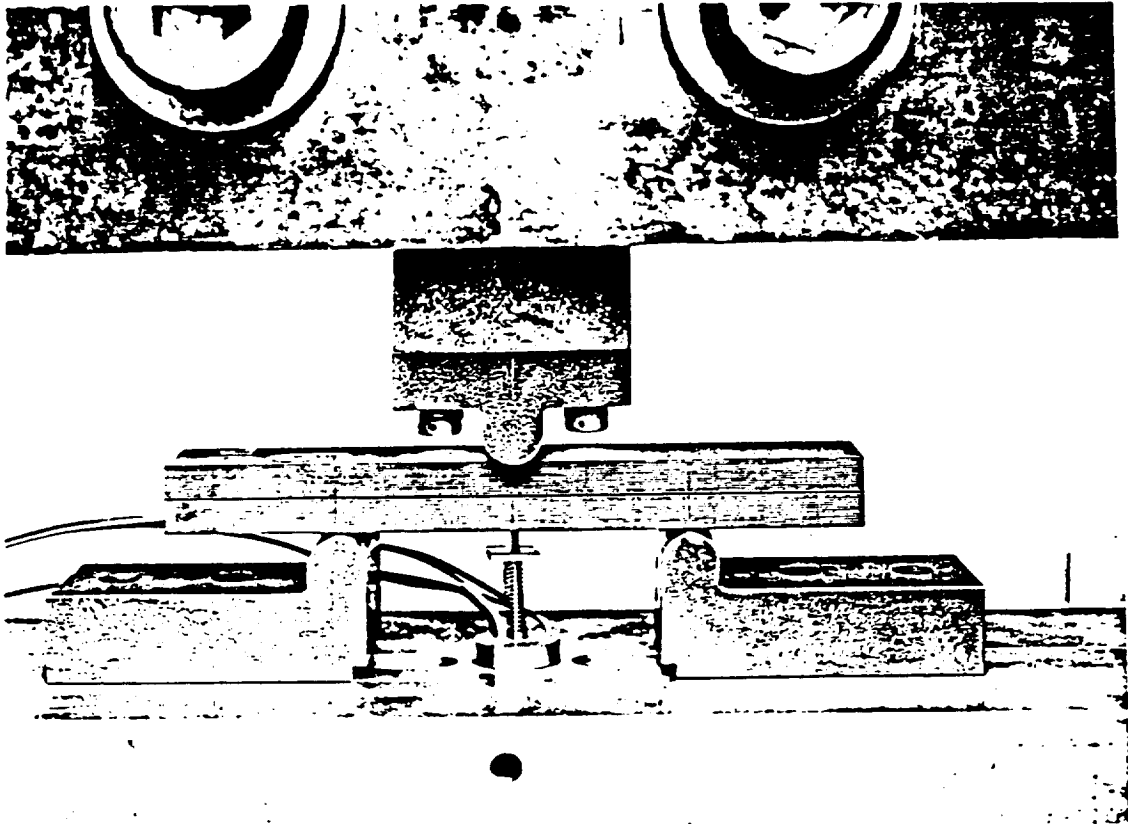
Figure 44.   Three-point bend test fixture.
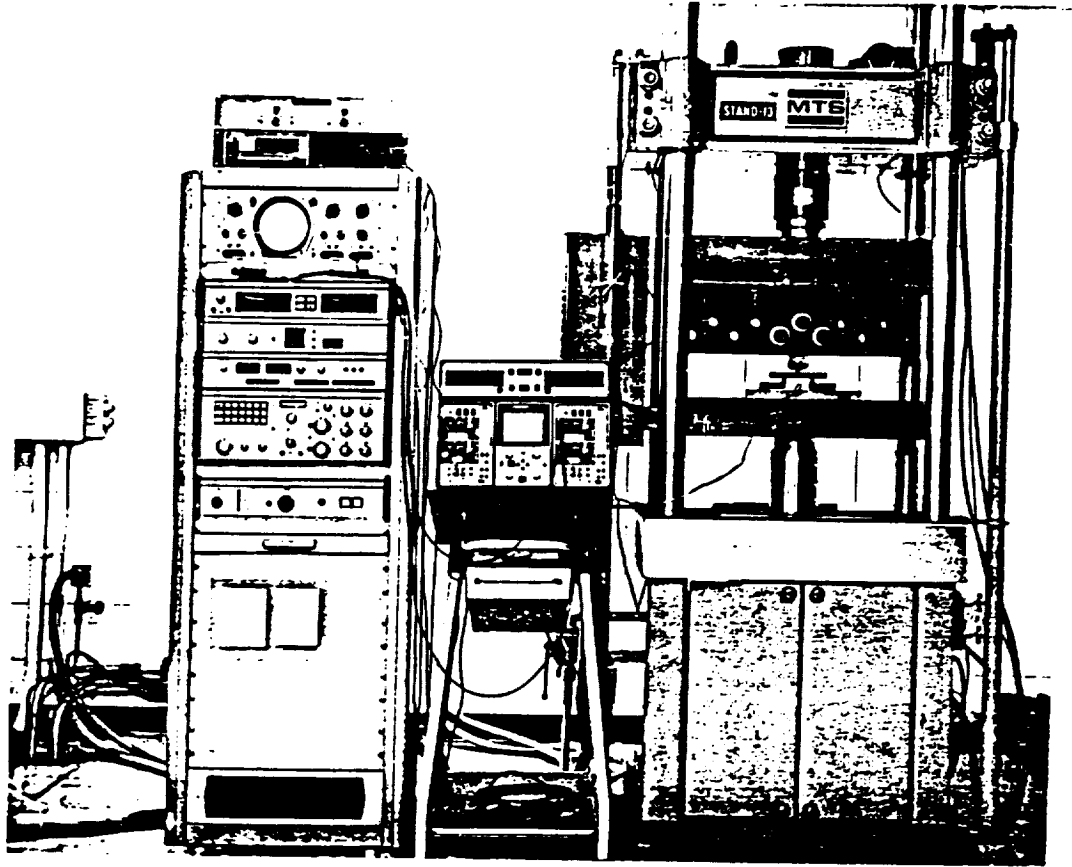
Figure 45. Testing equipment and experimental set-up.

Two different data acquisition units were used over the course of the testing program for collecting and storing the experimental data. Data from the preliminary tests was recorded using a Hewlett-Packard 3497A data acquisition unit and a Hewlett-Packard 9134/9826 computer. The data was subsequently converted to an IBM format for post-processing. The remaining tests utilized a Nicolet 4094 Digital Oscilloscope, XF-44 Disk Drive, and 4563 Plug-In Controls as shown in the center portion of Figure 45. The voltage versus time output format of the Nicolet system was converted to a time based load versus displacement format using the Vu-Point software package. The data was then writen to an ASCII file for further post-processing.

5.3 Results

5.3.1 Displacements

The collected experimental data was post-processed in order to generate applied load versus beam displacement and load versus local deformation, i.e., indentation curves. As discussed in the previous section, two displacement measurements were taken, one from a DCDT displacement transducer and one from the stroke of the MTS testing machine. However, the measured displacements cannot be directly compared with the deformations predicted from the analytical solution. The transducer reading, for example, contained the summation of three components of displacement; the amount of bottom surface beam deflection at the midspan, the amount of indentation at the supports, and an intangible quantity related to the test fixture deformation. The summation of five displacement quantities was possibly recorded for the stroke measurement; the amount of indentation under the loading nose, the

indentation at the support points, the "lost motion" due to the machine compliance, fixture related deformations, plus the beam deflection.

In order to compare the displacements calculated from the elasticity solution with the experimentally measured deformations one needs to isolate the part of the calculated displacements which corresponds to the experimentally measured quantities. Different components of the experimentally measured displacements at the top and bottom beam surfaces, i.e., stroke (Δ_S) and DCDT (Δ_D), respectively, are shown in Figure 46 and can be written mathematically as:

$$\Delta_S = \delta_s + \delta_N + \delta_m + w_b \tag{1}$$

$$\Delta_D = \delta_s + \delta_d + w_b \tag{2}$$

where, as previously discussed, δ_s = support indentation, δ_N = nose indentation, δ_m = machine compliance plus fixture related deformations, δ_d = fixture related deformations, and w_b = bottom surface beam deflection. Subtracting equation (2) from equation (1) results in:

$$\Delta_S - \Delta_D = \delta_N + \delta_m - \delta_d \tag{3}$$

Rewriting this equation:

$$(\Delta_S - \delta_m) - (\Delta_D - \delta_d) = \delta_N \tag{4}$$

The amount of top surface indentation and deformation can now be found by taking the difference between the stroke and DCDT readings which have been adjusted for the system related motion by subtracting the machine compliance and fixture related deformations, respectively, i.e., equation (4).

The combined compliance of the MTS load frame, the crosshead system which included the L-shaped gripping plates, and the loading nose attached to the rectangular steel bar was experimentally determined by compressing the loading nose directly on the ram. To prevent
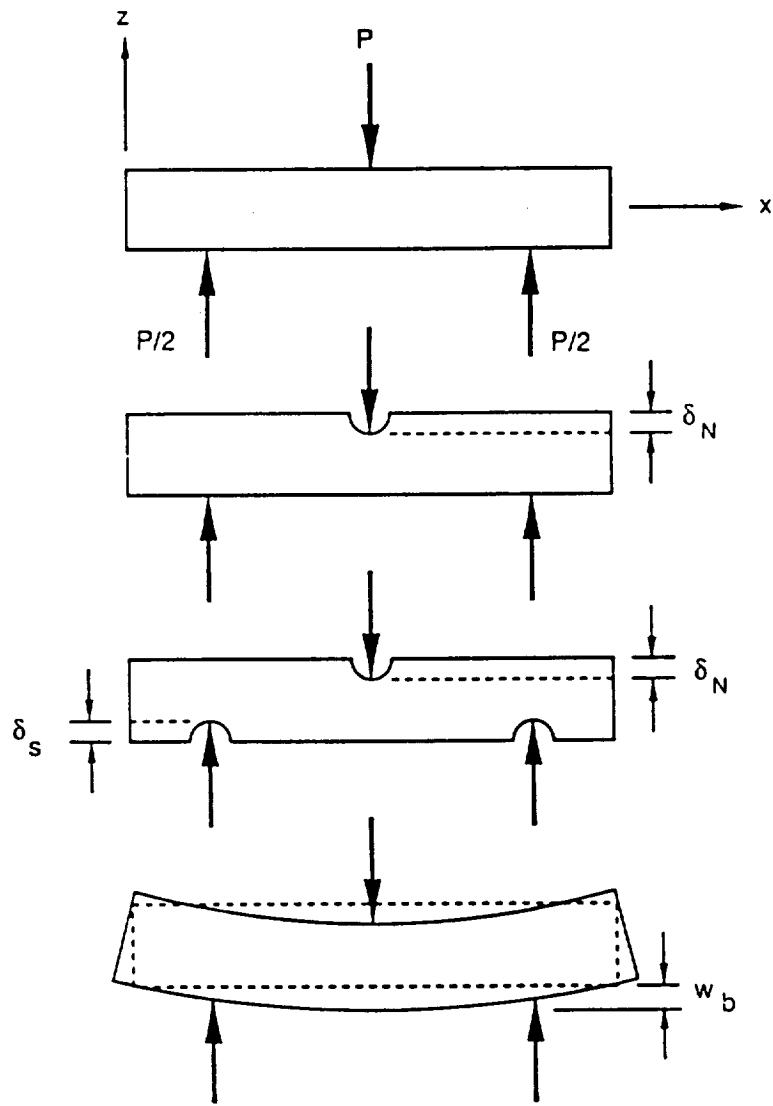
Figure 46. Measured displacement quantities in three-point bend specimen.

any damage to the ram's surface and to account for the base plate appendage of the test fixture a one inch steel plate was actually used as the contacting surface. The only remaining unaccounted for parts were the two supports. Consequently, a special three-point bend test was conducted to include any support related displacements. A block specimen was machined, from 4130 steel heat treated to a Rockwell hardness of 40, to an overall length $L=2.0$ inches, a height of 2.0 inches, and a width of 1.0 inch. The block was then subjected to three-point bend loading conditions with a span length of 1.5 inches. For this geometry, and recalling that the supports and loading nose only had a hardness of 20, there will be negligible bottom surface beam deflection and no indentation at the contact points. Therefore, any measured displacement will be related to motions in the test equipment and fixture themselves and not associated with any beam response. Figure 47 shows how the measured stroke motion (δ_m) and displacement transducer reading (δ_d) varied as a function of the applied load. When the load P was less than 13 kips an empirical relationship which fits the experimental data is given by:

$$
\begin{aligned}
\delta_d = &-5.3578 \text{x} 10^{-5} + 1.7268 \text{x} 10^{-3} P - 4.5208 \text{x} 10 -4 P^2 + 6.4143 \text{x} 10^{-5} P^3 - 4.3591 \text{x} 10^{-6} P^4 \\
&+ 1.1273 \text{x} 10^{-7} P^5 \\
\delta_m = &\; 1.8374 \text{x} 10^{-5} + 1.0906 \text{x} 10^{-2} P - 4.5661 \text{x} 10^{-3} P^2 + 1.1926 \text{x} 10^{-3} P^3 - 1.8566 \text{x} 10^{-4} P^4 \\
&+ 1.6756 \text{x} 10^{-5} P^5 - 8.0416 \text{x} 10^{-7} P^6 + 1.5818 \text{x} 10^{-8} P^7
\end{aligned}
\tag{5}
$$

and when P was greater than 13 kips this relationship becomes:

$$
\begin{aligned}
\delta_d = &\; 3.0021 \text{x} 10^{-3} + 1.1486 \text{x} 10^{-5} P + 8.5327 \text{x} 10^{-6} P^2 - 1.6137 \text{x} 10^{-7} P^3 \\
\delta_m = &\; 8.1801 \text{x} 10^{-3} + 1.0855 \text{x} 10^{-3} P - 1.6512 \text{x} 10^{-5} P^2 + 2.0153 \text{x} 10^{-7} P^3
\end{aligned}
\tag{6}
$$

The two relationships given by equations (5) and (6) were used to calculate the displacements unrelated to beam bending as a function of load intensity, which were then subtracted from the stroke and transducer measurements. Consequently, the displacements which are presented in Appendix A, Figures 89 through 128, include the beam deflection plus unknown amounts of indentation plus local deformations at the two supports and under the loading nose. The load-displacement results are presented for both the damage initiation test and the

ultimate failure test. All of the figures, 89-128, illustrate an excellent repeatability in the curves for the results of the two tests conducted with identical beam geometries.

The top surface displacements in the first four figures of Appendix A, 89-92 , are shown in Figure 48 and demonstrate that the $0°$ unidirectional beams have a nonlinear load-displacement relationship for the four aspect ratios tested. In the smaller aspect ratio beams the nonlinear behavior is not thought to be structure related but to be a result of nonlinear contact effects and matrix nonlinearity in the vicinity of the loading nose. When the specimens have a larger aspect ratio, the nonlinearity is thought to be related to the shear deformations and the material nonlinearity due to the softening behavior of graphite/epoxy under axial compression. For the large aspect ratio beams the response is governed by bending effects and compressive bending stresses exist above the midplane of the beam. Consequently, the softening behavior generally observed in uniaxial compression specimens is also seen in beam specimens due to the compressive bending stresses.

The results presented in Figures 93-128 of Appendix A are the load-displacement curves for the cross-ply and quasi-isotropic beams. All of these curves demonstrate a linear load-displacement relationship up to the initiation of damage, disregarding the initial nonlinear portion of the curves. The only exceptions to this type of behavior are seen for the 1.0 inch span length cross-ply beam, and the 0.5 inch span length $[0/\pm45/90]_{1ss}$ and $[0/\pm60]_{2as}$ specimens, in Figures 95, 108, and 122, respectively. Recall that the initiation of damage was defined to occur when the applied loading first experiences a reduction in magnitude. The initial nonlinear portion of the curves is believed to be a result of very localized contact related deformations and unrelated to the beam's global response.

The applied load is plotted as a function of the indentation calculated from equation (4), δ_N, for all tested laminates in Figures 129 through 137 of Appendix A. The results tend to show the local indentation at the top surface to be independent of the span length and the stacking sequence up until damage has been initiated. The indentation at the supports, δ_s, can be ex-
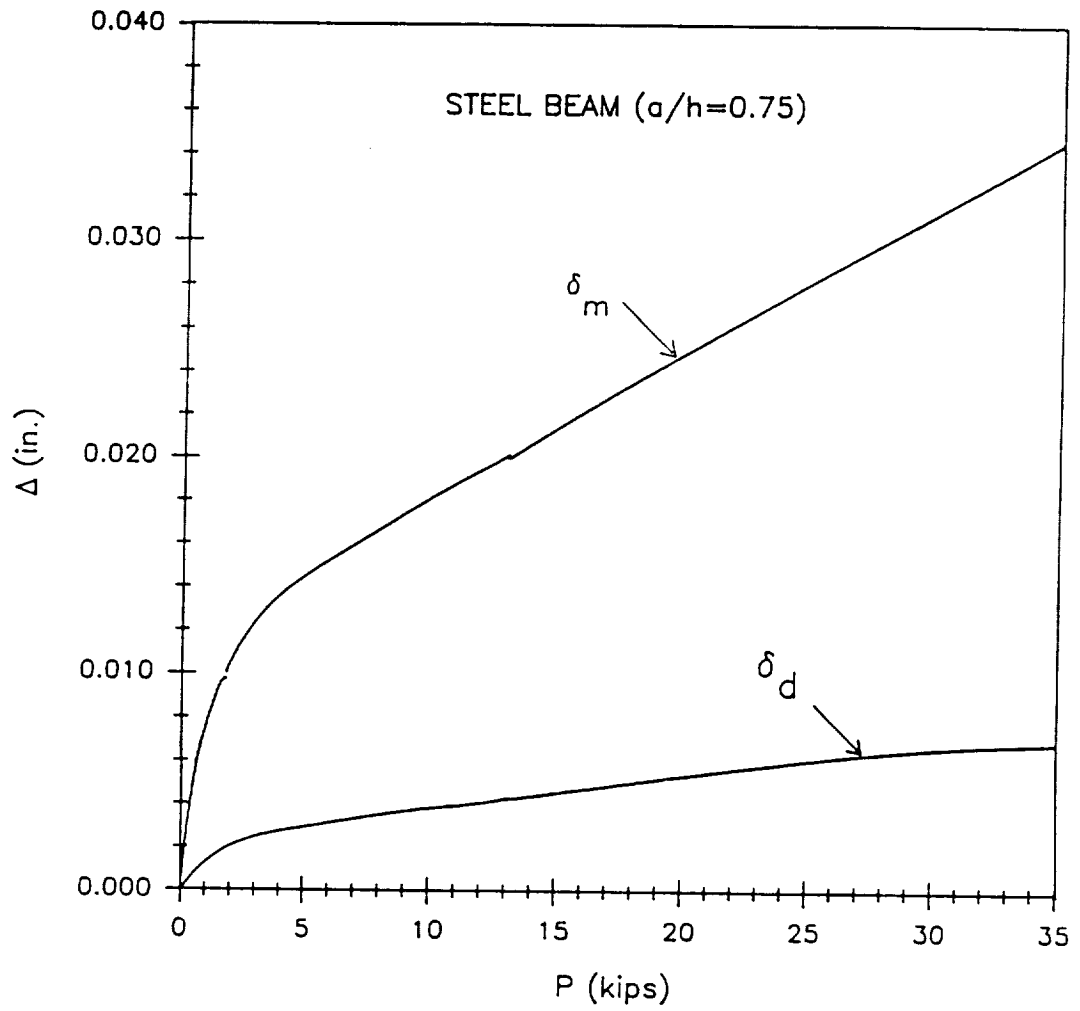
Experimental Investigation

Figure 47. Load versus experimental displacements for a 4130 steel beam having an aspect ratio of 0.75.
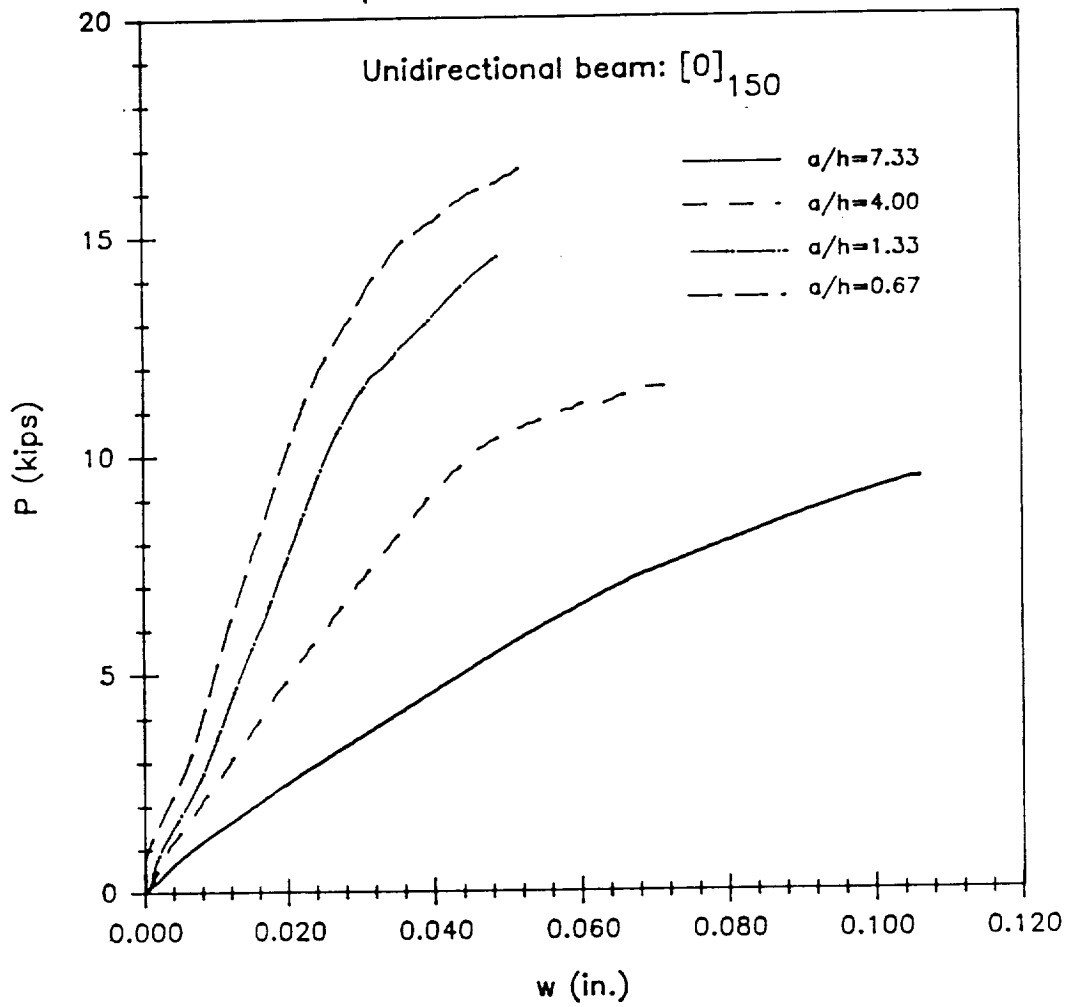
Figure 48. Load versus top surface displacements for the unidirectional beams and four different aspect ratios.

pressed in terms of the indentation at the top surface in the following manner. Assuming a Hertzian type of pressure distribution at the contact points and a spherical indenter, the indentation under the load nose, δ_N, will be proportional to the contact force raised to the two-thirds power (Love [10]), i.e.,

$$\delta_N = k_n P^{2/3} \tag{7}$$

where the proportionality constant, k_n, depends on the material system of the beam. Using equation (7), the unknown indentation at the support points, δ_s , can be expressed in terms of the top surface indentation, δ_N. Since the force at the supports is equal to one half of the applied load on the top surface, the indentation at the supports, δ_s is:

$$\delta_s = k_n \left(\frac{P}{2} \right)^{2/3} = \left(\frac{1}{2} \right)^{2/3} \delta_N \tag{8}$$

For the case of a cylindrical indenter, Sankar [37] showed that the indentation will be proportional to the contact force raised to the one-half power. Therefore, for three-point bend experiments the 2/3 power in equations (7) and (8) should be replaced by 1/2.

5.3.2 Ultimate Failure Loads

Figures 49 through 51 show the dependence of the maximum load on the span length-to-depth aspect ratio and the type of laminate. As previously discussed in this chapter, the test matrix was classified into four different groups. The results for the first group are presented in Figure 49 and illustrate the ultimate load as a function of aspect ratio for different classes of laminates. When comparing the cross-ply results to the unidirectional 0° results it is observed that the cross-ply laminates have a greater load carrying capacity for the smaller aspect ratios but have a lower ultimate load than the unidirectional beam results as the aspect ratio becomes large. The dependence of the ultimate load on the a/h aspect ratio for the two quasi-isotropic

laminates shown in Figure 49, i.e., $[0/\pm45/90]_{2ss}$ and $[0/\pm60]_{3ss}$, is similar. For the larger aspect ratios the two quasi-isotropic stacking sequences have ultimate failure loads which are comparable to the cross-ply beam results. However, as the span length-to-depth aspect ratio is reduced the quasi-isotropic beams have larger ultimate loads in comparison to both the $0°$ unidirectional and cross-ply beam results.

The second group of beams was classified on the premise of studying beam thickness effects and the results for the ultimate load as a function of aspect ratio are shown in Figure 50. According to the test matrix given in Table 1, the $[0/\pm45/90]$ and $[0/\pm60]$ repetitive ply groupings were used to lay-up laminated beams having three different overall thicknesses of 1.00, 0.60, and 0.24 inches. In Figure 50, the open symbols are for the $[0/\pm45/90]$ quasi-isotropic laminates and the filled symbols are for the $[0/\pm60]$ quasi-isotropic laminates. Also, the circles correspond to the 1.00 inch thick beams, the triangles represent the 0.60 inch thick beams, and the squares are for the 0.24 inch thick beams. Similar to what was stated above for the quasi-isotropic laminates in Figure 49, for a given beam thickness the dependence of the ultimate load on a/h is much the same between the $[0/\pm45/90]$ and $[0/\pm60]$ laminates. The only exception being for the case of a 0.24 inch thick beam having an aspect ratio of 2.08 where the $[0/\pm60]_{ss}$ beam's ultimate load is almost double that of the $[0/\pm45/90]_{ss}$ beam. The results presented in Figure 50 show that the beam's thickness significantly affects the relationship between the ultimate load and the aspect ratio. This figure illustrates that for a given a/h aspect ratio the three different beam thicknesses produce three different failure loads. For example, for an aspect ratio of approximately 5.0 the ultimate failure loads for the $[0/\pm60]$ beams with thicknesses of 1.05, 0.6, and 0.24 inches were 10.51, 8.54, and 3.05 kips, respectively. However, the difference in the failure loads is seen to decrease as the aspect ratio of the beam increases. Consequently, the a/h ratio does not uniquely describe the failure loads and caution must be exercised when using the span length-to-depth aspect ratio as a nondimensional scaling parameter, especially for the case of small a/h ratios.

Figure 51 illustrates the effect of grouping plies together on the ultimate load, i.e., the effect of increasing the relative thickness of a given ply orientation with respect to the laminate thickness. The laminates in the third classification group were considered and the results for the ultimate load as a function of a/h are shown in this figure. The open symbols correspond to the interspersed stacking sequence, whereas the filled symbols are for the grouped stacking sequence. The $[0/\pm45/90]$ laminates are represented by circles and the $[0/\pm60]$ laminates by triangles. For the range of aspect ratios tested and for both of the quasi-isotropic laminates, grouping the plies together reduced the ultimate load when compared to the ungrouped laminates having the same total number of plies. The percentage of load reduction was larger for the $[0/\pm45/90]$ laminates than for the $[0/\pm60]$ laminates except for the case of an aspect ratio equal to 0.50. Also, the percentage of load reduction decreases as the aspect ratio of both the quasi-isotropic beams is reduced. The $[0/\pm45/90]$ laminates have a maximum reduction of 51% for the largest aspect ratio tested, decreasing to 0% for the smallest aspect ratio. A 26% reduction is seen for the largest aspect ratio $[0/\pm60]$ beam and decreases to approximately 15% for the remaining aspect ratios tested. It is also interesting to note that as stated before the two different quasi-isotropic laminates have similar load carry capability if the layers are distributed throughout the laminate.

5.3.3 Damage Susceptibility

The susceptibility of a laminated beam to damage when subjected to an applied load is a measure of how easily damage is induced. The damage susceptibility of the three-point bend specimens was determined by investigating the dependence of the damage initiation load on the aspect ratio for the different lay-ups. As in the case for the ultimate loads presented above, the classification scheme for the test matrix is used for presenting the experimental data in Figures 52 through 54. The damage susceptibility for different classes of laminates is shown in Figure 52, beam thickness effects in Figure 53, and stacking sequence effects in
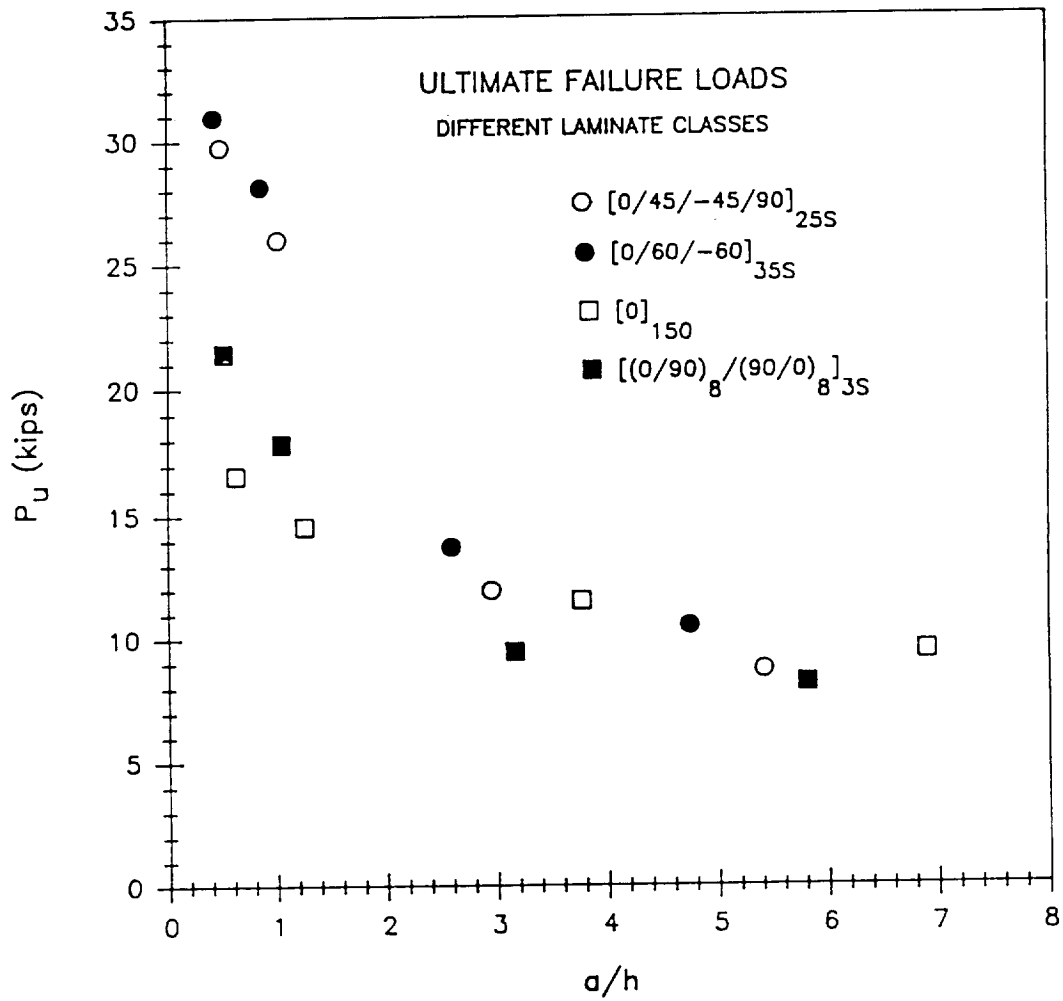
Figure 49. Ultimate failure load as a function of span length-to-depth aspect ratio for different classes of laminates.
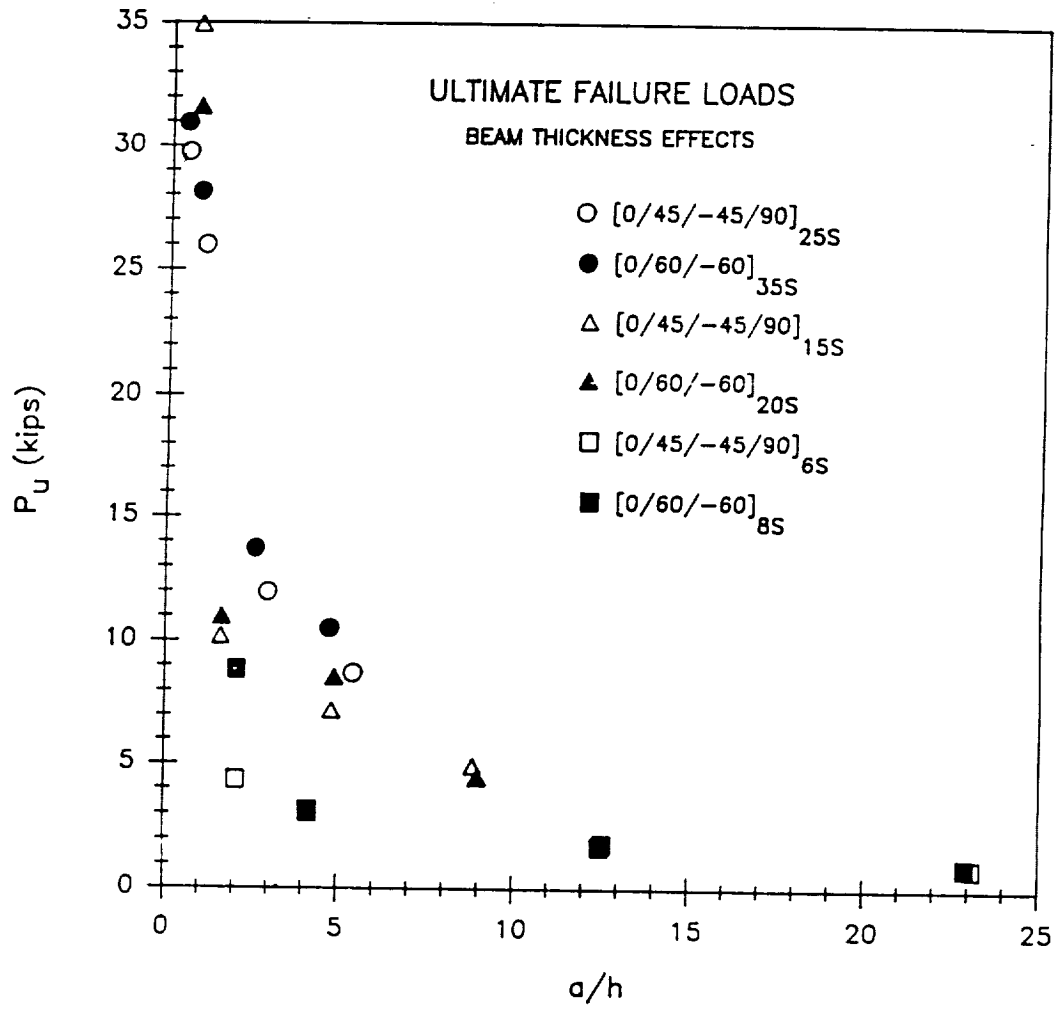
Figure 50. Ultimate failure load as a function of span length-to-depth aspect ratio and beam thickness effects.
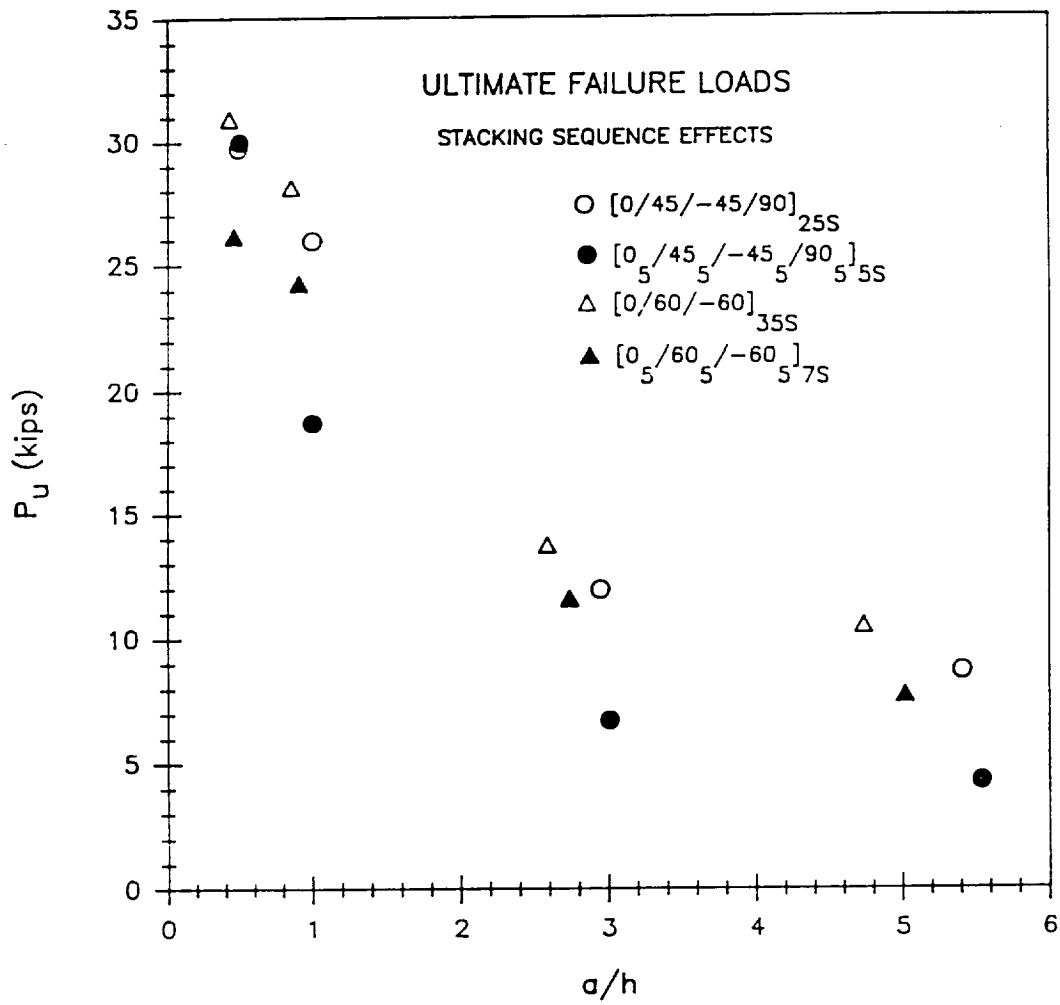
Figure 51. Ultimate failure load as a function of span length-to-depth aspect ratio and stacking sequence effects.

Figure 54. From Figure 52 and for a large aspect ratio, the cross-ply beam is seen to be the most susceptible to damage in comparison to the 0° unidirectional beam. For the smallest aspect ratio tested, the 0° unidirectional beam is more damage susceptible than the cross-ply and quasi-isotropic laminates. When comparing the two quasi-isotropic laminates, Figure 52 shows that the $[0/\pm45/90]_{2ss}$ laminated beam is more susceptible to damage than the $[0/\pm60]_{3ss}$ beam when the span length-to-depth aspect ratio is greater than 2.50. When the aspect ratio becomes less than 2.50 the dependence of the damage initiation load on a/h demonstrates the $[0/\pm60]_{3ss}$ beams to be more damage susceptible than the $[0/\pm45/90]_{2ss}$ beams.

Figure 53 illustrates the dependence of the damage initiation load on the aspect ratio for the six quasi-isotropic laminates having an interspersed stacking sequence. For the entire range of aspect ratios tested, the 0.24 inch thick beams are seen to be the most damage susceptible for a given a/h ratio. Also, the dependence of the damage initiation load on a/h is the same for the $[0/\pm45/90]_{ss}$ and $[0/\pm60]_{ss}$ laminates. The results for the 0.60 inch thick beams indicate that the $[0/\pm45/90]_{1ss}$ laminated beams have a lower damage initiation load than the $[0/\pm60]_{2ss}$ beams for a/h between 1.0 and 8.0, and are therefore more damage susceptible. In comparison to the previous discussion for the ultimate failure loads, the beam thickness effects on the dependence of the damage initiation load on a/h are seen to be even more significant. In other words, for a given a/h the differences between the damage initiation loads for the different beam thicknesses are greater than the differences seen in the ultimate failure loads.

The effects of grouping plies together on the damage susceptibility are depicted by the results in Figure 54. In this figure, the damage initiation load is plotted as a function of the aspect ratio for the grouped and interspersed quasi-isotropic stacking sequences. Similar trends are seen in the dependence of the damage initiation load on a/h as were described for the ultimate failure loads. The grouped stacking sequences are observed to be more damage susceptible than the corresponding interspersed laminates. Also, for the larger aspect ratios,

Figure 54 shows that the [0/45/ − 45/90] laminates are more susceptible to damage in comparison to the [0/60/ − 60] laminated beams.

5.3.4 Damage Tolerance

Once damage is present in the laminated beam, how well it is tolerated with regard to ultimate failure defines the beams tolerance to damage. A measure of a laminated beam's tolerance to damage is the ratio of the load which produces the initial damage to the load measured at ultimate failure. A ratio equal to one would correspond to a beam configuration which is considered to be highly damage intolerant. On the other hand, a value less than one would mean the beam is still capable of carrying loads or resistant to the applied load once damage has initiated. For the $0°$ unidirectional beams the ratio of initial damage load to the ultimate load was approximately equal to one, i.e., intolerant to damage, except for the case of an aspect ratio equal to 0.67, where this ratio was 0.89. As a result of the beam thickness effects described above, comparisons between the different stacking sequences in Table 1 must be restricted to beams having equivalent thicknesses.

The dependence of the damage tolerance, as defined above, on the beam's a/h aspect ratio is shown in Figure 55 for the beams having an overall thickness approximately equal to 1.0. There is some scatter in the data, especially for the cross-ply results, but it appears that for a span length-to-depth aspect ratio greater than 5.0 and for the three-point bend specimen configuration these laminates will have a low damage tolerance. When the aspect ratio is reduced, the beam's resistance to the applied load increases after the initial damage has occurred until the span length-to-depth aspect ratio becomes equal to 1.0. The damage tolerance then begins to decrease for smaller span length-to-depth aspect ratios, e.g., the ratio of the damage initiation load to the ultimate failure load for the $[0/\pm45/90]_{2ss}$ beams was equal to 0.81 for a/h = 1.0 and 0.92 for a/h = 0.5. The results presented in Figure 55 also show that

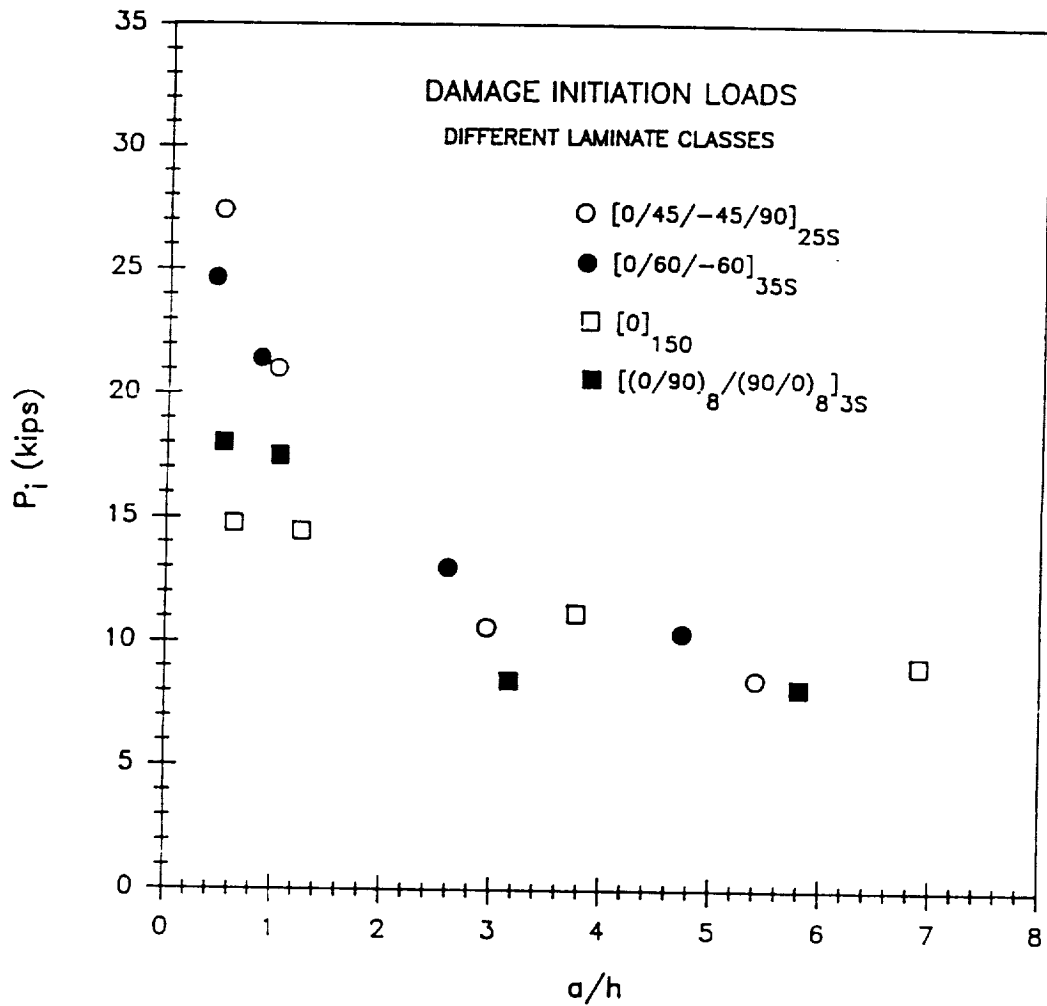**Figure 52.** Damage initiation load as a function of span length-to-depth aspect ratio for different classes of laminates.

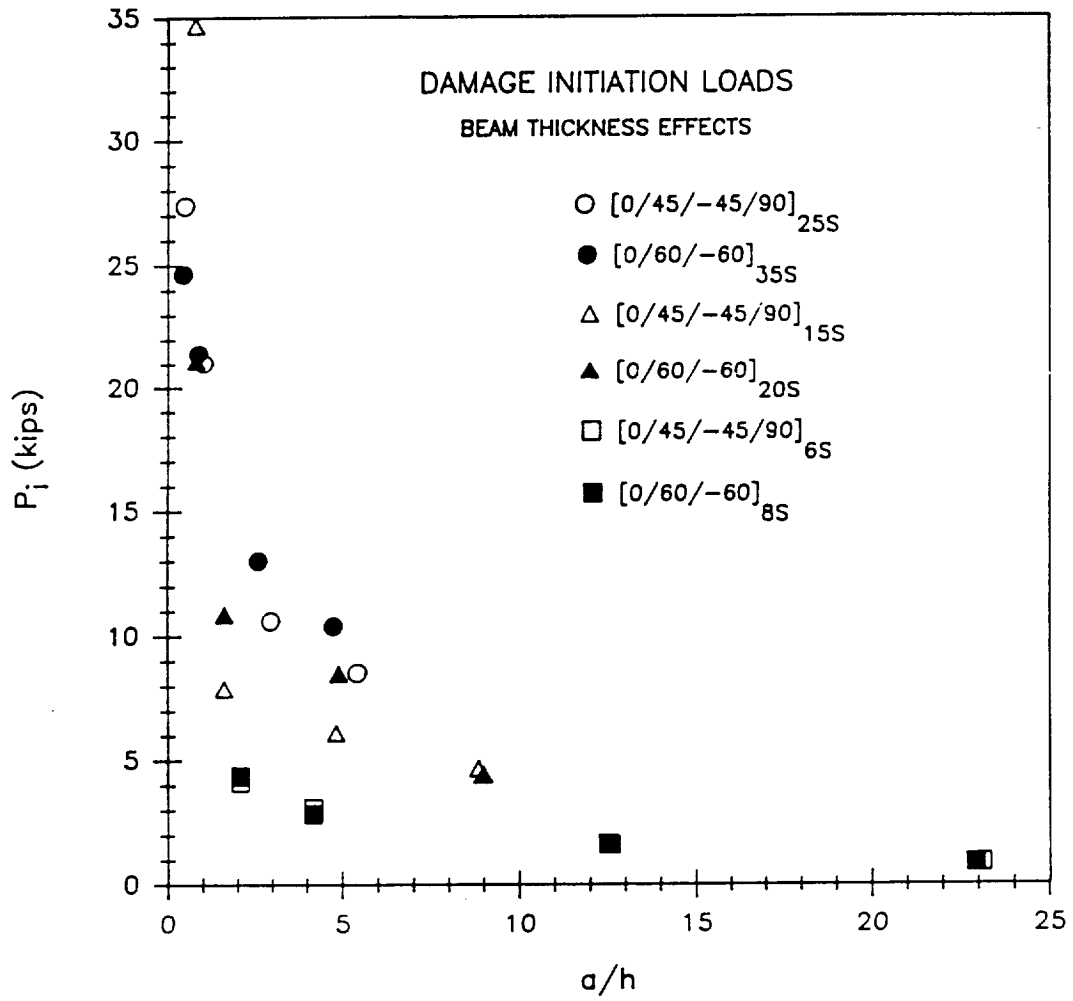**Figure 53.** Damage initiation load as a function of span length-to-depth aspect ratio and beam thickness effects.

DAMAGE INITIATION LOADS

STACKING SEQUENCE EFFECTS

○ $[0/45/-45/90]_{25S}$

● $[0_5/45_5/-45_5/90_5]_{5S}$

△ $[0/60/-60]_{35S}$

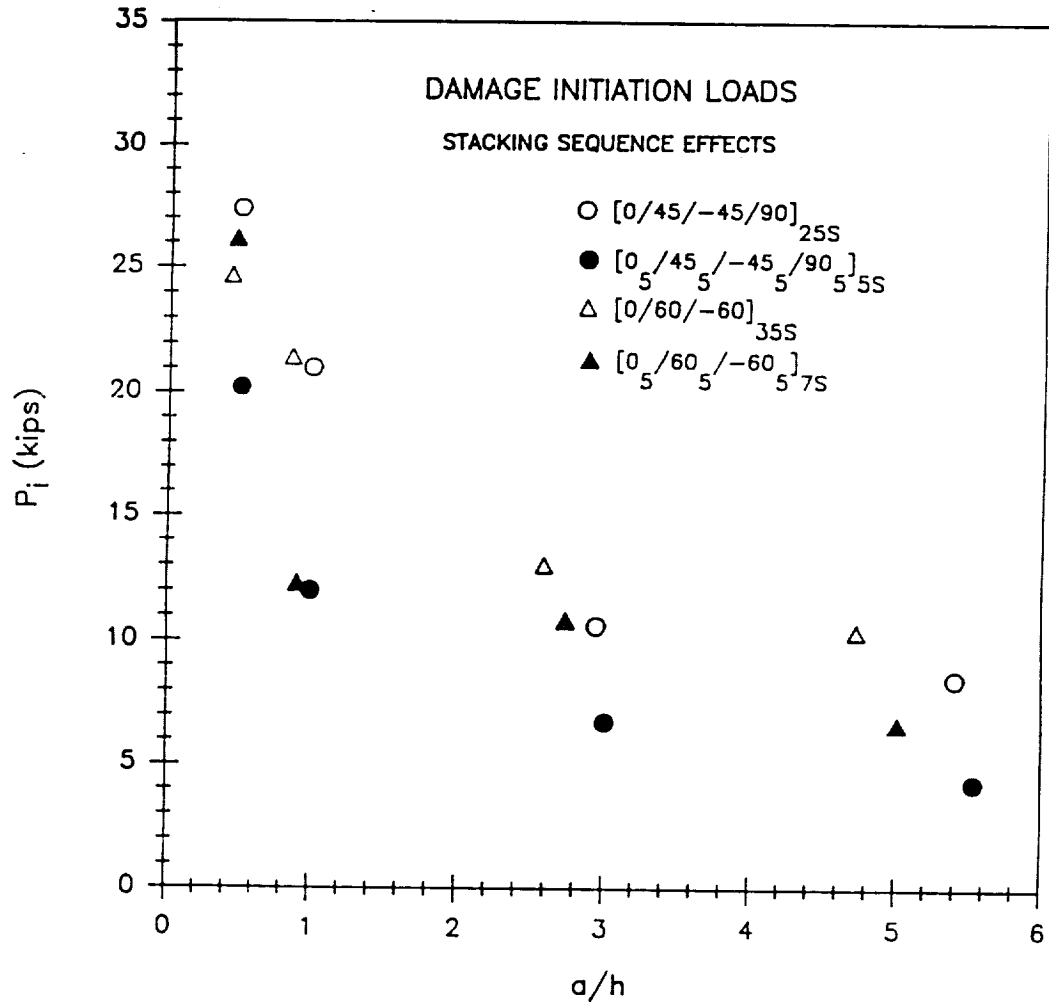▲ $[0_5/60_5/-60_5]_{7S}$

P_i (kips)

a/h

Figure 54. Damage Initiation load as a function of span length-to-depth aspect ratio and stacking sequence effects.

for aspect ratios greater than 1.0 the $[0_5/60_5/ - 60_5]_{7s}$ laminated beam has the largest damage tolerance. For aspect ratios smaller than 1.0, the $[0_5/45_5/ - 45_5/90_5]_{5s}$ grouped stacking sequence is more tolerant to damage than the other 1.0 inch thick laminates. However, for a/h greater than 3.0 this laminate has a low damage tolerance. When comparing the two interspersed quasi-isotropic laminates, the dependence of the damage tolerance on the a/h aspect ratio is very much the same. In addition, for the range of aspect ratios shown in Figure 55, the cross-ply beam in general is the least tolerant to damage.

For the case of a 0.6 inch thick beam, the results are presented in Figure 56. With the exception of a very small a/h aspect ratio, the $[0/\pm60]_{20s}$ laminate is seen to have a very low damage tolerance. The dependence of the damage tolerance on a/h for the $[0/\pm45/90]_{15s}$ beam has a contrasting behavior to that of the $[0/\pm60]_{20s}$ beam and is very similar to the 1.0 inch thick $[0/\pm45/90]_{25s}$ beam. The $[0/\pm45/90]_{15s}$ stacking sequence is seen to be damage intolerant for a large a/h but as a/h decreases the tolerance to damage increases. Figure 57 illustrates the dependence of the damage tolerance on the aspect ratio for the 0.24 inch thick beams. The results indicate that both the $[0/\pm45/90]_{6s}$ and the $[0/\pm60]_{8s}$ laminates have a very low damage tolerance for the entire range of aspect ratios tested. The only exception being, as in the case of the $[0/\pm60]_{20s}$ beam discussed above, for the $[0/\pm60]_{8s}$ beam having an a/h aspect ratio equal to 2.08.

5.4 Damage Descriptions

After the specimens were tested and their damage initiation and maximum failure loads recorded, they were inspected for damage using the optical microscope as described previously. Flexural failure mechanisms, which have been reported in the literature and discussed in Chapter 2, can generally be classified in terms of three basic modes: tensile mode,
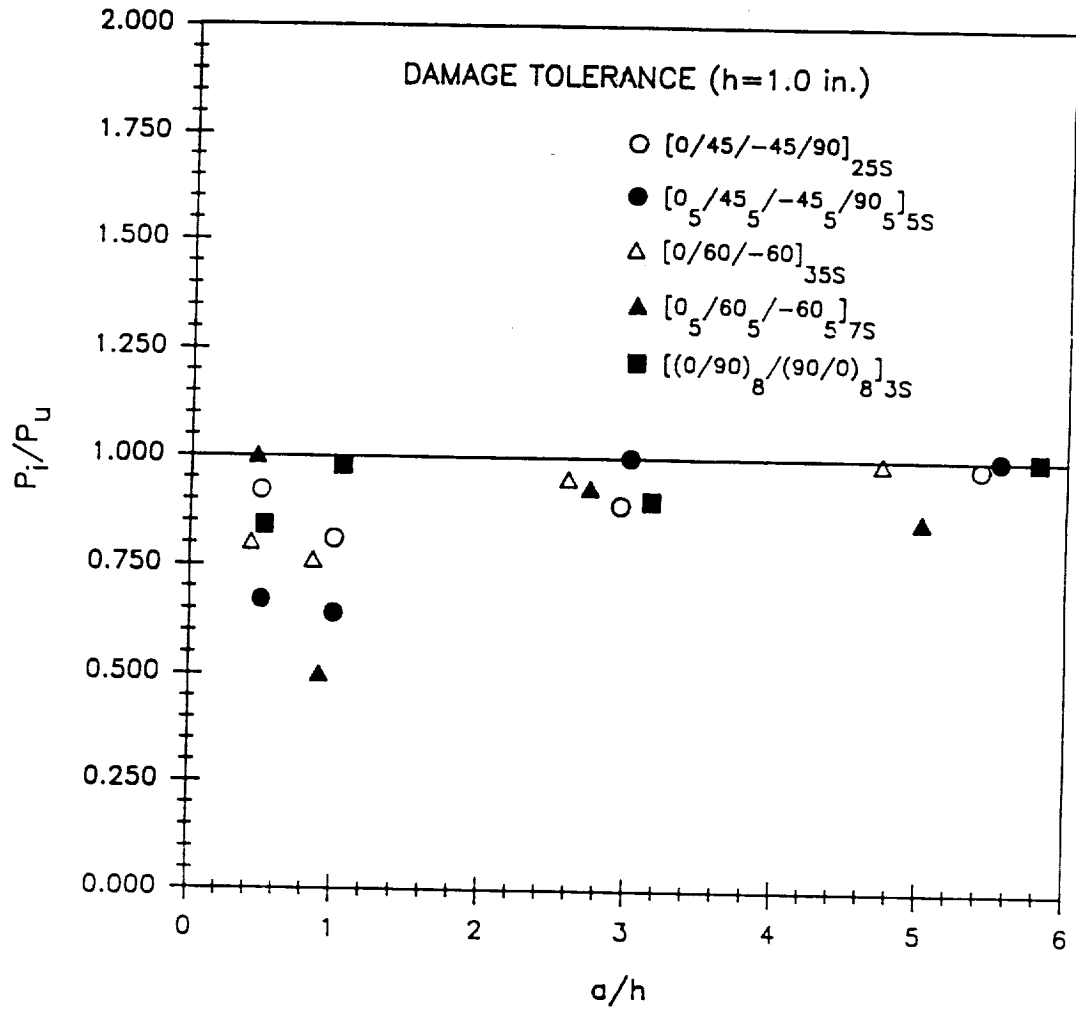
Figure 55. Damage tolerance for the laminated beams having an overall height equal to 1.0 inches.
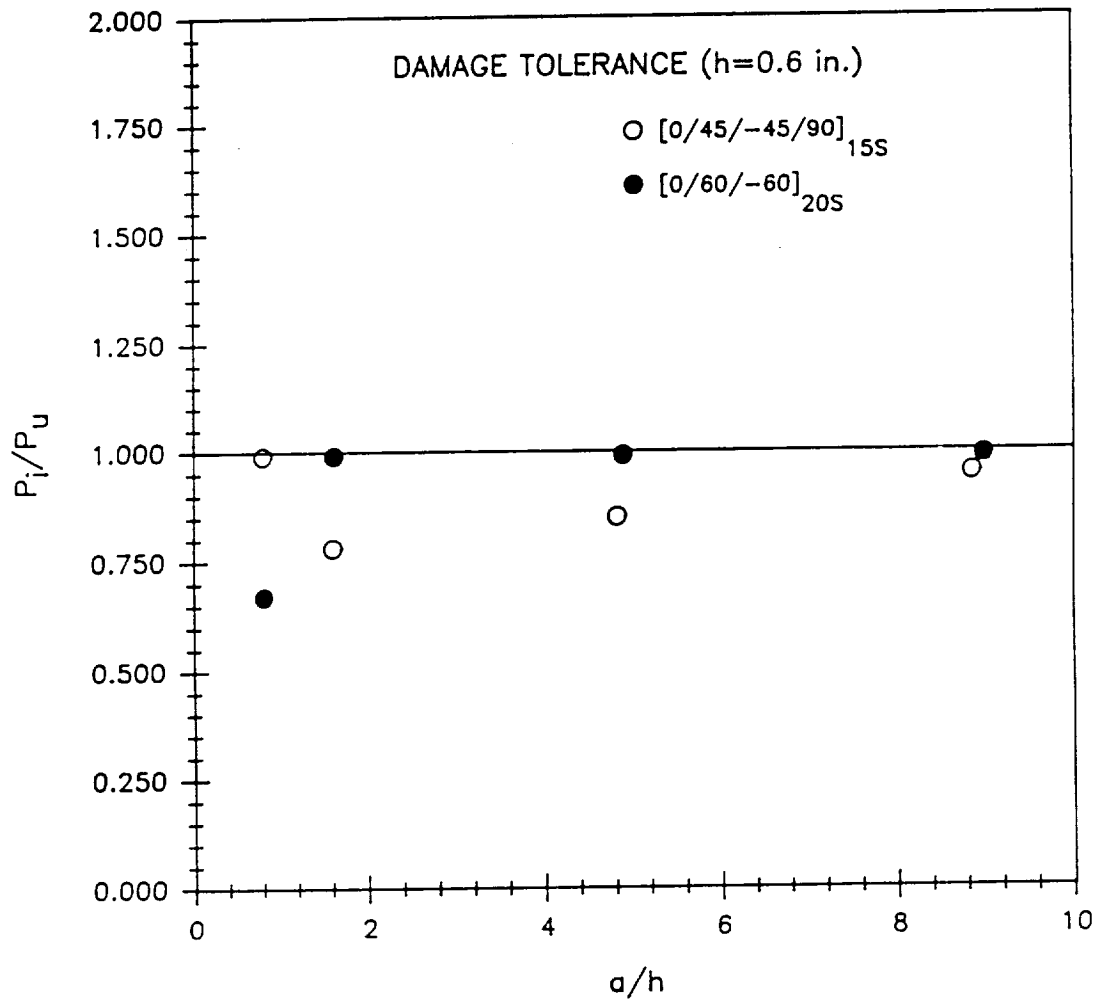
Figure 56. Damage tolerance for the laminated beams having an overall height equal to 0.6 inches.

DAMAGE TOLERANCE (h=0.24 in.)

○ $[0/45/-45/90]_{6S}$

● $[0/60/-60]_{8S}$

P_i/P_u

a/h

2.000
1.750
1.500
1.250
1.000
0.750
0.500
0.250
0.000

0   5   10   15   20   25

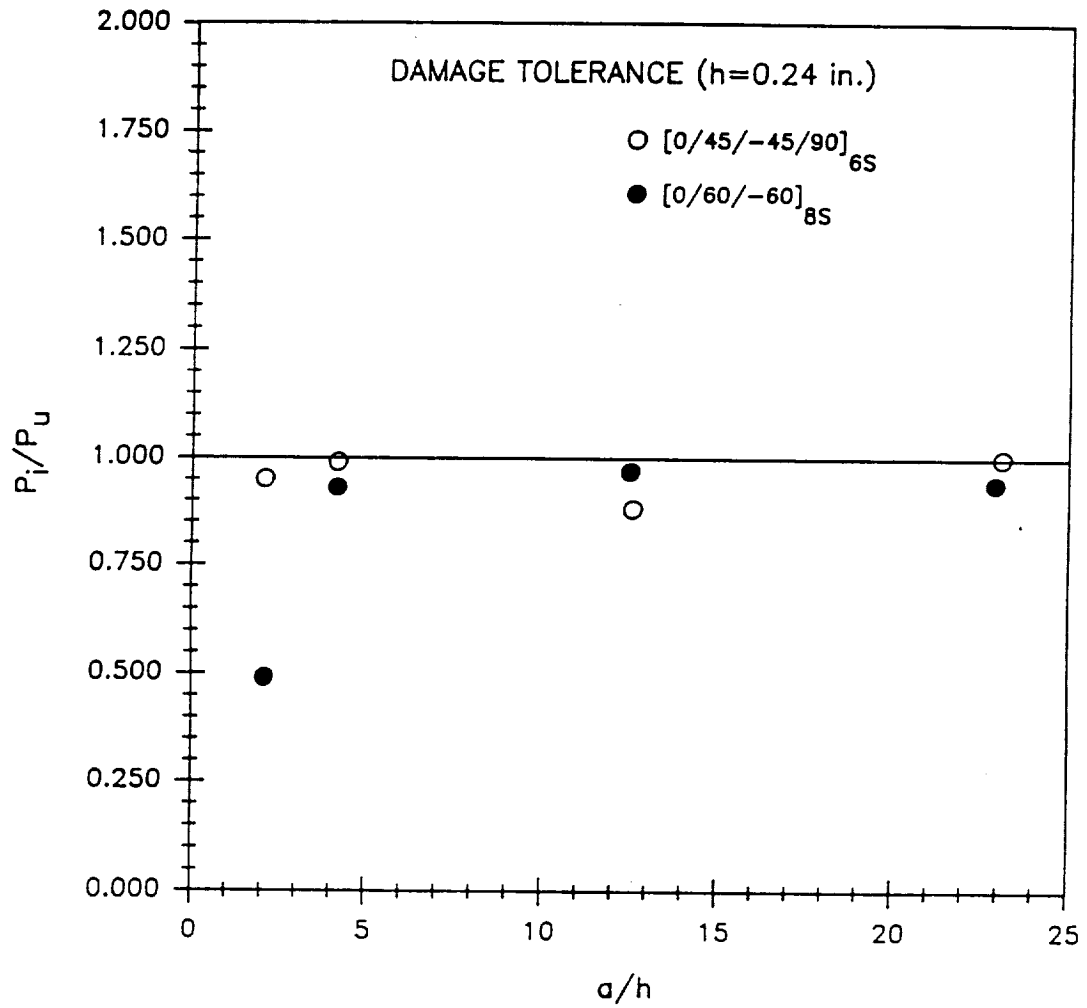**Figure 57.** Damage tolerance for the laminated beams having an overall height equal to 0.24 inches.

compressive mode, and/or shear mode. Combinations of the three basic modes have also been observed in failed specimens. The predominant combined mode discussed in the literature involves compression and shear in the form of kink bands in unidirectionally-aligned carbon-fiber reinforced plastic beams and has reportedly led to interlaminar failures [39]. It was also stated that for a constant span length and varying beam thicknesses, thin laminates generally failed on bottom due to tensile bending stresses, whereas, thick laminates failed near the top due to contact stresses [42]. The visual inspection of the damaged specimens was performed to determined which laminate geometries given in Table 1 were associated with each of the basic modes stated above. Also, the inspection was carried out to indentify any previously unreported damage modes corresponding to a particular geometry.

5.4.1 Unidirectional Beams

For the case of a $0°$ unidirectional beam having an aspect ratio of a/h = 7.33 the initiation of damage was very localized, located directly under the loading nose, and in the form of fiber buckling. Subsequently, testing the same beam configuration monotonically to failure produced shear kink bands which originated at the top surface in the vicinity of the applied load. In addition to the kink band formations, delaminations which extended to the end face of the beam were seen at approximately h/3 down from the top surface and at the midplane (z = 0.0). The observed kink band appeared to occur after the beam delaminated at the midplane. The midplane delamination in effect created two thinner beams which under the three-point bend loading experienced an increased compressive bending stress which buckled the fibers. Also, it should be noted that the delamination or longitudinal split in the xy-plane did not remain at a constant z-location across the width of the specimen but seemed to cross from one layer to another, as shown in Figure 58.
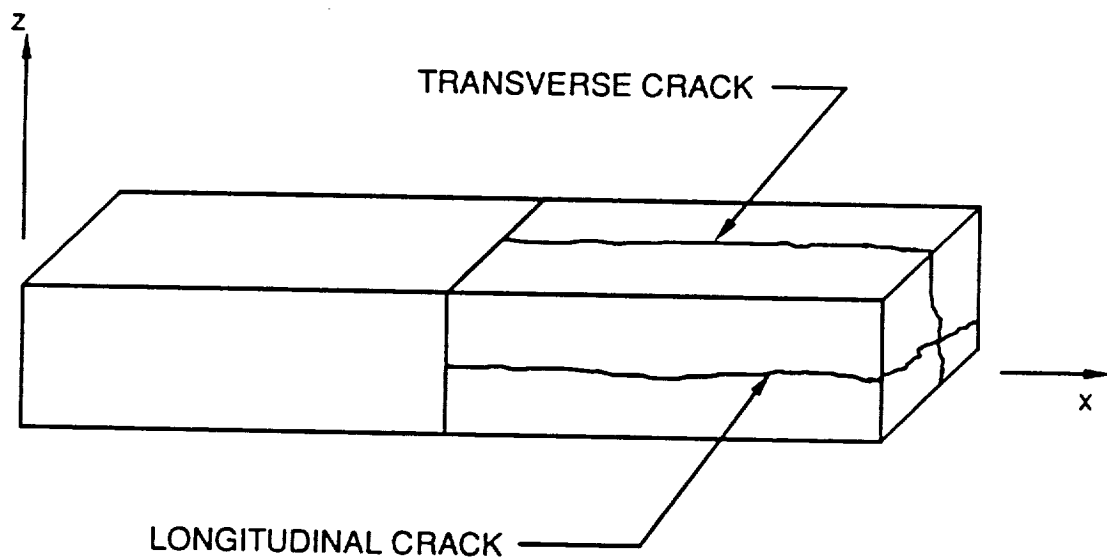
Figure 58. Longitudinal and transverse cracks in a unidirectional beam.

When the span length-to-depth aspect ratio of a 0° unidirectional beam was reduced to 4, damage was initiated by longitudinal cracks occurring at approximately 1/3 of the beam's total thickness down from the top surface. Ultimate failure for this beam geometry corresponded to the longitudinal cracks described above forming a delamination. There were also through the thickness or transverse cracks in the xz-plane of the beam (see Figure 58) which traversed the entire beam length. However, there was no evidence of fibers buckling as in the case of the previous beam. This may be attributed to the existence of large compressive stresses along the fiber direction for large a/h ratio specimens. Similar types of damage were observed when the supports were located 1.0 inches apart which corresponded to an aspect ratio of 1.33. Short longitudinal cracks were seen at 1/3 of the beam's thickness down from the top and at the midplane but no large delaminations were present. A transverse crack through the thickness, as depicted in Figure 58, was the predominant form of damage. There was no distinquishable difference between the observed damage states in the beam tested for damage initiation and in the beam tested up to ultimate failure. Further reducing the span length-to-depth aspect ratio to 0.67 yielded much the same observable damage but with the addition of short longitudinal cracks appearing near the bottom surface between the two supports.

5.4.2 Cross-Ply Beams

The next series of beams to be visually inspected under the microscope were the $[(0/90)_8/(90/0)_8]_{3s}$ cross-ply beams for which only the monotonic test to failure was conducted. For the specimen tested with an aspect ratio of 5.73, a kink band consisting of buckled fibers in the 0° plies under the loading nose (similar to the unidirectional beam) and matrix cracks in the adjacent 90° plies were observed. The kink band was located in the vicinity of the applied load and terminated at the first 90/90 interface, 16 plies down from the top surface, where a delamination was seen as depicted in the photograph of Figure 59. A second delamination

was present at the first 90/90 interface past the midplane with no evidence of fiber buckling or matrix cracking. Positioning the supports for an aspect ratio of 3.12 resulted in similar forms of damage but having a different location in the beam. Sandwiched between two delaminations which occurred at depths corresponding to 32 and 48 ply thicknesses was the formation of a kink band. A second kink band was seen to be located at a depth of 80 plies which traversed 32 plies before another delamination was present. Both bands of broken fibers and matrix cracks were located near the midspan of the beam.

The type of damage observed in the specimens changed when the span length-to-depth aspect ratio was reduced to 1.04. The type of damage was predominately shear related and there was no longer any evidence of kink band formations. Matrix cracking in the 90° plies and short interlayer seperations appeared throughout the entire depth of the beam between the support locations as shown in Figure 60. For the beams tested with an aspect ratio equal to 0.52 there was severe crushing of the beam under the loading nose. The damage was concentrated around the contact area with no evidence of damage beneath the first grouping of 16 plies.

5.4.3 Quasi-Isotropic Beams, [0/45/-45/90]

All of the remaining beams to be investigated were quasi-isotropic laminates. For the $[0/\pm45/90]_{28s}$ specimens, the damage states were primarily shear related in the form of matrix cracks and delaminations. When the aspect ratio was equal to 5.5, the damage initiation test resulted in a delamination at the third 90/0 interface from the top surface of the beam. For the monotonic test up to failure, fiber breakage was seen in conjunction with matrix cracking in the off-axis and 90° layers. There were also short longitudinal cracks appearing at the interfaces adjacent to the matrix cracking. This type of damage started under the loading nose and continued along an approximately 45° path until the fourth repeating ply sequence was
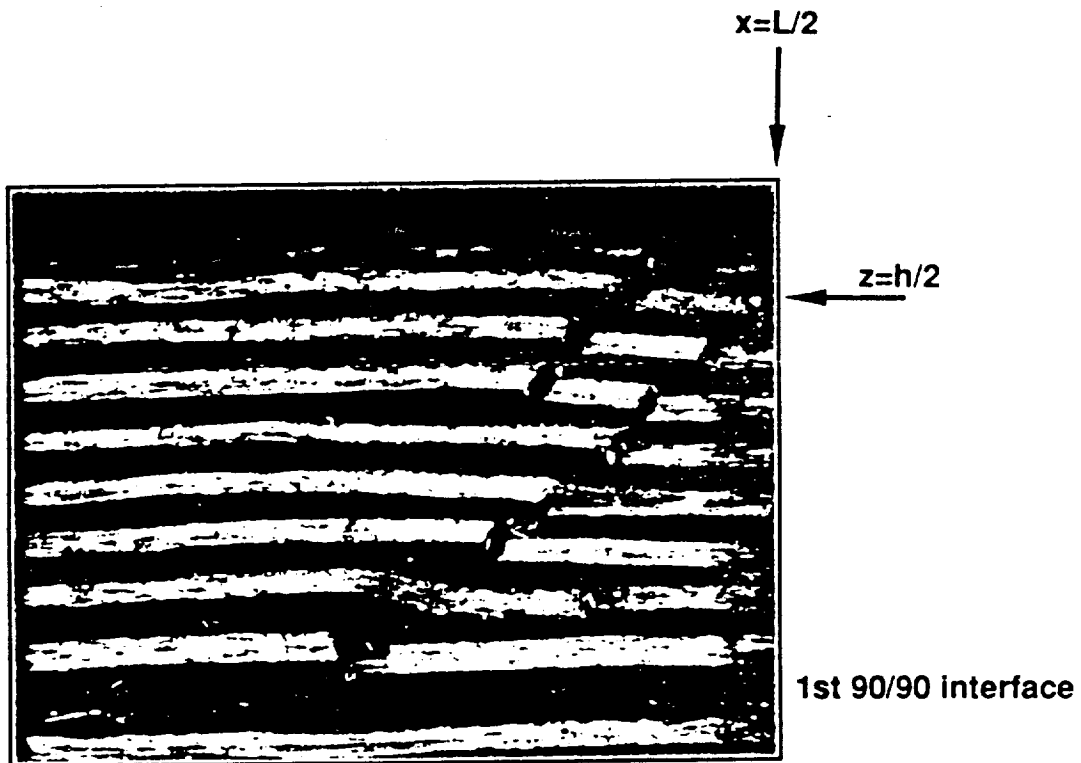
Figure 59. Kink band formation in a cross-ply beam.
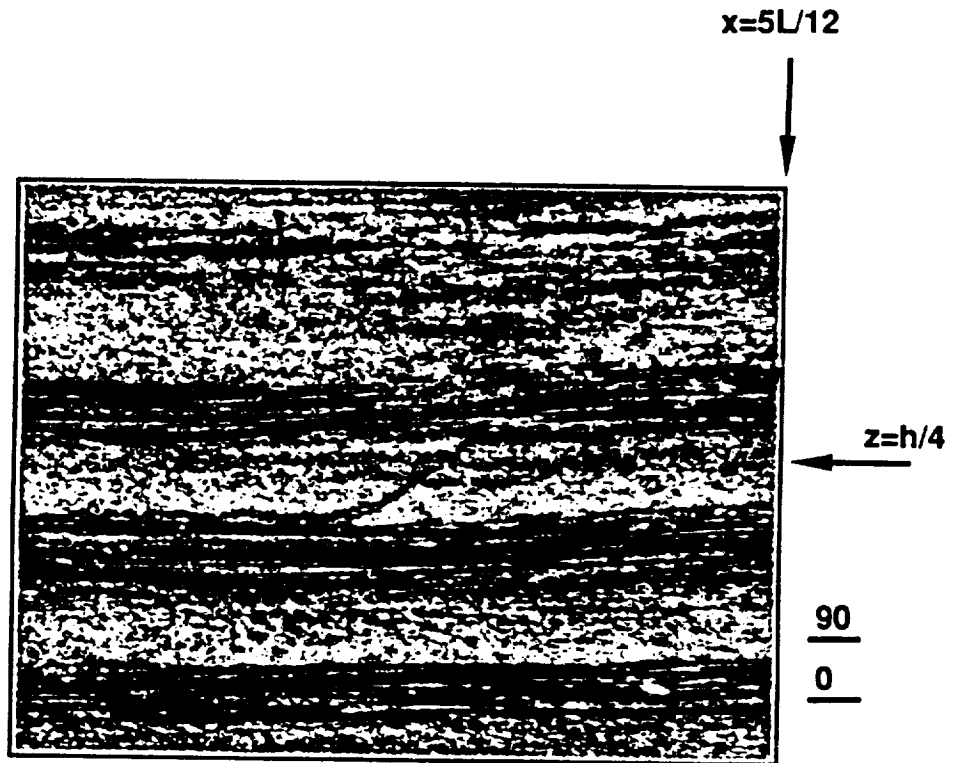
x=5L/12

z=h/4

90

0

Figure 60.   Matrix cracks and short delaminations in a cross-ply beam.

reached where a delamination occurred at the 45/-45 interface. Ultimately, the beam completely delaminated at the midplane.

The predominant damage seen for the case of an aspect ratio equal to 3.0 was in the form of delaminations. In the damage initiation test the beam delaminated at the fifth 0/45 interface down from the top surface. The second test, which was up to failure, produced additional delaminations in the fifth repetitive ply sequence and at the midplane. For the beams tested with an aspect ratio equal to 1.0, damage was initiated by matrix cracking in the off-axis plies located in the top two ply groupings as shown in Figure 61. Post-test inspection of the beam loaded to ultimate failure showed extensive damage in the top eight layers in the vicinity of the applied load. There were matrix cracks in the off-axis plies and a large delamination at the first 90/0 interface. The matrix cracking continued beneath this delamination and was observed in other off-axis and 90° plies extending all the way to the support location at the bottom surface. For an aspect ratio of 0.5, there was no discernable difference between the damage initiation test and the ultimate failure test as both specimens were severely crushed in the first 24 layers under the load.

The next two series of beams to be visually inspected for damage were the $[0/\pm45/90]_{1SS}$ and $[0/\pm45/90]_{6S}$ laminated beams. These two laminates contained the same basic ply grouping as the previous ones but had overall heights of 0.60 and 0.24 inches, respectively. Consequently, a broader range of span length-to-depth aspect ratios was achieved as shown in Table 1. For the $[0/\pm45/90]_{1SS}$ laminated beam having an aspect ratio of 9.17, the damage was similar to the $[0/\pm45/90]_{2SS}$ beam tested with an aspect ratio equal to 5.5. Damage was initiated by a delamination at the third 90/0 interface from the top surface. The ultimate failure test produced matrix cracks in the $\pm45°$ and 90° plies which started where the loading nose lost contact with the top surface and terminated at a depth of 12 plies.

Moving the supports to achieve an aspect ratio of 5.00 resulted in a combination of delaminations and matrix cracks. The specimen tested for damage initiation delaminated at the
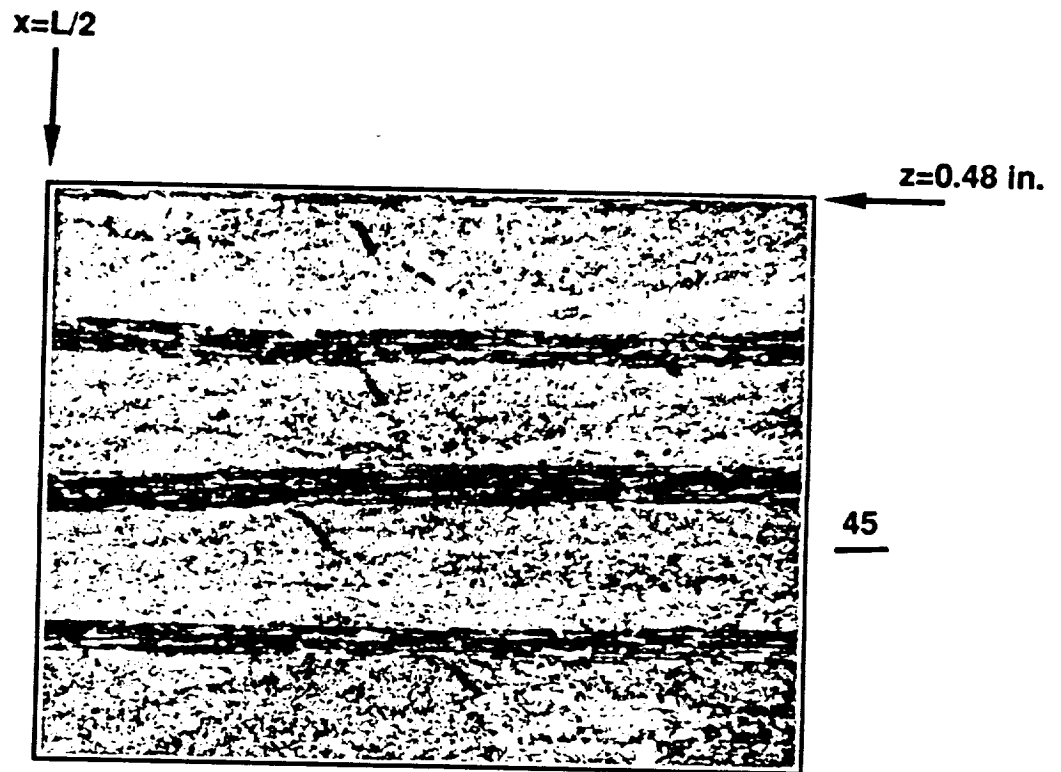
x=L/2

z=0.48 in.

45

Figure 61.   Matrix cracking in the off-axis plies of a quasi-isotropic beam.

interfaces adjacent to the 90° plies located at the midplane as shown in Figure 62. In addition to this delamination, the presence of matrix cracks in the 90° plies located at the beam's midplane were observed in the specimen tested up to ultimate failure. The observed damage for the case of an aspect ratio equal to 1.67 was much the same with the initial delamination occurring at the midplane. However, the ultimate failure test showed extensive matrix cracking in the 90° plies located away from the midplane in comparison to the beam having an aspect ratio of 5.00 where the cracks were concentrated at the midplane. As described for the 0.5 aspect ratio 1.0 inch thick $[0/\pm45/90]_{2ss}$ beam, for an aspect ratio of 0.83 there was severe crushing and delaminations in the top 16 layers under the point of load application.

The damage in the 48-ply 0.24 inch thick $[0/\pm45/90]_{ts}$ laminated beams can be characterized as follows. When the span length-to-depth aspect ratio was equal to 22.92, visual inspection of the specimen tested for damage initiation yielded no observable damage. The second specimen tested experienced ultimate failure as a result of extensive damage located at the back-face. This was in the form of a tensile failure mode with the 0° fibers breaking and numerous delaminations in the bottom half of the beam, all of which occurred at interfaces associated with a 0° ply. Also, there were matrix cracks located in the $\pm45°$ off-axis plies and the 90° plies located below the midplane. For the beam geometries tested with an aspect ratio of 12.50 the observed initial and ultimate failure damage states were very similar to the damage described for the previous beam geometry.

In cases where the beam had an aspect ratio equal to 4.17 the damage was initiated by matrix cracks in the third 90° ply located from the bottom surface and half-way between the load and support points as depicted by the photograph in Figure 63. In conjunction with the matrix cracks there were short delaminations at the interfaces located above and below the 90° ply stated above. When an identical specimen geometry was tested up to ultimate failure the type of observed damage was the same as seen in the damage initiation test but was more extensive throughout the beam. The damage state in the 2.08 aspect ratio beams was much the same as described for the 4.17 aspect ratio specimens.
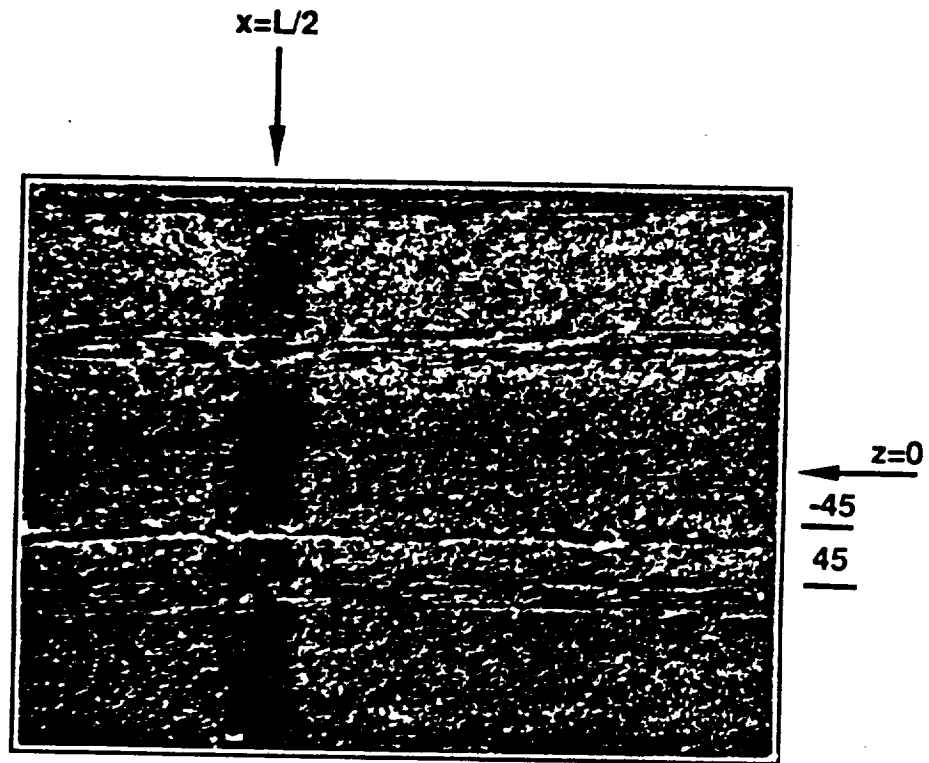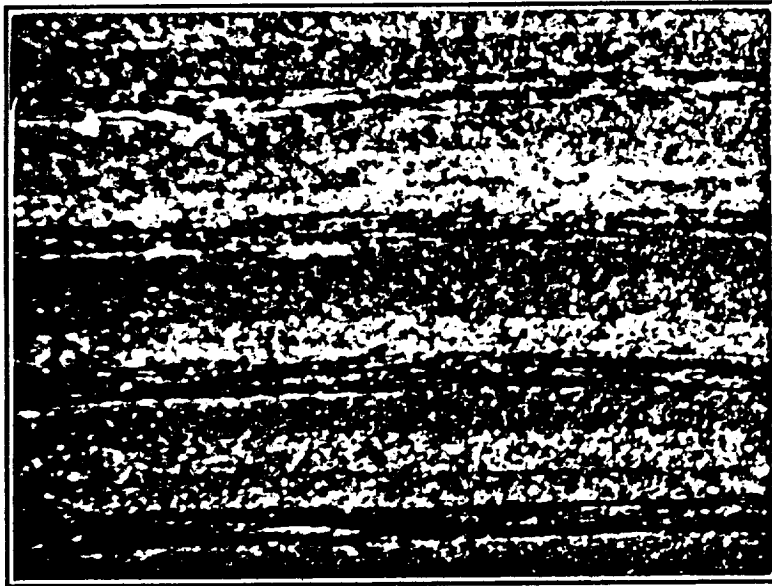
Figure 62. Delaminations near the midplane of a quasi-isotropic beam.

x=5L/12

z=0

90

Figure 63.   Matrix cracks in a 90 degree ply for a quasi-isotropic beam.

5.4.4 Quasi-Isotropic Beams, [0/60/-60]

The next series of laminated beams tested were also quasi-isotropic but differed in that their stacking sequence was based on a 0/±60 ply grouping. The thickest beams studied were the [0/±60]$_{38s}$ laminates which were approximately the same thickness as the 1.0 inch thick [0/±45/90]$_{25s}$ beams. When the span length-to-depth aspect ratio was equal to 5.24 the damage, shown in Figure 64, could be characterized by an initial delamination at the third -60/0 interface from the top surface. Visual inspection of the beam after being tested to ultimate failure showed additional damage with a kink band starting to form under the load point. Below the initial delamination there were broken fibers in the next three 0° layers in conjunction with matrix cracks in the ±60° plies and several small delaminations. The type of damage described above resembles the mode observed for the [0/±45/90]$_{25s}$ beam having an aspect ratio of 5.5.

When the 2.86 aspect ratio beams were tested, the primary form of damage was a delamination which was comparatively the same as in the [0/±45/90]$_{25s}$ specimens. The damage initiation test showed a delamination occurring at the fifth -60/0 interface relative to the top surface. Several other delaminations were seen when a second specimen was tested up to ultimate failure. Reducing the aspect ratio to 0.95 produced initial damage in the form of a delamination at the first -60/0 interface. In the test for ultimate failure the beam was severely crushed under the applied load. Moving the supports for an aspect ratio of 0.48 resulted in a similar damage state with crushing of the top two ply groupings for both the damage initiation test and the ultimate failure test.

The [0/±60]$_{20s}$ beams tested had the same span length-to-depth aspect ratios as the [0/±45/90]$_{15s}$ beams listed in Table 1. Figure 65 illustrates that the initial damage for the 9.17 aspect ratio beams was in the form of matrix cracking in the top ±60° ply grouping located approximately where the loading nose lost contact with the top surface. A delamination was

x=3L/8
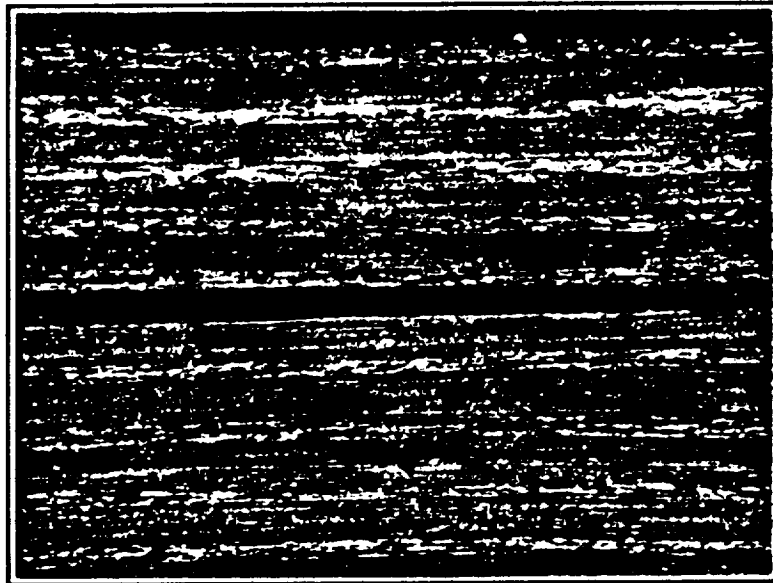
z=0.465 in.

Figure 64.   Delamination near the top surface of a quasi-isotropic beam.

also seen at the first -60/0 interface adjacent to the matrix cracks. Additional damage oc-curred in the ultimate failure test when the third and fourth 0° layers from the top surface buckled. When the span length-to-depth aspect ratio was equal to 5.00 and the damage initi-ation test was performed, the specimen delaminated at the seventh -60/0 interface from the top surface. The ultimate failure of an identical specimen produced added damage in the form of a kink band with fiber buckling and matrix cracks seen in the layers above the initial de-lamination. The only observable damage in the specimens having an aspect ratio equal to 1.67, for both the initiation of damage and ultimate failure tests, was a small delamination at the fourth -60/0 interface under the loading nose. For the case of a 0.83 aspect ratio specimen, damage was initiated by a very localized delamination directly under the load at the first and second 0/60 interface from the top surface. Severe crushing under the load, fiber breakage, and numerous delaminations in the first 24 plies were seen in the specimen tested to failure.

Visual inspection of the failed $[0/\pm60]_{4s}$ specimens produced the following forms of damage. The initiation of damage in the 22.92 aspect ratio beam was a delamination located at the fifth 0/60 interface from the bottom surface. Ultimate failure for this beam geometry was associ-ated with back-face damage consisting of a combination of tensile and shear failure modes with fiber breakage, matrix cracking, and delaminations in the bottom five ply groupings. Positioning the supports for an aspect ratio of 12.50 changed the initiation of damage to a short delamination at the midplane and was located approximately half-way between the load and support points. The specimen which was tested monotonically to failure showed very little additional damage other than the type seen in the damage initiation test. It should be noted that it was difficult to assess the extent of damage in these specimens because of the large number of voids that were present.

In the specimen tested up to the initiation of damage and having an aspect ratio equal to 4.17, cracks were observed in the $\pm60°$ plies located at the midplane as shown in Figure 66. Testing a second specimen to failure produced the same type of damage as was seen in the damage initiation test. Similar damage states were observed when the span length-to-depth aspect
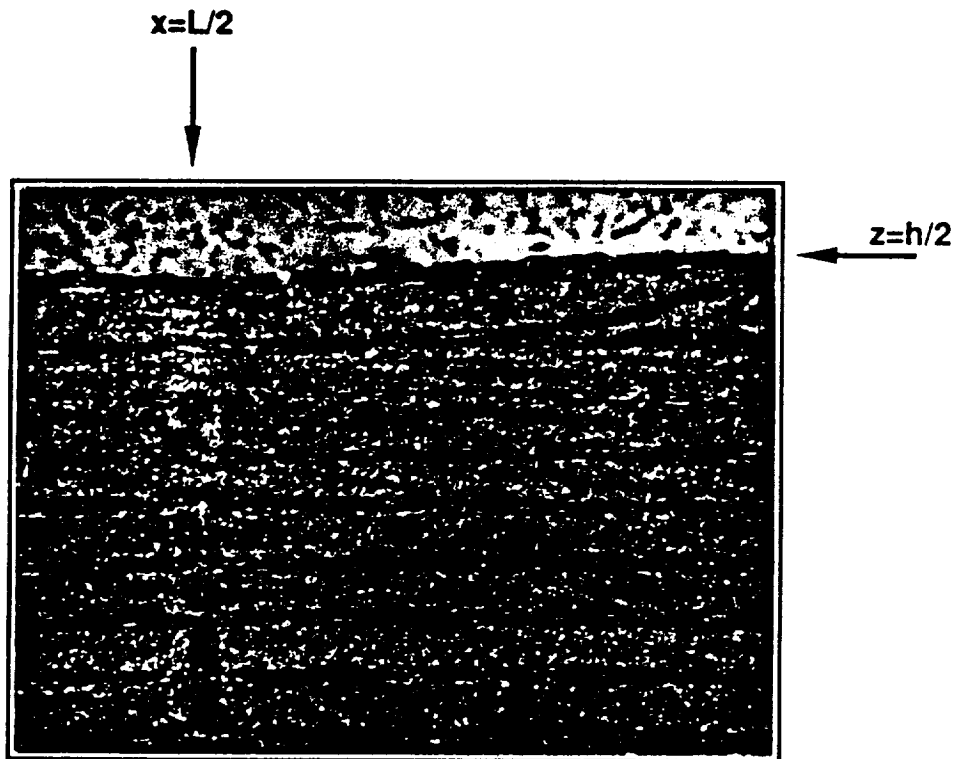
Experimental Investigation

x=L/2

z=h/2

Figure 65.   Matrix cracks in the off-axis plies of a quasi-isotropic beam.

ratio was reduced to 2.08 but the damage was more extensive. At ultimate failure the matrix cracks in the $\pm 60°$ plies extended along a line from the load point to the support point.

5.4.5 Quasi-Isotropic Beams, Grouped Stacking Sequence

By grouping five plies together having the same fiber orientation, e.g., $[0_5/45_5/-45_5/90_5]_{ss}$, the overall height of the beam did not change in comparison to the $[0/\pm 45/90]_{2ss}$ laminate. This was also true for the 210 ply laminates based on the $0/\pm 60$ ply grouping. For the grouped $[0_5/45_5/-45_5/90_5]_{ss}$ stacking sequence and an aspect ratio of 5.5, the initial damage is shown in Figure 67 and was a combination of delaminations and matrix cracks in the $90°_5$ and off-axis layers located at the midplane of the beam and close to the midspan. The same type of damage was seen in the specimen tested monotonically to failure with the delaminations and matrix cracks being larger in number. The specimens having a $[0_5/60_5/-60_5]_{7s}$ grouped stacking sequence and tested with an aspect ratio equal to 5.5 had similar damage characteristics. Damage in the beams having a grouped stacking sequence differed from the interspersed case by not having fiber breakage in the top $0°$ plies. Also, in contrast to the damage being located near the top surface for the interspersed beams, the damage was concentrated more at the midplane for the grouped stacking sequence.

For the case of a beam having an aspect ratio of 3.0, the observed initial damage in both of the grouped laminates was in the form of matrix cracks in the $90°_5$ and off-axis plies located at the midplane. The ultimate failure of the specimens was associated with an extensive branching or staircase pattern of matrix cracks and short longitudinal cracks at the adjacent interfaces and is illustrated in Figure 68. The effect of grouping plies together on the damage characteristics was a change from a predominantly interlaminar shear mode for the interspersed specimens to a matrix shear mode.

Experimental Investigation

x=5L/12

z=0

-60
60

Figure 66.   Matrix cracks in the off-axis plies of a quasi-isotropic beam.
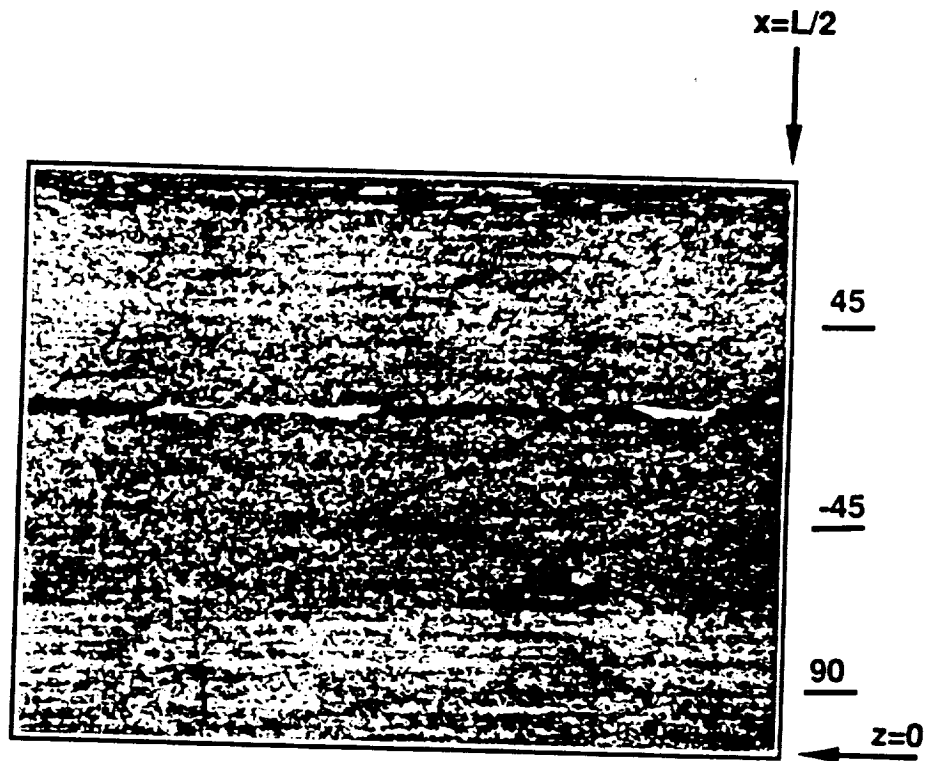
x=L/2

45

-45

90

z=0

Figure 67. Matrix cracks and delaminations in a quasi-isotropic beam.
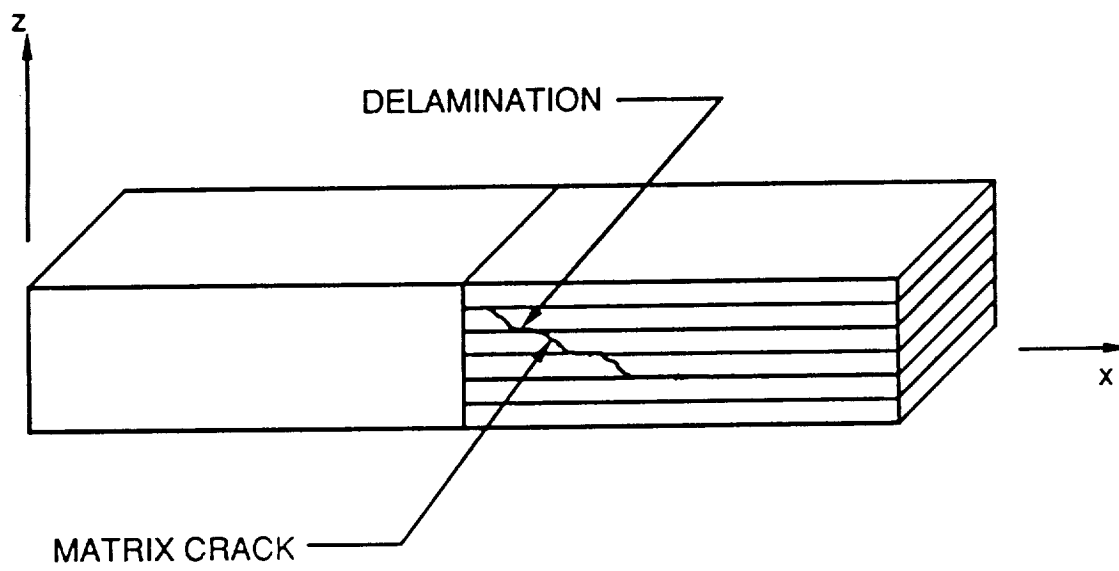
Figure 68.   Staircase pattern of matrix cracks and short delaminations.

Testing the 1.0 aspect ratio specimen, and conducting the test for damage initiation, produced the same type of damage as described for the 3.0 aspect ratio beam. However, the matrix cracks were located in the first ply grouping near the applied load. The ultimate failure test showed no additional damage. The observed damage modes for the grouped stacking sequence were very similar to the previously described damage modes in the beams having an interspersed lamination. When the span length-to-depth aspect ratio was equal to 0.5, the initial damage consisted of the same matrix cracks as described for the case of an aspect ratio equal to 1.0. When identical specimens were tested up to failure, the beams experienced crushing in the first repetitive ply sequence, e.g., $0_5/45_5/-45_5/90_5$ and $0_5/60_5/-60_5$. Comparatively, this was the same type of damage as described for the interspersed beams. Consequently, increasing the effective layer thickness by grouping plies together did not significantly alter the observed damage states for the shorter span length-to-depth aspect ratios of 1.0 and 0.5.

5.5 Summary

The experimental investigation was conducted in order to define the damage states in various laminated beam geometries subjected to three-point bend loading conditions. The experimental data consisted of top and bottom surface displacements at the midspan and the applied load. After reducing the data, load-displacement and load-indentation plots were generated and the damage initiation load and ultimate failure load defined. The behavior of the load-displacement and load-indentation curves was categorized as being linear up to the initiation of damage with the exception of the $0°$ unidirectional beams. The dependence of the initial damage and ultimate failure loads on the beam's span length-to-depth aspect ratio were identified. Also, the damage susceptibility and the damage tolerance of the tested laminates

were discussed. In general, it was shown that the damage initiation load and ultimate failure load decreased as the beam's a/h aspect ratio increased.

To investigate the effects of stacking sequence, beam thickness, and relative layer thickness on the load dependencies stated above, the different laminated beams in the test matrix were classified into four groups. The results showed that there were significant beam thickness effects and that the a/h aspect ratio did not uniquely define the damage initiation nor the ultimate failure load. For a given a/h aspect ratio, the 0.24 inch thick beams had the lowest ultimate load and were the most susceptible to damage. However, the beam thickness effects described above decreased as the aspect ratio increased. Also, it was shown that increasing the relative layer thickness in a laminated beam increased its damage susceptibility and decreased its load carrying capacity. In addition, the grouped $[0_5/45_5/-45_5/90_5]_{ss}$ beams had lower ultimate loads and were more susceptible to damage than the $[0_5/60_5/-60_5]_{7s}$ beams. When the laminates had an interspersed stacking sequence and the same thickness, their load carrying capabilities were similar. For the laminates having a thickness approximately equal to 1.0 inches, the $[0_5/60_5/-60_5]_{7s}$ stacking sequence was the most tolerant to damage, whereas the cross-ply beams were the least tolerant. In general, the damage tolerance was seen to decrease with increasing aspect ratio.

A post-test visual inspection of the damaged specimens was conducted using an optical microscope and photomicrographs were taken to document the damage. The damage which was observed indicated that several different mechanisms can occur depending on the beam geometry and stacking sequence. The dependence of the type of damage on the beam configuration is summarized in Table 2 for the unidirectional and cross-ply beams, and in Tables 3 and 4 for the $[0/\pm45/90]$ and $[0/\pm60]$ quasi-isotropic beams, respectively. The observed initial damage in each specimen is indicated by a superscript "i", whereas, the remaining marked boxes correspond to subsequent damage seen in the ultimate failure test. Also, when the observed damage was concentrated at one particular location, the location is noted in

parentheses. In specimens where the damage was extensive or occurred at several different locations, no mention is made of any location.

The 0° unidirectional orthotropic beams failed by either buckling of fibers and delaminations or transverse splitting. The change in the observed damage from a midspan delamination to a transverse split occurred when the span length-to-depth ratio became less than 4.0. The appearance of kink bands and delaminations were typical for the higher aspect ratio cross-ply beams. For the cases when the span length was less than 3.0 inches, matrix cracking in the 90° plies was the predominant form of damage. For the quasi-isotropic laminates, the initial damage states were comprised of either delaminations, matrix cracks in the off-axis and 90° plies, or a combination of these two. Initial damage in the form of delaminations was primarily seen in the interspersed stacking sequences and when the overall beam thickness was equal to 1.0 and 0.6 inches. When a grouped stacking sequence was used and when the 0.24 inch thick interspersed laminated beams were tested the initial damage was generally in the form of matrix cracks in the off-axis plies. Also, for the 0.24 inch thick specimens having an aspect ratio equal to 22.92 or 12.50, a tensile failure mode was observed with damage occurring at the back-face and fibers breaking in the bottom 0° plies. Based on these observations it was expected that a detailed investigation of the local stress distributions would be required in order to explain the damage seen in the laminated beams.

Table 2. Observed damage in the unidirectional and cross-ply beams

Specimen configuration		Delamination	Matrix crack, 90°	Matrix crack, 45° or 60°	Matrix crack + delamination	Kink band	Tensile, 0°	Crushing
Stacking sequence	Aspect ratio							
[0]₁₅₀	7.33	x (midplane)						
	4.00	x						
	1.33	x						
	0.67	x				x^i		
[(0/90)₈/(90/0)₈]3S	5.73	x^i (1ˢᵗ 90/90)						
	3.12	x^i (1ˢᵗ 0/0)						
	1.04	x	x^i (1ˢᵗ 90/90)			x (1ˢᵗ 16 plies) x		
	0.52							x

Table 3. Observed damage in the [0/45/-45/90] quasi-isotropic beams

Specimen configuration		Delamination	Matrix crack, 90°	Matrix crack, 45° or 60°	Matrix crack + delamination	Kink band	Tensile, 0°	Crushing
Stacking sequence	Aspect ratio							
[0/45/-45/90]$_{25S}$	5.50	x^i (3rd 90/0)						
	3.00	x^i (5th 0/45)		x				
	1.00	x		x^i (1st 2 groups)				x
	0.50							
[0/45/-45/90]$_{15S}$	9.17	x^i (3rd 90/0)						
	5.00	x^i (midplane)						
	1.67	x^i (midplane)	x					x
	0.83		x					
[0/45/-45/90]$_{6S}$	22.92				x (z < 0)		x (z = -h/2)	
	12.50				x (z < 0)		x (z = -h/2)	
	4.17		x^i (10th 90)					
	2.08		x^i (10th 90)					x
[0$_5$/45$_5$/-45$_5$/90$_5$]$_{1S}$	5.50							
	3.00							
	1.00		x^i (midplane)	x^i (midplane)	x^i (midplane)			
	0.50		x^i (1st group)		x^i (1st group)			x

Table 4.   Observed damage in the [0/60/-60] quasi-isotropic beams

Specimen configuration — Stacking sequence	Aspect ratio	Delamination	Matrix crack, 90°	Matrix crack, 45° or 60°	Matrix crack + delamination	Kink band	Tensile, 0°	Crushing
$[0/60/-60]_{35S}$	5.24	x^j (3rd -60/0)			x			
	2.86	x^j (5th -60/0)						
	0.95	x^j (1st -60/0)						x
	0.48							x
$[0/60/-60]_{20S}$	9.17	x^j (7th -60/0)			x^j (1st group)			
	5.00	x^j (4th -60/0)						
	1.67	x^j (2nd 0/60)				x		x
	0.83							
$[0/60/-60]_{8S}$	22.92	x^j (12th 0/60)		x				
	12.50	x^j (midplane)						
	4.17			x^j (midplane)			x (z = -t/2)	
	2.08			x^j (midplane)				
$[0_5/60_5/-60_5]_{7S}$	5.24			x^j (midplane)	x^j (midplane)			
	2.86				x^j (1st group)			
	0.95				x^j (1st group)			
	0.48							x

Chapter VI

Analytical/Experimental Correlation

The results of the experimental program for testing laminated beams under quasi-static three-point bend loading conditions were presented in the previous chapter. The post-test inspections of the damaged specimens yielded the primary failure modes and types of damage which occurred in the beams. In order to correlate the analytically predicted stresses and displacements, using the solution procedure given in Chapter 3, with the experimental data the applied boundary conditions must simulate the actual test conditions as accurately as possible. The solution previously derived was based on a stress formulation in the mathematical theory of elasticity with the tractions being prescribed on the boundary. Therefore, the applied tractions must represent the manner in which load was introduced into the specimens during testing. The loading nose and supports have a finite radius of curvature creating contact between a rigid cylinder and a laminated beam. No attempt is made here to explicitly solve the associated mixed boundary-value contact problem but merely to utilize previously published results to model the traction distributions in the contact region.

6.1 Modelling of Boundary Conditions

6.1.1 Elliptical Stress Distribution

When the radius of the indenter, i.e., loading nose and supports, is small compared to the curvature of the target, i.e., beam, the Hertzian solution for the contact stress distribution on an orthotropic half-plane can be used. This is an elliptical type of distribution [34] which can be expressed as follows:

$$f(x)_i = \frac{2P}{\pi db} \sqrt{1 - 4\left(\frac{x - c_i}{d}\right)^2} \qquad c_i - \frac{d}{2} \leq x \leq c_i + \frac{d}{2}$$
$$= 0 \qquad\qquad\qquad\qquad 0 \leq x < c_i - \frac{d}{2} \tag{1}$$

where P is the applied contact force, b is the beam's width, c_i is the distance from the origin to the center of the ellipse, and d is the contact length (see Figure 69). The subscript i ranges from 1 to 2 and corresponds to the top and bottom surfaces, respectively. For three-point bend loading conditions, $c_1 = \frac{L}{2}$. Following the solution procedure in Chapter 3, equation (1) must be written in the form of a Fourier series expansion and in terms of the nondimensional co-ordinate system. The Fourier series coefficients were determined using the Guassian quadrature numerical integration technique with the following result:

$$f_i(\xi) = -\frac{2P}{bd}\left[\frac{\beta}{2} + \frac{2\beta}{\pi}\sum_{m=1}^{M}\sum_{n=1}^{N} w_n f_i(t_n) \cos p_m \xi\right] \tag{2}$$

where

$$f_i(t_n) = \sqrt{1 - t_n^2}\, \cos p_m\left(\frac{dt_n}{2L} + \delta_i \right) \tag{3}$$

and where w_n and t_n are the corresponding Gauss weights and points, respectively. The remaining quantities are the same as previously defined in Chapter 3, e.g., $M = 400$ terms which was determined based on the convergence study. As shown in Figure 69, the major axis of the elliptical stress distribution is proportional to the applied load and the minor axis is equal to the associated contact length.

6.1.2 Contact Length

A relationship between the applied contact force and the resulting contact length was derived by Sankar [37] for the contact between a rigid cylinder and an orthotropic beam. The solution was obtained by considering approximate Green's functions for the surface displacements in an orthotropic half-plane and subsequently superposing these with beam theory deflections. His results are presented here and were implemented to theoretically determine the contact length for a given load. The contact length is related to the load and beam material properties by:

$$d = \frac{2}{\sqrt{k_c\left(\frac{1}{P} - \gamma\right)}} \tag{4}$$

where

$$\gamma = \frac{Ra}{4E_1 I} \qquad I = \frac{1}{12}bh^3 \tag{5}$$

$$k_c = \frac{1}{2k_h R} \qquad k_h = \frac{\lambda_1 + \lambda_2}{\pi E_3} \tag{6}$$

and where R is the indenter radius. The beam dimensions b, h, and a were given in Figure 4, and $\lambda_{1,2}$ are the roots to the following characteristic equation:

$$S_{11}\lambda^4 - (2S_{13} + S_{55})\lambda^2 + S_{33} = 0 \qquad (7)$$

where the S_{ij} are the compliance terms in the principal material directions. It should also be noted that for a small indenter radius the contact length of equation (4) may be approximated using the following relationship:

$$d \cong \sqrt{\frac{4P}{k_c}} \qquad (8)$$

For the purpose of correlating the experimental data with this analysis, an estimate of the contact length was obtained experimentally by placing pieces of carbon paper and graph paper between the loading nose and the beam's top surface. The decision to verify the theoretical contact length was made after the test program was initiated. Consequently, the contact lengths for the 0° unidirectional, cross-ply, $[0/\pm45/90]_{2ss}$, and the $[0_5/45_5/-45_5/90_5]_{ss}$ laminates are not included in the experimental results. For the remaining stacking sequences in Table 1, the carbon replica of the contact patch was measured and compared with the value from equation (4). The results are given in Figure 70 for all of the aspect ratios tested and for both the damage initiation test and the ultimate failure test. The results shown in Figure 70 illustrate a satisfactory correlation between theory and experiment for the contact length, especially for the lightly loaded specimens. The scatter in the experimental data may be attributed to the beam's textured surface finish. Consequently, it was difficult to exactly measure the contact length due to the ill-defined boundaries of the carbon transferred to the graph paper near the edge of the contact area. The discrepancy which occurred for the higher load levels is thought to be the result of damage and crushing of the beam's top surface. It should also be noted that the experimentally measured contact length did not appear to depend on the stacking sequence of the beam.
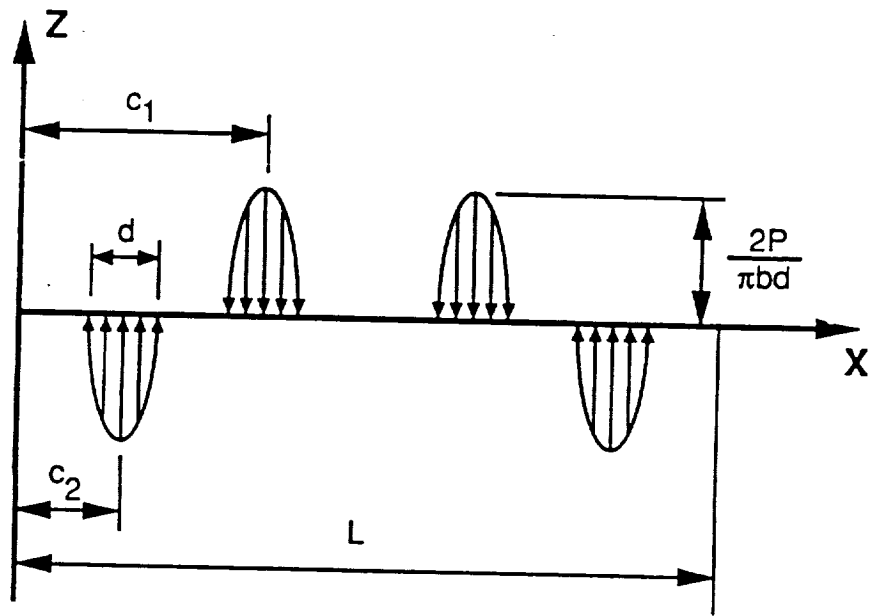
Figure 69. Elliptical traction distribution.
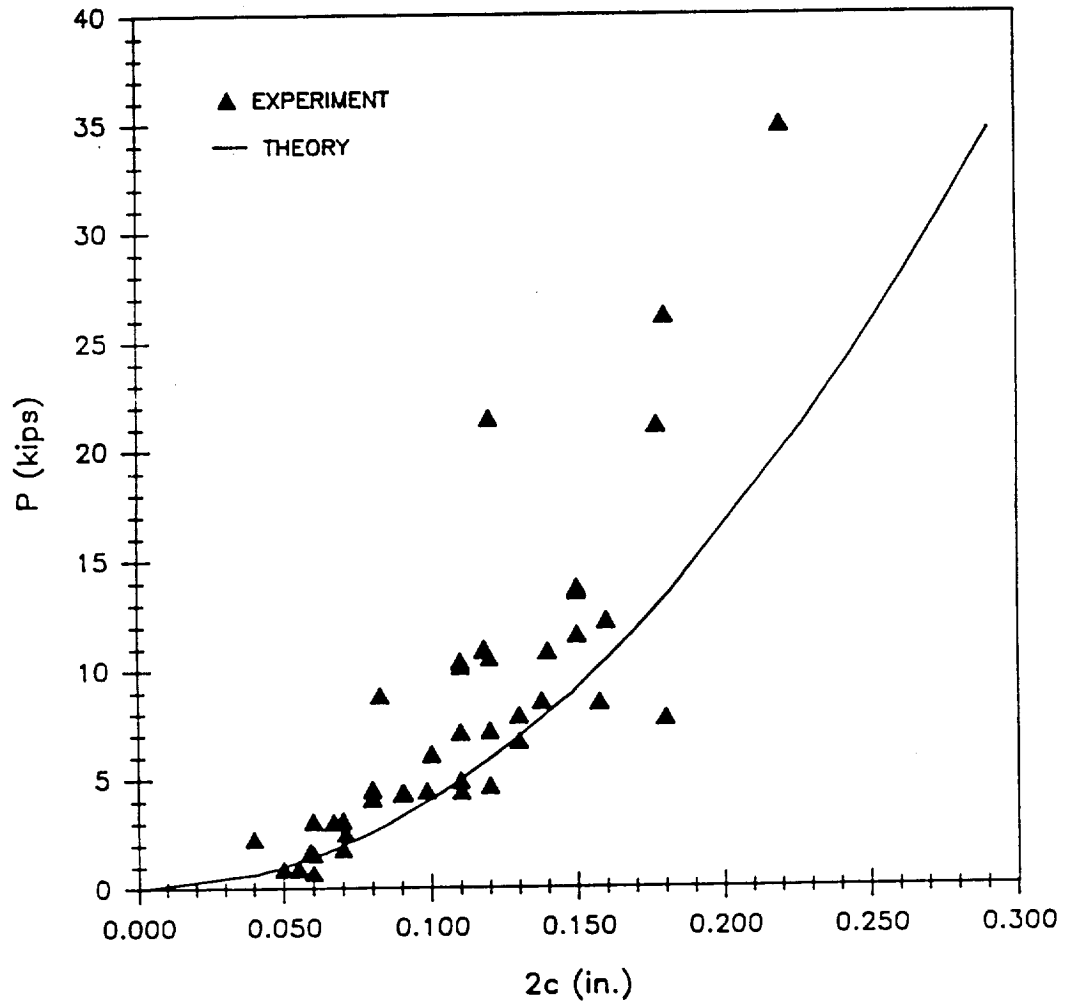
Figure 70. Comparison of experimentally measured contact length with theory.

6.2 Displacements

The elliptical traction distribution given by equation (2) and the contact length given by equation (4) were used in analytically predicting the beam displacements and stresses. The elasticity solution was based on the assumption of linear elastic material behavior but equation (4) shows that a nonlinear relationship exists between the applied load and the contact length. To account for this nonlinearity, a step-wise incremental loading procedure was implemented, where for a given applied load increment the corresponding contact length was calculated using equation (4). The top and bottom surface displacements were then calculated at the midspan and then another load step was used. Essentially this procedure modelled the nonlinear response in a piece-wise linear fashion.

6.2.1 Midspan Deflection

The load versus displacement plots in Figure 89-92 of Appendix A are the experimental results for the 0° unidirectional beams corresponding to the four different aspect ratios listed in Table 1. The incremental procedure discussed above was used to analyze the unidirectional beams and the theoretical midspan displacements are compared to the experimental results in Figures 71-74. The experimental procedure described in Chapter 5 measured displacements at both the top and bottom surfaces of the beam. Therefore, the elasticity solutions for the w displacement were calculated at z equal to h/2 and -h/2 (see Figure 4). As discussed in Chapter 5, the experimental curves have been corrected for machine and fixture related displacements.

The results presented in Figure 71 are for an aspect ratio equal to 7.33. Reasonably good agreement between the theoretical predictions and the experimental data is demonstrated in

C-3

the initial linear portions of the plots. This is true for both the top and bottom surface displacements. For beam geometries corresponding to aspect ratios of 4.00, 1.33, and 0.67 inches, the load versus displacement relationships are shown in Figures 72, 73, and 74, respectively. In specimens having small a/h aspect ratios, the beam's response is governed by local deformations and the bending effects are negligible. Therefore, the poor correlation between the elasticity solution and the experimental displacements is believed to partially be a result of local nonlinear effects at the support points and under the loading nose. Also, the damage described in Chapter 5 indicated the existance of a three-dimensional stress state. Consequently, the two-dimensional linear elastic analysis cannot accurately predict the local displacements for these particular beam configurations. In addition, there is some uncertainty in the experimentally measured quantities and the actual boundary conditions associated with the test environment. Similar discrepancies were seen between the experimental and theoretical displacements in the other laminated beams which were tested.

6.2.2 Indentation

In the classical problem considered by Hertz [2], i.e., contact between two solid isotropic bodies, the amount of indentation was defined as the relative displacement of the two centers of mass of the two contacting bodies. This quantity was discussed in Chapter 1 to be proportional to the contact force raised to the two-thirds power for both isotropic bodies [2] and for graphite/epoxy laminates [1] with a spherical steel indenter.

Sankar [37] considered the contact problem between a rigid cylinder and an orthotropic beam as previously described in Section 6.1.2 for determining the contact length. In addition, Sankar derived an expression for the amount of indentation at the top surface of the beam. This approach was based on modifying an orthotropic half-plane solution to account for the beam
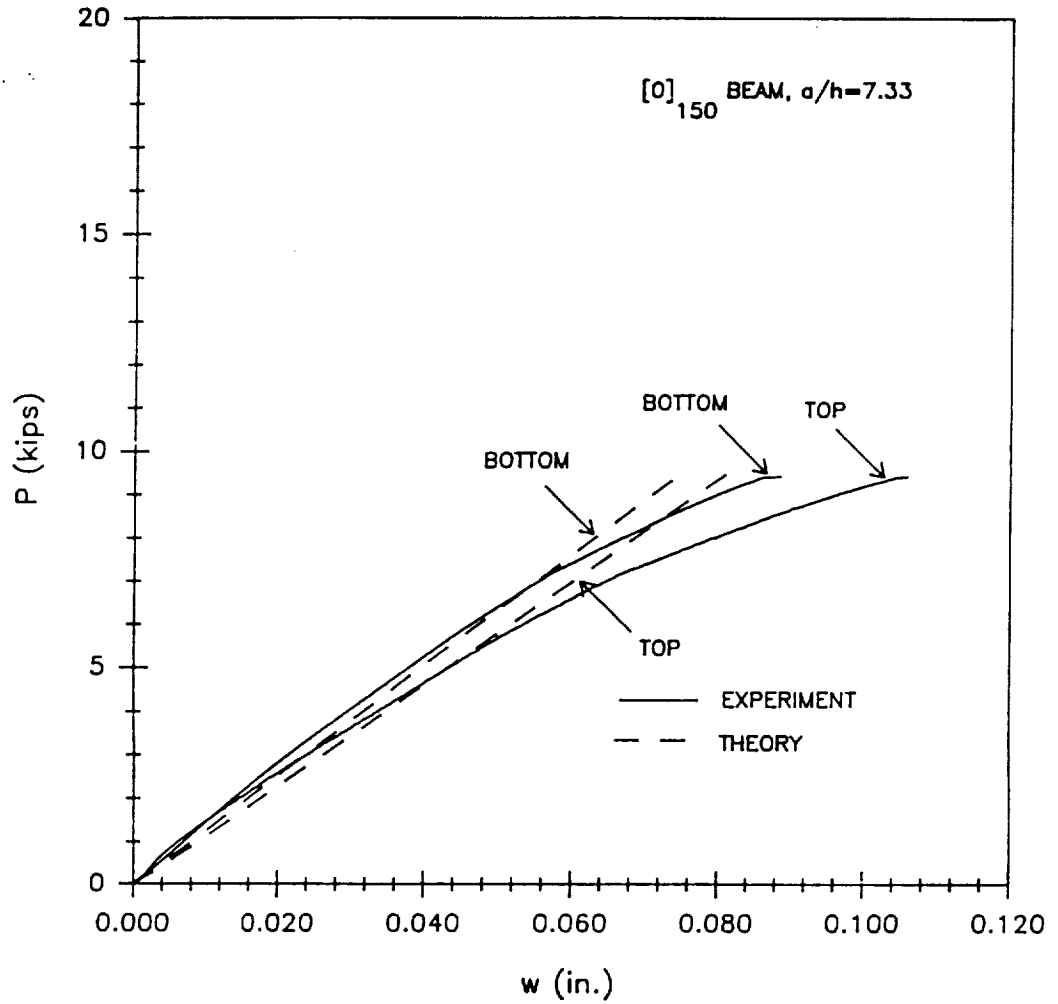
Figure 71. Load versus displacement for a unidirectional beam having an aspect ratio equal to 7.33.
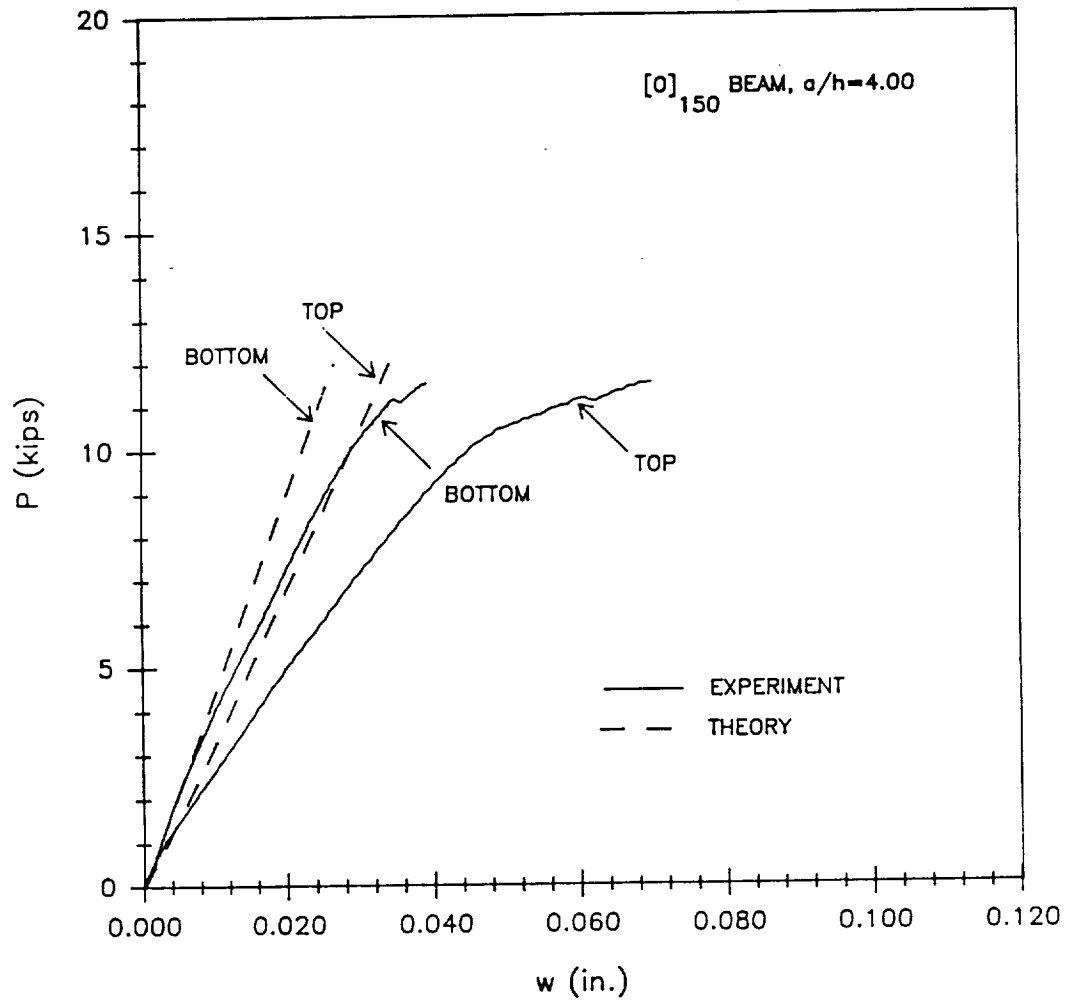
Figure 72. Load versus displacement for a unidirectional beam having an aspect ratio equal to 4.00.
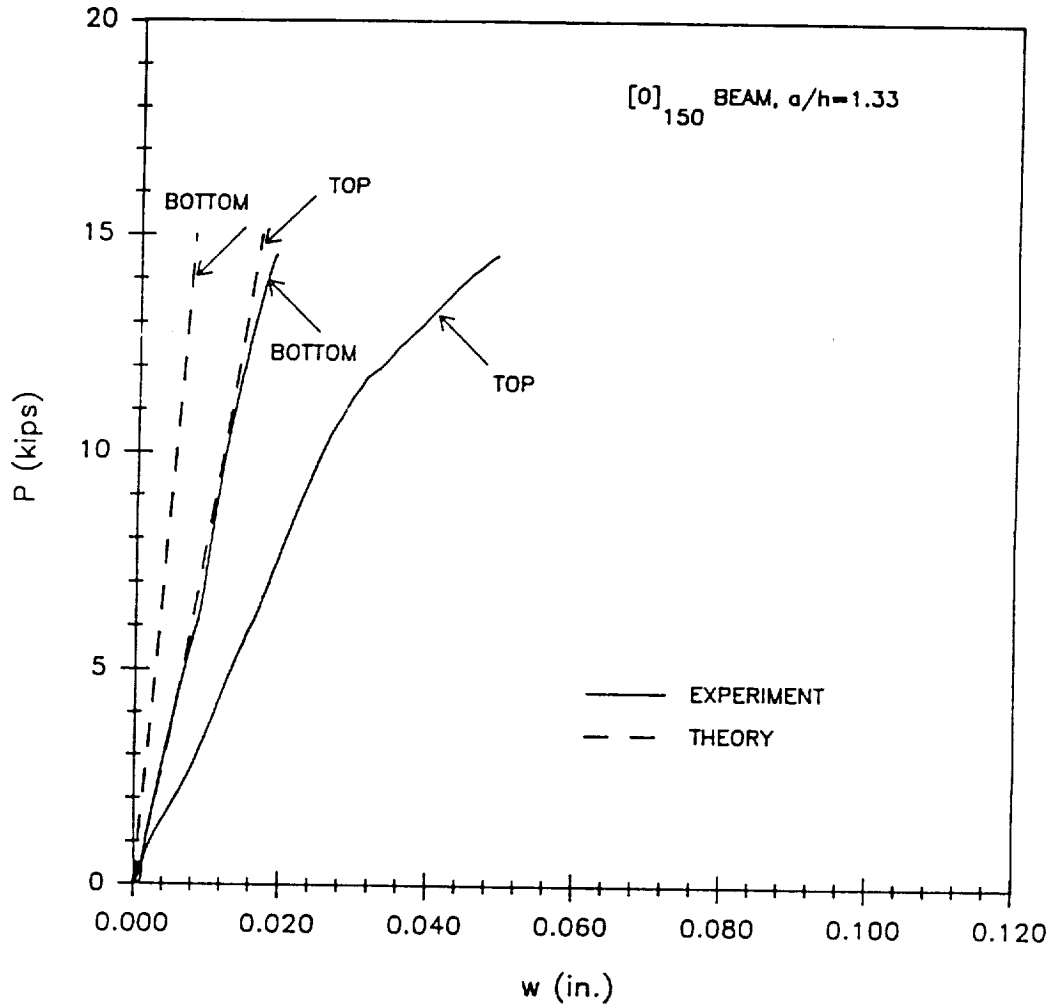
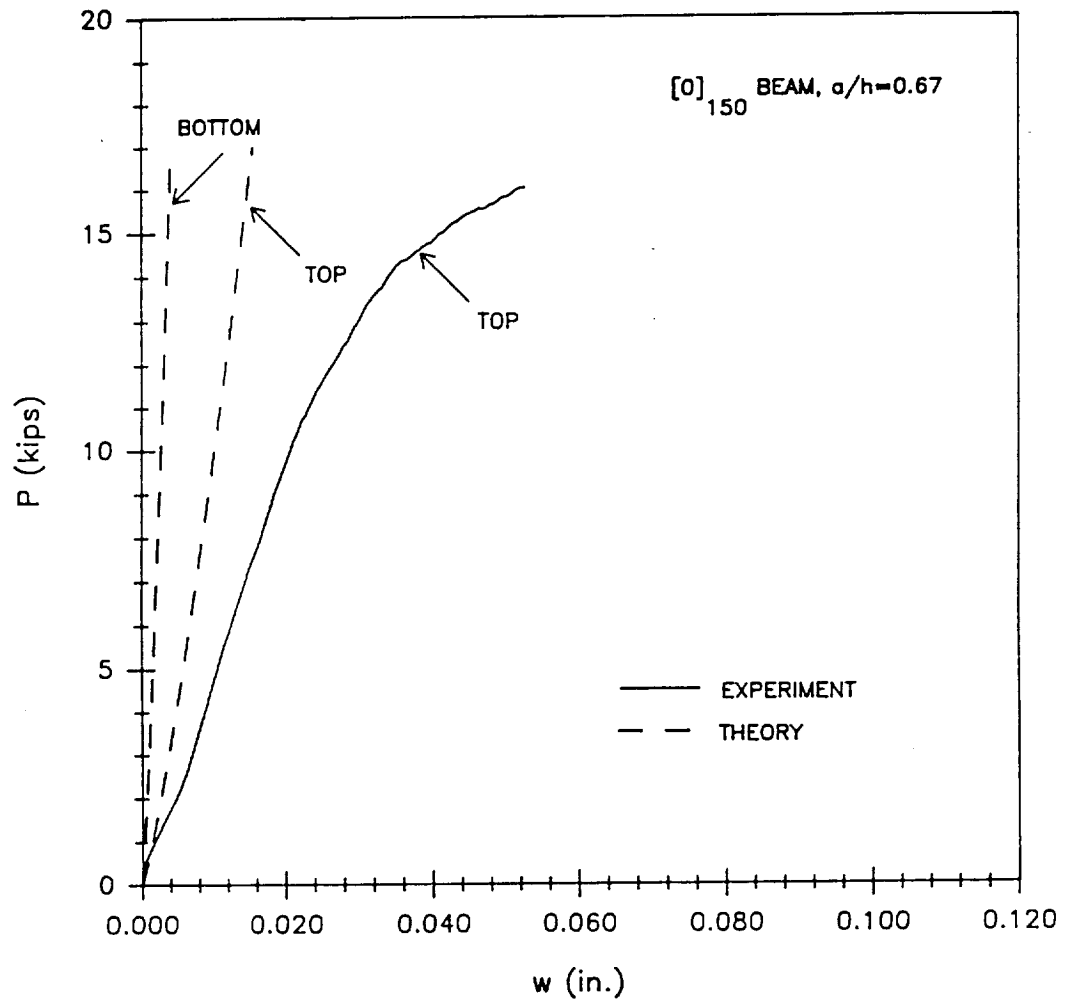**Figure 73.** Load versus displacement for a unidirectional beam having an aspect ratio equal to 1.33.

Figure 74. Load versus displacement for a unidirectional beam having an aspect ratio equal to 0.67.

deflection. The equation derived by Sankar [37] for the indentation in an orthotropic half-plane is given by:

$$\alpha_h = -\frac{4Pk_h}{\pi d} \int_{-d/2}^{d/2} \sqrt{1 - \left(2\frac{\xi}{d}\right)^2} \left\{ \log | -\xi| - \log |\frac{a}{2} - \xi| \right\} d\xi \tag{18}$$

where d is the contact length given by equation (4) and k_h is defined in equation (6). For a given contact length, d, the indentation in an orthotropic beam was derived by Sankar [37] to be equal to:

$$\alpha_b = \frac{\alpha_h}{1 + \frac{\gamma k_c d^2}{4}} \tag{19}$$

where γ and k_c are given by equations (5) and (6), respectively. Sankar noted that the lower limit on the beam's span length-to-depth aspect ratio was approximately 8 for this technique to be valid. This was based on using classical beam theory as an approximation to the global response. An upper limit was stated to exist which corresponded to the case of a very slender beam whose response was governed by beam deflections and not the local indentation.

The amount of indentation can also be obtained using the elasticity solution presented in Chapter 3. The following expression which was used assumes the indentation to be equal to the difference between the top and bottom surface displacements at the midspan of the beam, i.e.,

$$\alpha_e = w(L/2, h/2) - w(L/2, -h/2) \tag{20}$$

The use of equation (20) is analagous to the experimental procedure described in Chapter 5 which led to the results illustrated in Figures 129-137 of Appendix A. Qualitatively, the experimental results in Figures 129-137 indicate the indentation to be independent of the span

length-to-depth aspect ratio and also independent of the stacking sequence. In Figure 75, the relationships between the applied load and the indentation calculated from equation (20) are shown for a $0°$ unidirectional beam having various aspect ratios. For a/h > 1, the theoretical results presented in this figure demonstrate the insensitivity of the indentation to the aspect ratio as stated above for the experimental results. However, a poor correlation between the elasticity solution and the experimental data is illustrated in Figure 76. The results depicted are for a $0°$ unidirectional beam having a 3.0 inch span length which corresponds to an aspect ratio of 4.0. Sankar's solution given by equation (19) is also shown in Figure 76 and also results in a large discrepancy between theory and experiment. Similar behavior was seen in the analytical/experimental correlation for the other laminates.

Predictions for the indentation based on Sankar's equation are larger than the experimental values, whereas the elasticity solution for a laminated beam underestimates the indentation. The discrepancy between Sankar's theory and the experiment is thought to be partially due to approximating the global response by the classical beam theory. The results from the elasticity solution developed in the present study are based on the difference between the top and bottom surface displacements. Consequently, the same correlation difficulties which were discussed for the midspan deflection also apply to the indentation.

The results presented for the midspan beam deflection and the top surface indentation illustrated the difficulties encountered in achieving a good correlation between theoretical predictions and experimental data. Numerous attempts aimed towards improving this correlation were made. Analytically, the elasticity solution for the w-component of displacement was verified using the results from a three-dimensional FEM model for a $0°$ unidirectional beam. Satisfactory agreement was seen for the z-displacement along the entire span length and for both top and bottom surfaces. Analytically and experimentally, displacements must be calculated and measured relative to some fixed point in space in order to be meaningful. The elasticity solution developed in Chapter 3 assumed rigid supports and a rigid loading nose, whereas in the test environment the load frame and test fixture are nonrigid. However, the
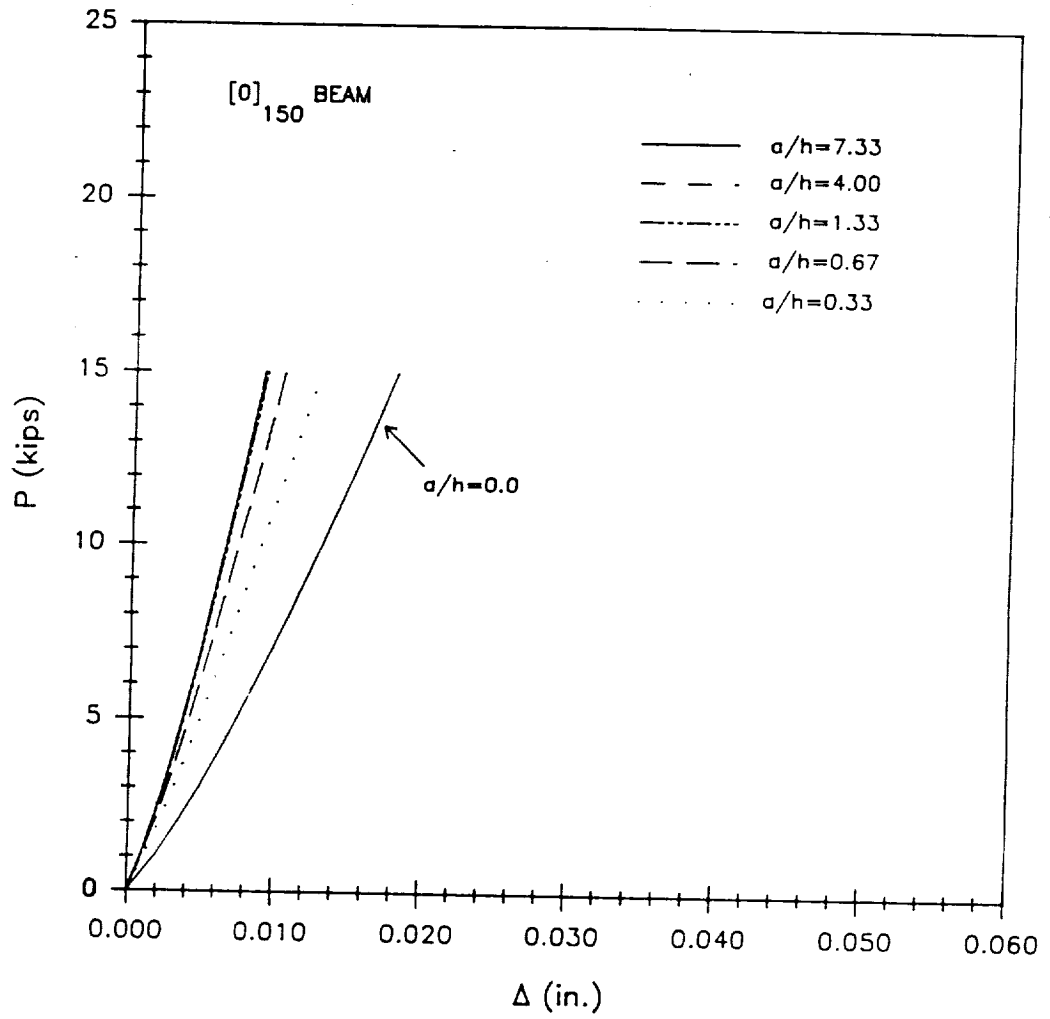
Figure 75. Elasticity solution for indentation in a unidirectional beam and different aspect ratios.
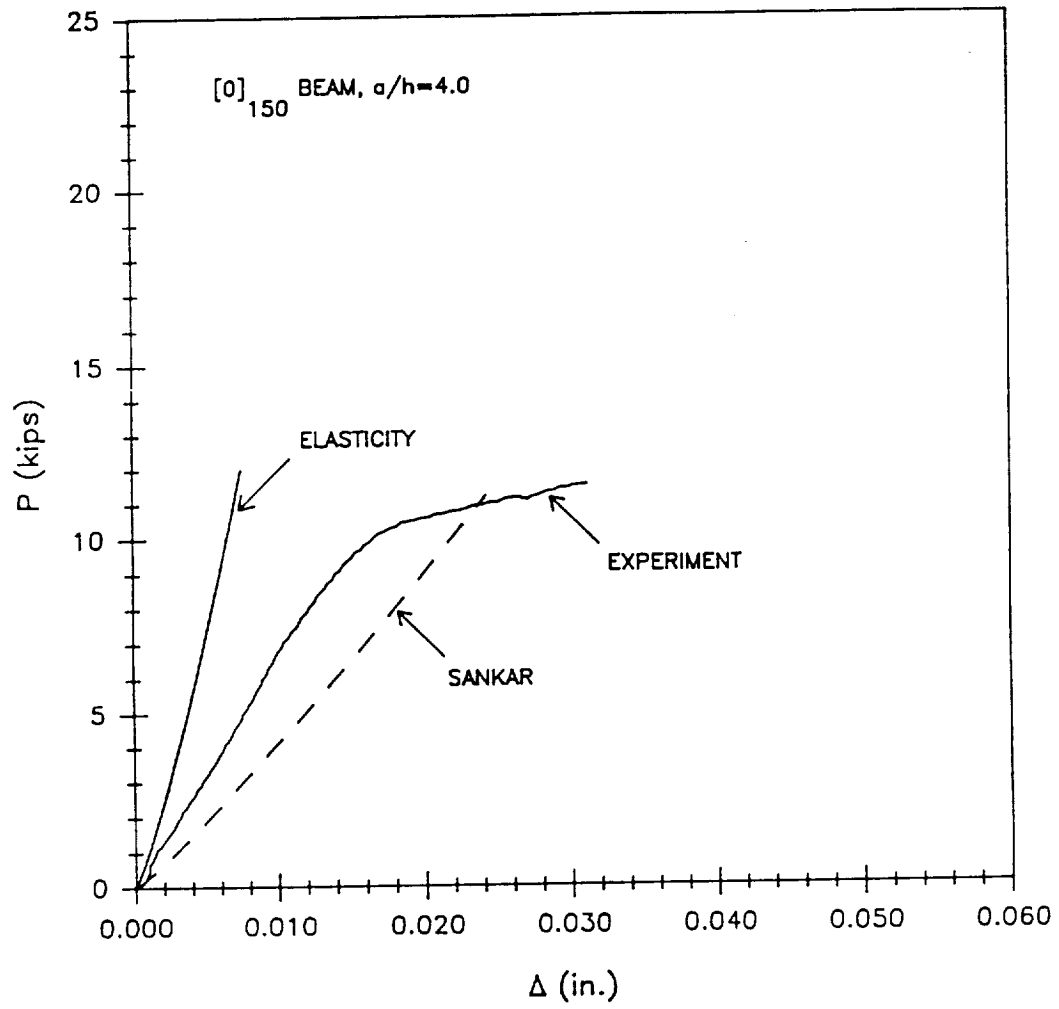
Figure 76. Comparison between theory and experiment for indentation in a unidirectional beam having a aspect ratio of 4.0.

effects of a nonrigid load frame and test fixture were presumably taken into account as discussed in Chapter 5. Subsequently, it was verified that the experimental and analytical results were measured relative to the same point. Nevertheless, as previously stated there is still some uncertainty in the experimentally measured quantities and the modelling of the actual boundary conditions.

6.3 Damage Initiation

The objective of the present study is to develop methodologies which can be used to obtain a better understanding of damage in laminated composite beams. A combined experimental/analytical approach is used where the analytical procedure for calculating ply-level stress states was presented in Chapter 3. For the beam configurations given in Table I, the damage susceptibility, ultimate failure loads, and initial damage modes were experimentally determined and the results presented in Chapter 5. The experimental results and an analysis of the different test specimen geometries can both be used to rank the damage susceptibility of the different laminates and capture the different damage modes. In correlating the experimental and analytical results, the discrepancies discussed above between the experimental and theoretical displacements are not expected to affect the accuracy of analytically ranking the different laminates.

Correlating the predicted stress distributions with the initation loads for different damage states can be approached several different ways. One approach is to choose a component of stress or combination of stresses, on the basis of one experiment, which might have caused initiation of damage at a given load level. The experimentally measured damage initiation load is then used to analytically determine the magnitude of the chosen stress component at the damage site to be used in predicting the damage initiation load for the observed mode.

On the basis of this criterion, load magnitudes are then calculated which would cause damage initiation in other specimen geometries. An alternative approach is similar to the procedure described above but averages the results from all specimen geometries that have the same type of initial damage. The damage criterion is then based on the average value of the chosen stress component, and the analysis applied to beam geometries which were not tested to determine their damage initiation load. The predicted loads are then plotted as a function of the span length-to-depth aspect ratio, a/h, to use as damage initiation envelopes. If there are specimens which exhibit the same type of damage for a given range of a/h aspect ratios then the predictive model should produce a damage envelope which agrees with the experiments. If the type of damage changes beyond a certain range of a/h aspect ratios then another curve is generated to predict damage initiation based on a different criterion.

Damage initiation loads were calculated for the 0° unidirectional beams using the first approach discussed above and the results from the a/h = 7.33 aspect ratio beam geometry. For the remaining stacking sequences, the second approach was implemented using the following procedure. The summary of different damage states given in Tables 2, 3, and 4 demonstrated that the investigation of several different damage mechanisms was required to predict the damage initiation loads. Subsequently, the damaged specimens were classified into four groups on the basis of similar damage mechanisms. The first group consisted of all the laminated beams which had a span length-to-depth aspect ratio less than 1.00 (see Table 1). The type of damage observed in these laminates was in the form of localized crushing and a maximum contact pressure was assumed to be an applicable damage criterion. The second group of laminates was on the opposite end of the spectrum for the range of aspect ratios considered, i.e., a/h greater than 12.0. Four different beam configurations were included in this group, the $[0/\pm45/90]_{4s}$ and $[0/\pm60]_{4s}$ stacking sequences having aspect ratios equal to 12.50 and 22.92, all of which experienced a tensile failure mode. Consequently, the postulated criterion for predicting the damage initiation loads was based on a maximum tensile bending stress located at the back-face of the beam. The third class of beams was comprised of

laminate geometries which corresponded to initial damage in the form of a delamination. Finally, when the initial damage was described by matrix cracks in the 90° or off-axis plies the beam configuration was classified into the fourth group. For the specific stacking sequences and aspect ratios in the last two groups refer back to Tables 2, 3, and 4. The postulated damage initiation criteria for the third and fourth groups will be discussed later in this chapter. The next step in the procedure was to analytically determine the local stress states which corresponded to the damage initiation load and the damage location. Depending on the type of damage which was similar in each group, the results were examined to determine the component and magnitude of stress to use as a damage initiation criterion.

6.3.1 Unidirectional Beams

The observed damage states reported in Chapter 5 for the 0° unidirectional beams consisted primarily of delaminations at $z = h/6$ and at the midplane for the largest aspect ratios tested. Also, the results for the experimentally measured loads showed the damage initiation load to be equal to the ultimate failure load. Consequently, the criterion used for predicting damage initiation also applies for predicting ultimate failure and can be based on the magnitude of interlaminar shear stress, τ_{xz}, which causes a delamination. For the smaller aspect ratio beams tested, the observed damage was a transverse splitting in the xz-plane which seemed to initiate under the loading nose. Based on the two-dimensional elasticity analysis, calculated normal stresses along the x-direction under the loading nose are compressive and therefore can not cause splitting. Also, experimental observations indicate that, as opposed to the deformation patterns assumed by plane strain or generalized plane deformations, there is significant local out-of-plane deformation in the vicinity of the load nose. These observations suggest that the actual stress distribution under the load nose is three-dimensional and complex. It is possible that the observed splitting initiates slightly away from the load nose due to tensile stresses resulting from the local out-of-plane deformations. Therefore, the

two-dimensional analysis developed in Chapter 3 would not be expected to accurately predict the observed splitting failures.

For the prediction of delaminations the magnitude of the maximum shear stress, τ_{xz}, is used as a damage initiation criterion. The $a/h = 7.33$ beam configuration was analyzed to determine the magnitude of τ_{xz} at the midplane of the beam when subjected to the damage initiation load. The distribution of shear stress, τ_{xz}, along the beam's span and at the midplane shows the maximum value to be located half-way between the midspan and the supports. For a 0° unidirectional beam the global coordinates and material coordinates coincide and the τ_{xz} component of stress is equivalent to τ_{13}. The calculated maximum value was in good agreement with reported shear strengths of approximately 10 ksi for this material system. Consequently, a shear strength value, S_{13}, equal to 10 ksi was used to determine the applied load which would produce an interlaminar shear stress at the midplane having a magnitude of S_{13}. This criterion was also applied to other 0° unidirectional beams having different span lengths. The correlation between the predicted loads as a function of beam aspect ratio and the experimental results are shown in Figure 77. It is seen that the maximum shear stress criterion slightly over predicts the damage initiation load for the highest aspect ratio tested but in general a satisfactory correlation between theory and experiment was achieved.

6.3.2 Crushing Mode

For the elliptical traction distribution described in Section 6.1.1, the maximum contact pressure is equal to:

$$p_{max} = \frac{2P_i}{\pi bd} \tag{21}$$
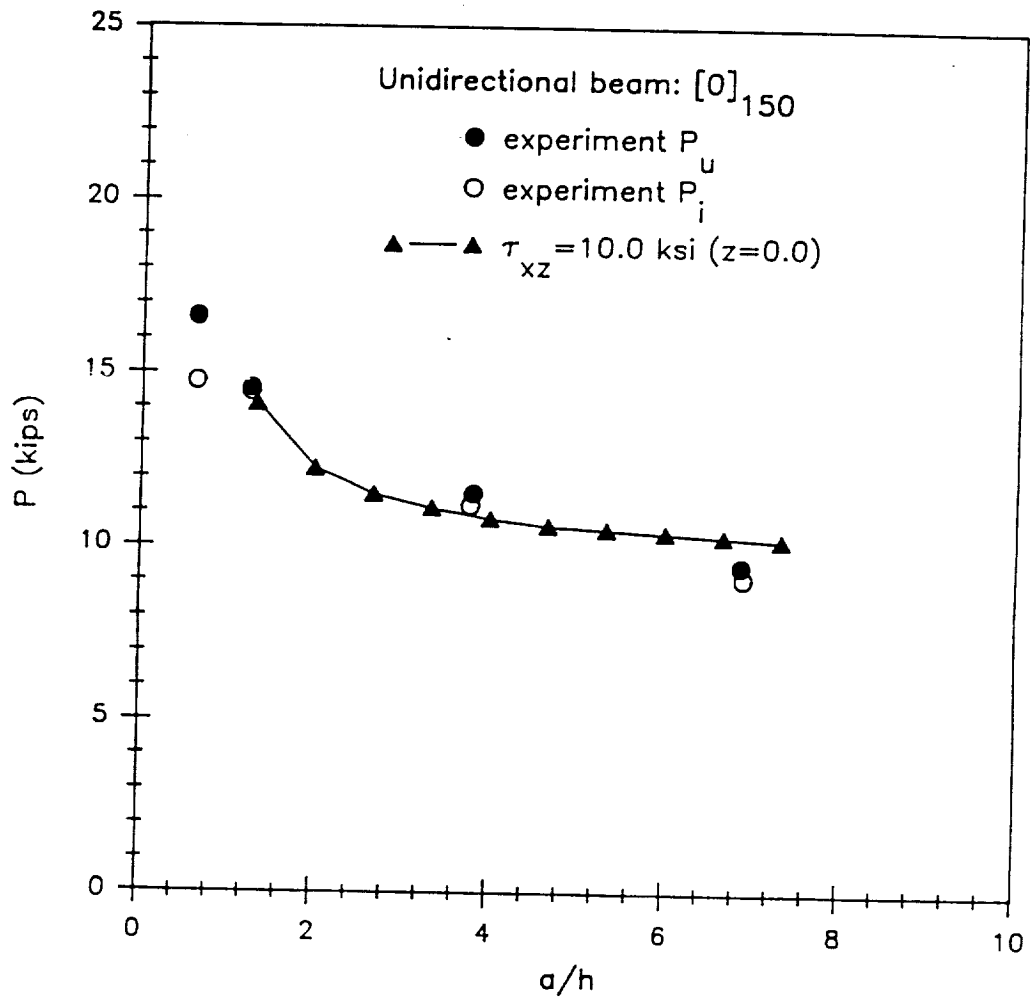
Figure 77. Damage initiation predictions for unidirectional beams as a function of the beam's a/h aspect ratio.

where P_i is the damage initiation load, b = 1.0 for a unit width, and d is equal to the contact length. The results for the maximum contact pressure calculated from equation (21) for the beams having an aspect ratio less than 1.0 are shown in Figure 78. The results range from a minimum of 54.623 ksi for the cross-ply beam to a maximum of 75.734 for the $[0/\pm45/90]_{1ss}$ beam. A criterion based on an average maximum contact pressure for the seven beams included in this group would predict damage initiation if the contact pressure was larger then 63.5 ksi. However, instead of a criterion based on an average value, a threshold value could be used which would predict crushing of a beam's top surface if the applied contact pressure exceeded 54 ksi.

An isotropic beam having similar geometry would likely fail along a slip line associated with the plane of maximum shear stress. In Chapter 4, it was shown that for an orthotropic beam the maximum shear stress contour was located directly under the loading nose and very high gradients existed. Therefore, a possible alternative to the contact pressure criterion for predicting the crushing damage mode would be a maximum shear stress criterion. For this group of seven beams, an average maximum shear stress value of 52.1 ksi was calculated at d/2 away from the midspan and near the top surface.

6.3.3 Tensile Mode

The magnitude of the tensile bending stress in the bottom 0° plies was assumed to be an appropriate damage initiation criterion for the second group of beams. The analytical stress calculations for the four beams in this group had an average maximum bending stress of 280 ksi when the beams were subjected to their damage initiation loads. A commonly reported value for the uniaxial tensile strength of an AS4/3501-6 graphite/epoxy 0° specimen is 300 ksi. The damage initiation loads which would produce an ultimate tensile bending stress of 300 ksi in the bottom 0° ply were determined. The results for the $[0/\pm45/90]_{6s}$ beams having a/h
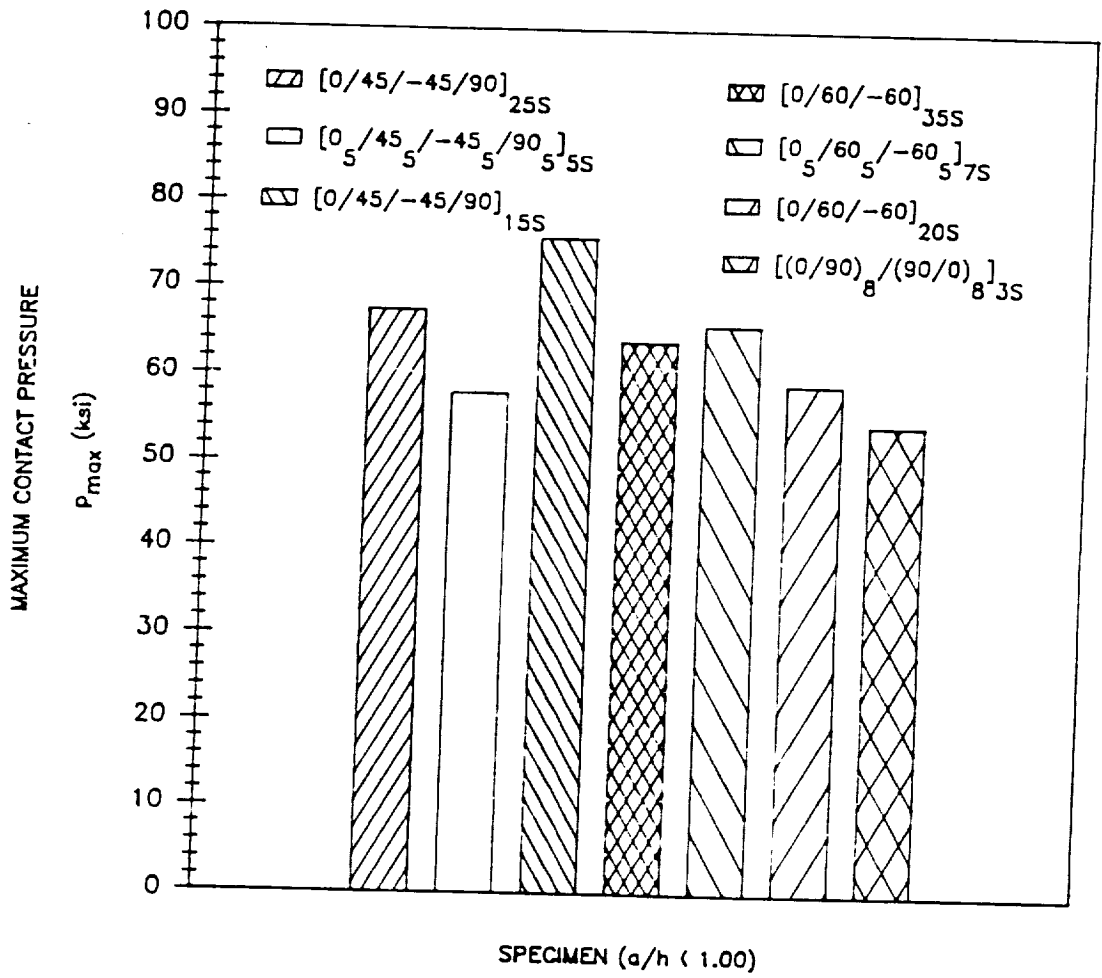
Figure 78. Maximum contact pressures for beams having an aspect ratio less than 1.0.

equal to 22.97 and 12.50 were 0.97 kips and 1.75 kips, respectively. For the $[0/\pm60]_{4s}$ beams having the same aspect ratios the results were 0.95 kips and 1.71 kips. These results are approximately 9% larger than the experimental results. Consequently, the damage initiation criterion based on the maximum tensile bending stress equal to 300 ksi accurately predicted the damage initiation loads for this group of specimens.

6.3.4 Delamination Mode

The third group of laminates was classified on the basis of a delamination type of damage mode. The proposed criterion for predicting the damage initiation loads was based on the interlaminar shear stress distribution along the interface which corresponded to the location of the delamination. In general, for the case of a large aspect ratio beam the delaminations were close to the midplane. The interlaminar shear stress, τ_{xz}, at that point is maximum half-way between the load and support points and the normal component of stress, σ_{zz}, is approximately equal to zero. However, as the aspect ratio becomes small, the delaminations occur at an interface which is above the midplane. The distribution of the interlaminar shear stress along these interfaces showed the maximum value to be located closer to the midspan and the applied loading. Consequently, the location of the maximum interlaminar shear stress coincided with a compressive normal stress, σ_{zz}, which would prevent the delamination. Moving along an interface which is located close to the top surface, away from the midspan and the load nose, the magnitudes of the compressive normal stress and the interlaminar shear stress decrease. Therefore, when evaluating the analytical results for the interlaminar shear stress distribution the z-location of the interface corresponding to the observed delamination is an important parameter in developing a valid damage criterion. For the smaller aspect ratios, the z-location of the delamination led to a damage initiation criterion being based on a magnitude of interlaminar shear which was not an absolute maximum value. The damage criterion for predicting damage initiation loads for this group of beams was subse-

quently based on an average value of the results shown in Figure 79, which was equal to 8.5 ksi.

6.3.5 Matrix Cracking Mode

For the group of laminated beams which experienced initial damage in the form of matrix cracks, cracks were experimentally observed in either the 90°, 45°, or 60° plies. Depending on the stacking sequence and the orientation of the fibers, different local states of stress can exist in a layer which can be related to the existence of matrix cracks. For the case of cracks in a 90° ply and considering the components of stress in the xz-plane, the stresses will be acting along the principal material directions in the transverse 23-plane. This corresponds to the component of stress σ_{22} being equal to σ_{xx} and τ_{23} equals τ_{xz}. Consequently, a criterion for predicting matrix cracks in a 90° ply located below the midplane can be based on the beam's bending stress, σ_{xx}, exceeding the transverse tensile stength of the material system. An alternative criterion, regardless of the crack's location, is the in-plane shear stress exceeding an allowable transverse shear strength. A resulting damage criterion which combines the above components of stress, σ_{xx}, τ_{xz} and also σ_{zz} is based on the principal stresses in two directions. The components of stress in the xz-plane are rotated to their principal directions along which the maximum and minimum normal stresses act. Also, the plane of maximum shear is determined. The damage initiation load can then be predicted based on the maximum principal normal stress reaching an allowable transverse tensile strength or based on an allowable shear stress. The numerical calculations for the principal stresses in the specimens with 90° ply matrix cracks were performed under the experimentally measured damage initiation load. The results for the maximum shear stress at the observed damage site are presented in Figure 80 and will be discussed later in this section.
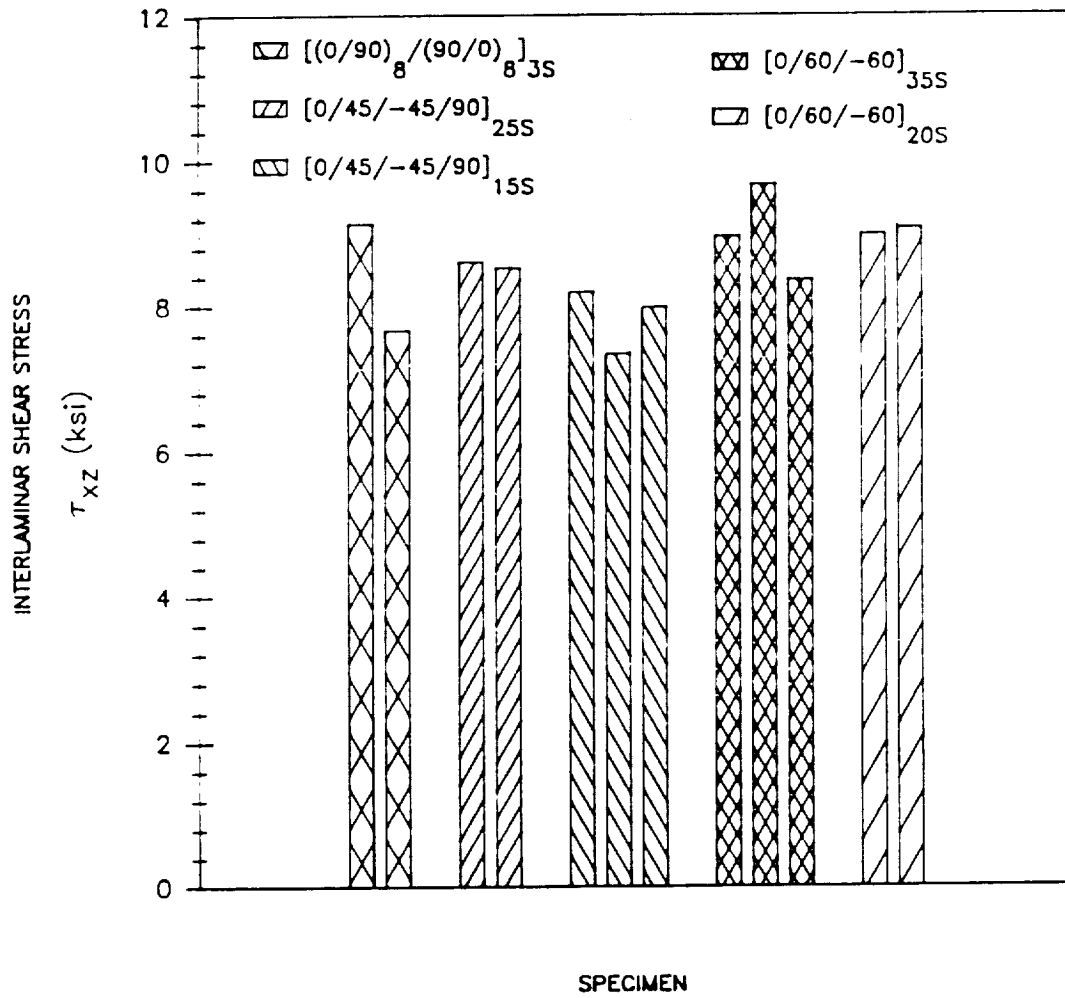
Figure 79. Interlaminar shear stress magnitudes for the group of beams which had a delamination.

In the case of a matrix crack in a 45° or 60° ply the development of a valid damage criterion is more involved than in the case of a 90° ply. In addition to considering the components of stress in the xz-plane, the components of stress in the xy-plane must be examined. The xy-plane components of stress can be rotated to the principal material directions in the 12-plane and a criterion can be formulated based on these results. However, in order to compare with the 90° results presented above, the principal stresses in the xz-plane were initially determined. The calculated values for the maximum shear stress in the plies having matrix cracks are shown in Figure 81 for the case of a 45° layer and in Figure 82 for the 60° layers.

The results presented in Figures 80-82 show that a wide range of maximum shear stress values were calculated at the location of the experimentally observed matrix cracks. Therefore, it appears that the maximum shear stress by itself does not explain the presence of matrix cracks in the damaged specimens. The results also indicate that for a given aspect ratio, comparable values of maximum shear stress were calculated for the 90°, 45°, and 60° plies containing matrix cracks. Consequently, in correlating the analytical stress predictions with the observed matrix cracks no distinction between different fiber orientations is required when only the stress components in the xz-plane are considered. However, the z-location of the matrix cracks and the beam's aspect ratio are seen to be important influencing factors which required further investigation. For the different beam configurations in this group, the matrix cracks in most of the higher aspect ratio beams were located in the neighborhood of the midplane. As the aspect ratio is decreased, cracks were also seen closer to the top surface and the loading nose, and the crack density or number of cracks increased. For the case of a small a/h aspect ratio, the extensive cracking made it difficult to define or pinpoint the location of the initial crack. Also for this geometry, there is a minimal amount of beam deflection and when a matrix crack occurs there is a corresponding minimal amount of energy released. Consequently, the manner in which the damage initiation load was determined, i.e., the first noticeable reduction in load carrying capacity, may actually overpredict the load at which the first crack appears.
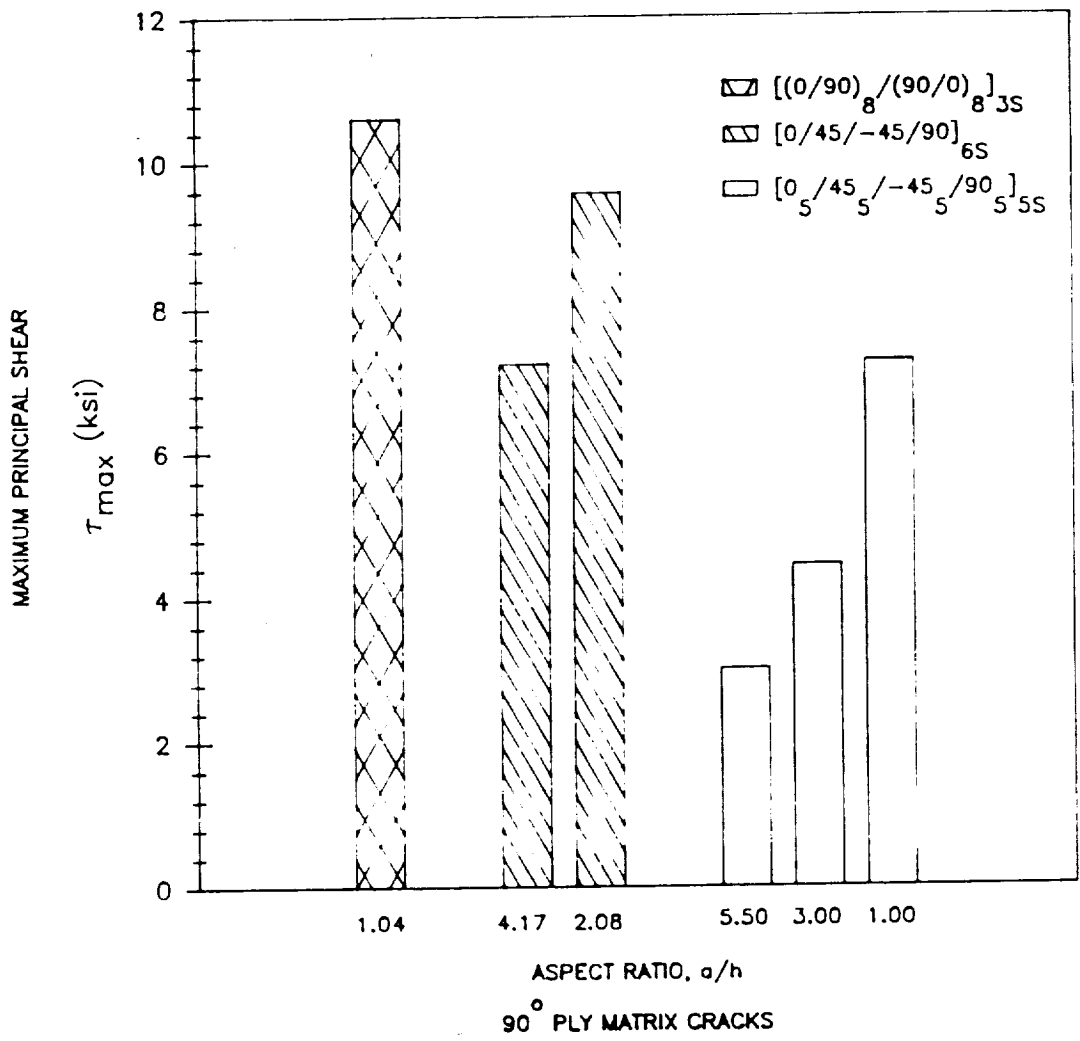
Figure 80.   Maximum shear stress, τ_{max} (ksi), in the 90 plies.
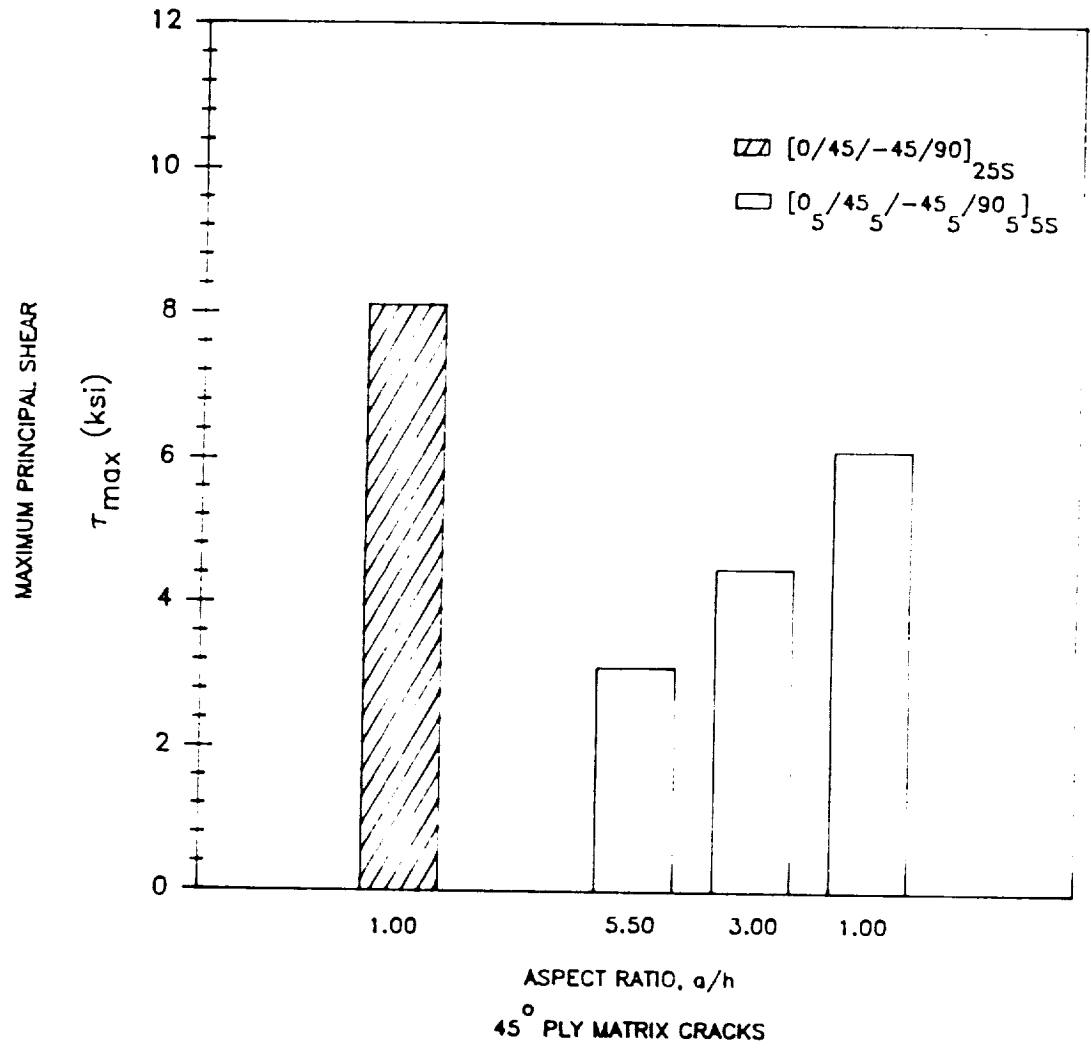
Figure 81. Maximum shear stress, τ_{max} (ksi), in the 45 plies.
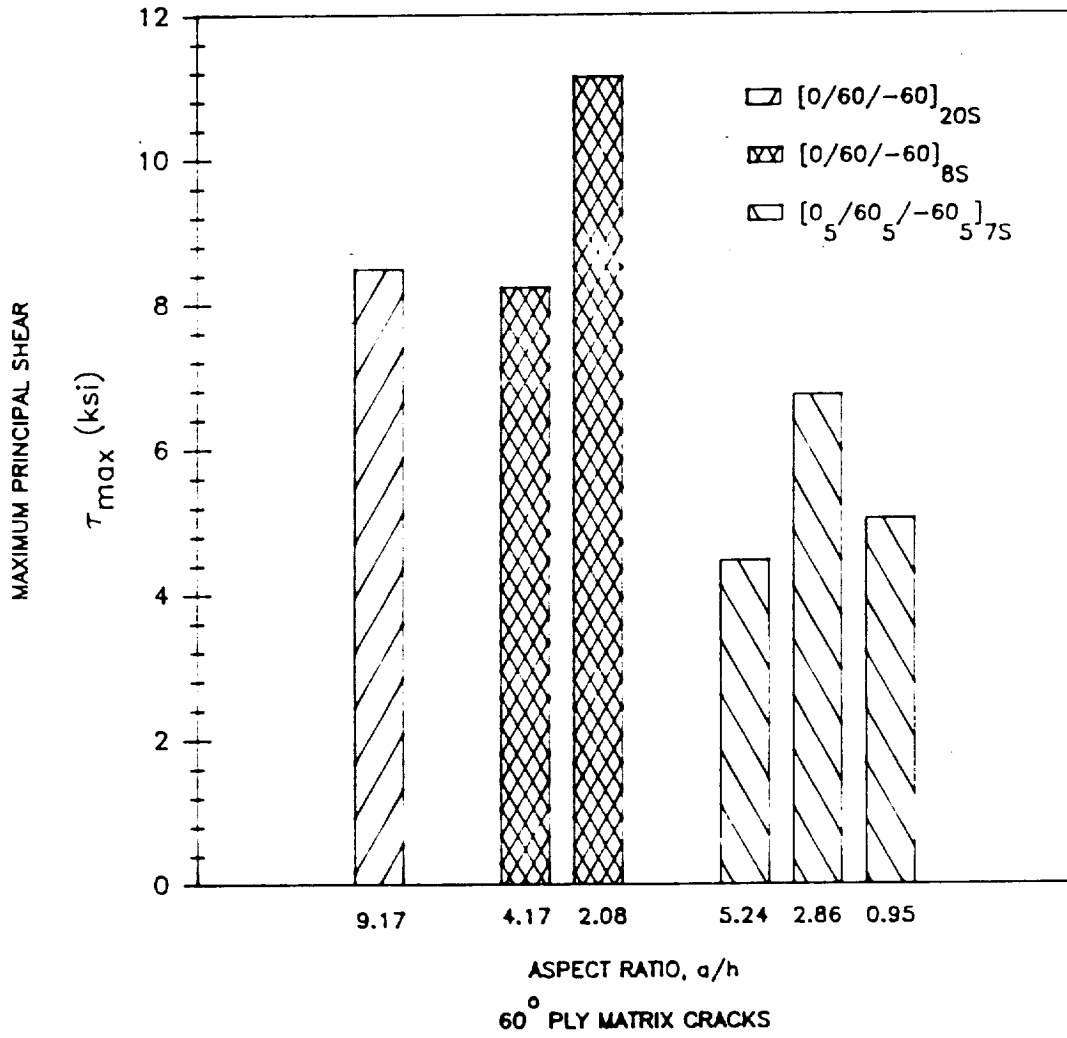
Figure 82. Maximum shear stress, τ_{max} (ksi), in the 60 plies.

To better understand the role which the in-plane shear stress, τ_{xz}, plays in the development of matrix cracks, stress profiles were generated along the span of the beam. The distributions of τ_{xz} were examined because the largest contribution in the expression for the maximum shear stress comes from τ_{xz} in comparison to the normal components of stress, σ_{xx} and σ_{zz}. An exception to this is when the value of the maximum shear stress is calculated at the midspan and close to the top surface where large axial compressive stresses exist. The distribution of τ_{xz} along the span of the beam was determined at different z-locations corresponding to the various layers in which matrix cracks were observed for the different beam geometries. The results for the span length profiles focused on the grouped stacking sequences which were shown in Tables 3 and 4 to have the largest percentage of specimens containing matrix cracks. In Figures 83-85 the distributions are presented for the $[0_5/45_5/ - 45_5/90_5]_{ss}$ laminated beams having aspect ratios of 1.00, 3.00, and 5.50, respectively. The five curves in each figure correspond to the five 45° plies located above the midplane. As mentioned above, similar profiles exist for the 90° plies in this stacking sequence and for the 60° plies in the $[0_5/60_5/ - 60_5]_{7s}$ stacking sequence. In all three of the figures, very large shear stress gradients exist in the neighborhood of the midspan and in the top 45° layer. However, the maximum value of shear stress in this layer may not necessarily result in a matrix crack because, as previously stated, there are large compressive stresses in this region. On the other hand, the existance of very large gradients correlates with the increase in crack density seen for the case of a small aspect ratio beam. Also, for a small aspect ratio beam the observed crack pattern can be described by a series of cracks extending along a line from the loading nose to the support points. The location of the peaks in the five τ_{xz} stress profiles shown in Figure 83 correlates with the above described cracking pattern. For the case of a large aspect ratio beam the observed cracking pattern was concentrated at the beam's midplane with several cracks located along a line drawn from the midspan to the end-face of the beam. This correlates with the τ_{xz} stress profiles shown in Figure 85, where for a large aspect ratio beam the profiles corresponding to the layers closest to the midplane have a fairly uniform stress distribution.

$[0_5/45_5/-45_5/90_5]_{5S}$

a/h=1.00

45° plies

τ_{xz} (ksi)

40
30
20
10
0
-10
-20
-30
-40

——————— z=0.462 in.
· · · · · z=0.363 in.
— — . z=0.262 in.
— — . z=0.162 in.
—·—··—·· z=0.063 in.

0.000   0.500   1.000   1.500   2.000   2.500   3.000

x (in.)
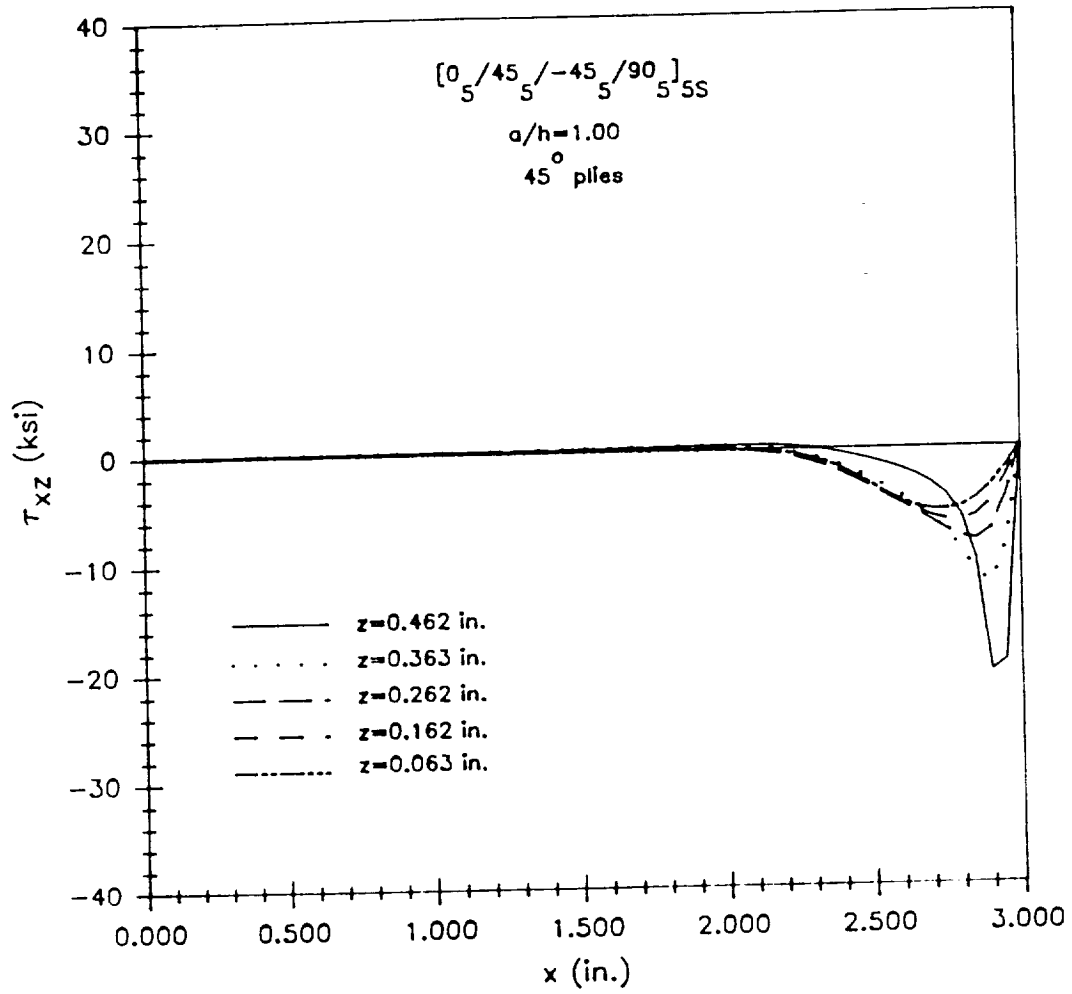
Figure 83.   Span length stress profile for τ_{xz} and an aspect ratio of a/h=1.00.
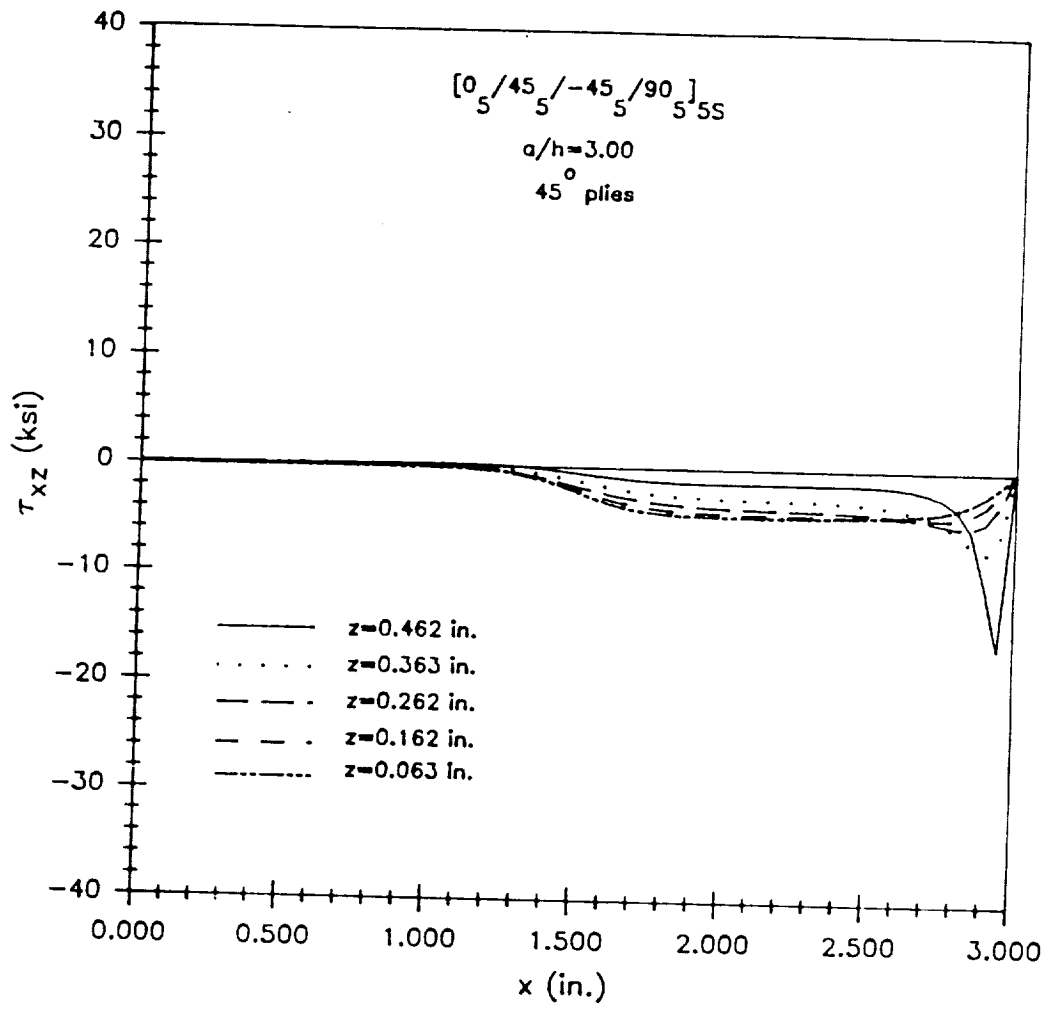
Figure 84. Span length stress profile for τ_{xz} and an aspect ratio of a/h = 3.00.
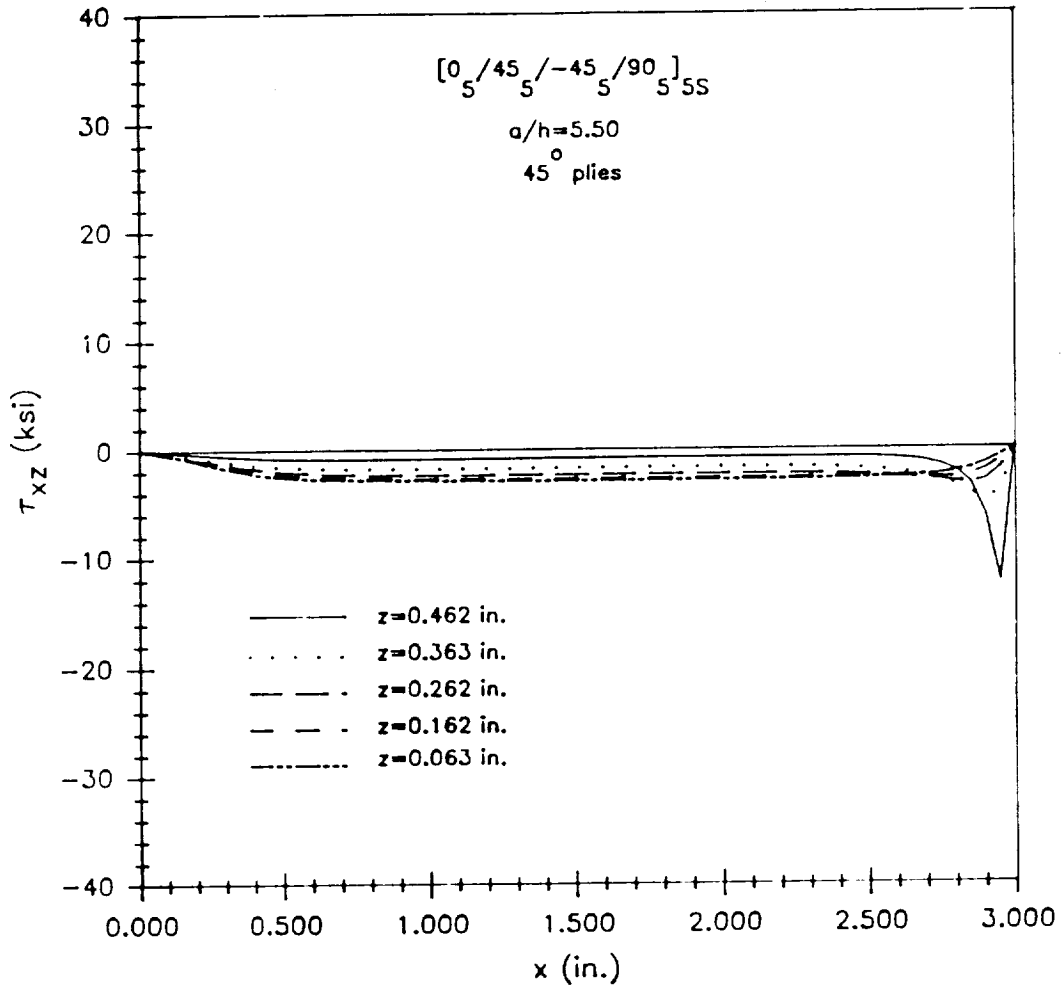
Figure 85.   Span length stress profile for τ_{xz} and an aspect ratio of a/h = 5.50.

6.4 Damage Susceptibility

The last issue addressed in the experimental/analytical correlation study is the damage susceptibility of the tested laminated beam geometries. As described in Chapter 5, damage susceptibility measures how easily damage is induced in a laminated beam when subjected to an applied load. After damage has been initiated, the damage tolerance defines the beam's ability to provide additional load carrying capacity and withstand additional damage. A qualitative assessment of the damage susceptibility and the damage tolerance of the beam geometries tested was discussed in Chapter 5 based on the experimentally measured damage initiation and ultimate failure loads. In this section, the analytical results for the through-the-thickness stress profiles are used to quantify some of the statements made on the basis of the experimental results.

Through-the-thickness stress profiles for the in-plane components of stress were generated for all of the quasi-isotropic beam configurations given in Table 1. The stress profiles are at an x-location corresponding to the location of initial damage and for an applied load equal to the damage initiation load. Generally, for damage that was concentrated at the beam's midplane, the x-location of the damage was half-way between the load and support points, whereas for specimens with damage located closer to the top surface the x-location of the damage was in the vicinity of the beam's midspan. The results for the bending stress, σ_{xx}, and the in-plane shear stress. τ_{xz} , are given in Appendix B. Of primary importance in correlating the previously described damage susceptibility (see Section 5.3.3) with the stress profiles is the shear component of stress, τ_{xz}. Recall that in sections 6.3.4 and 6.3.5 both the delaminations and matrix cracking modes of damage were explained in terms of the in-plane shear stress, τ_{xz} .

Based on the experimental results, for an a/h aspect ratio greater than 2.50 the $[0/\pm45/90]_{2ss}$ stacking sequence was more damage susceptible than the $[0/\pm60]_{3ss}$ laminate, i.e., the $[0/\pm45/90]_{2ss}$ beams had smaller damage initiation loads. The through-the-thickness τ_{xz} stress profiles for the two different stacking sequences under applied loads equivalent to their respective damage initiation loads and an x-location close to the midspan are compared in Figure 86. The results presented are for the case when the $[0/\pm45/90]_{2ss}$ and $[0/\pm60]_{3ss}$ had aspect ratios of 5.50 and 5.24, respectively. Because of the difference in the thickness of these two laminates, comparison of exactly equal a/h ratios was not possible. This figure illustrates that the two laminated beams have very similar stress profiles even though the $[0/\pm45/90]_{2ss}$ results are for a smaller damage initiation load (8.52 kips) compared to the damage initiation load of the $[0/\pm60]_{3ss}$ laminate (10.40 kips). Consequently, for a given load level the shear stress distribution in the $[0/\pm45/90]_{2ss}$ beam will have a larger magnitude in comparison to the $[0/\pm60]_{3ss}$ beam and therfore be more susceptible to damage initiation. Similar results were seen when the results for the $[0/\pm45/90]_{2ss}$ laminated beam having an aspect ratio of 3.00 were compared to the $[0/\pm60]_{3ss}$ beam having an aspect ratio of 2.86.

In the case of a/h ratios less than 2.50, however, the $[0/\pm60]_{3ss}$ laminated beams were more susceptible to damage than the $[0/\pm45/90]_{2ss}$ beams. Figure 87 compares the two through-the-thickness stress profiles at an x-location close to the midspan when the aspect ratio was equal to 0.50 for the $[0/\pm45/90]_{2ss}$ and 0.48 for the $[0/\pm60]_{3ss}$ beam. The comparable stress profiles at the two loads, 24.6 kips for the $[0/\pm60]_{3ss}$ laminate and 27.4 kips for the $[0/\pm45/90]_{2ss}$ laminate indicate that for the same applied load the $[0/\pm60]_{3ss}$ beam will have larger shear stresses, which correlates with the experimental results that the $[0/\pm60]_{3ss}$ beam is more susceptible to damage initiation. Also presented in Figure 87 are the results for the grouped stacking sequences, i.e., $[0_5/45_5/-45_5/90_5]_{ss}$ and $[0_5/60_5/-60_5]_{7s}$, having the same aspect ratios. Again it is seen that the analytical predictions for the distribution of τ_{xz} through-the-thickness are very similar between the different lamination sequences which had different damage initiation loads (20.2 kips for the $[0_5/45_5/-45_5/90_5]_{ss}$ beam compared to 26.1

kips for the $[0_s/60_s/-60_s]_{7s}$ beam). Therefore, based on the analytical stress profiles for a given applied load the $[0_s/45_s/-45_s/90_s]_{ss}$ beams will have a larger shear stress than the $[0_s/60_s/-60_s]_{7s}$ beams and thus be more damage susceptible. In addition, the profiles quantitatively support the experimental results which indicated the grouped stacking sequences to be more susceptible to damage than the interspersed stacking sequences. This is a direct consequence of the similar stress profiles and the differences in loads at which damage was initiated.

In contrast to the beams having an interspersed stacking sequence and an aspect ratio greater than 2.50 where the damage was located close to the top surface, the initial damage in the grouped stacking sequence beams was concentrated around the midplane. For the most part, based on the damage descriptions in Tables 3 and 4 and the damage initiation loads, the laminated beams having initial damage located at the midplane are more damage susceptible than the beams having initial damage located closer to the top surface. The τ_{xz} stress profiles for the $[0_s/45_s/-45_s/90_s]_{ss}$ and the $[0_s/60_s/-60_s]_{7s}$ beams having aspect ratios of 5.50 and 5.24, respectively, are shown in Figure 88. Since the damage was located near the midplane, the results are for an x-location halfway between the load and the supports and the profiles resemble a parabolic distribution. The $[0_s/60_s/-60_s]_{7s}$ profile has a slightly larger shear stress at the midplane in comparison to the $[0_s/45_s/-45_s/90_s]_{ss}$ results. However, due to the large difference in their damage initiation loads, 4.28 kips for the $[0_s/45_s/-45_s/90_s]_{ss}$ laminate versus 6.67 kips for the $[0_s/60_s/-60_s]_{7s}$ laminate, applying the same load to each laminate results in the $[0_s/45_s/-45_s/90_s]_{ss}$ beam having a larger shear stress which corresponds to this beam configuration being more susceptible to damage.

Analytical/Experimental Correlation
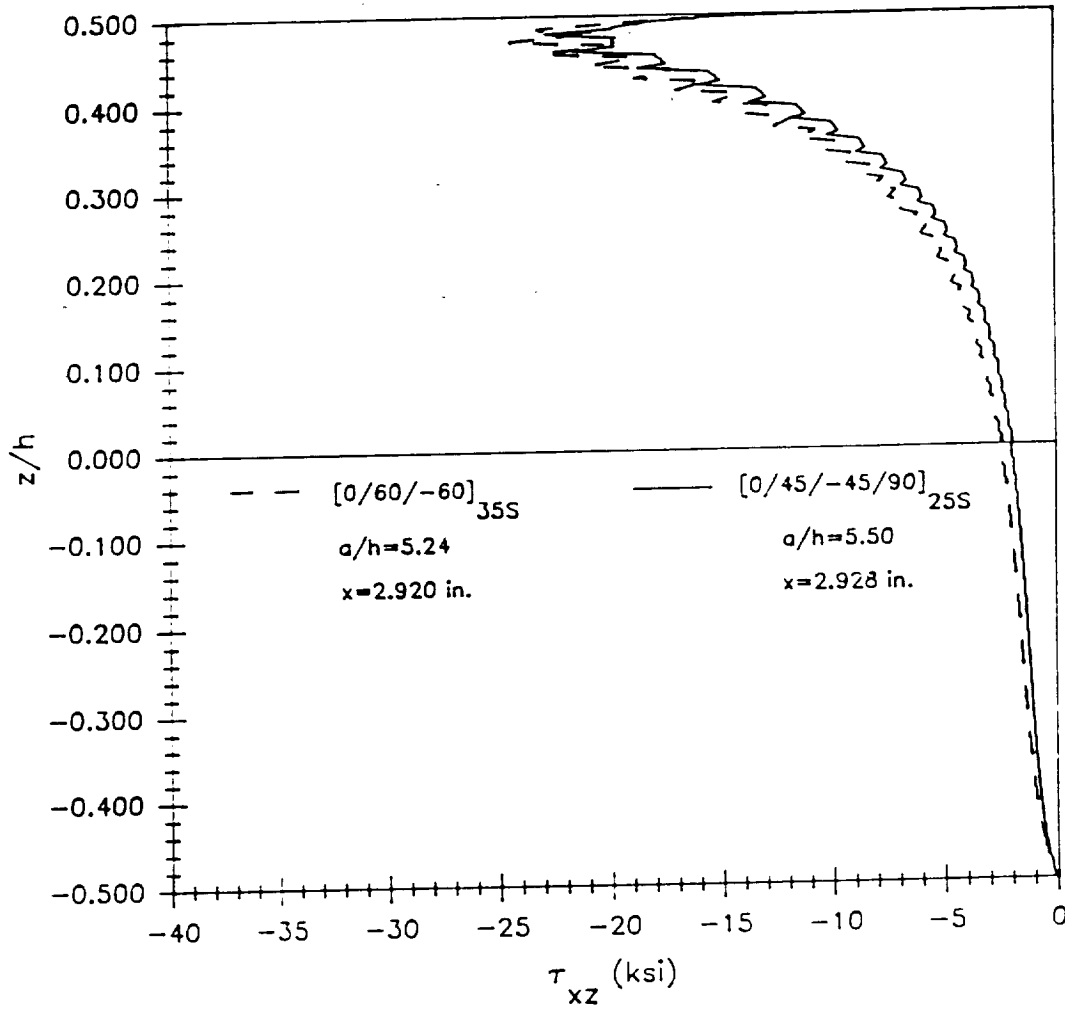
Figure 86. Through-the-thickness stress profiles for τ_{xz} and the beams having an interspersed stacking sequence and an aspect ratio of $a/h = 5.50$.

Analytical/Experimental Correlation
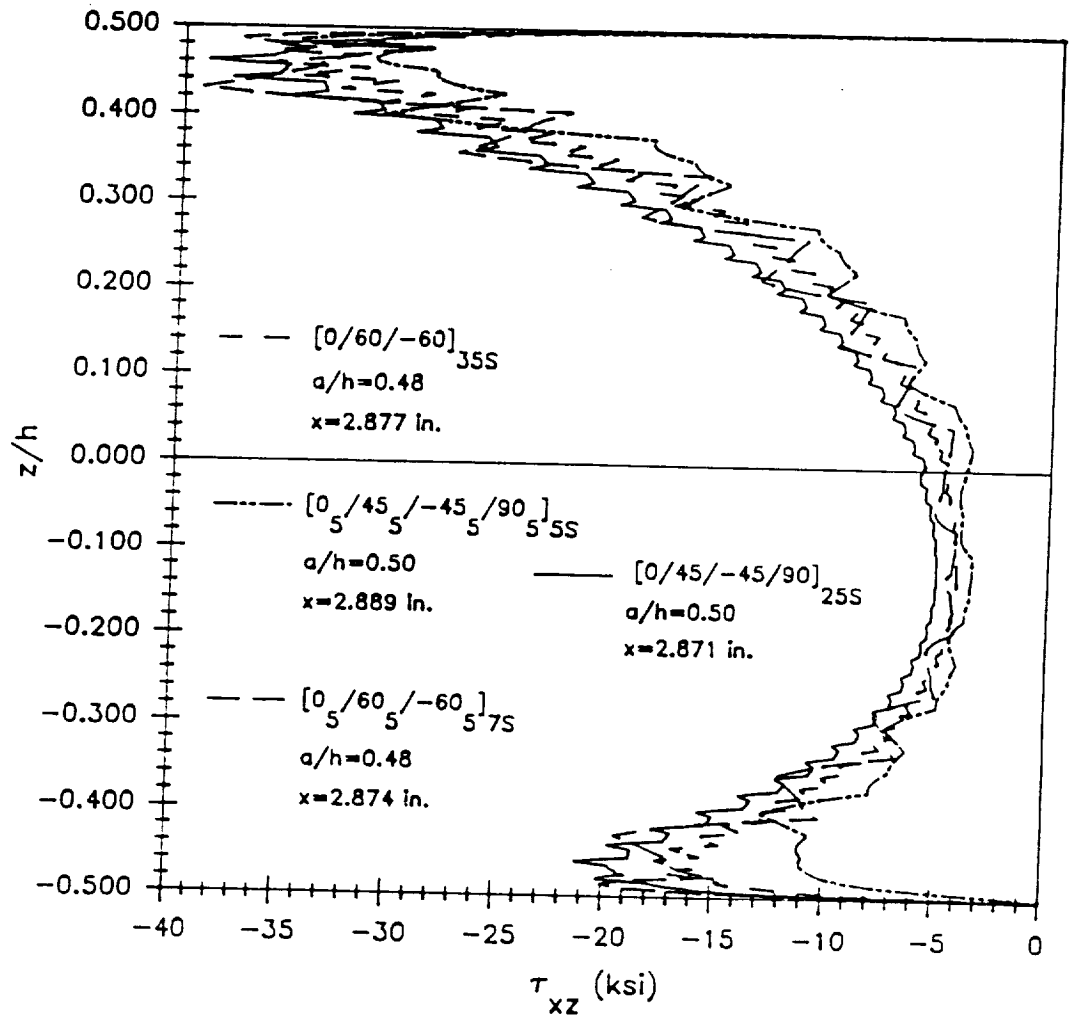
Figure 87.   Through-the-thickness stress profiles for τ_{xz} and an aspect ratio of a/h = 0.50.
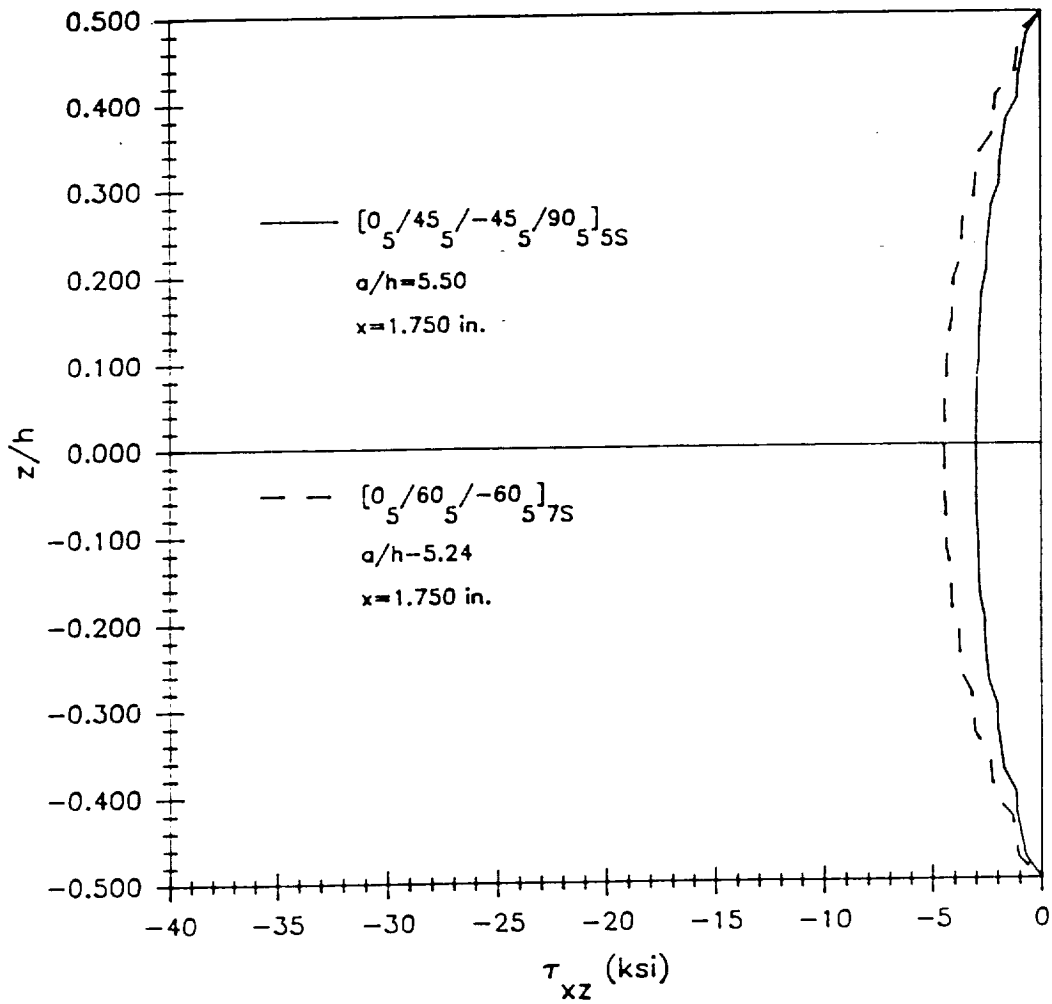
Figure 88. Through-the-thickness stress profiles for τ_{xz} and the beams having a grouped stacking sequence and an aspect ratio of a/h = 1.00.

Legend in figure:

$[0_5/45_5/-45_5/90_5]_{5S}$
a/h=5.50
x=1.750 in.

$[0_5/60_5/-60_5]_{7S}$
a/h-5.24
x=1.750 in.

Axis labels: z/h (vertical), τ_{xz} (ksi) (horizontal)

Analytical/Experimental Correlation

Chapter VII

Conclusions

7.1 Investigative Approach

7.1.1 Elasticity Solution

The investigation of damage states in laminated three-point bend specimens has been approached using a combination of experimental and theoretical research techniques. The mathematical theory of elasticity was the basis for developing the analytical solution to determine the stress distributions in a laminated beam. A stress formulation was used where the applied tractions were expressed in terms of a Fourier series and were representative of the contact stress distribution for static indentation. The static problem was considered as a first step towards understanding impact damage where a quasi-static loading was used to simulate a low velocity, large diameter impact. The expressions for the stresses and displacements were derived for the case of an arbitrary laminated beam of finite length and for

an assumed generalized plane deformation stress state. This was an extension of Whitney's [14] work for a homogeneous single-layered orthotropic beam under plane strain or plane stress conditions. The stress function approach in [14] was modified in the present study for a state of generalized plane deformation to properly account for off-axis plies in the stacking sequence. This required formulating an expression for a second stress function which resulted in two governing partial differential equations which were coupled. For the case of an orthotropic ply, a transversely-isotropic ply, or an isotropic ply the problem was reduced to plane strain conditions.

The solutions for the stresses and displacements were applied to each layer of the laminated beam and interfacial continuity of stresses and displacements were imposed. The applied tractions were prescribed on the top and bottom surfaces of the beam which corresponded to the loading and support points. The traction free end-face conditions were approximately satisfied by requiring the resultant forces and moments to vanish. Subsequently, a program was written and verified to correctly perform the necessary numerical calculations in the solution procedure. Convergence of the infinite series solution was based on the agreement between the applied traction on the top surface and the resulting σ_{xx} distribution along the same surface.

7.1.2 Preliminary Analyses

Prior to conducting the experimental phase of the research, a preliminary analytical study was performed to aid in developing a suitable test matrix. The preliminary analyses investigated the geometric, shear-coupling, and stacking sequence effects on the stress distributions in a laminated beam subjected to three-point bending Significant effects were seen in the displacements and the ply-level stress distributions depending on the fiber orientation, span length-to-depth aspect ratio, and whether or not a grouped or interspersed stacking sequence

was used. The location and magnitude of the maximum shear stress, τ_{xz}, was shown to be a strong function of the beam's stacking sequence. In general, the maximum shear stress was located below the top surface and was associated with very high gradients in the vicinity of the applied load.

The results for unidirectional laminates consisting of off-axis ply orientations showed significant shear coupling effects for a wide range of fiber orientations. The shear coupling effects were seen to increase the effective stiffness of the laminated beam, although these effects diminished as the beam's aspect ratio became small. For the generalized plane deformation stress state none of the components of stress are identically equal to zero, and it was seen that the out-of-plane shear stress, τ_{xy} in the off-axis layers was larger in magnitude than its in-plane counterpart. Consequently, the more complicated generalized plane deformation analysis, as compared to plane strain or plane stress, was required to accurately determine the local stress states when off-axis plies were used in the stacking sequence.

Stacking sequence effects on the local stress state were determined by considering grouped and interspersed quasi-isotropic stacking sequences. Continuous components of stress across the interface were seen to be independent of the aspect ratio when this ratio was greater than 1.0. When the aspect ratio was less than 1.0, the influence of the bottom support points was seen in the through-the-thickness stress profiles near the midspan. Conversely, the discontinuous components of stress strongly depended on the beam's aspect ratio. The effect of grouping plies of equal fiber orientation together was a reduction in the maximum bending stress and a reduction in the out-of-plane shear stress for the off-axis plies. However, as the aspect ratio of the beam became small, the differences between the grouped and interspersed beam's stress states decreased.

Conclusions

210

7.1.3 Experimental Study

The damage states in laminated beams subjected to a quasi-statically applied load were determined by conducting an experimental study on three-point bend specimen geometries. The test matrix covered a wide range of specimen length-to-thickness and support span-to-thickness ratios. The different stacking sequences used in the test matrix were 0° unidirectional, cross-ply, and various quasi-isotropic laminates having either a [0/±45/90] or a [0/±60] basic ply grouping and both interspersed and grouped layers were considered (see Table 1, Chapter 5). The experimental data consisted of the top and bottom surface displacements, and the damage initiation and ultimate failure loads. The dependence of the initial damage and ultimate failure load on the beam's aspect ratio were identified, and the issues of damage susceptibility and damage tolerance were addressed. Possible damage states were defined by a post-test visual inspection of the damaged specimens using an optical microscope.

7.2 Summary of Results

7.2.1 Displacements

The behavior of the load-displacement and load-indentation curves was experimentally seen to be linear up to the initiation of damage with the exception of the 0° unidirectional beams. The top surface local indentation in these curves was calculated by taking the difference between the measured top and bottom surface displacements after adjusting their values for non-beam related deformations. The analytical study for the displacements used an elliptical

traction distribution to model the contact at the load and support points, and an incremental loading procedure was used to update the contact length as a function of the applied loading. The minor axis of the ellipse was equal to the contact length which was analytically determined based on Sankar's [37] work for an orthotropic beam, and the major axis was proportional to the applied load.

Initially, the results from the unidirectional beam analysis for the midspan deflection were compared to the experimental results. For the largest aspect ratio of 7.33 reasonably good agreement was seen between the experimental data and the analytical prediction in the initial linear portion of the plot. However, a poor correlation between the elasticity solution and the experimental displacements was seen for the beam geometries having aspect ratios of 4.00, 1.33, and 0.67. The discrepancies were believed to be a result of some uncertainty in the experimentally measured quantities and the actual boundary conditions. Similar problems were encountered in correlating the experimental and theoretical displacements in the other beam configurations. The results for the indentation were based on the difference between the top and bottom surface displacements, and therefore the same correlation difficulties were encountered as discussed for the midspan deflection.

7.2.2 Damage Descriptions

Several different damage mechanisms were identified when the damaged specimens were visually inspected. The basic modes consisted of delaminations, matrix cracking, fiber breakage, and crushing. The dependence of the type of damage on the beam configuration was summarized in Tables 2-4, Chapter 5. The primary damage in the 0° unidirectional beams was a delamination at the midplane for the larger aspect ratios, and a transverse splitting mode for the smaller aspect ratios. The transverse splitting, i.e., a crack in the xz-plane of the beam, was indicative of a three-dimensional stress state existing for this particular geometry.

Consequently, the two-dimensional analysis developed in the present study was not expected to accurately predict the local stress states and no attempt was made towards correlating the experimentally observed damage with the theoretical stress distributions for the 0° unidirectional beams. However, a satisfactory correlation between theory and experiment was achieved for the delamination mode based on the magnitude of the maximum shear stress at the midplane.

The observed damage in the remaining laminates, i.e., cross-ply and quasi-isotropic, was correlated with the predicted stress distributions on the basis of the particular mode of damage. The crushing mode, which occurred in all of the beam configurations having an aspect ratio less than 1.0, was satisfactory explained quantitatively on the basis of the maximum contact pressure. The tensile mode or fiber breakage was an isolated case and was only observed in the 0.24 inch thick quasi-isotropic specimens having aspect ratios of 22.92 and 12.50. Accurate predictions for the damage initiation loads were obtained based on the maximum tensile bending stress in the bottom 0° ply exceeding the allowable tensile strength.

The group of beams which experienced a delamination largely consisted of laminates having an interspersed stacking sequence and a large aspect ratio. The interlaminar shear stress, τ_{xz}, at the interface where the delamination was located explained the delamination mode of damage. Careful consideration was given to the through-the-thickness location of damage due to the presence of compressive normal stresses which would prevent delamination. When the delaminations were located close to the top surface the maximum interlaminar shear stress coincided with large compressive normal stresses. Consequently, when correlating the experimental results with the analytical results a value for the interlaminar shear stress less than the absolute maximum value corresponded to the initial damage in the form of a delamination. Conversely, the matrix cracking mode of damage was predominantly seen in the grouped quasi-isotropic laminated beams. Similar to the delamination mode, the cracks in the higher aspect ratio beams were located near the midplane, whereas for smaller aspect ratios the cracks were concentrated closer to the top surface. Again, the through-the-

Conclusions

thickness location of the matrix cracks was an important factor because of the compressive normal stresses. The results for the maximum shear stress in the xz-plane indicated that this quantity did not explicitly explain the presence of matrix cracks in the off-axis plies. However, even though the analytical solution for the stresses accounted for the different fiber orientations, the maximum shear stress results indicated that no distinction between 90°, 45°, and 60° layers was required in the analytical/experimental correlation. This statement can be made when the components of stress in the xz-plane are solely considered. Clearly, if the components of stress in the xy-plane are considered then the there should be a definite dependence on the fiber orientation. Span length profiles for the shear stress τ_{xz} were generated to quantify the occurance of experimentally observed matrix cracks. The profiles exhibited very large gradients in the neighborhood of the midspan which correlated with the increase in crack density seen in the smaller aspect ratio beams. For a large aspect ratio beam the uniform distribution of τ_{xz} along the span in the layers closest to the midplane correlated with the experimentally observed cracking pattern.

7.2.3 Damage Susceptibility and Damage Tolerance

The susceptibility of a laminate to damage is a measure of how easily damage can be induced as a result of an applied load. Experimentally, this was determined by measuring the load at which the first sign of damage was observed. Once the initial damage is present, how well it is tolerated with regard to ultimate failure defines the beam's damage tolerance. A quantitative measure of damage tolerance is the ratio of the damage initiation load to the ultimate failure load. The linear elastic analysis used in the present study was limited to accurately predicting the stress distributions up to the initiation of damage. Consequently, the theoretical results were only used in correlating the stress distributions with the experimental results for damage susceptibility.

In comparing the damage initiation loads for the quasi-isotropic laminated beams having an interspersed stacking sequence and for a given a/h aspect ratio, the 0.24 inch thick beams were experimentally seen to be the most damage susceptible. For the most part, the quasi-isotropic beams having the [0/±45/90] basic ply grouping were more susceptible to damage than the [0/±60] beams. Also, the results indicated the grouped stacking sequence to be more damage susceptible than the interspersed stacking sequence. The analytical results for the through-the-thickness τ_{xz} shear stress distribution correlated with the experimentally determined damage susceptibility. The dependence of the load on the beam's aspect ratio showed that the a/h ratio did not uniquely define the damage initiation load nor the ultimate failure load. Consequently, the results presented for the damage tolerance compared the different beam configurations which had equal thicknesses but varying aspect ratios. For an overall beam thickness of approximately 1.0 inch, the damage tolerance of the different beam geometries was seen to increase as the aspect ratio decreased. However, for aspect ratios greater than 5.0 and less than 1.0 the beams were highly damage intolerant. In general, the cross-ply beams were the least tolerant to damage. For a/h greater than 1.0 the $[0_5/60_5/-60_5]_{7s}$ beams were the most tolerant, whereas for a/h less than 1.0 the $[0_5/45_5/-45_5/90_5]_{6s}$ beams had the largest damage tolerance. In comparing the $[0/±45/90]_{15s}$ and the $[0/±60]_{20s}$ beam results, which corresponded to a beam thickness equal to 0.6 inches, the $[0/±60]_{20s}$ stacking sequence was seen to be highly intolerant to damage. The results for the 0.24 inch thick beams indicated that both of the $[0/±45/90]_{6s}$ and the $[0/±60]_{8s}$ stacking sequences were highly damage intolerant.

The present experimental/analytical correlation study examined the beam displacements, damage modes, and damage susceptibility for a three-point bend specimen geometry. The results of this investigation clearly indicated that damage susceptibility and damage tolerance need to be differentiated, and that both of these quantities strongly depend on the type of laminate, aspect ratio, thickness, and stacking sequence for the specimen geometry considered. The results also showed that different damage modes can be produced depending on

the beam configuration, i.e., laminate type, aspect ratio, thickness and stacking sequence. In addition, the results of the correlation study indicated that the multilayer elasticity model can be used to rank damage susceptibility of different laminates and develop predictive capability for damage susceptibility. The correlation of the experimentally determined damage tolerance with the theoretical stress distributions was not performed because of the limitations in the analytical procedure. The linear elastic analysis developed in the present study can accurately predict the ply-level stresses up to the load at which damage is initiated. The problem of damage accumulation and the redistribution of stresses up to the ultimate failure load needs investigating to analytically predict damage tolerance. Also, to study the effects of different load paths on the initial damage states, the problem of different loading conditions, e.g., end loading, after damage has been initiated needs to be addressed.

Bibliography

1. Yang, S. H., and Sun, C. T., "Indentation Law for Composite Laminates", Composite Materials: Testing and Design (Sixth Conference), ASTM STP 787, I. M. Daniel, Ed., American Society of Testing and Materials, 1982, pp. 425-449.

2. Hertz, H., "Uber die Beruhrung fester Elastischer Korper", Journal Reine Angle Math, Crelle, Vol. 92, 1881, p. 155.

3. Tan, T. M., and Sun, C. T., "Use of Statical Indentation Laws in the Impact Analysis of Laminated Composite Plates", Trans. of the ASME, J. Appl. Mech., Vol. 52, March, 1985, pp. 6-12.

4. Schonberg, W. P., Keer, L. M., and Woo, T. K., "Low Velocity Impact of Transversely Isotropic Beams and Plates", Int. J. of Solids Structures, Vol. 23, No. 7, 1987, pp. 871-896.

5. Poe, C. C. Jr. and Illg, W., "Strength of a Thick Graphite/Epoxy Rocket Motor Case After Impact by a Blunt Object", NASA TM 89099, Feb., 1987.

6. Sokolnikoff, I. S., Mathematical Theory of Elasticity, 2nd. Ed., McGraw-Hill, New York, 1956.

7. Benjumea, R., and Sikarskie, D. L., "On the Solution of Plane Orthotropic Elasticity Problems by an Integral Method", J. App. Mech., Sept., 1972, pp. 801-808.

8. Rizzo, F. J., and Shippy, D. J., "A Method for Stress Determination in Plane Anisotropic Elastic Bodies", J. Comp. Matl., Vol. 4, 1970, pp. 36-61.

9. Green, A. E., and Zerna, W., Theoretical Elasticity, Second Ed., Clarendon Press, Oxford, England, 1968.

10. Love, A. E. H., A Treatise on the Mathematical Theory of Elasticity, Fourth Ed., Dover Publications, New York, N.Y., 1944.

11. Tarnopolskii, Iu. M., Zhigun, I. G., and Polyakov, V. A., "Distribution of Shearing Stresses Under Three-Point Flexure in Beams Made of Composite Materials", Polymer Mechanics, Vol. 13, No. 1, 1977, pp. 52-58.

12. Conway, H. D., "Some Problems of Orthotropic Plane Stress", J. Appl. Mech., Vol. 20, No. 1, 1953, pp. 72-76.

13. Kasano, H., Ogino, K., Matsumoto, H., and Nakahara, I., "Theoretical Analysis of an Orthotropic Rectangular Plate Under In-Plane Loading", Trans. Japan Society for Composite Materials, Vol. 6, 1980, pp. 33-42.

14. Whitney, J. M., "Elasticity Analysis of Orthotropic Beams Under Concentrated Loads", Composites Science and Technology, Vol. 22, 1985, pp. 167-184.

15. Sullivan, J. L., and Van Oene, H., "An Elasticity Analysis for the Generally and Specially Orthotropic Beams Subjected to Concentrated Loads", Comp. Sci. and Tech., Vol. 27, No. 2, 1986, pp. 133-155.

16. Kasano, H., Matsumoto, H., Nakahara, I., and Kiga, T., "Two- Dimensional Stress Analysis of an Orthotropic Beam Under Concentrated Loads", Trans. Japan Society for Composite Materials, Vol. 6, 1980, pp. 1-8.

17. Yu, J. G.,"Local Effects of a Concentrated Load Applied to Orthotropic Beams", J. Franklin Institute, Vol. 296, No. 3, 1973, pp. 191-206.

18. Rao, K. M., "Some Observations in the Behavior of Laminated Composite Beams", ASME, Trans., Journal of Applied Mechanics, Vol. 48, June, 1981, pp. 431-436.

19. Filon, L. N. G., Phil. Trans. Roy. Soc. (Ser. A), Vol. 198, 1902.

20. Chatterjee, S. N., Pindera, M. J., Pipes, R. B., and Dick, B., "Composite Defect Significance", MSC TFR 1312/1108, NADC 81034-60, Nov., 1982.

21. Pagano, N. J., "Exact Solutions for Composite Laminates in Cylindrical Bending", J. Composite Materials, Vol. 3, 1969, pp. 398-411.

22. Pagano, N. J, and Wang, A. S. D., "Further Study of Composite Laminates Under Cylindrical Bending", J. Composite Materials, Vol. 5, 1971, pp. 521-528.

23. Pagano, N. J., "Influence of Shear Coupling in Cylindrical Bending of Anisotropic Laminates", J. Comp. Matl., Vol. 4, 1970, pp. 330-343.

24. Lekhnitskii, S. G., Theory of Elasticity of an Anisotropic Elastic Body, Holden-Day, 1963.

25. Berg, C. A., Tirosh, J., and Israeli, M., "Analysis of Short Beam Bending of Fiber Reinforced Composites", Composite Materials: Testing and Design (2nd Conf.), ASTM STP 497, American Society for Testing Materials, 1972, pp. 206-218.

26. Sandorff, P. E., "Saint-Venant Effects in an Orthotropic Beam", J. Composite Materials, Vol. 14, 1980, pp. 199-212.

27. Mitchell, J. H., Proc. London Math. Soc., Vol. 32, p. 35 (n.d.).

28. Timoshenko, S. P., and Goodier, J. N., Theory of Elasticity, 3rd. ed., McGraw-Hill, 1970.

29. Whitney, J. M., Browning, C. E., and Mair, A., "Analysis of the Flexure Test for Laminated Composite Materials", Composite Materials: Testing and Design: Proc. of the Third Conference, American Society for Testing and Materials, ASTM STP 546, 1974, pp. 30-45.

30. Whitney, J. M., and Pagano, N. J., "Shear Deformations in Heterogeneous Anisotropic Plates", J. App. Mech., Vol. 37, Dec., 1970, pp. 1031-1036.

31. Pagano, N. J., "Analysis of the Flexure Test of Bidirectional Composites", J. Comp. Matl., Vol. 1, 1967, pp. 336-342.

32. Adams, D. F., and Miller, A. K., "The Influence of Transverse Shear on the Static Flexure and Charpy Impact Response of Hybrid Composite Materials", J. Matl. Sci., Vol. 11, 1976, pp. 1697-1710.

33. Sveklo, V. A., "Boussinesq Type Problems for the Anisotropic Half-Space", J. App. Math. Mech., Vol. 28, 1964, pp. 908-913.

34. Willis, J. R., "Hertzian Contact of Anisotropic Bodies", J. Mech. Phys. Solids, Vol. 14, 1966, pp. 163-176.

35. Chen, W. T., "Stresses in Some Anisotropic Materials Due to Indentation and Sliding", Int. J. Solids Struc., Vol. 5, 1969, pp. 191-214.

36. Miller, G. R., "A Green's Function Solution for Plane Anisotropic Contact Problems", J. App. Mech., Trans. ASME, Vol. 53, June, 1986, pp. 386-389.

37. Sankar, B. V., "Contact Stresses in an Orthotropic Beam", Proc. of the American Society for Composites", Sept., 1987, pp. 489-499.

38. Sankar, B. V., "Smooth Indentation of Orthotropic Beams", Composite Science and Technology (submitted), Aug., 1988.

39. Parry, T. V. and Wronski, A. S., "Kinking and Tensile, Compressive and Interlaminar Shear Failure in Carbon-Fibre-Reinforced Plastic Beams Tested in Flexure", J. of Materials Science, Vol. 16, Feb., 1981, pp. 439-450.

40. Shih, G. C. and Ebert, L. J., "Flexural Failure Mechanisms and Global Stress Plane for Unidirectional Composites Subjected to Four- Point Bending Tests", Composites, Vol. 17, No. 4, Oct., 1986, pp. 309- 320.

41. Mallick, P. K., and Broutman, L. J., "Impact Properties of Laminated Angle Ply Composites", Eng. Frac. Mech., Vol. 8, No. 4, 1976, pp. 631-641.

42. Greszczuk, L. B., and Chao, H., "Impact Damage In Graphite-Fiber-Reinforced Composites", Composite Materials: Testing and Design (Fourth Conference), ASTM STP 617, American Society for Testing and Materials, 1977, pp. 389-408.

43. Browning, C. E., Abrams, F. L., and Whitney, J. M., "A Four-Point Shear Test for Graphite/Epoxy Composites", Composite Materials: Quality Assurance and Processing, ASTM STP 797, C. E. Browning, Ed., American Society for Testing and Materials, 1983, pp. 54-74.

Appendix A

Experimental Load-Displacement Data
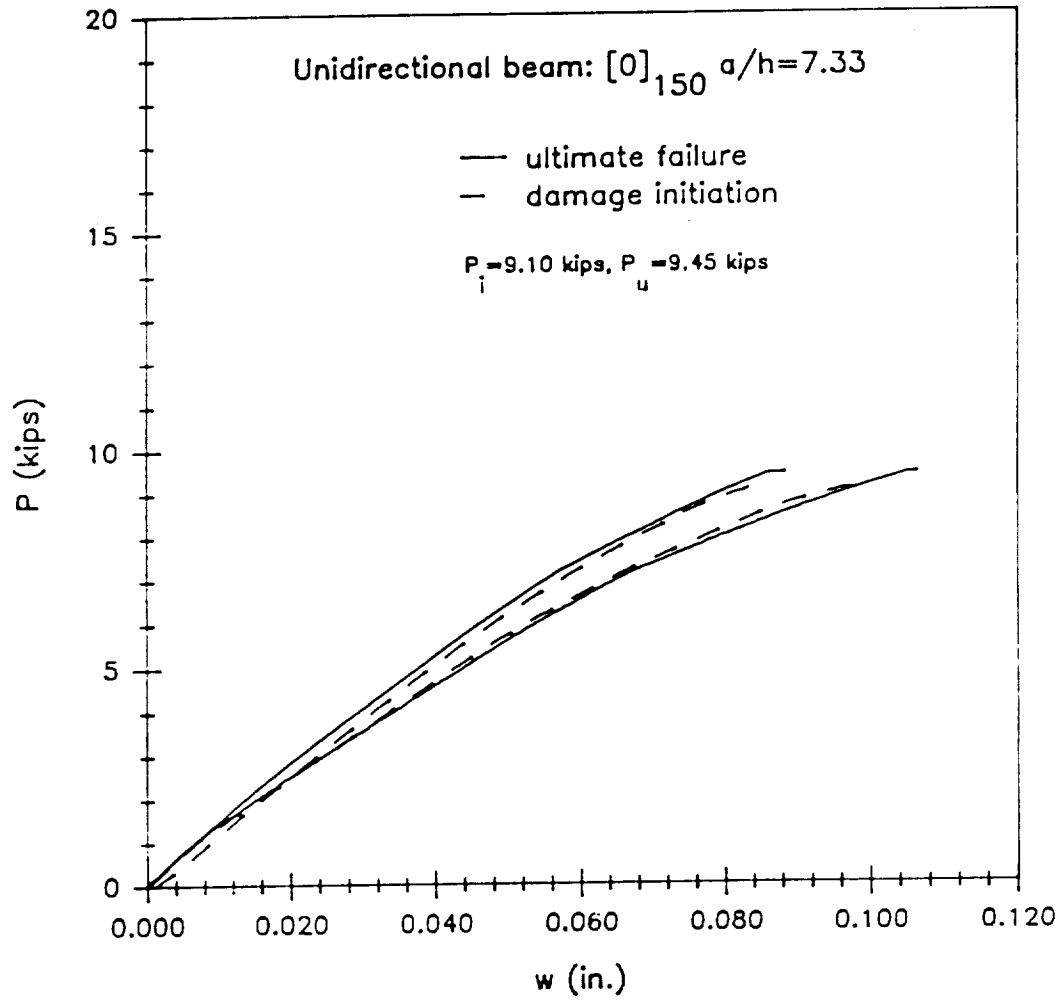
Figure 89. Load versus displacement for the $[0]_{150}$ laminate with an aspect ratio of 7.33.

Experimental Load-Displacement Data

221
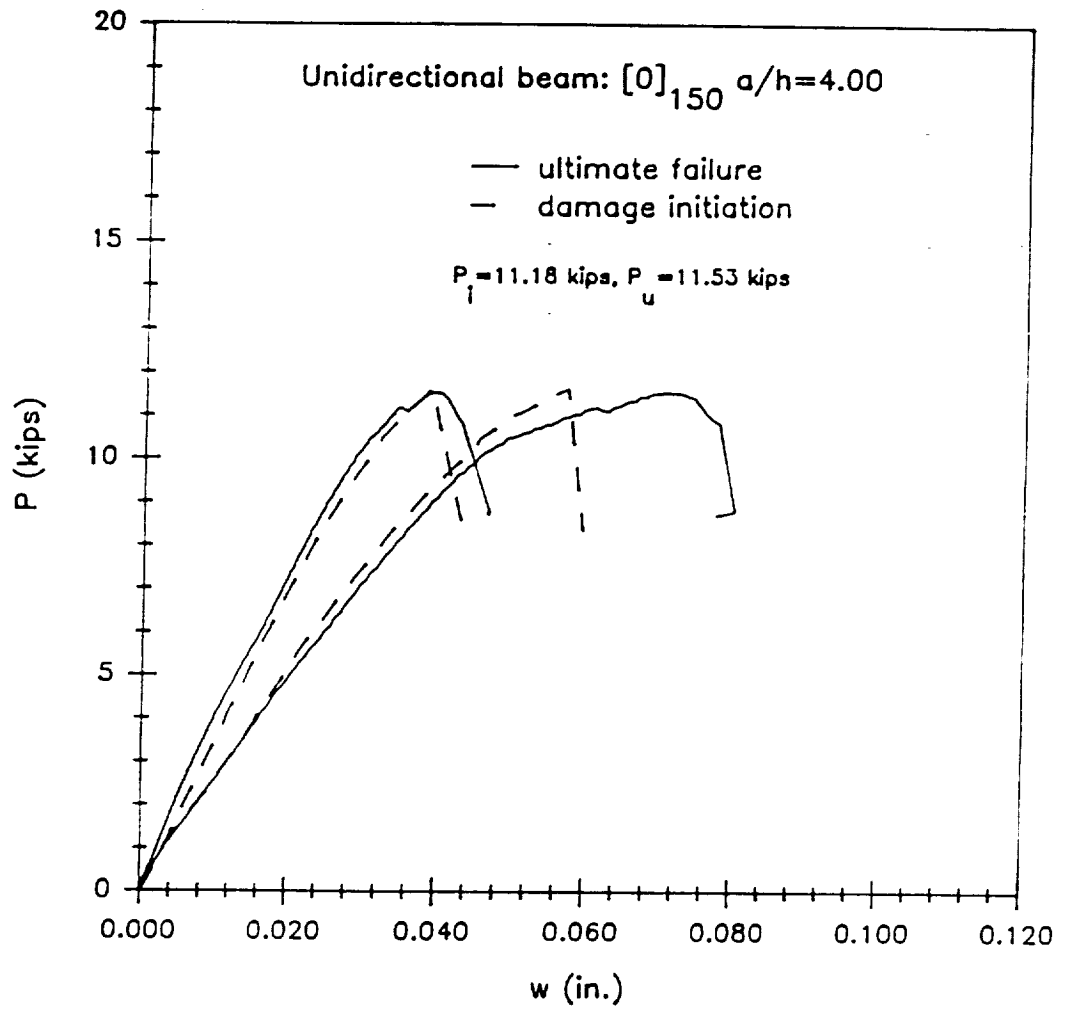
Figure 90.   Load versus displacement for the $[0]_{150}$ laminate with an aspect ratio of 4.00.

Unidirectional beam: $[0]_{150}$ a/h=1.33

— ultimate failure
— damage initiation

P (kips)

P_i=14.44 kips, P_u=14.55 kips

w (in.)
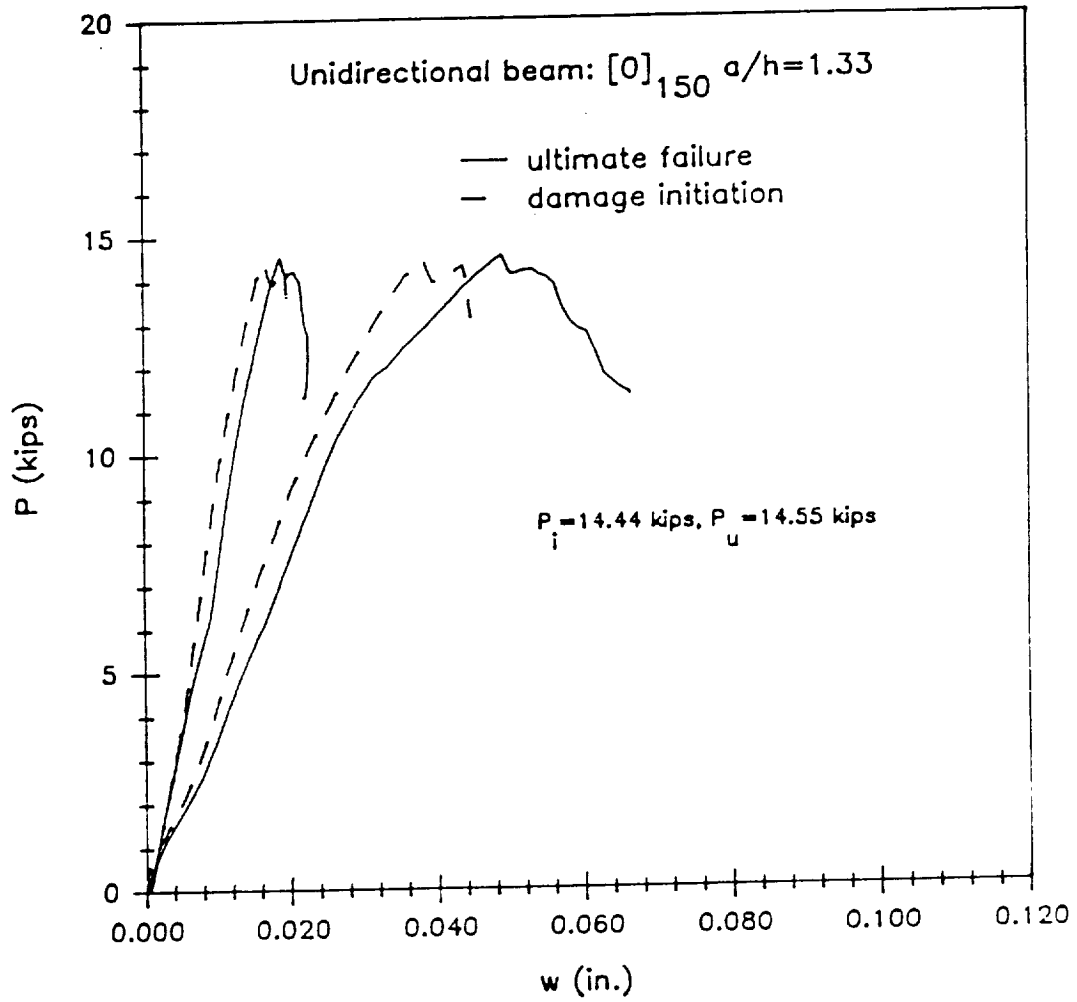
Figure 91. Load versus displacement for the $[0]_{150}$ laminate with an aspect ratio of 1.33.
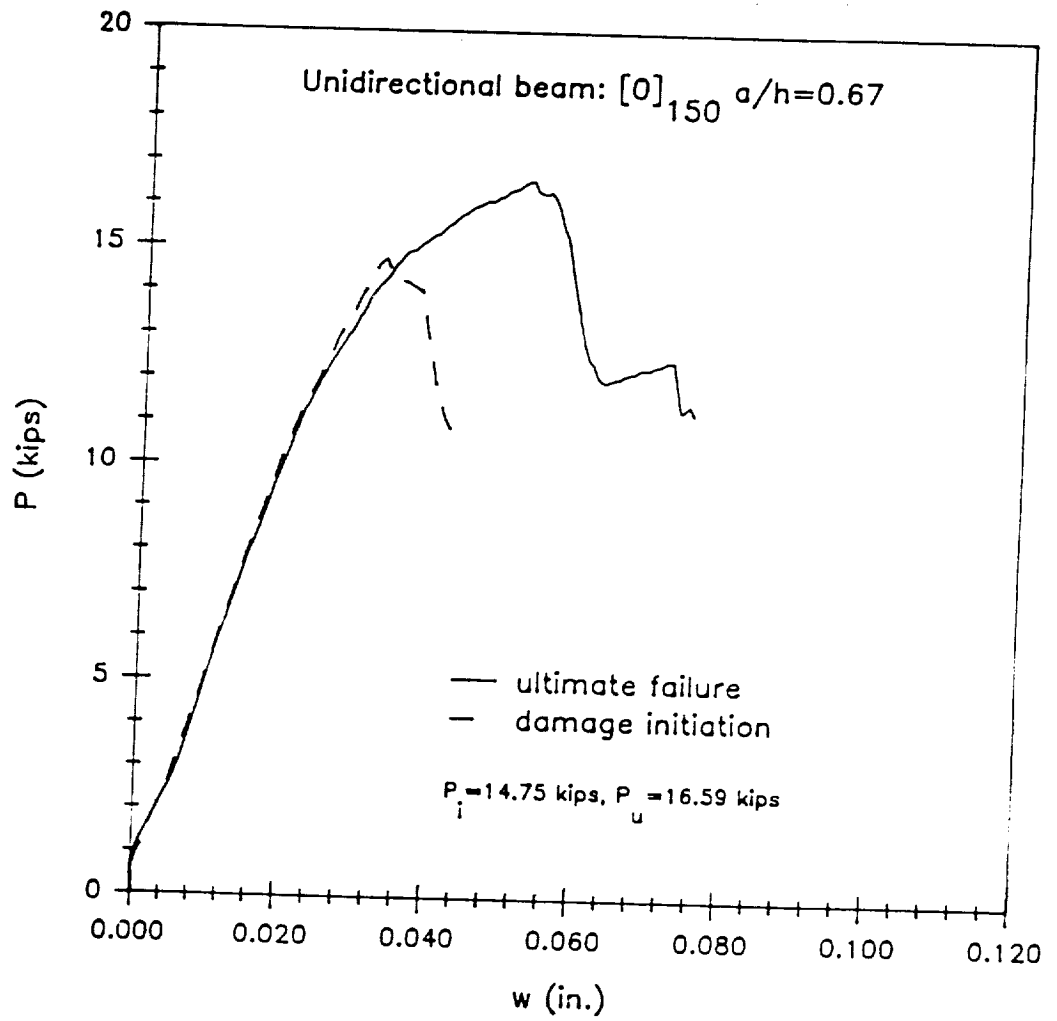
Figure 92. Load versus displacement for the [0]₁₅₀ laminate with an aspect ratio of 0.67.
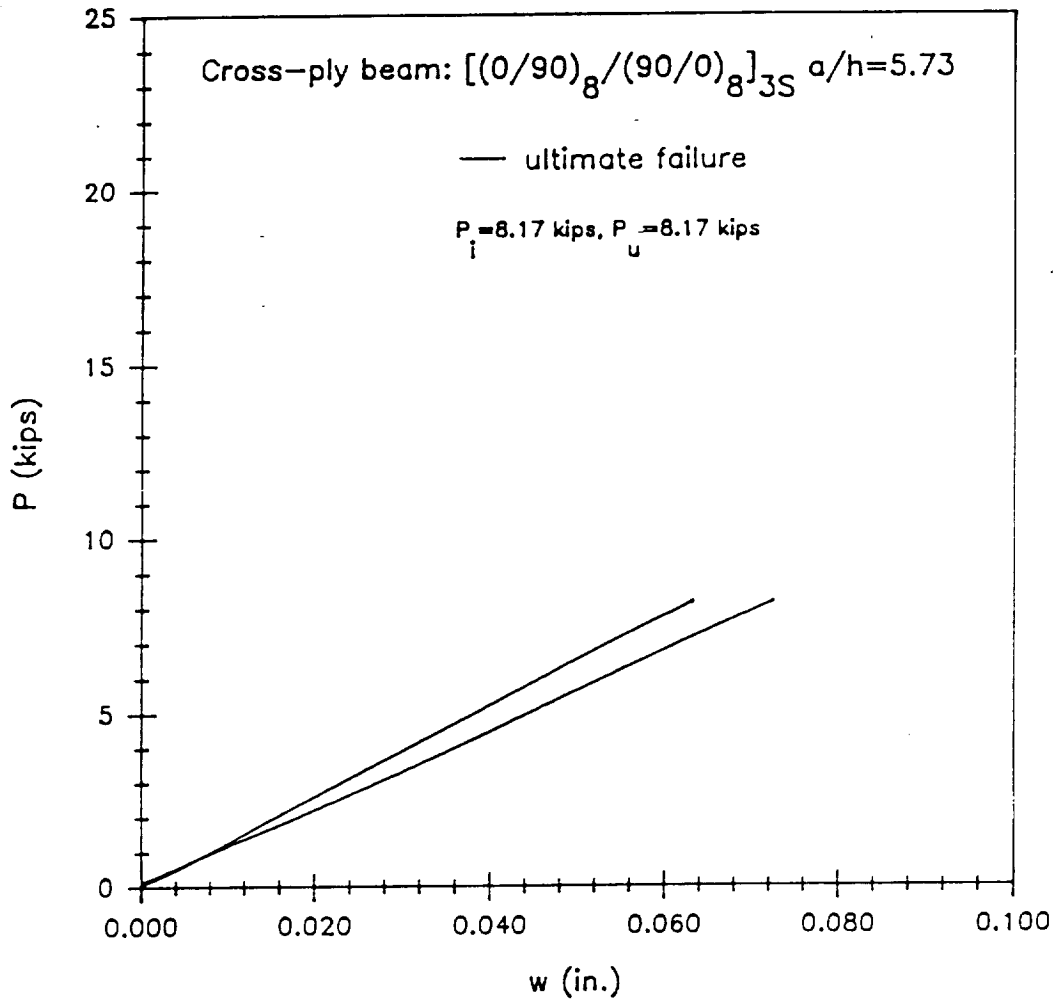
Figure 93. Load versus displacement for the $[(0/90)_8/(90/0)_8]_{3S}$ laminate with an aspect ratio of 5.73.
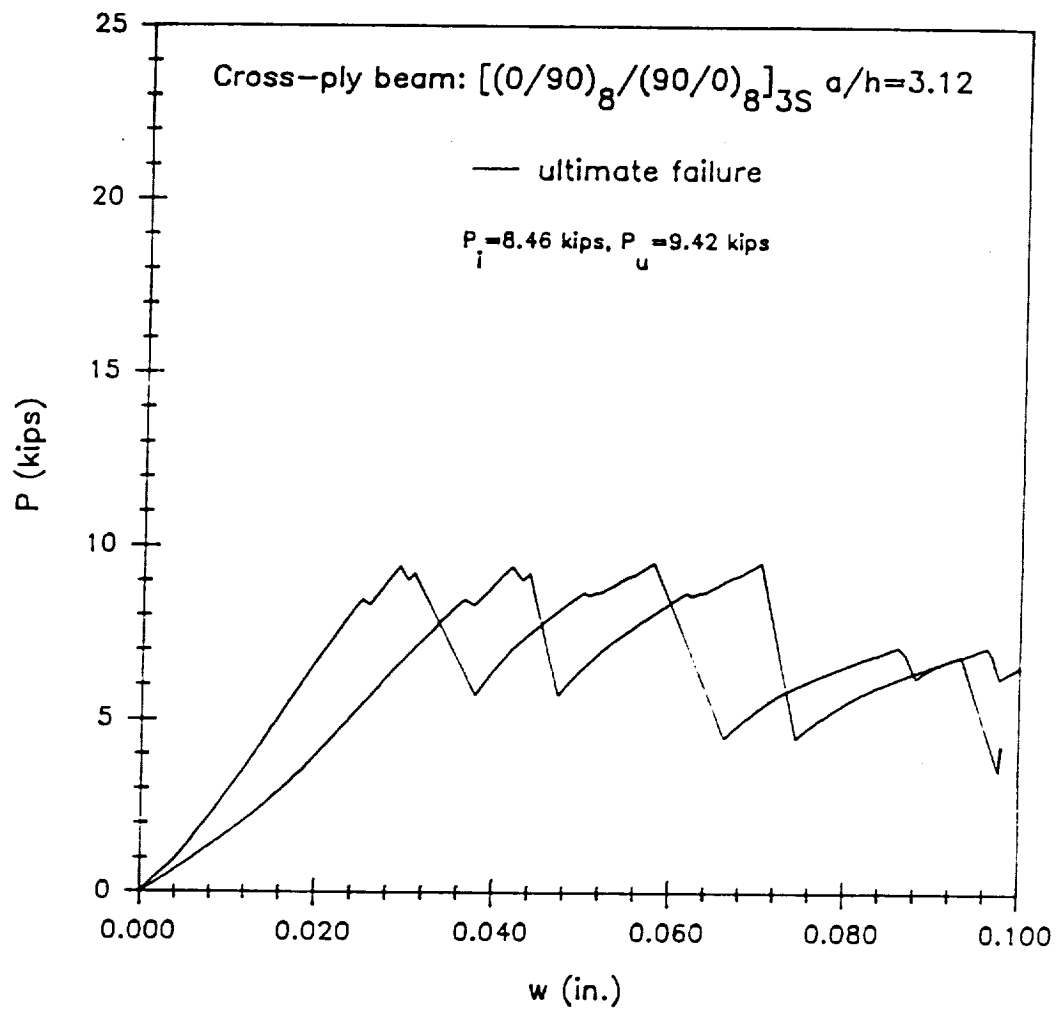
Figure 94. Load versus displacement for the [(0/90)₈/(90/0)₈]₃ₛ laminate with an aspect ratio of 3.12.
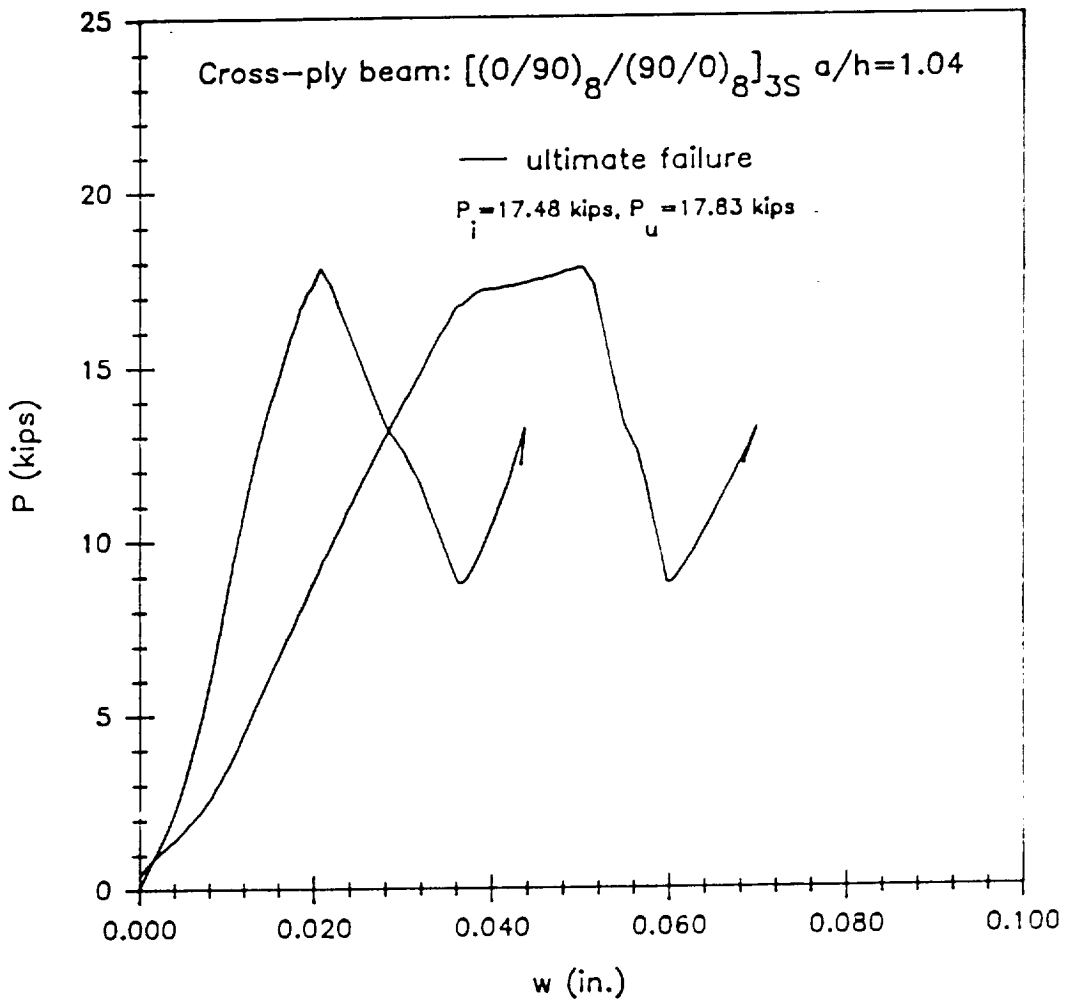
Figure 95. Load versus displacement for the $[(0/90)_8/(90/0)_8]_{3S}$ laminate with an aspect ratio of 1.04.

The plot contains the following annotations:

Cross-ply beam: $[(0/90)_8/(90/0)_8]_{3S}$ a/h=1.04

— ultimate failure

P_i=17.48 kips, P_u=17.83 kips
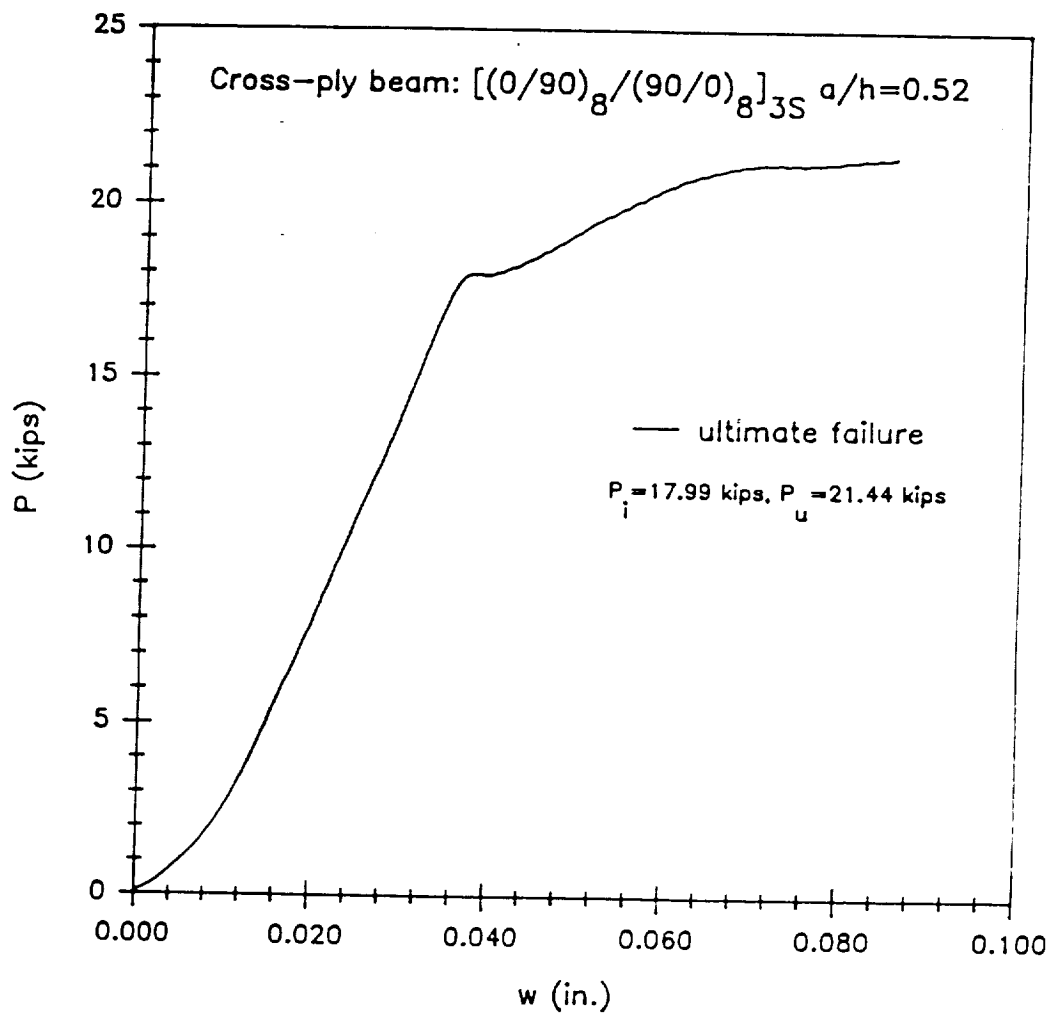
Figure 96. Load versus displacement for the $[(0/90)_8/(90/0)_8]_{3S}$ laminate with an aspect ratio of 0.52.
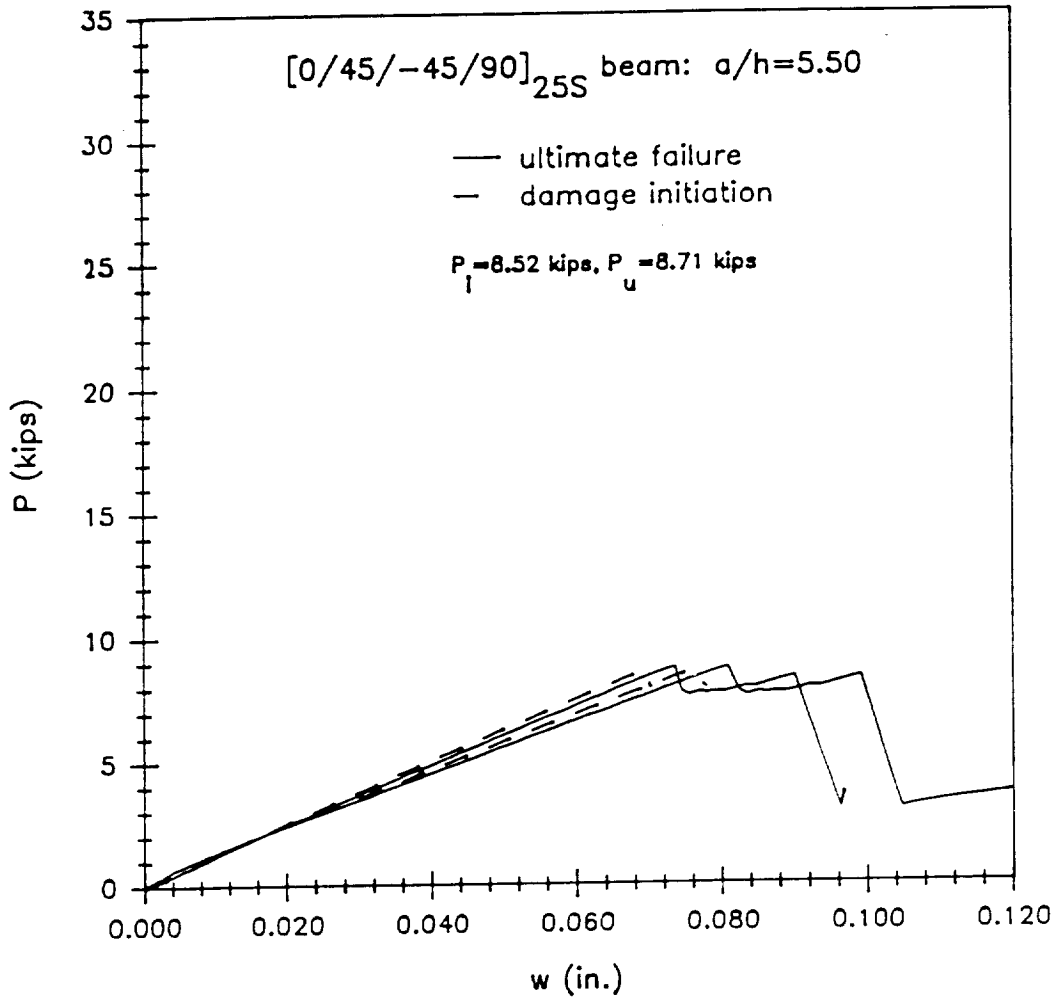
Figure 97.   Load versus displacement for the [0/45/-45/90]$_{25S}$ laminate with an aspect ratio of 5.50.
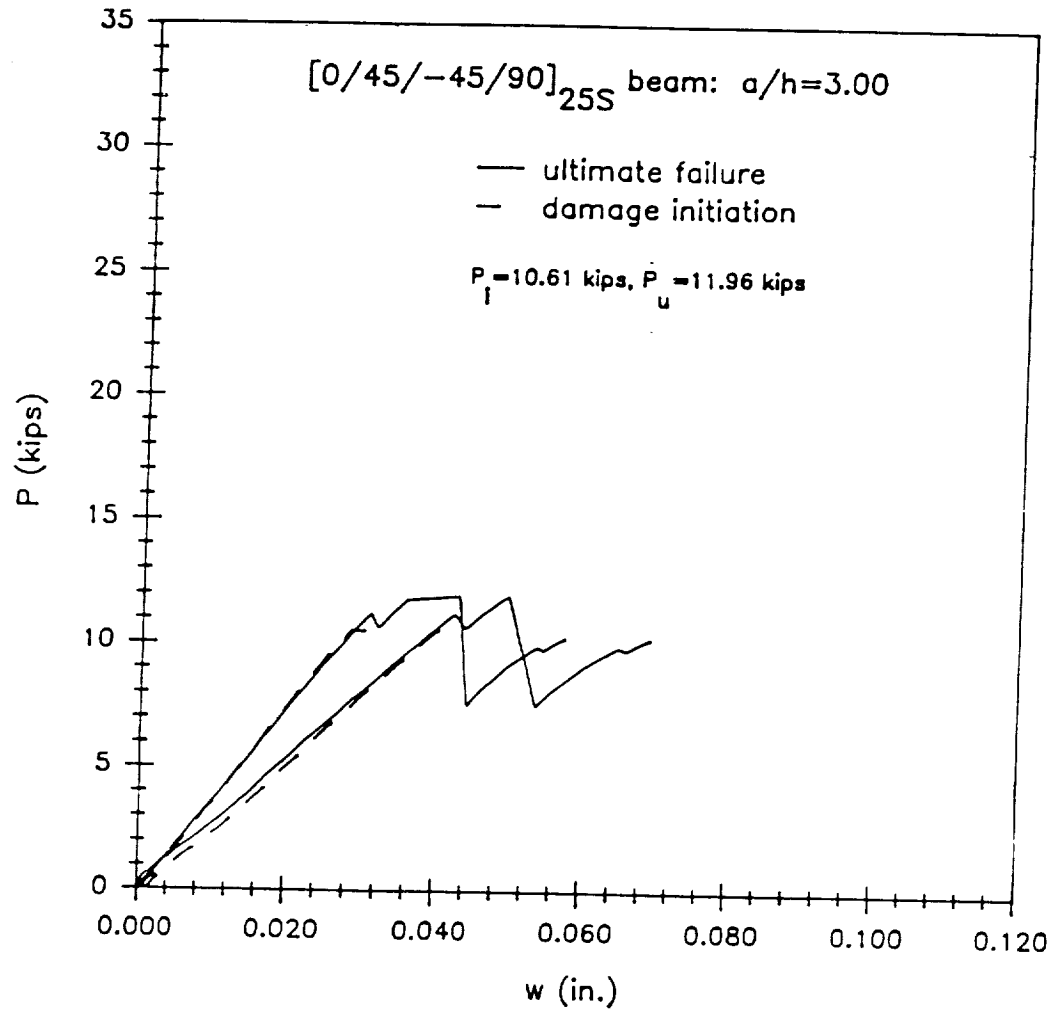
Figure 98. Load versus displacement for the [0/45/-45/90]$_{25S}$ laminate with an aspect ratio of 3.00.
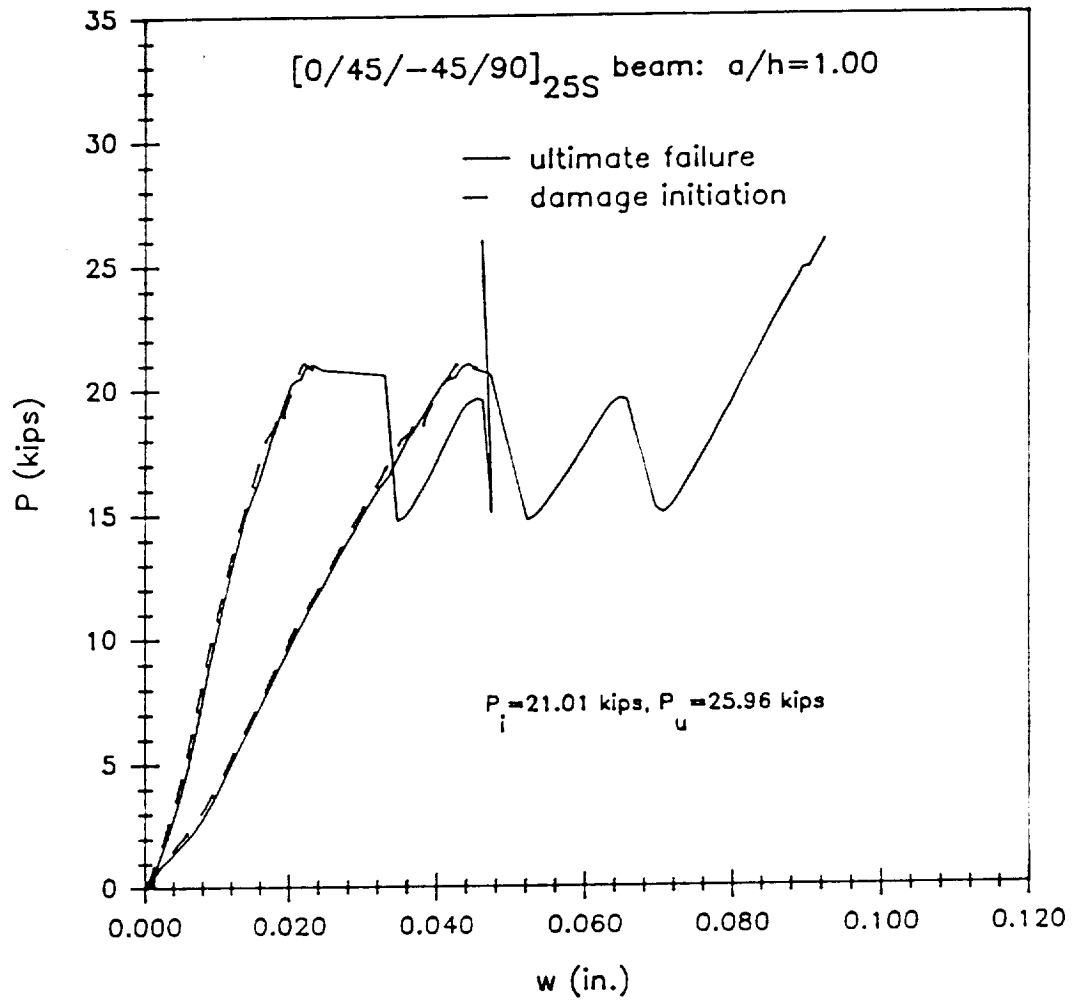
Figure 99. Load versus displacement for the [0/45/-45/90]$_{25S}$ laminate with an aspect ratio of 1.00.
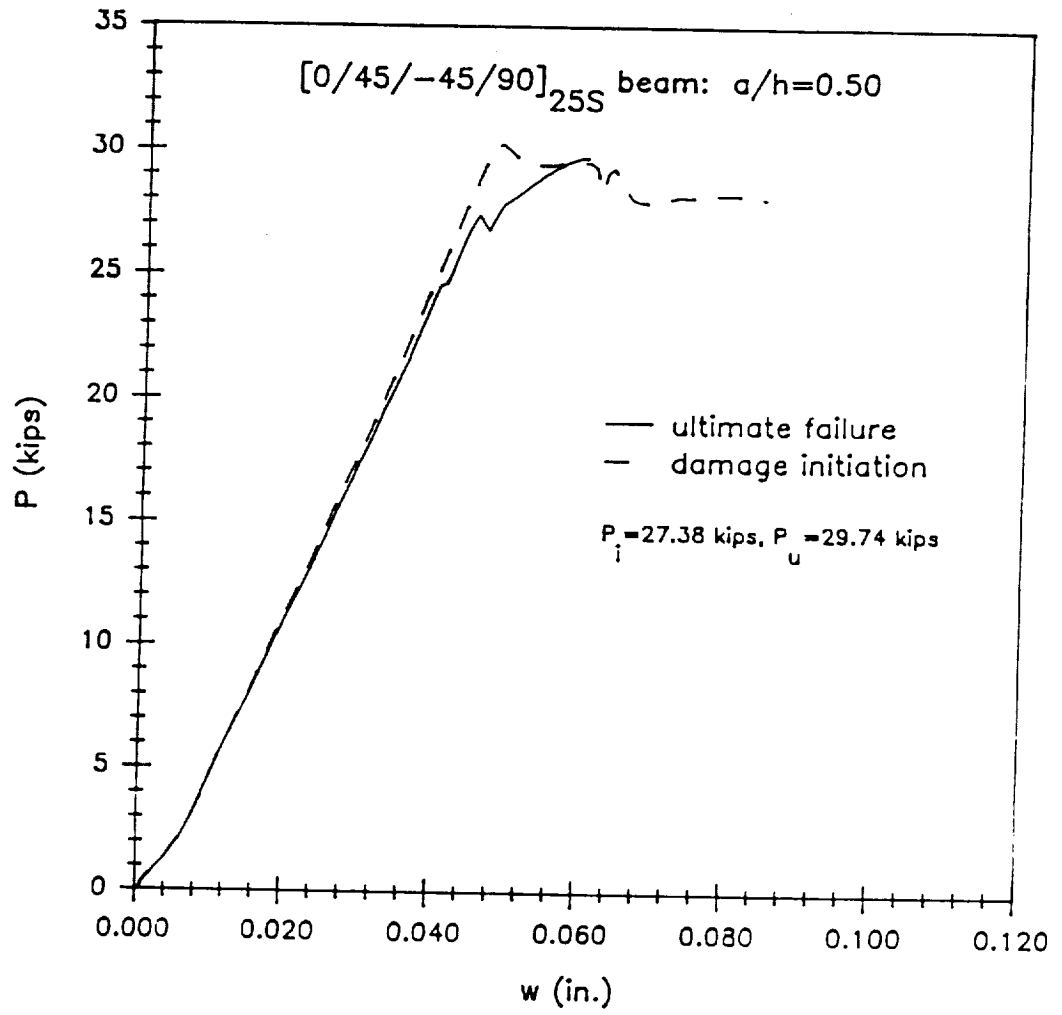
Figure 100. Load versus displacement for the [0/45/-45/90]$_{25S}$ laminate with an aspect ratio of 0.50.
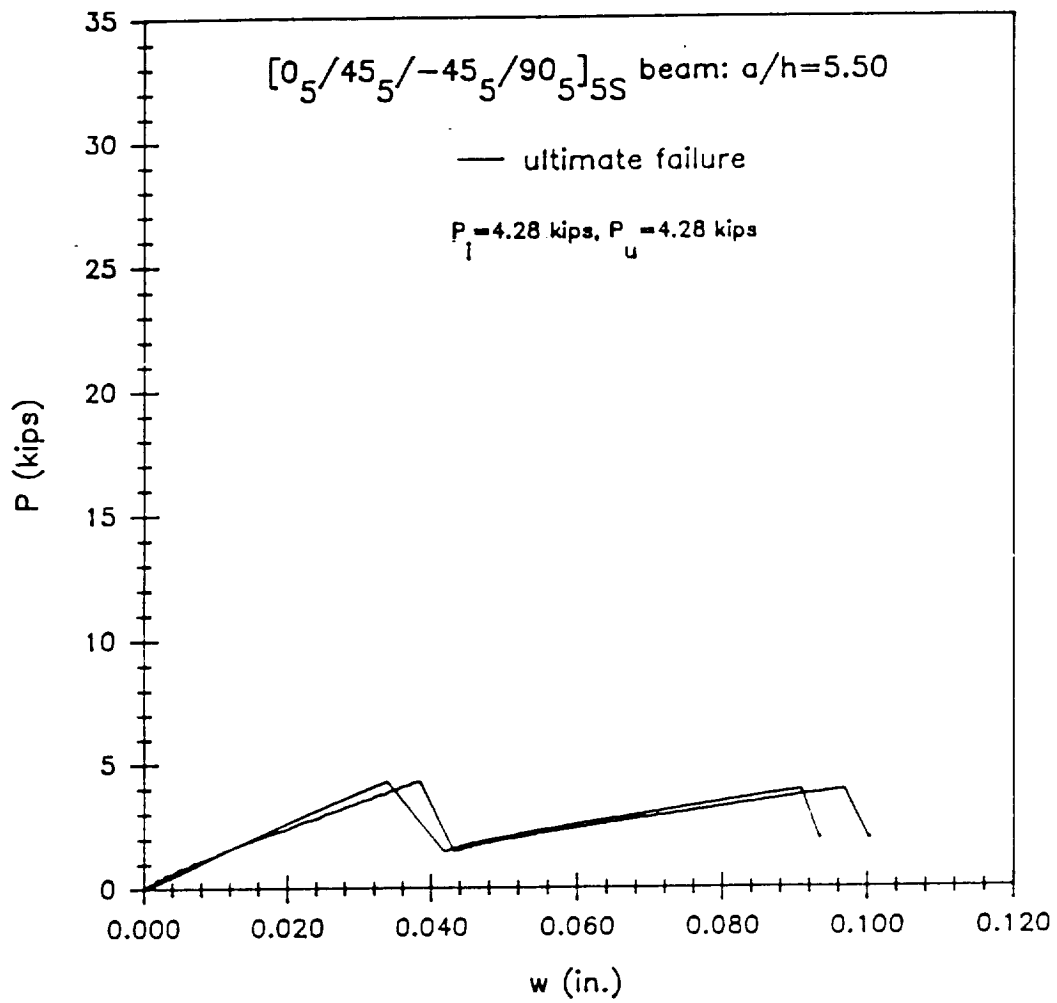
Figure 101. Load versus displacement for the [0/45/-45/90] grouped laminate with an aspect ratio of 5.50.
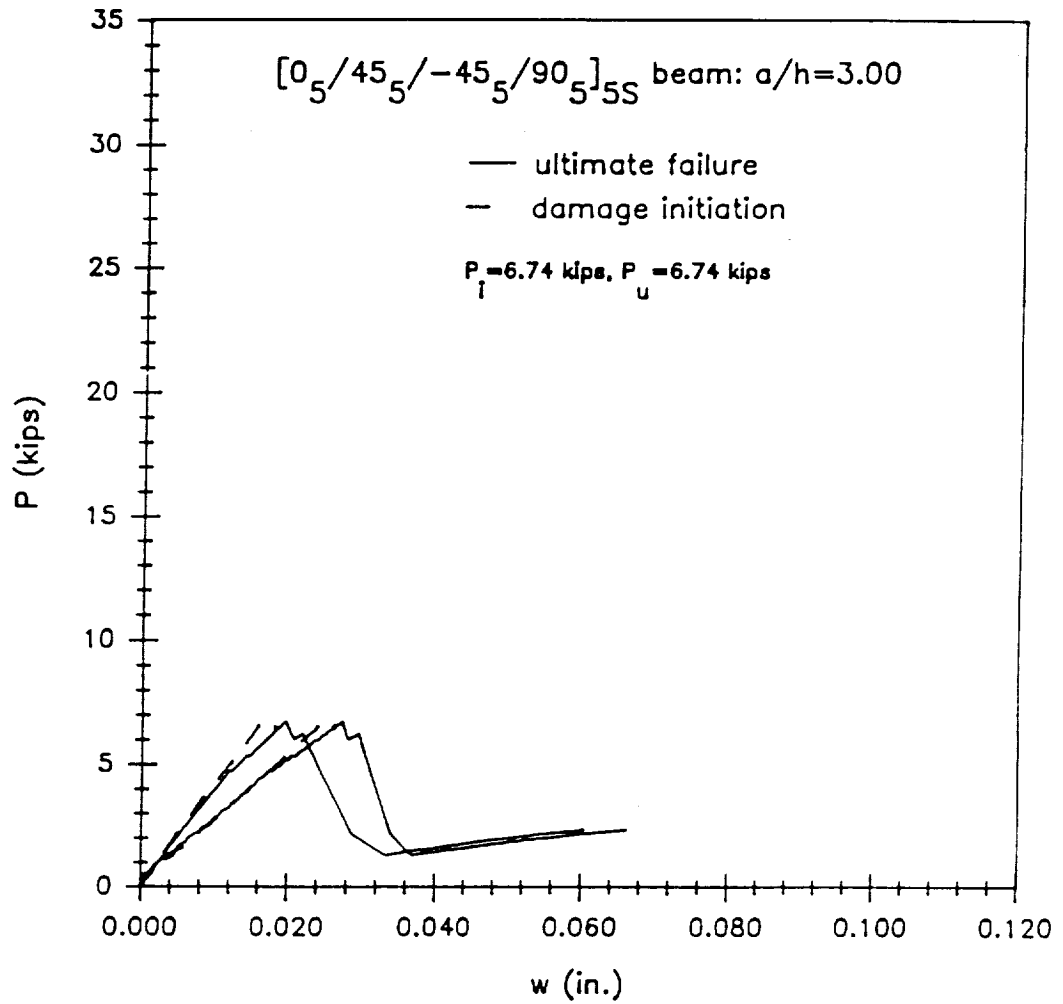
Figure 102. Load versus displacement for the [0/45/-45/90] grouped laminate with an aspect ratio of 3.00.
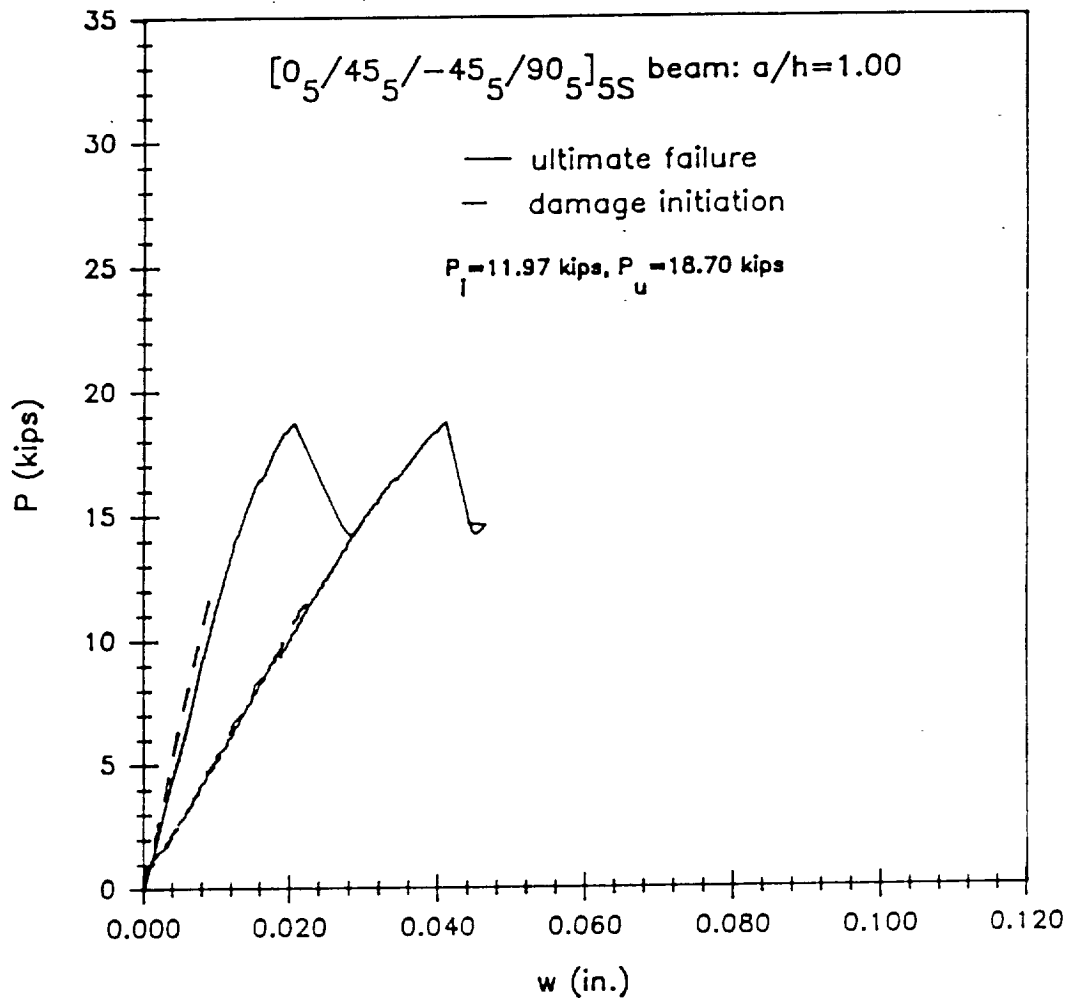
Figure 103. Load versus displacement for the [0/45/-45/90] grouped laminate with an aspect ratio of 1.00.
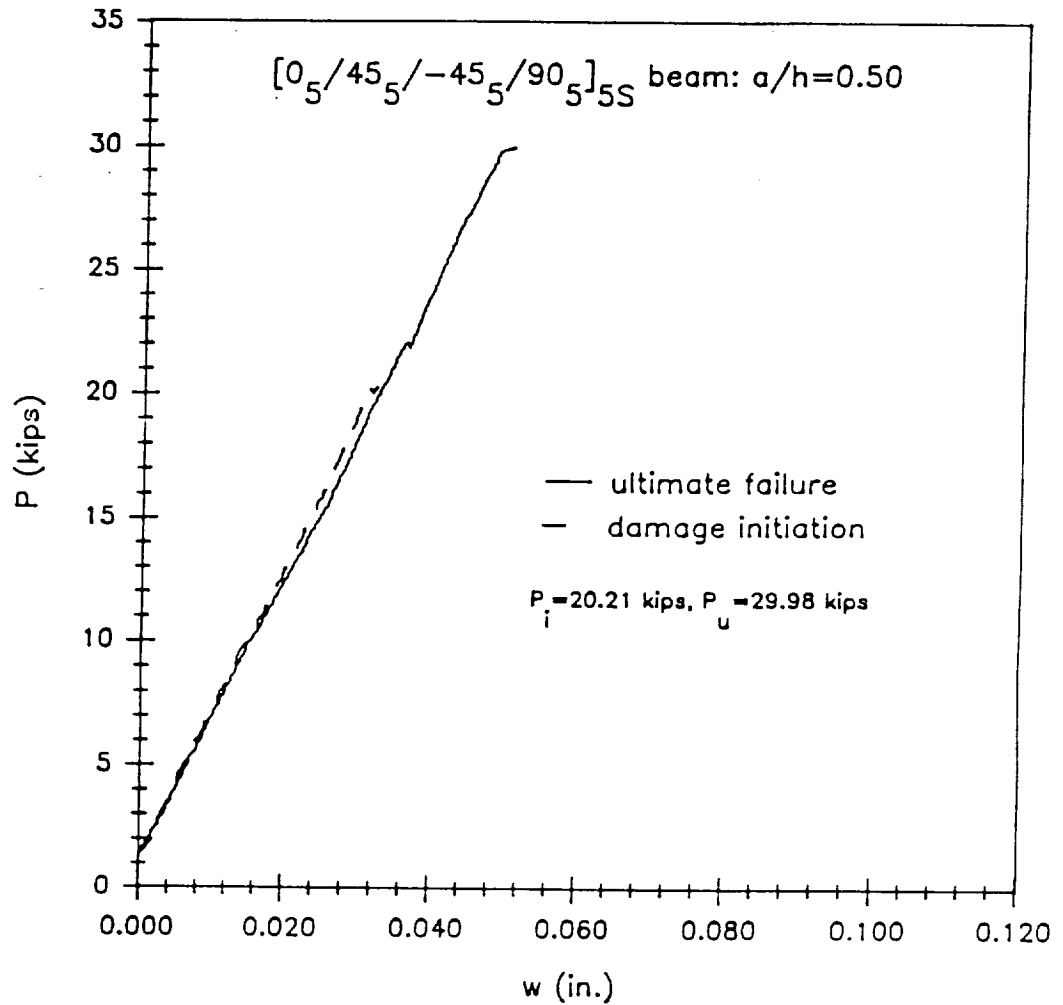
Figure 104. Load versus displacement for the [0/45/-45/90] grouped laminate with an aspect ratio of 0.50.
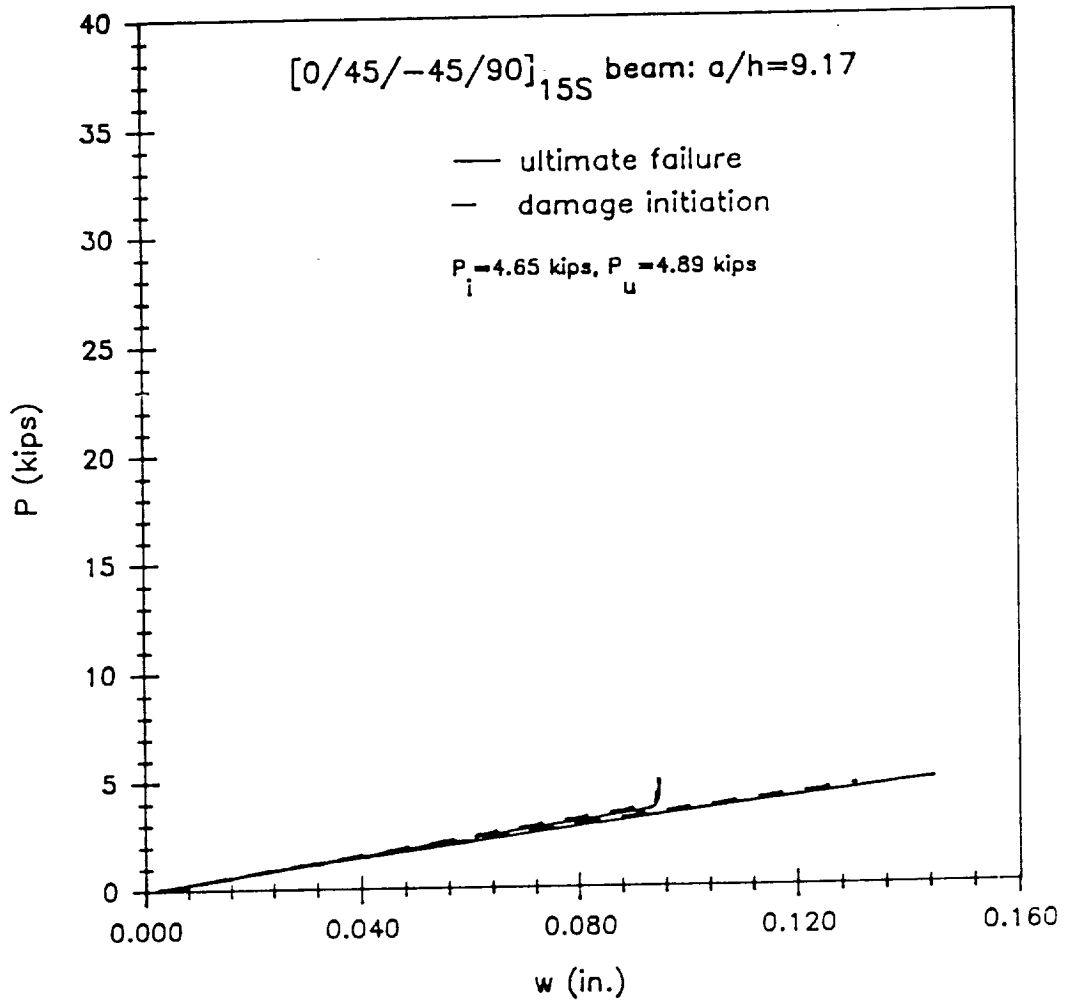
Figure 105. Load versus displacement for the [0/45/-45/90]₁₅ₛ laminate with an aspect ratio of 9.17.

$[0/45/-45/90]_{15S}$ beam: a/h=5.00

—— ultimate failure

— damage initiation

P_l=6.10 kips, P_u=7.17 kips

P (kips)

40

35

30

25

20

15

10

5

0

0.000   0.040   0.080   0.120   0.160

w (in.)
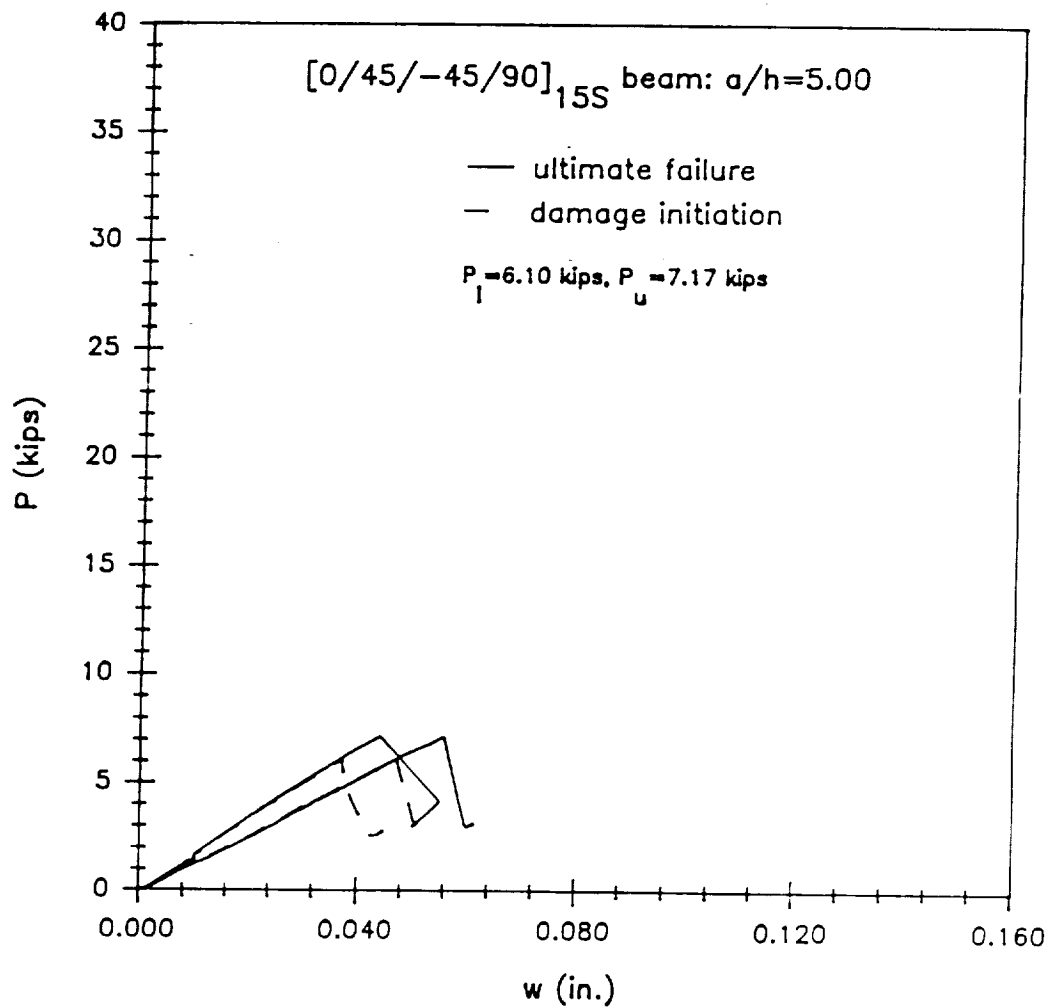
Figure 106. Load versus displacement for the $[0/45/-45/90]_{15S}$ laminate with an aspect ratio of 5.00.
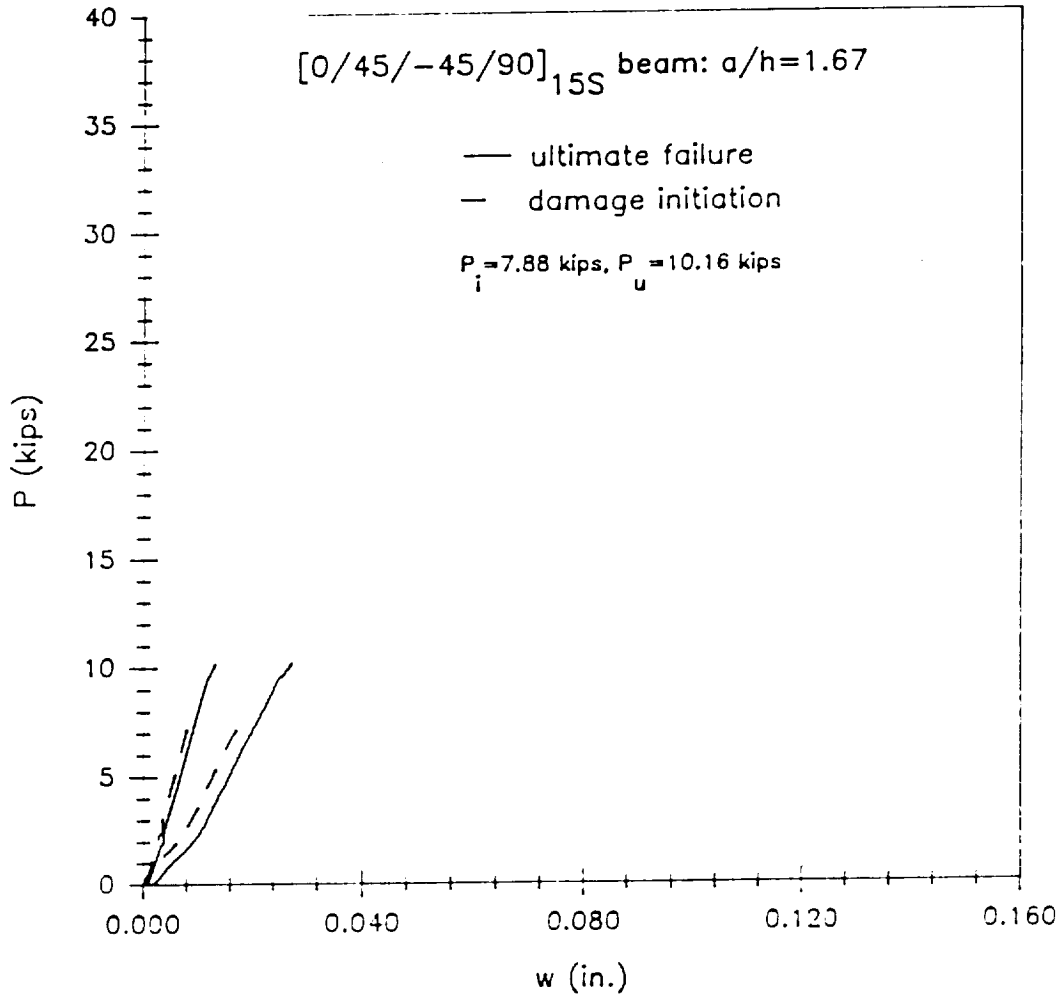
Figure 107. Load versus displacement for the [0/45/-45/90]$_{15S}$ laminate with an aspect ratio of 1.67.
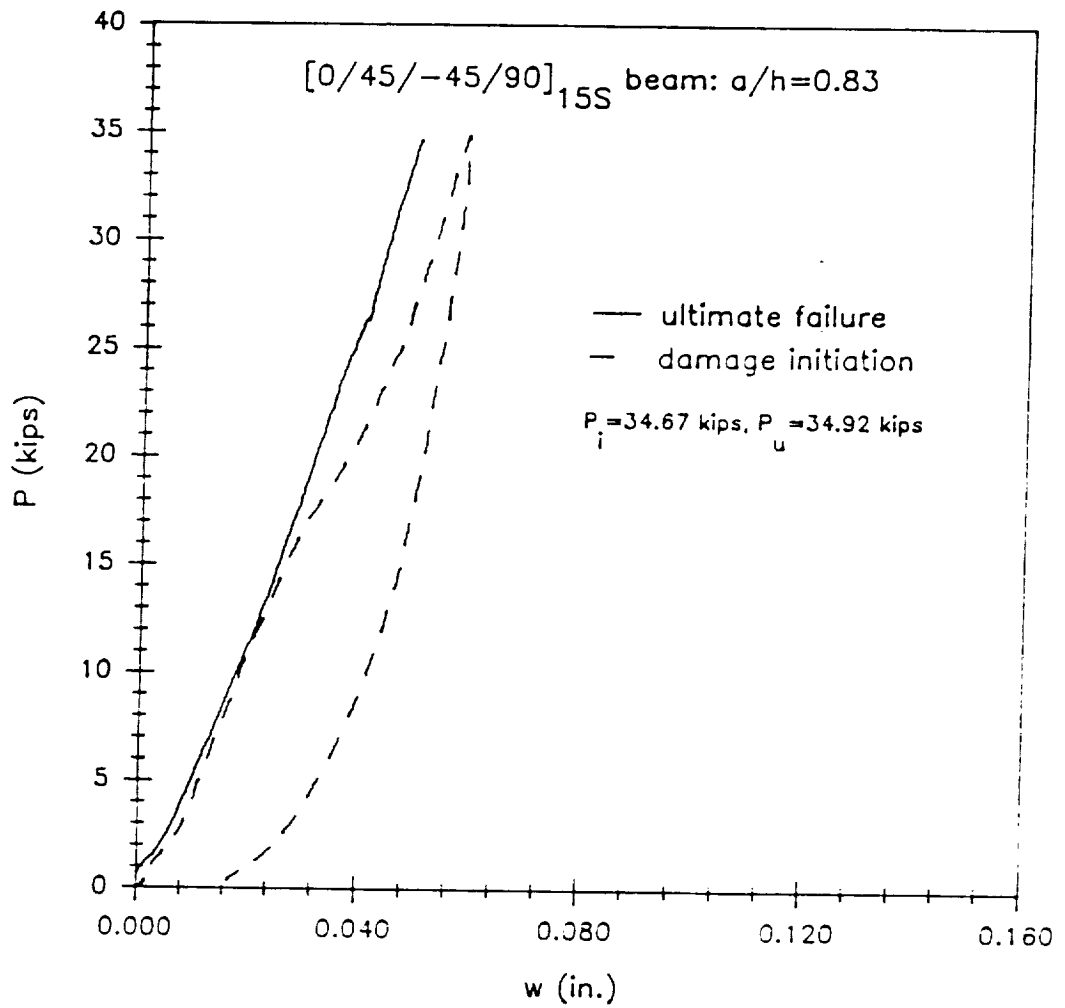
Figure 108. Load versus displacement for the $[0/45/-45/90]_{15S}$ laminate with an aspect ratio of 0.83.
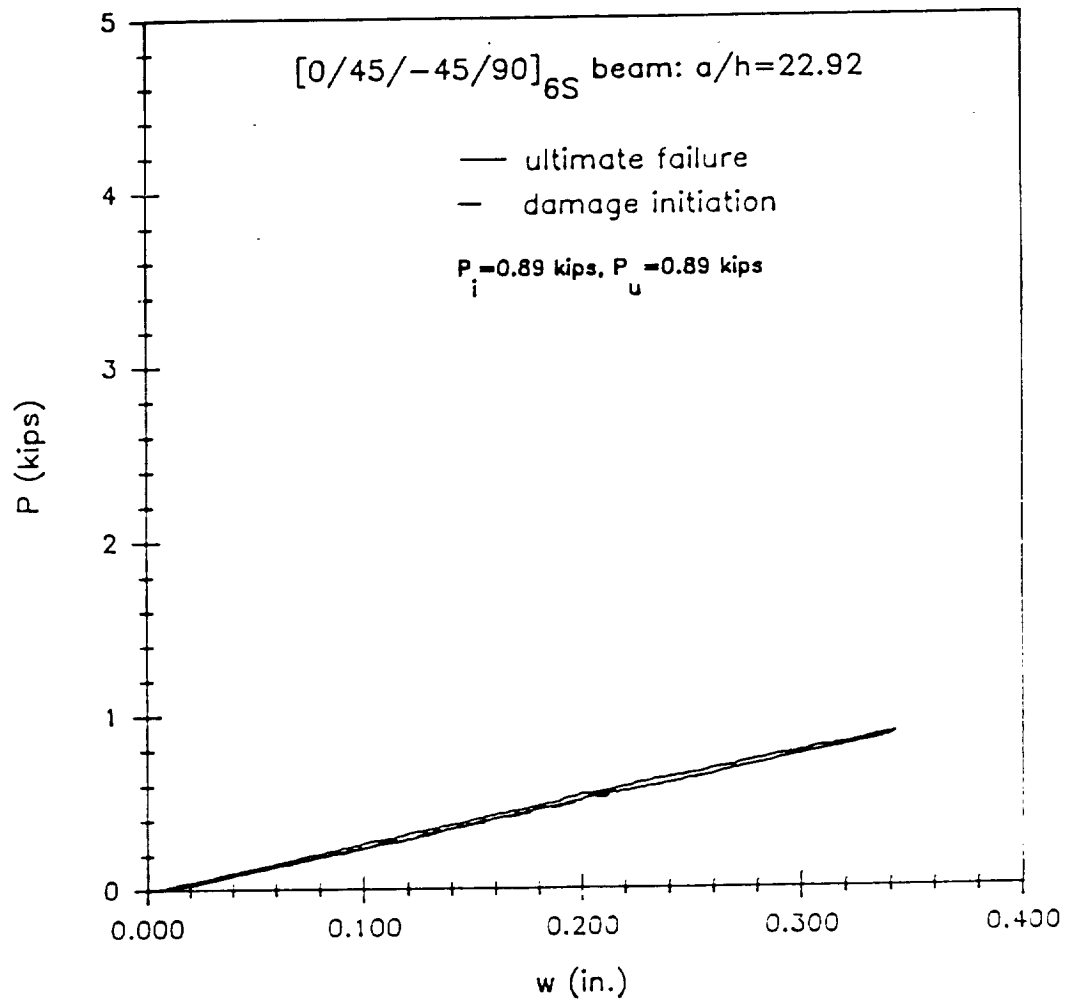
Figure 109. Load versus displacement for the [0/45/-45/90]₆ₛ laminate with an aspect ratio of 22.92.
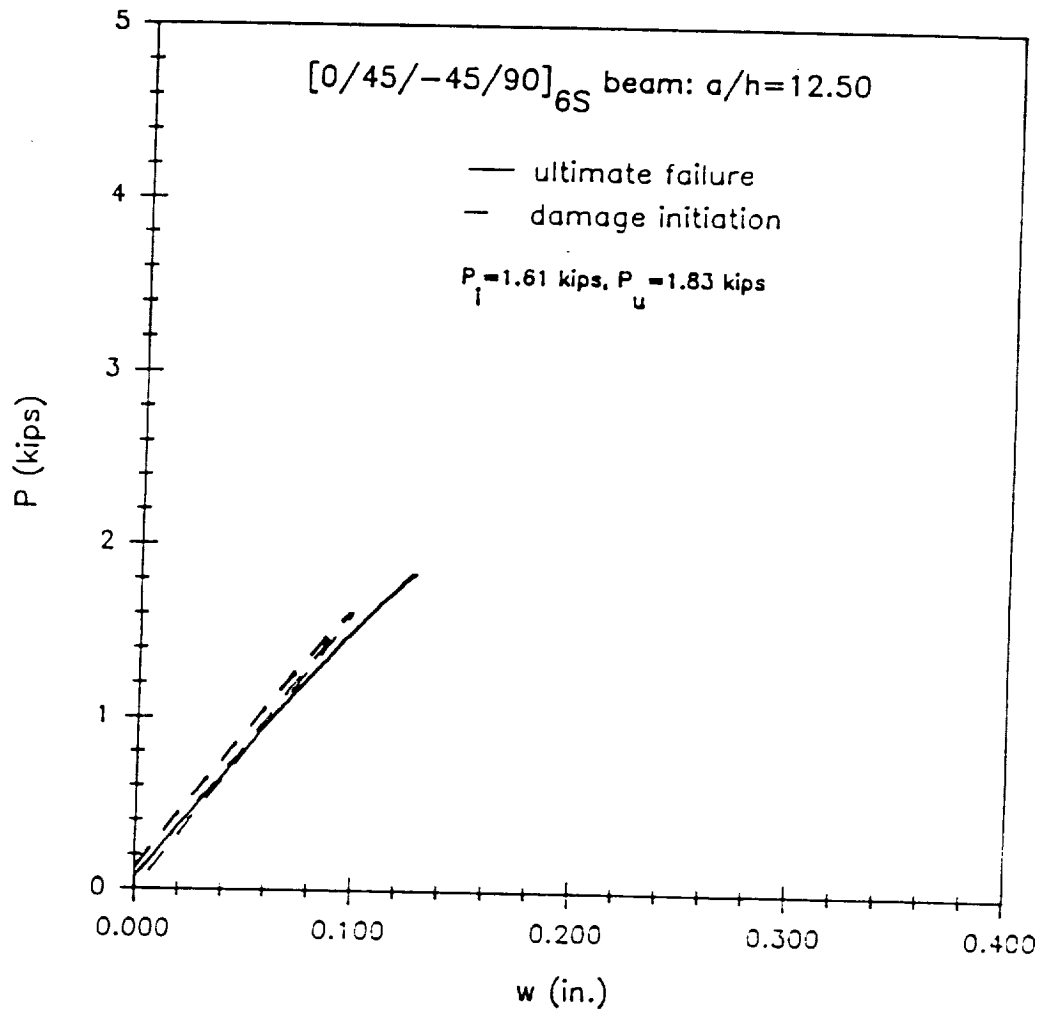
Figure 110. Load versus displacement for the [0/45/-45/90]$_{6S}$ laminate with an aspect ratio of 12.50.

$[0/45/-45/90]_{6S}$ beam: $a/h=4.17$

— ultimate failure

— damage initiation

$P_i=3.08$ kips, $P_u=3.11$ kips
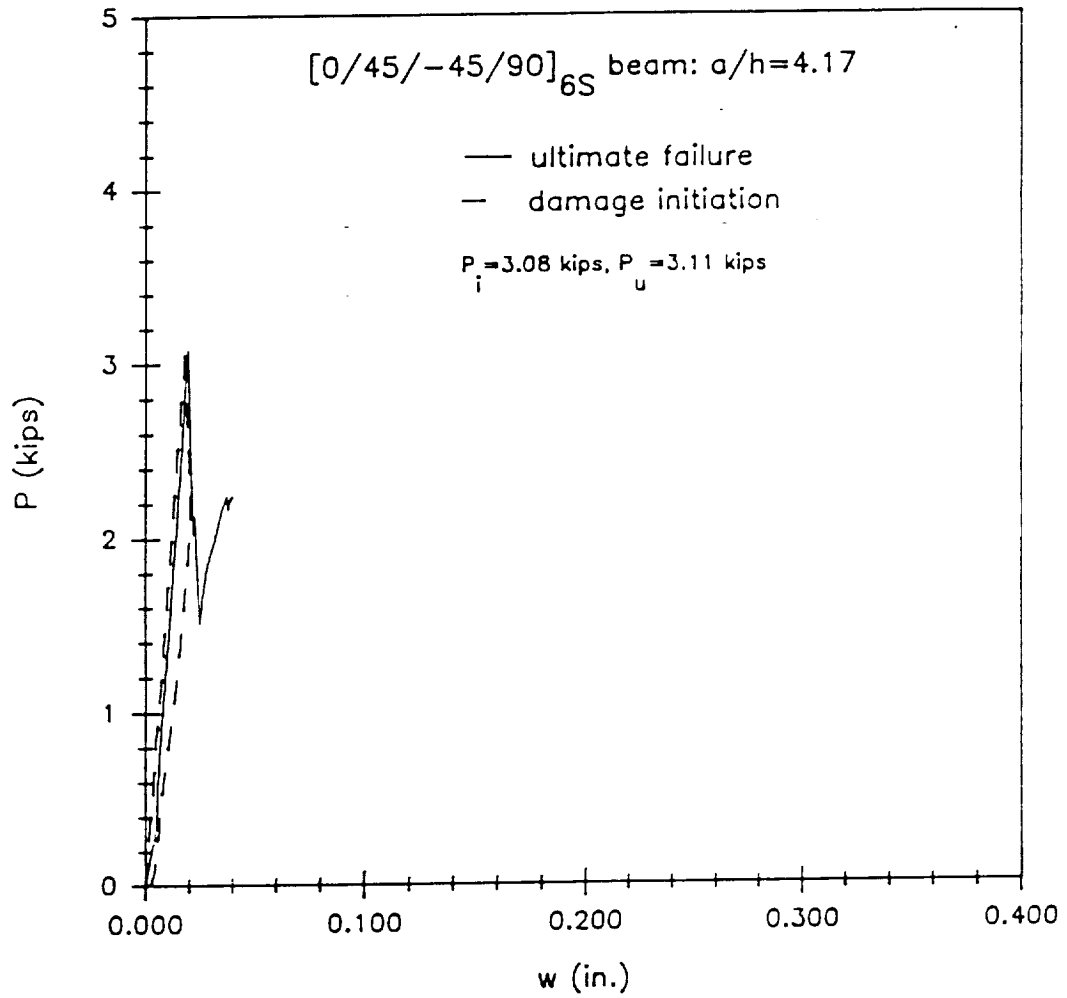
Figure 111. Load versus displacement for the $[0/45/-45/90]_{6S}$ laminate with an aspect ratio of 4.17.
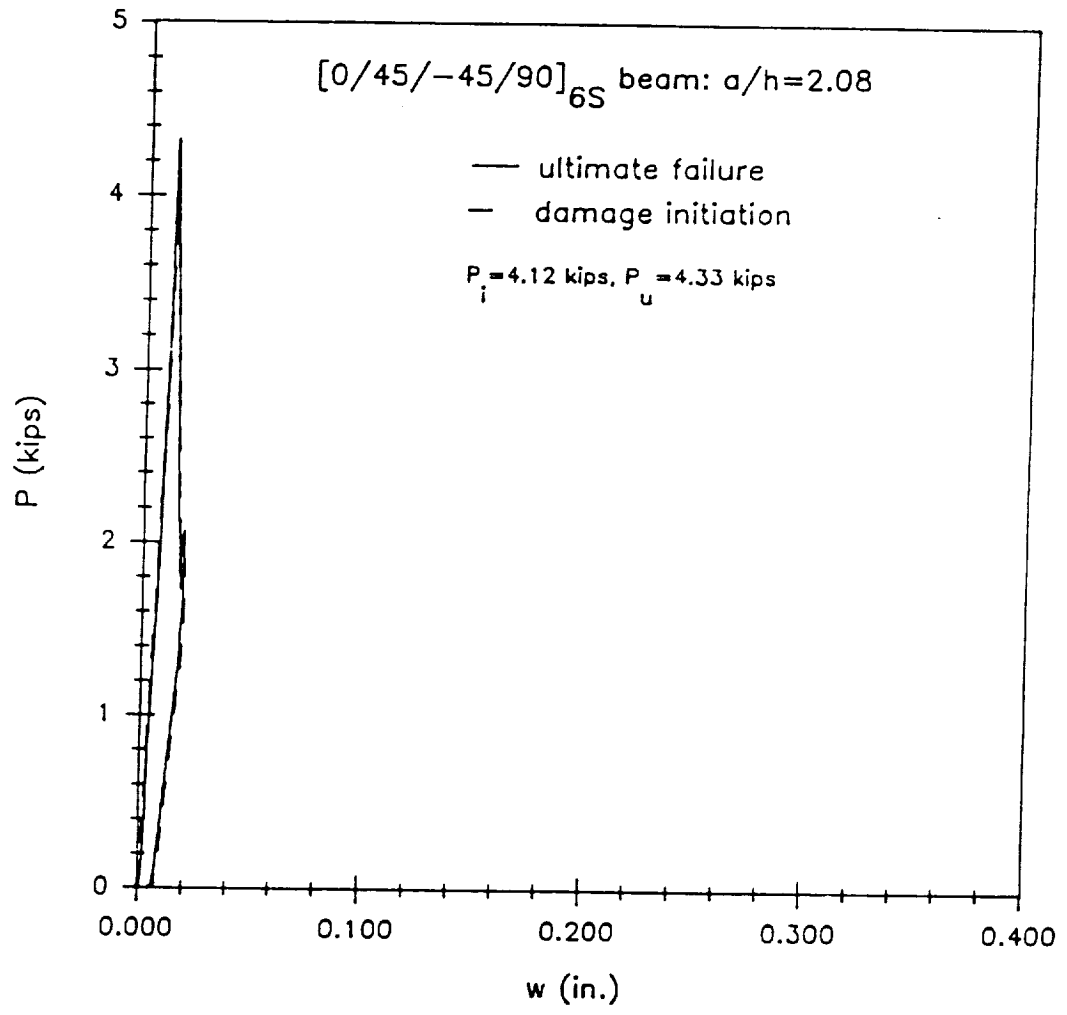
Figure 112. Load versus displacement for the [0/45/-45/90]$_{6S}$ laminate with an aspect ratio of 2.08.
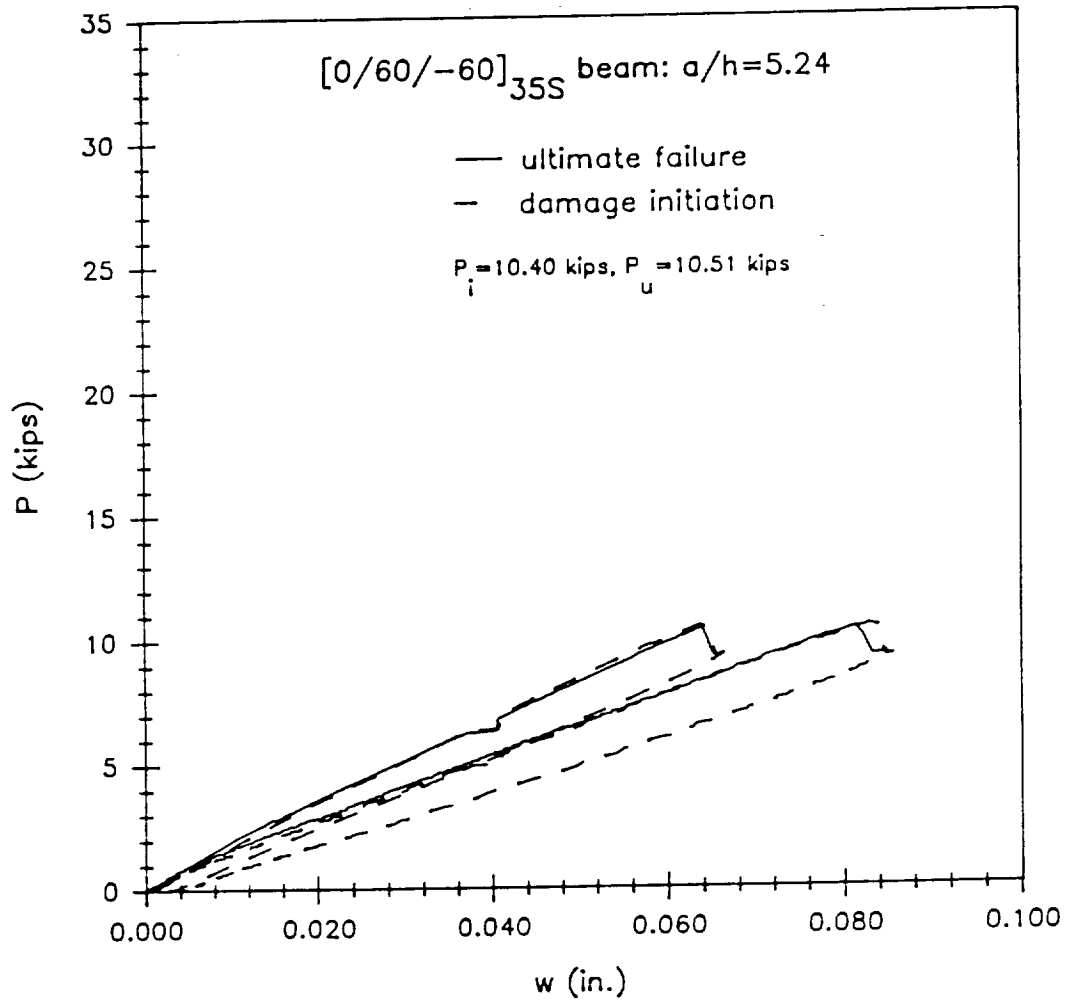
Figure 113. Load versus displacement for the $[0/60/-60]_{35S}$ laminate with an aspect ratio of 5.24.
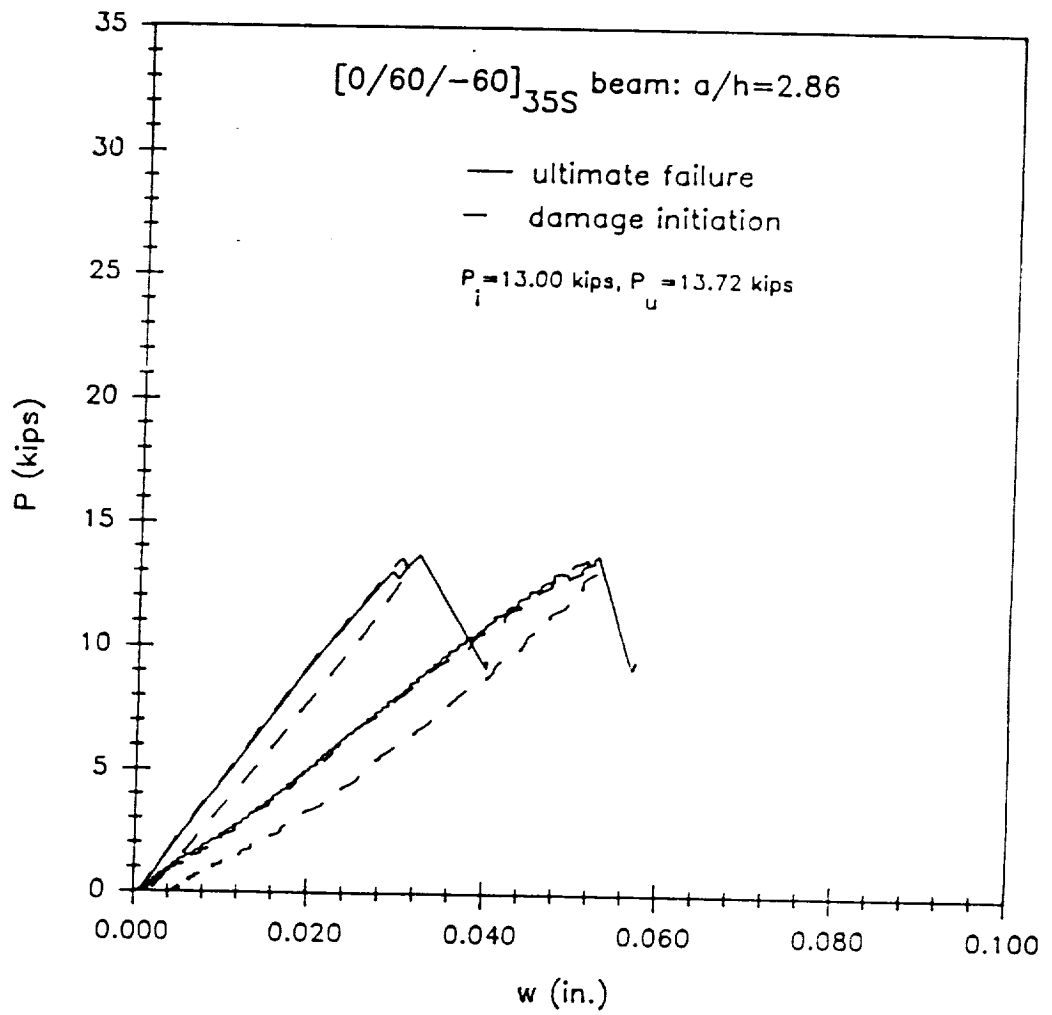
Figure 114. Load versus displacement for the [0/60/-60]$_{35S}$ laminate with an aspect ratio of 2.86.
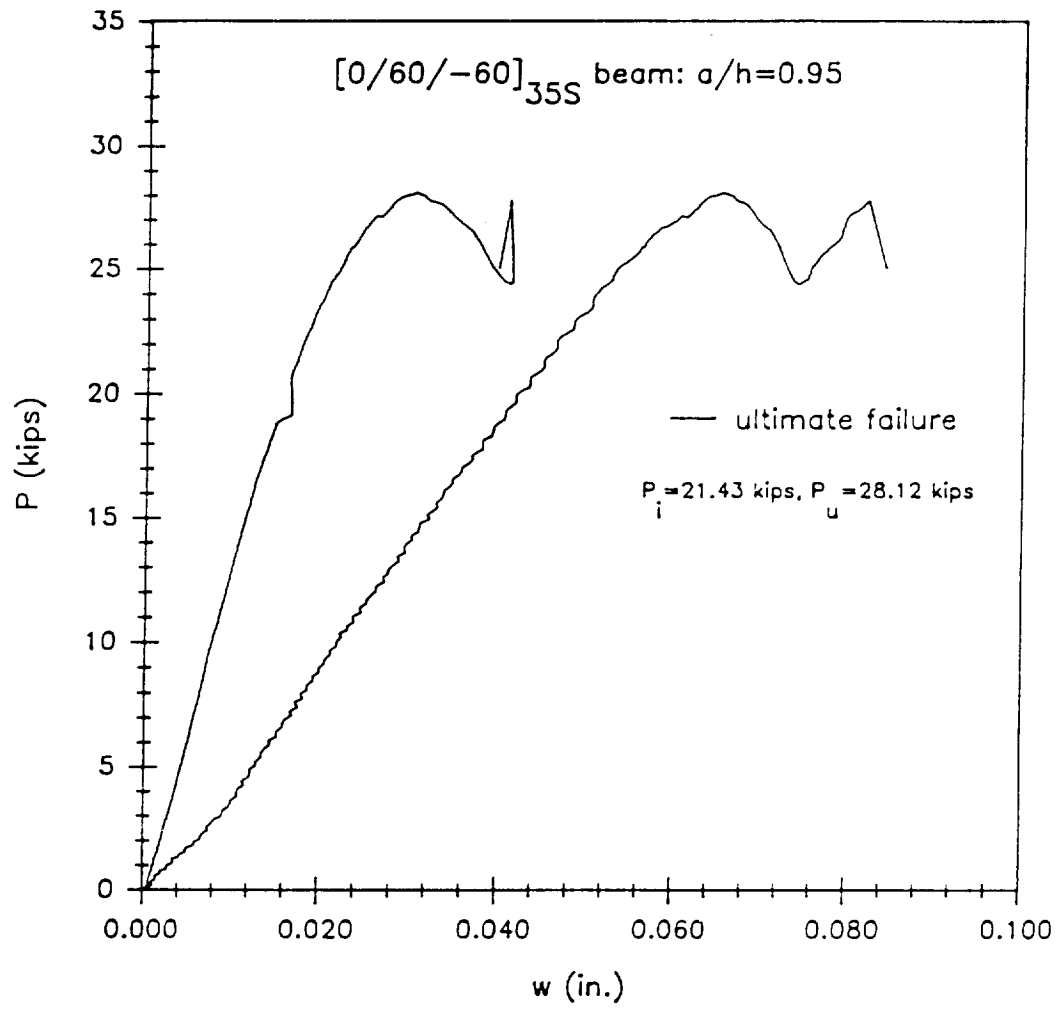
Figure 115. Load versus displacement for the $[0/60/-60]_{35S}$ laminate with an aspect ratio of 0.95.
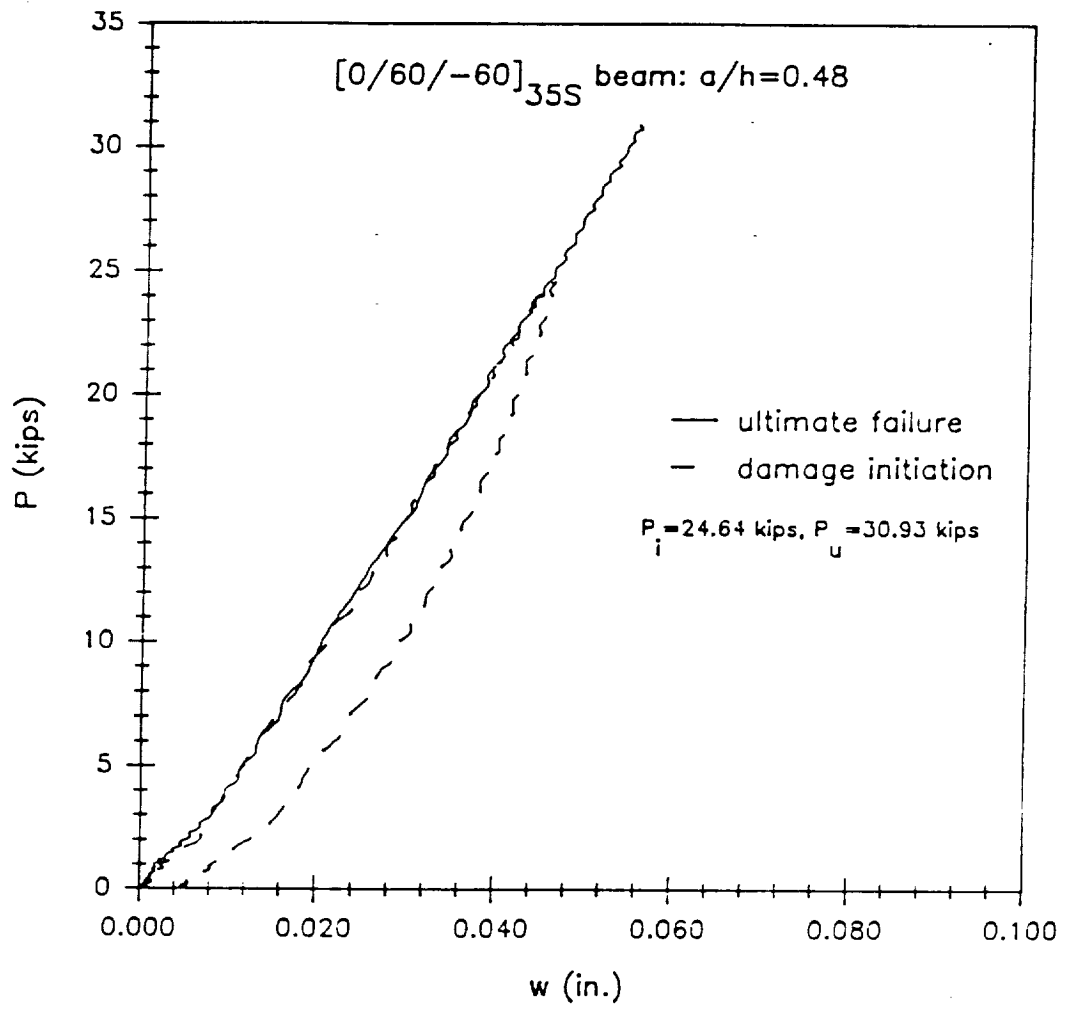
Figure 116. Load versus displacement for the [0/60/-60]$_{35S}$ laminate with an aspect ratio of 0.48.
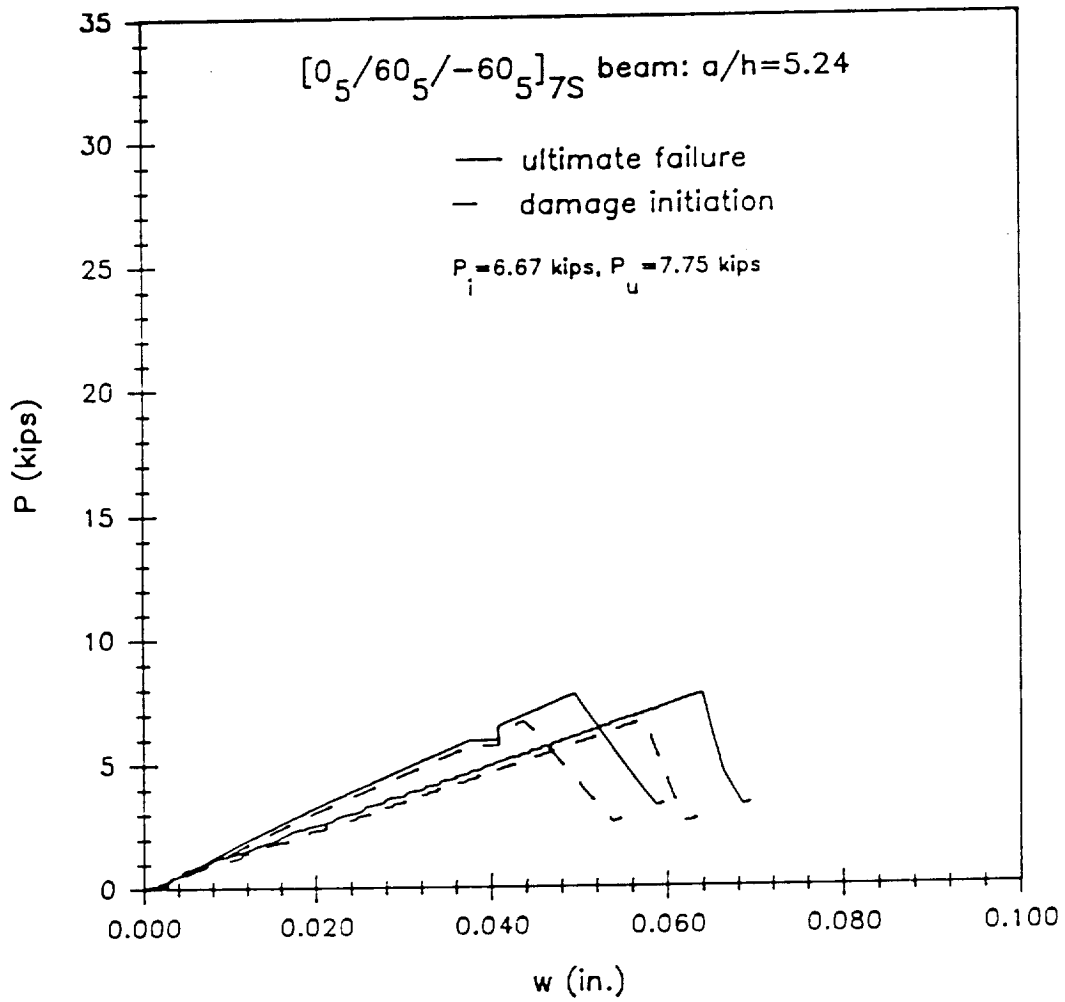
Figure 117. Load versus displacement for the [0/60/-60] grouped laminate with an aspect ratio of 5.24.
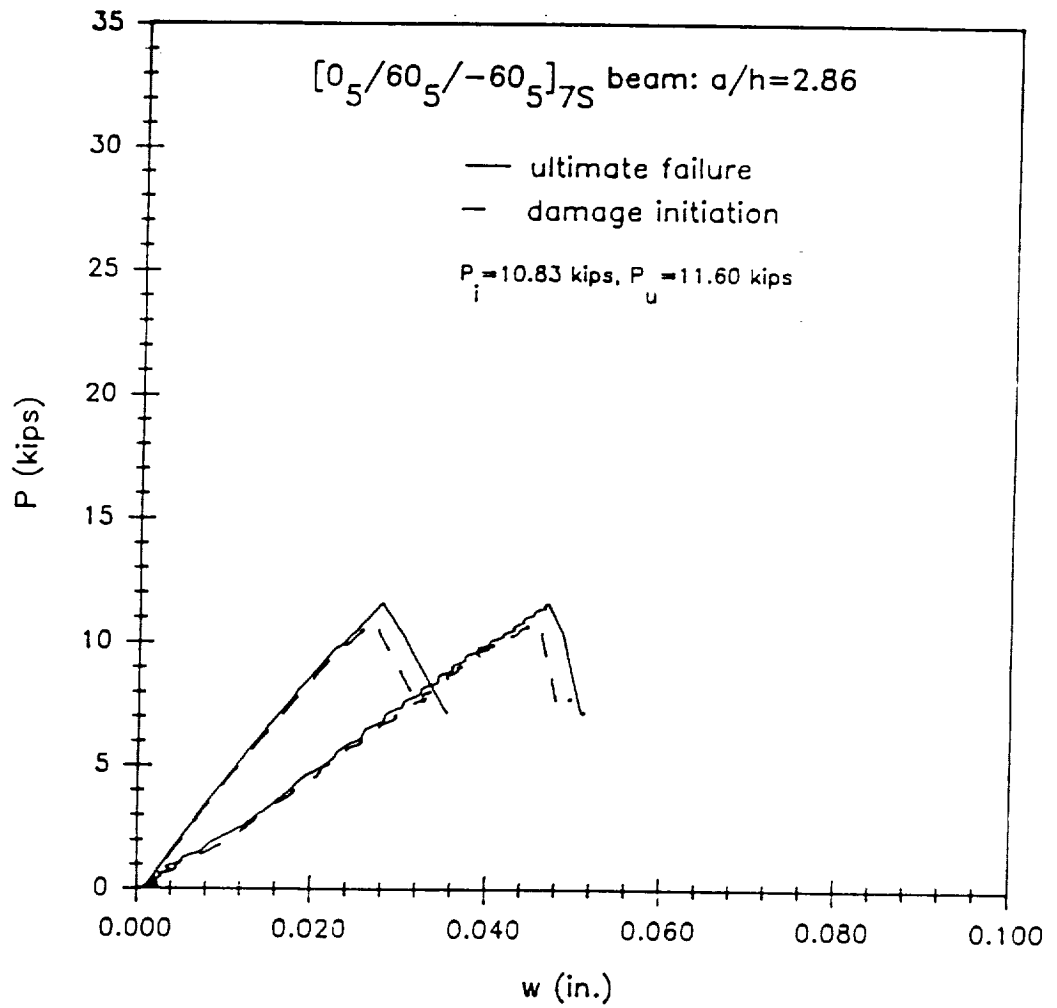
Figure 118. Load versus displacement for the [0/60/-60] grouped laminate with an aspect ratio of 2.86.
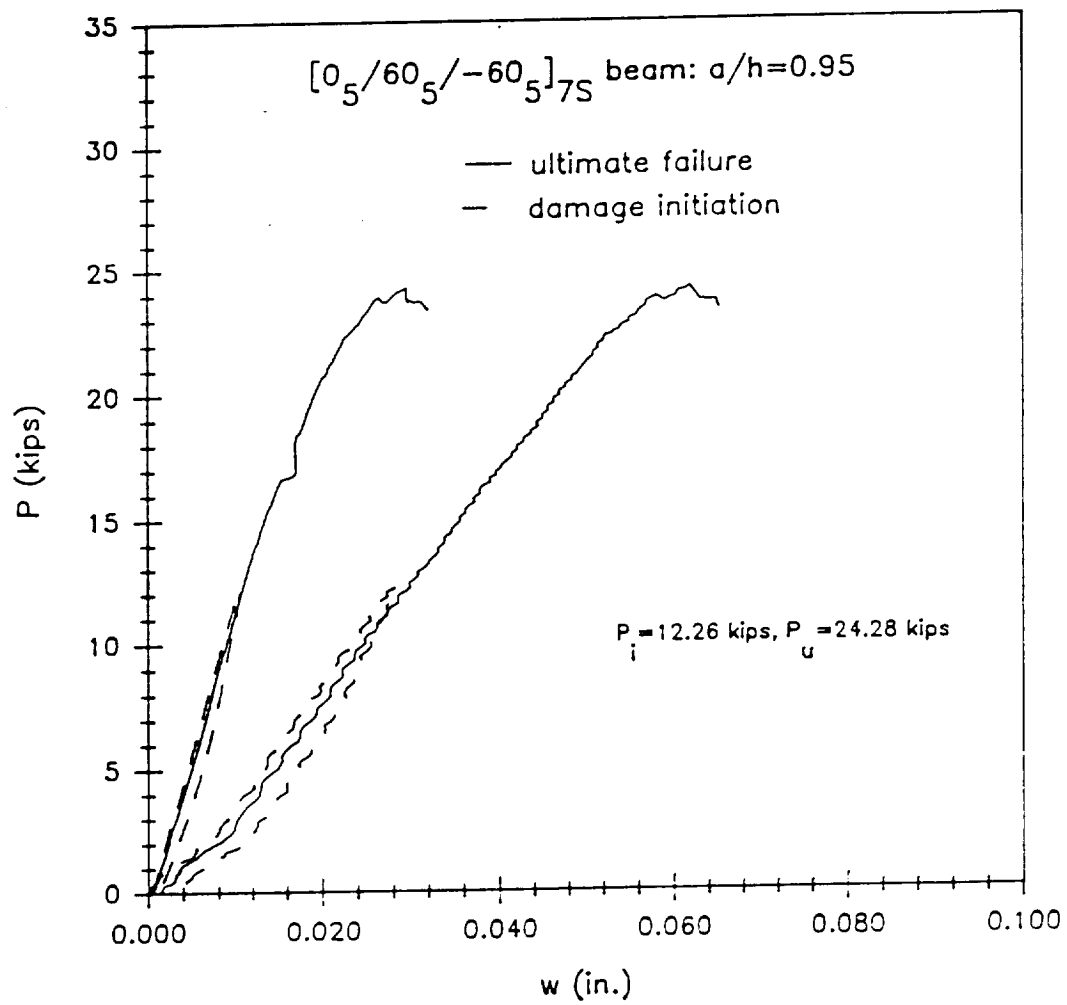
Figure 119. Load versus displacement for the [0/60/-60] grouped laminate with an aspect ratio of 0.95.
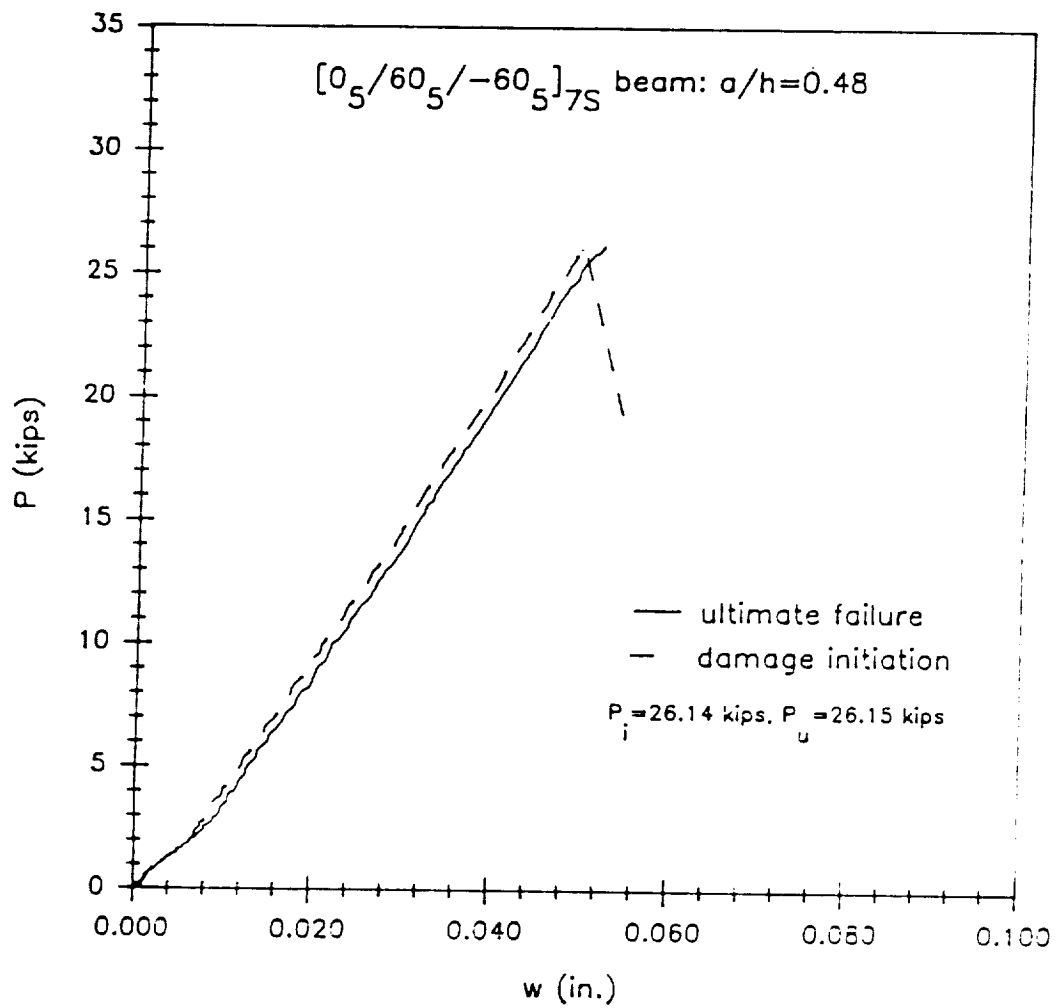
Figure 120. Load versus displacement for the [0/60/-60] grouped laminate with an aspect ratio of 0.48.
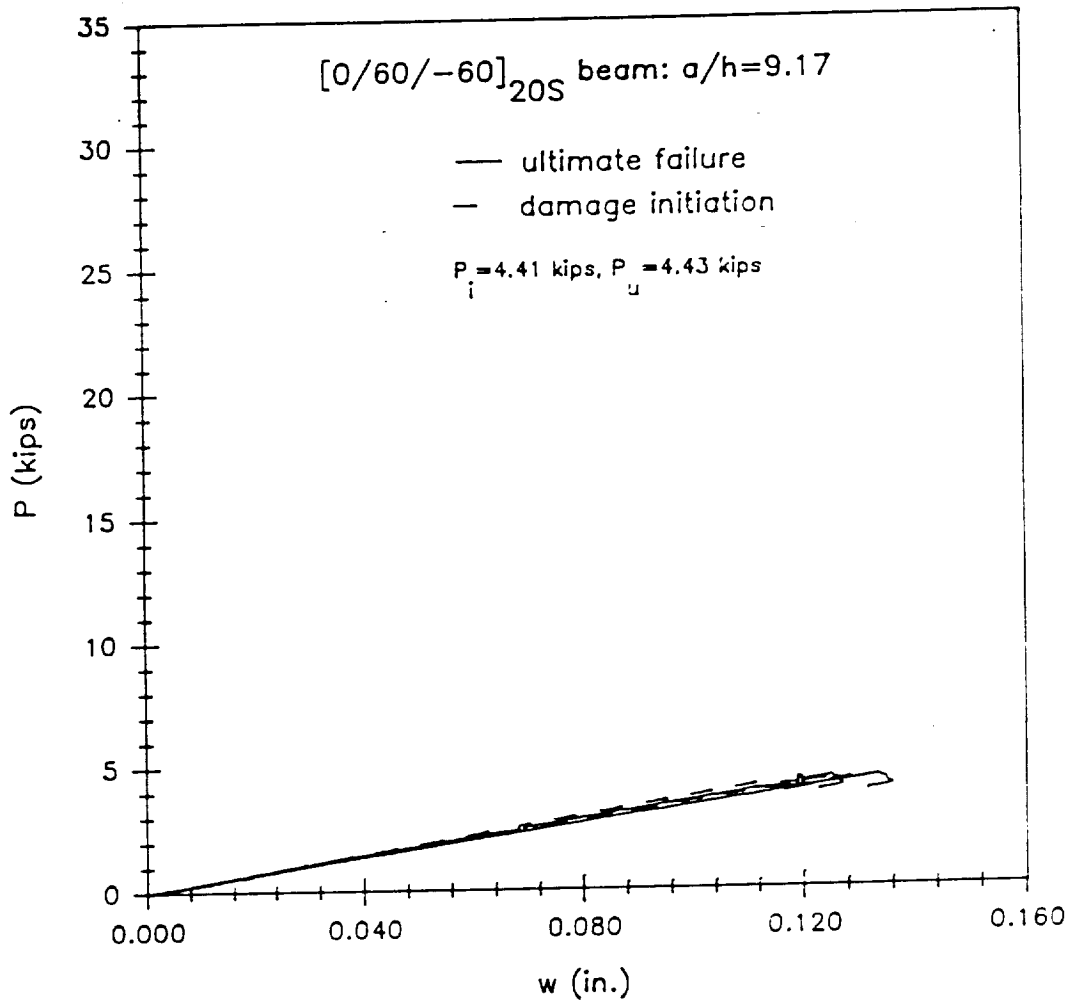
Figure 121.   Load versus displacement for the [0/60/-60]$_{20S}$ laminate with an aspect ratio of 9.17.

Experimental Load-Displacement Data

253
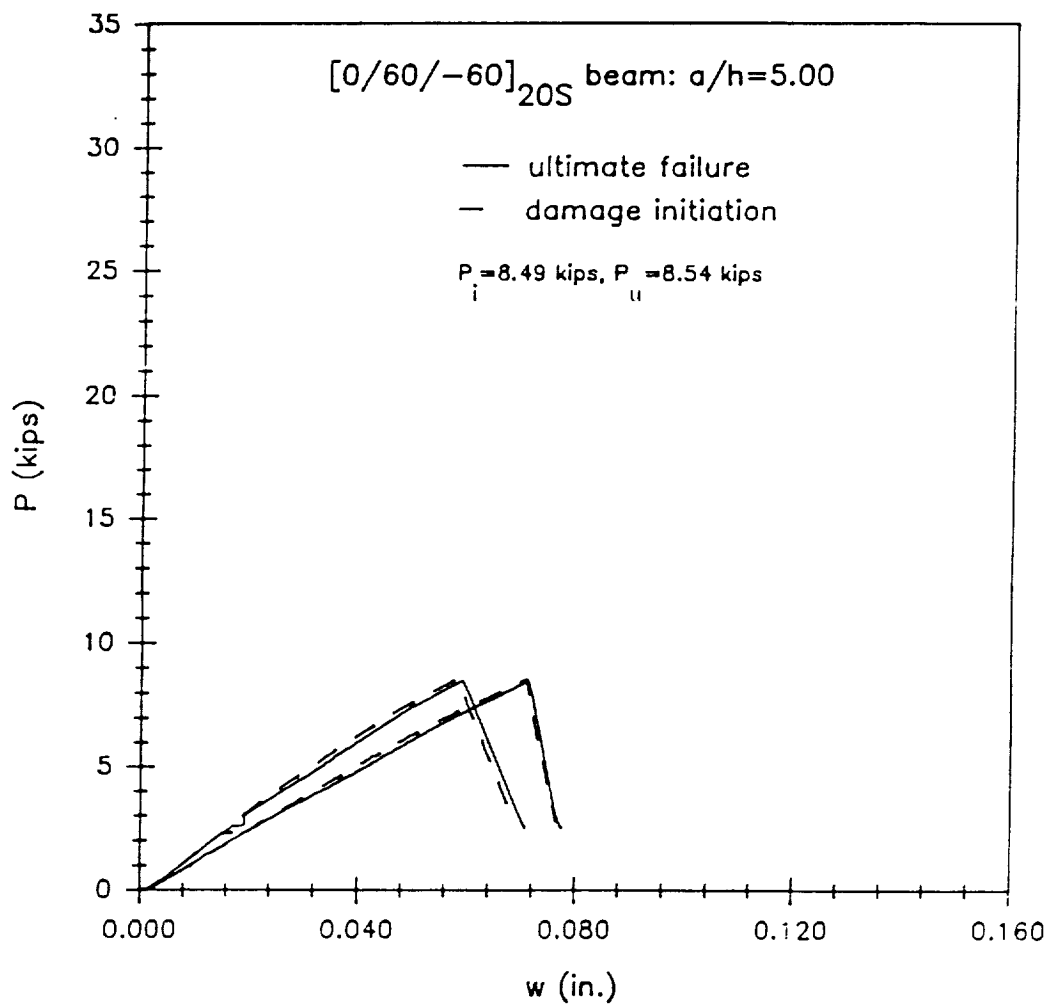
Figure 122.   Load versus displacement for the [0/60/-60]$_{20S}$ laminate with an aspect ratio of 5.00.
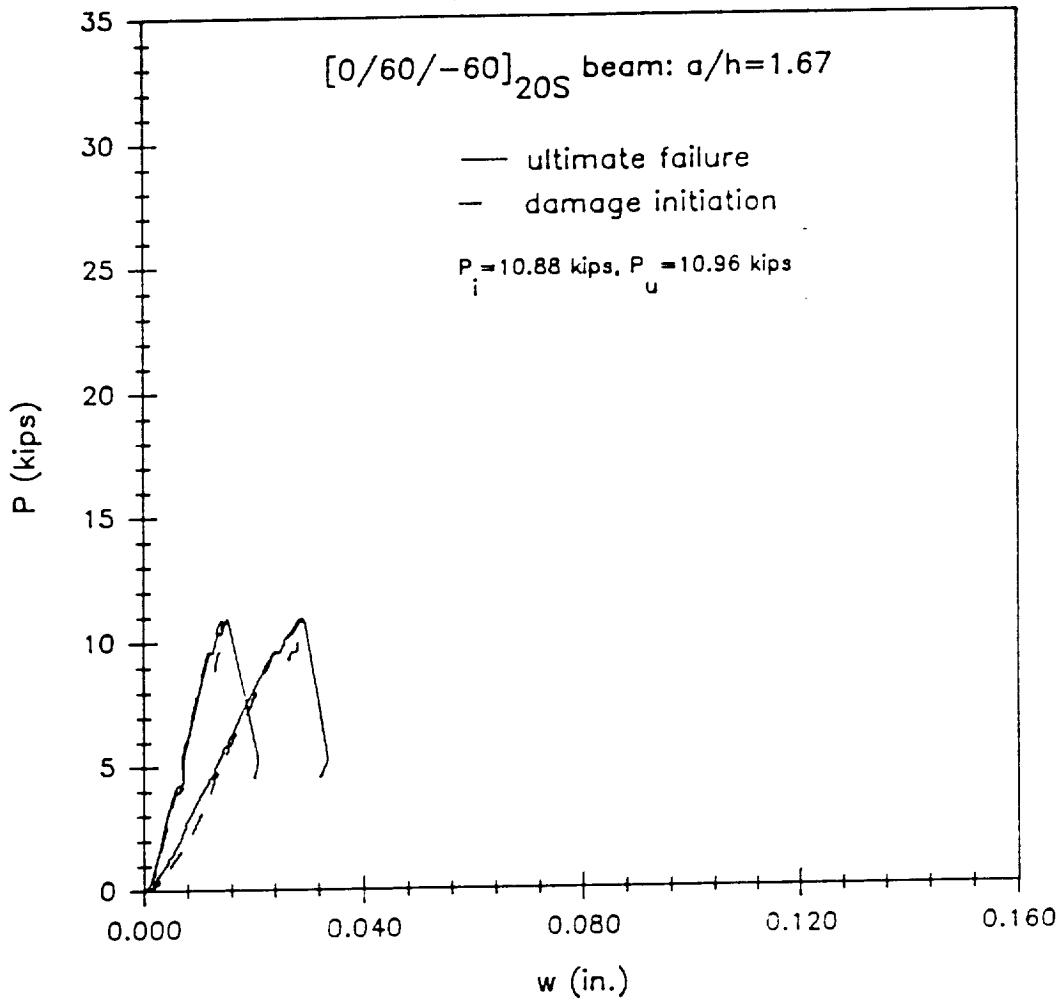
Figure 123.   Load versus displacement for the [0/60/-60]$_{20S}$ laminate with an aspect ratio of 1.67.
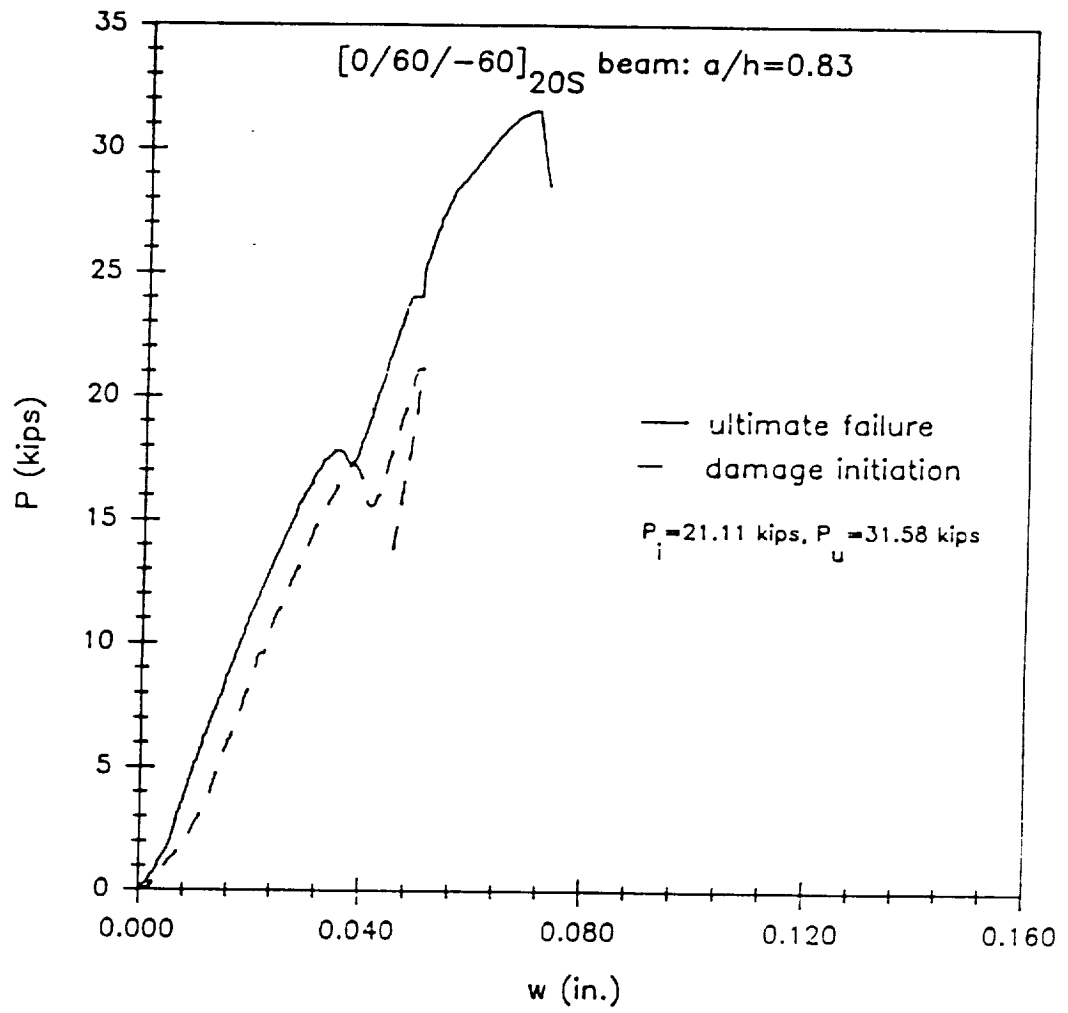
Figure 124. Load versus displacement for the [0/60/-60]$_{20S}$ laminate with an aspect ratio of 0.83.
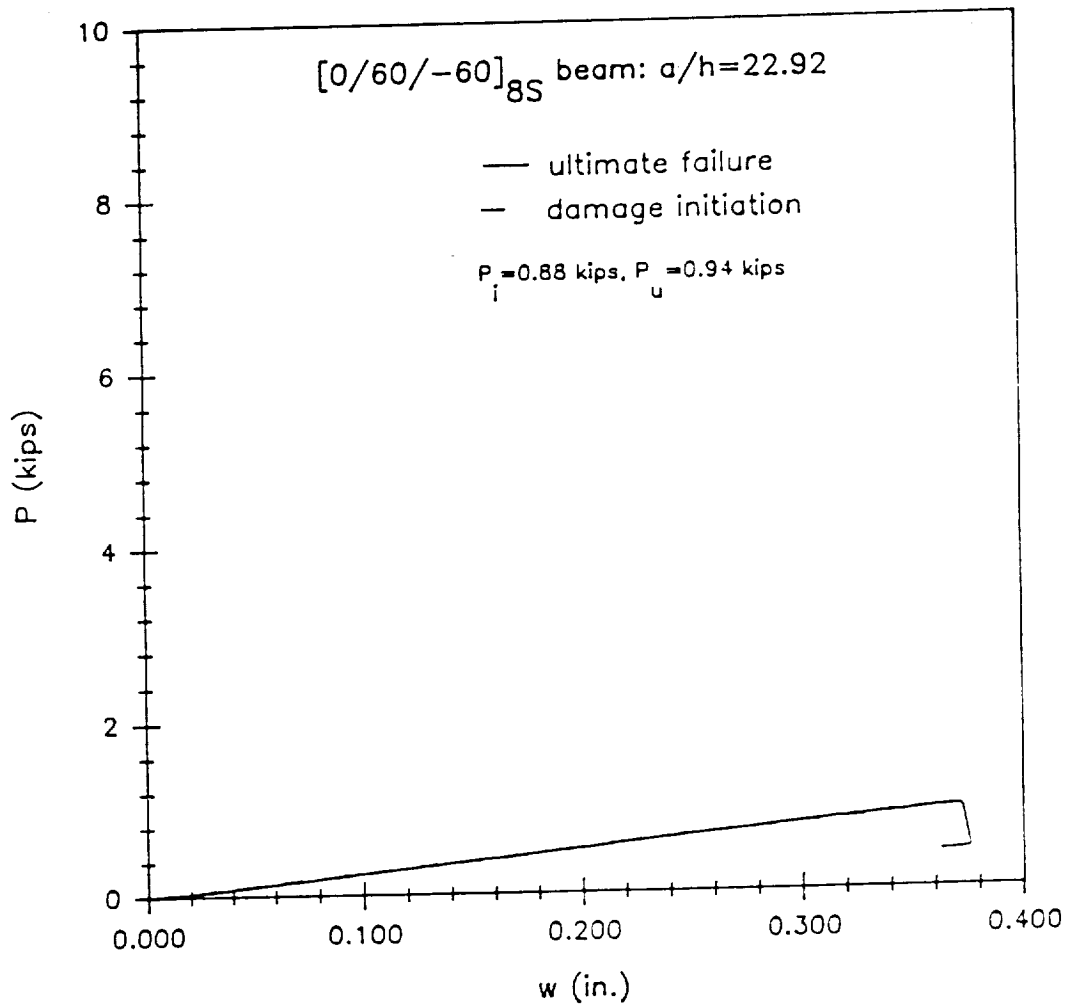
Figure 125.   Load versus displacement for the [0/60/-60]$_{8S}$ laminate with an aspect ratio of 22.92.

$[0/60/-60]_{8S}$ beam: $a/h = 12.50$

— ultimate failure
— damage initiation

$P_i = 1.66$ kips, $P_u = 1.71$ kips

P (kips)

10

8

6

4

2

0

0.000   0.100   0.200   0.300   0.400

w (in.)
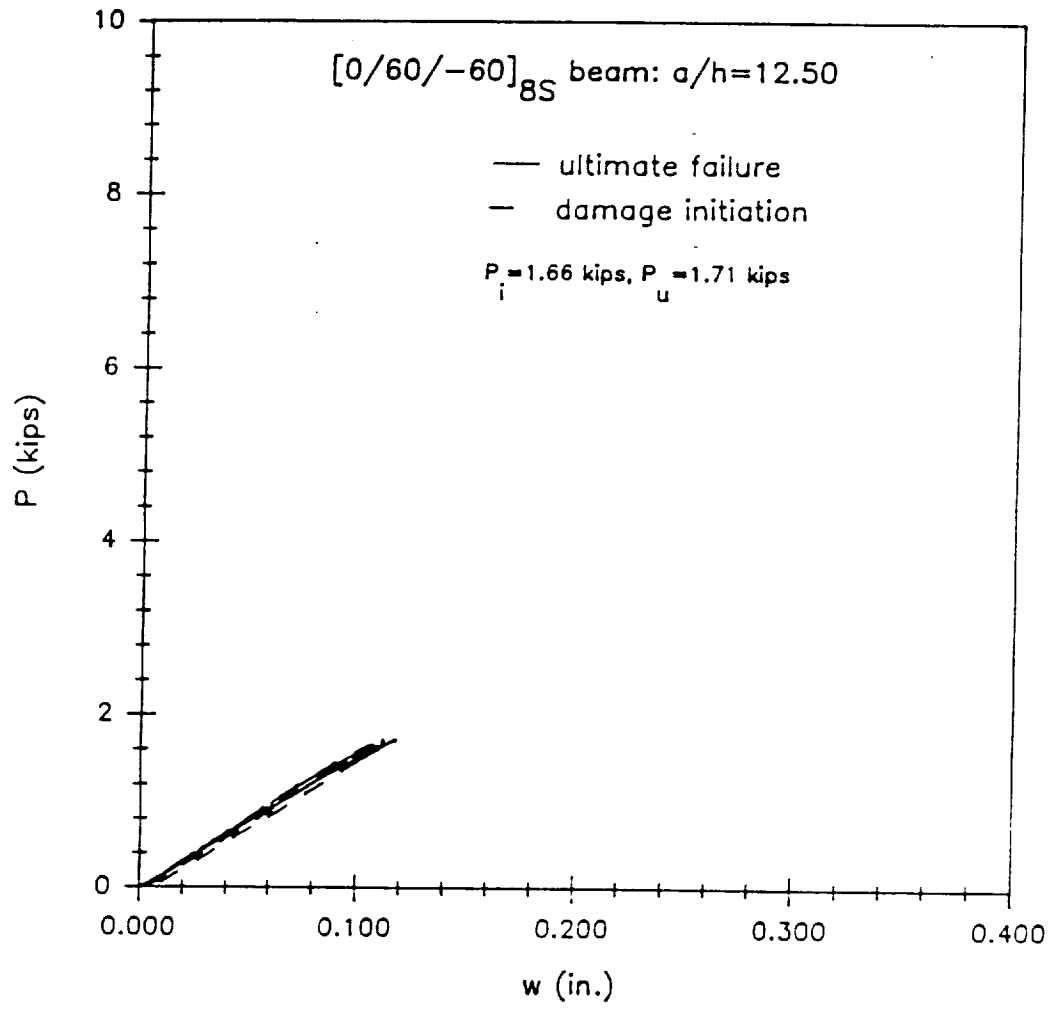
Figure 126. Load versus displacement for the $[0/60/-60]_{8S}$ laminate with an aspect ratio of 12.50.

Experimental Load-Displacement Data
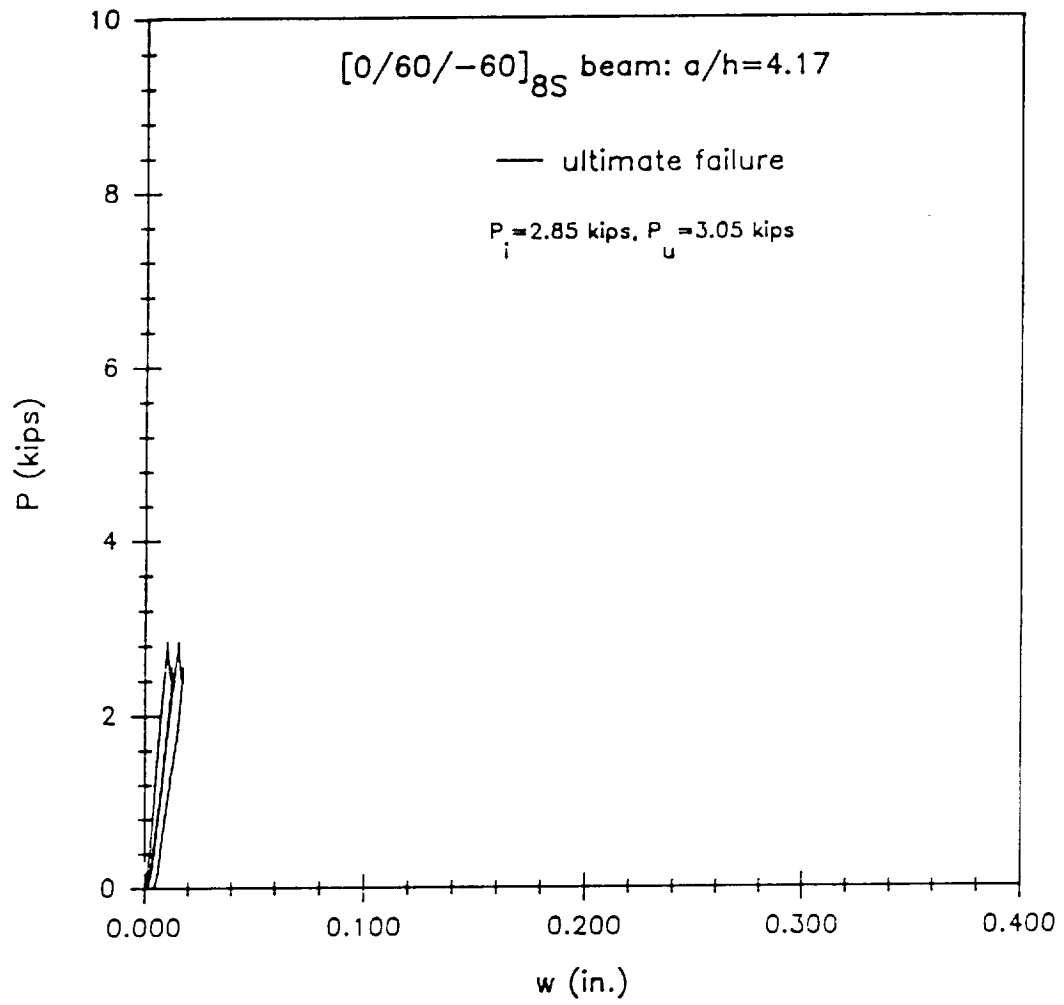
Figure 127. Load versus displacement for the [0/60/-60]$_{8S}$ laminate with an aspect ratio of 4.17.
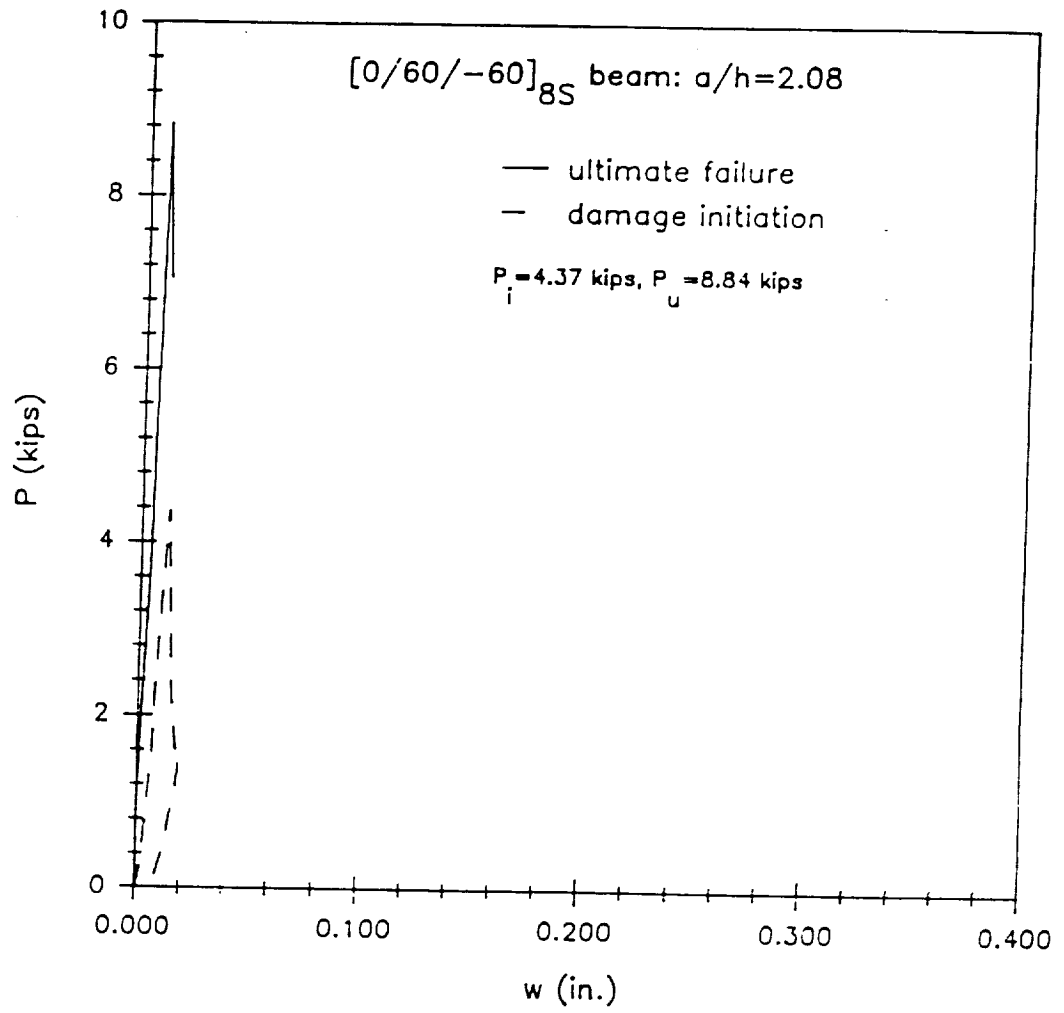
Figure 128. Load versus displacement for the [0/60/-60]$_{8S}$ laminate with an aspect ratio of 2.08.
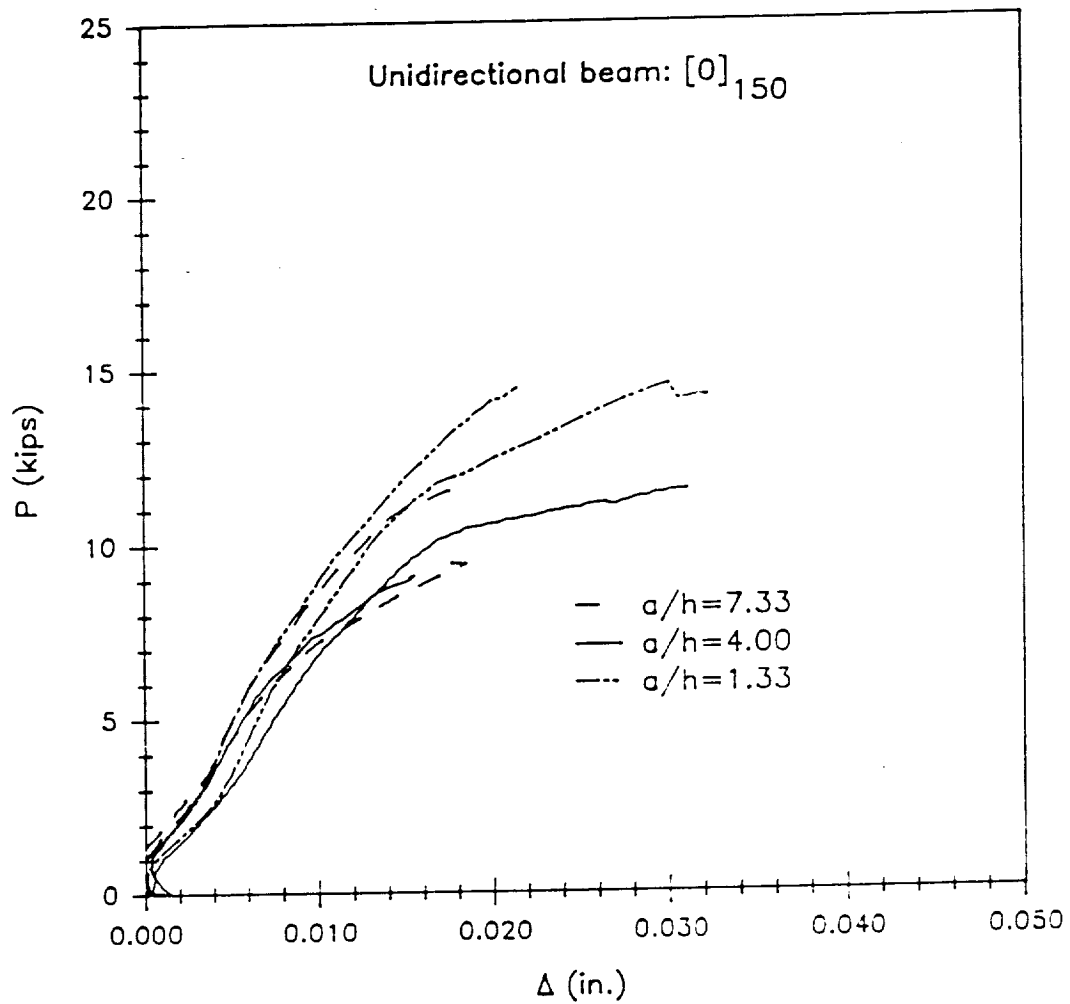
Figure 129. Load versus indentation for the $[0]_{150}$ laminate.
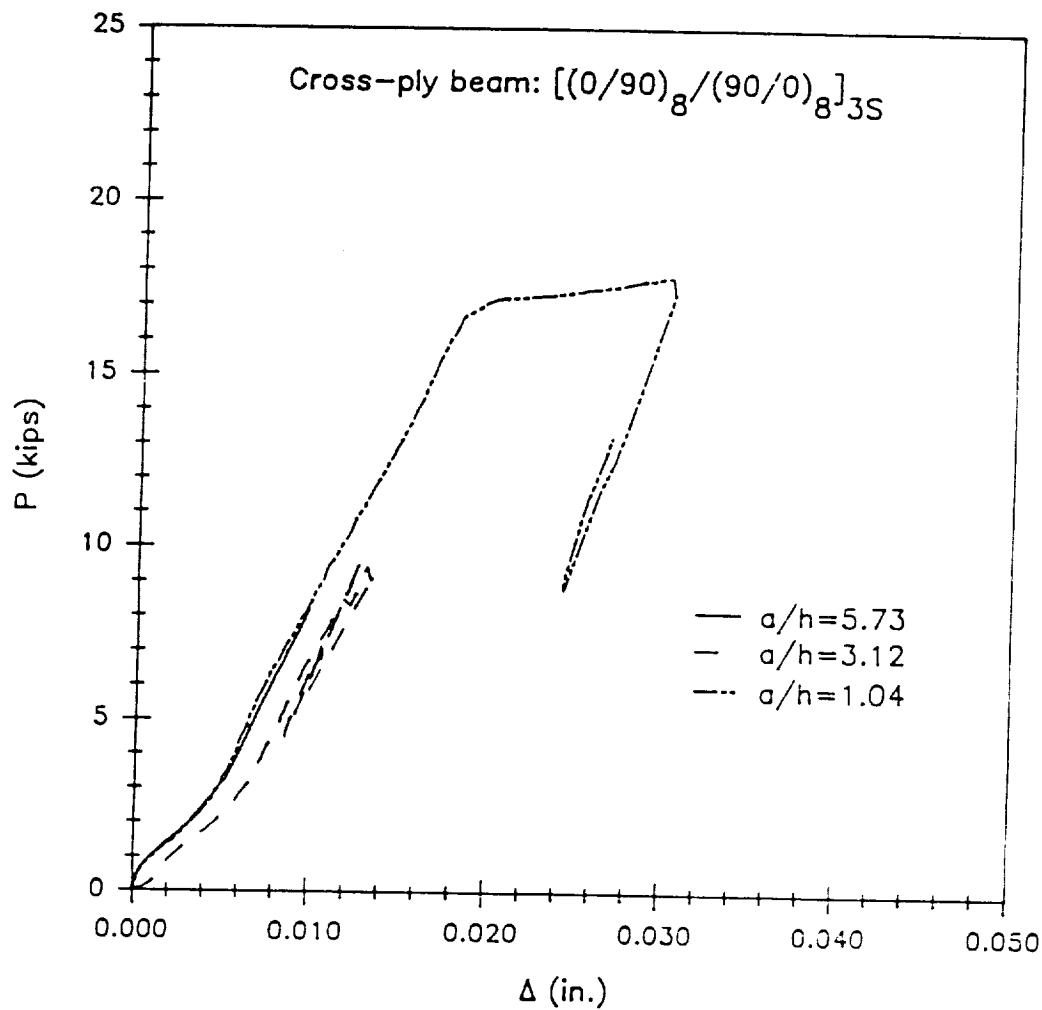
Figure 130. Load versus indentation for the $[(0/90)_8/(90/0)_8]_{3S}$ laminate.
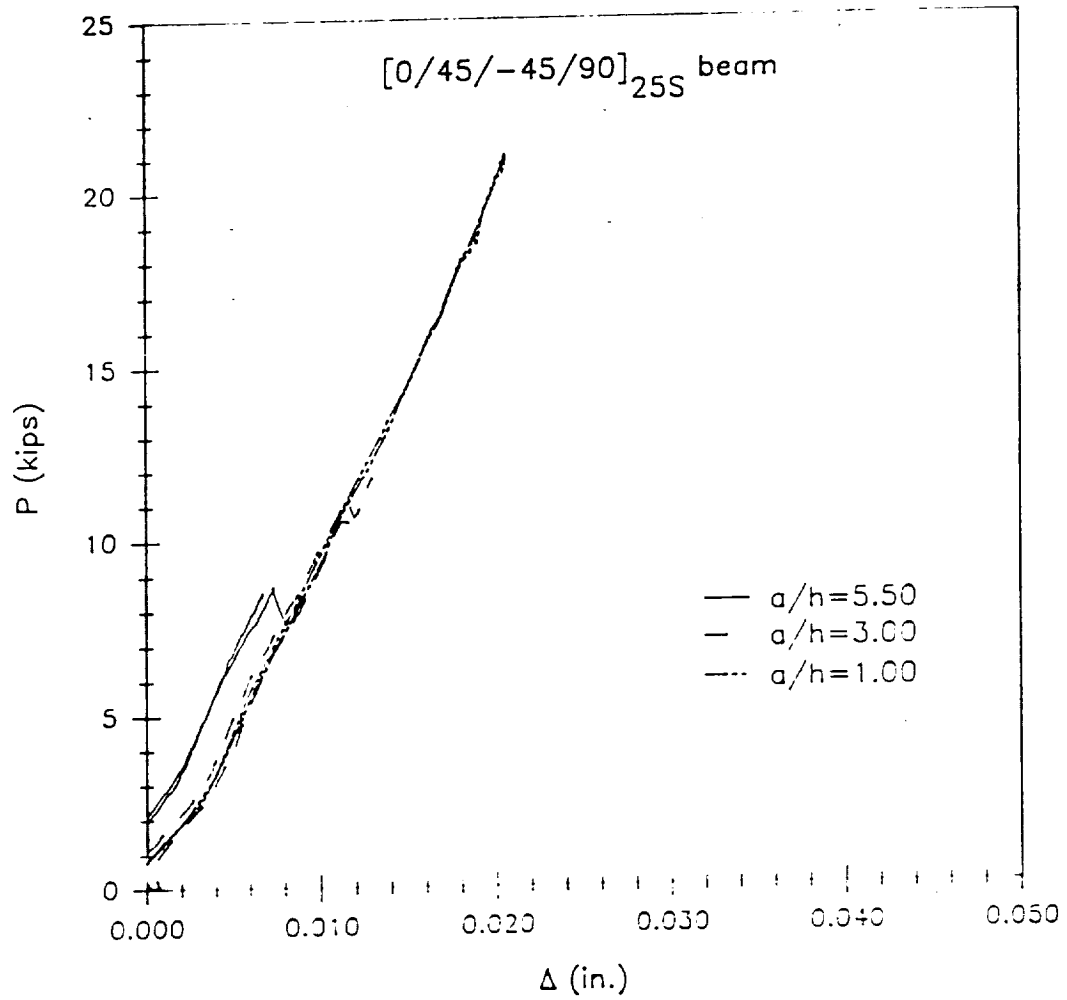
Figure 131. Load versus indentation for the [0/45/-45/90]$_{25S}$ laminate.
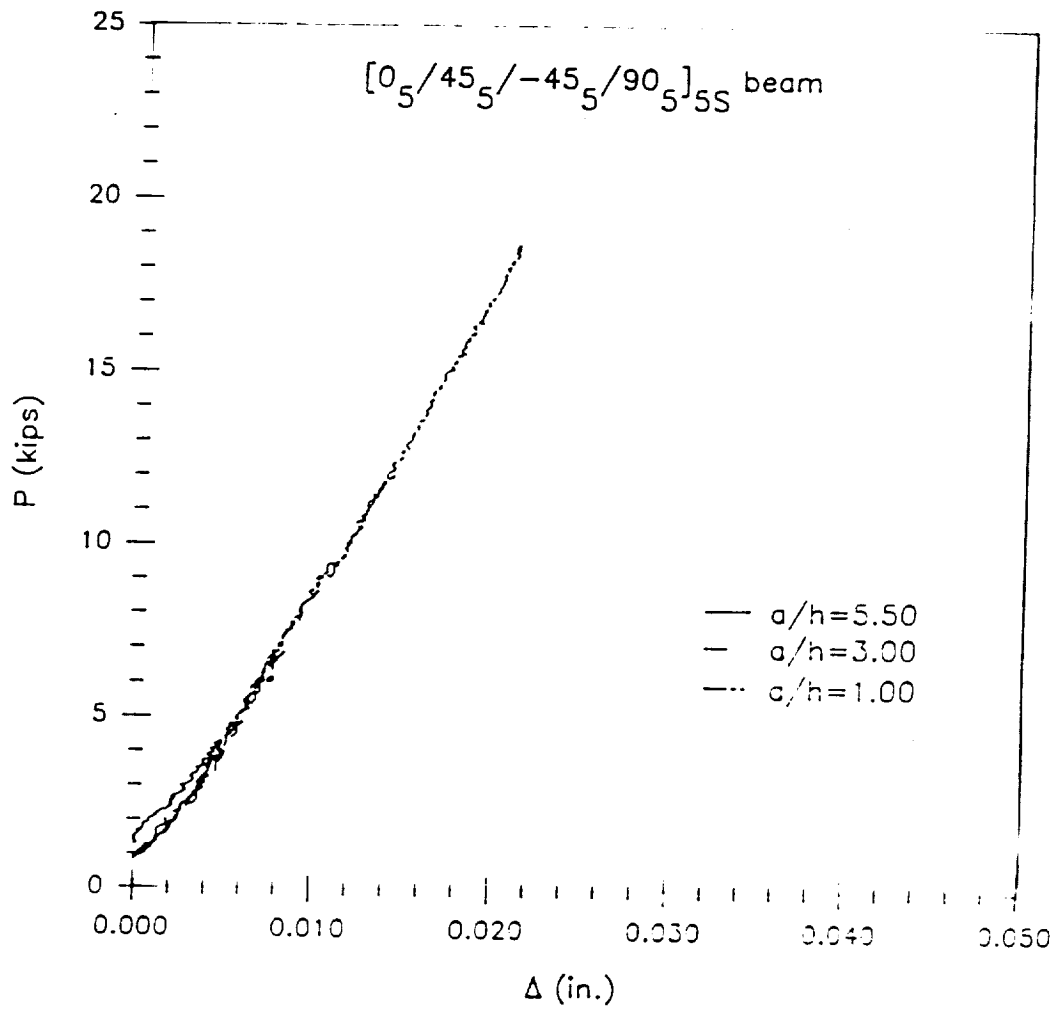
Figure 132. Load versus indentation for the [0/45/-45/90] grouped laminate.
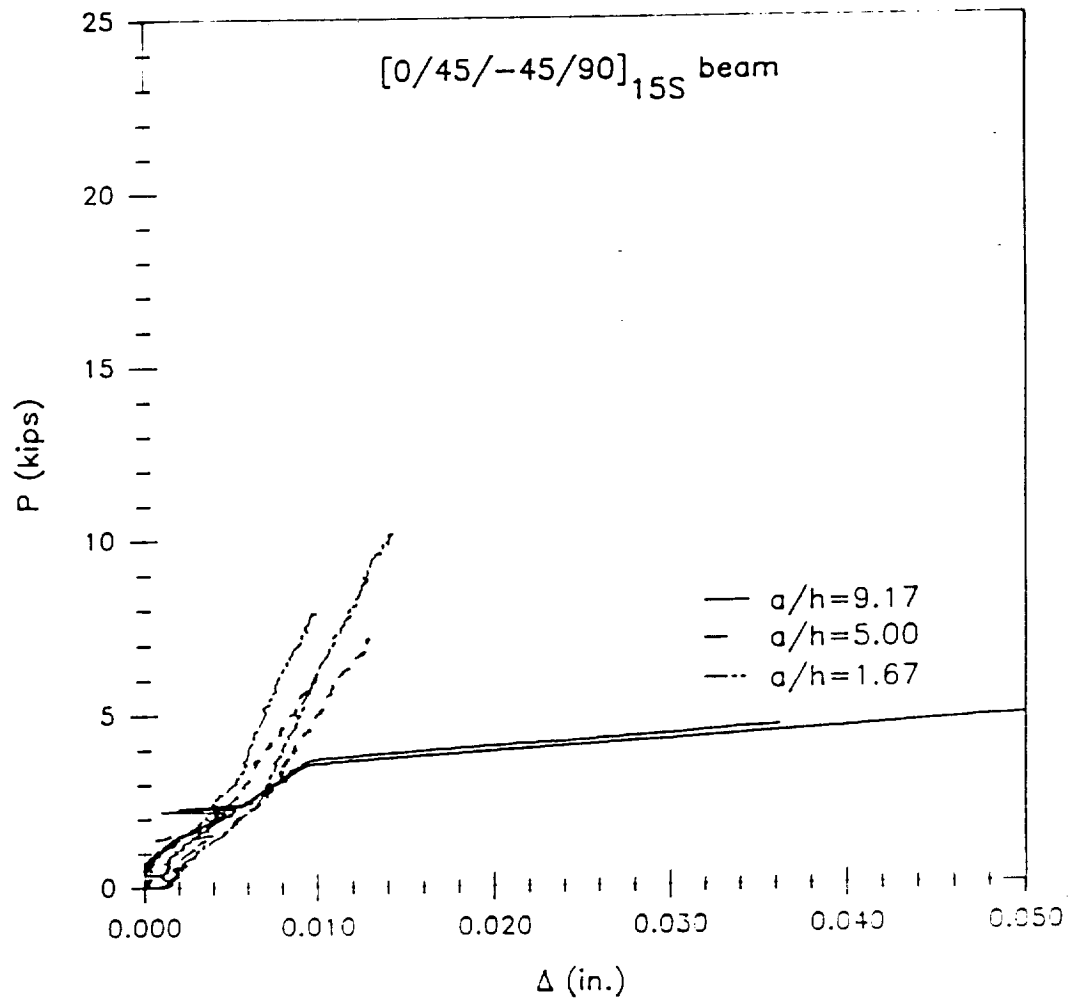
Figure 133. Load versus indentation for the [0/45/-45/90]$_{15S}$ laminate.
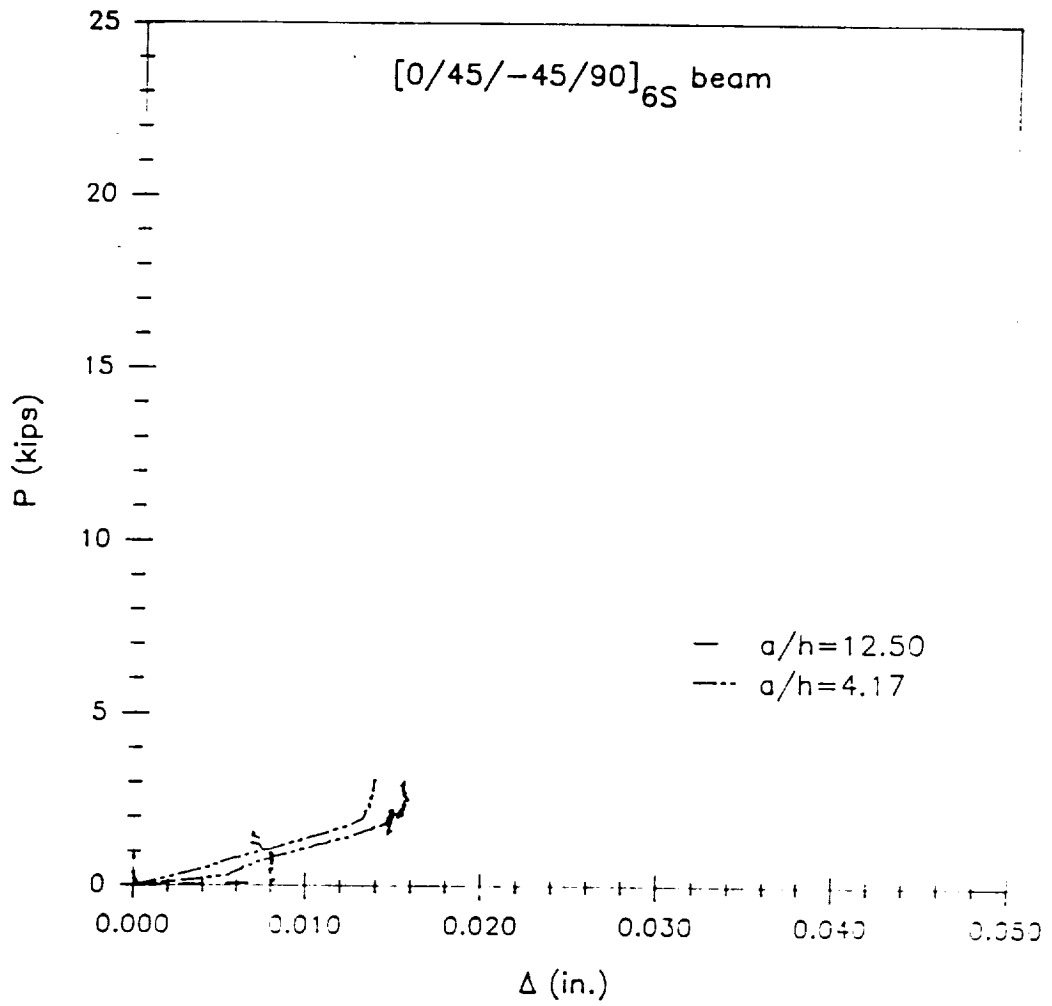
Figure 134. Load versus indentation for the [0/45/-45/90]₆ₛ laminate.
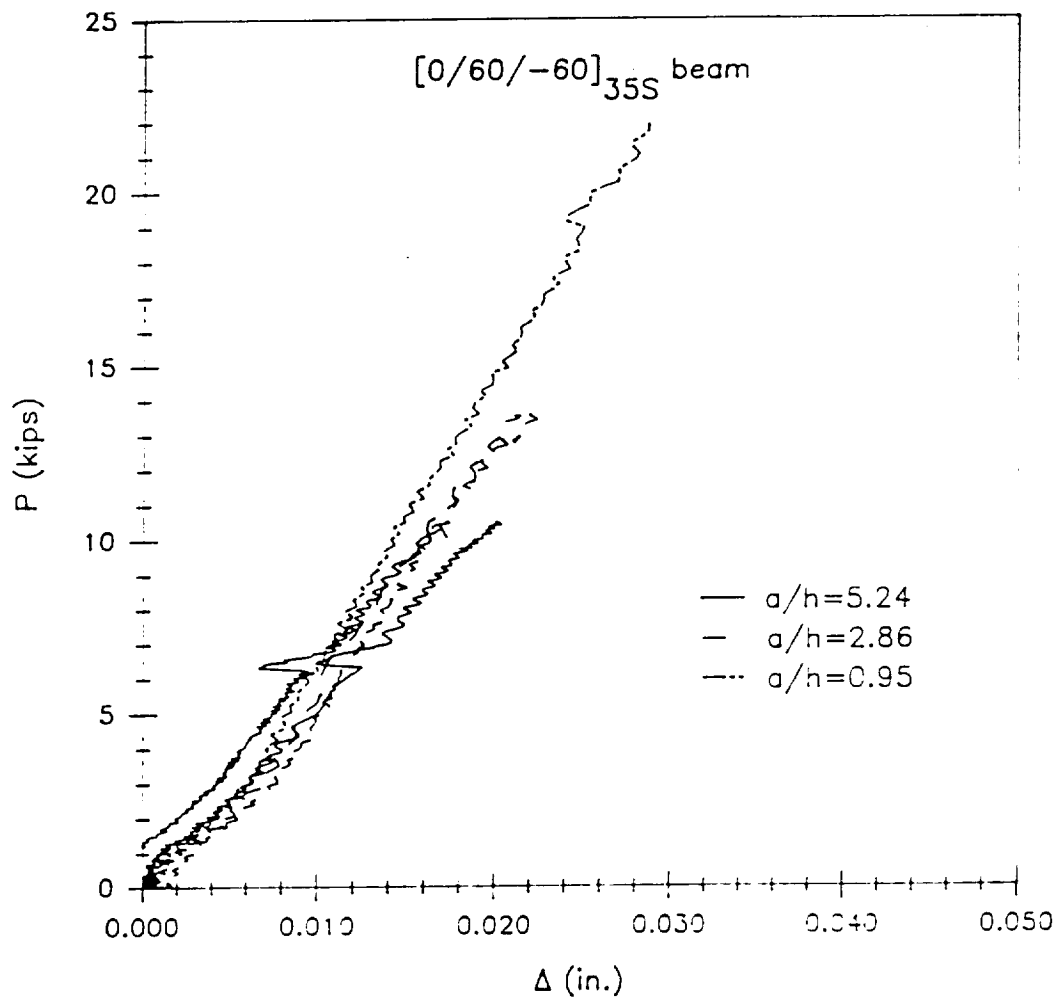
Figure 135. Load versus indentation for the [0/60/-60]$_{35S}$ laminate.
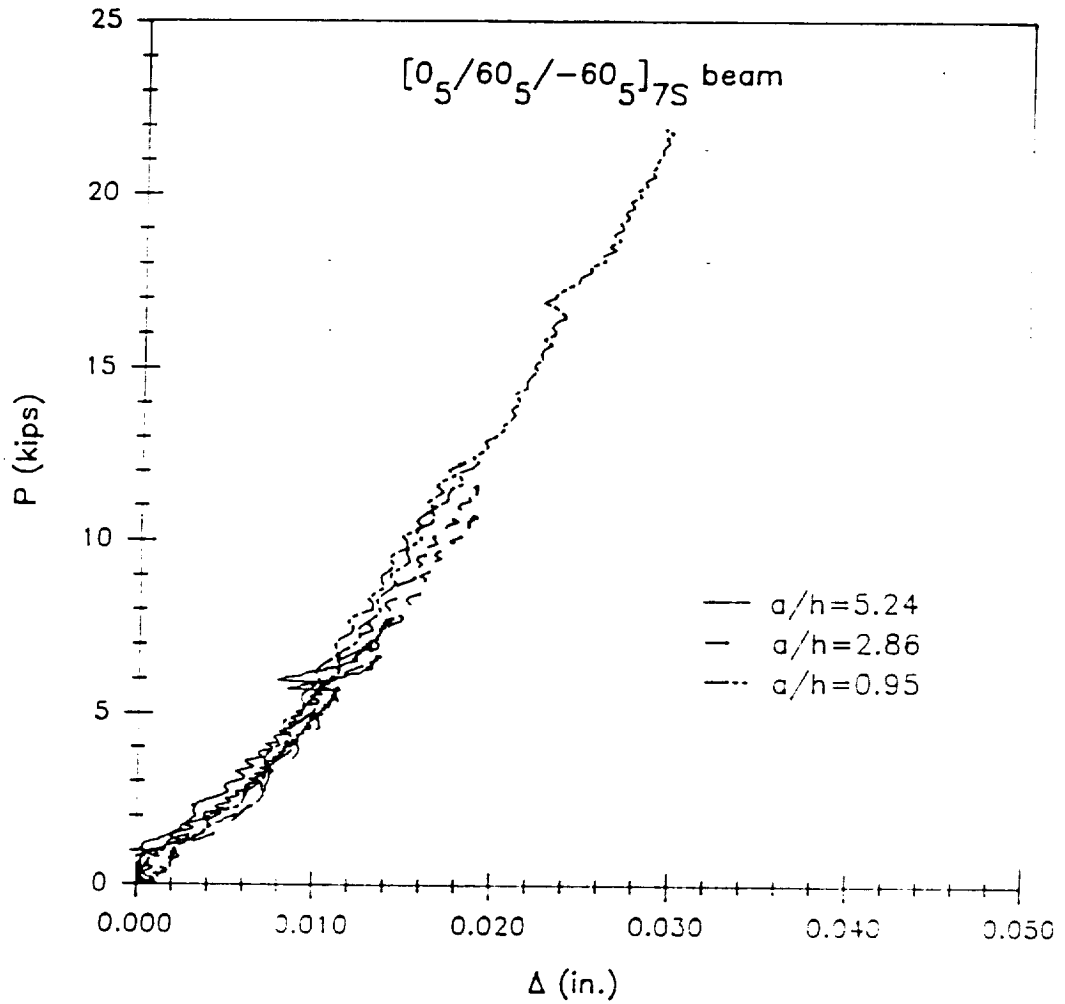
Figure 136. Load versus indentation for the [0/60/-60] grouped laminate.
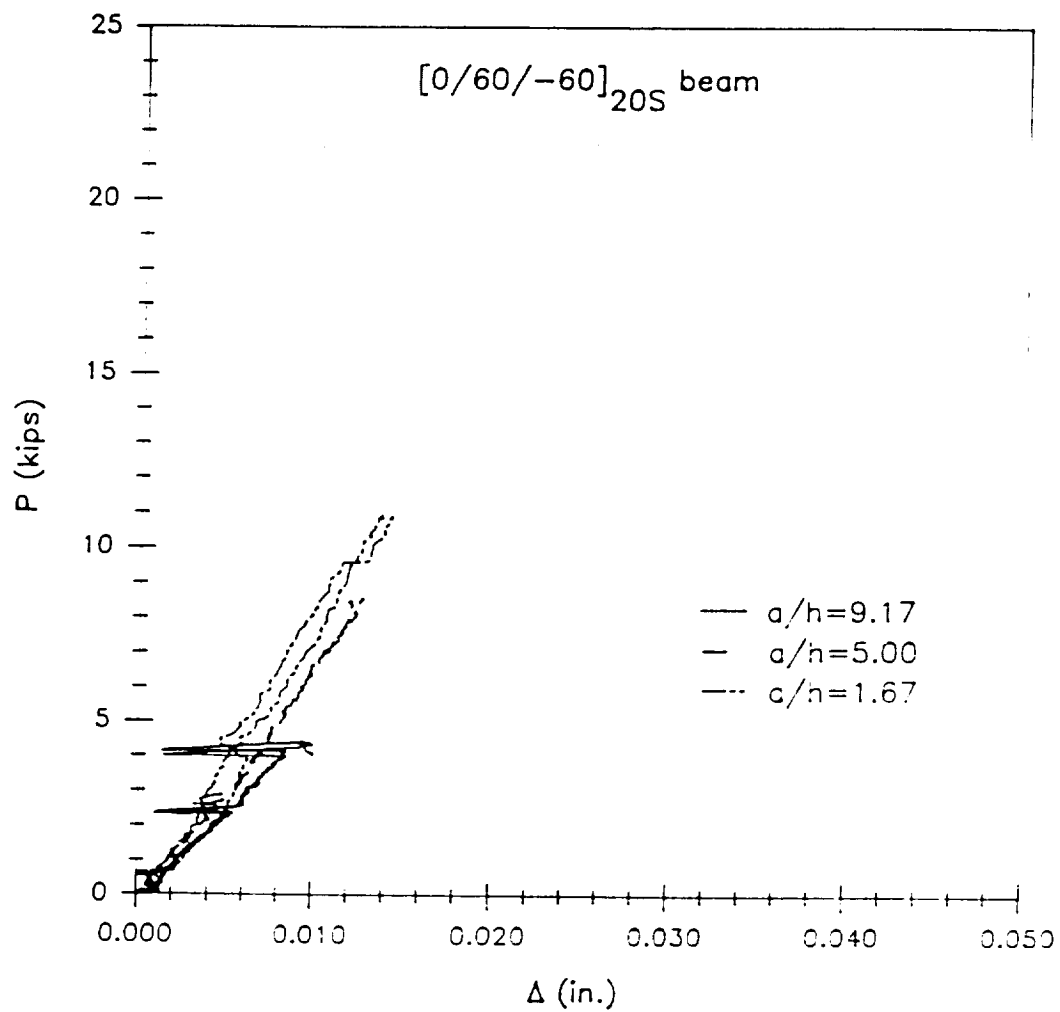
Figure 137. Load versus indentation for the [0/60/-60]$_{20S}$ laminate.
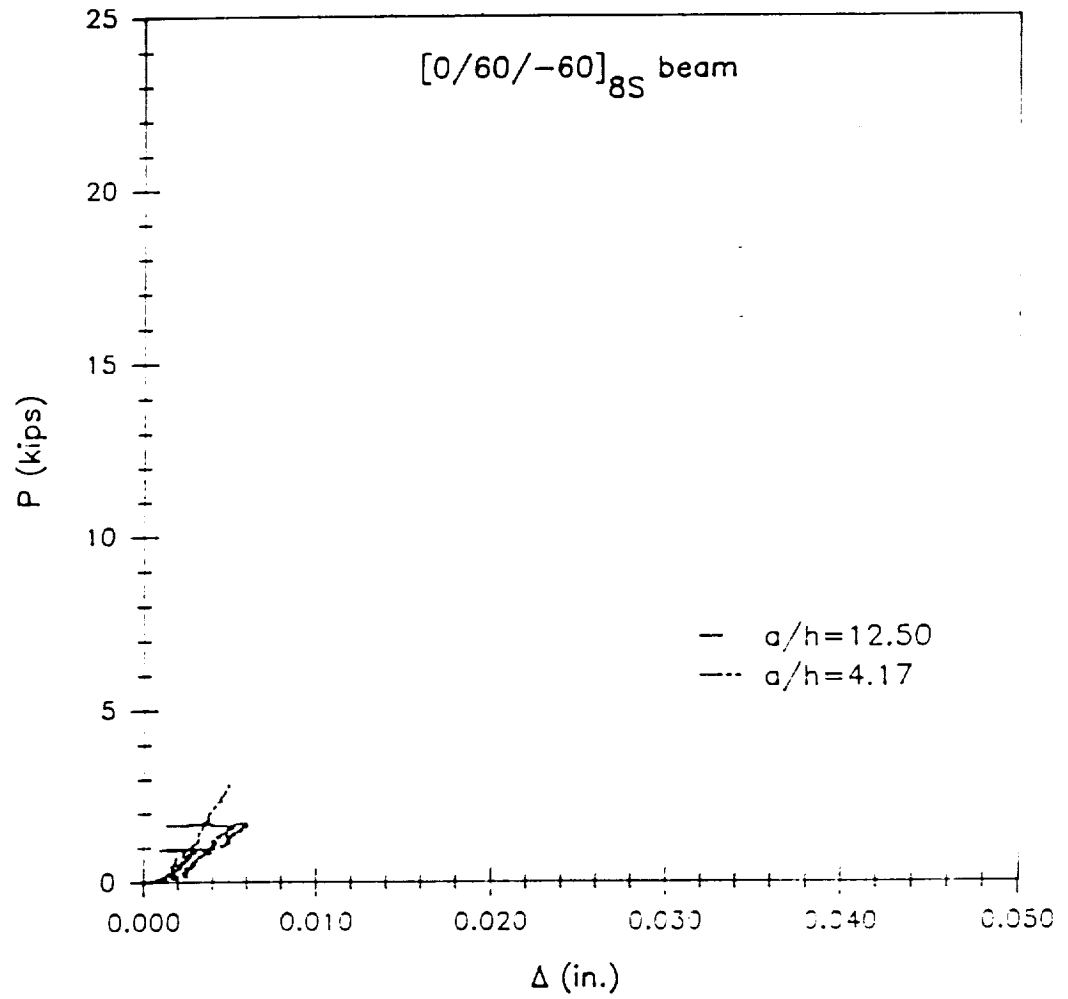
Figure 138.   Load versus indentation for the [0/60/-60]₈S laminate.

Appendix B

Through-the-Thickness Stress Distributions

C-4
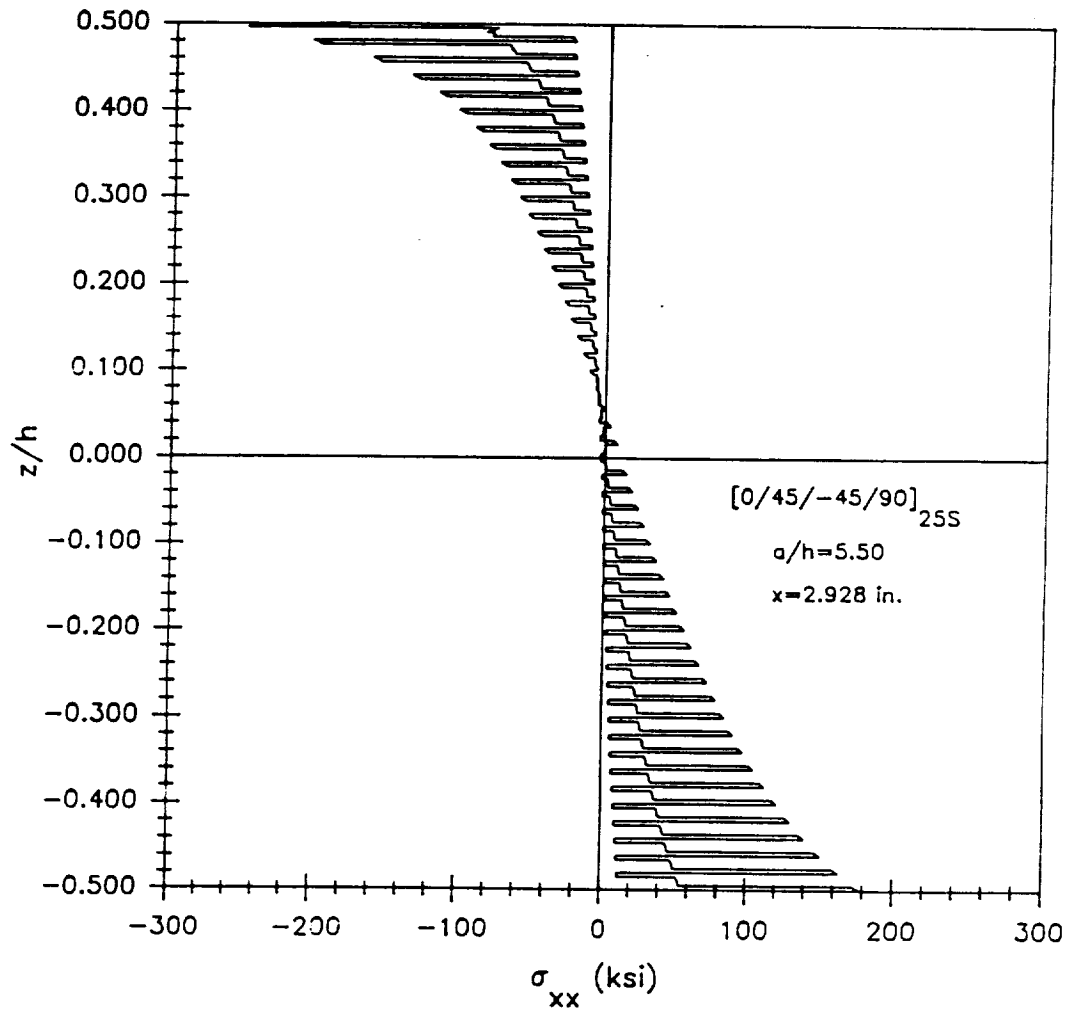
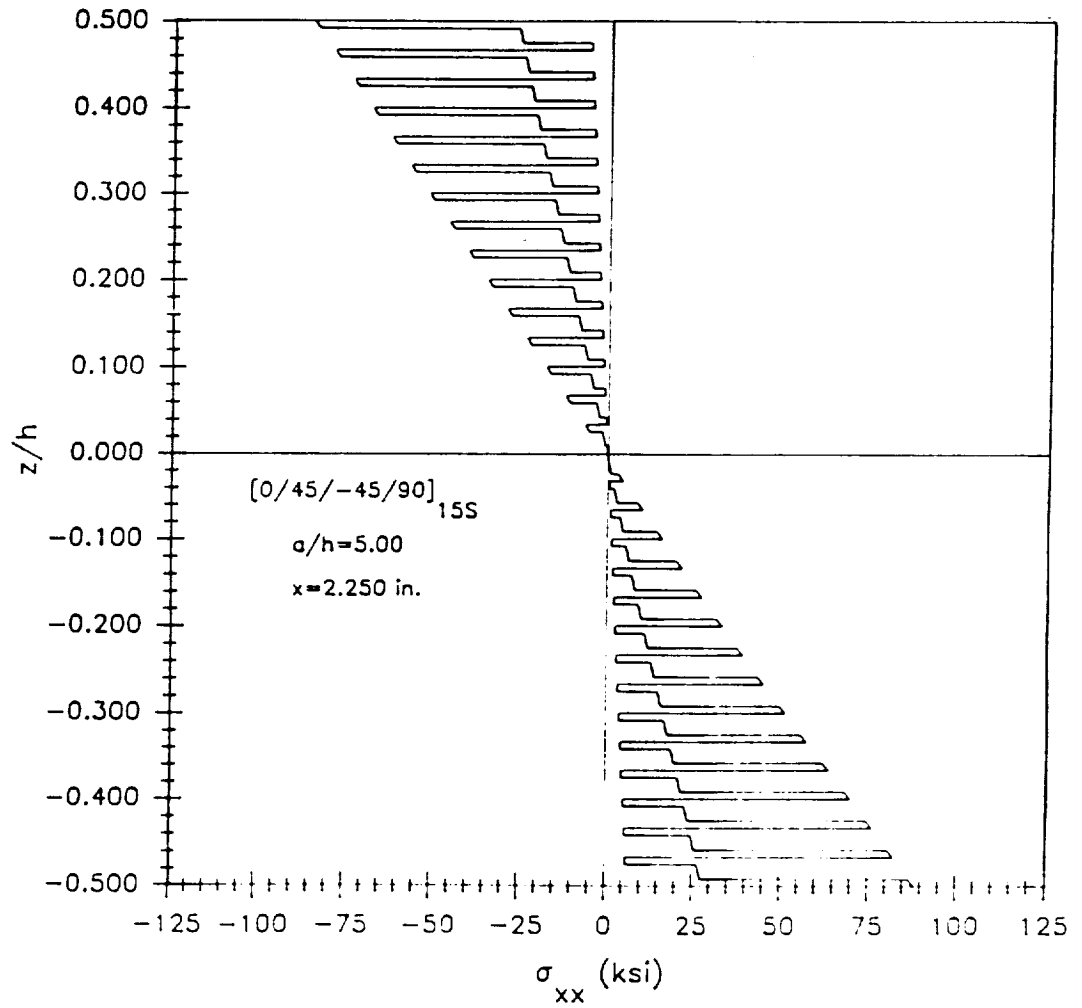**Figure 139.** Through-the-thickness distribution for σ_{xx} in the $[0/45/-45/90]_{25S}$ laminate with an aspect ratio of 5.50.
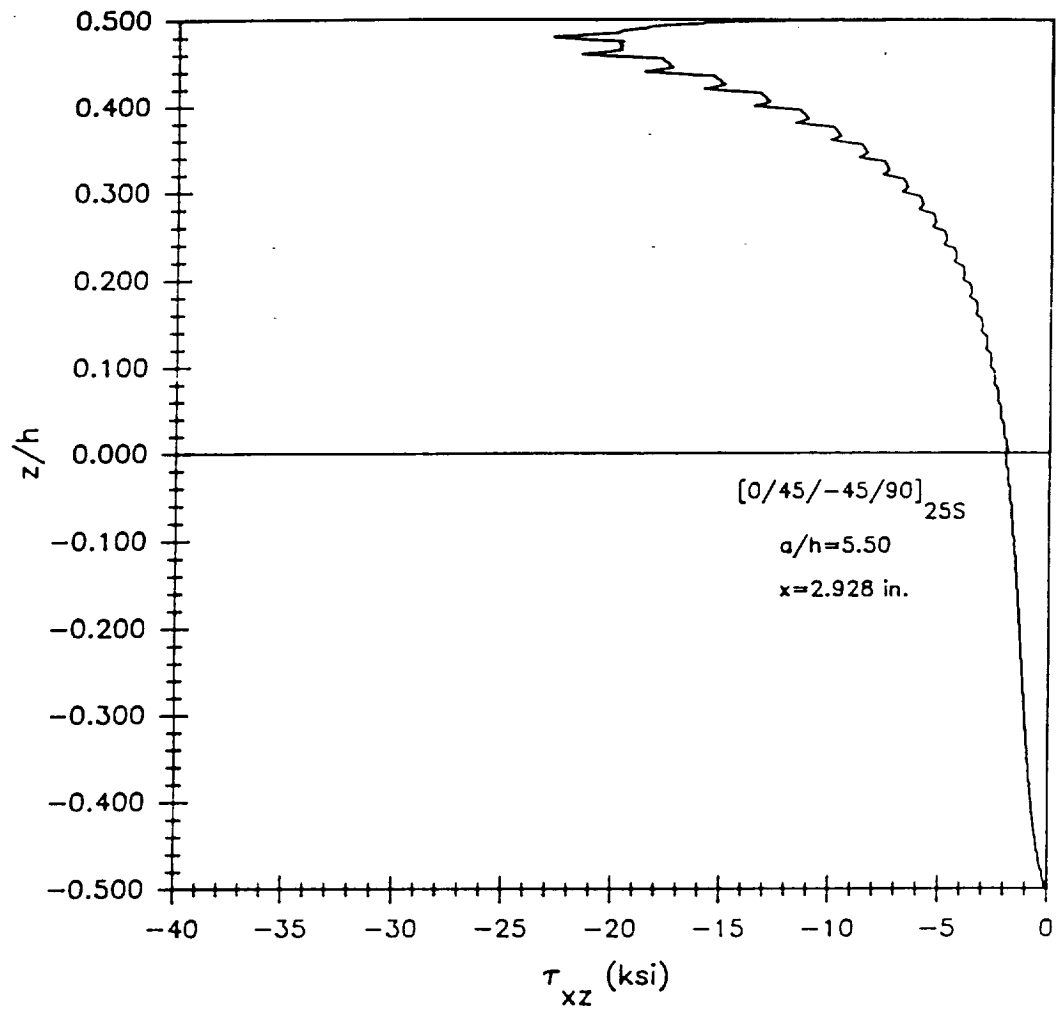
Figure 140. Through-the-thickness distribution for τ_{xz} in the $[0/45/-45/90]_{25S}$ laminate with an aspect ratio of 5.50.
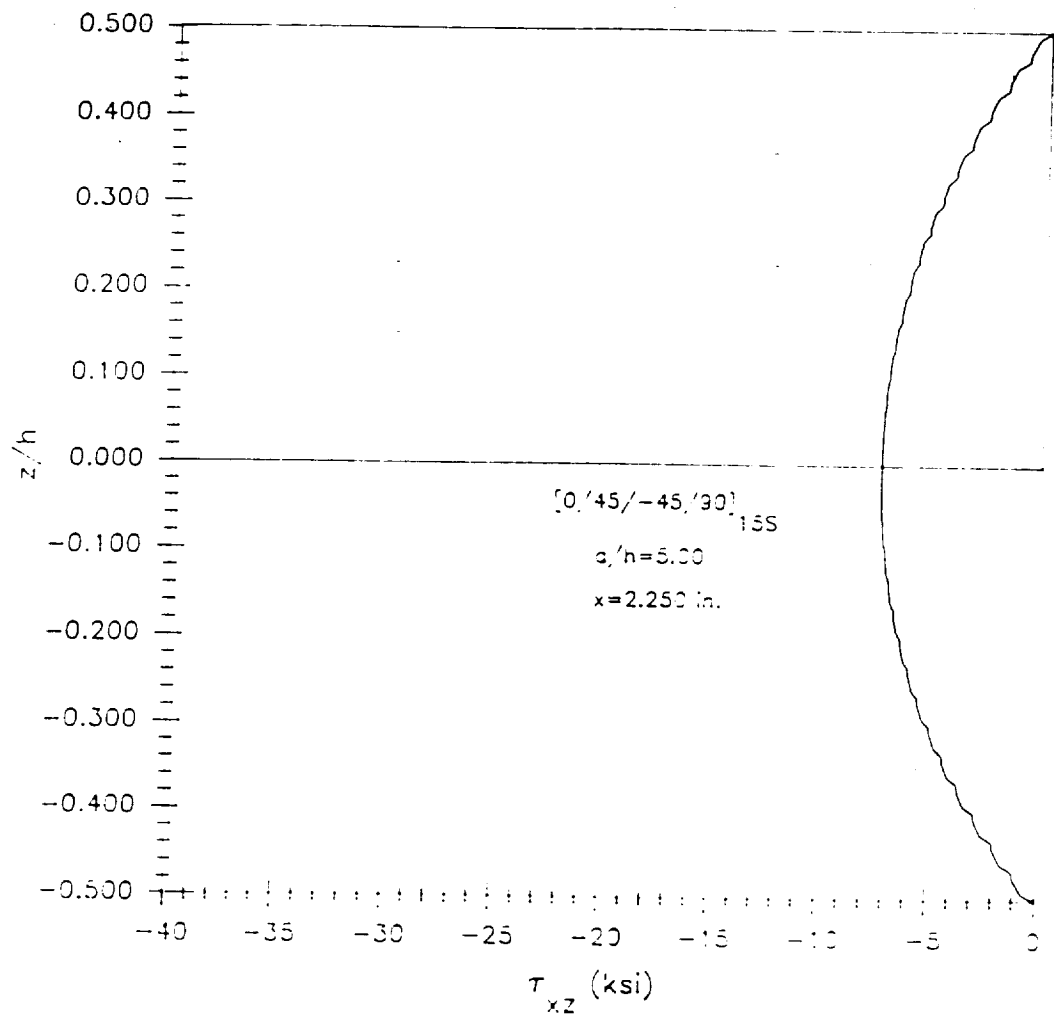
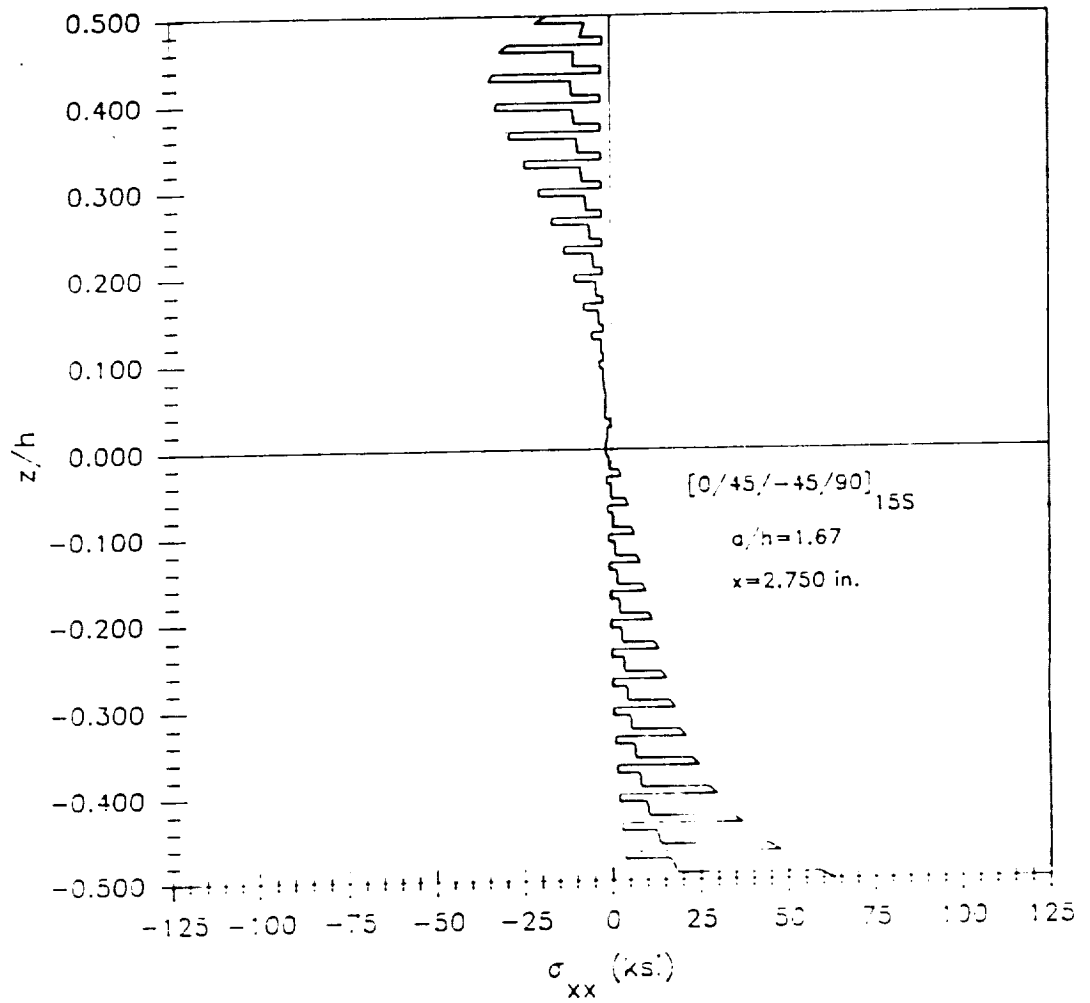Through-the-Thickness Stress Distributions
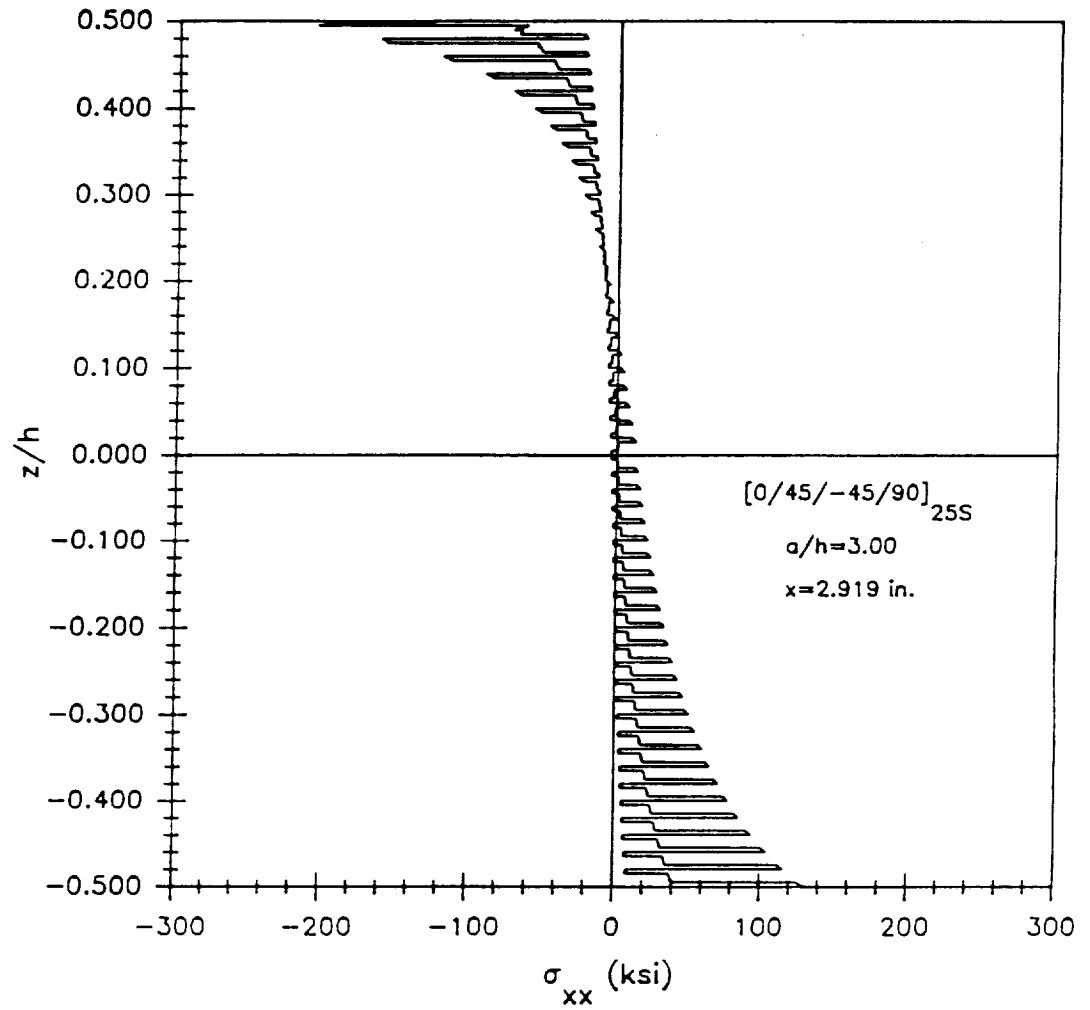
Figure 141. Through-the-thickness distribution for σ_{xx} in the $[0/45/-45/90]_{25S}$ laminate with an aspect ratio of 3.00.
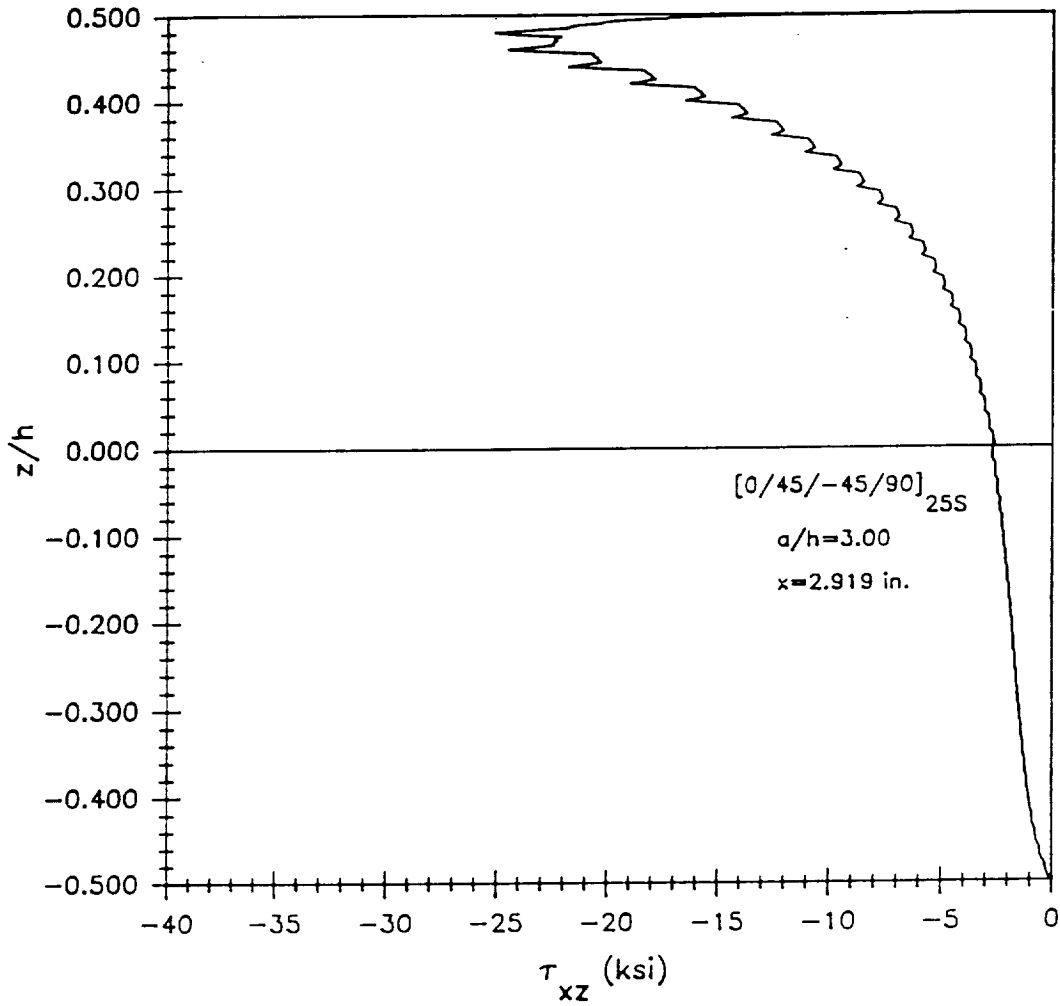
Figure 142. Through-the-thickness distribution for τ_{xz} in the $[0/45/-45/90]_{25S}$ laminate with an aspect ratio of 3.00.
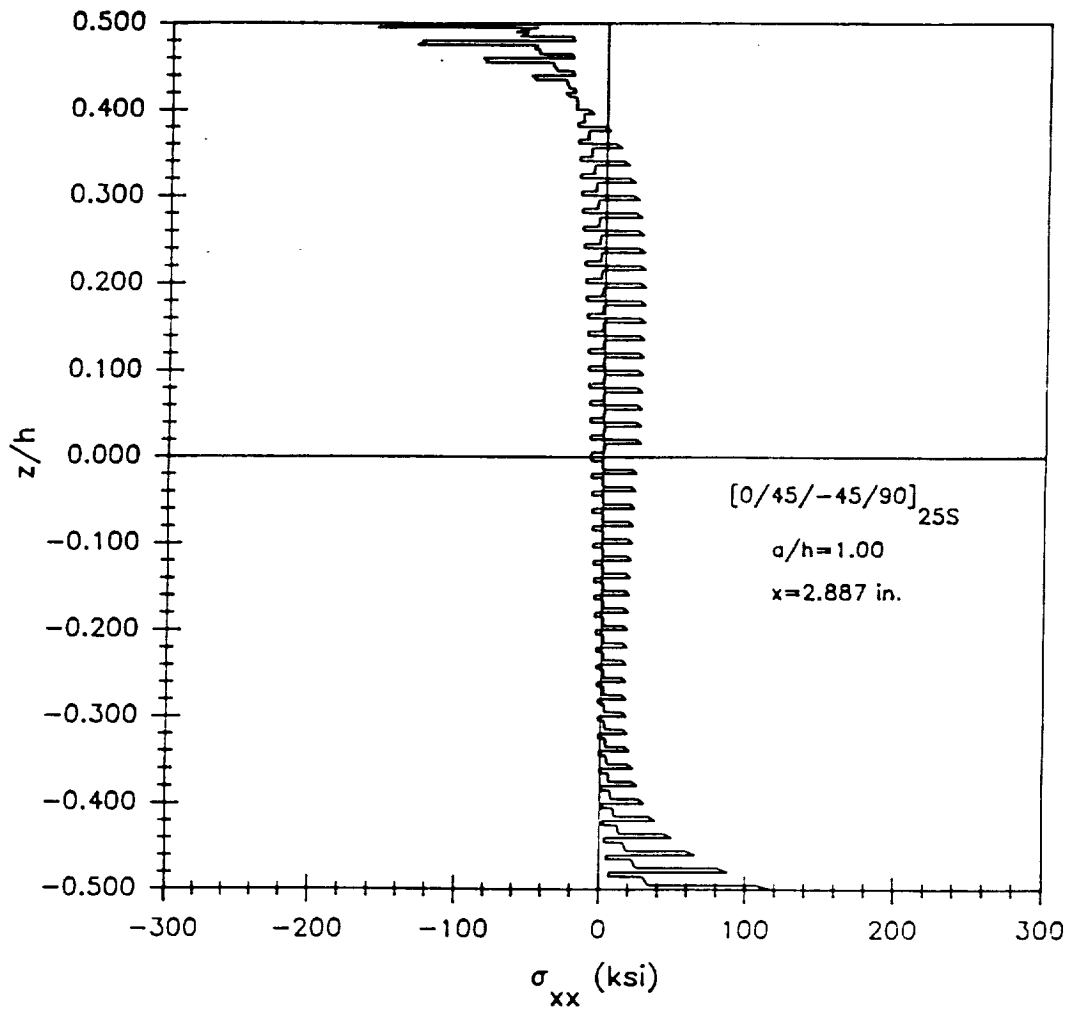
Figure 143. Through-the-thickness distribution for σ_{xx} in the [0/45/-45/90]$_{25S}$ laminate with an aspect ratio of 1.00.
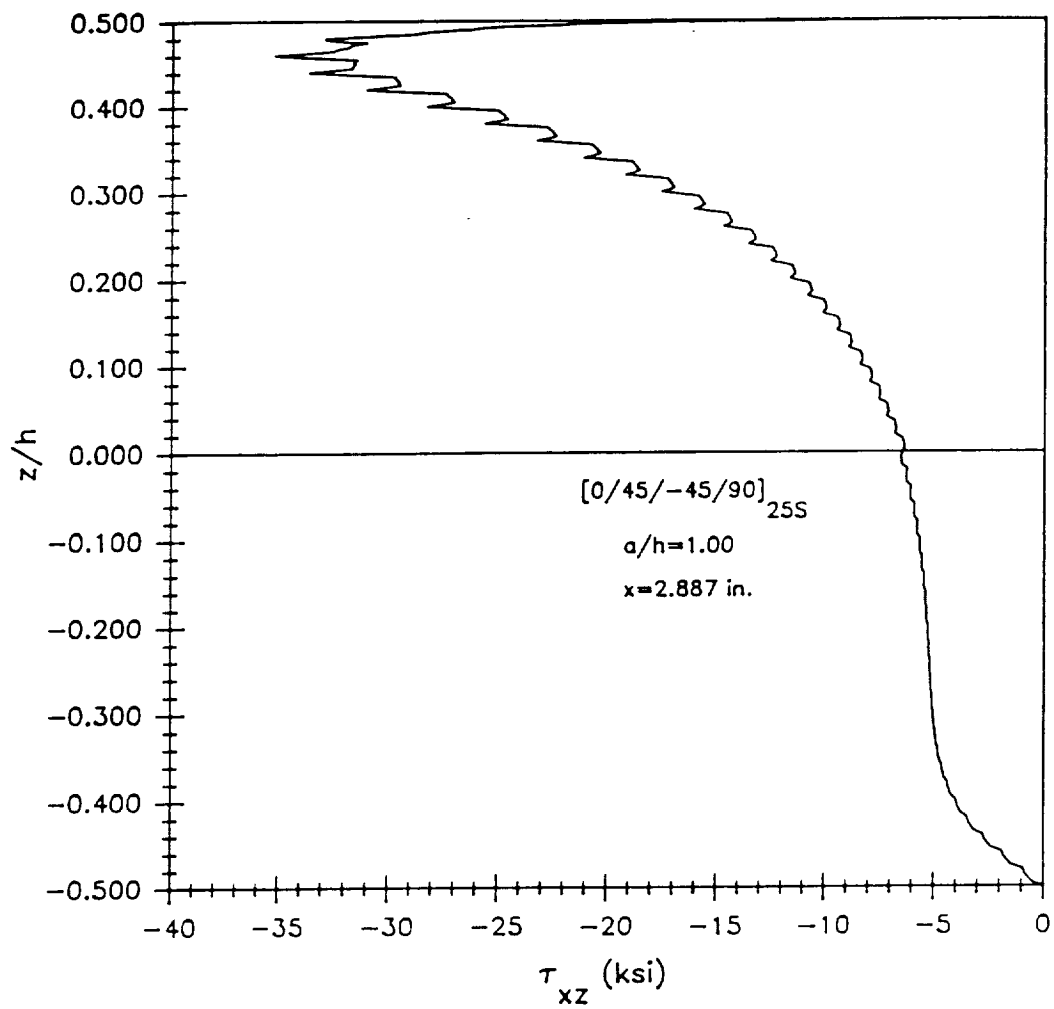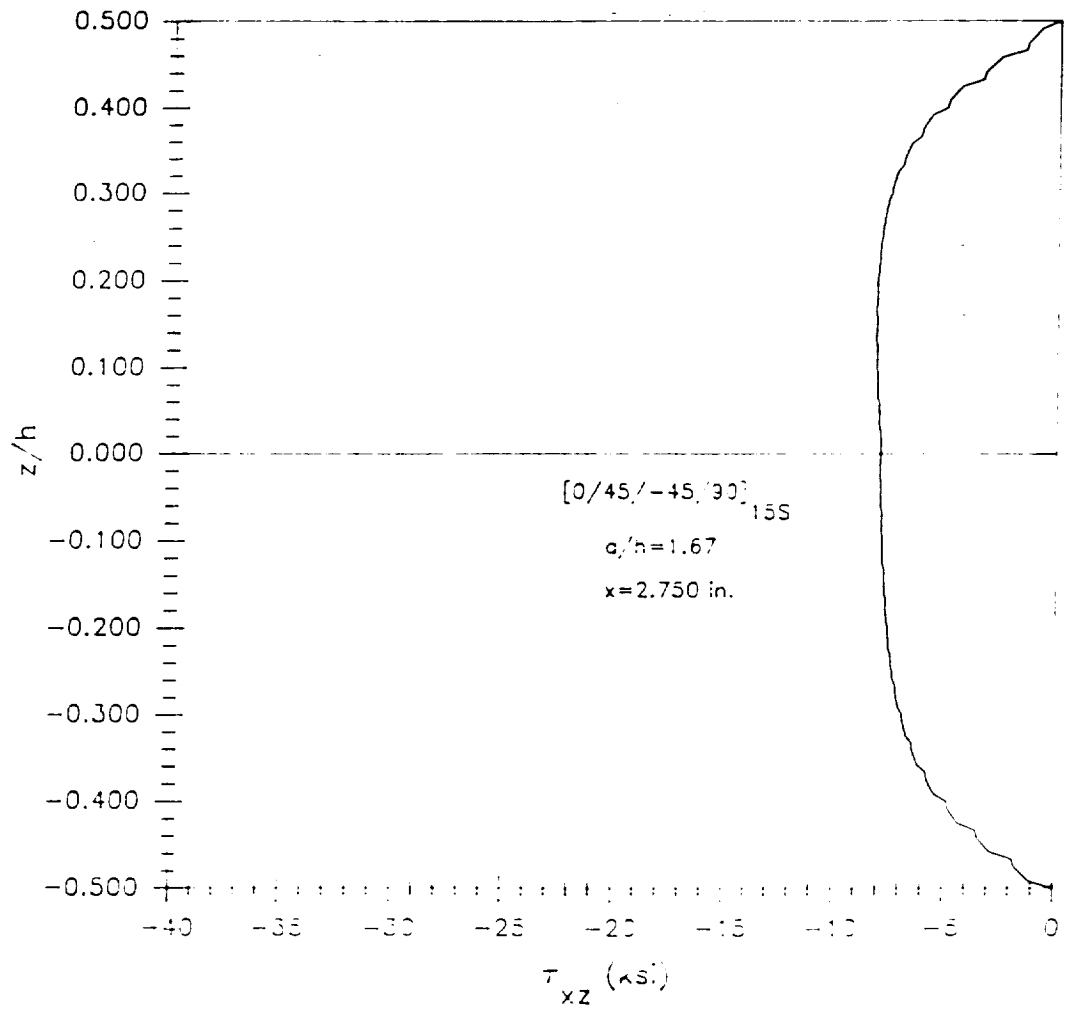
Figure 144. Through-the-thickness distribution for τ_{xz} in the $[0/45/-45/90]_{25S}$ laminate with an aspect ratio of 1.00.
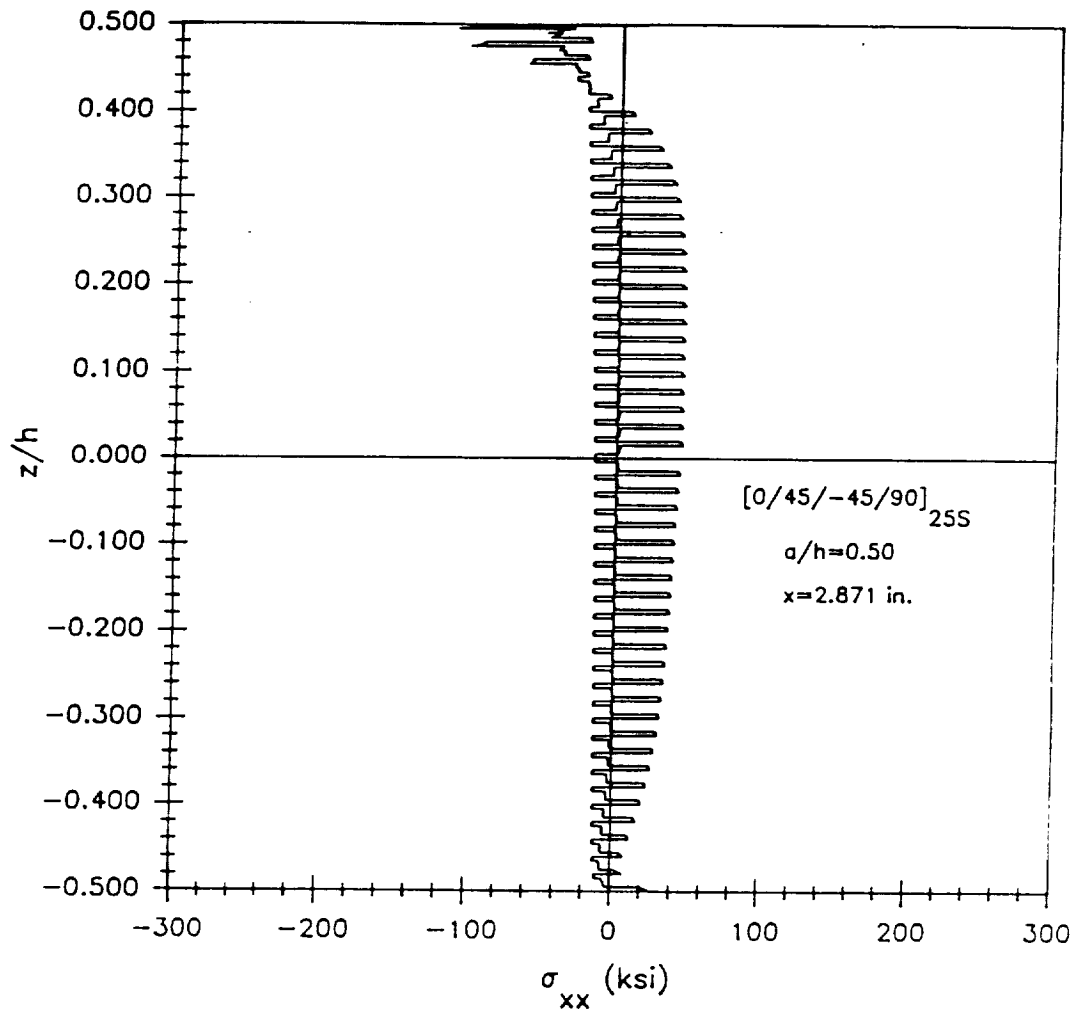
Figure 145. Through-the-thickness distribution for σ_{xx} in the $[0/45/-45/90]_{25S}$ laminate with an aspect ratio of 0.50.
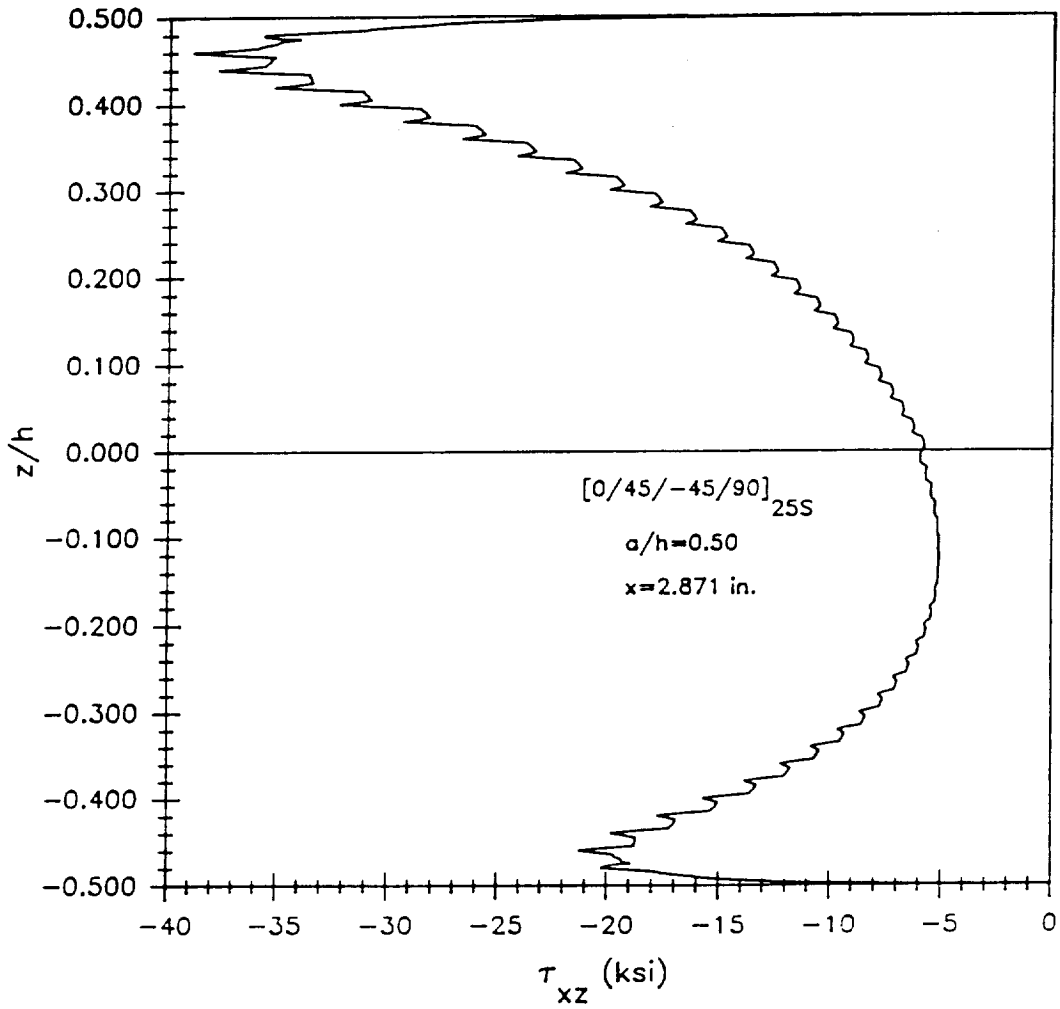
Figure 146. Through-the-thickness distribution for τ_{xz} in the $[0/45/-45/90]_{25S}$ laminate with an aspect ratio of 0.50.
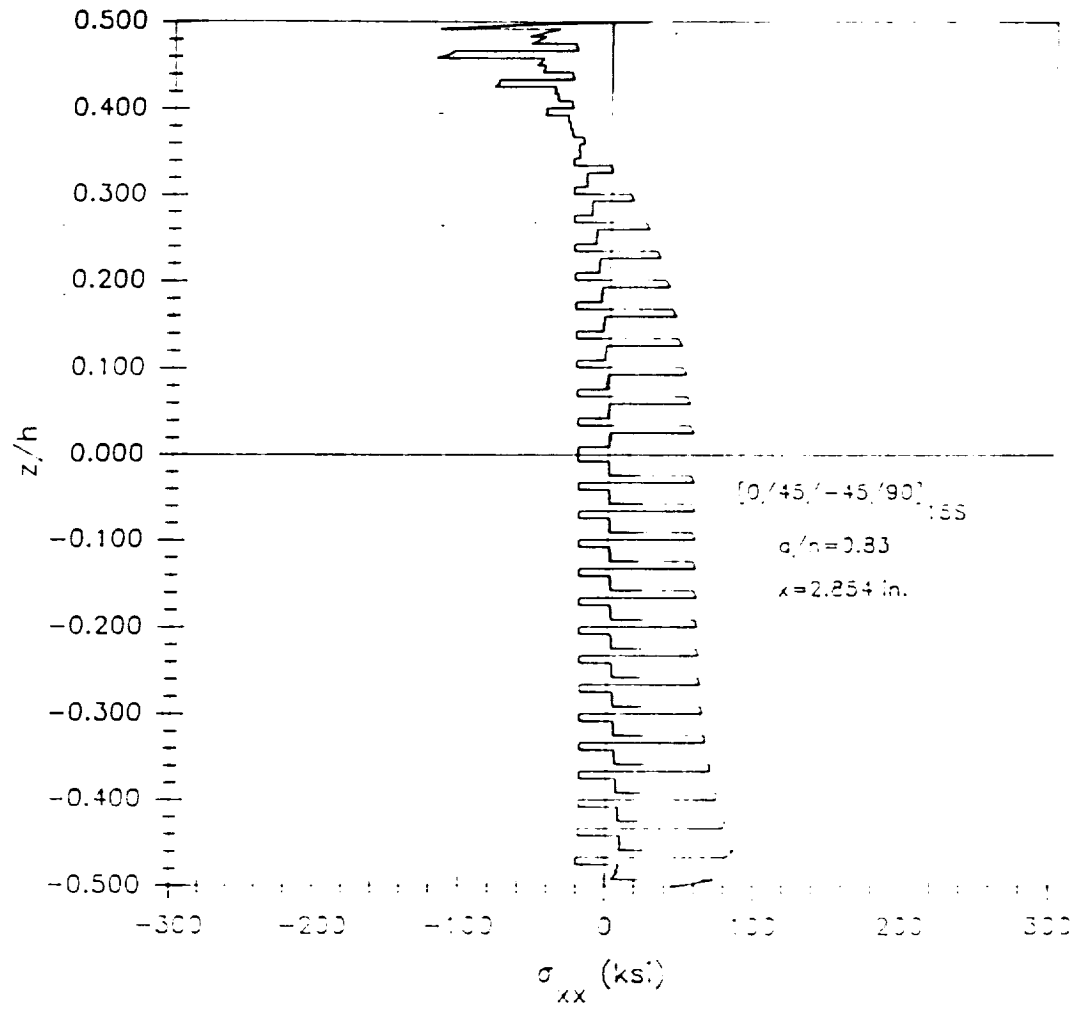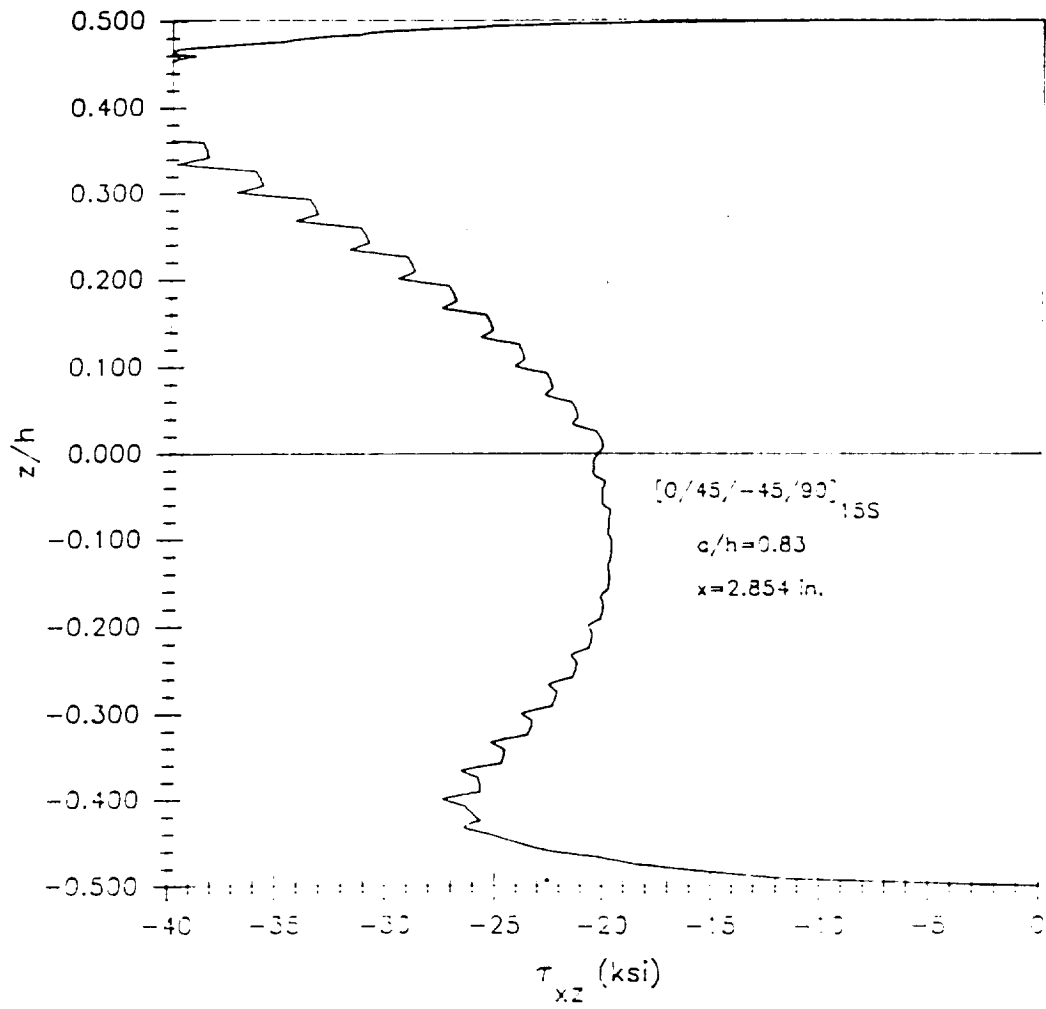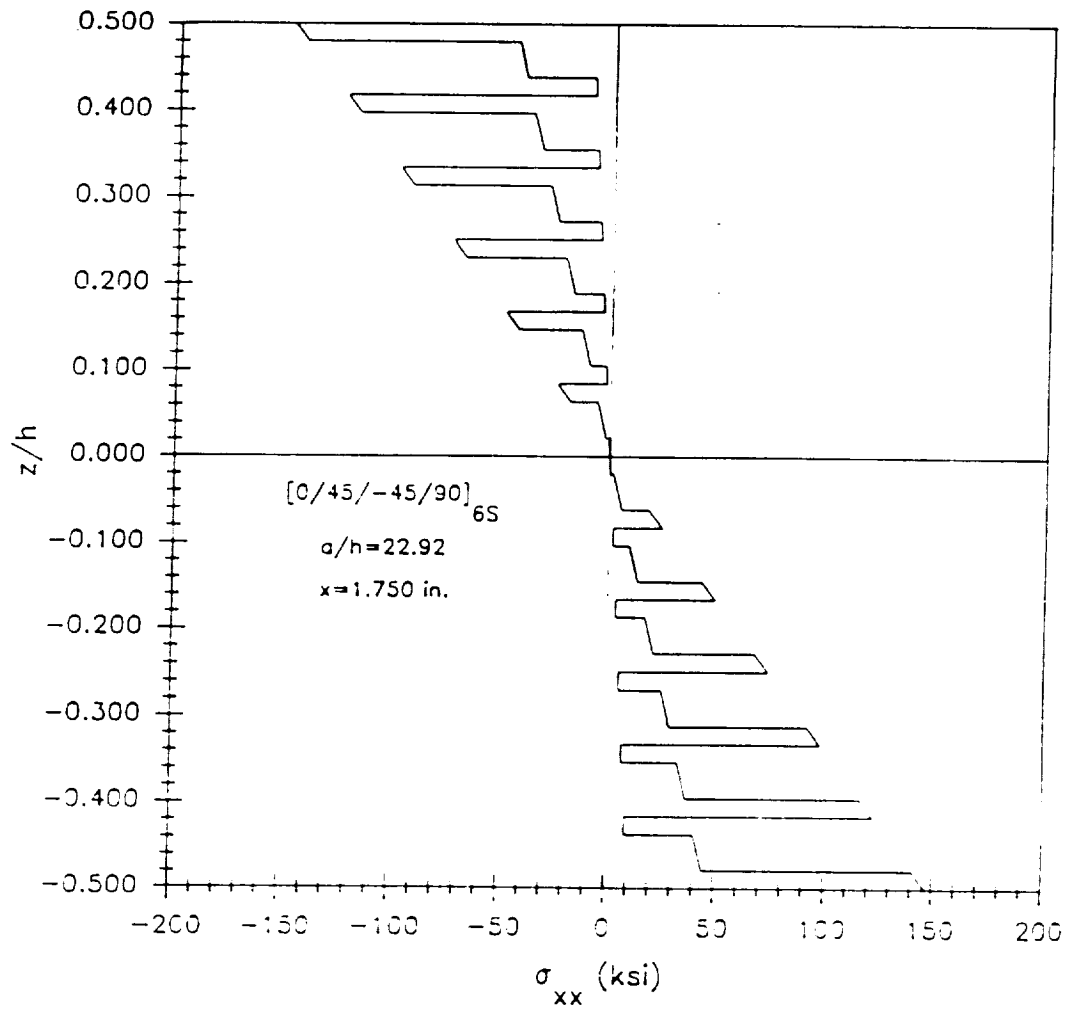
Through-the-Thickness Stress Distributions
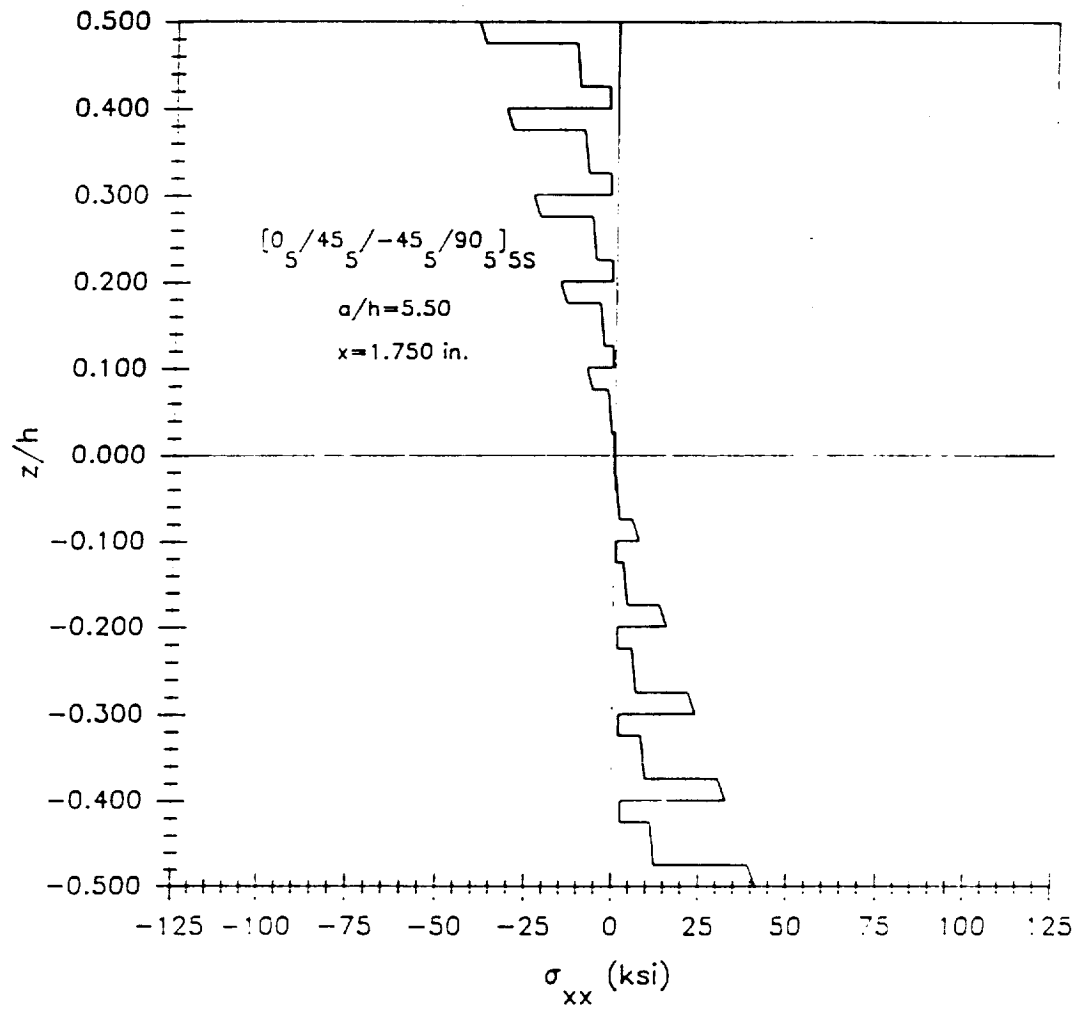
Figure 147. Through-the-thickness distribution for σ_{xx} in the [0/45/-45/90] grouped laminate with an aspect ratio of 5.50.

Through-the-Thickness Stress Distributions
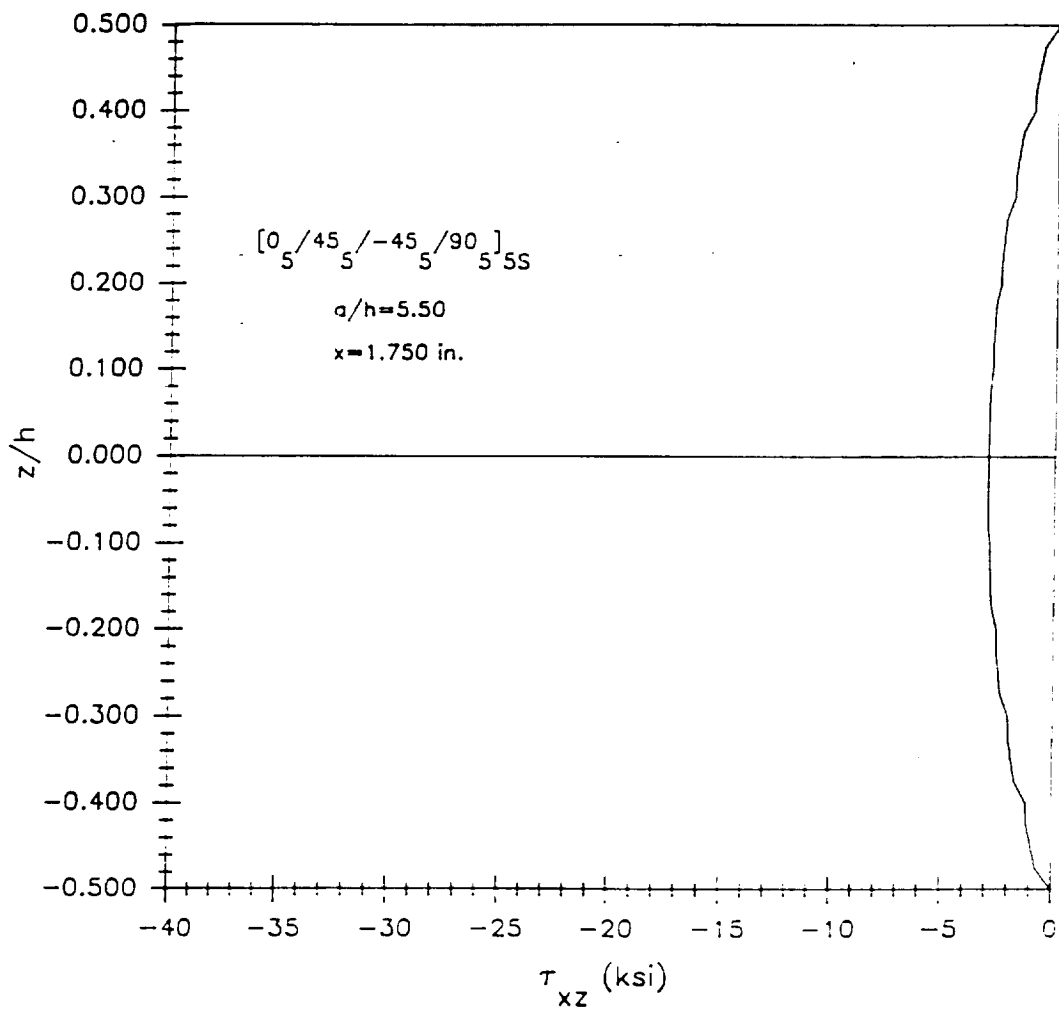
Figure 148. Through-the-thickness distribution for τ_{xz} in the [0/45/-45/90] grouped laminate with an aspect ratio of 5.50.
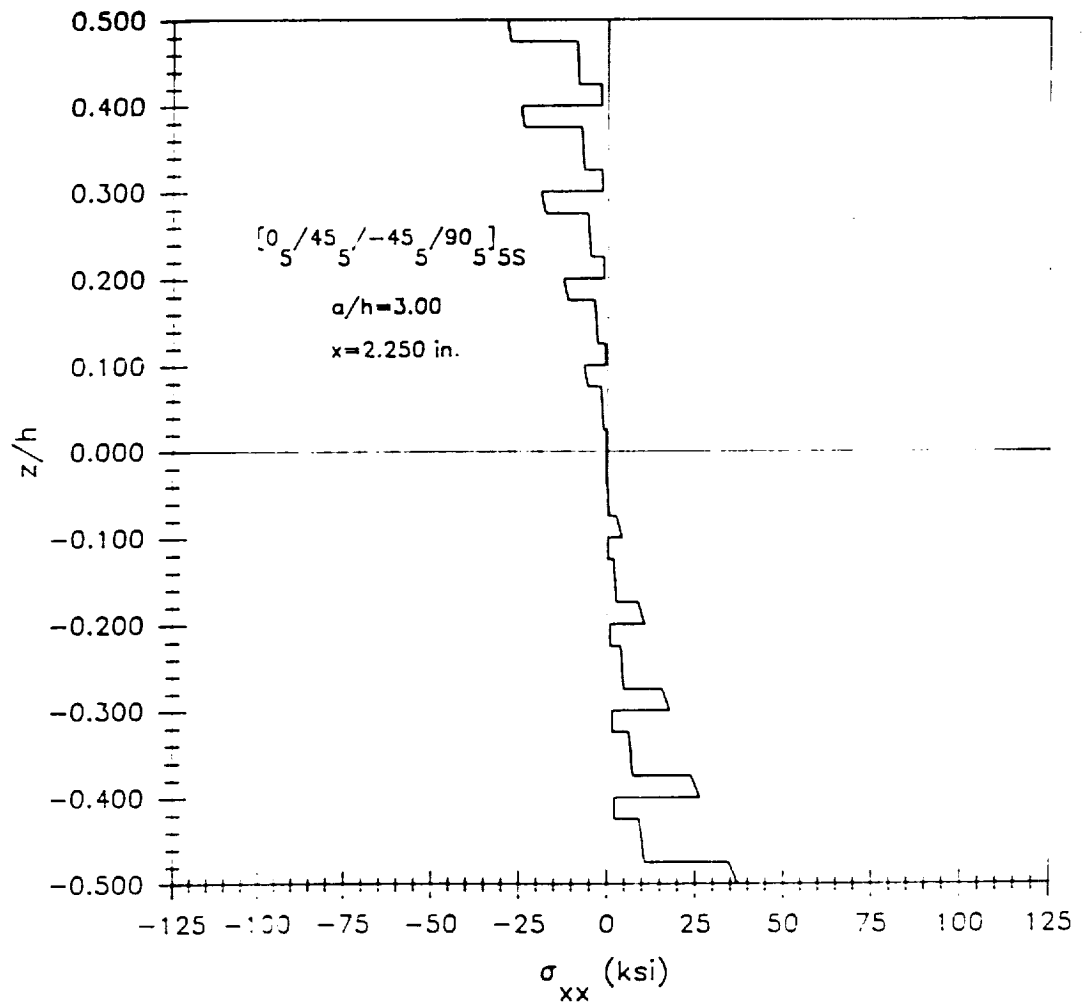
Figure 149. Through-the-thickness distribution for σ_{xx} in the [0/45/-45/90] grouped laminate with an aspect ratio of 3.00.
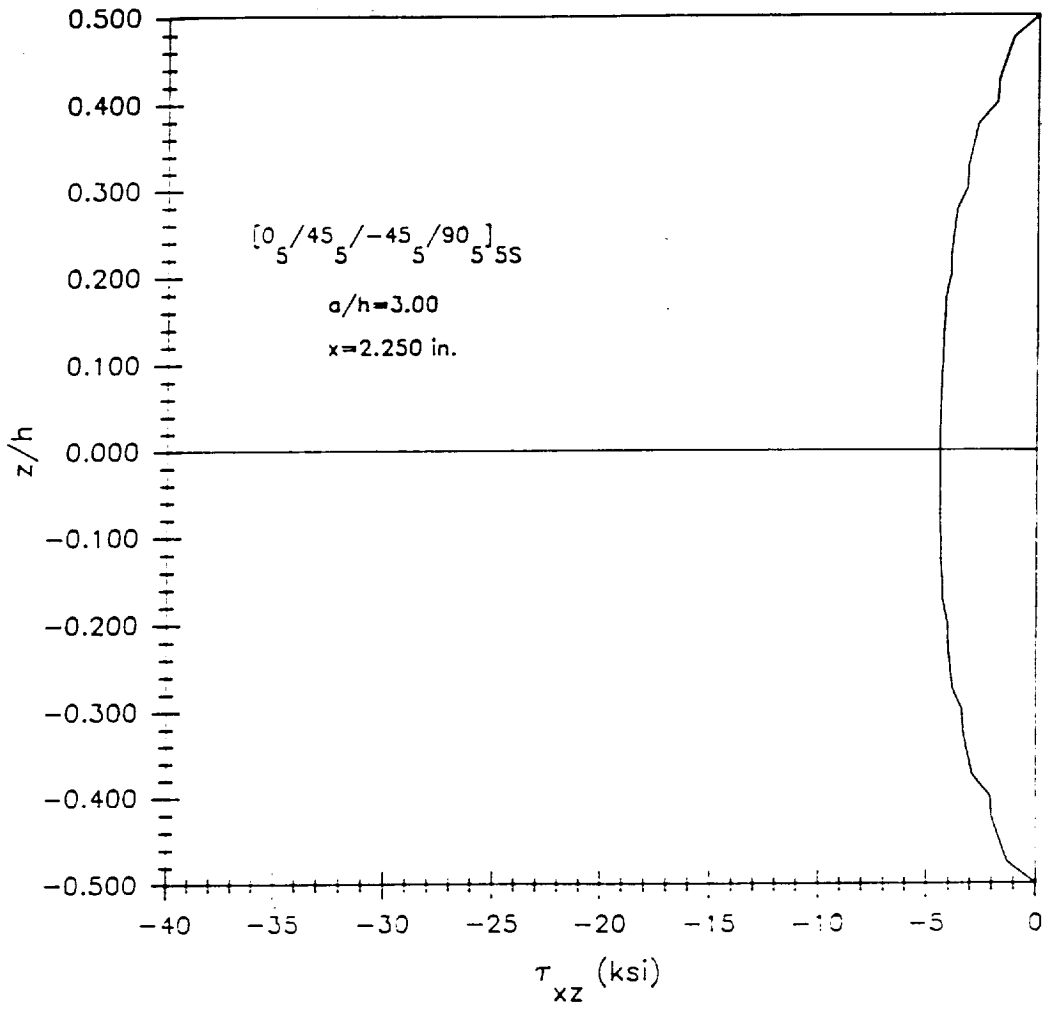
Figure 150. Through-the-thickness distribution for τ_{xz} in the [0/45/-45/90] grouped laminate with an aspect ratio of 3.00.
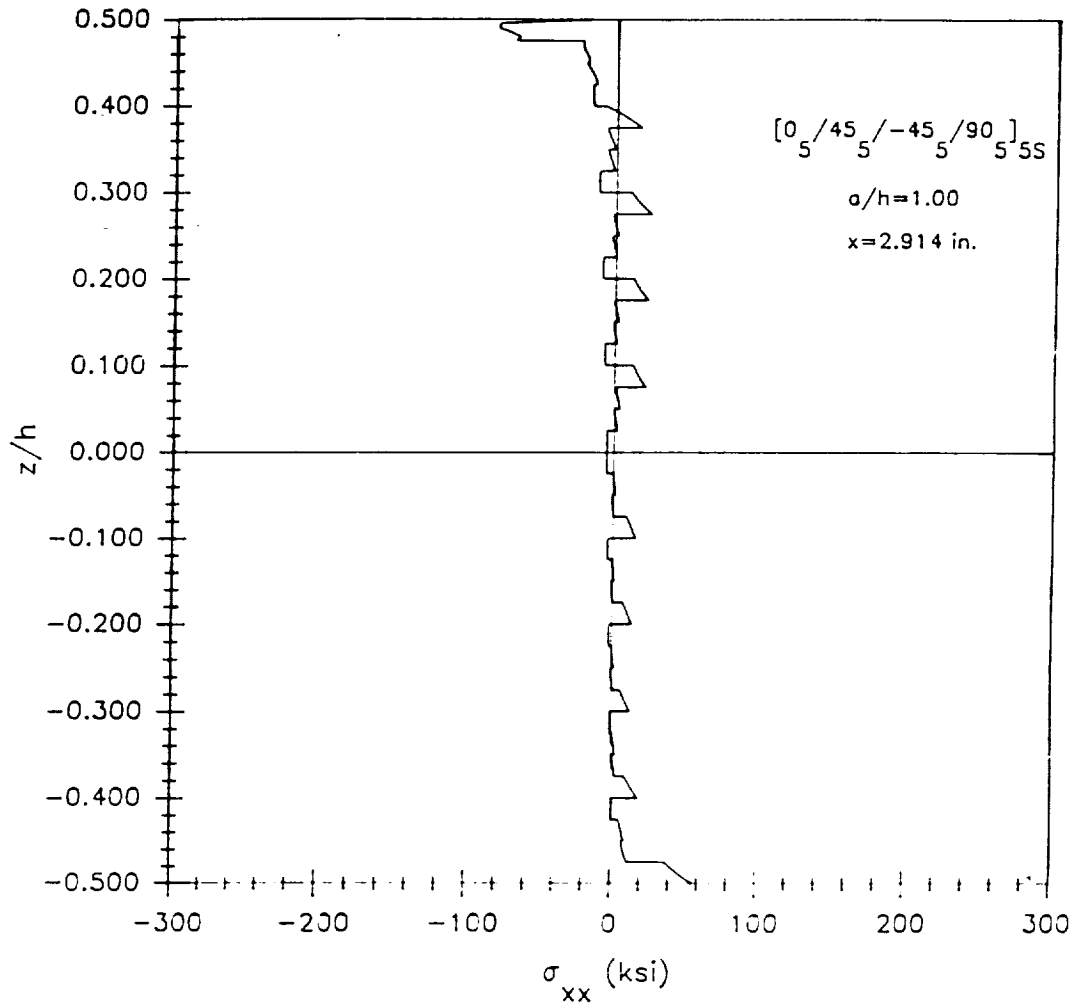
Figure 151. Through-the-thickness distribution for σ_{xx} in the [0/45/-45/90] grouped laminate with an aspect ratio of 1.00.
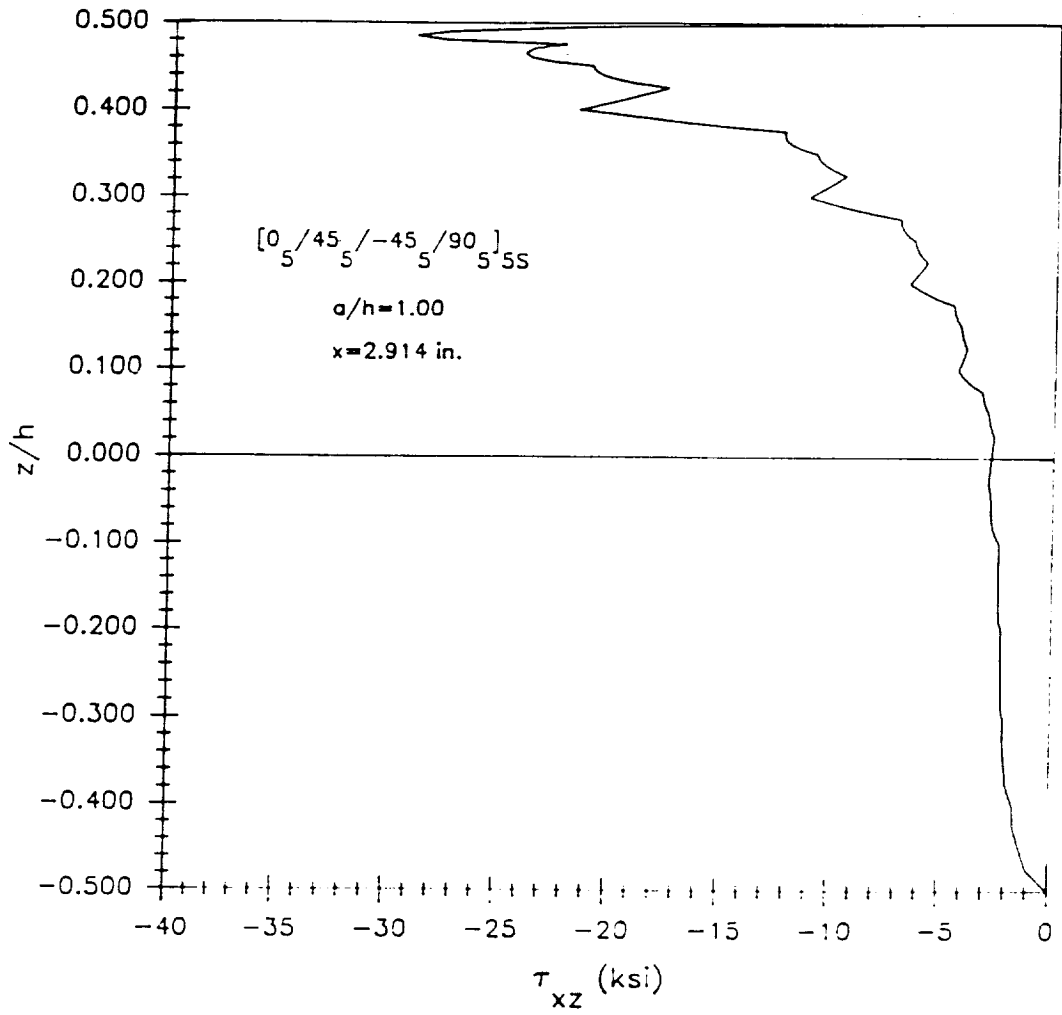
Figure 152. Through-the-thickness distribution for τ_{xz} in the [0/45/-45/90] grouped laminate with an aspect ratio of 1.00.
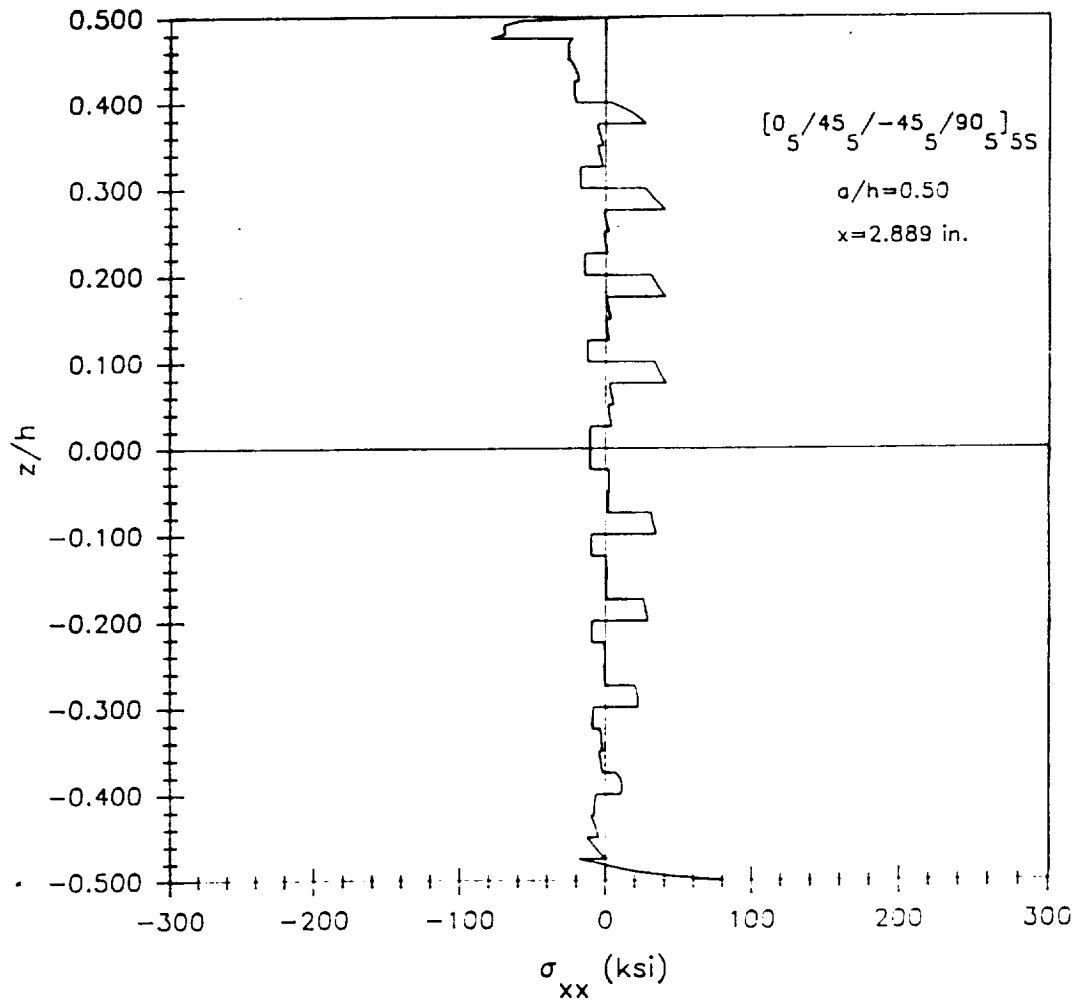
Figure 153. Through-the-thickness distribution for σ_{xx} In the [0/45/-45/90] grouped laminate with an aspect ratio of 0.50.

0.500

0.400

0.300

$[0_5/45_5/-45_5/90_5]_{5S}$

0.200

a/h=0.50

x=2.889 in.

0.100

z/h 0.000

−0.100

−0.200

−0.300

−0.400

−0.500

−40 −35 −30 −25 −20 −15 −10 −5 0

τ_{xz} (ksi)
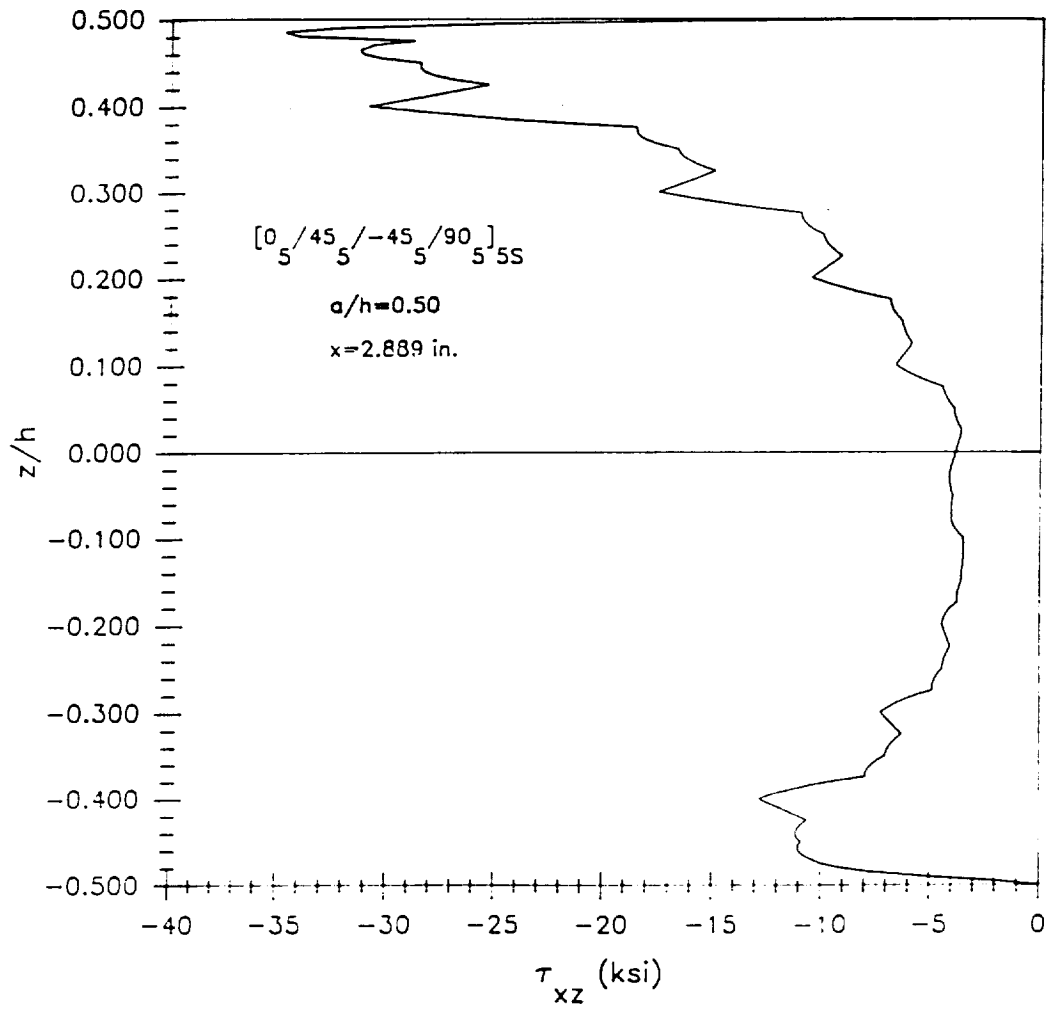
Figure 154. Through-the-thickness distribution for τ_{xz} in the [0/45/-45/90] grouped laminate with an aspect ratio of 0.50.
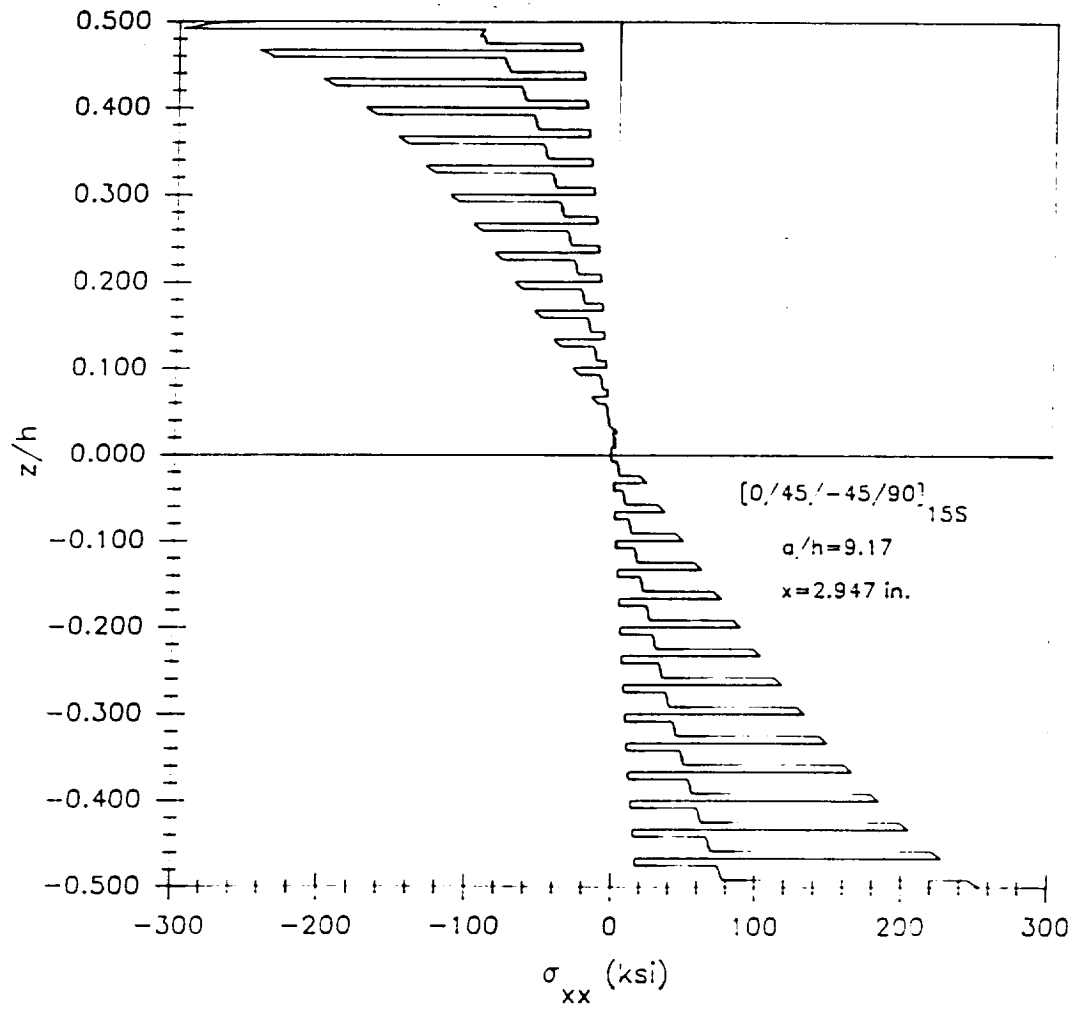
Figure 155. Through-the-thickness distribution for σ_{xx} in the $[0/45/-45/90]_{15S}$ laminate with an aspect ratio of 9.17.
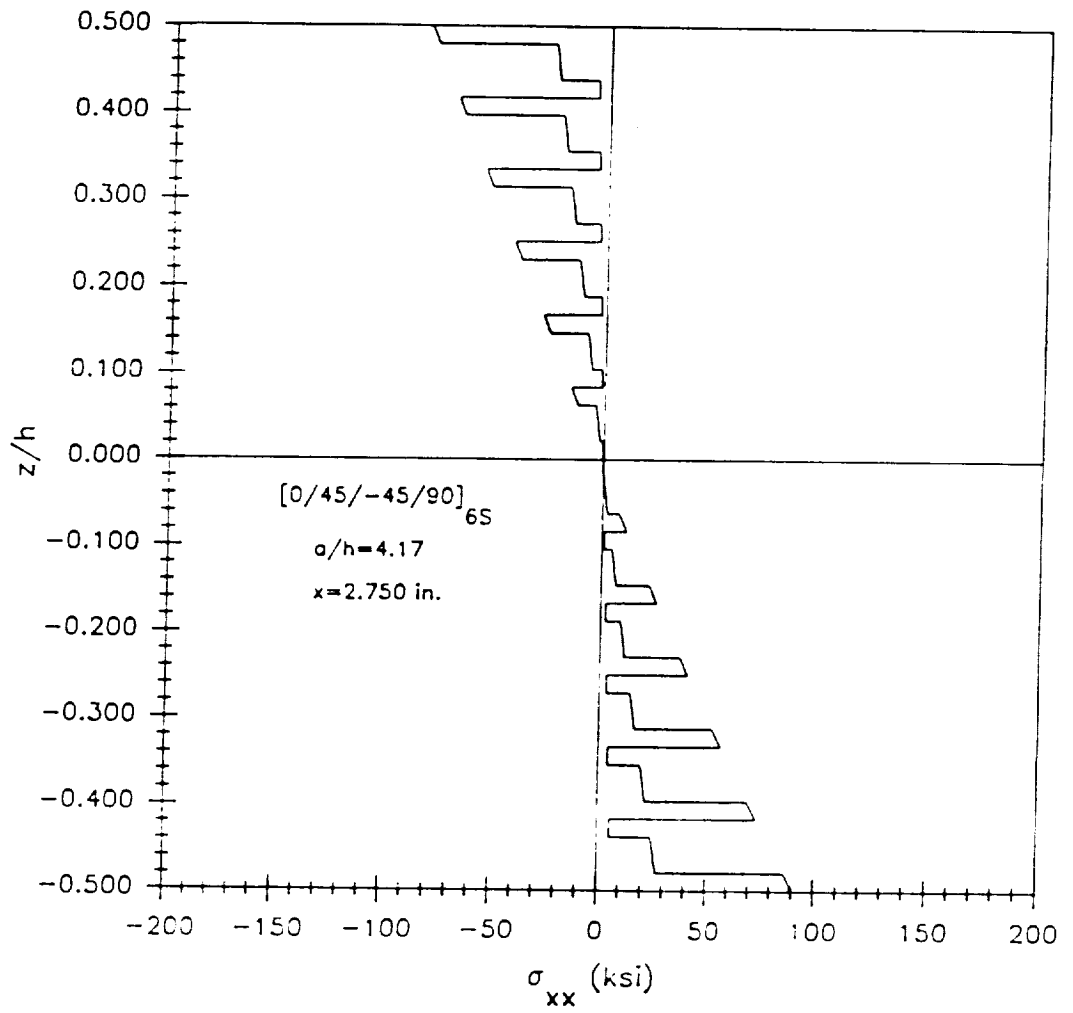
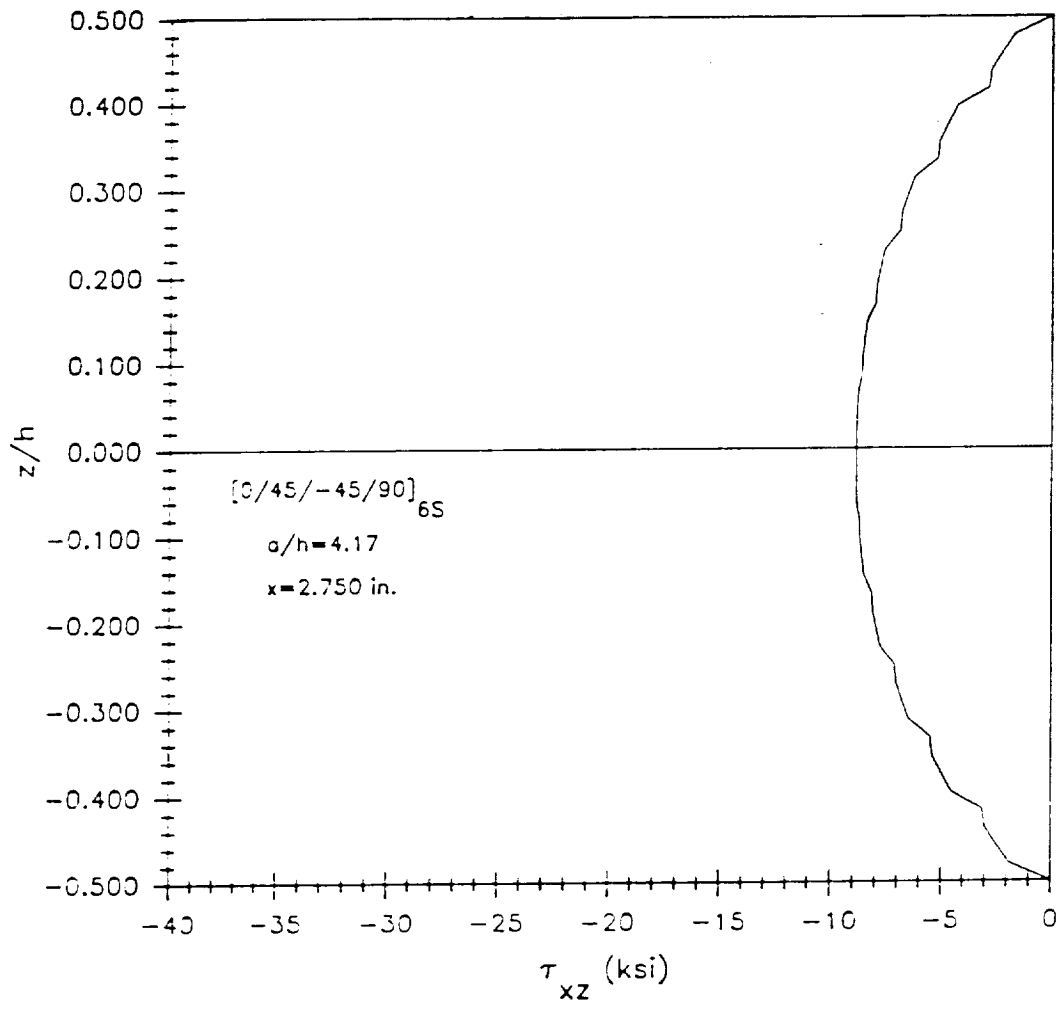Through-the-Thickness Stress Distributions
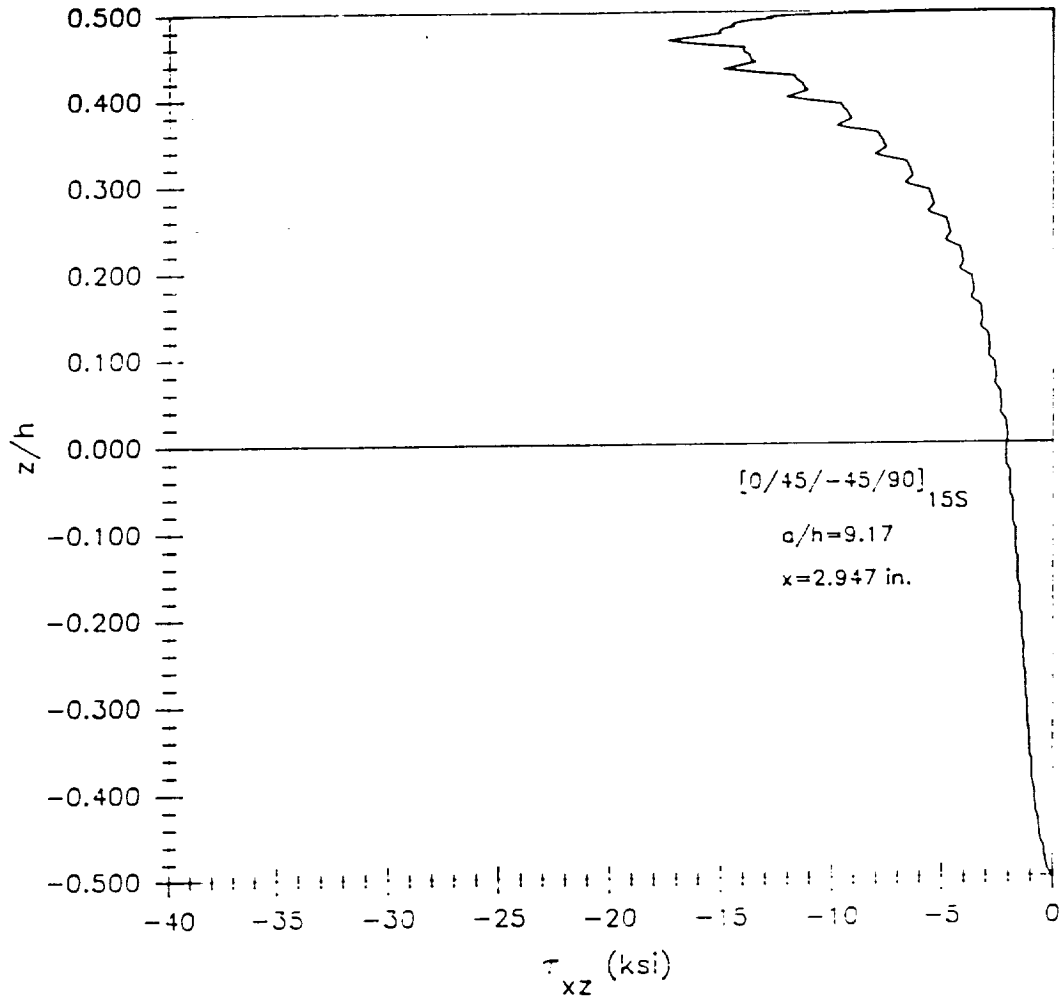
Figure 156. Through-the-thickness distribution for τ_{xz} in the $[0/45/-45/90]_{15S}$ laminate with an aspect ratio of 9.17.

Figure 157. Through-the-thickness distribution for σ_{xx} in the $[0/45/-45/90]_{15S}$ laminate with an aspect ratio of 5.00.

Through-the-Thickness Stress Distributions

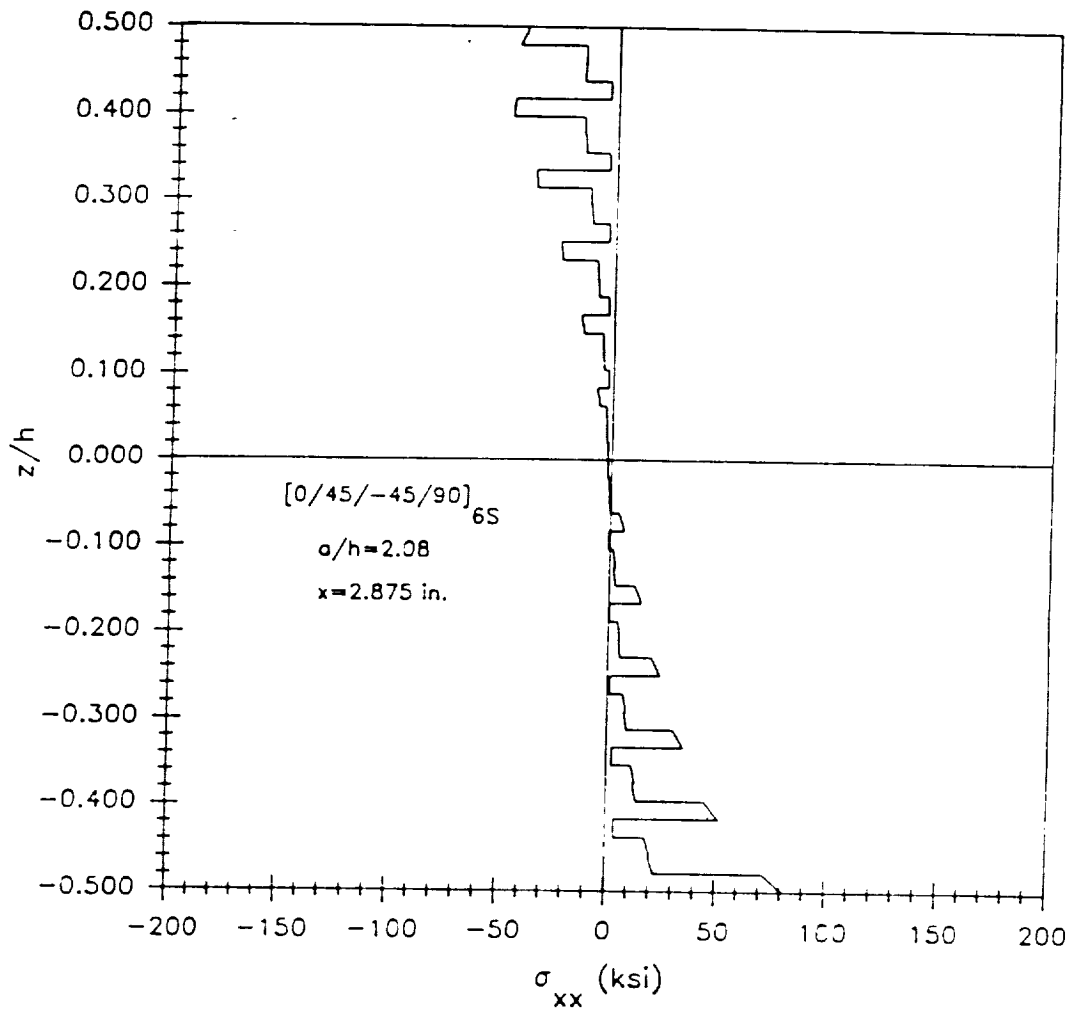**Figure 158.** Through-the-thickness distribution for τ_{xz} in the $[0/45/-45/90]_{15S}$ laminate with an aspect ratio of 5.00.

Through-the-Thickness Stress Distributions

Figure 159. Through-the-thickness distribution for σ_{xx} in the $[0/45/-45/90]_{15S}$ laminate with an aspect ratio of 1.67.

Figure 160. Through-the-thickness distribution for τ_{xz} in the $[0/45/-45/90]_{15S}$ laminate with an aspect ratio of 1.67.
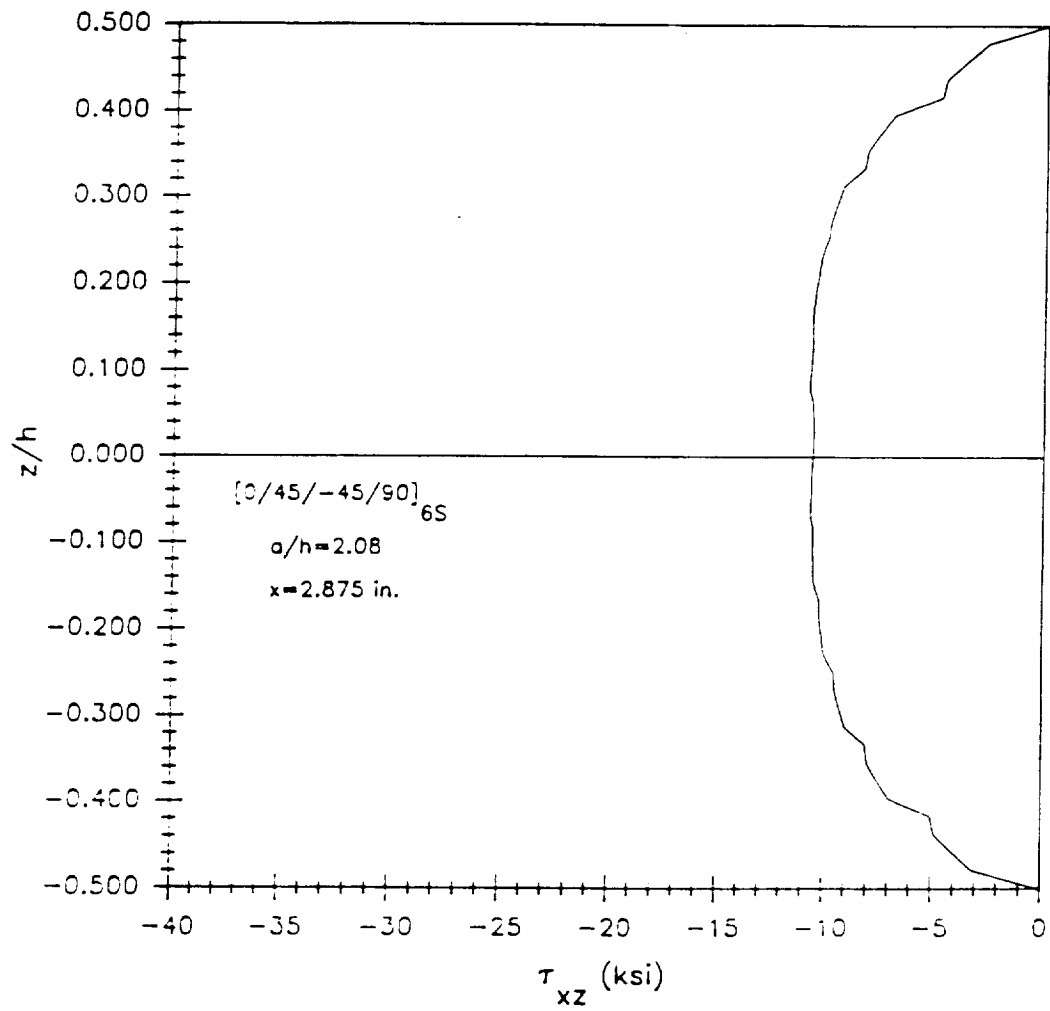
Figure 161. Through-the-thickness distribution for σ_{xx} in the [0/45/-45/90]$_{15S}$ laminate with an aspect ratio of 0.83.

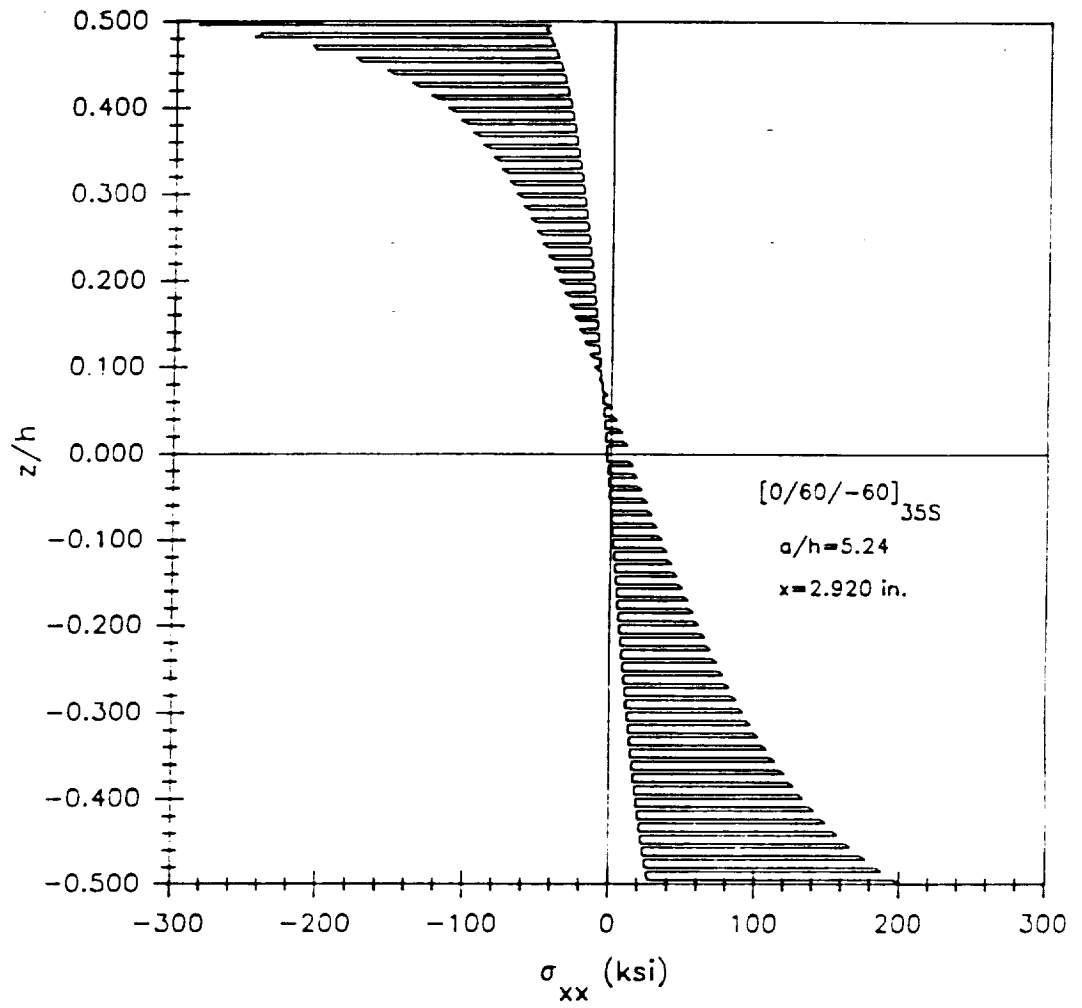**Figure 162.** Through-the-thickness distribution for τ_{xz} in the $[0/45/-45/90]_{15S}$ laminate with an aspect ratio of 0.83.

Figure 163. Through-the-thickness distribution for σ_{xx} in the $[0/45/-45/90]_{6S}$ laminate with an aspect ratio of 22.92.
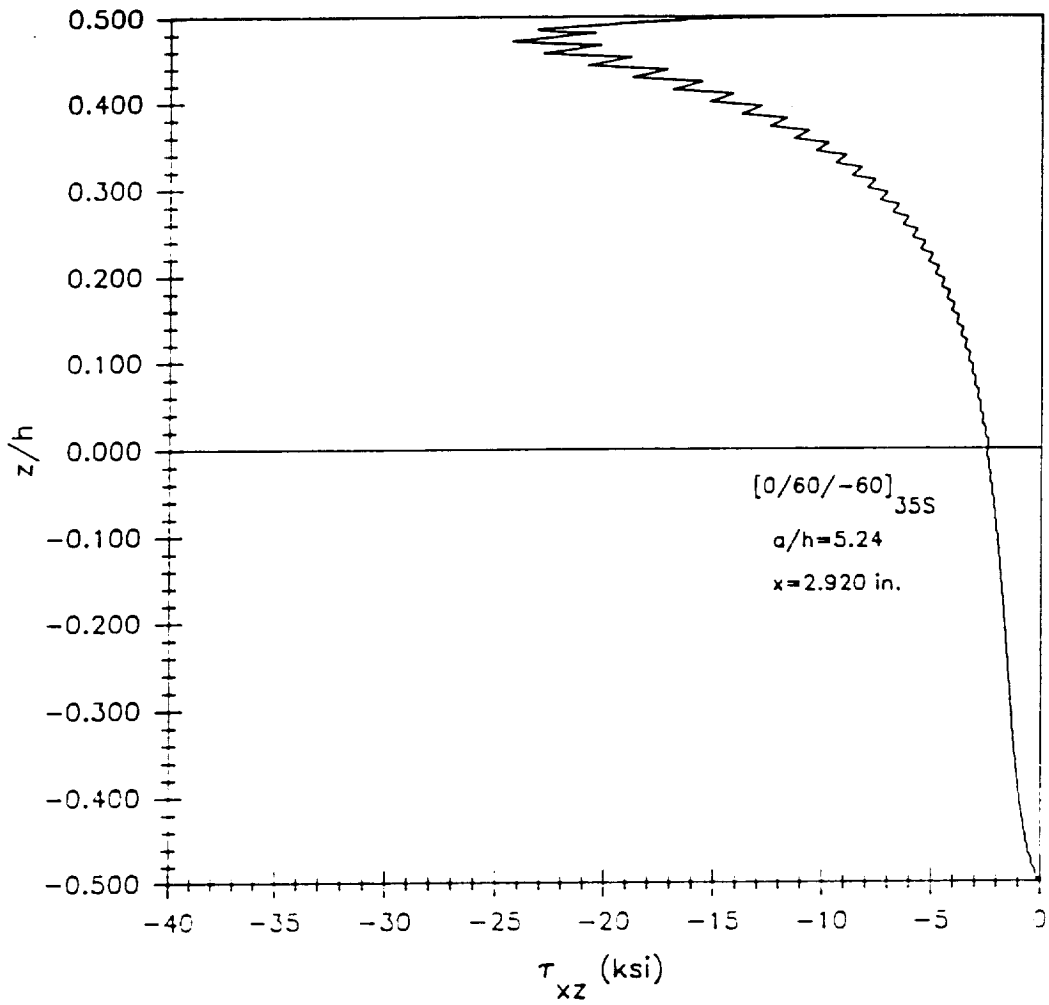
Figure 164. Through-the-thickness distribution for τ_{xz} in the $[0/45/-45/90]_{6S}$ laminate with an aspect ratio of 22.92.
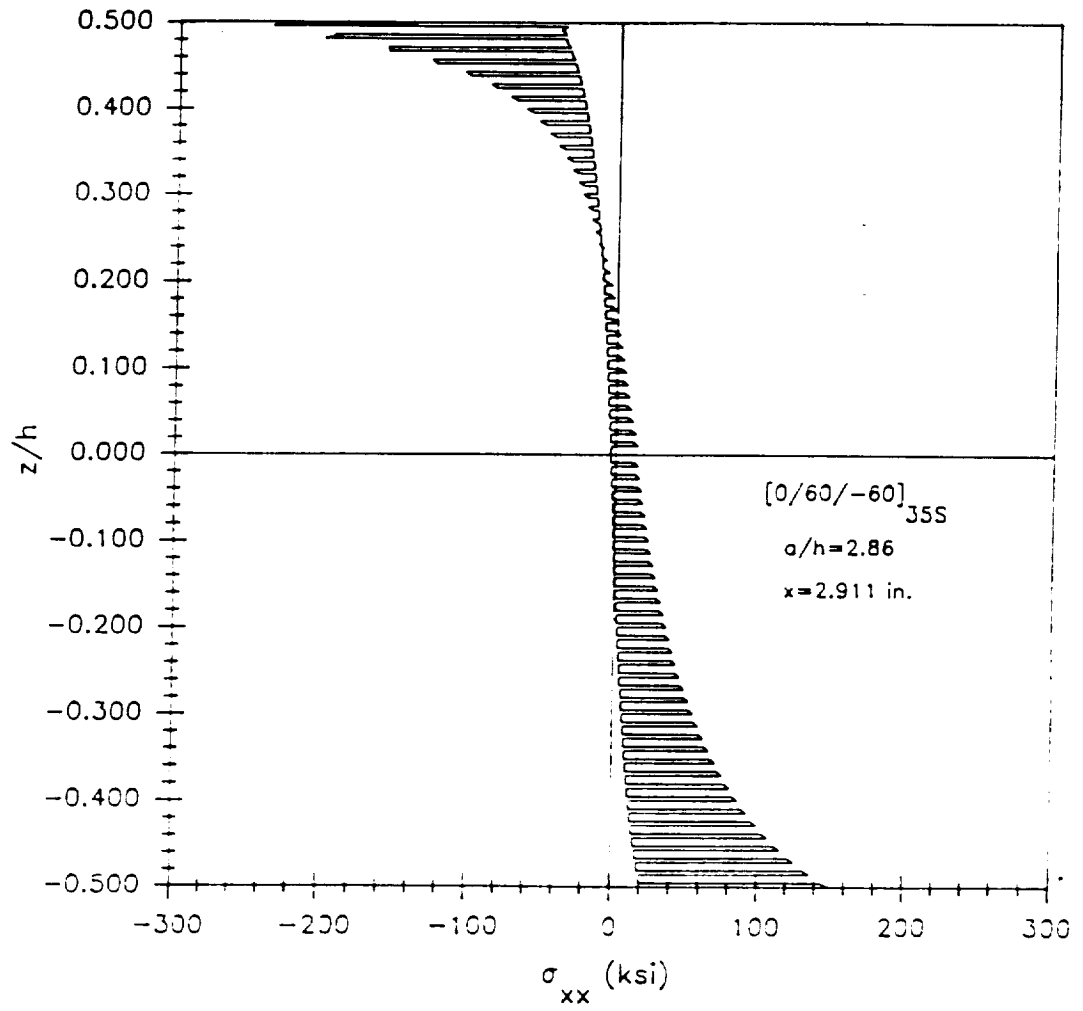
Through-the-Thickness Stress Distributions

Figure 165. Through-the-thickness distribution for σ_{xx} in the $[0/45/-45/90]_{6S}$ laminate with an aspect ratio of 12.50.

ORIGINAL PAGE IS
OF POOR QUALITY
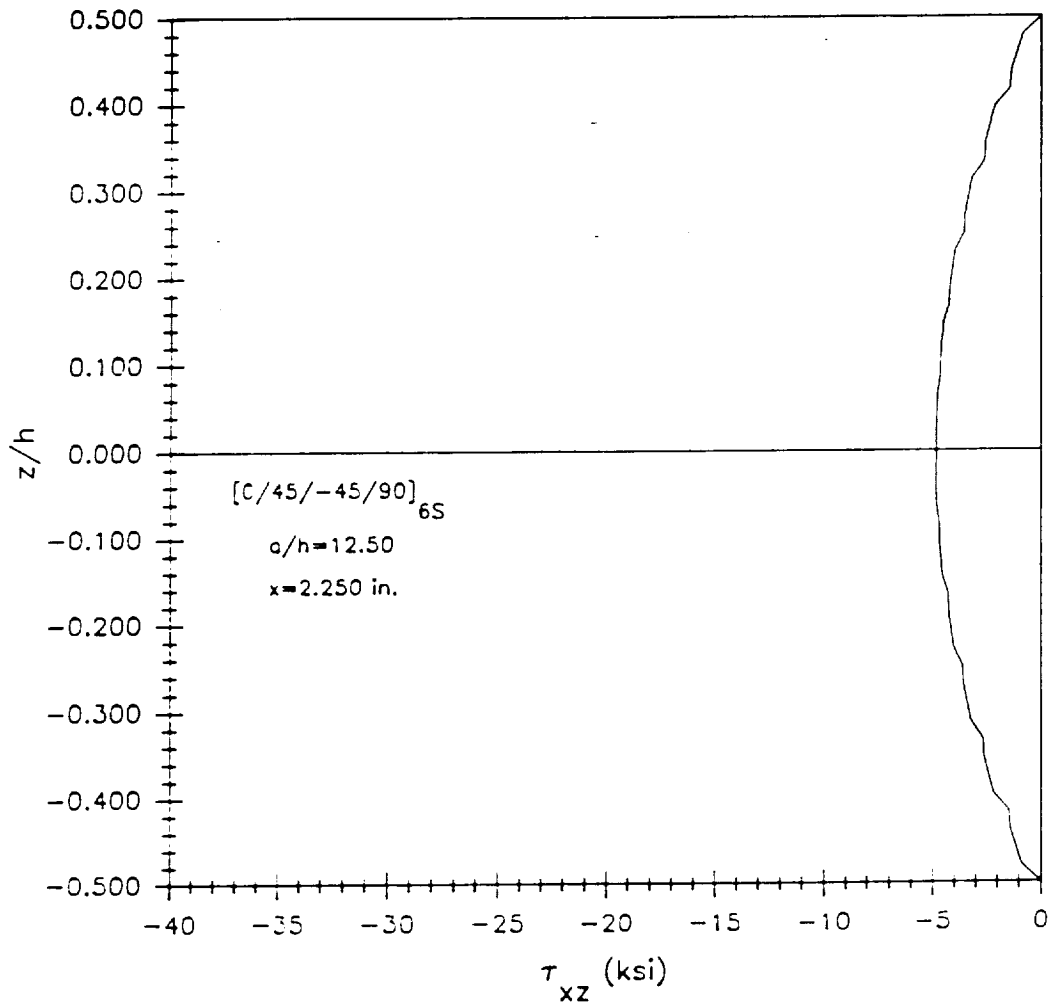
Figure 166. Through-the-thickness distribution for τ_{xz} in the $[0/45/-45/90]_{6S}$ laminate with an aspect ratio of 12.50.

Through-the-Thickness Stress Distributions

Figure 167. Through-the-thickness distribution for σ_{xx} in the $[0/45/-45/90]_{6S}$ laminate with an aspect ratio of 4.17.
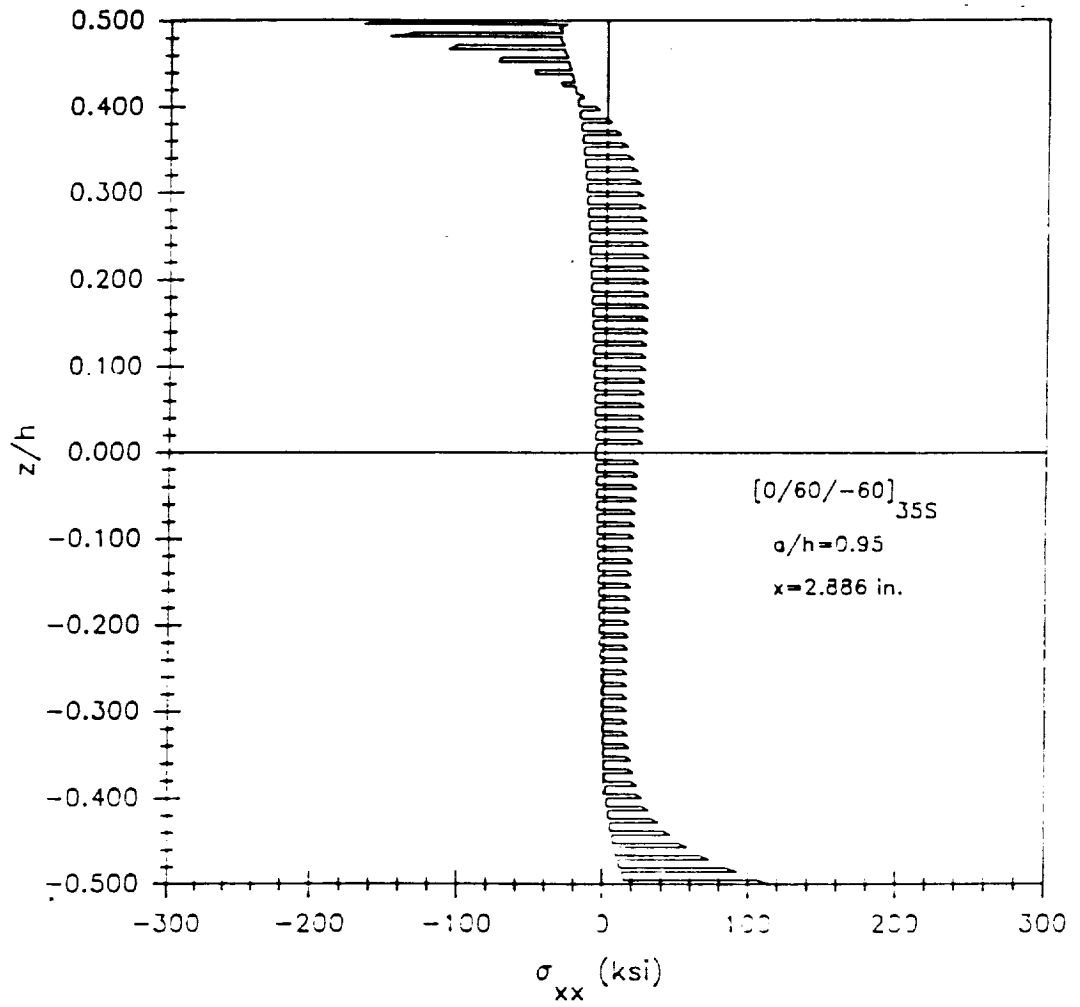
Figure 168. Through-the-thickness distribution for τ_{xz} in the $[0/45/-45/90]_{6S}$ laminate with an aspect ratio of 4.17.

Through-the-Thickness Stress Distributions

Figure 169. Through-the-thickness distribution for σ_{xx} in the $[0/45/-45/90]_{6S}$ laminate with an aspect ratio of 2.08.

Figure 170. Through-the-thickness distribution for τ_{xz} in the $[0/45/-45/90]_{6S}$ laminate with an aspect ratio of 2.08.

Figure 171. Through-the-thickness distribution for σ_{xx} in the $[0/60/-60]_{35S}$ laminate with an aspect ratio of 5.24.
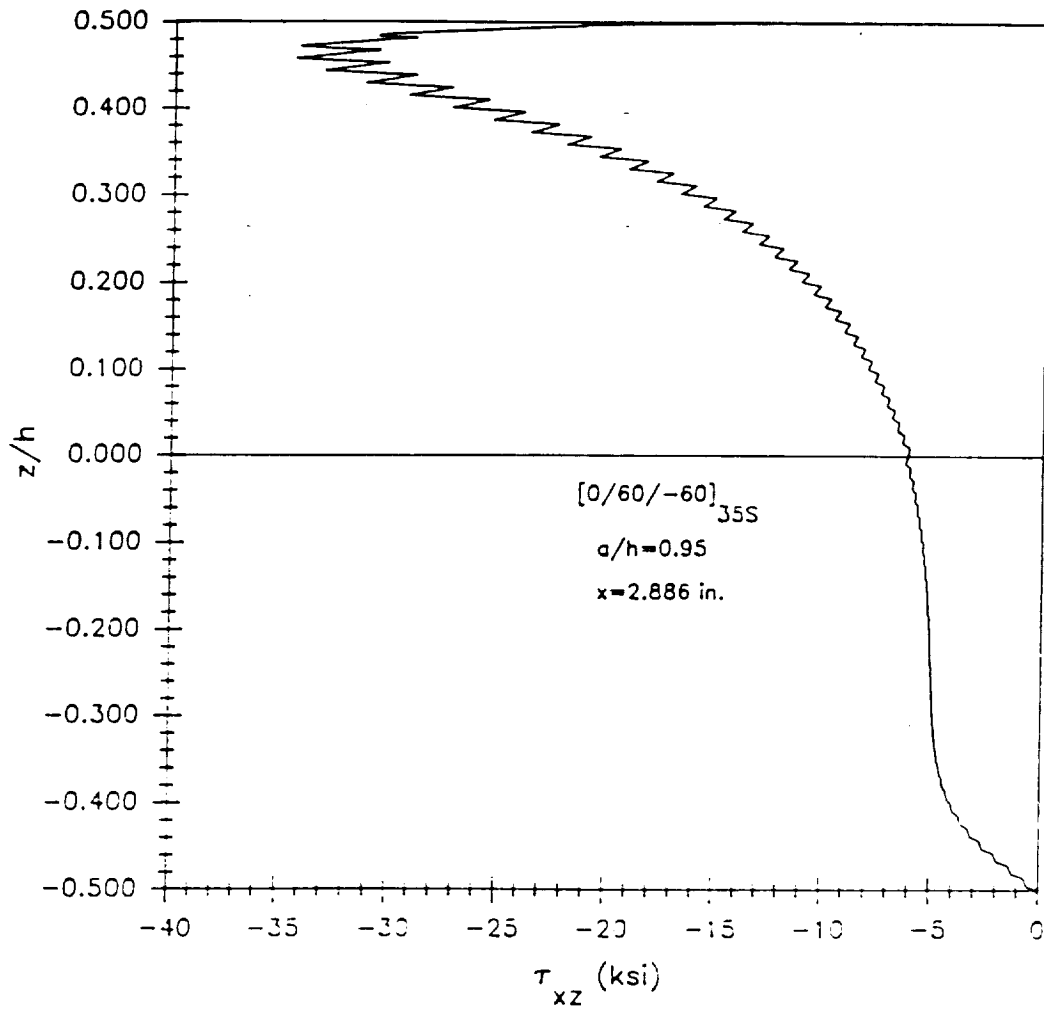
Figure 172. Through-the-thickness distribution for τ_{xz} in the $[0/60/-60]_{35S}$ laminate with an aspect ratio of 5.24.
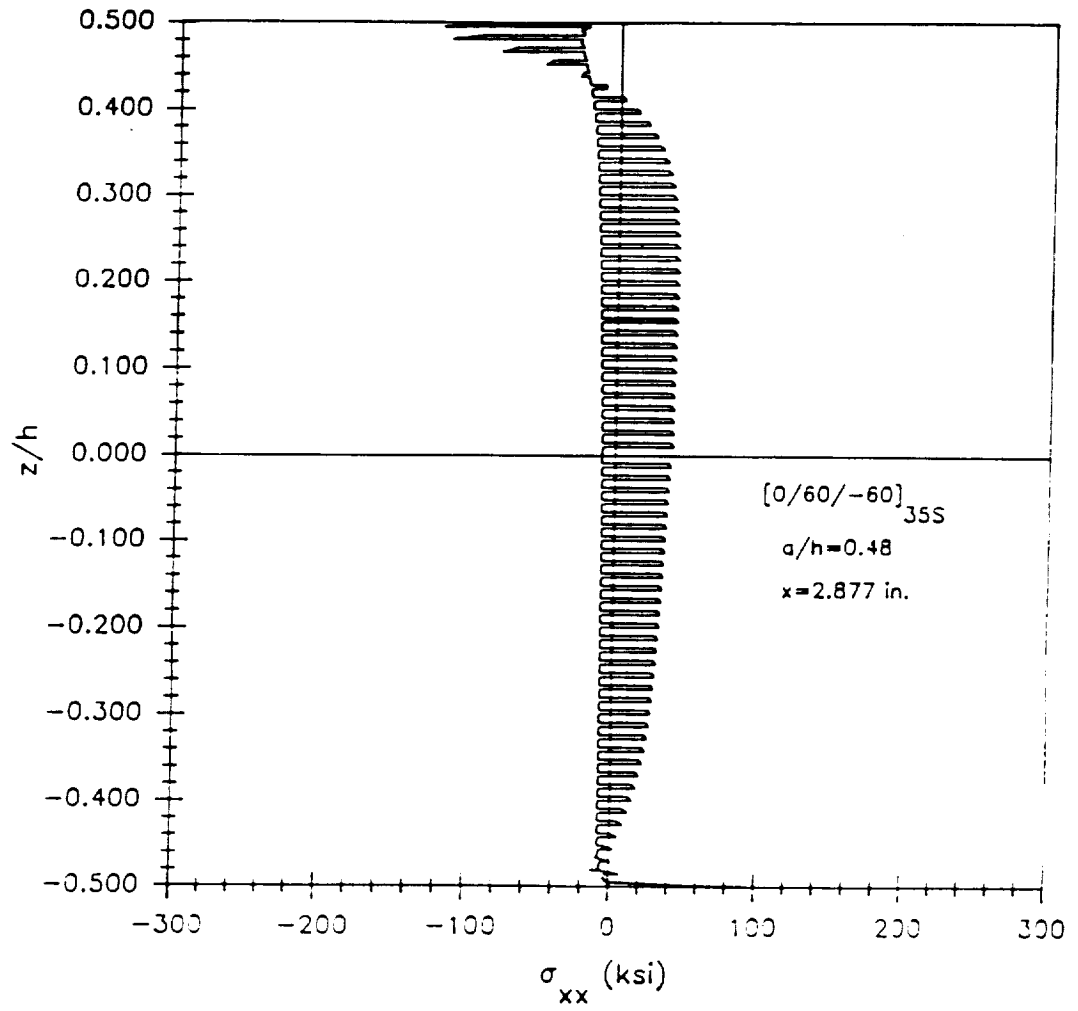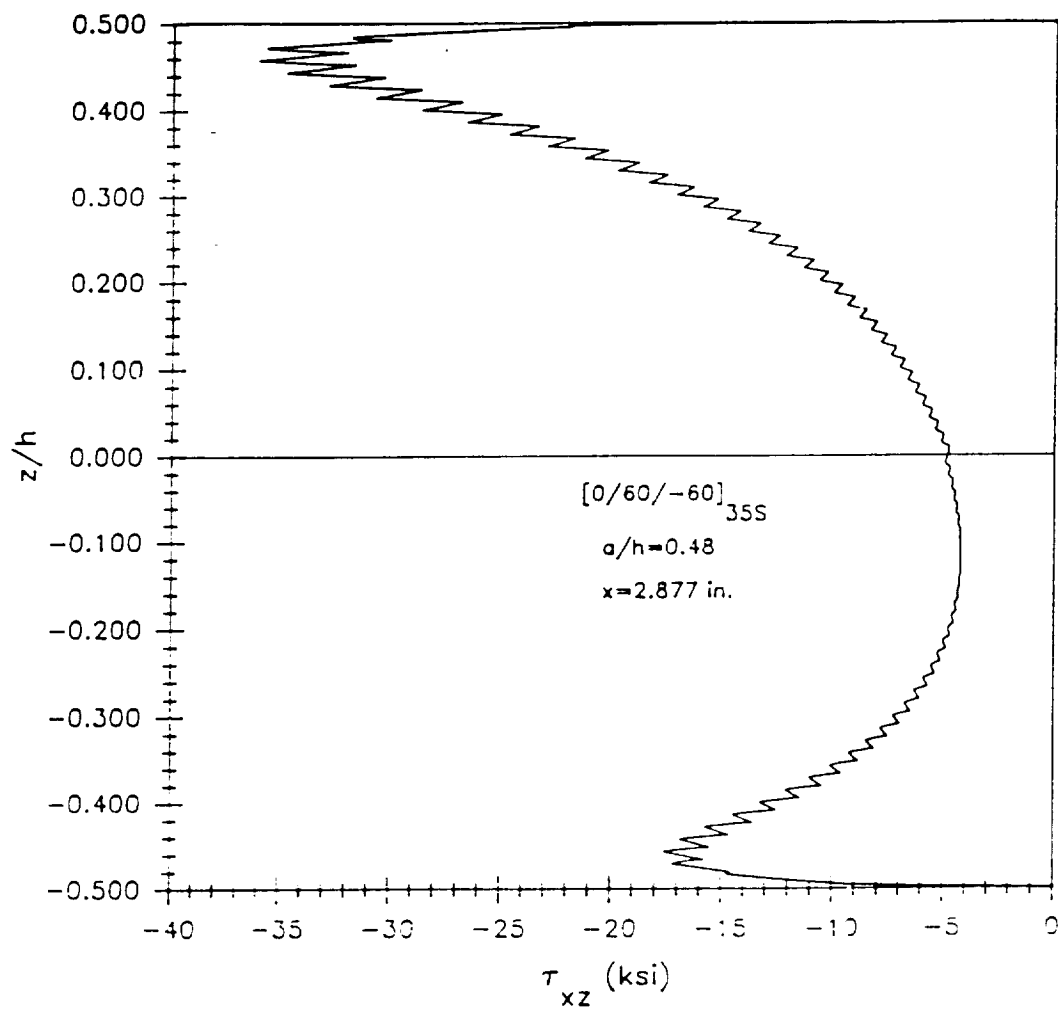
Figure 173. Through-the-thickness distribution for σ_{xx} in the $[0/60/-60]_{35S}$ laminate with an aspect ratio of 2.86.
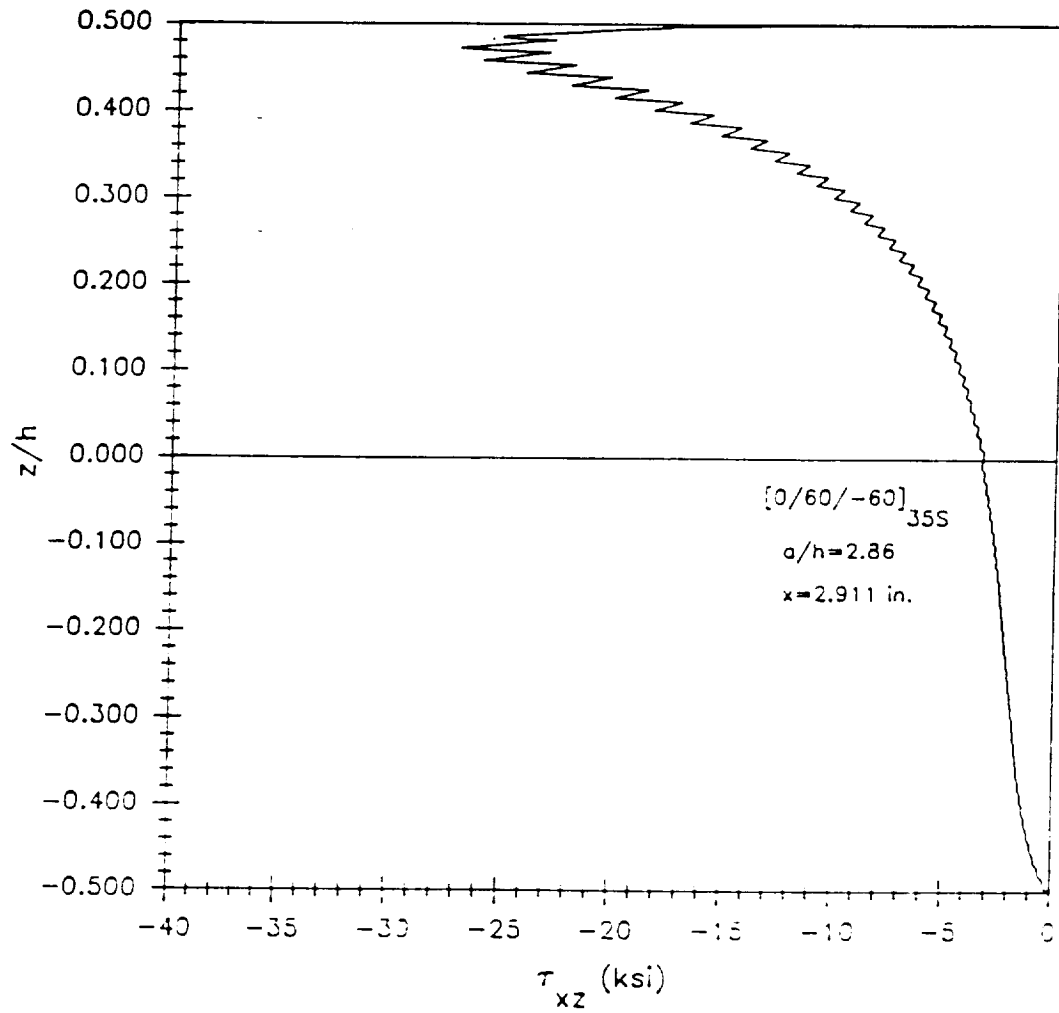
Figure 174. Through-the-thickness distribution for τ_{xz} in the $[0/60/-60]_{35S}$ laminate with an aspect ratio of 2.86.

Figure 175. Through-the-thickness distribution for σ_{xx} in the $[0/60/-60]_{35S}$ laminate with an aspect ratio of 0.95.

Figure 176. Through-the-thickness distribution for τ_{xz} in the $[0/60/-60]_{35S}$ laminate with an aspect ratio of 0.95.
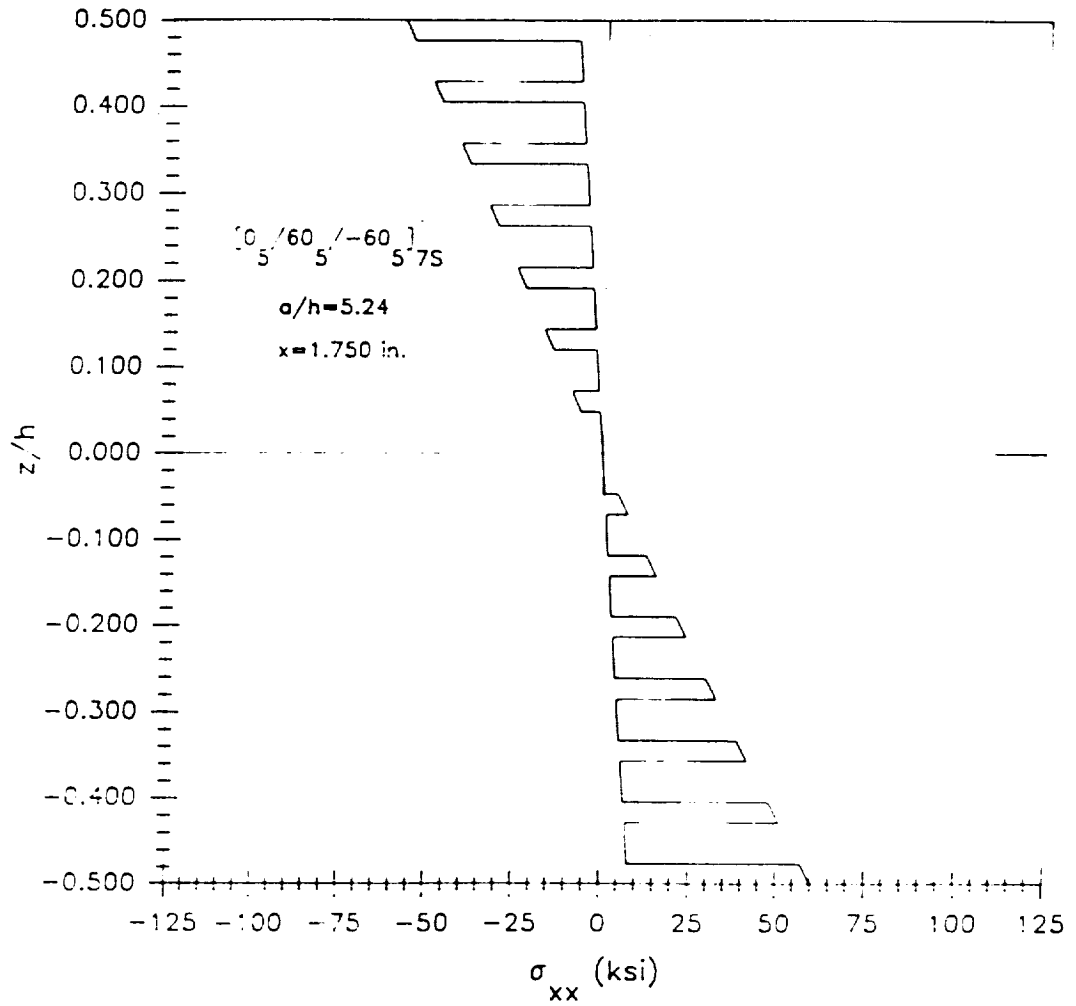
Figure 177. Through-the-thickness distribution for σ_{xx} in the $[0/60/-60]_{35S}$ laminate with an aspect ratio of 0.48.

Figure 178. Through-the-thickness distribution for τ_{xz} in the $[0/60/-60]_{35S}$ laminate with an aspect ratio of 0.48.

Figure 179. Through-the-thickness distribution for σ_{xx} in the [0/60/-60] grouped laminate with an aspect ratio of 5.24.
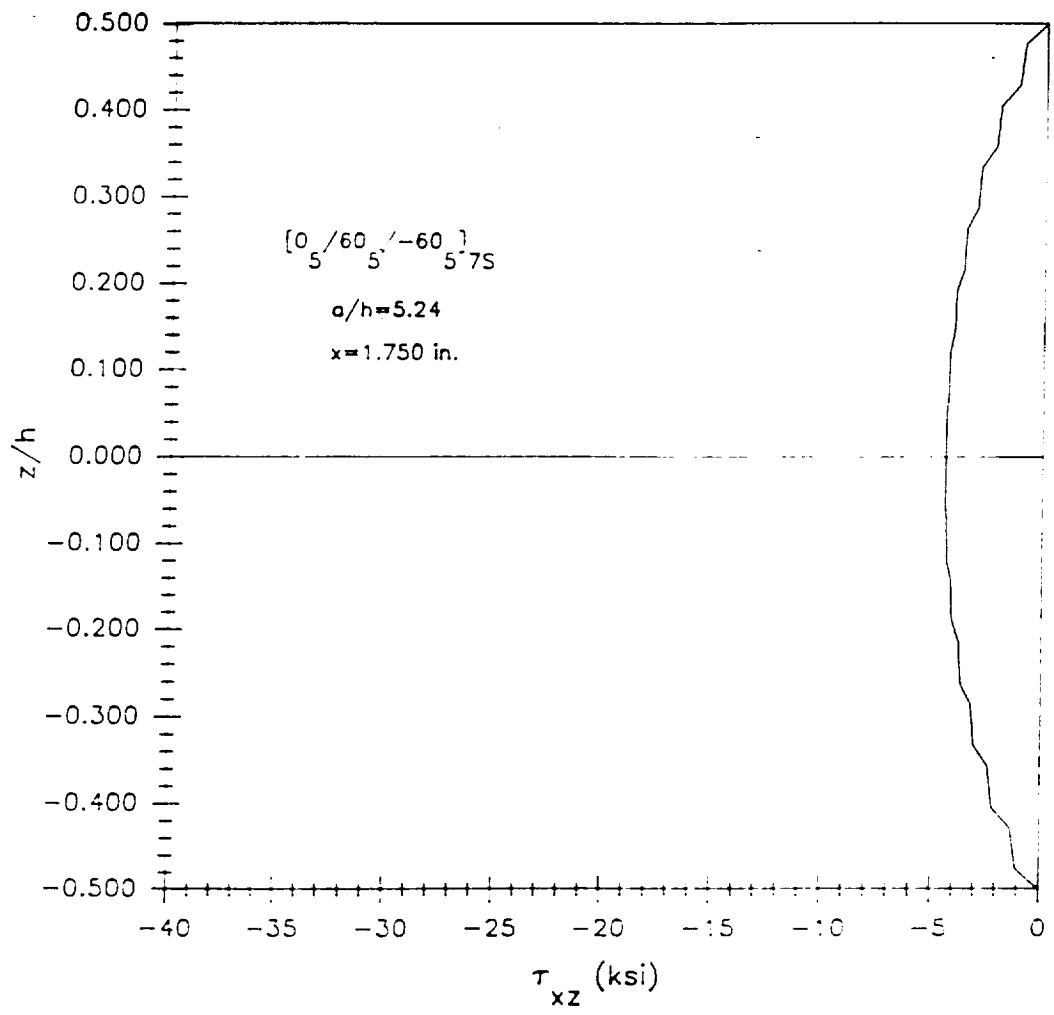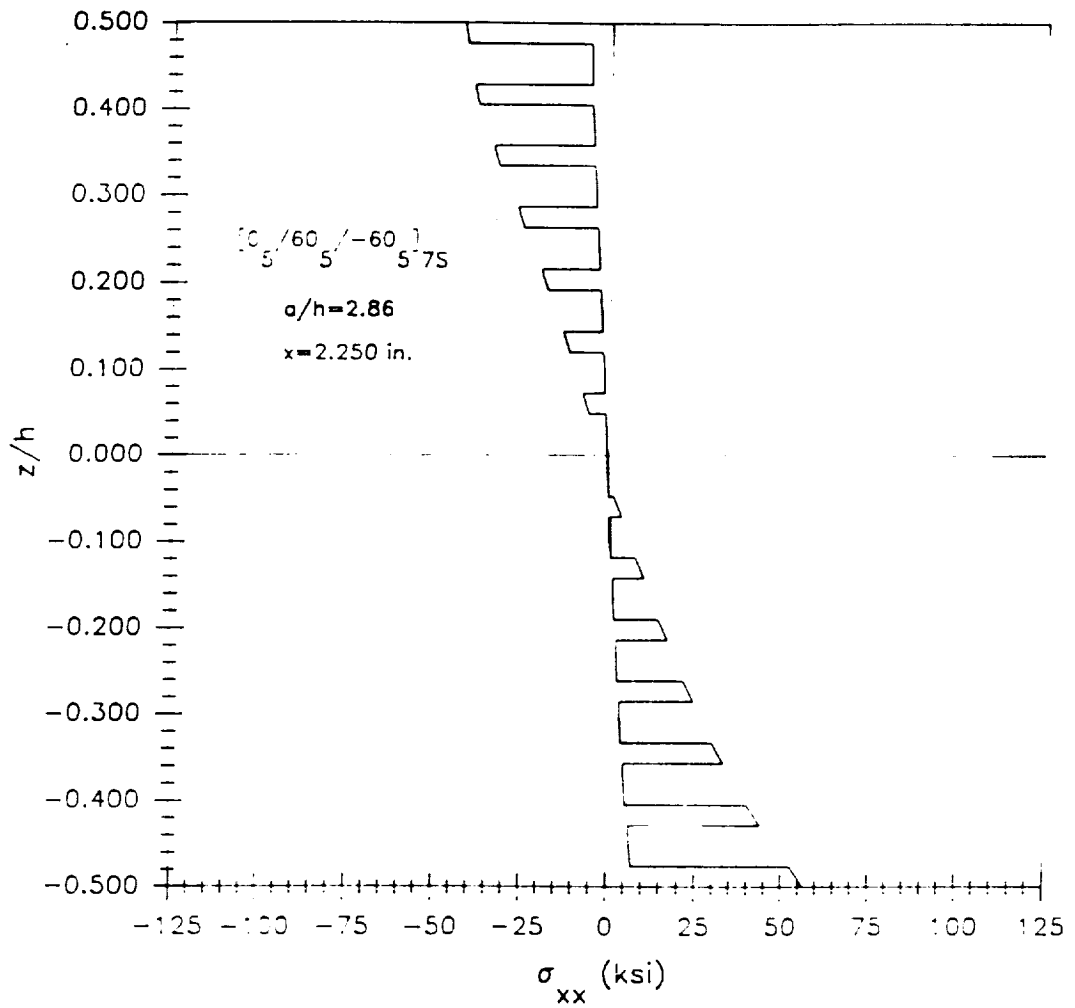
0.500

0.400

0.300

$[0_5/60_5/-60_5]_{7S}$

0.200

a/h=5.24

x=1.750 in.

0.100

z/h 0.000

−0.100

−0.200

−0.300

−0.400

−0.500

−40   −35   −30   −25   −20   −15   −10   −5   0

τ_{xz} (ksi)

Figure 180. Through-the-thickness distribution for τ_{xz} in the [0/60/-60] grouped laminate with an aspect ratio of 5.24.

Figure 181. Through-the-thickness distribution for σ_{xx} in the [0/60/-60] grouped laminate with an aspect ratio of 2.86.
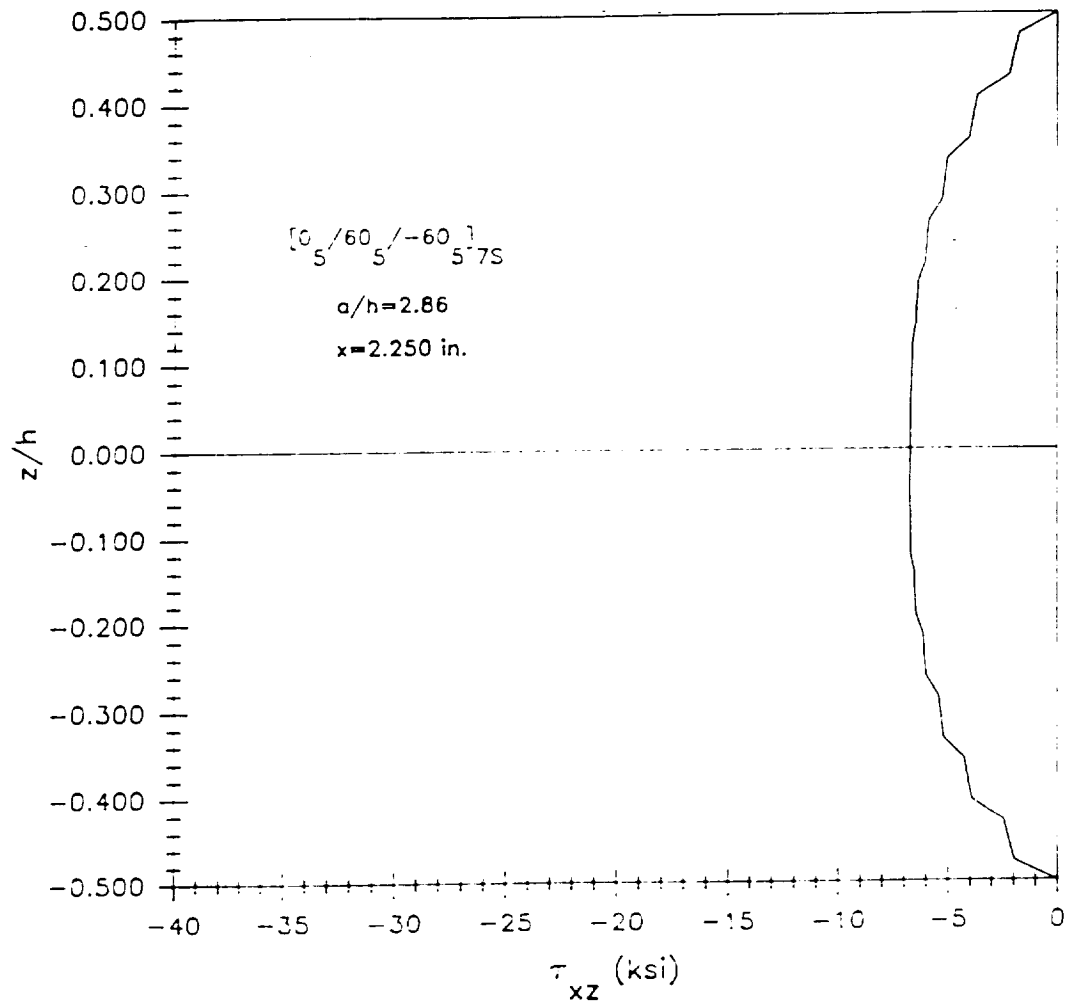
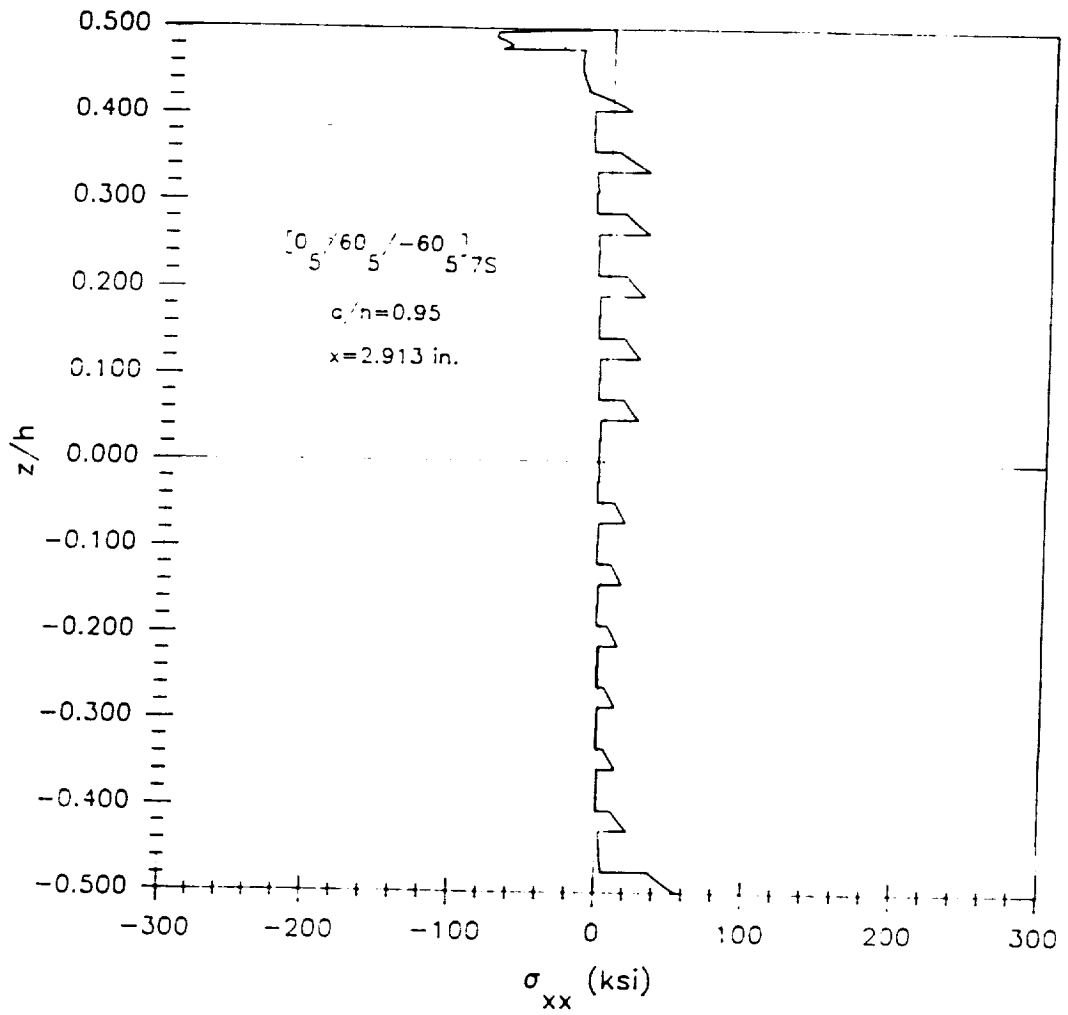**Figure 182.** Through-the-thickness distribution for τ_{xz} in the [0/60/-60] grouped laminate with an aspect ratio of 2.86.
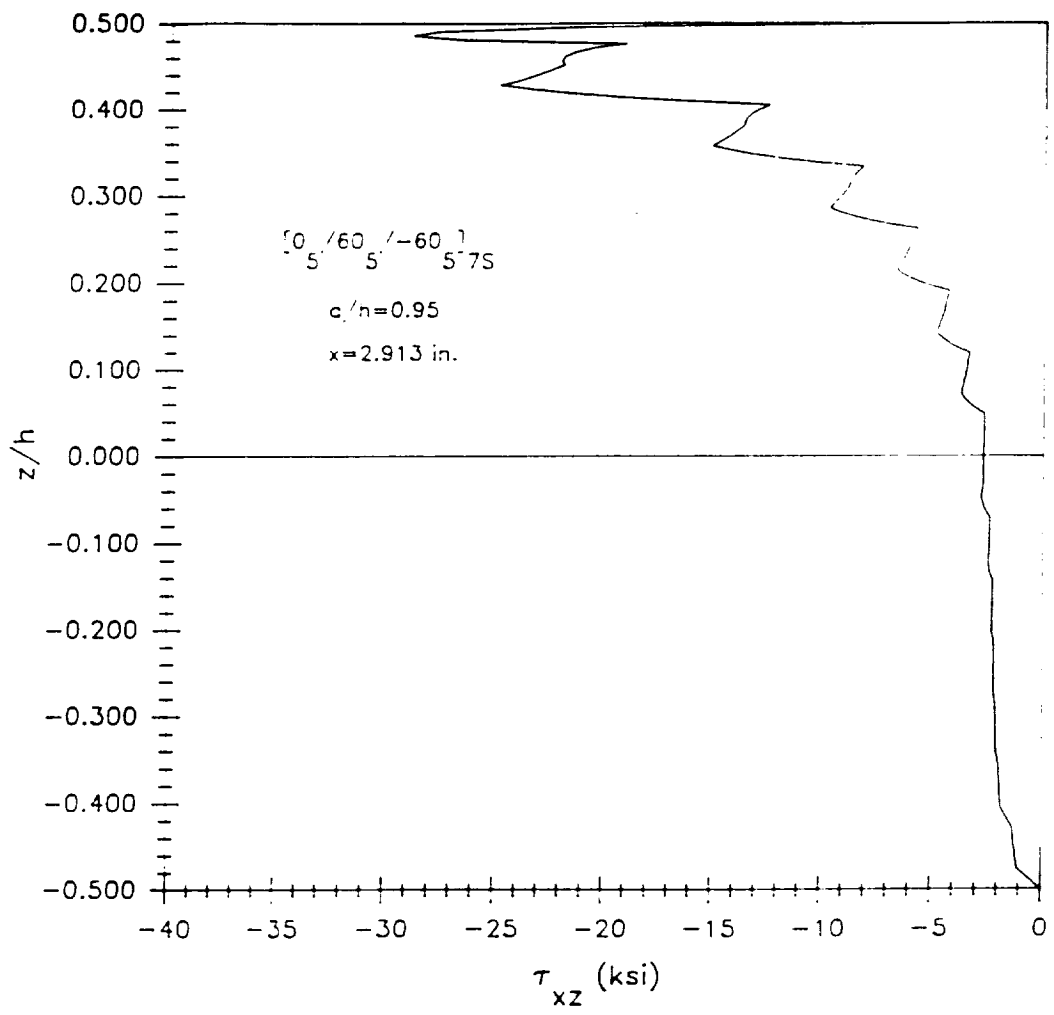
0.500

0.400

0.300

0.200

0.100

0.000

-0.100

-0.200

-0.300

-0.400

-0.500

z/h

$[0_5/60_5/-60_5]_{7S}$

c/n=0.95

x=2.913 in.

-300   -200   -100   0   100   200   300

σ_{xx} (ksi)

Figure 183. Through-the-thickness distribution for σ_{xx} in the [0/60/-60] grouped laminate with an aspect ratio of 0.95.

Figure 184. Through-the-thickness distribution for τ_{xz} in the [0/60/-60] grouped laminate with an aspect ratio of 0.95.
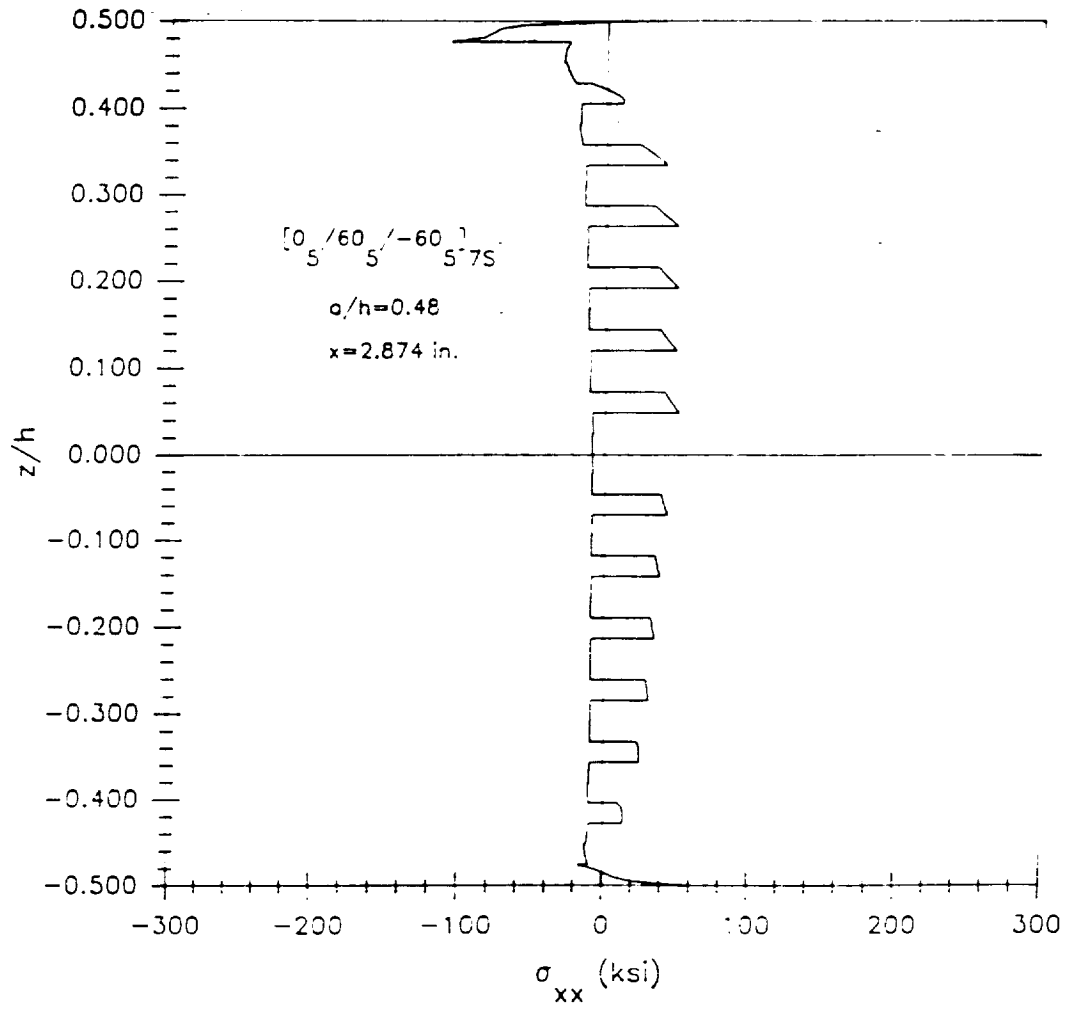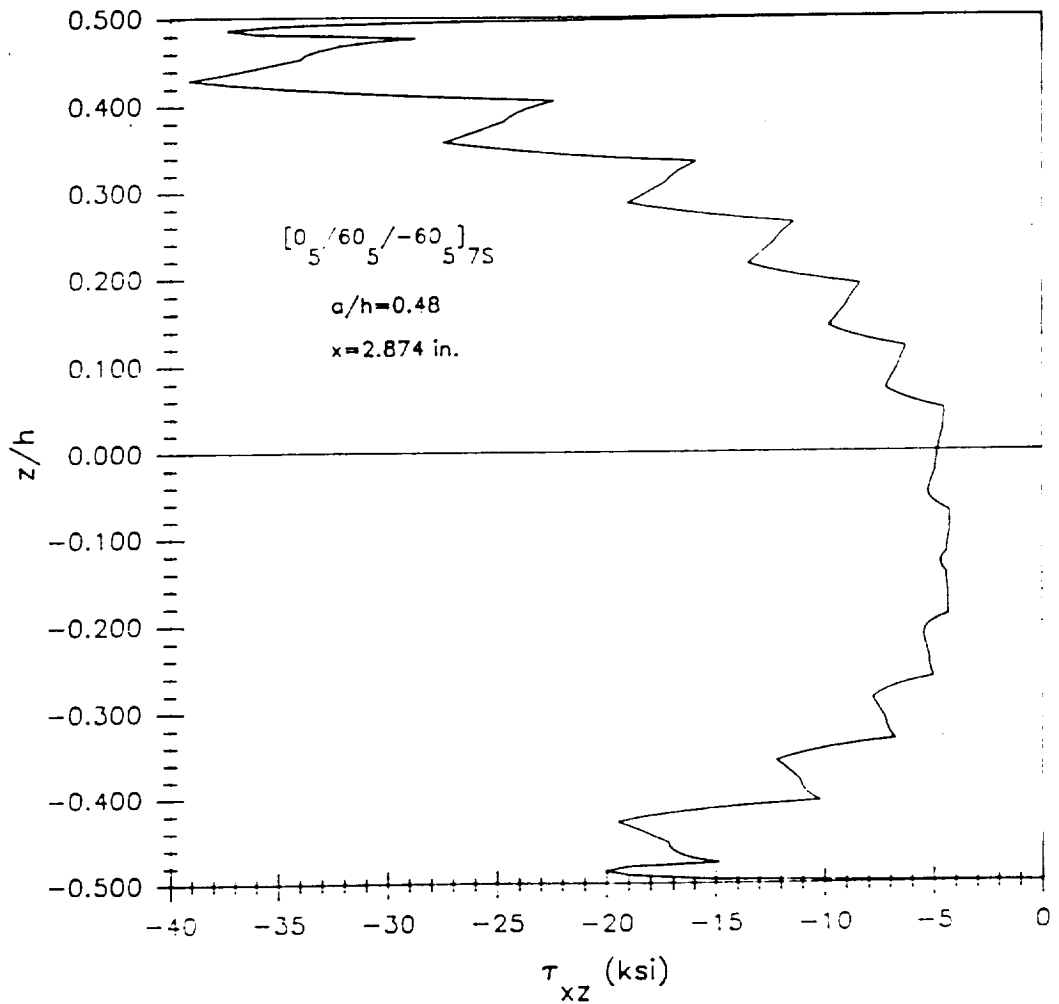
Figure 185. Through-the-thickness distribution for σ_{xx} in the [0/60/-60] grouped laminate with an aspect ratio of 0.48.

Plot annotations:
$[0_5/60_5/-60_5]_{7S}$
$a/h=0.48$
$x=2.874$ in.

y-axis: z/h (0.500, 0.400, 0.300, 0.200, 0.100, 0.000, -0.100, -0.200, -0.300, -0.400, -0.500)

x-axis: σ_{xx} (ksi) (-300, -200, -100, 0, 100, 200, 300)

Figure 186. Through-the-thickness distribution for τ_{xz} in the [0/60/-60] grouped laminate with an aspect ratio of 0.48.
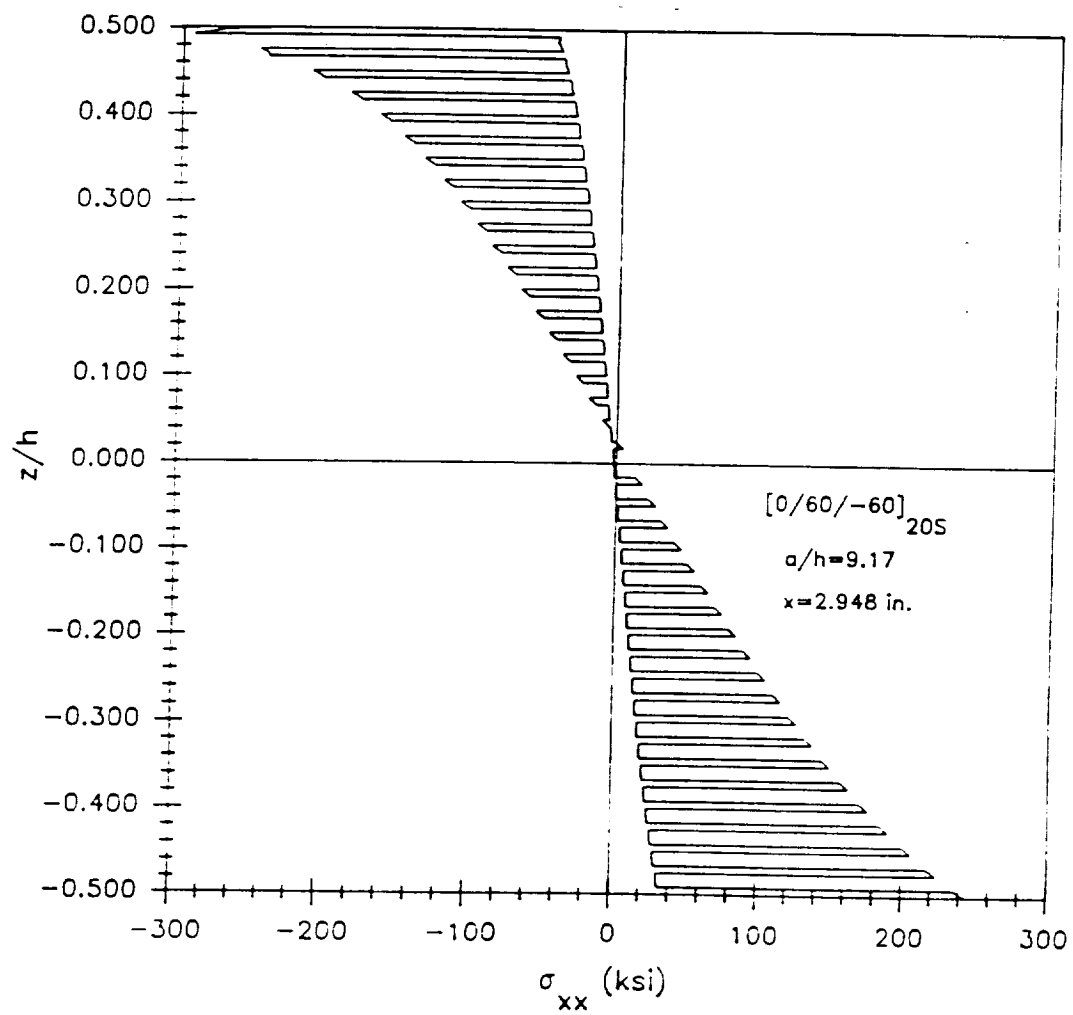
Figure 187. Through-the-thickness distribution for σ_{xx} in the $[0/60/-60]_{20S}$ laminate with an aspect ratio of 9.17.
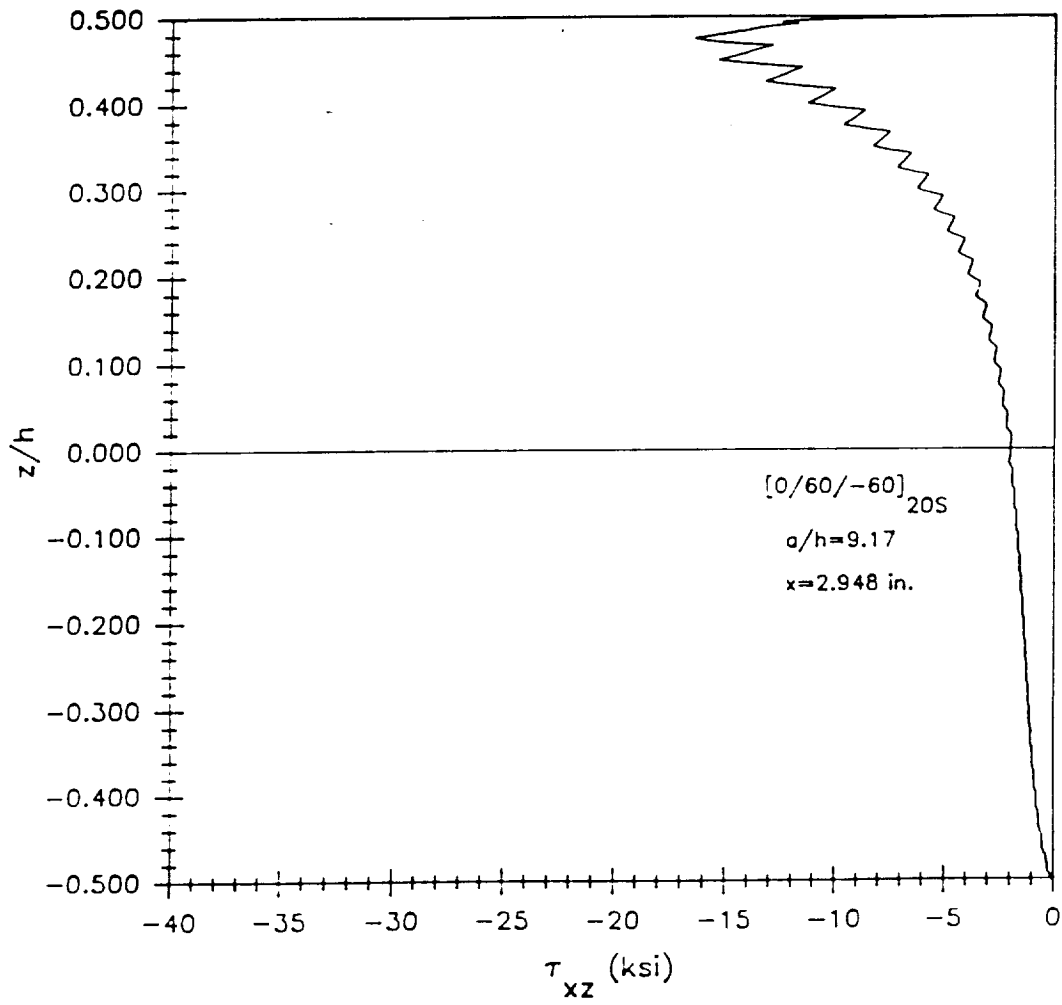
Figure 188.   Through-the-thickness distribution for τ_{xz} in the $[0/60/-60]_{20S}$ laminate with an aspect ratio of 9.17.
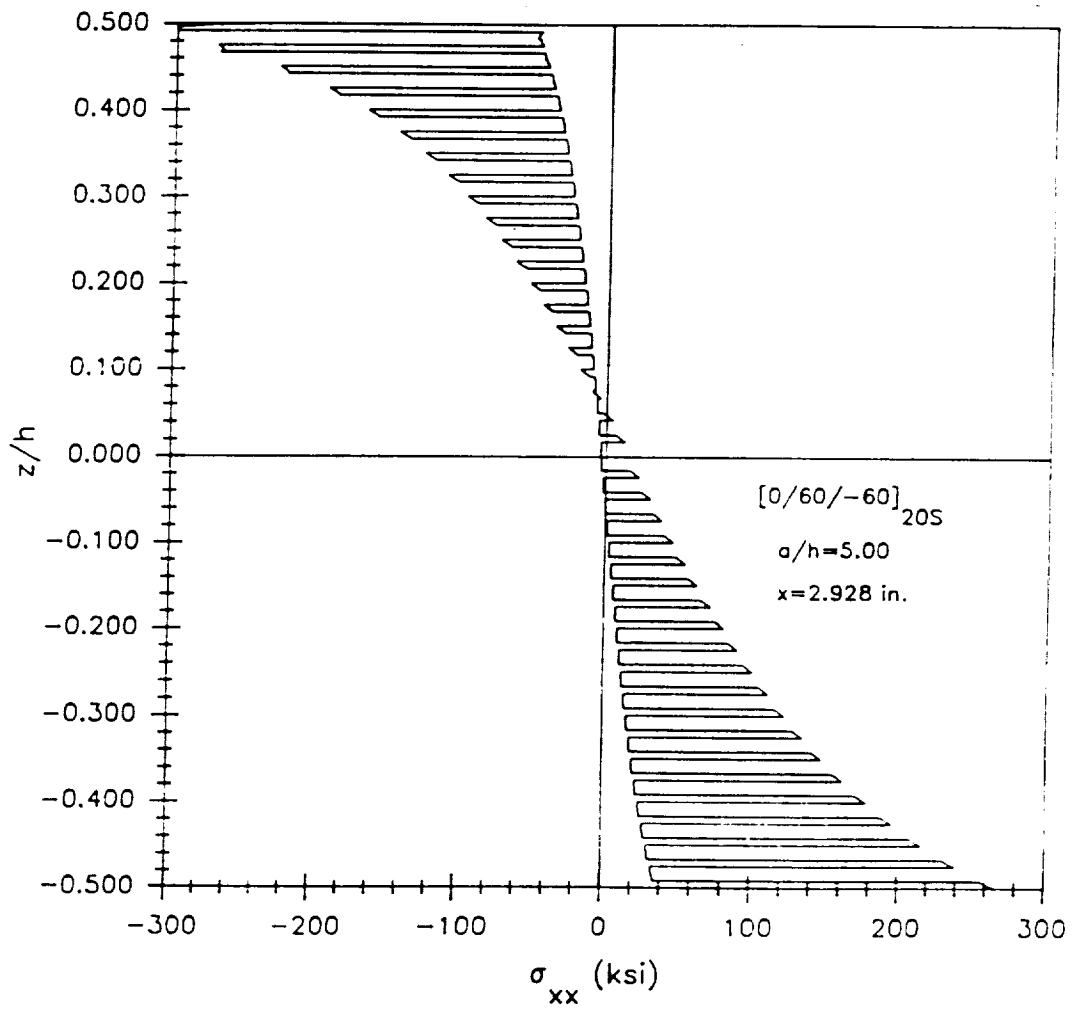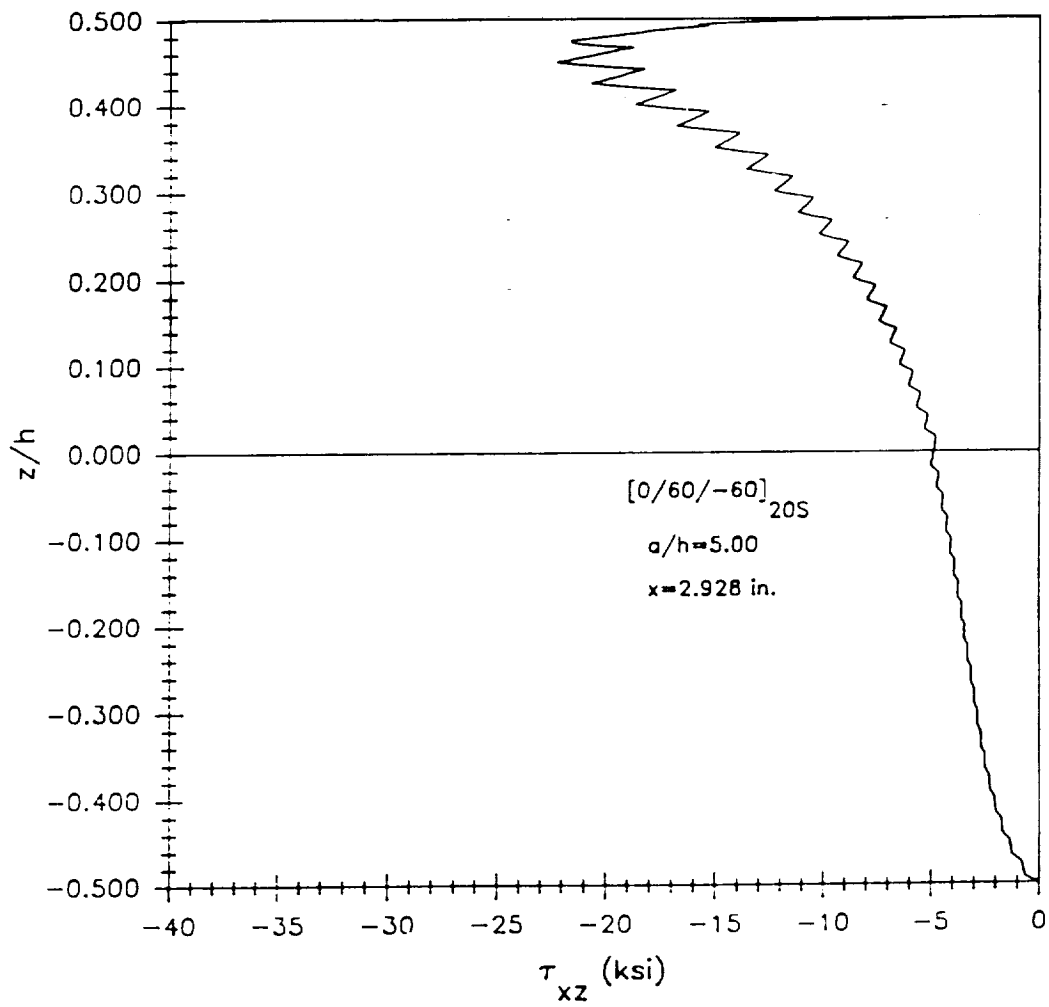
Figure 189. Through-the-thickness distribution for σ_{xx} in the $[0/60/-60]_{20S}$ laminate with an aspect ratio of 5.00.

Figure 190. Through-the-thickness distribution for τ_{xz} in the $[0/60/-60]_{20S}$ laminate with an aspect ratio of 5.00.

Figure 191. Through-the-thickness distribution for σ_{xx} in the $[0/60/-60]_{20S}$ laminate with an aspect ratio of 1.67.

Figure 192. Through-the-thickness distribution for τ_{xz} in the $[0/60/-60]_{20S}$ laminate with an aspect ratio of 1.67.
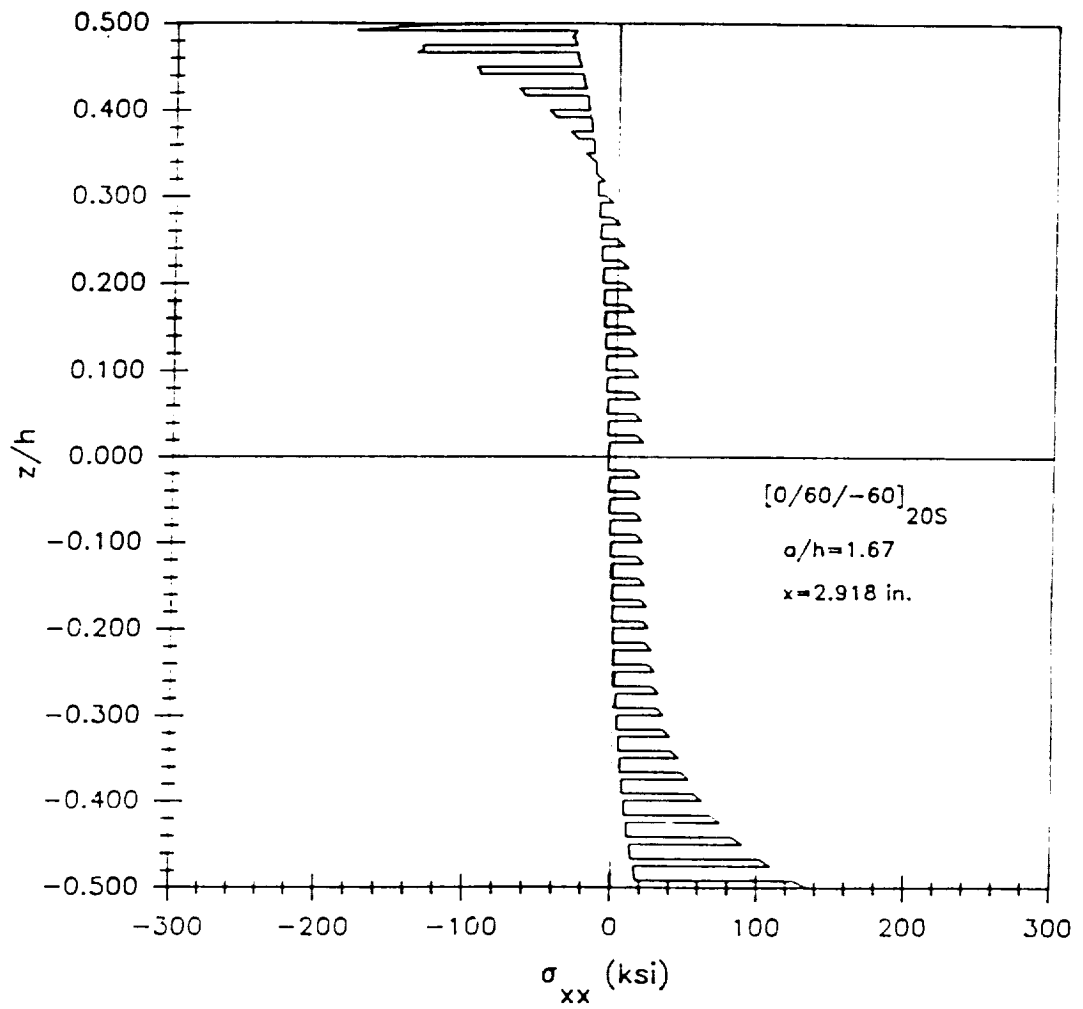
Figure 193. Through-the-thickness distribution for σ_{xx} in the $[0/60/-60]_{20S}$ laminate with an aspect ratio of 0.83.

Figure 194. Through-the-thickness distribution for τ_{xz} in the $[0/60/-60]_{20S}$ laminate with an aspect ratio of 0.83.
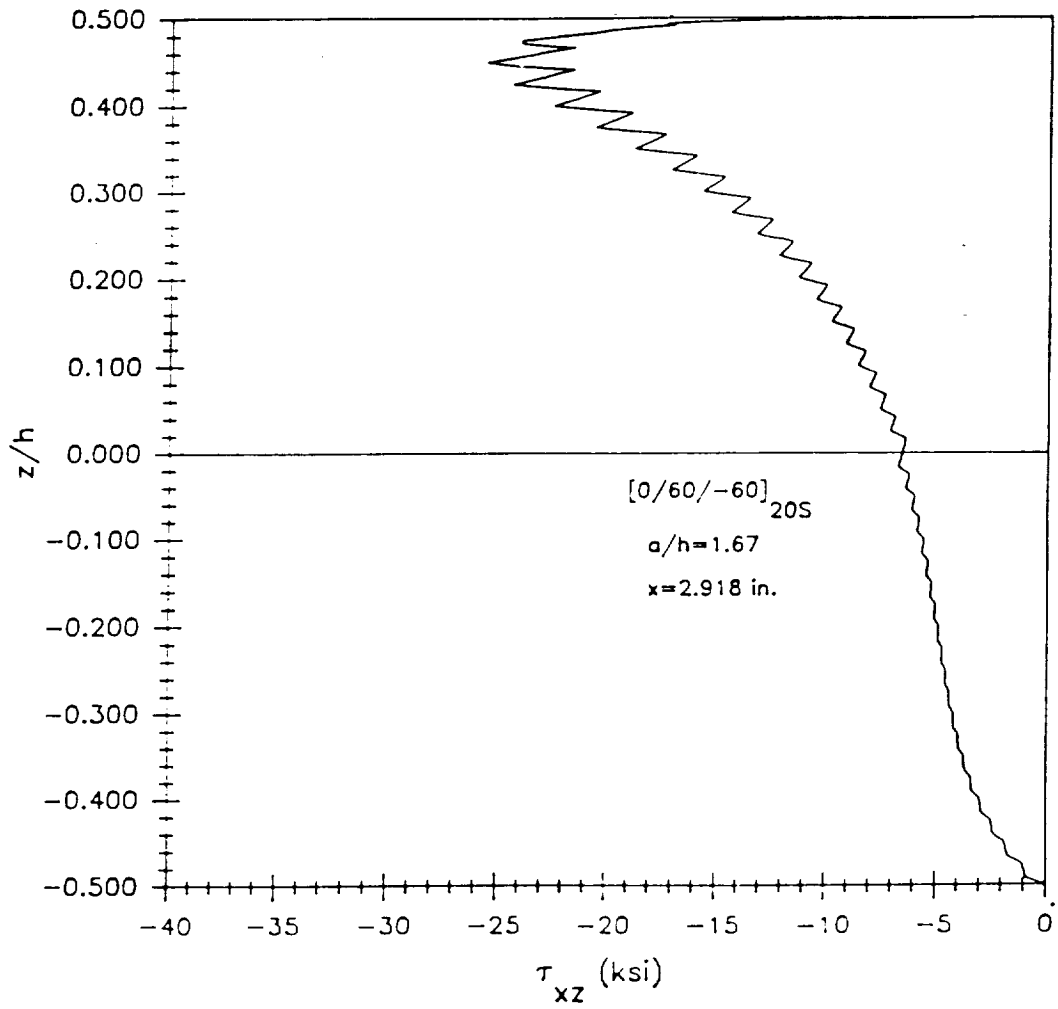
Figure 195. Through-the-thickness distribution for σ_{xx} in the $[0/60/-60]_{8S}$ laminate with an aspect ratio of 22.92.
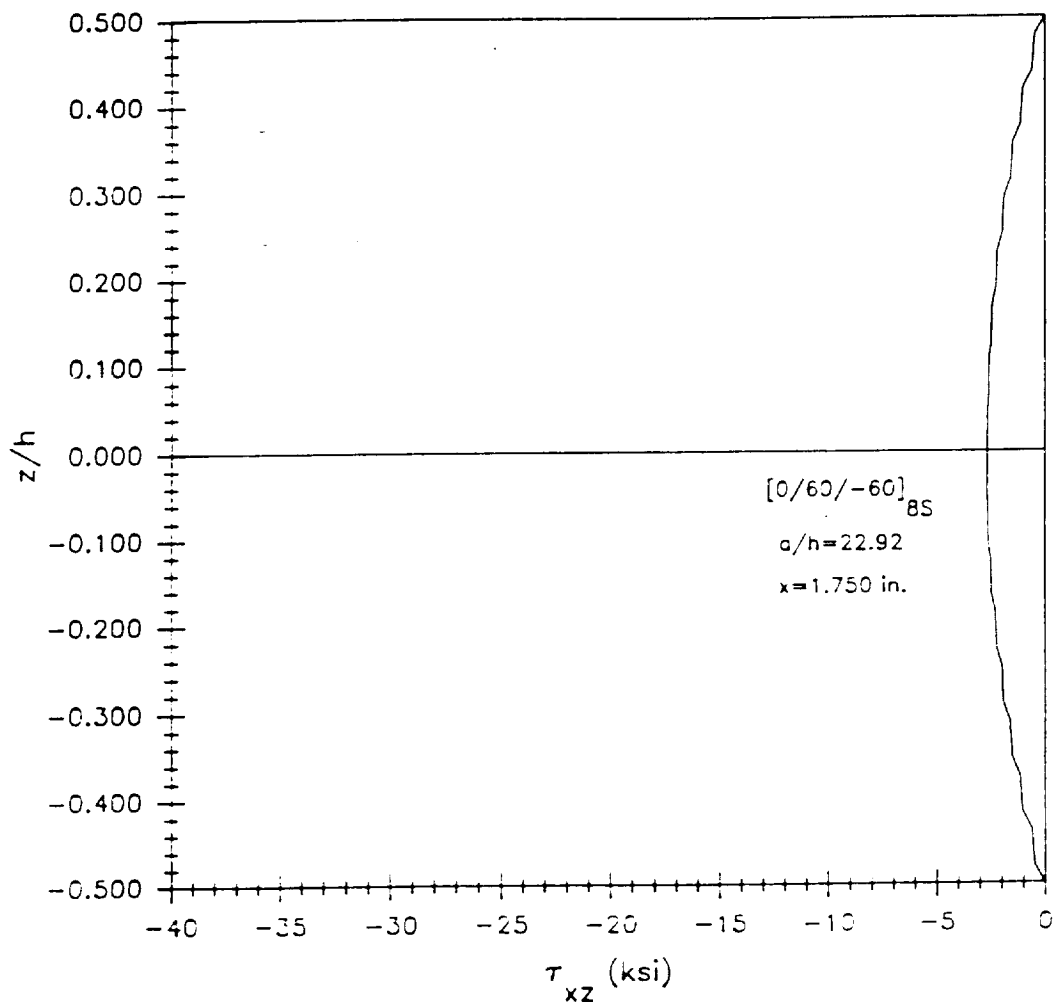
Figure 196. Through-the-thickness distribution for τ_{xz} in the $[0/60/-60]_{8S}$ laminate with an aspect ratio of 22.92.
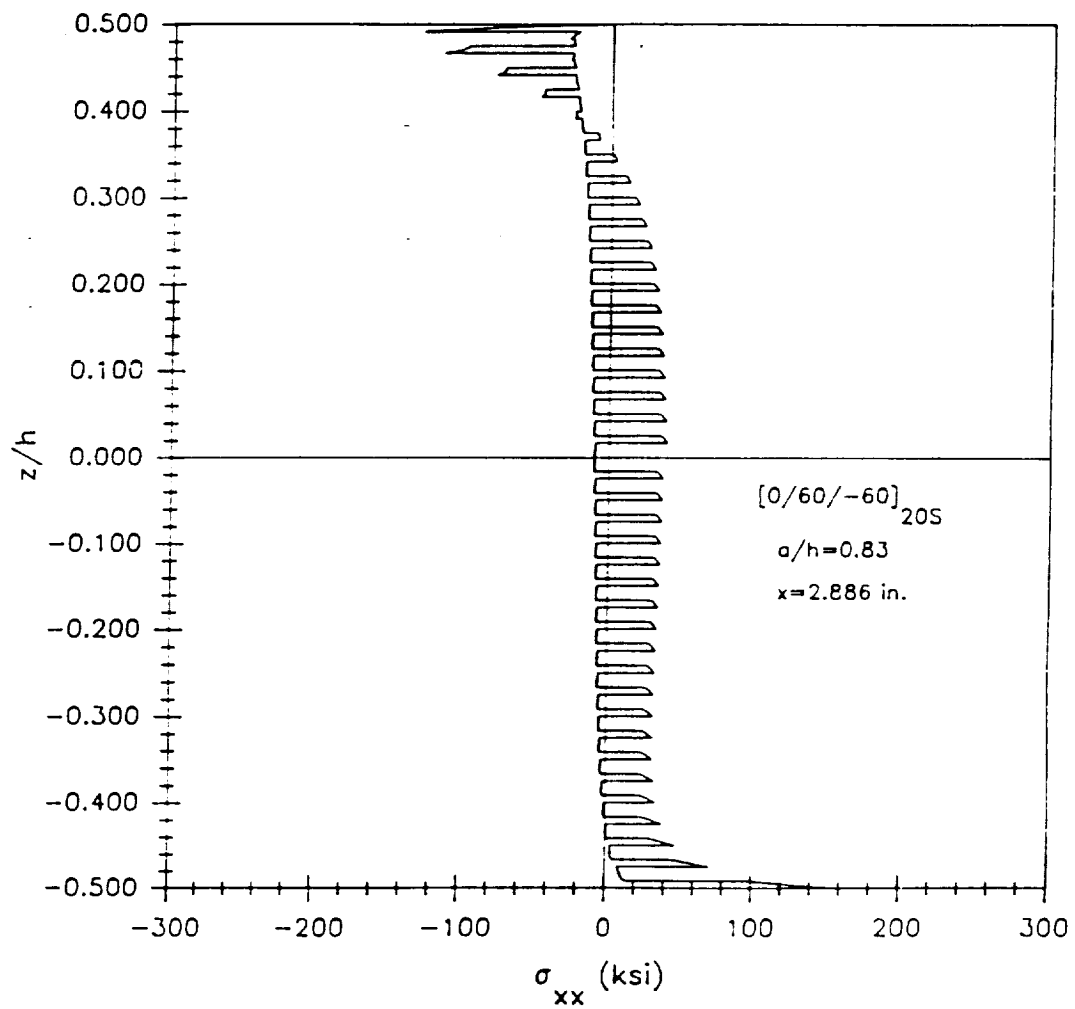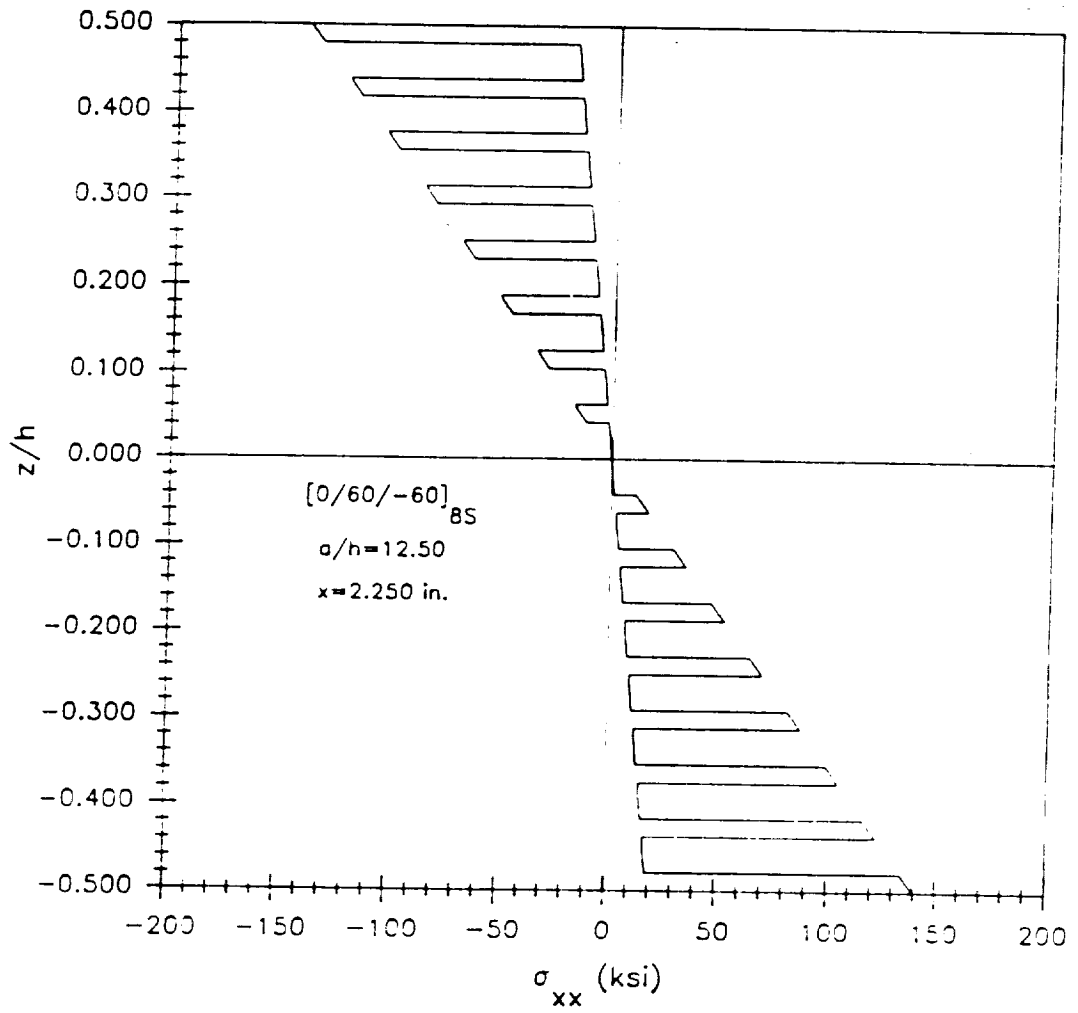
Figure 197. Through-the-thickness distribution for σ_{xx} in the $[0/60/-60]_{8S}$ laminate with an aspect ratio of 12.50.
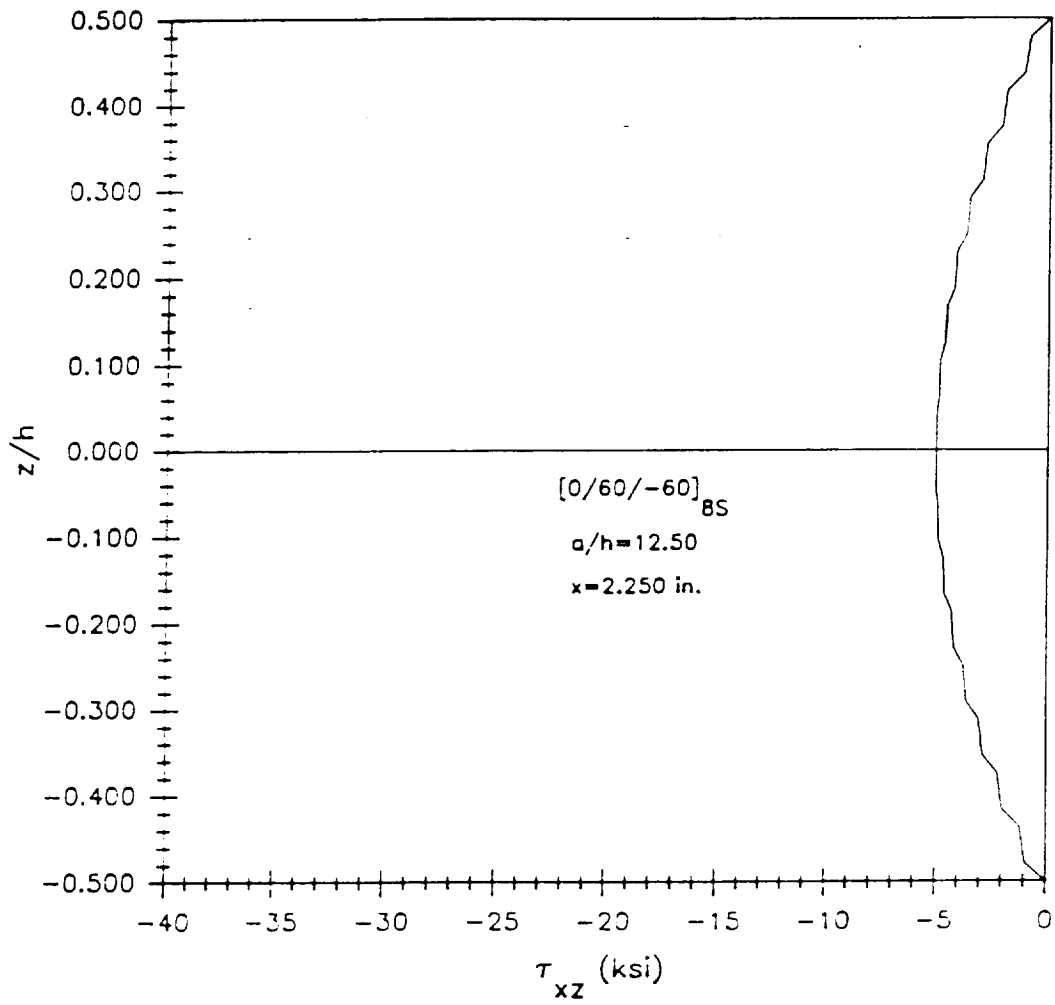
Figure 198. Through-the-thickness distribution for τ_{xz} in the $[0/60/-60]_{8S}$ laminate with an aspect ratio of 12.50.
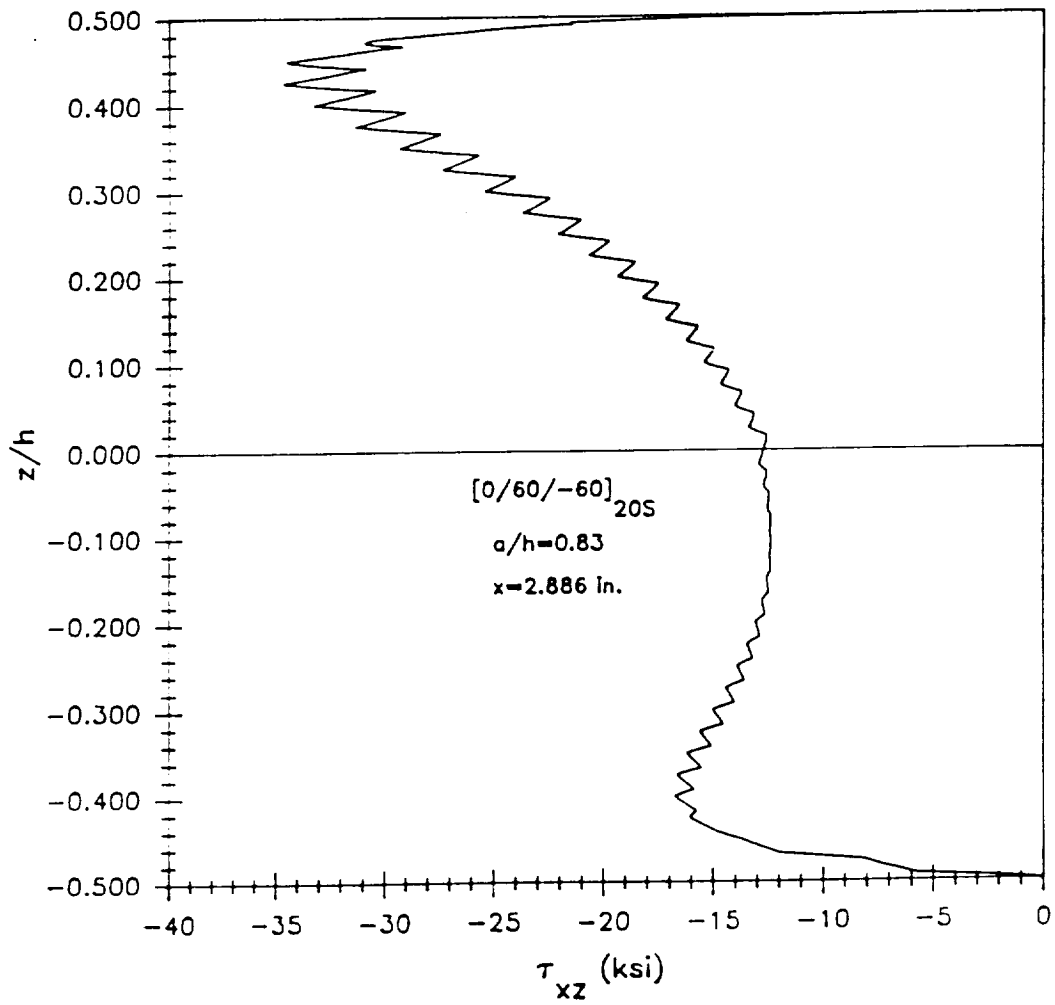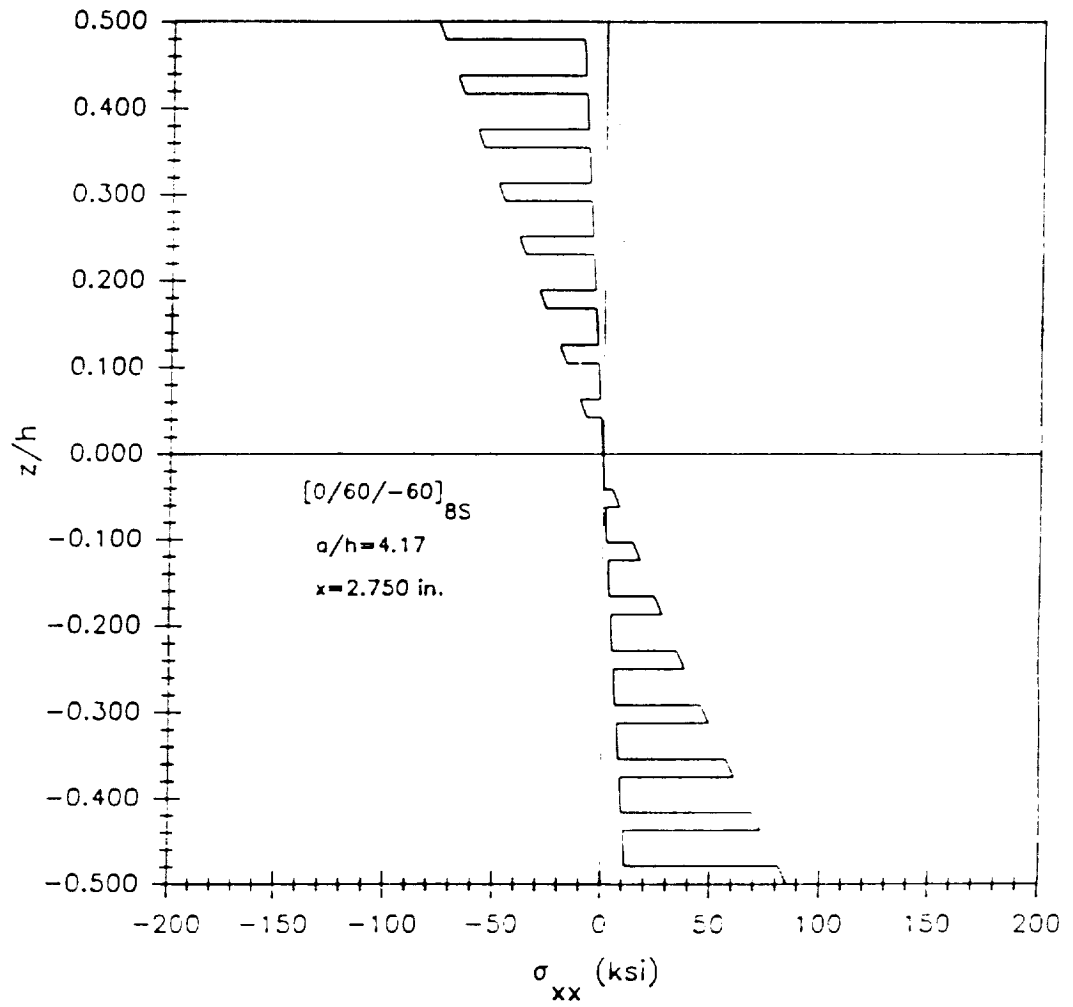
Figure 199. Through-the-thickness distribution for σ_{xx} in the $[0/60/-60]_{8S}$ laminate with an aspect ratio of 4.17.

0.500

0.400

0.300

0.200

0.100

z/h 0.000

-0.100

-0.200

-0.300

-0.400

-0.500

-40   -35   -30   -25   -20   -15   -10   -5   0

τ_{xz} (ksi)
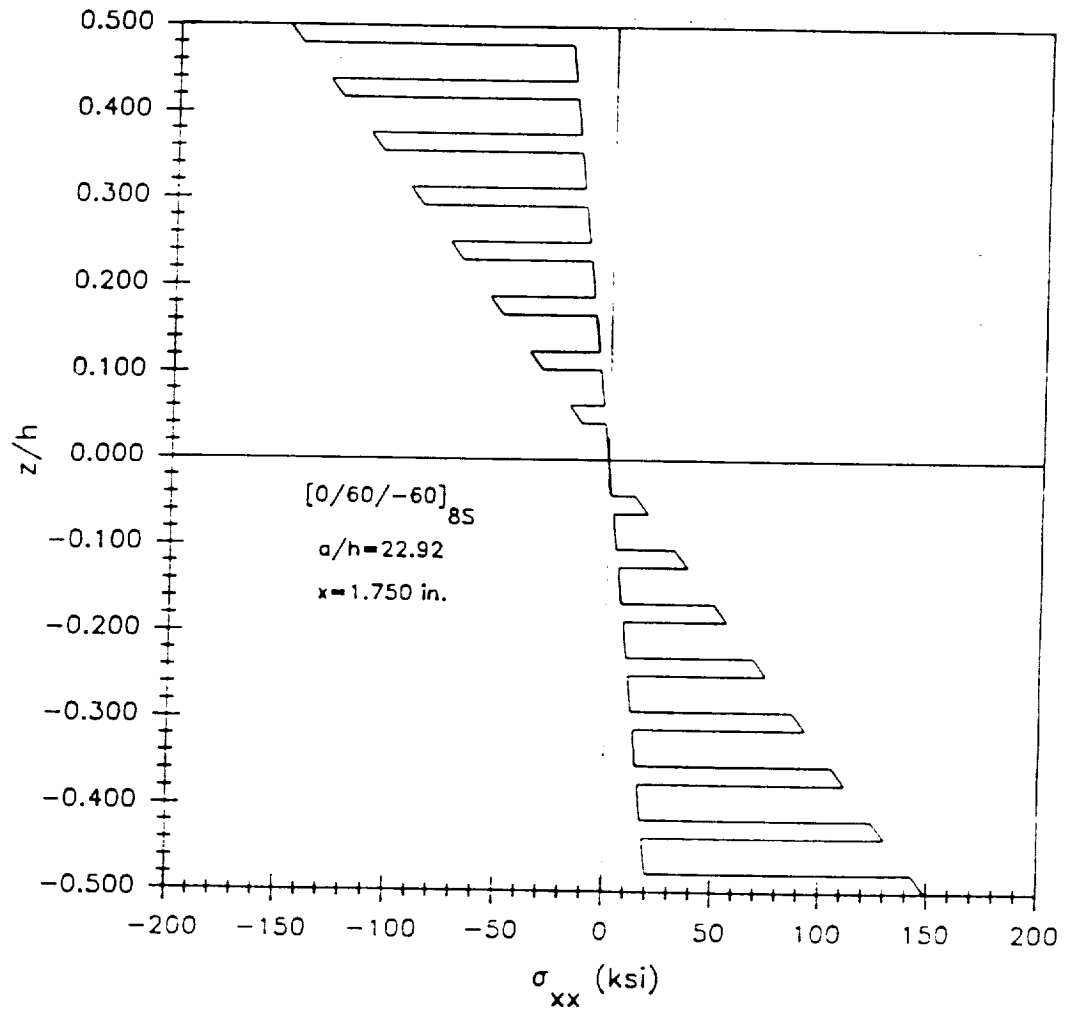
$[0/60/-60]_{8S}$

a/h=4.17

x=2.750 in.

Figure 200. Through-the-thickness distribution for τ_{xz} in the $[0/60/-60]_{8S}$ laminate with an aspect ratio of 4.17.

Figure 201. Through-the-thickness distribution for σ_{xx} in the $[0/60/-60]_{8S}$ laminate with an aspect ratio of 2.08.

Figure 202. Through-the-thickness distribution for τ_{xz} in the $[0/60/-60]_{8S}$ laminate with an aspect ratio of 2.08.
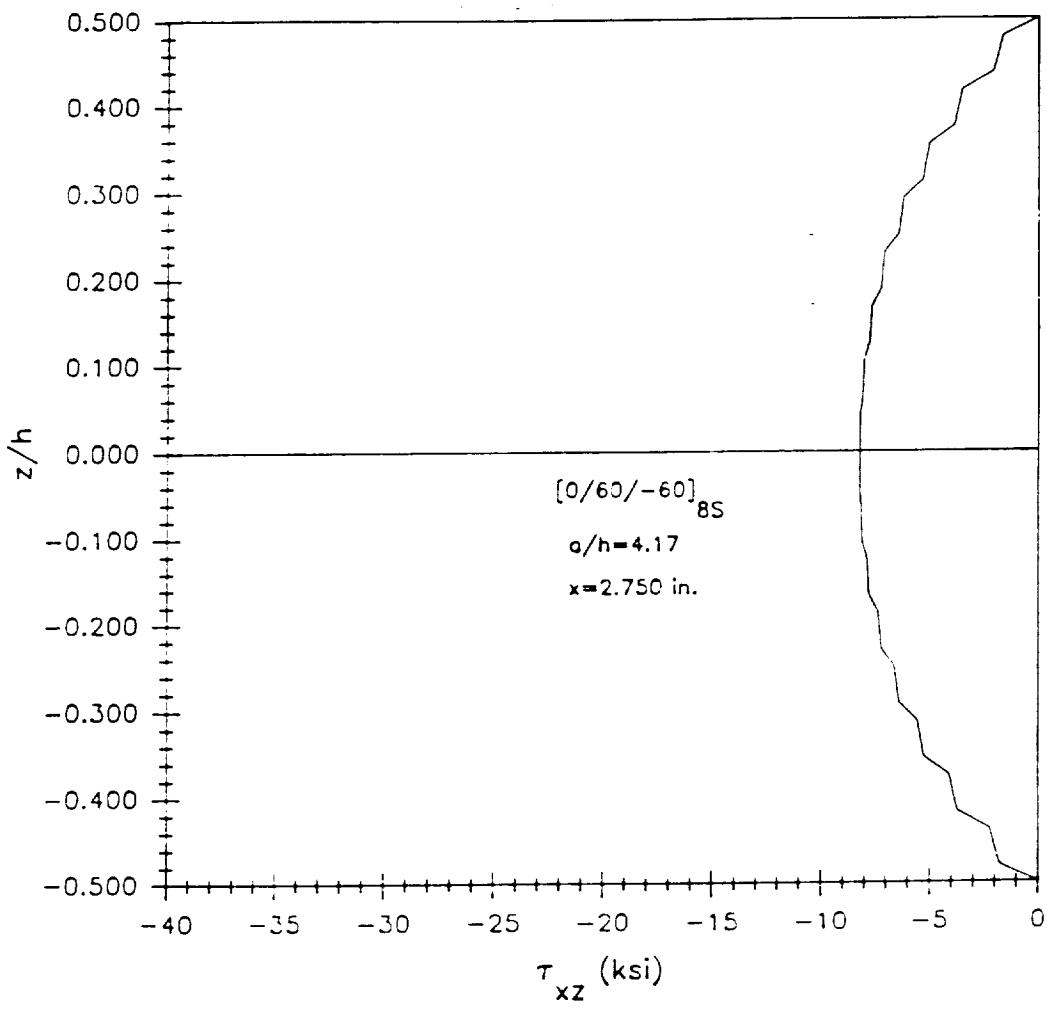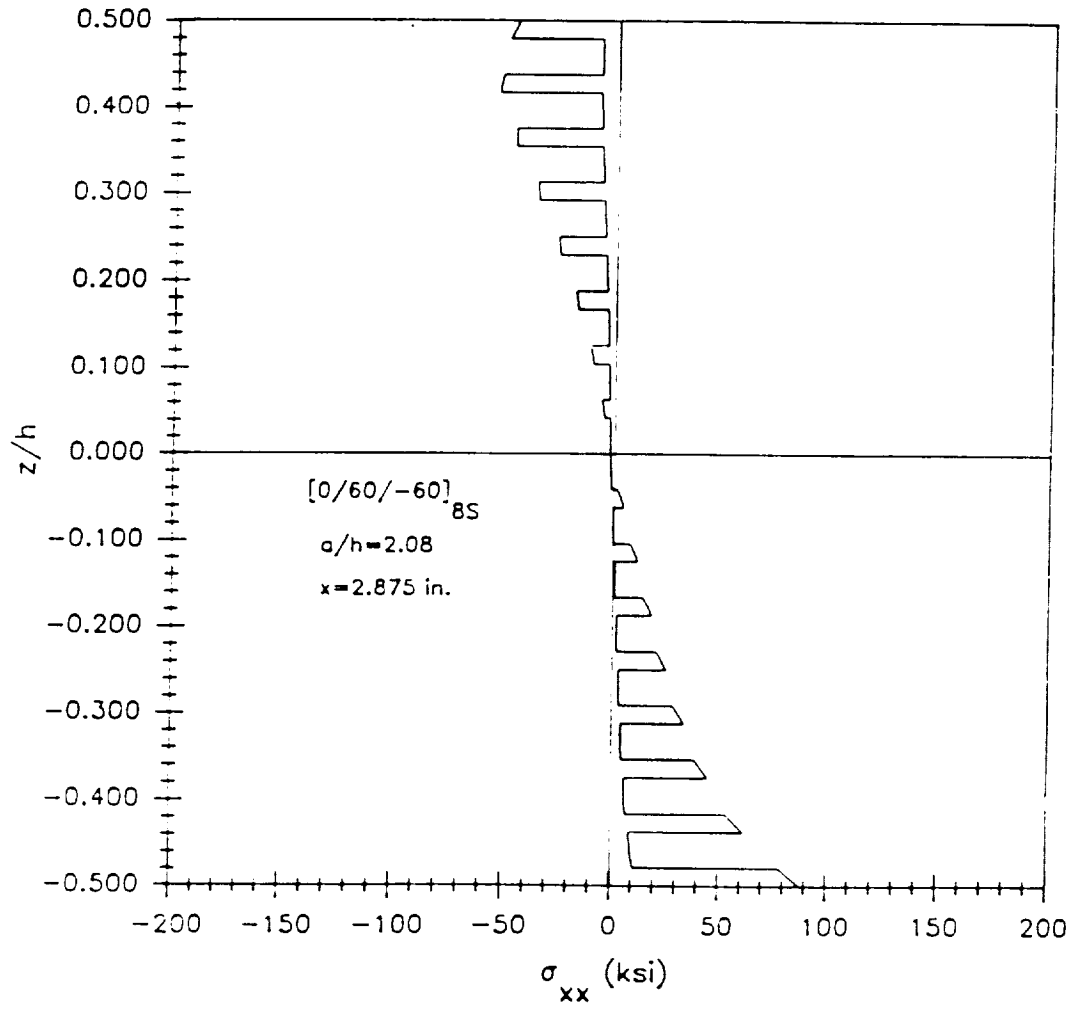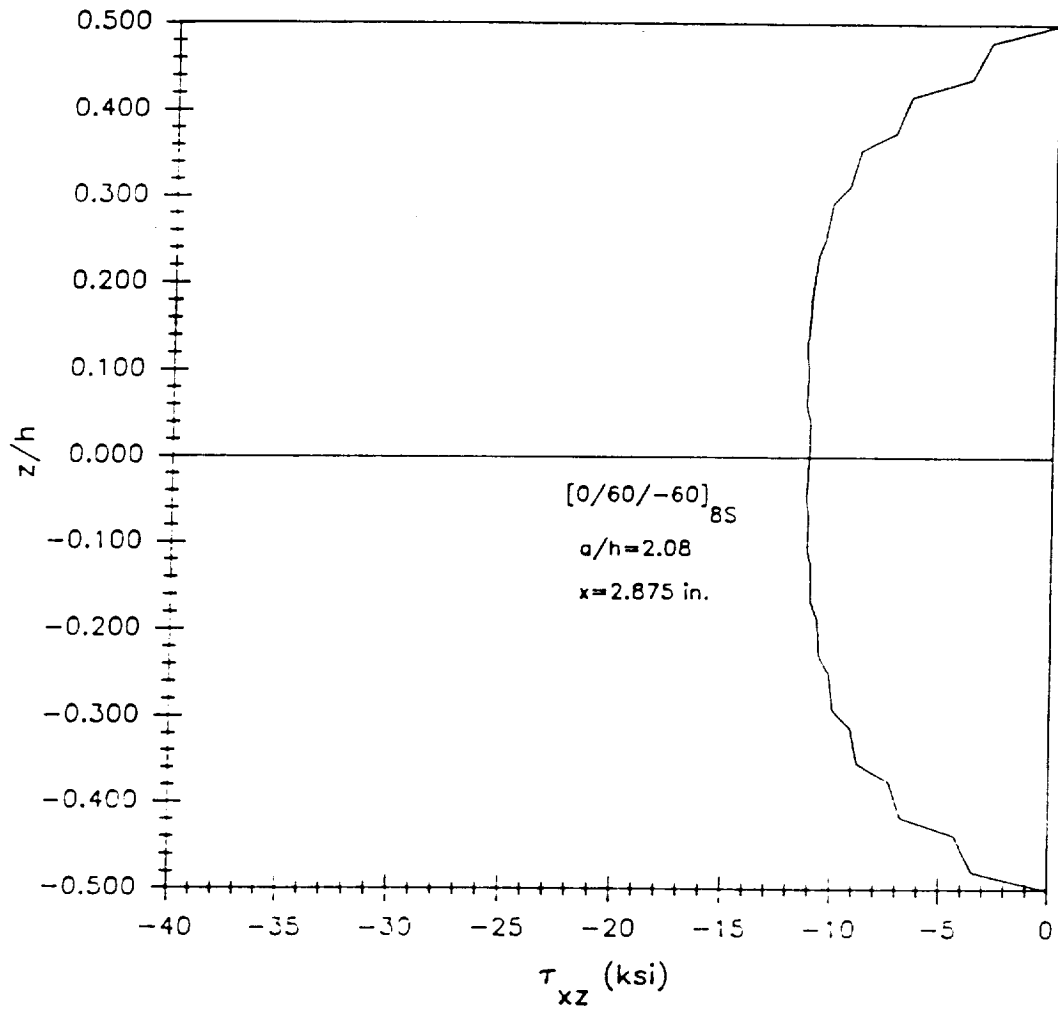
BIBLIOGRAPHIC DATA SHEET	1. Report No. VPI-E-90-11 CCMS-90-06	2. Interim Report 79	3. Recipient's Accession N
4. Title and Subtitle Damage States in Laminated Composites Three-Point Bend Specimens - An Experimental-Analytical Correlation Study			5. Report Date July 1990
			6.
7. Author(s) J.M. Starbuck, Z. Gürdal, M.J. Pindera and C.C. Poe			8. Performing Organization No. VPI-E-90-11
9. Performing Organization Name and Address Department of Engineering Science and Mechanics Virginia Polytechnic Institute and State University Blacksburg, VA 24061-0219			10. Project/Task/Work Unit
			11. Contract/Grant No. NAG-1-343
12. Sponsoring Organization Name and Address Mechanics of Materials Branch NASA Langley Research Center Hampton, VA 23665-5225			13. Type of Report & Period Covered Interim Report 8/87-12/89
			14.

15. Supplementary Notes

16. Abstracts

Damage states in laminated composites were studied by considering the model problem of a laminated b subjected to three-point bending. A combination of experimental and theoretical research techniques was to correlate the experimental results with the analytical stress distributions. The analytical solution procedure based on the stress formulation approach of the mathematical theory of elasticity. The solution procedure is pable of calculating the ply-level stresses and beam displacements for any laminated beam of finite length the generalized plane deformation or plane stress state assumption. The beam lamination can be any arbi combination of monoclinic, orthotropic, transversely-isotropic, and isotropic layers. Prior to conducting the perimental phase of the study the results from preliminary analyses were examined. Significant effects in ply-level stress distributions were seen depending on the fiber orientation, aspect ratio, and whether or r grouped or interspersed stacking sequence was used.

The experimental investigation was conducted to determine the different damage modes in laminated tl point bend specimens. The test matrix consisted of three-point bend specimens of 0° unidirectional, cross-ply quasi-isotropic stacking sequences. The dependence of the damage initiation loads and ultimate failure l were studied, and their relation to damage susceptibility and damage tolerance of the beam configuration discussed. Damage modes were identified by visual inspection of the damaged specimens using an optica croscope. The four fundamental damage mechanisms identified were delaminations, matrix cracking, breakage, and crushing. The correlation study between the experimental results and the analytical results performed for the midspan deflection, indentation, damage modes, and damage susceptibility. The correlation primarily based on the distribution of the in-plane component of shear stress, τ_{xz}. The exceptions were for the of a very small aspect ratio (less than 1.0) where the crushing model of damage was predicted based o maximum contact pressure, and for very large aspect ratios (greater than 12.0) where a maximum tensile bei stress criterion was used for predicting the damage initiation loads.

17. Key Words and Document Analysis.   17a. Descriptors

anisotropic elasticity, stress functions, failure of composites, thick composites, interlaminar shear stress

17b. Identifiers/Open-Ended Terms

17c. COSATI Field/Group

18. Availability Statement	19. Security Class (This Report) UNCLASSIFIED	21. No. of Pa 356
	20. Security Class (This Page UNCLASSIFIED	22. Price

VIRGINIA TECH CENTER FOR
COMPOSITE MATERIALS AND STRUCTURES

The Center for Composite Materials and Structures s a coordinating organization for research and educational activity at Virginia Tech. The Center was 'ormed in 1982 to encourage and promote continued advances in composite materials and composite structures. Those advances will be made from the base of individual accomplishments of the forty members who represent ten different departments in two colleges.

The Center functions through an Administrative Board which is elected yearly and a Director who is elected for a three-year term. The general purposes of the Center include:

- collection and dissemination of information about composites activities at Virginia Tech,
- contact point for other organizations and individuals,
- mechanism for collective educational and research pursuits,
- forum and agency for internal interactions at Virginia Tech.

The Center for Composite Materials and Structures is supported by a vigorous program of activity at Virginia Tech that has developed since 1963. Research expenditures for investigation of composite materials and structures total well over seven million dollars with yearly expenditures presently approximating two million dollars.

Research is conducted in a wide variety of areas including design and analysis of composite materials and composite structures, chemistry of materials and surfaces, characterization of material properties, development of new material systems, and relations between damage and response of composites. Extensive laboratories are available for mechanical testing, nondestructive testing and evaluation, stress analysis, polymer synthesis and characterization, material surface characterization, component fabrication, and other specialties.

Educational activities include eight formal courses offered at the undergraduate and graduate levels dealing with the physics, chemistry, mechanics, and design of composite materials and structures. As of 1984, some 43 Doctoral and 53 Master's students have completed graduate programs and several hundred Bachelor-level students have been trained in various aspects of composite materials and structures. A significant number of graduates are now active in industry and government.

Various Center faculty are internationally recognized for their leadership in composite materials and composite structures through books, lectures, workshops, professional society activities, and research papers.

MEMBERS OF THE CENTER

Aerospace and Ocean Engineering
Raphael T. Haftka
Eric R. Johnson
Rakesh K. Kapania

Chemical Engineering
Donald G. Baird

Chemistry
John G. Dillard
James E. McGrath
Larry Taylor
Thomas C. Ward
James P. Wightman

Civil Engineering
Richard M. Barker

Electrical Engineering
Ioannis M. Besieris
Richard O. Claus

Engineering Science and Mechanics
Robert Czarnek
David Dillard
Norman E. Dowling
John C. Duke, Jr.
Daniel Frederick
O. Hayden Griffin, Jr.
Zafer Gurdal
Robert A. Heller
Edmund G. Henneke, II
Michael W. Hyer
Robert M. Jones
Liviu Librescu
Alfred C. Loos
Don H. Morris
John Morton
Ali H. Nayfeh
Daniel Post

J. N. Reddy
Kenneth L. Reifsnider
C. W. Smith
Wayne W. Stinchcomb
Surot Thangjitham

Industrial Engineering and Operations Research
Joel A. Nachlas

Materials Engineering
S. B. Desu
D. P. H. Hasselman
Robert E. Swanson

Mathematics
Werner E. Kohler

Mechanical Engineering
Charles E. Knight
John B. Kosmatka
J. Robert Mahan
Craig A. Rogers
Curtis H. Stern

Inquiries should be directed to:

Center for Composite Materials and Structures
College of Engineering
Virginia Tech
Blacksburg, VA 24061-0230
Phone: (703) 231-4969